Measuring and Analysing the directional spectrum of ocean waves

Stephen F. Barstow, Jean-Raymond Bidlot, Sofia Caires, Mark A. Donelan, William M. Drennan, Hélène Dupuis, Hans C. Graber, J. Jim Green, Oistein Gronlie, Christine Guérin, et al.

COST — the acronym for European cooperation in the field of scientific and technical research — is the oldest and widest European intergovernmental network for cooperation in research. Established by the Ministerial Conference in November 1971, COST is currently used by the scientific communities of 35 European countries to cooperate in common research projects supported by national funds. The funds provided by COST — less than 1 % of the total value of the projects — support the COST cooperation networks (COST actions) through which, with only around EUR 20 million per year, more than 30 000 European scientists are involved in research having a total value which exceeds EUR 2 billion per year. This is the financial worth of the European added value which COST achieves. A 'bottom up' approach (the initiative of launching a COST action comes from the European scientists themselves), 'à la carte participation' (only countries interested in the action participate), 'equality of access' (participation is open also to the scientific communities of countries not belonging to the European Union) and 'flexible structure' (easy implementation and light management of the research initiatives) are the main characteristics of COST. As precursor of advanced multidisciplinary research, COST has a very important role for the realisation of the European research area (ERA), anticipating and complementing the activities of the framework programmes, constituting a 'bridge' towards the scientific communities of emerging countries, increasing the mobility of researchers across Europe and fostering the establishment of 'networks of excellence' in many key scientific domains, such as physics, chemistry, telecommunications and information science, nanotechnologies, meteorology, environment, medicine and health, forests, agriculture and social sciences. It covers basic and more applied research and also addresses issues of pre-normative nature or of societal importance.

COST is supported by the EU framework programme

Publications Office
Publications.eu.int

ISBN 92-898-0003-8

14

15

QS-NA-21367-EN-C

EC

COST Action 714

Measuring and analysing the directional spectra of ocean waves

EUR 21367

European cooperation in the field of scientific and technical research

Meteorology

Measuring and analysing the directional spectra of ocean waves

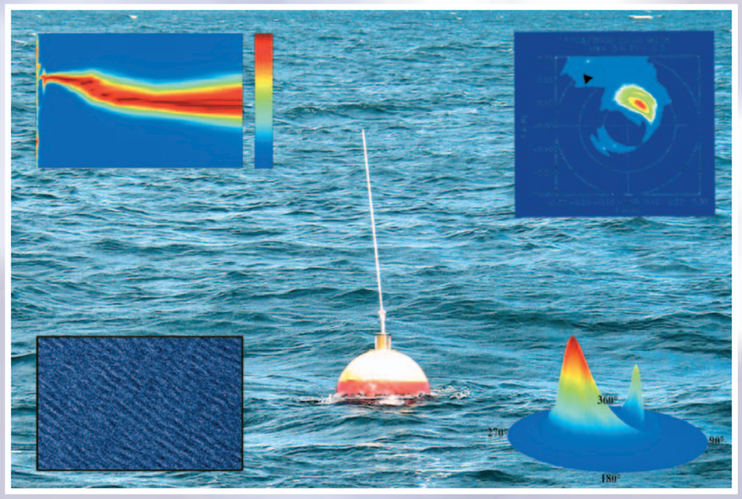

COST Action 714

EUR 21367

SALES AND SUBSCRIPTIONS

Publications for sale produced by the Office for Official Publications of the European Communities are available from our sales agents throughout the world.

How do I set about obtaining a publication?

Once you have obtained the list of sales agents, contact the sales agent of your choice and place your order.

How do I obtain the list of sales agents?

- Go to the Publications Office website http://publications.eu.int/
- Or apply for a paper copy by fax (352) 2929 42758

Contact: Mr Pavol Nejedlik (Science Officer)

COST Office, 149 Avenue Louise, B-1050 Brussels
Tel. (32-2) 53-33830; fax (32-2) 53-33890
E-mail: pnejedlik@cost.esf.org
Website: http://cost.cordis.lu

COST
European cooperation in the field of scientific and technical research

COST Action 714

Measuring and analysing the directional spectra of ocean waves

Working Group 3

Editors

Danièle Hauser, Kimmo Kahma, Harald E. Krogstad,
Susanne Lehner, Jaak A. J. Monbaliu,
Lucy R. Wyatt

(From the European COST Action 714)

2005 EUR 21367 EN

Cataloguing data can be found at the end of this publication.

Luxembourg: Office for Official Publications of the European Communities, 2005

ISBN 92-898-0003-8

Printed in Luxembourg

PRINTED ON WHITE CHLORINE-FREE PAPER

MEASURING AND ANALYSING THE DIRECTIONAL SPECTRUM OF OCEAN WAVES

Editors

Danièle Hauser, Kimmo K. Kahma, Harald E. Krogstad, Susanne Lehner, Jaak Monbaliu and Lucy R. Wyatt

Contributors

Stephen F. Barstow
Jean-Raymond Bidlot
Sofia Caires
Mark A. Donelan
William M. Drennan
Hélène Dupuis
Hans C. Graber
J. Jim Green
Øistein Grønlie
Christine Guérin
Klaus-Werner Gurgel
Heinz Günther
Danièle Hauser
Kenneth Hayes
Katrin Hessner
Danielle Hoja
Delphine Icard
Kimmo K. Kahma
William C. Keller
Harald E. Krogstad
Jean-Michel Lefèvre
Susanne Lehner
Anne Karin Magnusson
Jaak Monbaliu
José Carlos Nieto Borge
Heidi Pettersson
William J. Plant
Céline Quentin
Konstanze Reichert
Magnar Reistad
Wolfgang Rosenthal
Øyvind Saetra
Johannes Schulz-Stellenfleth
Edward J. Walsh
Alain Weill
Judith Wolf
C. Wayne Wright
Lucy R. Wyatt

The affiliations and addresses are given on page 456.

Contents

Preface

The importance of directional wave information has been recognised for a long time. However, for decades good measurements of directional spectra were limited almost exclusively to special research campaigns. Collecting directional wave climates from various sites and putting directional wave data to operational use were not a common practice.

The situation has now improved. Many new instruments and analysis techniques have been developed for both in situ implementation and for remote sensing. It has become possible to extend the use of directional information over a much wider range, including many practical applications.

This has opened up new possibilities. But it has also highlighted the difficulties associated with the directional spectrum. None of the present instruments can provide all the data that is required to calculate the directional spectrum in a robust way. Clever analysis techniques have been introduced that use physical and mathematical constraints to extract the directional spectrum from the limited data available. Each instrument and each analysis method has its own advantages and shortcomings, and the results are not necessarily comparable. If one wants to make use of the directional information, one needs an understanding of the properties of the instruments and the methods as well as the differences between them.

COST action 714, supported by the European Commission, had the objective to promote the development of measurement techniques and the use of directional wave measurements. The action was launched in 1996, and, in the end, representatives of ten European countries (Belgium, Finland, France, Italy, Germany, The Netherlands, Norway, Portugal, Spain, United Kingdom) participated in it. Within the action a working group was created with the title *Intercomparisons of Spectral Properties of Surface Waves* for the purpose of improving the understanding of measurement techniques, methods of analysis, and comparisons between different instruments.

The working group decided to publish its work in the form of a book describing the theory of directional wave spectra and the various instruments and analysis methods used to measure them, as well as comparisons between different instruments. The aim of the book is to give a comprehensive and up-to-date review of the instruments and methods of analysis available today for measuring the directional spectrum of ocean waves. In addition to the texts by members of the working group, the book contains contributions

by other ocean wave experts.

The book was edited by K.K. Kahma, D. Hauser, H. E. Krogstad, S. Lehner, J. Monbaliu, and L. Wyatt. It consists of two parts. Part I covers the theory of directional spectra of ocean waves, the methods and instruments to measure it, techniques for the statistical intercomparison of directional wave data, and spectral wave modelling. The technical editor for Part I was H. E. Krogstad, who has also written much of it. Part II, with J. Monbaliu as the technical editor, covers intercomparison studies between the various types of wave measurement techniques. The editors gratefully acknowledge all the authors who agreed to contribute to this book.

The whole book was externally reviewed by Gerbrant van Vledder and Heinz Günther who contributed insightful comments. In addition, Evert Bouws, and Heidi Pettersson gave particularly valuable and detailed reviews.

The editors gratefully acknowledge the support of the succesive Scientific Secretaries of the COST Action on Meteorology: Jean Labrousse, Andrei Hocevar, Zoltan Dunkel and Pavol Nejedlik as well as of the members of the COST Technical Committee on Meteorology, Charles Dupuy and Sylvain Joffre. Thanks are also due to the Evaluation Committee of COST 714, Jeanette Onvlee, Gerbrant van Vledder and Olavo Rasquinho, for helpful advice.

The editors thank all the hosts of the working group meetings and the editors meetings.

Harald E. Krogstad and Susanne Lehner thank Professors Mark A. Donelan and Hans Graber at the Rosenstiel School of Marine and Atmospheric Science, University of Miami, USA for hospitality during their sabbatical stay there in the spring of 2002.

The people who helped in the collection of the data used in this book are too numerous to mention individually; each contribution is greatly appreciated.

The group's hope is that this book will help all those who need directional wave data for various applications by showing them what kinds of measurements are available today, and how one may draw useful and robust conclusions from them.

Helsinki 18.10.2003

Kimmo K. Kahma

The following persons participated in at least one of the meetings of the working group:

Evert Bouws (KNMI,The Netherlands), Sofia Caires (Univ. of Sheffield, UK), Patricia Cavaco (Portugal), Mark Donelan (RSMAS, USA), William Drennan (RSMAS, USA), Hans Graber (RSMAS, USA), Carlos Guedes Soares (Instituto Superior Técnico, Portugal), Danièle Hauser (CETP, France), Kimmo K. Kahma (FIMR, Finland, chairman), Harald E. Krogstad (NTNU, Norway), Jean-Michel Lefèvre (Météo-France, France), Susanne Lehner (DLR, Germany), Ann-Karin Magnusson (DMNI, Norway), Vladimir Makin (KNMI, The Netherlands), Jaak Monbaliu (KUL, Belgium), Heidi Pettersson (FIMR, Finland), Céline Quentin (CETP, France), Wolfgang Rosenthal (GKSS, Germany), José-Carlos Santas Lopez (Cedex, Spain), Johannes Schulz-Stellenfleth (DLR, Germany), Aart Voorrips (KNMI, The Netherlands), Alain Weill (CETP, France), Lucy Wyatt (University of Sheffield, UK).

Part I

MEASURING AND ANALYSING THE DIRECTIONAL SPECTRUM OF OCEAN WAVES

Theory, Instruments and Methods of Analysis

Technical Editor Harald E.Krogstad

Chapter 1

Introduction

1.1 Motivation

Kimmo K. Kahma

There is a wide range of applications where knowledge of waves and the wave climate are needed. These range from engineering applications such as the design and operational safety of harbours, ships, and offshore structures to coastal management including, e.g. coastal stability and pollution.

The directional wave spectrum describes the complex and chaotic phenomenon of wind-generated ocean waves in terms of contributions from waves propagating in different directions with different wavelengths. At the present time, it is the fundamental quantity of wave modelling and the quantity that allows us to calculate the consequences of interactions between waves and other matter. The forces on piles, breakwaters and offshore structures, the response of ships, platforms and floating breakwaters to waves, wave-induced erosion: all of these depend on properties of the directional spectrum. Wave model verification and data assimilation into a wave model are best done using the information contained in the directional wave spectrum. The role of waves in air-sea interaction cannot be properly treated without knowledge of the directional properties of waves.

While the concept of the directional spectrum is about 50 years old, for decades good measurements of directional spectra were a major achievement. Some of the pioneering contributions to the concept of the directional spectrum and its measurement and application, are the books Ocean Wave Spectra (Anon., 1963), Kinsman (1965), Pierson (1976), and Phillips (1977), and conference proceedings, e.g. Wiegel (1982), Biel (1991), and, in particular, the series of WAVES conferences (Anon., 1974; Magoon and Hemsley,

1993; Edge, 1997, 2001).

During the last two decades significant advances have been made in measuring the directional wave spectrum, and a large number of measuring devices working on different principles are now available. The classical methods such as spatial arrays and pitch-and-roll buoys have been complemented by new technologies such as the displacement and GPS buoys, acoustic Doppler current meters, microwave and marine radars, coastal HF radars, and real and synthetic aperture radars. Global coverage of directional wave information is now available using the synthetic aperture radar from satellites. Some of these instruments can be considered as well established, whereas others are still under development.

Directional wave measurements can now be made at a reasonable cost. The directional wave climate is being measured at several sites, and it has become feasible to make directional wave measurements for operational use. This means that it is now possible to extend the use of directional information into a much wider range of applications than before.

At the same time, the inherent difficulties associated with measuring and analysing directional spectra have not disappeared. None of the instruments used today can provide all the data needed to make a robust estimate of the complete directional spectrum. Assumptions must be made about the properties of the directional spectrum in order to extract the spectrum from the measured data, and these assumptions, different ones for different instruments, together with noise and imperfect responses of the instruments, have a significant effect on the result. What is needed is an understanding of the strengths and weaknesses of each instrument and method of analysis, so that it is possible to judge which parameters can be robustly determined, and which properties of the directional spectrum are merely indicative.

The standard measuring techniques provide partial information on the directional spectrum, but do not provide a robust estimate of the full directional spectrum. The average wave direction is usually well defined, has a clear interpretation, and various instruments agree reasonably well. The variability in wave direction, often referred to as the spreading, and the various analytical descriptions of the spectra are more ambiguous, and conclusions from them should be drawn with caution. Engineering design should not rely on one particular description of the directional shape of the spectrum. For any directional property other than the mean direction a combination of different methods of measurement and analysis is needed.

The purpose of the present book is to give a comprehensive and up-to-

date review of the instruments and methods of analysis available today for measuring the directional spectrum of ocean waves. At the same time, the material clearly reflects the interests and expertise of the authors, and the list of references is by no means complete. Ocean surface wave research is in a very active stage and directional measurement campaigns are going on at the time of writing. The theory and measurement of non-linear waves is becoming the hot topic. These ongoing developments are not represented here, and they will take some time to have any influence on operational wave measurement instruments and methods.

The theoretical background and the operating principles of various instruments are described in Part I. In this chapter we begin with a descriptive introduction to the directional spectrum and its interpretation. An introduction to the classical mathematical model of the sea surface is then presented in Chapter 2, followed by a more detailed and rigorous mathematical treatment of the subject. An alternative to the classical theory, the wave packet model of the sea surface, is also discussed in Chapter 2.

There are two fundamentally different approaches to the measurement of waves: local *in situ* measurements and remote sensing. Methods of the first type are described in Chapter 3, and the related instruments in Chapter 4. Radar measurements are discussed in Chapter 5. In Chapter 6, the principles of wave modelling are briefly reviewed, as they form a part of certain inversion methods for the synthetic aperture radar (SAR), as well as being an important way to complement directional measurements. Finally, the complicated problem of comparing directional spectra is discussed in Chapter 7.

In Part II the actual performance of different instruments and comparisons between them are discussed.

1.2 Wind-generated Waves and the Directional Spectrum

Kimmo K. Kahma

The sea surface in the presence of wind-generated waves can be visualised as an irregular collection of crests and troughs (Fig. 1.1). Often one can see neither a well-defined wavelength or wave direction, nor a fixed wave height. The crests are short, and aligned in different directions. The waves move, but not all in the same direction, and the waves themselves do not retain

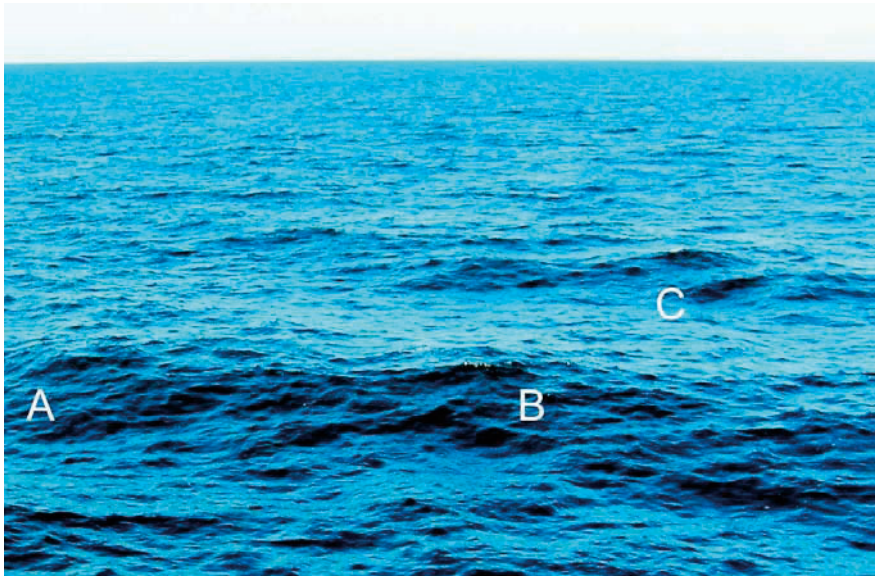

Figure 1.1: The sea surface of wind-generated waves is an irregular collection of short-crested waves. The crests at points A and B are nearly orthogonal. At point C there are two crests that propagate at different angles.

their shape: the position and height of an individual crest is not predictable for more than a few wavelengths. The directional spectrum is a way to describe this irregular and unpredictable surface.

As a starting point we first look at a simple harmonic cosine wave on a two-dimensional surface:

$$\eta(\mathbf{x}, t) = a \cos\left(\mathbf{k} \cdot \mathbf{x} - \omega t + \varphi\right), \tag{1.1}$$

where a is the amplitude, $k = 2\pi/\lambda$ the wavenumber, λ the wavelength, $\omega = 2\pi/T$ the (angular) frequency, T the wave period and φ is the phase of the wave, see Fig. 1.2(a).

The wavelength, amplitude, period, phase, and direction define the plane cosine wave. Another way of plotting this information is shown in Fig. 1.2(b). The distance from the centre gives the (angular) frequency. Long waves and long periods are near the centre, short periods are at the perimeter. The direction from the centre shows the direction towards which the waves are going. If this were a three-dimensional plot, using the square of the amplitude of the wave for the third dimension, it would be similar to a plot of the

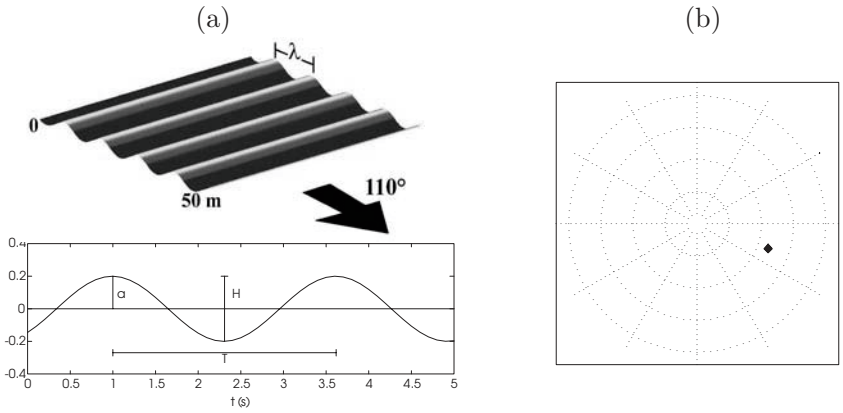

Figure 1.2: (a) Top: Plane cosine wave propagating to direction 110° from north. Bottom: Surface displacement of the wave at a fixed point: wave period (T), wave amplitude (a), and wave height (H). (b) Directional spectrum of the single cosine wave. The grid circles have 1 rad/s steps, radials 30° steps; north is up, east right. The distance from the centre gives the (angular) frequency $\omega = 2\pi/T$, here 2.4 rad/s. Long waves and long periods are near the centre, short periods at the perimeter.

directional spectrum.

Cosine waves are possible solutions of the linearised equations modelling the motion of the water and the boundary conditions (i.e physical properties of the air/water interface) at the surface. A sum of cosine waves

$$\eta(\mathbf{x}, t) = \sum_{n=1}^{N} a_n \cos\left(\mathbf{k}_n \cdot \mathbf{x}_n - \omega_n t + \varphi_n\right) \tag{1.2}$$

is also a solution of the linearised equations, and it can be used as a model of the sea surface. The classical drawing by Pierson *et al.* (1955) shows how many waves of different wave lengths and directions add up to a sum that resembles the ocean surface (Fig.1.3).

Tides in the ocean can be successfully described by just a sum of cosine waves. Wind-generated waves are more complicated. They are not predictable in the way tides are. Whereas for tides the heights of 'spikes' in the directional spectrum, one for each cosine wave, could be represented by the wave amplitude as in (Fig. 1.2b), this is not a practical definition for wind waves. One cannot predict the positions of the crests, or the heights of individual waves. The form of the surface itself is unpredictable: only

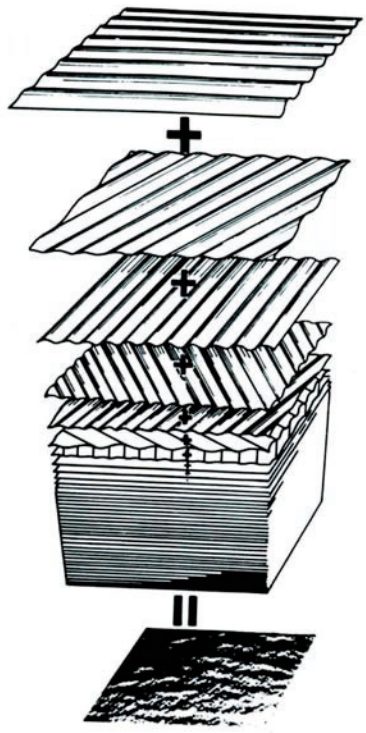

Figure 1.3: A sum of cosine waves makes the sea. Copy of the classic drawing from Pierson *et al.* 1955.

statistical properties such as mean water level, and variance of surface displacement (or mean wave energy per square metre) can be predicted. In other words, even if one could make a perfectly controlled experiment in which all the boundary conditions are kept the same, still the individual wave heights would not be the same from one experiment to another.

To describe, in a statistical sense, the wind-generated waves by a spectrum this random element has to be taken into account. This can be done by using infinitely many cosine waves, letting them have random phases independent of each other, and defining the continuous spectrum in a such way that it will provide the distribution of the variance density of the surface displacement. Below we present a descriptive overview of the subject; the mathematical definitions will be given in Chapter 2.

If we ignore the directional properties of the wave field the non-directional wave spectrum will give the distribution of the variance density as a function of frequency, ω (Fig. 1.4). The variance that is associated with the wave components on a given frequency interval can be found by integrating the spectrum over that interval. It is not possible to attribute this variance to any particular cosine wave, but if the frequency interval is relatively small one can get an idea of the wave amplitude associated with that frequency band by noting that the variance of a cosine wave is $\frac{a^2}{2}$. For the overall wave height of the wave field this approximation based on a single cosine wave will be misleading, and the sea state parameter used to describe the visually estimated average of wave heights is called *significant wave height*, H_s, and defined as $H_s = 4\sqrt{m_0}$, where m_0 is the variance of the surface displacement. Another important sea state parameter is the *peak wave period* $T_p = 2\pi/\omega_p$ that corresponds to the period of the maximum energy of the spectrum.

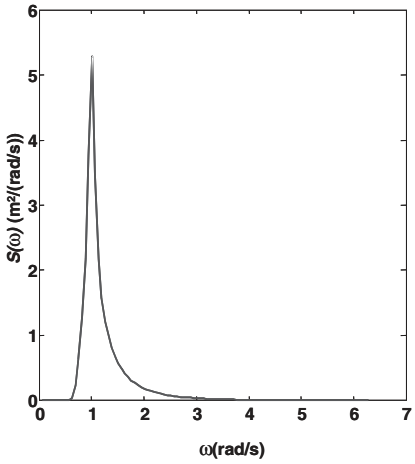

Figure 1.4: Typical shape of the frequency spectrum of ocean waves.

In the case of the directional spectrum the variance density is a function of both frequency and direction. Figure 1.1 shows how the two crests at point "C" differ in direction, and they both have a large angle with respect to the crests at points "A" and B". A wide range of directions is needed to model the real sea surface by a sum of cosine waves, and the directional spectrum will thus have the general shape shown in Fig. 1.5. The commonly used directional sea state parameters are the mean wave direction at the peak of the spectrum θ_{1p}, and directional spreading at the peak σ_{1p}. The

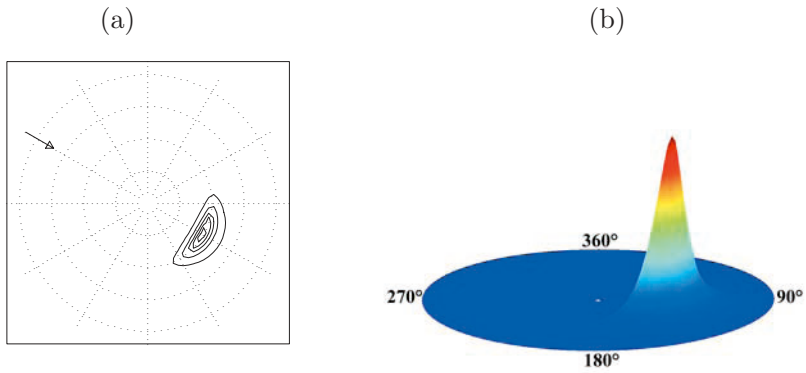

Figure 1.5: (a) Directional spectrum, linear contour plot. The frequency scale circles have 1 rad/s steps. The circles correspond to approximately 60 m, 15 m, 7 m, and 4 m wavelengths. Wind direction is denoted by the arrow. (b) Linear perspective view from south.

latter corresponds to the standard deviation of the directional distribution. Compared with the other parameters the directional spreading is a much less stable parameter, and it depends both on the instrument and on the analysis method. Both mean direction and spreading can also be defined as functions of frequency. In that respect they clearly differ from the integral parameters such as significant wave height and peak wave period.

There are unfortunately two conventions for the direction when waves are discussed. In the literature wind is always coming from, and current is always going to the direction named, but for waves the direction may be given either way. Fortunately, where the directional wave spectrum is concerned, the prevailing notation is to show where the waves are going to, i.e. the waves move the same way as the current. This notation for the directional wave spectrum is consistently used in this book.

In the past directional wave measurements were rare, and the wind direction was often given as an indication of the direction of growing waves. It was then natural to use the same notation when the wave direction was observed visually, and later, when measured mean direction has become available, the practice has continued. Mariners in particular traditionally speak about the direction from which waves are coming, whereas wave modellers prefer the direction waves are going to. In Part II both notations are used, depending on the context, when referring to mean (not spectral) directions.

1.3 Wind-wave Systems

Kimmo K. Kahma and Heidi Pettersson

1.3.1 The Development of Wind Wave Systems

When the wind begins to blow, at first short waves are generated. These quickly grow, and the apparent wavelength increases. A *wave system* is formed that consists of waves of various heights and directions. If the wind is steady, the spectrum will have the general shape of Fig. 1.5. Local effects, such as shoreline geometry, or very strong gradients in the wind, will affect the growth of the waves. Still, the physics of wave growth controls the shape of actively growing waves sufficiently strongly that in most cases the spectrum of a single wave system can be reasonably approximated by a spectral form that is described by a small number of parameters: significant wave height H_s, period of the dominant waves T_p, the propagation direction θ_{1p}, and directional spreading at the peak σ_{1p}. As measurement of these parameters requires fewer assumptions than the full directional spectrum, they play a central rôle in the comparisons made in this book.

When the wind decays, or the waves propagate to an area where the wind speed is much lower, the waves become swell. Very short waves are dissipated, but swell waves continue to propagate until they arrive at a shore. If the wind direction changes significantly, again the existing wave system becomes swell, and a new wave system is generated on top of it. A typical ocean wave field is composed of several wave systems, and its directional spectrum has multiple peaks. A spectrum with two wave systems is shown in Fig. 1.6. The dominant waves of the actively growing wave system travel southwest, but there are many waves travelling in other directions, too, and the narrower swell system is travelling northeast.

Swell waves usually are not steep and therefore do not directly interact very much with each other or with the growing wind sea. When this is true, the wave growth is similar even in the presence of various types of swell.

When the waves turn into swell, the properties of the individual wave components are to some extent retained. But there are changes to the overall spectrum as shorter waves fall behind the faster, longer waves, and waves travelling in different directions become spatially separated. As swell propagates the swell spectrum becomes increasingly more concentrated both in direction and in frequency. Thus, the swell wave system can with some ac-

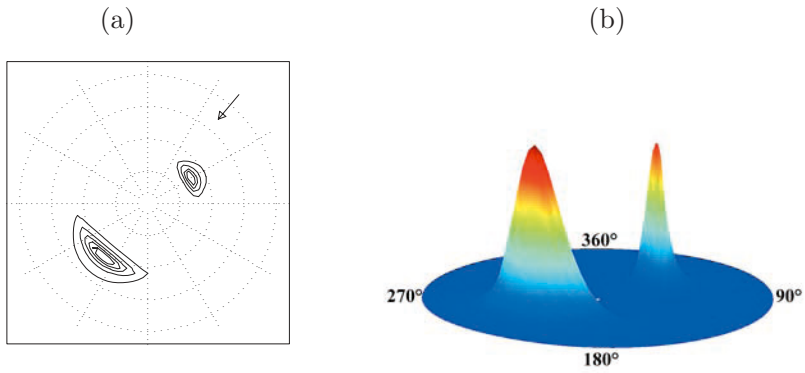

Figure 1.6: Directional spectrum showing two wave systems. (a) Linear contour plot, frequency scale circles have 1 rad/s steps. (b) Linear perspective plot.

curacy be approximated by a small number of parameters, and the whole complicated directional spectrum can be expressed as a sum of several wave systems, each one described by the characteristic parameters $\{H_s, T_p, \theta_{1p}, \sigma_{1p}\}$. These parameters capture the properties of the directional spectrum that are less dependent of the instrument and analysis method, and, if they are sufficient from the point of view of the application, they provide a robust way to describe the sea. This technique of decomposing the wave field into separate wave systems is called *partitioning*. It is discussed in more detail in Part II, Chapter 10, where different partitioning techniques are compared.

1.3.2 Directional Spectrum of Wind Wave Systems

As already mentioned in Sec. 1.1, there are many different types of instruments to measure the directional properties of the waves. Wave buoys measure the surface displacement at one point together with the slope or the horizontal movements caused by the orbital velocities of the waves. This gives only a small fraction of the information needed, and the calculated directional spectrum is based on additional assumptions (cf. Chapter 3). Some types of radar, on the other hand, are able to provide spatial data that can be transformed into a directional spectrum using much fewer assumptions, although at the cost of other limitations (Chapter 5). At the moment no instrument exists that can measure all the data required to determine the directional spectrum without additional assumptions. These

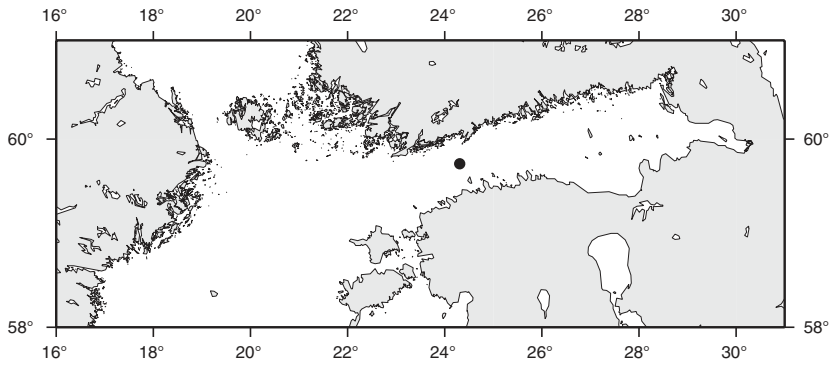

Figure 1.7: A map showing the point of the measurements in the Gulf of Finland.

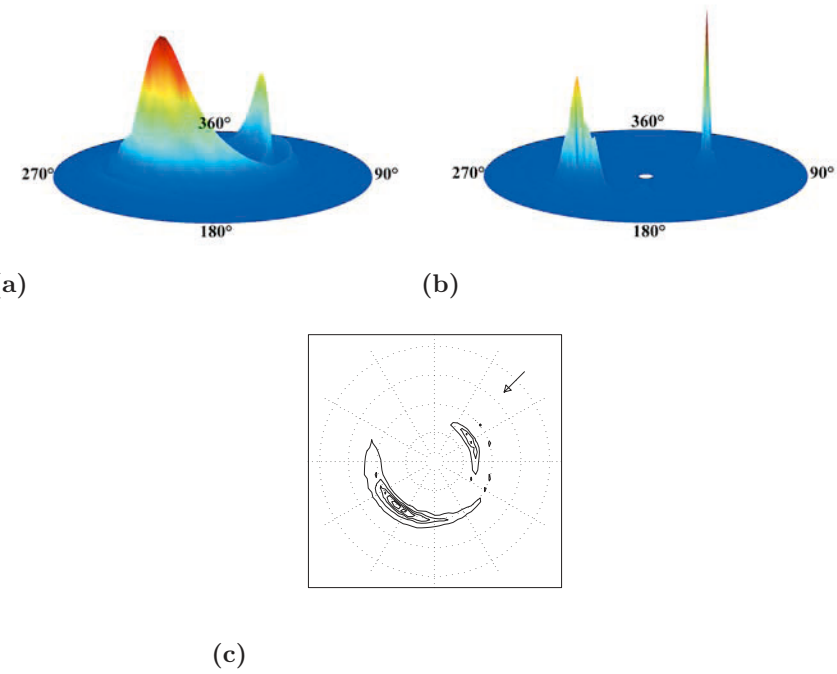

Figure 1.8: Directional spectrum of two wave systems measured by a wave buoy: (a) Maximum likelihood method (MLM). (b) Maximum entropy method (MEM). (c) Contour plot (MLM method).

assumptions can significantly influence the look of the acquired spectrum.

To illustrate this Fig. 1.8 shows the directional spectrum calculated from the three components provided by a directional wave buoy, located as shown in Fig. 1.7, using two different methods. At this location a spectrum might be expected to include waves propagating along the Baltic Sea to the north-east or south-west depending on the wind direction. The methods are called the maximum likelihood method (MLM), and the maximum entropy method (MEM). More about these methods and their underlying assumptions will be found in Chapter 2, Section 2.5.2, and in Chapter 3. Here we note only that the MLM spectrum has a directional distribution that is wider than the MEM spectrum. If it were possible to measure the directional spectrum directly without assumptions, the true spectrum would be expected to differ in its details from both of these spectra. Both show that, in this case, there are wind waves to the south-west and a swell to the north-east.

Chapter 2

The Directional Wave Spectrum

Harald E. Krogstad

The present chapter contains a review of the stochastic model of ocean waves and the corresponding wave spectra. The directional wave spectrum is first introduced as a suitable limit involving superimposed regular waves, and then as the leading order solution of the full equations and boundary conditions for the ocean surface. The main wave parameters derived from the directional spectrum are defined, and a short treatment of the transformation of the spectra for wave fields in the presence of currents has also been included.

Wave packet based models represent an interesting alternative to the Fourier based models. Wave packets are localised events, and these models form the basis for new and promising ways of analysing ocean wave measurements, see Chapter 3.

The general mathematical theory for directional distributions is outlined in Section 2.5 along with a summary of some of the model distributions.

The final section shows examples of surface simulations based on various directional spectra.

2.1 The Directional Spectrum Concept

"The basic law of the seaway is the apparent lack of any law". This citation, attributed to Lord Rayleigh by Kinsman (1965), illustrates the general state of knowledge about the wind waves on the ocean surface up to the Second World War. Although of fundamental concern to sailors all times, the mathematical theory for the confused sea was not really developed until

the mid to late fifties. The first attempts to consider a random superposition of regular waves go back to the mid forties where Barber and Ursell carried out a spectral analysis of data from a bottom mounted pressure recorder by means of a completely mechanical device (Barber and Ursell, 1948). Later, spectral analysis of records of sea elevation at a single point could be carried out with analog devices and finally digitally. The book by Kinsman (1965) gives a vivid account on how the idea of a random sea gradually emerged. The conceptual model of the surface, comprising superimposed regular waves with random amplitudes, directions and phases, was introduced in a very much cited paper by Longuet-Higgins (1957), and we shall use the Longuet-Higgins model for our introduction to concept of a directional wave spectrum.

As will be treated in more details in Sec. 2.2, and found in almost any book about ocean waves, it is possible to linearise the differential equations and nonlinear boundary conditions defining surface water waves. The linearised equations have solutions where the surface elevation, $z = \eta(\mathbf{x}, t)$, is a running cosine wave,

$$\eta(\mathbf{x}, t) = a \cos\left(\mathbf{k} \cdot \mathbf{x} - \omega t + \varphi\right), \tag{2.1}$$

where x is the horizontal location, t is time, ω is the (angular) frequency, and $\mathbf{k}$ is the wavenumber. The frequency is given from the dispersion relation, $\omega = \sigma(k)$, $\sigma(k) = \sqrt{gk \tanh(kh)}$, $k = |\mathbf{k}|$. The wave is travelling on the surface of a sea with depth h, in the direction $\mathbf{k}/k$, with wavelength $2\pi/k$, frequency ω, and amplitude a. The phase angle, φ, defines the elevation at a fixed point and time, but does not affect any of the physical properties of the wave. Since the equations are linear, sums of waves are also solutions:

$$\eta(\mathbf{x}, t) = \sum_{n=1}^{N} a_n \cos\left(\mathbf{k}_n \cdot \mathbf{x}_n - \omega_n t + \varphi_n\right), \ \omega_n = \sigma(k_n). \tag{2.2}$$

Again the dispersion relation connects $\mathbf{k}$ and ω, such that it is enough to specify the direction of $\mathbf{k}_n$, say θ_n, and ω_n.

The first step towards a random model of the surface is to assume that the phases $\{\varphi_n\}$ are independent and uniformly distributed random variables. The expectation ($\mathbb{E}$) and the variance (Var) may then be obtained as

$$\mathbb{E}\left(a\cos\left(\mathbf{k}\cdot\mathbf{x}-\omega t+\varphi\right)\right)=\frac{1}{2\pi}\int_0^{2\pi}a\cos\left(\mathbf{k}\cdot\mathbf{x}-\omega t+\varphi\right)d\varphi=0,$$

$$\begin{aligned}\mathrm{Var}\left(a\cos\left(\mathbf{k}\cdot\mathbf{x}-\omega t+\varphi\right)\right)&=\mathbb{E}\left(\left[a\cos\left(\mathbf{k}\cdot\mathbf{x}-\omega t+\varphi\right)\right]^2\right) &(2.3)\\&=\frac{1}{2\pi}\int_0^{2\pi}\left(a\cos\left(\mathbf{k}\cdot\mathbf{x}-\omega t+\varphi\right)\right)^2d\varphi\\&=\frac{a^2}{2}. &(2.4)\end{aligned}$$

Moreover, from the linearity of the expectation,

$$\mathbb{E}\left(\eta(\mathbf{x},t)\right)=0, \tag{2.5}$$

$$\mathrm{Var}\left(\eta(\mathbf{x},t)\right)=\mathbb{E}\left(\eta^2(\mathbf{x},t)\right)=\sum_{n=1}^{N}\frac{a_n^2}{2}. \tag{2.6}$$

We can introduce a primitive "spectrum" for the surface in Eqn. 2.2 as the function

$$\Psi(\mathbf{k})=\sum_{n=1}^{N}\frac{a_n^2}{2}\delta(\mathbf{k}-\mathbf{k}_n), \tag{2.7}$$

where the two-dimensional Dirac δ-function satisfies

$$\int\delta(\mathbf{k})f(\mathbf{k})d\mathbf{k}=f(\mathbf{0}). \tag{2.8}$$

Note that Ψ contains *all* non-random information about η. In particular,

$$\mathrm{Var}\left(\eta(\mathbf{x},t)\right)=\int_{\mathbf{k}}\Psi(\mathbf{k})d\mathbf{k}. \tag{2.9}$$

Instead of a finite number of waves, we can now imagine a continuous collection of waves and assume that $\Psi(\mathbf{k})$ is a ordinary function. The corresponding integral for η becomes more difficult to express, but for all practical purposes, it is sufficient to think of some kind of "generalised sum" obtained as the limit of Eqn. 2.2 when $N\to\infty$ and $a_n\to 0$.

The corresponding function Ψ is called the *wavenumber spectrum*. A word of caution should be stated here since "spectrum" is used quite ambiguously in the engineering literature. This will also be explained in more detail in Section 2.2.

The wavenumber spectrum is a function of the wavenumber, which defines the wave's propagation direction, wavelength and, by means of the dispersion

relation, frequency. A peak in the wave spectrum around $\mathbf{k} = \mathbf{k}_0$ indicates a major contribution of waves moving in the direction of $\mathbf{k}_0$. In general, if A is a certain region in the wavenumber plane, $\int_A \Psi(\mathbf{k})d\mathbf{k}$ is equal to the part of the variance that comes from wave components with $\mathbf{k} \in A$. It is, however, not possible to attribute "components" in Ψ to specific regular waves as we could for a finite number of waves. The wavenumber spectrum hence represents a *variance density*. By multiplying $\Psi(\mathbf{k})$ with the density ρ and the acceleration of gravity g, it becomes an *energy density*, since the total energy of the wave field per area unit is $\rho g \operatorname{Var}(\eta)$ (Massel, 1995).

Although wavenumber is familiar in geophysics and remote sensing, engineers tend to think in term of wave *frequency*. Because of the dispersion relation, the polar representation of the wavenumber may be substituted by frequency and direction:

$$\begin{aligned}\int_{\mathbf{k}} \Psi(\mathbf{k})d\mathbf{k} = & \\ &= \int_{k=0}^{\infty}\int_{\theta=0}^{2\pi} \Psi(k,\theta)k\,dk\,d\theta \\ &= \int_{\omega=0}^{\infty}\int_{\theta=0}^{2\pi} \Psi(k(\omega),\theta)k(\omega)\frac{dk}{d\omega}d\omega\,d\theta\end{aligned} \tag{2.10}$$

The wavenumber spectrum expressed in terms of angular frequency ω and the wave direction, θ, is called the *directional wave spectrum*,

$$\begin{aligned}E(\omega,\theta) &= \Psi(k(\omega),\theta)k(\omega)\frac{dk(\omega)}{d\omega} \\ &= \Psi(k(\omega),\theta)\frac{k(\omega)}{c_g(k)}.\end{aligned} \tag{2.11}$$

Here $c_g = \frac{\partial\omega}{\partial k}$ is the group velocity of the waves. The function E can further be split in a product

$$E(\omega,\theta) = S(\omega)D(\theta,\omega), \tag{2.12}$$

where the angular dependent part D is called the *directional distribution* and normalised such that

$$\int_0^{2\pi} D(\theta,\omega)d\theta = 1. \tag{2.13}$$

The function $S(\omega)$ is called the *frequency spectrum* or simply the wave spectrum. Since there is a direct correspondence between ω and k, it is possible to go back and forth between E and Ψ.

2.1.1 Gaussian Linear Wave Theory

The central limit theorem states that a sum of independent stochastic variables tend to be Gaussian. Then, since the surface is thought to be a sum of many random waves, it is quite reasonable to assume that it is Gaussian, and this defines what is commonly referred to as *Gaussian linear wave theory*.

In Gaussian linear wave theory, the surface is completely characterised in a statistical sense by the directional spectrum. This applies in particular to the so-called sea state parameters that are used in ocean engineering. Introducing the spectral moments

$$m_k = \int_0^\infty \omega^k S(\omega) d\omega, \tag{2.14}$$

we shall define the *significant waveheight*, H_s, as $H_s = 4\sqrt{m_0}$ and the *mean wave period*, $T_z = 2\pi\sqrt{m_0/m_2}$. It should, however, be mentioned that these definitions are not universally accepted. The significant waveheight is alternatively defined as the mean of the 1/3 largest waves, and then denoted $H_{1/3}$. Moreover, H_s is written H_{m0} to signify its relation to m_0. The mean wave period defined above is in the same way often denoted T_{m02}. In addition, traditionally T_z has been used for the mean zero-upcrossing period derived from a time record of the surface elevation. The *peak wave period* corresponds to the maximum of $S(\omega)$, $T_p = 2\pi/\omega_p$, $\omega_p = \arg\max_\omega S(\omega)$. Several other period parameters, like $T_{m01} = m_0/m_1$ and $T_{m-10} = m_0/m_{-1}$ are also in use. We refer to Tucker (1991), Massel (1995), and Goda (2000) for a more complete discussion of the wave parameters and their relations. It should also be mentioned that ocean engineering books tend to use frequency f in Hz instead of angular frequency ω in rad/s.

The most important directional sea state parameters are the *mean wave direction* and the *directional spread*. The parameters correspond to the mean and standard deviation of angular stochastic variables with probability density D. Since D depends on ω, the parameters are in general frequency dependent. The mean direction is defined as

$$\theta_1(\omega) = \arg\left(\int_0^{2\pi} \cos(\theta) D(\theta,\omega) d\theta + i \int_0^{2\pi} \sin(\theta) D(\theta,\omega) d\theta\right), \tag{2.15}$$

and the directional spread is

$$\begin{aligned}\sigma_1(\omega) &= \sqrt{2\,(1 - r_1(\omega))},\\ r_1(\omega) &= \left(\left(\int_0^{2\pi} \cos(\theta) D(\theta,\omega) d\theta \right)^2 \right.\\ &\qquad \left. + \left(\int_0^{2\pi} \sin(\theta) D(\theta,\omega) d\theta \right)^2 \right)^{1/2}. \end{aligned} \tag{2.16}$$

These expressions for the directional parameters are discussed in more detail in Sec. 2.5, in particular how they relate to the ordinary definitions of the mean and standard deviation of probability distributions. Like H_s and T_z, there are also alternative definitions found in the engineering literature.

Simple directional distributions are well characterised in terms of θ_1 and σ_1, but similarly to ordinary probability distributions, the parameters may be somewhat misleading for more complicated distributions.

If one wave system, say a local wind sea, dominates on the surface, the waves have periods around $T_p = 2\pi/\omega_p$. Similarly, the dominant wavenumber is

$$\mathbf{k}_p = k_p \left(\cos\theta_1(\omega_p) \;,\; \sin\theta_1(\omega_p) \right), \tag{2.17}$$

where k_p is obtained from the dispersion relation. Thus, the dominant wavelength is $\lambda_p = 2\pi/k_p$ and the propagation direction $\theta_1(\omega_p)$. If several wave systems co-exist, as is quite common with wind sea and swell in the open ocean, the sea state is usually well characterised in terms of $\{H_s, T_z, T_p, \theta_1(2\pi/T_p), \sigma_1(2\pi/T_p)\}$ for each system separately.

Again we refer to Tucker (1991), Massel (1995), Young (1999), and Goda (1997, 2000) for a discussion of analytic forms of S and D used in ocean and coastal engineering. The directional distribution is discussed in more details in Section 2.5.

For completeness, we mention that in addition to the sea state parameters, the whole probabilistic structure of the Gaussian linear wave theory surface may be expressed in terms of the directional spectrum E (Longuet-Higgins, 1957). This theory is however outside the scope of the present treatment.

The linear theory makes it simple to create computer simulations of surfaces corresponding to given directional wave spectra (Goda, 2000). Some examples of ocean surfaces from synthetic and measured wavenumber spectra will be shown in Section 2.6.

Gaussian linear wave theory is a surprisingly good model for ocean waves, and forms the basis for most stochastic wave analysis in ocean engineering and naval architecture (Goda, 2000). It also forms the basis for most of the material found in the present book. Nevertheless, linear wave theory assumes that the ocean waves are solutions of linear equations which they in fact are not. In the following section the wave spectrum will therefore be introduced in a more rigorous way than in the comments following Eqn. 2.9.

2.2 The General Stochastic Model

It is possible to give a rigorous derivation of the various wave spectra by assuming that the ocean surface is a *stochastic field* solution to the full nonlinear equations for surface waves. Linear wave theory is then recovered as the leading order term of the full solution.

The ocean surface varies over several scales. The shortest scales are those associated with the detailed motion of the surface, that is, the individual waves. In analogy with the stochastic theory of turbulence, these fast variations are considered random, and for scales of the order of 10 km and 0.5 hour, it is appropriate to model the surface in the open ocean as a horizontally homogeneous and stationary stochastic field. Here, and in the following, stationarity refers to *weak* stationarity. *Homogeneity* refers to spatial invariance in the statistical sense, whereas *stationarity* refers to time invariance. No significant changes in the statistical properties are supposed to occur over these spatial and temporal scales. However, in cases such as rapidly varying storm conditions, the stationarity becomes questionable. Similarly, wave conditions in strong current shear or near coastal areas, where depth variations are significant, may be very inhomogeneous (Goda, 2000). In such situations the spectral theory breaks down in principle, although in practice, analyzing the data with the stationarity and homogeneity assumption may nevertheless be reasonable, as the results will be representative for some kind of average conditions.

A zero mean stationary and homogeneous random surface has a *spectral representation* in the form of a stochastic Fourier-Stieltjes integral),

$$\eta(\mathbf{x},t) = \int_{\mathbf{k},\omega} e^{i(\mathbf{k}\cdot\mathbf{x}-\omega t)} dB(\mathbf{k},\omega), \tag{2.18}$$

where B is the *spectral amplitude*. This is the proper way of writing the sum in Eqn. 2.2 when $N \to \infty$ and $a_i \to 0$. The exponential function

$\exp\{i(\mathbf{k}\cdot\mathbf{x}-\omega t)\}$ is a complex running wave, but there is in general no dispersion relation connecting ω and $\mathbf{k}$. The spectral amplitude is not a function, but rather an orthogonal stochastic measure. This means that if C is a set in the wavenumber/frequency space, $\mathbf{R}^2\times\mathbf{R}$, $B(C)$ is a stochastic variable. Moreover,

$$\begin{aligned}\mathbb{E}[B(C)] &= 0,\\ \mathbb{E}[B(C)\overline{B(D)}] &= 0 \text{ if } C\cap D=\emptyset,\\ \mathrm{Var}(\eta) &= \mathbb{E}[B(\mathbf{R}^2\times\mathbf{R})\overline{B(\mathbf{R}^2\times\mathbf{R})}]\end{aligned} \tag{2.19}$$

(The over-bar means complex conjugate). The spectrum of η, χ, is called the *wavenumber/frequency spectrum*, and is defined by

$$\chi(C)=\mathbb{E}[B(C)\overline{B(C)}], C\in\mathbf{R}^2\times\mathbf{R}. \tag{2.20}$$

The definition is often written in the convenient short hand notation

$$d\chi(\mathbf{k},\omega)=\mathbb{E}[dB(\mathbf{k},\omega)\overline{dB(\mathbf{k},\omega)}], \tag{2.21}$$

(Phillips, 1977). A simpler and in fact equivalent definition of the three dimensional spectrum is as the Fourier transform of the covariance function, $\rho(\mathbf{x},t)$, of the surface,

$$\rho(\mathbf{x},t)=\mathbb{E}[\eta(x,t)\eta(\mathbf{0},0)]=\int_{\mathbf{k},\omega}e^{i(\mathbf{k}\cdot\mathbf{x}-\omega t)}d\chi(\mathbf{k},\omega). \tag{2.22}$$

Similarly to the surface, it is also possible to obtain stochastic field solutions for the velocity potential. The velocity potential $\Phi(\mathbf{x},z,t)$ is defined for $z\in[-h,\eta(\mathbf{x},t)]$ and if we assume inviscid, irrotational and incompressible flow and no mean current, the wave induced potential must satisfy Laplace's equation, $\nabla^2\Phi=0$ with $\partial\Phi/\partial z=0$ at $z=-h$. It is easily shown that the general solution of the Laplace equation in this case will have a spectral representation

$$\Phi(\mathbf{x},z,t)=\int_{\mathbf{k},\omega}\frac{\cosh(k(z+h))}{\cosh(kh)}e^{i(\mathbf{k}\cdot\mathbf{x}-\omega t)}dA(\mathbf{k},\omega), \tag{2.23}$$

where the spectral amplitude A is unknown. Note that the z-dependence in the integrand is known and that A is independent of z. Since η and Φ are real functions, both B and A must be conjugate symmetric, *e.g.*, $dB(\mathbf{k},\omega)=\overline{dB(-\mathbf{k},-\omega)}$. Similarly, χ and ρ are real and symmetric, and $\chi\geq 0$.

The potential and the surface elevation are connected by the *kinematic* and *dynamic boundary conditions* at the free surface ($\Phi_z = \partial\Phi/\partial z$, etc.)

$$\begin{aligned} \eta_t &= \Phi_z - (\Phi_x\eta_x + \Phi_y\eta_y) \ \text{ for } z = \eta(\mathbf{x}, t), \\ \Phi_t &+ (\Phi_x^2 + \Phi_y^2 + \Phi_z^2)/2 + g\eta = 0 \ \text{ for } z = \eta(\mathbf{x}, t), \end{aligned} \tag{2.24}$$

where g is the acceleration due to gravity (Phillips, 1977). Putting Eqns. 2.18 and 2.23 into Eqns. 2.24 and solving for the spectral amplitudes represents a formidable problem which is usually treated by perturbation analysis. By expanding η and Φ, as well as the boundary conditions in terms of a small parameter equal to the mean slope of the surface, one obtains a set of perturbation equations which may be solved recursively. The leading order solution requires

$$\begin{aligned} dA &= -\frac{i\omega}{k}\, dB, \\ \omega^2 &= gk\tanh(kh). \end{aligned} \tag{2.25}$$

By further assuming that η is Gaussian, we recover Gaussian linear wave theory. In Gaussian linear wave theory, B and χ are so-called *singular* measures supported by the double trumpet-shaped *dispersion surface* in $(\mathbf{k}, \omega)$–space,

$$\Xi = \{(\mathbf{k}, \omega); \omega = \pm\sigma(k)\}\,, \tag{2.26}$$

(in the absence of currents). This, and the symmetry of χ, may be used to eliminate ω as an independent variable and express χ only in terms of $\mathbf{k}$,

$$d\chi(\mathbf{k}, \omega) = \left[\frac{\Psi(\mathbf{k})}{2}\delta\left(\omega - \sigma(k)\right) + \frac{\Psi(-\mathbf{k})}{2}\delta\left(\omega + \sigma(k)\right)\right] d\mathbf{k}. \tag{2.27}$$

The function $\sigma(k) = +\sqrt{gk\tanh(kh)}$ is called the *intrinsic frequency,* and Ψ is the wavenumber spectrum from Sec. 2.1,

$$\Psi(\mathbf{k})d\mathbf{k} = 2\int_{d\mathbf{k},\ \omega>0} d\chi(\mathbf{k}, \omega). \tag{2.28}$$

When carrying the stochastic perturbation expansion of the wave field to higher orders, the arithmetic quickly gets very complicated. Exposition of the expansions up to the third order in amplitudes and fourth order in the spectra may be found in Mitsuyasu *et al.* (1979a) and Laing (1985). By assuming a Gaussian first order solution, third order averages vanish, and the leading nonlinear contribution, χ_2, in the spectrum is of the fourth order

in average wave slope. The spectrum χ_2 may be expressed as a generalised convolution of the Gaussian linear wave theory spectrum, χ_1, formally,

$$\chi_2(\mathbf{k},\omega) = \int_{\mathbf{k}_1,\omega_1} F_1(\mathbf{k},\omega,\mathbf{k}_1,\omega_1) d\chi_1(\mathbf{k},\omega_1) d\chi_1(\mathbf{k}-\mathbf{k}_1,\omega-\omega_1). \quad (2.29)$$

In addition, the first order dispersion surface is slightly shifted:

$$(gk-\omega^2) = \int_{\mathbf{k}_1,\omega_1} F_2(\mathbf{k},\omega,\mathbf{k}_1,\omega_1) d\chi_1(\mathbf{k}_1,\omega_1) \quad (2.30)$$

(for deep water). The functions F_1 and F_2 are rather complicated expressions of wavenumber.

It is possible to extend the definition of the wavenumber spectrum and the frequency spectrum to this more general situation by defining

$$\Psi(\mathbf{k})d\mathbf{k} = 2\int_{d\mathbf{k},\ \omega>0} d\chi(\mathbf{k},\omega), \quad (2.31)$$

and

$$S(\omega)d\omega = 2\int_{\mathbf{k},[\omega,\omega+d\omega]} d\chi(\mathbf{k},\omega),\ \omega>0. \quad (2.32)$$

The factor 2 ensures that the integrals of Ψ and S are equal to $\mathrm{Var}(\eta)$. The directional spectrum $E(\omega,\theta)$ does not have an obvious definition since there is no unique dispersion relation.

If the sea state is changing rapidly, the assumptions about stationarity and homogeneity become questionable. Nevertheless, a well-defined frequency spectrum exists if the conditions are sufficiently stationary in time. Also, Ψ may be defined in non-homogeneous conditions, as long as we are thinking in terms of the linear model.

In Gaussian linear wave theory, quantities like surface slope, surface velocity, pressure etc. are connected to the surface elevation by linear filters. In general, time and space invariant filters are represented by transfer functions in the wavenumber/frequency domain. In the present case, this amounts to

$$X(\mathbf{x},t) = \int_{\mathbf{k},\omega} T_X(\mathbf{k},\omega) e^{i(\mathbf{k}\cdot\mathbf{x}-\omega t)} dB(\mathbf{k},\omega), \quad (2.33)$$

where T_X is the *transfer function* linked to X. The transfer functions may be derived from the solution of regular sine-waves and are found in most textbooks about ocean waves. Some of the most important ones are listed in Table 2.1. The elevation and slope transfer functions actually have general validity, whereas velocity and pressure require linear wave theory.

Property	Notation	Transfer function
Elevation:	η	1
Slope in the x-direction:	$\partial\eta/\partial x$	ik_x
Slope in the y-direction:	$\partial\eta/\partial y$	ik_y
Velocity in the x-dir. at $z = 0$:	u	$\omega k_x/k$
Velocity in the y-dir. at $z = 0$:	v	$\omega k_y/k$
Velocity in the z-dir. at $z = 0$:	w	$-i\omega$
Pressure	p	$\rho g \frac{\cosh(k(z+h))}{\cosh(kh)}$

Table 2.1: The transfer functions of linear wave theory

2.3 Linear Waves on Uniform Currents

A uniform current advecting the surface wave system will change the impression of the waves for an observer at rest. Similarly, waves are experienced differently on board a moving ship, depending on the speed and the direction of the ship. The impact of currents on the spectrum is found, *e.g.* in Kitaigorodskii *et al.* (1975), and is most easily analyzed using the general stochastic model.

Consider a random ocean surface η passing a stationary observer with a uniform speed $\mathbf{U}$. The observer then sees a surface

$$\eta(\mathbf{x}, t) = \eta_0(\mathbf{x} - \mathbf{U}t, t), \tag{2.34}$$

where "0" refers to quantities in a system moving along with the current.

If the surface has a spectral representation $\eta_0(\mathbf{x}, t) = \int_{\mathbf{k},\sigma} e^{i(\mathbf{k}\cdot\mathbf{x}-\sigma t)} dB_0(\mathbf{k}, \sigma)$, the surface in a fixed frame of observations will be

$$\eta(\mathbf{x}, t) = \int_{\mathbf{k}} \int_{\omega} e^{i(\mathbf{k}\cdot(\mathbf{x}-\mathbf{U}t)-\sigma t)} dB_0(\mathbf{k}, \sigma), \tag{2.35}$$

and the correlation function changes to

$$\begin{aligned} \rho(\mathbf{x}, t) &= \mathbb{E}[\eta(\mathbf{x}, t)\eta(\mathbf{0}, 0)] \\ &= \int_{\mathbf{k}} \int_{\sigma} e^{i(\mathbf{k}\cdot(\mathbf{x}-\mathbf{U}t)-\sigma t)} d\chi_0(\mathbf{k}, \sigma) \\ &= \int_{\mathbf{k}} \int_{\omega} e^{i(\mathbf{k}\cdot\mathbf{x}-\omega t)} d\chi(\mathbf{k}, \omega), \end{aligned} \tag{2.36}$$

where

$$d\chi(\mathbf{k}, \omega) = d\chi_0(\mathbf{k}, \omega - \mathbf{U}\cdot\mathbf{k}). \tag{2.37}$$

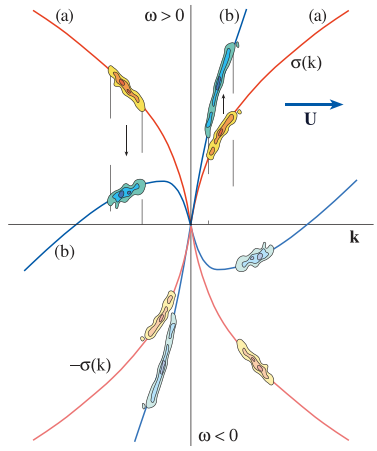

Figure 2.1: Modifications of the dispersion relation and the spectrum due to a steady current. See text for explanations.

The transformation of the spectrum is visualised by considering χ as a mass distribution; χ is then obtained from χ_0 by moving slices orthogonal to $\mathbf{U}$ a vertical distance $\mathbf{U} \cdot \mathbf{k} = Uk\cos(\theta - \beta)$, where β is the direction of the current. The Jacobian of the transformation is 1, reflecting that this does not compress or dilute the spectral mass.

If linear wave theory is valid, the observed spectrum (and similarly the spectral amplitude) will be supported on a *modified* dispersion shell

$$\Xi = \{(\mathbf{k}, \omega); \omega = \pm\sigma(k, h) + \mathbf{U} \cdot \mathbf{k}\}. \tag{2.38}$$

Figure 2.1 shows a two-dimensional plot of the dispersion relation without current (curve a), and the dispersion relation in presence of a current along the positive horizontal axis (curve b). The Doppler shift due to the current can be seen in the curve b. Comparing both curves (a and b), the encounter frequency $\omega(\mathbf{k}; h, \mathbf{U})$ is higher than the intrinsic frequency for the wave components travelling predominantly with the current, $\mathbf{k} \cdot \mathbf{U} > 0$, and less than the intrinsic frequency when $\mathbf{k} \cdot \mathbf{U} < 0$. The Doppler shift vanishes when $\mathbf{k}$ is orthogonal to $\mathbf{U}$. Without the current, the spectrum, visualised in the figure by chunks of mass, is located near a. The current moves the chunks vertically to curve b. Note that the spectrum always remains symmetric relative to the origin.

We then consider the transformation of the wave spectra when linear wave theory is valid. The definitions of Ψ and S (Eqns. 2.31 and 2.32) are the

same, but the expressions relating the spectra in the two systems of observations are not obvious. First of all, the solution for k in the dispersion relation for fixed ω and θ may no longer be unique. Also, the transformation of χ_0 to χ may bring part of the spectrum across the plane $\omega = 0$. This corresponds to the apparent flip in the wave propagation direction experienced if we are in a boat with a speed exceeding the wave speed. From Eqns. 2.31 and 2.37, it follows that

$$\begin{aligned}\Psi(\mathbf{k})d\mathbf{k} &= 2\int_{d\mathbf{k},\ \omega>0} d\chi(\mathbf{k},\omega) = 2\int_{d\mathbf{k},\ \omega>0} d\chi_0(\mathbf{k},\omega-\mathbf{U}\cdot\mathbf{k}) = \\ &= \{\Psi_0(\mathbf{k})H\left(\sigma(k)+\mathbf{U}\cdot\mathbf{k}\right) \\ &\quad + \Psi_0(-\mathbf{k})H\left(-\sigma(k)+\mathbf{U}\cdot\mathbf{k}\right)\}\, d\mathbf{k}, \end{aligned} \tag{2.39}$$

where $H(x) = 1$ when $x > 0$, and 0 otherwise. It is always possible to compute Ψ from Ψ_0, whereas the opposite transformation requires that the terms on the right hand side are not non-zero simultaneously. This will be the case if Ψ_0 is confined to a bounded region in the $\mathbf{k}$-plane and the current is sufficiently small, or if $\Psi_0(\mathbf{k}) \neq 0 \Longrightarrow \Psi_0(-\mathbf{k}) = 0$.

For the frequency spectrum, the situation is even more complicated since the equation

$$\pm\sigma(k) + \mathbf{U}\cdot\mathbf{k} = \omega \tag{2.40}$$

will have 3 solution branches for $k = k(\omega,\theta)$ when ω is less than the frequency $\omega_{\lim}$ for which the intrinsic group velocity $\frac{\partial\sigma}{\partial k}$ is equal to U ($\omega_{\lim} = \frac{g}{4U}$ in deep water). The dimensionless apparent frequency $\omega U/g$ is plotted against the dimensionless intrinsic frequency and θ for deep water in Fig. 2.2. The contour lines are the solution branches for $\sigma = \sigma(\omega,\theta)$, apart from the solution of $-\sigma(k) + Uk\cos\theta = \omega$, which is to the right of the graph.

Using the expression for $\Psi(\mathbf{k})$ we obtain

$$\begin{aligned} S(\omega)d\omega &= 2\int_{\mathbf{k},[\omega,\omega+d\omega]} d\chi(\mathbf{k},\omega) \\ &= \int_{\sigma(k)+\mathbf{U}\mathbf{k}\in\,[\omega,\omega+d\omega]} \Psi_0(\mathbf{k})d\mathbf{k} \\ &\quad + \int_{-\sigma(k)+\mathbf{U}\mathbf{k}\in\,[\omega,\omega+d\omega]} \Psi_0(-\mathbf{k})d\mathbf{k}. \end{aligned} \tag{2.41}$$

The first integral will be over two separate strips for $\omega < \omega_{\lim}$, whereas the second integral corresponds to the components with apparently flipped propagation directions.

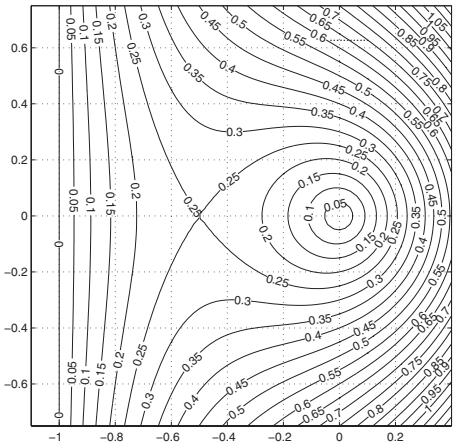

Figure 2.2: Contour plot of the dimensionless apparent frequency $\omega U/g$ as a function of the dimensionless intrinsic frequency $\sigma U/g$ and the wavenumber direction, θ. The x-axis shows $(\sigma U/g) \times \cos(\theta)$ and the y-axis $(\sigma U/g) \times \sin(\theta)$. A vector from the origin has modulus $\sigma U/g$ and direction θ.

Let us for simplicity assume that $\omega < \omega_{\text{lim}}$, neglect the last integral in Eqn. 2.41, and also the outer solution in the first integral. Then the area element over the strip $\sigma(k) + \mathbf{Uk} \in [\omega, \omega + d\omega]$ can be expressed as

$$(dk)(kd\theta) = \frac{d\omega}{|d\omega/dk|}(kd\theta) = \frac{d\omega}{|c_g(k) + U\cos(\theta - \beta)|}kd\theta \tag{2.42}$$

and

$$S(\omega)d\omega = \int_{\sigma(k)+\mathbf{Uk}\in\,[\omega,\omega+d\omega)} \Psi_0(k,\theta)kdkd\theta \tag{2.43}$$

$$= d\omega \int_0^{2\pi} \Psi_0(k(\omega,\theta),\theta)\frac{k(\omega,\theta)}{|c_g(k(\omega,\theta)) + U\cos(\theta-\beta)|}d\theta, \tag{2.44}$$

where $k(\omega, \theta)$ is the (smallest) solution of

$$\sigma(k) + kU\cos(\theta - \beta) = \omega. \tag{2.45}$$

Introducing the directional spectrum,

$$\Psi_0(k,\theta) = \frac{c_g(k)}{k}S_0(\sigma(k))D_0(\theta,\sigma(k)), \tag{2.46}$$

this leads to a relation

$$S(\omega) = \int_0^{2\pi} S_0(\sigma(k)) D_0(\theta, \sigma(k)) \frac{c_g(k)}{|c_g(k) + U\cos(\theta - \beta)|} d\theta \tag{2.47}$$

In order to compute the frequency spectrum, it is therefore necessary to know the full directional spectrum in the system following the current. In this case, it is actually reasonable to define an *apparent* directional spectrum as

$$S(\omega)D(\omega, \theta) = \frac{c_g(k)}{|c_g(k) + U\cos(\theta - \beta)|} S_0(\sigma(k)) D_0(\theta, \sigma(k)), \tag{2.48}$$

where $k = k(\omega, \theta)$ is the solution of Eqn. 2.45. These expressions get more involved if one has to take into account all terms in Eqn. 2.41 (Kitaigorodskii *et al.*, 1975), and it is then not necessarily possible to solve for S_0 and D_0.

2.4 Wave Packet-Based Stochastic Models

The stochastic models we have discussed have so far been based on the Fourier transform, which in essence is an expansion in terms of trigonometric functions. Trigonometric functions have excellent frequency, but poor time location ability, and *wavelet analysis* has over the recent years become an interesting alternative. Wavelets are localised both in frequency and time and may be used for identifying local events in a signal as well as for representing signals in terms of wavelet expansions (Kaiser, 1999).

It turns out that the idea of modelling stochastic signals by adding deterministic or stochastic families of "wavelet-like" functions at random times or locations is older than the stochastic Fourier expansions introduced by N. Wiener in the thirties and later developed into the modern theory of 2nd order stationary stochastic processes and fields. The starting point appears to have been *shot-noise* from vacuum tubes which occurs as randomly located impulses $\{\delta(t - t_j)\}$. After the pulses have passed through a linear filter, the output signal takes the form

$$X(t) = \sum_j h(t - t_j), \tag{2.49}$$

where h is the impulse response of the filter. The mean and variance of X as a regular stochastic process when the intensity of the pulses (to be defined below) is constant, were derived by Campell (1909). Further properties of

X are nicely summarised in the classic papers by S. O. Rice (1944, 1945). In particular, if the density of points is large enough to ensure that many terms in the sum occur at any selected point, $X(t)$ will approach a Gaussian variable.

With the development of soliton and envelope soliton solutions to idealised ocean surface wave equations in 1960s and 1970s, the idea of building stochastic models of the ocean surface based on such solutions is appealing, and explored in a paper by E. Mollo-Christensen and A. Ramamonjiarisoa (1978). In Eqn. 2.49, h would then be the wave packet, and t would have to be replaced by randomly placed locations and time instants, $(\mathbf{x}_j, t_j)$. However, no simple wave packet solution for surface waves is known. For simplicity, Mollo-Christensen and Ramamonjiarisoa assumed packets in the form of plane Stokes-like waves, $\varphi(\mathbf{k}\cdot\mathbf{x}-\omega t)$, multiplied by a moving Gaussian shaped envelope,

$$h(\mathbf{x},t) = G(\mathbf{x}-\mathbf{V}t)\varphi(\mathbf{k}\cdot\mathbf{x}-\omega t)\,. \tag{2.50}$$

The model was studied by direct numerical simulations, without using the results of the Rice paper.

Wave packet solutions of the form in Eqn. 2.50 do not satisfy surface wave equations, although reasonably chosen forms may exist approximately unchanged on the surface for some time. It is important to notice that a representation of the ocean surface analogous to Eqn. 2.49 is linear in form, whereas real soliton solutions are genuinely nonlinear with the non-linearity balancing the dispersion. Although soliton solutions may be added and even pass unaffected through each other, apart from a phase shift, the interaction mechanism is nonlinear, and realistic models where the ocean surface is composed as a linear sum of non-linear solitons is not possible.

Nevertheless, the apparent groupiness often seen in real ocean waves suggests wave packet models, and in the present section we shall briefly review how such models may be built and recall some of their simplest properties. It should, however, be realised that these stochastic models are weakly stationary, and thus do not lead to a new class of processes. Whether a representation of the form in Eqn. 2.49 is preferable to the more familiar Fourier representation will depend on the circumstances.

The Wavelet Directional Method (WDM) treated in Chapter 3 is an estimation method for ocean wave spectra based on wavelet decompositions of the surface. The time localised analysis of the method makes it usable even in cases where the waves are clearly non-stationary.

2.4.1 The Spectrum of Wave Packet Models

In the present section we introduce wave packet models more formally and derive an expression for the spectrum of a stochastic surface based on such a model when the surface is stationary.

The shot-noise process is a physical realisation of what today is called a *Poisson point process*. More generally, a realisation of a *homogenous Poisson field* is a collection of points $\Lambda = \{x_i\}$, randomly and uniformly distributed in space, say $\mathbb{R}^N$, such that the number of points from Λ in any set A, $\#(\Lambda \cap A)$, is Poisson distributed with mean equal to $\nu_i m(A)$,

$$P(\#(\Lambda \cap A) = n) = \frac{(\nu_i m(A))^n}{n!} \exp(-\nu_i m(A)), \; n = 0, 1, \cdots . \tag{2.51}$$

Here $m(A)$ is the size (measure) of A, and $\nu_i > 0$ is a constant called the *intensity* of the field. When realisations of a homogeneous Poisson field are passed through a stationary filter with impulse response function h, the output is, as already stated in Eqn. 2.49,

$$X(x) = \sum_i h(x - x_i). \tag{2.52}$$

It may be proved that the spectrum of X is simply

$$S_{XX}(\kappa) = \nu_i |\mathcal{F}h(\kappa)|^2, \tag{2.53}$$

where $\mathcal{F}h$ is the Fourier transform of h (Rice, 1944, 1945). The formula suggests that the spectrum of the Poisson field is equal to ν_i, and hence, that the field is true *white noise*.

When x is time, a classic filtering problem is to determine (causal) filters with impulse response h fitting a positive target function g such that $g(\kappa) = |\mathcal{F}h(\kappa)|^2$. Since such an h exists for all reasonable functions g, there always exist processes of the form in Eqn. 2.52 fitting a given spectrum as in Eqn. 2.53.

More generally, assume that not only the locations but also the filters vary from point to point. Let h be described in terms of a stochastic variable Φ which is independent and identically distributed at all points, and independent from the Poisson field itself. Assume further that the probability density of Φ is $p_\Phi(\phi)$. The filtered process resulting from a combined realisation of Λ and Φ is then

$$X(x) = \sum_{x_j \in \Lambda} h(x - x_j, \Phi_j). \tag{2.54}$$

From the general properties of superimposed Poisson fields it follows that the spectrum of X is simply

$$S_{XX}(\kappa) = \nu_i \int p_\Phi(\phi) \left|\mathcal{F}h(\kappa,\phi)\right|^2 d\phi. \tag{2.55}$$

As an example, let h have the form of a wave packet,

$$h(x) = g(x)\cos(kx), \tag{2.56}$$

where g is the packet envelope and k a wavenumber taken from a distribution $\Psi(k)$. The Fourier transform of h will be $\mathcal{F}h(\kappa) = \frac{1}{2}(\mathcal{F}g(\kappa+k) + \mathcal{F}g(\kappa-k))$, and the spectrum is hence

$$S_{XX}(\kappa) = \frac{\nu_i}{4}\int_k \Psi(k)\left|\mathcal{F}g(\kappa+k) + \mathcal{F}g(\kappa-k)\right|^2 dk. \tag{2.57}$$

Two limiting cases are of interest. If the k-distribution is narrow, say $\Psi(k) \backsim \delta(k-k_0)$, then

$$S_{XX}(\kappa) \approx \frac{\nu_i}{4}\left|\mathcal{F}g(\kappa+k_0) + \mathcal{F}g(\kappa-k_0)\right|^2. \tag{2.58}$$

and the shape of the spectrum of X is governed by the Fourier transform of the envelope.

At the other extreme, if g has a broad Gaussian bell-shape, then the Fourier transform is correspondingly narrow, $\left|\mathcal{F}g(\kappa)\right|^2 \backsim a\delta(\kappa)$ and

$$S_{XX}(\kappa) \approx a\frac{\nu_i}{4}\left(\Psi(\kappa) + \Psi(-\kappa)\right). \tag{2.59}$$

In this case, there is thus a close correspondence between S_{XX} and Ψ, independent of the detailed shape of g.

In summary, if the wave packet is broad, the spectrum is approximately equal to the (symmetrised) wavenumber distribution $\Psi(\kappa)$. However, $S_{XX}(\kappa)$ will always be a smeared version of the wavenumber distribution and, as the wave packet gets more narrow, its Fourier transform broadens and the spectrum also broadens. When the Fourier transform of the packet gets substantially *broader* than the k–distribution, the spectrum of the surface inherits the shape of the squared Fourier transform of the envelope, independent of the k–distribution.

2.4.2 Wave Packet Models and Linear Wave Theory

Since the wave packet based models in essence are linear, it appears that the models would be most useful in connection with linear wave theory. In order to apply the above theory to ocean surface models, we consider a filtered Poisson field in space and time such that

$$\eta(\mathbf{x},t) = \sum_{(\mathbf{x}_i,t_i)\in\Lambda} w(\mathbf{x}-\mathbf{x}_i, t-t_i, \Phi_i). \tag{2.60}$$

The simplest wave packet that satisfies the equations of linear wave theory is the analytic deep water solution of Pierson and Neumann (1966),

$$w_{PN}(\mathbf{x},t) = p(\mathbf{e}_0\cdot\mathbf{x}, t, \omega_0), \tag{2.61}$$

where ω_0 is the centre frequency and $\mathbf{e}_0$ the propagation direction. The function p has the analytical expression

$$\begin{aligned} p(x,t,\omega_0) &= \frac{1}{D^{1/4}}\exp\left[-\frac{4\omega_0^2}{g^2 D t_0^2}\left(x-\frac{gt}{2\omega_0}\right)^2\right] \\ &\times \sin\left(-\frac{\omega_0^2 x}{Dg}+\frac{\omega_0 t}{D}+\frac{4t^2x}{Dgt_0^4}-\frac{1}{2}\arctan\left(\frac{4x}{gt_0^2}\right)\right), \end{aligned} \tag{2.62}$$

where $D = 1+16x^2/\left(t_0^4 g^2\right)$ (Donelan, *et al.*, 1996). The resulting plane wave propagates in direction $\mathbf{e}_0$, and

$$p(0,t,\omega_0) = \exp\left(-(t/t_0)^2\right)\sin(\omega_0 t). \tag{2.63}$$

The Fourier transform of $w_{PN}(\mathbf{x},t)$ is a δ–curve situated on the dispersion shell such that its projection onto the wave number plane is the line though the origin defined by $\mathbf{e}_0$.

The simplest way to write down a 3D analogue of this packet which satisfies linear wave theory and is localised also in the transverse direction, is to sum packets going in slightly different directions. This will not displace the Fourier transform from the dispersion shell, and such a packet may, *e.g.*, be written

$$w(\mathbf{x},t) = \int_\theta D(\theta)\, w_{PN}(\mathbf{e}_0(\theta)\cdot\mathbf{x}, t, \omega_0)d\theta, \tag{2.64}$$

where $D(\theta)$ is a continuous directional distribution.

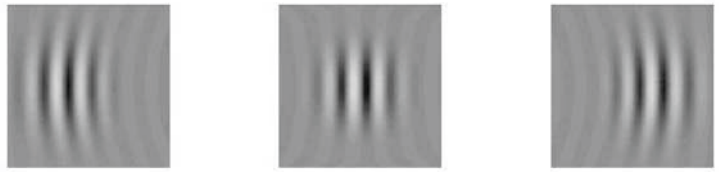

Figure 2.3: Three dimensional wave group before, at and after $t = 0$. Note the converging and diverging crests and the slight change in wavelength over the group.

The 3D wave packet will have a Fourier transform completely situated on the dispersion shell, now in the form of a *surface* δ–function. Obviously, its Fourier transform is just a weighed integral of the curve δ–function Fourier transforms of $w_{PN}(\mathbf{e}_0(\theta) \cdot \mathbf{x}, t, \omega_0)$.

A simple example of a wave group based on directionally super-imposed Pierson-Neumann wave packets is given in Fig. 2.3. A model of the ocean surface consisting of such wave packets placed randomly in space and time will thus satisfy linear wave theory exactly. Depending on the density of the packets, it will also be more or less Gaussian, at least when observed at a fixed point. Some technicalities will occur because of the singularity of the Fourier transform of the group, but the spectrum of the surface may, as before, be expressed by means of a density situated on the dispersion surface. Since a broad wave group will have a localised Fourier transform, it is obvious that any given ocean surface may be approximated arbitrarily well (in a stochastic sense) by a suitable collection of wavelets of the above form.

It may be noted that no wave packet of permanent form, say

$$w(\mathbf{x}, t) = \varphi(\mathbf{k}_0 \cdot \mathbf{x} - \omega_0 t), \tag{2.65}$$

could have a Fourier transform located only on the (curved) linear wave theory dispersion surface, since the Fourier transform of $\varphi(\mathbf{k}_0 \cdot \mathbf{x} - \omega_0 t)$ will be located on the *cone* defined by $|\omega| = \frac{\omega_0}{k_0} |\mathbf{k}|$.

As already mentioned above, the advantages of using wave packet based models are uncertain. There is a direct connection to wavelet analysis, and we return to this in Chapter 3. In a two-dimensional picture or a temporal series of images of the surface, wave groups, like the linear group based on the Pierson/Neumann solution, may be identified by a *matched filter* analysis. The time-dependence of the shape of the group should even make it possible to identify groups both before, at and after the focussing

2.5 Directional Distributions

Engineers have considered various analytic forms of the frequency spectrum for a long time, but the directional distribution has received somewhat less attention (Goda, 1999). In general, directional distributions in real spectra have complicated shapes and depend strongly on frequency. The present section reviews the theory of directional distributions from a purely theoretical point of view. General properties are summarised in Sec. 2.5.1, whereas Sec. 2.5.2 surveys various analytical distributions and their interrelationship. Constructing directional distributions from a subset of Fourier coefficients is discussed in Sec. 2.5.3.

2.5.1 General Theory

A *directional distribution* is a non-negative function with integral 1 on the interval $[0, 2\pi)$. Directional distributions may be viewed as probability distributions of an angular variable, and the theory for angular probability distributions has been treated in detail in the book of K.V. Mardia (1972). We consider distributions in the form of functions, with a possible additional sum of δ-functions,

$$D(\theta) = D_c(\theta) + \sum_{n=1}^{N} d_n \delta(\theta - \theta_n) \tag{2.66}$$

where $d_n > 0$, $D_c(\theta) \geq 0$, and

$$\int_0^{2\pi} D_c(\theta) d\theta + \sum_{n=1}^{N} d_n = 1. \tag{2.67}$$

Distributions of the δ-function type define *unidirectional* wave fields, and a finite sum of δ-functions signifies finitely many unidirectional wave fields occurring simultaneously.

The distribution D may be expanded in a Fourier series,

$$D(\theta) = \frac{1}{2\pi}[1 + 2\sum_{n=1}^{\infty}\{a_n \cos(n\theta) + b_n \sin(n\theta)\}] = \frac{1}{2\pi}\sum_{n=-\infty}^{\infty} c_n e^{-in\theta}, \tag{2.68}$$

where

$$\begin{aligned} a_n &= \int_0^{2\pi} D(\theta)\cos(n\theta)\,d\theta,\ b_n = \int_0^{2\pi} D(\theta)\sin(n\theta)\,d\theta, \\ c_n &= \int_0^{2\pi} D(\theta)e^{+in\theta}\,d\theta. \end{aligned} \tag{2.69}$$

Note that $c_0 = 1$, and since D is real, $c_n = a_n + ib_n = \bar{c}_{-n}$. It is also convenient to write $c_n = r_n \exp(in\theta_n)$ which leads to the alternate expression

$$D(\theta) = \frac{1}{2\pi}[1 + 2\sum_{n=1}^{\infty} r_n \cos(n\,(\theta - \theta_n))]. \tag{2.70}$$

In Fourier analysis, there is a complete theory for the Fourier series of non-negative functions. Since

$$|c_n| \le \int_0^{2\pi} |D(\theta)e^{-in\theta}|\,d\theta = \int_0^{2\pi} D(\theta)\,d\theta = c_0 = 1, \tag{2.71}$$

we note that all Fourier coefficients of a directional distribution have to be less than or equal to 1. It is known (*The Riemann-Lebesgue lemma*) that $c_n \underset{n\to\infty}{\to} 0$ for functions. However, for a δ-function this is not the case.

There are also a series of slightly more subtle facts about the Fourier series of positive functions which we state here without further proof. The most basic result is that $\{c_n\}_{n=-\infty}^{\infty}$ is the Fourier coefficients of a non negative function if and only if the sequence is *positive semi-definite*, *i.e.*

$$\sum_{k,n=-\infty}^{\infty} c_{n-k} z(n)\bar{z}(k) \ge 0 \tag{2.72}$$

for all finite sequences $\{z(n)\}$ on the integers (This is what is usually known as Bochner's Theorem). An equivalent statement is that the matrices

$$[c_0], \tag{2.73}$$

$$\begin{bmatrix} c_0 & \bar{c}_1 \\ c_1 & c_0 \end{bmatrix}, \tag{2.74}$$

$$\begin{bmatrix} c_0 & \bar{c}_1 & \bar{c}_2 \\ c_1 & c_0 & \bar{c}_1 \\ c_2 & c_1 & c_0 \end{bmatrix}, \tag{2.75}$$

$$\cdots$$

are all non-negative definite. These requirements enforce in turn a sequence of inequalities on the coefficients:

$$|c_n| \leq c_0 \quad \text{for all } n,$$
$$|c_1^2 - c_0 c_2| \leq c_0^2 - |c_1|^2, \tag{2.76}$$
$$|c_n - c_{n-1}|^2 \leq 2c_0(c_0 - \Re(c_1)), \tag{2.77}$$
$$\ldots$$

As will be clear in Chapter 3, such inequalities are important when checking data and algorithms.

A sequence of functions $\{k_n(\theta)\}_{n=1}^{\infty}$ is called an *approximate identity* or a *δ-sequence* if it has the property that

$$\lim_{n \longrightarrow \infty} \int_{-\pi}^{\pi} k_n(\theta) f(\theta) d\theta = f(0) \tag{2.78}$$

for all continuous functions f. A sequence of directional distributions is a δ-sequence if and only if the Fourier coefficients

$$\left(\hat{k}_n\right)(m) \underset{n \to \infty}{\longrightarrow} 1 \text{ for all } m. \tag{2.79}$$

(From Eqn. 2.77 it is actually possible to show that $\hat{k}_n(m) \underset{n \to \infty}{\longrightarrow} 1$ for $m = 0$, 1 suffices for positive functions).

A directional distribution is called *unimodal* if it has only one maximum, otherwise it is *bi-modal* or *multimodal*. We shall say that a distribution is *symmetric* if it is symmetric about a certain direction. If the distribution is symmetric about $\theta = 0$, its Fourier series has the form

$$D(\theta) = \frac{1}{2\pi}[1 + 2\sum_{n=1}^{\infty} r_n \cos(n\theta)]. \tag{2.80}$$

It is also possible to prove that if a symmetric distribution is unimodal, then $r_2 < r_1$ (The opposite is not true in general).

For probability distributions on the line, the mean (μ) and the spread or standard deviation (σ) are the most important parameters. The analogous quantities for angular distributions are defined in Mardia (1972). The mean value is taken to be the *vectorial mean* over D, *i.e.* the direction, θ_1, of the vector (α_1, β_1) defined by

$$(\alpha_1, \beta_1) = \left(\int_0^{2\pi} \cos(\theta) D(\theta) d\theta, \int_0^{2\pi} \sin(\theta) D(\theta) d\theta \right). \tag{2.81}$$

Thus, the direction θ_1 is equal to $-\arg(c_1)$.

Similarly, for probability distributions $p(x)$ on $(-\infty, \infty)$, the variance is defined as

$$\mathrm{Var}X = \int_{-\infty}^{\infty} (x - \mathbb{E}(X))^2 p(x) dx. \tag{2.82}$$

However, the corresponding function $p(\theta) = \theta^2$ is not periodic, and it is necessary to replace θ^2 by some periodic expression which approximates θ^2 for small θ's, *e.g.*

$$2(1 - \cos(\theta)) = 4\sin^2(\theta/2) = \theta^2 - \frac{1}{12}\theta^4 + \mathcal{O}(\theta^6), \tag{2.83}$$

$$(1 - \cos(2\theta))/2 = \sin^2(\theta) = \theta^2 - \frac{1}{3}\theta^4 + \mathcal{O}(\theta^6). \tag{2.84}$$

If (2.83) and (2.84) are inserted into the definition of variance, we obtain

$$\sigma_1^2 = \int_0^{2\pi} 2(1 - \cos(\theta - \theta_1)) D(\theta)\, d\theta = 2(1 - (a_1^2 + b_1^2)^{1/2}), \tag{2.85}$$

$$\sigma_2^2 = \int_0^{2\pi} \sin^2(\theta - \theta_1) D(\theta)\, d\theta = \frac{1}{2}(1 - (a_2^2 + b_2^2)^{1/2}). \tag{2.86}$$

Both expressions involve only one pair of Fourier coefficients. The square root of the variance is called the *directional spread*, and denoted by σ_1 and σ_2, respectively, *i.e.*,

$$\sigma_1 = (2(1 - r_1))^{1/2}, \tag{2.87}$$

$$\sigma_2 = (\frac{1}{2}(1 - r_2))^{1/2}, \tag{2.88}$$

$$r_i = (a_i^2 + b_i^2)^{1/2}. \tag{2.89}$$

Since $0 \leq r_i \leq 1$, $\max(\sigma_1) = \sqrt{2}$ rads $\approx 81^\circ$ and $\max(\sigma_2) = \sqrt{1/2}$ rads$\approx 40.5^\circ$.

Sometimes higher order parameters such as angular *skewness* and *kurtosis* are used to describe the shape of the distributions (Kuik *et al.*, 1987). However, these higher order moments are difficult to interpret and unstable when it comes to estimation, and they will not discussed further.

There is a general recipe for constructing all directional distributions. The method is based on the classical work of Schur on orthogonal polynomials and has found new applications in the so-called Burg Maximum Entropy (ME) spectral estimation method (Burg, 1975). Recall that $c_0 = 1$ and that

$|c_1| \leq 1$. This means that in general we may only choose c_1 from within a disc in the complex plane with centre at the origin and radius equal to 1. If c_0 and c_1 have been determined, Eqn. 2.76 yields

$$|c_2 - c_1^2| \leq 1 - |c_1|^2. \tag{2.90}$$

Thus, c_2 must be chosen within a circle with centre at c_1^2 and radius equal to $\left(1 - |c_1|^2\right)$. As is easily seen, c_2 will also be less than or equal to 1. A similar expression is valid in general, namely

$$|c_{N+1} - \bar{\gamma}_c \phi| \leq \rho_N, \tag{2.91}$$

$$\rho_N^2 = (1 - \gamma^H \phi) \frac{\det(R_N)}{\det(R_{N-1})}, \tag{2.92}$$

where

$$\begin{aligned} \gamma &= (c_1, \ldots, c_N)^t, \\ \gamma_c &= (c_N, \ldots, c_1), \\ \phi &= (\phi_1, \ldots, \phi_N)^t, \\ R_{N-1}\phi &= \gamma, \end{aligned}$$

and

$$R_N = \begin{bmatrix} 1 & \bar{c}_1 & \cdots & \bar{c}_N \\ c_1 & \ddots & \ddots & \vdots \\ \vdots & \ddots & & \bar{c}_1 \\ c_N & \cdots & c_1 & 1 \end{bmatrix}. \tag{2.93}$$

(superscript t means transposed and H means Hermitian transposed). The region for c_{N+1} is a circle centered at $o_N = \bar{\gamma}_c \phi$ with radius ρ_N and we have a recursion of the form

$$c_{N+1} = o_N + s_N \rho_N \tag{2.94}$$

where $\{s_N\}$ is a sequence of complex numbers where $|s_n| \leq 1$. The numbers $\{s_N\}$ are called the *Schur coefficients*. Any such sequence gives rise to a positive semi-definite sequence of Fourier coefficients and hence a non-negative directional distribution. *Vice versa*, all distributions define a corresponding Schur sequence (Akhieser and Krein, 1962).

Functions having only a finite number of Schur coefficients different from 0 correspond to the Burg maximum entropy family of directional distributions. The *Burg entropy* is defined

$$H_B(D) = \int_0^{2\pi} \ln D(\theta) d\theta. \tag{2.95}$$

It can be proved (see, *e.g.* Kay, 1988, p.182) that the solution to the problem

$$D_B = \arg\max_D \{H_B(D)\} \tag{2.96}$$

subject to

$$\int_0^{2\pi} e^{-n\theta} D(\theta) d\theta = c_n,\ n = 0, ..., N, \tag{2.97}$$

is given by

$$\begin{aligned} D(\theta) &= \frac{1}{2\pi} \frac{\sigma_e^2}{|1 - \phi_1 e^{-i\theta} - \cdots - \phi_N e^{-iN\theta}|^2}, \\ \sigma_e &= 1 - \phi_1 \bar{c}_1 - \cdots - \phi_N \bar{c}_N, \end{aligned} \tag{2.98}$$

where $\phi_1, ..., \phi_N$ is found from the equation above, $R_{N-1}\phi = \gamma$, also called the *Yule-Walker equation*. This problem is equivalent to finding the maximum entropy spectrum for a complex stochastic process as observed in Lygre and Krogstad (1986).

It is also possible to base an expression for D on the conventional *Shannon entropy* (Hashimoto and Konube, 1986),

$$H_S(D) = -\int_0^{2\pi} D(\theta) \ln D(\theta) d\theta. \tag{2.99}$$

In this case, there is no analytic expression for the distribution unless $N = 1$. However, the functional form is

$$D(\theta) = \exp(-\sum_{j=0}^{2N+1} \lambda_j e_j(\theta)), \tag{2.100}$$

where the functions $e_j(\theta)$ are the sine and cosine function with arguments up to $N\theta$, and λ_j are Lagrange multipliers, which have to be obtained by solving for the (non-linear) constraints (Hashimoto and Konube, 1986).

2.5.2 Classes of Directional Distributions

Below we discuss various directional distributions met in ocean wave analysis. Apart from the double δ-function discussed at the end, all distributions are unimodal.

A class of stochastic variables on the real line where a sum of independent variables from the class leads to a variable of the same class, is called *stable*.

The normal and Cauchy variables are examples of stable classes. Symmetric stable variables have characteristic functions (i.e. the Fourier transform of their distributions) proportional to $\exp(-|bt|^\alpha)$, $0 \leq \alpha \leq 2$. Note that $\alpha = 2$ corresponds to the normal distribution and $\alpha = 1$ to the Cauchy distribution (Lukacs, 1970).

Any integrable function on the real line, $f(x)$, $-\infty < x < \infty$, may be "wrapped up" into a 2π-periodic function by means of the operator W defined by the sum

$$Wf(\theta) = \sum_{n=-\infty}^{\infty} f(\theta + 2\pi n). \tag{2.101}$$

With suitable definitions, the Fourier coefficients of the periodic function Wf equal the Fourier transform of f on the integers, $\widehat{Wf}(m) = \hat{f}(m)$, $m = \cdots, -1, 0, 1, \cdots$, and this suggests a simple method for constructing directional distributions from probability distributions on the real line. The *wrapped stable distributions* are thus defined by the expression

$$D(\theta) = \frac{1}{2\pi}\left[1 + 2\sum_{n=1}^{\infty} x^{n^\alpha} \cos(n\theta)\right], \tag{2.102}$$

where $0 \leq x \leq 1$ and $0 \leq \alpha \leq 2$. Fourier coefficients are simply $r_n = x^{n^\alpha}$, $n = 1, 2, \cdots$, and the directional spread, σ_1, becomes

$$\sigma_1 = \left[2\,(1 - x)\right]^{1/2}, \tag{2.103}$$

independent of α. Two cases are of special interest. The wrapped Cauchy distribution ($\alpha = 1$) turns out to be identical to the *Poisson distribution* in potential theory (not to be confused with the Poisson distribution in statistics). The distribution has a simple Fourier series and a closed form expression:

$$\begin{aligned} D(\theta, x) &= \frac{1}{2\pi}\left[1 + 2\sum_{n=1}^{\infty} x^n \cos(n\theta)\right] \\ &= \frac{1}{2\pi}\frac{1 - x^2}{1 - 2x\cos\theta + x^2} \quad , \; 0 < x < 1. \end{aligned} \tag{2.104}$$

It may be proved that the Poisson distribution is equal to the Burg maximum entropy distribution when the mean direction and the directional spread (*i.e.* σ_1) are given.

For $\alpha = 2$ we obtain the *Wrapped normal distribution* with a simple Fourier series but with no simple closed form,

$$D_2(\theta) = \frac{1}{2\pi}\left[1 + 2\sum_{n=1}^{\infty} e^{-\frac{n^2\sigma^2}{2}} \cos(n\theta)\right],\ \sigma = [-2\log|r_1|]^{1/2}. \tag{2.105}$$

The Fourier coefficients are thus $r_n = e^{-\frac{n^2\sigma^2}{2}}$, $n = 1, 2, \cdots$, and

$$\sigma_1 = [2\,(1 - e^{-\sigma^2/2})]^{1/2}. \tag{2.106}$$

Note that $\sigma_1 \approx \sigma$ for small values of σ. Obviously, if the original distribution on the line is centered around the origin and the directional spread is small, only the central term in the sum $D(\theta) = \sum_{n=-\infty}^{\infty} f(\theta + 2\pi n)$ will be significant, and $D(\theta) \approx f(\theta)$, $|\theta| < \pi$.

The limiting stable distribution for $\alpha = 0$ is a δ-function on top of a uniform background,

$$D_{\alpha=0}(\theta) = \frac{1-x}{2\pi} + x\delta(\theta). \tag{2.107}$$

The very first attempt to describe the directional properties of ocean waves suggested the simple functions $D\,(\theta) = \cos\theta$ or $\frac{2}{\pi}\cos^2\theta$ for $|\theta| \le \pi/2$, and 0 for $\pi/2 \le |\theta| \le \pi$ (see, *e.g.* Pearson *et al.*, 1955). A general class of distributions of this form is the *cos-k distributions* defined for $k > 0$ as

$$D_{(k)}\,(\theta) = \begin{cases} \frac{\Gamma(k+1)}{2^k\Gamma^2\left(\frac{k+1}{2}\right)} \cos^k(\theta)\,, & |\theta| \le \frac{\pi}{2}, \\ 0, & \text{otherwise.} \end{cases} \tag{2.108}$$

It may be proved that that the Fourier coefficients for the cos-k distribution are given by

$$r_n = \frac{B\left(\frac{k+2}{2}, \frac{k+2}{2}\right)}{B\left(\frac{k+n+2}{2}, \frac{k-n+2}{2}\right)}, \tag{2.109}$$

where $B(\cdot,\cdot)$ is the Beta-function (Gradshteyn and Ryzhik, formula 3.631–9, 1965). In particular,

$$r_1 = \frac{2\Gamma^2\left(\frac{k}{2}+1\right)}{(k+1)\,\Gamma^2\left(\frac{k+1}{2}\right)} = 1 - \frac{1}{2\,(k+1)} + \frac{1}{16\,(k+1)^2} + \cdots, \tag{2.110}$$

$$r_2 = \frac{k}{k-2}. \tag{2.111}$$

Nowadays, the cos-k distribution is often replaced by the *cos-2s distribution*, which also occurs in early papers about directional wave spectra (Longuet-Higgins *et al.*, 1963). The distribution has the closed form expression

$$D(\theta, s) = \frac{\Gamma(s+1)}{2\sqrt{\pi}\,\Gamma(s+1/2)}\,\cos^{2s}(\theta/2), \tag{2.112}$$

and the Fourier coefficients take the form

$$r_n = \frac{[\Gamma(s+1)]^2}{\Gamma(s+n+1)\,\Gamma(s-n+1)}, \tag{2.113}$$

where the parameter s is given as $s = |r_1|/(1-|r_1|)$. In particular,

$$\sigma_1 = \left(\frac{2}{s+1}\right)^{1/2}. \tag{2.114}$$

It is easily verified that $D_{(k)}(\theta) = 2D(2\theta, s = k/2)$, $|\theta| \leq \pi/2$, and that the two distributions are in practice indistinguishable when $k = (s-1)/2$ is larger than about 5. Because of the similarity between the two distributions, only the cos-2s distribution has been considered below.

The Poisson distribution was the maximum entropy distribution (given c_1) when the Burg entropy was used. The *von Mises distribution* is obtained when the Shannon entropy (Eqn. 2.99) is used instead (Mardia, 1972):

$$D(\theta, \kappa) = \frac{1}{2\pi I_0(\kappa)} e^{\kappa\cos\theta} = \frac{1}{2\pi}\left[1 + 2\sum_{n=1}^{\infty}\frac{I_n(\kappa)}{I_0(\kappa)}\cos(n\theta)\right]. \tag{2.115}$$

Here, the parameter κ is described as the concentration parameter, whereas the function $I_n(\kappa)$ is the modified Bessel function of the first kind and order n. For $\kappa \to 0$, the von Mises distribution approaches the uniform distribution on the circle since $I_0(0) = 1$.

The *sech-2 distribution* suggested by Donelan *et al.* (1985) is quite similar to the von Mises distribution. It is based on *sech-2* distribution on the real line,

$$f(x) = \frac{\beta}{2\cosh^2(\beta x)}, \tag{2.116}$$

where β governs the width. In Donelan's original paper, the distribution was truncated to the interval $[-\pi, \pi]$, thus requiring an additional normalisation parameter,

$$D(\theta, \beta) = \frac{1}{\tanh(\beta\pi)}\,\frac{\beta}{2\cosh^2(\beta\theta)}. \tag{2.117}$$

An alternative is to apply the wrapping formula $D(\theta) = \sum_{n=-\infty}^{\infty} f(\theta + 2\pi n)$ in which case the Fourier coefficients can be obtained analytically,

$$r_n = \frac{n\pi/2\beta}{\sinh(n\pi/2\beta)}. \tag{2.118}$$

The *Boxcar* (or *Steklov*) *distribution* is defined as

$$D(\theta, a) = \frac{1}{2a}, |\theta| \leq a,\ 0 \text{ otherwise.} \tag{2.119}$$

The Fourier coefficients are easily seen to be $r_n = \frac{\sin(na)}{na},\ n = 1, 2, \cdots$, so that the directional spread is

$$\sigma_1 = [2\ \left(1 - \frac{\sin a}{a}\right)]^{1/2}. \tag{2.120}$$

An equally simple distribution is the *triangular distribution*:

$$D(\theta, a) = \frac{1}{a^2}\,(a - |\theta|),\ 0 \leq |\theta| \leq a,\ = 0,\ \text{otherwise,} \tag{2.121}$$

with Fourier coefficients $r_n = \frac{2}{n^2 a^2}\,[1 - \cos(na)],\ n = 1, 2, \cdots$, and the directional spread equal to

$$\sigma_1 = \frac{1}{a}\,[2\,(a^2 - 2\,(1 - \cos a))]^{1/2}. \tag{2.122}$$

We finally list the *double δ-function* with peaks at $\theta = \pm a$:

$$D(\theta, a) = \frac{1}{2}\,[\delta(\theta + a) + \delta(\theta - a)] \quad ,\ -\pi \leq \theta \leq \pi. \tag{2.123}$$

Using the definition of the δ-function, we obtain $r_n = \cos(na)$, and

$$\sigma_1 = [2\,(1 - \cos(a))]^{1/2}. \tag{2.124}$$

The distributions are summarised in Table 2.2 and the Fourier coefficients in Table 2.3.

Graphs of some of the distributions in a logarithmic scale are shown in Fig. 2.4.

Distribution	Expression $D(\theta)$	Parameter range
cos-k	$\frac{\Gamma(k+1)}{2^k\Gamma^2\left(\frac{k+1}{2}\right)}\cos^k(\theta)$, $\lvert\theta\rvert \le \frac{\pi}{2}$, 0 otherwise.	$0 < k$
cos-2s	$\frac{\Gamma(s+1)}{2\sqrt{\pi}\Gamma(s+1/2)}\cos^{2s}\left(\frac{\theta}{2}\right)$	$0 < s$
Wrapped normal	$\frac{1}{2\pi}[1 + 2\sum_{n=1}^{\infty} x^{n^2}\cos(n\theta)]$	$0 < x < 1$
sech-2	$\frac{1}{\tanh(\beta\pi)}\frac{\beta}{2\cosh^2(\beta\theta)}$	$0 < \beta$
Poisson	$\frac{1}{2\pi}\frac{1-x^2}{1-2x\cos(\theta)+x^2}$	$0 < x < 1$
von Mises	$\frac{1}{2\pi I_0(\kappa)}e^{\kappa\cos(\theta)}$	$0 < \kappa$
Boxcar	$\frac{1}{2a}, \lvert\theta\rvert \le a$, 0 otherwise.	$0 < a < \pi$
Triangular	$\frac{1}{a^2}(a - \lvert\theta\rvert)$, $0 \le \lvert\theta\rvert \le a$, 0, otherwise	$0 < a < \pi$
Double δ-function	$\frac{1}{2}[\delta(\theta + a) + \delta(\theta - a)]$	$0 < a < \pi/2$

Table 2.2: Some families of directional distributions.

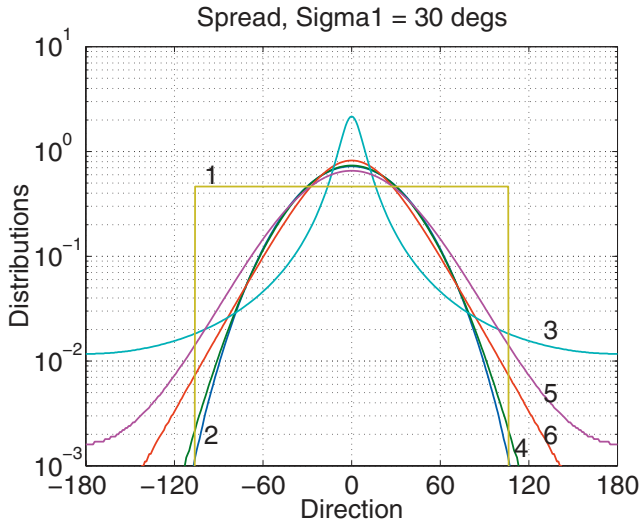

Figure 2.4: The shape of some of the directional distributions in Table 2.3: Boxcar (1) ; cosine-2s (2) ; Poisson (3) ; Wrapped Normal (4); von Mises (5) ; sech-2 (6).

2.5.3 Distributions Based on Four Fourier Coefficients

Instruments which measure the first four (real) Fourier coefficients of the directional distribution are quite common, and we shall therefore discuss this case in some detail. Although the mean direction and the directional spread are defined from the first pair of Fourier coefficients, the second pair provides important additional information.

We recall that $c_0 = 1$ and, from Eqn. 2.76, that the four first Fourier coefficients, $c_1 = a_1 - ib_1$, $c_2 = a_2 - ib_2$, have to fulfill the following inequalities:

$$|c_1| \leq 1, \tag{2.125}$$

$$|c_2 - c_1^2| \leq 1 - |c_1|^2. \tag{2.126}$$

It follows from the general theory that if any of these inequalities degenerates to an equality, the distribution is necessarily a sum of up to two δ-functions. In fact, the double peaked δ-distribution mentioned in the previous chapter represents the limit case: $c_2 = 2c_1^2 - 1 = c_1^2 - (1 - c_1^2)$.

In practice, we thus usually have $|c_1| < 1$ and $|c_2 - c_1^2| < 1 - |c_1|^2$ (but even in this case, D may be a sum of *more* than two δ-functions). When $|c_1|$ approaches 1 or $|c_2 - c_1^2|$ approaches $1 - |c_1|^2$, the distributions get gradually more spiky.

Various distributions show different functional relationships between the first two Fourier coefficients, $r_1 = |c_1|$ and $r_2 = |c_2|$. As a consequence, a plot of the calculated Fourier coefficients from a data set can tell us something about the shape of the underlying distribution. A summary of the r_2 vs. r_1 relationships for the distributions in Table 2.2 is given in Table 2.3.In Fig. 2.5, $r_2^{1/2}$ is plotted against r_1 for all distributions described in Table 2.3.

As mentioned in Sec. 2.5.1, unimodal, symmetric distributions fulfill $r_2 \leq r_1$, thus introducing an upper bound for such distributions in the $r_2 - r_1$ graph. The lower bound is found from the inequality 2.126. As mentioned above, the lower bound coincides with the relationship between r_1 and r_2 for the double δ-function. The Boxcar relation is, incidentally, the lower bound for unimodal symmetric distributions.

For a given a pair of Fourier coefficients c_1 and c_2, the remaining Fourier coefficients have to be contained in a sequence of discs in the complex plane as explained in Sec. 2.5.1. Examples of various distributions with the same four Fourier coefficients are shown in Fig. 2.6. In this example, only c_3 is actually varied, and the displayed functions are computed from Eqn. 2.98.

Distribution	Fourier coefficients r_k	Fourier coefficient relations
cos-k	$\frac{B\left(\frac{k+2}{2},\frac{k+2}{2}\right)}{B\left(\frac{k+n+2}{2},\frac{k-n+2}{2}\right)}$	$r_1 \backsim 1-\frac{1}{2(k+1)}+\frac{1}{16(k+1)^2}+\cdots,$ $r_2=\frac{k}{k+2}$
cos-2s	$\frac{\Gamma^2(s+1)}{\Gamma(s+k+1)\Gamma(s-k+1)}$	$r_2=-r_1\,\frac{1-2c_1}{2-c_1}$
Wrapped normal	x^{k^2}	$r_2=r_1^4.$
Wrapped sech-2	$\frac{k\pi/2\beta}{\sinh(k\pi/2\beta)}$	$r_2=r_1\frac{1}{\cosh(\pi/2\beta)}$
Poisson	x^k	$r_2=r_1^2.$
von Mises	$\frac{I_k(\kappa)}{I_0(\kappa)}$	$r_2=1-2r_1/\kappa,\ r_1=\frac{I_1(\kappa)}{I_0(\kappa)}$
Boxcar	$\frac{\sin(ka)}{ka}$	$r_2=r_1[1-\frac{1}{4}r_1a^2],\ r_1=\frac{\sin(a)}{a}$
Triangular	$\frac{2}{k^2a^2}\,[1-\cos(ka)]$	$r_2=r_1[1-\frac{1}{4}r_1a^2],\ r_1=\frac{2}{a^2}\,[1-\cos(a)]$
Double δ-function	$\cos(ka)$	$r_2=2r_1^2-1$

Table 2.3: Fourier coefficients for the distributions in Table 2.2 (The wrapped sech-2 distribution is used for simplicity).

With only c_1 and c_2 available, the Burg maximum entropy directional distribution (Eqn. 2.97) is

$$D(\theta)=\frac{1}{2\pi}\,\frac{\sigma_e^2}{|1-\phi_1e^{-i\theta}-\phi_2^{-2i\theta}|^2}, \tag{2.127}$$

where

$$\phi_1=(c_1-c_2\bar{c}_1)/(1-|c_1|^2),\phi_2=c_2-c_1\phi_1,\sigma_e=1-\phi_1\bar{c}_1-\phi_2\bar{c}_2.$$

The maximum entropy distribution is actually the distribution which is closest to the uniform distribution and, at the same time, consistent with the data, i.e. the given Fourier coefficients. This shows up in Fig. 2.6. In fact, the vast majority of distributions constructed in this way come out quite spiky and quite different from what one expects to find for ocean wave spectra.

Of the various distributions given in Sec. 2.5.2, only the Poisson distribution will be reproduced when the corresponding Fourier coefficients are used in the ME formula.

When applied to the Fourier coefficients of the cos-2s or the boxcar distribution for instance, the Burg maximum entropy distribution will produce 2 peaks. This is illustrated in Fig. 2.7 for the cos-2s distribution.

Using the fact that $c_1 = r_1$ (and $|c_2| = r_2$) for distributions which are

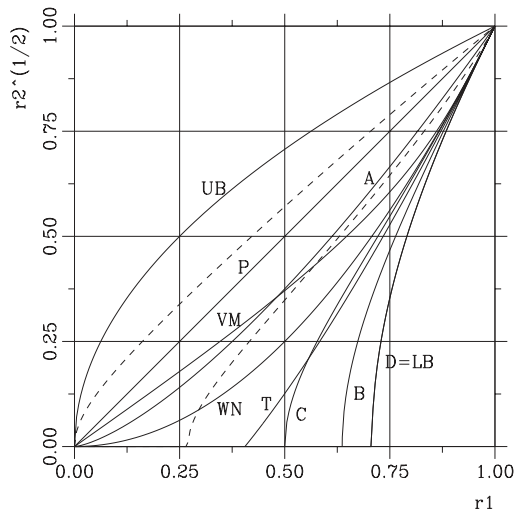

Figure 2.5: The relation between r_1 and $\sqrt{r_2}$ for the distributions in Table 2.3. P: Poisson; VM: von Mises; WN: Wrapped normal; A: wrapped stable distribution of index 1.5; T: Triangular distribution; C: cosine-2s; B: Boxcar; D: Double $\delta-$function; LB: Lower bound; UB: Upper bound for unimodal, symmetric distributions. The dashed lines mark the boundaries for unimodal ME-distributions (see text).

symmetric about zero, we have from Eqn. 2.128 that

$$\phi_1 = \frac{r_1}{1-r_1^2}(1-c_2),\ \phi_2 = \frac{c_2-r_1^2}{1-r_1^2}. \tag{2.128}$$

By a straightforward manipulation, it turns out that for the distribution in Eqn. 2.127 to have only one peak, the Fourier coefficients have to fulfill the following inequality:

$$\left|\frac{r_1\,(1-c_2)^2}{4\,(c_2-r_1^2)\,(1-r_1^2)}\right| \geq 1. \tag{2.129}$$

This inequality corresponds to choosing c_2 from a region bounded by the curves

$$(c_2)_{max} = 1 + \frac{2}{r_1}\,(1-\sqrt{1+r_1})\,(1-r_1^2), \tag{2.130}$$

$$(c_2)_{min} = 1 - \frac{2}{r_1}\,(1-\sqrt{1-r_1})\,(1-r_1^2). \tag{2.131}$$

In Fig. 2.5 we have plotted the boundaries (dashed lines) along with some illustrative distributions from Sec. 2.5.2. The Poisson distribution is reproduced by the ME-expression, which is thus always unimodal. The cos-2s

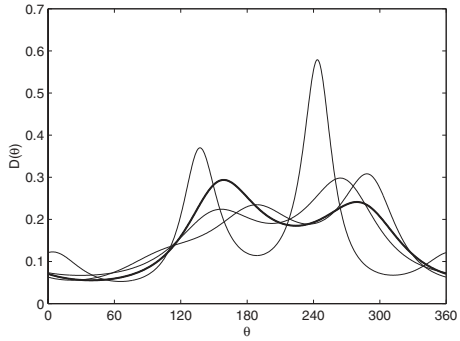

Figure 2.6: The figure shows the Burg ME distribution (thick line) and three additional distributions (thin lines), all having the same c_1 and c_2.

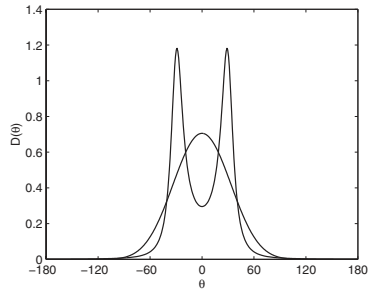

Figure 2.7: The Burg ME estimate produces a double-peaked distribution when the Fourier coefficients of the cos-2s-distribution is input.

distribution for $r_1 > 0.5$ falls completely outside the region, whereas the wrapped normal crosses the region for $r_1 \approx 0.30$.

The peak splitting tendency of the Burg entropy distribution is sometimes considered to be a weakness. However, this distribution is only optimal in the ME metric when the Fourier coefficients are all we know. If we had additional *a priori* information, *e.g.* that the distribution is unimodal, this information should be included in the estimation procedure.

It is noted in Fig. 2.5 that, apart from the Poisson distribution (and wrapped stable distributions for $\alpha < 2$), the rest of the distributions approach the lower bound when r_1 increases. It turns out that this behaviour depends on how well the distributions are concentrated around their mean. A family

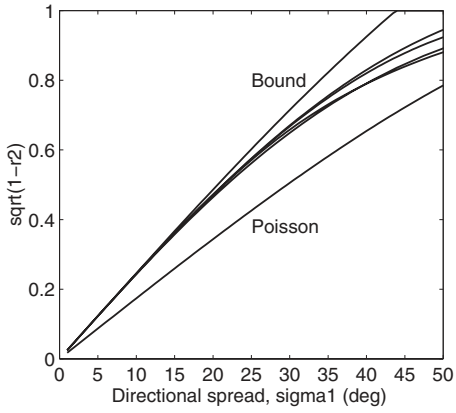

Figure 2.8: Relation between σ_1 and $\sqrt{1-r_2}$ for the distributions in Fig. 2.5.

of directional distributions is *well-focussed* if

$$\lim_{\sigma_1 \to 0} \frac{\int_{-\pi}^{\pi} (\theta - \theta_1)^4 D(\theta - \theta_1, \sigma_1) d\theta}{\int_{-\pi}^{\pi} (\theta - \theta_1)^2 D(\theta - \theta_1, \sigma_1) d\theta} = 0. \tag{2.132}$$

By a Taylor expansion it is then easy to show that

$$\lim_{\sigma_1 \to 0} \frac{1 - r_2}{1 - r_1} = 4, \tag{2.133}$$

which implies

$$\sqrt{1 - r_2} \approx 2^{1/2} \sqrt{2(1 - r_1)} = 2^{1/2} \sigma_1, \tag{2.134}$$

when σ_1 is small. Apart from the wrapped stable family for $\alpha < 2$, all distributions mentioned above are easily seen to be well-focussed. As illustrated in Fig. 2.8 by expanding the upper right corner of Fig. 2.5, the rather sad message is that it is very difficult to distinguish between narrow, well-focussed distributions by considering merely r_1 and r_2.

2.6 Numerical Simulation of Ocean Surfaces

Computer simulations of ocean surfaces corresponding to ideal or measured directional wave spectra is a nice way to obtain a feeling for the directional wave spectrum. The simplest way is to use a sum of plane waves with different amplitudes, wavelengths and direction, but this quickly becomes rather

computer expensive. The current section shows examples of simulations based on simple Gaussian linear wave theory, but more advanced simulation programs are also available (Sharma, 1979).

The simulation is an instantaneous realisation of the ocean surface, $z = \eta(\mathbf{x}, 0)$, and the spectrum of the surface is obtained from the corresponding covariance function,

$$\begin{aligned}\rho(\mathbf{x}, 0) &= \mathbb{E}\left(\eta(\mathbf{x}, 0)\eta(\mathbf{0}, 0)\right) = \int_{\mathbf{k},\omega} e^{i\mathbf{k}\cdot\mathbf{x}} d\chi(\mathbf{k}, \omega) \\ &= \int_{\mathbf{k},\omega>0} e^{i\mathbf{k}\cdot\mathbf{x}} d\chi(\mathbf{k}, \omega) + \int_{\mathbf{k},\omega<0} e^{i\mathbf{k}\cdot\mathbf{x}} d\chi(\mathbf{k}, \omega) \\ &= \frac{1}{2}\int_{\mathbf{k}} \left(\Psi(\mathbf{k}) + \Psi(-\mathbf{k})\right) e^{i\mathbf{k}\cdot\mathbf{x}} d\mathbf{k}.\end{aligned} \tag{2.135}$$

The spectrum of $\eta(\mathbf{x}, 0)$ is therefore $\Psi_0(\mathbf{k}) = \frac{1}{2}\left(\Psi(\mathbf{k}) + \Psi(-\mathbf{k})\right)$, and symmetric with respect to $\mathbf{k}$. The asymptotic properties of the two-dimensional discrete Fourier transform is similar to the one-dimensional transform (Brillinger, 1975). Therefore, the two-dimensional discrete Fourier transforms are zero mean complex Gaussian variables with a variance proportional to $\Psi_0(\mathbf{k})$. The simulations here uses a square of the surface, 512×512 points with a sampling distance $\Delta x = \Delta y = 5\,\mathrm{m}$. For ordinary open ocean directional spectra, the sampling is fine enough to eliminate significant sampling errors and the simulation area $\sim 2.5 \times 2.5\,\mathrm{km}$ is large enough to avoid significant spectral bias.

The input spectra consist of synthetic and real directional wave spectra. Figure 2.9, upper part, shows a simulated surface with a directional spectrum of the form

$$E(\omega, \theta) = S_J(\omega) D(\theta, \omega) \tag{2.136}$$

where S_J is a JONSWAP spectrum (Hasselmann *et al.*, 1973) with $H_s = 3\,\mathrm{m}$, $T_p = 10\,\mathrm{s}$, and a directional distribution close to a cos-2s distribution (For technical reasons, the distribution is the limiting unimodal ME-distribution defined by the Fourier coefficient in Eqn. 2.131). The contour plot to the right shows the wavenumber spectrum and the circles are from outer to inner 50 m, 100 m, 200 m, and 400 m. The directional spreading varies with dimensionless frequency according to the Mitsuyasu *et al.* (1979b) relation, with a spreading at the peak, $\sigma_1(\omega_p) = 10°$. In the lower part, the directional distributions have been changed to Poisson distributions which have a narrow peak and heavier tails. The directional spread $\sigma_1(\omega)$ is the same in these two cases, and this illustrates that it is quite important to know also the shape of the directional distribution.

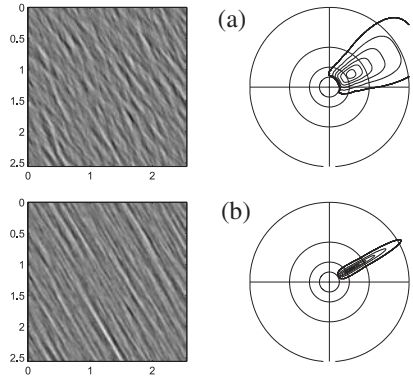

Figure 2.9: *Upper:* Simulation of a two-dimensional random surface with a directional spectrum typical for wind-driven waves. *Lower*: Same directional spectrum, apart from the *shape* of the directional distribution which now replaced by a Poisson distribution. The gray level is proportional to surface height and the horizontal dimensions are indicated in kilometres. The contour plot shows the corresponding wavenumber spectrum, see text.

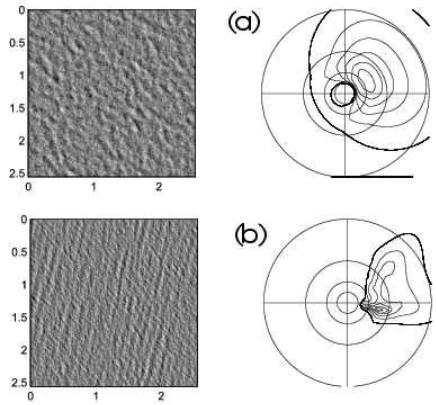

Figure 2.10: *Upper:* Similar to Fig. 2.9(a), but with $\sigma_1(\omega_p)$ increased to 30°. *Lower:* Simulation of a mixed sea state consisting of two fields.

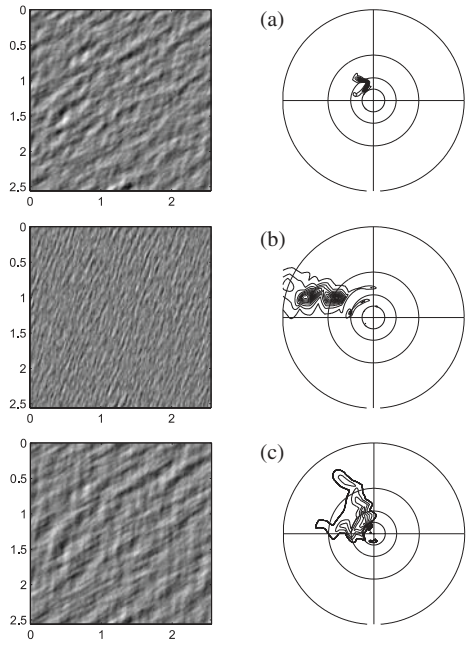

Figure 2.11: Surface simulations based on real spectra similar to Fig. 2.9. *Upper:* Long, swell-like waves; *middle*: Two almost co-linear wave fields; *lower*: Complex sea state consisting of 2–3 fields from different directions.

The spectra for the next simulation (Fig. 2.10, upper part) is similar to Fig. 2.9, but the spreading at ω_p, $\sigma_1(\omega_p)$, has now been increased to 30°. The crest lengths are seen to be considerably shorter. In Fig. 2.10, lower part, the simulation shows a mixed sea state with slightly different peak periods (7 and 9 s).

In Fig. 2.11 is shown simulations resulting from real, open ocean spectra. The surfaces would look similar for any significant waveheight, and approximate peak wavenumbers and wave directions may be inferred from the plots.

Figure 2.12 shows a real optical image wave observation next to a computer simulation. Although the exact in-situ conditions for the observation are not known, it is most likely a wind generation case (as was used for the computer simulation), and the surfaces look quite similar.

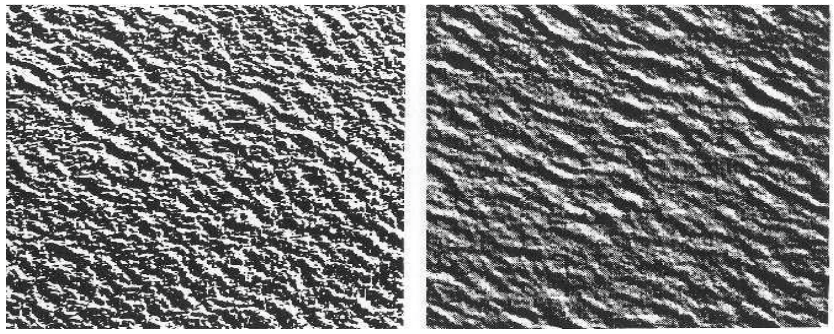

Figure 2.12: *Left:* Aerial photograph of a real wave field off the Norwegian coast (courtesy of *Norsk luftfoto og fjernmåling*); *right*: simulated surface with a JONSWAP spectrum and a *cos-2s* distribution with parameters characteristic for wave generation (Adjusted horizontal scales and aligned wave directions).

Chapter 3

Analysis of In-situ Wave Measurements

This chapter reviews general methodologies and algorithms for the analysis of *in situ* wave measurements. Emphasis is put on principles and overall properties, and not on details pertaining to individual instruments.

The ultimate goal would be to come up with an estimate of the *full* frequency-wavenumber spectrum χ of the surface without an *a priori* dispersion relation. However, to be able to do so with a reasonable accuracy, an $\mathcal{O}$(1 hour, 1 s sampling interval) time series of an $\mathcal{O}(1\,\mathrm{km}^2,\ 1\,\mathrm{m}$ sampling distance) area of the sea would be required. This has so far been out of question although scanning radars are approaching such a limit (Krogstad and Barstow, 1999c). Mathematically, the estimation of the wave spectrum represents an *inverse problem*: how do we obtain as much information as possible about the spectrum from incomplete information.

The following section considers the estimation of directional wave spectra from a spatial array of wave recorders. It also discusses measurements taken in steady currents as well as some of the theory for the sampling variability of directional parameters. We then give a brief description of the wavelet method which has been suggested as an alternative to the conventional methods. The wavelet method is particularly convenient when the measurement array is moving in an irregular, but traceable way during the recording period, since it only uses small parts of the time series simultaneously. The final section summarises questions related to the practical analysis and treatment of wave measurements like system calibration, filters and data consistency checks.

3.1 Conventional Analysis of Wave Measurement Arrays

Harald E. Krogstad

3.1.1 The Basic Algorithms

The starting point is the spectral representation of a stationary and homogeneous sea surface,

$$\eta(\mathbf{x},t) = \int_{\mathbf{k},\omega} e^{i(\mathbf{k}\cdot\mathbf{x}-\omega t)} dB(\mathbf{k},\omega), \tag{3.1}$$

and the corresponding velocity potential,

$$\Phi(\mathbf{x},z,t) = \int_{\mathbf{k},\omega} \frac{\cosh(k(z+h))}{\cosh(kh)} e^{i(\mathbf{k}\cdot\mathbf{x}-\omega t)} dA(\mathbf{k},\omega). \tag{3.2}$$

However, the connection between the spectral amplitudes and the spectra for the surface and the velocity potential is non-linear, and apart from some special types of measurements (*e.g.*, spatial arrays of wave staffs or heave/pitch/roll buoys), it will be necessary to assume linear wave theory.

Conventional in-situ measurements consist of a set of simultaneously recorded time series of some wave properties, like elevation, slope, velocity etc., taken at fixed, but possibly different spatial locations. This will be the basic assumption in the following. The recordings, which we for the moment assume are taken continuously from $t = -\infty$ to $+\infty$, $\mathbf{Y}(t) = \{Y_i(t)\}_{i=1}^N$, are then a *multivariate stochastic process*. Under the above assumption of linear wave theory, and also in some general situations, $\mathbf{Y}(t)$ is connected to the surface elevation by linear, time-invariant filters,

$$Y_i(t) = \int_{\mathbf{k},\omega} T_i(\mathbf{k},\omega) e^{i(\mathbf{k}\mathbf{x}_i-\omega t)} dB(\mathbf{k},\omega),\ i = 1,\cdots N. \tag{3.3}$$

It is convenient to include the spatial location factors $\{e^{i\mathbf{k}\cdot\mathbf{x}_i}\}$ in the transfer functions. The stationarity of the wave field implies that $\mathbf{Y}(t)$ will also be stationary. The spectrum of $\mathbf{Y}(t)$, $\mathbf{\Sigma}(\omega)$, which is a matrix-valued function of frequency containing all auto and cross spectra, can be expressed in short form as

$$\mathbf{\Sigma}(\omega)d\omega = \int_{\mathbf{k},[\omega,\omega+d\omega]} \mathbf{T}(\mathbf{k},\omega)\mathbf{T}^H(\mathbf{k},\omega))d\chi(\mathbf{k},\omega), \tag{3.4}$$

where "H" denotes Hermitian transposed.

In practice, the recordings will be *sampled* with a sampling frequency, say ω_s and with M points in each series,

$$\mathbf{W}(m) = \mathbf{Y}(m\frac{2\pi}{\omega_s}),\ m = 0, \cdots, M-1. \tag{3.5}$$

The total recording interval, $2\pi M/\omega_s$ is typically about 30 minutes, which is usually quite long compared to the correlation time in the series. This means that the series are *well-recorded* in the sense that the asymptotic properties of the discrete Fourier transform,

$$\widehat{\mathbf{W}}(k) = \sum_{m=0}^{M-1} e^{-2\pi ikm/M}\mathbf{W}(m),\ k = 0, \cdots, M-1, \tag{3.6}$$

of $\mathbf{W}$ apply to a high degree of accuracy. The asymptotic theory implies, in particular, that for the set of frequencies, $\omega_m = m\omega_s/M, |m| < M/2$, computed by the discrete Fourier transform, $\widehat{\mathbf{W}}(\omega_m)$ are zero mean, multivariate complex Gaussian variables with a covariance matrix (apart from a scaling factor) defined by Eqn. 3.4,

$$\mathbb{E}\left(\widehat{\mathbf{W}}(\omega_m)\widehat{\mathbf{W}}(\omega_m)^H\right) = \Sigma(\omega_m). \tag{3.7}$$

Moreover, $\widehat{\mathbf{W}}(\omega_m)$ is virtually independent of $\widehat{\mathbf{W}}(\omega_{m'})$ if $m \neq \pm m'$ (Brillinger, 1975). Ocean wave spectra are reasonably smooth functions and the *standard estimate* of the cross spectrum is

$$\widehat{\mathbf{\Sigma}}(\omega) = \frac{2}{\nu}\sum_{\beta=1}^{\nu/2} \widehat{\mathbf{W}}(\omega_\beta)\widehat{\mathbf{W}}^H(\omega_\beta), \tag{3.8}$$

where ω_β runs over $\nu/2$ frequencies surrounding ω (Note the use of a "hat" both for the Fourier transform and the estimator $\hat{a}$ for a parameter a). Since the Fourier coefficients are Gaussian, $\widehat{\mathbf{\Sigma}}(\omega)$ has a *complex Wishart distribution* with ν degrees of freedom (Brillinger, 1975). In practice, there are often electronic or mechanical filters which bias the estimate of $\mathbf{\Sigma}$, and it is mandatory to correct for these before the analysis proceeds (see Sec. 3.3 below).

The *maximum likelihood* (ML) estimate of the cross spectrum amounts to maximising the likelihood function, which, after taking the logarithm and leaving out irrelevant terms and the dependence on ω, takes the form

$$L(\widehat{\mathbf{\Sigma}}, \mathbf{\Sigma}) = -\log|\mathbf{\Sigma}| - \mathrm{tr}(\mathbf{\Sigma}^{-1}\widehat{\mathbf{\Sigma}}). \tag{3.9}$$

Thus,

$$\mathbf{\Sigma}_{ML} = \arg \max_{\mathbf{\Sigma} \in \mathcal{D}_\Sigma} L(\widehat{\mathbf{\Sigma}}, \mathbf{\Sigma}), \tag{3.10}$$

where $\mathcal{D}_{\mathbf{\Sigma}}$ is the domain of feasible matrices,

$$\begin{aligned} \mathcal{D}_{\mathbf{\Sigma}} \quad = \quad & \Big\{ \mathbf{\Sigma}; \mathbf{\Sigma}(\omega) d\omega = \int_{\mathbf{k},[\omega,\omega+d\omega]} \mathbf{T}(\mathbf{k},\omega)\mathbf{T}^H(\mathbf{k},\omega)) d\chi(\mathbf{k},\omega), \\ & \chi \text{ feasible} \Big\}. \end{aligned} \tag{3.11}$$

Feasible spectra are positive measures, symmetric with respect to the origin. It is easily seen that $\mathcal{D}_{\mathbf{\Sigma}}$ is a convex subset of the positive semi-definite matrices. The un-constrained maximum $\mathbf{\Sigma}_{ML}$ of $L(\widehat{\mathbf{\Sigma}}, \mathbf{\Sigma})$ over all positive semi-definite matrices is obtained for $\mathbf{\Sigma}_{ML} = \hat{\mathbf{\Sigma}}$, but in general the solution of Eqn. 3.10 is quite awkward (Burg *et al.* 1982).

The naive approach of trying to solve a discrete version of the integral equation

$$\frac{1}{\Delta\omega} \int_{\mathbf{k},[\omega,\omega+\Delta\omega]} \mathbf{T}(\mathbf{k},\omega)\mathbf{T}^H(\mathbf{k},\omega)) d\chi(\mathbf{k},\omega) = \widehat{\mathbf{\Sigma}}(\omega) \tag{3.12}$$

directly for χ will always fail. No solution exists if $\widehat{\mathbf{\Sigma}}(\omega)$ does not belong to $\mathcal{D}_{\mathbf{\Sigma}}$, and direct solutions of Fredholm integral equations are generally quite ill-conditioned.

An obvious simplification will be to assume linear wave theory, no currents and a directional spectrum of the form $E(\omega, \theta) = S(\omega)D(\theta, \omega)$. The transfer functions may then be written in terms of ω and θ and the cross spectrum expressed as

$$\mathbf{\Sigma}(\omega) = S(\omega) \int_0^{2\pi} \mathbf{T}(\omega,\theta)\mathbf{T}^H(\omega,\theta)) D(\theta,\omega)\, d\theta. \tag{3.13}$$

The direction-independent parts may be factored out, $T_i(\omega, \theta) = R_i(\omega)h_i(\theta, \omega)$, and the cross spectral matrix written $\mathbf{\Sigma} = S\mathbf{R}\mathbf{\Phi}\mathbf{R}^H$, where $\mathbf{R} = \text{diag}(R_1, \cdots, R_N)$, and

$$\mathbf{\Phi}(\omega) = \int_0^{2\pi} \mathbf{h}(\theta,\omega)\mathbf{h}(\theta,\omega)^H D(\theta,\omega)\, d\theta. \tag{3.14}$$

This splits the estimation of E into an estimate for S and an independent estimate for D for each frequency. However, even solving the resulting integral equation for D,

$$\int_0^{2\pi} \mathbf{h}(\theta,\omega)\mathbf{h}(\theta,\omega)^H D(\theta,\omega) d\theta = \hat{\mathbf{\Phi}}(\omega), \tag{3.15}$$

is still ill-conditioned, and requires inverse problem techniques. This may consist of solving the equation approximately and, at the same time, apply a *regularisation* device which keeps the solution from becoming too irregular. Omitting the dependence of ω, this is often written in general terms as

$$\hat{D} = \arg\min_{D\in\mathcal{D}} \left\{ L(\hat{\mathbf{\Phi}}, \Phi(D)) + \lambda N(D) \right\} \tag{3.16}$$

where $L(\Phi(D), \hat{\mathbf{\Phi}})$ measures the fit to the observed data and $N(D)$ is a *suitability* measure. The parameter λ signifies the relative weighting between the two terms and the minimisation is taken over the feasible set of distributions, $D(\theta) \geq 0$, $\int_0^{2\pi} D(\theta)d\theta = 1$ (see, *e.g.* Long, 1986). In the present case, L could be a weighted Euclidian norm or the negative likelihood function for the Wishart distribution of $\hat{\mathbf{\Phi}}$. Similarly, the suitability measure could be a measure of smoothness,

$$N(D) = \int_0^{2\pi} |\frac{d^2D}{d\theta^2}(\theta)|^2 d\theta, \tag{3.17}$$

or *a priori* information as in the so-called *Tikhonov regularization* (Engl *et al.*, 1996),

$$N(D) = \int_0^{2\pi} |D(\theta) - D_0(\theta)|^2 d\theta. \tag{3.18}$$

Here D_0 is a preferred model for the directional distribution and this choice, together with a covariance weighted metric for the Fourier coefficients of D, was investigated for buoy data by Long and Hasselmann (1979).

Later various entropy measures have been proposed, such as the (negative) Shannon and Burg entropies. The Shannon entropy allows a priori information to be taken into account by the so-called *relative cross-entropy* defined as

$$N(D) = \int_0^{2\pi} D(\theta) \log\left(D(\theta)/D_0(\theta)\right) d\theta. \tag{3.19}$$

Related to the inverse problem/entropy methods are also the Bayesian techniques advocated by Hashimoto (1997) and Hashimoto and Tokuda (1999).

Once the directional distribution has been estimated, the frequency spectrum may be obtained from Eqn. 3.15, *e.g.* by

$$\hat{S(\omega)} = \sum_1^N \sigma_{ii}(\omega)/\phi_{ii}(\omega), \tag{3.20}$$

where $\phi_{ii}(\omega)$ is computed from the directional estimate. However, in many cases, more direct ways of estimating $S(\omega)$ exist.

The above methods for estimating the directional distribution, which consist of solving the optimisation problem for D numerically for each frequency, tend to be rather computer-intensive and have mostly been applied only to special studies. However, in the limit $\lambda \to 0$, the data equations are forced to hold exactly, *e.g.*, $L(\Phi(D), \hat{\mathbf{\Phi}}) = \left\| \Phi(D) - \hat{\mathbf{\Phi}} \right\| = 0$, and then $N(D)$ is minimised among the remaining feasible solutions. For some instruments, this can be carried out with negligible computing efforts, and the single point triplet is such a system.

The single point triplet measures three linearly independent quantities of the wave field at a common horizontal location. The most common triplets are the heave/pitch/roll buoy (Longuet-Higgins *et al.*, 1963), and a combination consisting of two orthogonal velocity recordings and a pressure recorder. All triplets are analyzed in the same way, and we discuss the technique by considering the heave/pitch/roll buoy. After a rotation of the data into a fixed coordinate frame and elimination of tracking errors, the buoy records η, $\partial\eta/\partial x$, and $\partial\eta/\partial y$ at a fixed horizontal point. Incidentally, in this particular case, due to the general validity of the corresponding transfer functions, data from a heave/pitch/roll buoy may be analyzed without assuming linear wave theory (Barstow and Krogstad, 1984). However, if one assumes that linear wave theory is valid and an unspecified dispersion relation $k = k(\omega)$, the cross spectral matrix of the three time series is easily seen to be

$$\mathbf{\Sigma} = S \begin{pmatrix} 1 & -ika_1 & -ikb_1 \\ ika_1 & k^2(1+a_2)/2 & k^2 b_2/2 \\ ikb_1 & k^2 b_2/2 & k^2(1-a_2)/2 \end{pmatrix}. \tag{3.21}$$

Here the Fourier coefficients of D have been introduced and the dependence on ω has been omitted for clarity. If no further information about the spectrum is available, we are able to obtain S, the first four Fourier coefficients of D, and the wavenumber k, all as functions of frequency.

It was proved in Glad and Krogstad (1992) that the estimators introduced

by Long (1980) are ML estimators in the sense of Eqn. 3.10:

$$\begin{aligned}
\hat{S} &= \hat{\sigma}_{hh}, \\
\hat{k} &= [(\hat{\sigma}_{xx} + \hat{\sigma}_{yy})/\hat{\sigma}_{hh}]^{1/2}, \\
\hat{a_1} &= \Im\hat{\sigma}_{hx}/(\hat{\sigma}_{hh} \cdot \hat{k}), \\
\hat{b_1} &= \Im\hat{\sigma}_{hy}/(\hat{\sigma}_{hh} \cdot \hat{k}), \\
\hat{a_2} &= (\hat{\sigma}_{xx} - \hat{\sigma}_{yy})/(\hat{\sigma}_{xx} + \hat{\sigma}_{yy}), \\
\hat{b_2} &= 2\Re\hat{\sigma}_{xy}/(\hat{\sigma}_{xx} + \hat{\sigma}_{yy}).
\end{aligned} \tag{3.22}$$

(h = elevation, x = x-slope, y = y-slope, and $\Im$ and $\Re$ denote imaginary and real parts). Although k should in principle be given from the dispersion relation, there are good reasons to keep it independent since $\hat{k}$ is an estimate of the root mean square wavenumber at the frequency in question, and hence represents a test of the validity of linear wave theory (and, above all, the calibration of the instrument). In fact, the ratio between the computed wavenumber, $\hat{k}$, and the wavenumber from linear wave theory is often called the dispersion ratio or the *check ratio*, *e.g.* in deep water,

$$r(\omega) = \frac{\hat{k}(\omega)}{\omega^2/g}. \tag{3.23}$$

By restricting the wavenumber to the linear wave theory dispersion relation, the solution of the ML estimation problem has to be carried out numerically, but the modified estimators for the remaining parameters show somewhat improved performance (Glad and Krogstad, 1992). The Fourier coefficients in Eqn. 3.22 are always consistent with the requirements of a positive function, and it is therefore easy to obtain expressions for D by the methods discussed in the previous chapter, *e.g.*, the Burg entropy estimate.

The ML estimators have the interesting property that functions of the estimators are ML-estimators as well. This means that derived directional parameters like the mean direction and directional spread computed from the estimated Fourier coefficients will also be ML-estimators.

Returning to Eqn. 3.10 for more general arrays of wave recorders, little progress in using the ML-formulation directly has been reported. The first attempts to extract spectra from spatial arrays suggested non-negative Hermitian forms for D of the type

$$\widehat{D}(\theta) = \gamma^H(\theta)\widehat{\mathbf{\Phi}}\gamma(\theta), \tag{3.24}$$

where the vector of weights γ is independent of $\mathbf{\Phi}$ (Kinsman, 1965). However, these linear estimators are today mostly replaced by *data adaptive* estimators introduced by J. Capon (Capon, 1969, 1979). Capon suggested a method for seismic array processing which later has become known as the *Maximum likelihood method* (MLM) for directional wave spectra. The term maximum likelihood stems from the fact that the method may be derived as the maximum likelihood estimate of a plane regular wave from a certain direction in a background of uniform noise. The method was introduced in the context of ocean wave spectra by Davies and Regier (1977), Jeffreys *et al.* (1981), Borgman (1982), and Isobe *et al.* (1984), and the estimate has the form

$$D_{MLM}(\theta) = \kappa\gamma^H(\theta)\mathbf{\Phi}\gamma(\theta) = \kappa/\mathbf{h}^H(\theta)\mathbf{\Phi}^{-1}\mathbf{h}(\theta),$$
$$\kappa^{-1} = \int_0^{2\pi} (\mathbf{h}^H(\theta)\mathbf{\Phi}^{-1}\mathbf{h}(\theta))^{-1} d\theta. \tag{3.25}$$

In practice, the standard estimate is used for $\mathbf{\Phi}$ since the expression gives a non-negative directional estimate as long as $\widehat{\mathbf{\Phi}}$ is positive semi-definite. Arrays containing redundancies require use of *generalized inverses* for $\mathbf{\Phi}$, $\mathbf{\Phi}^g$, due to numerical instabilities when it becomes nearly singular (Krogstad, 1988).

The MLM directional estimate is simple to compute and is by far the most common method for spatial arrays. Nevertheless, the estimate has an obvious drawback. If one starts with a directional distribution D, and then computes the matrix, $\mathbf{\Phi}_D = \int_0^{2\pi} \mathbf{h}(\theta)\mathbf{h}(\theta)^H D(\theta) d\theta$, the MLM-distribution based on $\mathbf{\Phi}_D$ will have a smeared appearance compared to D. This observation led S. Pawka (1983) to suggest an iterative improvement of D_{MLM} related to deconvolution, and this may be taken further by inverse problem techniques.

Let $\mathbf{\Phi}_D = \int_0^{2\pi} \mathbf{h}(\theta) D(\theta) \mathbf{h}(\theta)^H d\theta$ and consider the non-linear operator $M : D \to D_{MLM}$ defined by

$$D \to \mathbf{\Phi}_D \to D_{MLM} = \kappa/\mathbf{h}^H \Phi_D^g \mathbf{h}. \tag{3.26}$$

The operator is in general not 1-1 since any function orthogonal to $\{h_i h_j^*\}_{i,j=1,N}$ may be added to D without affecting $M(D)$ as long as D is kept non-negative with an integral equal to 1. Again, the solution of

$$M(D) = \hat{D}_{MLM} \tag{3.27}$$

is ill-conditioned. One type of regularisation would be to introduce a functional of the form

$$J(D) = \left\| M(D) - \hat{D}_{MLM} \right\|^2 + \lambda N(D), \tag{3.28}$$

but the simplest method is the modified *Landweber iteration method* (Engl *et al.*, 1996):

$$D_{n+1} = \max[0, D_n + \omega_R(\widehat{D}_{MLM} - M(D_n))], \quad D_0 = \widehat{D}_{MLM}, \quad n = 1, 2, \cdots, \tag{3.29}$$

$$\int_0^{2\pi} D_{n+1}(\theta) d\theta = 1. \tag{3.30}$$

Here ω_R is a relaxation parameter and the result is truncated for negative values in order to keep D non-negative. The degree of regularisation is governed by *the number of iterations*, and too many iterations tend to develop instabilities in D. Typically 2-4 iterations seem to suffice, but an in depth theoretical study of this *iterative maximum likelihood method* (IMLM) has not been carried out, see however Krogstad *et al.* (1988) and Haug and Krogstad (1993).

It is possible to combine the ML spectral estimation based on Eqn. 3.10 with the Burg maximum entropy theory for directional distributions. For given set of Schur coefficients and its corresponding directional distributions, it is possible to maximise Eqn. 3.10 and hence obtain ML distributions restricted to this class. For single point triplets, the method corresponds to the standard analysis method (Eqn. 3.22) combined with the Burg ME directional estimate. Numerical experiments with the method for general arrays show very good properties, and this type of regularisation appears to be considerably more stable than the Landweber iteration used in the IMLM (Haug and Krogstad, 1993).

The Maximum Entropy estimation technique may also be applied directly to general spatial arrays (Nwogu, 1986). However, the numerical difficulties appears to be considerable, and the technique has not gained widespread use.

Array algorithms which first estimate Fourier coefficients and subsequently use them in, for example, a maximum entropy directional distribution have not shown better performance than the simpler IMLM-algorithm discussed above. In fact, Fourier coefficients computed by a numerical integration of the IMLM-distribution typically show less sampling variability than directly estimated Fourier coefficients.

As opposed to single point triplets, the resolution of a spatial array in general depends on the wavelength. For the MLM, it has been observed that the array performance degrades for wavelengths shorter than array extension due to spatial aliasing. Moreover, varying directional sensitivity will occur for highly non-symmetric arrays. This means that the directional estimate depends on the array orientation. These effects, which are difficult to investigate theoretically, may be analyzed by numerical simulations. Although full time series simulations are possible, it is more convenient to simulate cross spectra directly. Based on the asymptotic properties of the discrete Fourier transform discussed above, this is carried out as follows. Given the array defined in terms of the transfer functions, $\mathbf{T} = \mathbf{Rh}$, and the target directional distribution, D, the exact cross spectrum (apart from non-directional parts) is given by

$$\mathbf{\Phi} = \int_0^{2\pi} \mathbf{h}(\theta)\mathbf{h}(\theta)^H D(\theta) d\theta. \tag{3.31}$$

The simulated matrix is now easily obtained as $\hat{\mathbf{\Phi}} = \sum_{i=1}^{\nu/2} \mathbf{w}_i \mathbf{w}_i^H$, where $\mathbf{w}_i = \mathbf{L}\mathbf{e}_i$ and $\mathbf{L}$ is the Cholesky factor of $\mathbf{\Phi}$, $\mathbf{\Phi} = \mathbf{L}\mathbf{L}^H$. For redundancies in the array, $\mathbf{L}$ may be rank-deficient. The vector $\mathbf{e}_i$ consists of independent complex Gaussian variables with unit variance.

We finally note that other direction-of-arrival algorithms (Pisarenko, MUSIC etc., see Kay, 1988) appear to be less suitable in the present setting.

3.1.2 Measurements in Steady Currents or From Moving Platforms

The transformation of wave spectra in uniform currents was treated in Chapter 2. Measurements are also influenced by currents, or equivalently, by motion of the instrument.

If we for simplicity consider a uniformly moving wavefield with velocity $\mathbf{U}$ in Eqn. 3.3, the measurement location will change by $\mathbf{x} = -\mathbf{U}t$. The mean value (*e.g.* for current measurements) may now be non-zero, and hence,

$$\mathbf{Y}(t) = \mathbb{E}(\mathbf{Y}) + \int_{\mathbf{k},\omega} \mathbf{T}(\mathbf{k},\omega) e^{-i(\mathbf{k}\mathbf{U}+\omega)t} dB_0(\mathbf{k},\omega), \tag{3.32}$$

where a zero refers to quantities in the system moving with the current. The correlation functions of the measurements are collected in the matrix

function

$$\rho(t) = \mathbb{E}\left[(\mathbf{Y}(t) - \mathbb{E}(\mathbf{Y}))\,(\mathbf{Y}(0) - \mathbb{E}(\mathbf{Y}))^H\right] \tag{3.33}$$

$$= \int_{\mathbf{k},\omega} \mathbf{T}(\mathbf{k},\omega)\mathbf{T}(\mathbf{k},\omega)^H e^{-i(\mathbf{U}\cdot\mathbf{k}+\omega)t} d\chi_0(\mathbf{k},\omega) \tag{3.34}$$

$$= \int_{\mathbf{k},\omega} \mathbf{T}(\mathbf{k},\omega-\mathbf{U}\cdot\mathbf{k})\mathbf{T}(\mathbf{k},\omega-\mathbf{U}\cdot\mathbf{k})^H e^{-i\omega t} d\chi_0(\mathbf{k},\omega-\mathbf{U}\cdot\mathbf{k}) \tag{3.35}$$

$$= \int_{\mathbf{k},\omega} \mathbf{T}(\mathbf{k},\omega-\mathbf{U}\cdot\mathbf{k})\mathbf{T}(\mathbf{k},\omega-\mathbf{U}\cdot\mathbf{k})^H e^{-i\omega t} d\chi(\mathbf{k},\omega), \tag{3.36}$$

where the spectrum χ is the surface spectrum in the system at rest. The cross spectrum is then the Fourier transform of the measurements,

$$\begin{aligned}\mathbf{\Sigma}(\omega)d\omega &= \int_{\mathbf{k},[\omega,\omega+d\omega]} \mathbf{T}(\mathbf{k},\omega-\mathbf{U}\cdot\mathbf{k})\mathbf{T}(\mathbf{k},\omega-\mathbf{U}\cdot\mathbf{k})^H d\chi(\mathbf{k},\omega) \\ &= \int_{\mathbf{k},[\omega,\omega+d\omega]} \mathbf{T}(\mathbf{k},\sigma(k))\mathbf{T}(\mathbf{k},\sigma(k))^H d\chi(\mathbf{k},\omega),\end{aligned} \tag{3.37}$$

where $\sigma(k)$ is as before the intrinsic frequency, $\sigma(k) = \omega - \mathbf{U}\cdot\mathbf{k}$. Apart from modified transfer functions, Eqn. 3.37 is identical to Eqn. 3.4. The general estimation procedure would then be to form the cross spectra of the measurements as usual and then invert Eqn. 3.37 for an estimate of χ. In the final step, χ_0 is obtained from χ by the simple transformation $d\chi_0(\mathbf{k},\omega-\mathbf{U}\cdot\mathbf{k}) = d\chi(\mathbf{k},\omega)$.

In the case of linear wave theory and a small current ($\omega < \omega_{\text{lim}}$), the transformed spectra may be applied directly:

$$\begin{aligned}\mathbf{\Sigma}(\omega) &= \frac{1}{2}\int_{\theta=0}^{2\pi} \mathbf{T}(\mathbf{k},\sigma(k))\mathbf{T}(\mathbf{k},\sigma(k))^H \Psi(k,\theta)\frac{k}{|c_g(k) + U\cos(\theta-\beta)|}d\theta \\ &= \frac{1}{2}S(\omega)\int_{\theta=0}^{2\pi} \mathbf{T}(\mathbf{k},\sigma(k))\mathbf{T}(\mathbf{k},\sigma(k))^H D(\omega,\theta)d\theta.\end{aligned}$$

When the apparent directional spectrum, $S(\omega)D(\omega,\theta)$, has been found, it is transformed back to the frame moving with the current by solving for S_0 and D_0 by the equation

$$S(\omega)D(\omega,\theta) = \frac{c_g(k)}{|c_g(k) + U\cos(\theta-\beta)|}S_0(\sigma(k))D_0(\theta,\sigma(k)). \tag{3.38}$$

Moored platforms like buoys tend to do horizontal excursions during the measurements. In general, the motion of a moored buoy is quite complicated

and dependent on the weight of the mooring and its attachment to the buoy. The amount of insight it is possible to get by simple analysis is therefore limited. Below we consider a situation where the position of the each sensor changes by the same amount, as would be the case for single point triplets like moored buoys.

Starting again with the spectral representation, the time series from a horizontally moving instrument may be written as

$$\mathbf{Y}(t) = \int_{\mathbf{k},\omega} \mathbf{T}(\mathbf{k},\omega) e^{i(\mathbf{k}\cdot\mathbf{x}(t)-\omega t)} dB(\mathbf{k},\omega). \tag{3.39}$$

Let us first consider what happens when B and $\mathbf{x}(t)$ are independent, zero mean Gaussian variables. It is easily seen that $\mathbb{E}(\mathbf{Y}(t)) = 0$, and that $\mathbf{Y}(t)$ is still stationary with a correlation function

$$\begin{aligned}\rho(t) &= \int_{\mathbf{k},\omega} \mathbf{T}(\mathbf{k},\omega)\mathbf{T}(\mathbf{k},\omega)^H K(\mathbf{k},t) e^{-i\omega t} d\chi(\mathbf{k},\omega),\\ K(\mathbf{k},t) &= E\left(e^{i\mathbf{k}(\mathbf{x}(t)-\mathbf{x}(0))}\right)\end{aligned}$$

The effect on the spectrum is thus somewhat tricky, although as long as the excursions are small compared to the wave length, that is $|\mathbf{k}\mathbf{x}(t)| << 1$, the effect should not be very pronounced.

Another possibility is that the horizontal excursions are connected to the surface elevation by a linear filter,

$$\mathbf{x}(t) = \int_{\mathbf{k},\omega} e^{-i\omega t} \mathbf{T}_{\mathbf{x}}(\mathbf{k},\omega) dB(\mathbf{k},\omega). \tag{3.40}$$

When excursions are small compared to the wavelength, we may write

$$\begin{aligned}\mathbf{Y}(t) &= \int_{\mathbf{k},\omega} \mathbf{T}(\mathbf{k},\omega)\Big(1 + i\mathbf{k}\cdot\mathbf{x}(t)\\ &\qquad -\frac{1}{2}(\mathbf{k}\cdot\mathbf{x}(t))^2 + \cdots\Big) e^{-i\omega t} dB(\mathbf{k},\omega),\end{aligned} \tag{3.41}$$

and by inserting the spectral representation for $\mathbf{x}(t)$, we obtain a non-zero second order contribution to the mean value,

$$\begin{aligned}E\left(\mathbf{Y}(t)\right) &= 2\Im\Bigg(\int_{\mathbf{k},\omega>0} \mathbf{T}(\mathbf{k},\omega)\left(k_1\overline{T_{\mathbf{x}_1}(\mathbf{k},\omega)}\right.\\ &\qquad \left.+k_2\overline{T_{\mathbf{x}_2}(\mathbf{k},\omega)}\right) d\chi(\mathbf{k},\omega)\Bigg) + h.o.t.\end{aligned} \tag{3.42}$$

However, since $E\left((\mathbf{k}\cdot\mathbf{x}(t))^2 dB\right) = 0$, the next non-vanishing contribution is of *fourth order*. Exactly the same happens for the covariance function. The final result is a covariance function corresponding to a horizontally stationary instrument and a correction term where the leading order vanish. To the leading order, the correlation functions, and hence also the spectra, are identical to those of an ideal instrument.

Individual random motion of the various recorders in an array is harder to analyse without going to computer simulations. In general, location errors in the specification of spatial arrays has been observed to have serious effects for the estimation of directional parameters like the directional spread.

3.1.3 The Sampling Variability of Directional Parameters

Sampling variability is inherent in all kinds of parameter estimation. For a single time series, the sampling variability of estimated spectra is well known. The estimated spectrum is approximately χ^2-distributed with degrees of freedom (DOF) equal to twice the number of periodogram ("raw-spectrum") values over which the periodogram is smoothed. In the case of estimating say, the directional spread in a directional spectrum, the expression for the spread is fairly complicated and the sampling variability is harder to find. In the present section we review some of what is known about the sampling variability of directional parameters.

Since directional spectral estimation involves computing auto and cross spectra from several time series, the simple theory for single time series does not apply. However, as mentioned above, time series in ocean wave measurements are generally long compared to the typical correlation distance in the series and in addition, the underlying spectra are reasonably smooth. (Wind wave spectra from very extreme seas or narrow swell spectra may be somewhat questionable in this respect). Hence, the sampling variability of the cross spectrum estimates is then governed by the complex Wishart distribution.

The only instrument where a complete asymptotic theory of the sampling variability of the directional parameters exists is the single point triplet. The theory was developed by R. B. Long around 1980 and we shall for completeness recall some of Long's results below (Long, 1980). Consider a heave/pitch/roll buoy and let

$$\sigma^T = \left[\begin{array}{cccccc} \sigma_{hh} & \sigma_{xx} & \sigma_{yy} & \Im(\sigma_{xh}) & \Im(\sigma_{yh}) & \Re(\sigma_{xy}) \end{array}\right], \tag{3.43}$$

$$\mathbf{d}(\sigma) = \begin{bmatrix} a_1 \\ b_1 \\ a_2 \\ b_2 \end{bmatrix} = \begin{bmatrix} \Im(\sigma_{xh})/\sqrt{\sigma_{hh}(\sigma_{xx}+\sigma_{yy})} \\ \Im(\sigma_{yh})/\sqrt{\sigma_{hh}(\sigma_{xx}+\sigma_{yy})} \\ (\sigma_{xx}-\sigma_{yy})/(\sigma_{xx}+\sigma_{yy}) \\ 2\Re(\sigma_{xy})/(\sigma_{xx}+\sigma_{yy}) \end{bmatrix}. \tag{3.44}$$

By a Taylor expansion of the estimate $\widehat{\mathbf{d}}$ around the expectation value, we obtain to first order

$$\widehat{\mathbf{d}} = \mathbf{d}(\widehat{\sigma}) = \mathbf{d}(\sigma) + \mathbf{D}(\sigma)\delta\sigma + ... \tag{3.45}$$

where

$$D_{ij} = \frac{\partial d_i}{\partial \sigma_j}. \tag{3.46}$$

To the same order we thus obtain that $\mathbb{E}(\widehat{\mathbf{d}}) = \mathbf{d}$, and the covariance matrix of $\widehat{\mathbf{d}}$, $\mathbf{V}$, is given by

$$\mathbf{V} = \mathbf{D}\mathbb{E}(\delta\sigma\delta\sigma^T)\mathbf{D}^T = \mathbf{D}\mathbf{U}\mathbf{D}^T. \tag{3.47}$$

The covariance matrix $\mathbf{U}$ is found by means of the Wishart distribution of $\widehat{\mathbf{\Sigma}}$ and the elements in $\mathbf{V}$ may be expressed explicitly as in Table 3.1.

$V_{11} = \frac{1}{2\nu}\left[a_1^2 z_1 - 2a_1b_1b_2 - a_2(2a_1^2-1)+1\right]$
$V_{22} = \frac{1}{2\nu}\left[b_1^2 z_1 - 2a_1b_1b_2 + a_2(2b_1^2-1)+1\right]$
$V_{12} = \frac{1}{2\nu}\left[a_1b_1z_1 - b_2(r_1^2-1)\right]$
$V_{13} = \frac{1}{\nu}\left[a_1a_2z_2 - a_1(a_1^2-b_1^2+a_2^2-1) - b_1b_2(a_2+1)\right]$
$V_{23} = \frac{1}{\nu}\left[b_1a_2z_2 - b_1(a_1^2-b_1^2-a_2^2+1) - a_1b_2(a_2-1)\right]$
$V_{14} = \frac{1}{\nu}\left[a_1b_2(z_2-a_2) - b_1(2a_1^2+b_2^2-a_2-1)\right]$
$V_{24} = \frac{1}{\nu}\left[b_1b_2(z_2+a_2) - a_1(2a_1^2+b_2^2+a_2-1)\right]$
$V_{33} = \frac{1}{\nu}(a_2^2-1)(r_2^2-1)$
$V_{44} = \frac{1}{\nu}(b_2^2-1)(r_2^2-1)$
$V_{34} = \frac{1}{\nu}a_2b_2(r_2^2-1)$
$V_{ij} = V_{ji}$
$z_1 = 2(r_1^2-1) + \frac{1}{2}(r_2^2-1),\ z_2 = (r_1^2-1) + \frac{1}{2}(r_2^2+1)$ $r_1^2 = a_1^2+b_1^2,\ r_2^2 = a_2^2+b_2^2$

Table 3.1: Elements of the covariance matrix for estimates of the Fourier coefficients. The numbering 1 - 4, refers to $\widehat{a}_1, \widehat{b}_1, \widehat{a}_2, \widehat{b}_2$, respectively. ν is the DOF in the cross spectral estimates. The table is copied from Long (1980).

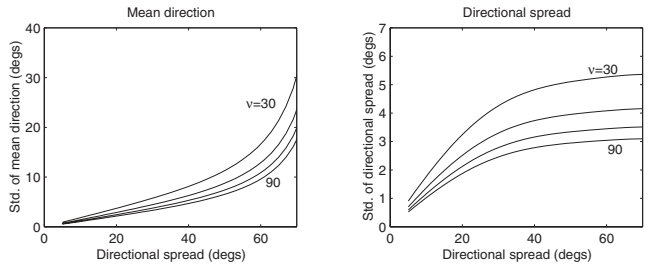

Figure 3.1: The sampling variability for estimates of the mean direction and the directional spread shown for degrees of freedom (ν) equal to 30, 50, 70, and 90.

The statistical properties for the estimates of the directional spread $\widehat{\sigma_1}$ may be derived by the same method utilizing the $\mathbf{V}$ matrix:

$$\mathrm{Var}(\widehat{\sigma_1}) = \frac{1}{2}[(1-r_1)^3\,\mathrm{Var}(s)], \tag{3.48}$$

where

$$\begin{aligned}\mathrm{Var}(s) \;=\; & \frac{1}{(1-r_1)^4}\Bigg\{r_1^4 + \frac{1}{4}r_1^2(r_2^2-1) \\ & +(\frac{1}{2}r_1^{-2}-1)[r_1^2 + a_2(a_1^2-b_1^2) + 2a_1b_1b_2]\Bigg\}\frac{1}{\nu}.\end{aligned} \tag{3.49}$$

Similarly, the asymptotic variability for the mean wave direction is given by

$$\mathrm{Var}(\theta_1) = \frac{1}{r_1^4}[r_1^2 - a_2(a_1^2-b_1^2) - 2a_1b_1b_2]\,\frac{2}{\nu}. \tag{3.50}$$

The asymptotic sampling variability for estimating the mean direction and the directional spread for a cos-2s distribution is shown in Fig. 3.1. It is important to note that the sampling variability is strongly dependent on actual shape of the directional distribution. It is therefore not possible to give a simple answer to questions about the directional resolution of single point triplets. How well asymptotic expressions work out in practice is always a question, and Munthe-Kaas and Krogstad (1985) carried out a simulation study to test Long's asymptotic expressions. The idea of the simulation is to assume a given directional distribution which in turn leads to a (theoretical) directional spectrum. It is easy to simulate possible estimated cross spectra by means of the fast Fourier transform, and from there estimate directional Fourier coefficients and other parameters.

The study confirmed Long's theory apart from very narrow or very broad distributions. In some cases, the sampling distribution was also observed to be considerably skew. For the few multi-modal directional distributions tested, the asymptotic theory appeared to fit the simulations.

When it comes to more general arrays, the sampling variability for Fourier coefficients and derived parameters is much harder to obtain. A fairly comprehensive study of a 4 and 5 element laser array was carried out in the WADIC project (unpublished project report), and an overall conclusion was that the sampling variability for the array was comparable to that of the buoys.

3.1.4 The Sampling Variability of the Directional Distribution

For directional estimates of the form $D(\theta) = \gamma(\theta)^H \hat{\mathbf{\Sigma}} \gamma(\theta)$, where γ is independent of $\hat{\mathbf{\Sigma}}$, the sampling variability is simply $\mathrm{Var}(\hat{D}(\theta)) = \frac{2}{\nu}(\mathbb{E}\hat{D}(\theta))^2$ (Capon, 1979). It has been suggested that a similar expression should be valid in the data adaptive case as well. Unfortunately, this does not appear to be the case. Below we review some results obtained by Ingrid Glad in her masters thesis dealing with the ME method applied to heave/pitch/roll buoy data (Glad, 1990).

If the theoretical directional distribution is fairly uniform, the Fourier coefficients obtained by the standard method are small, and the ME-directional estimate is, to first order, simply the truncated Fourier series:

$$\widehat{D}(\theta) \approx \frac{1}{2\pi} \frac{1}{1 - \widehat{c}_1 e^{-i\theta} - \widehat{c}_1^* e^{i\theta} - \widehat{c}_2 e^{-2i\theta} - \widehat{c}_2^* e^{2i\theta}} \tag{3.51}$$

$$\approx \frac{1}{2\pi}(1 + \widehat{c}_1 e^{-i\theta} + \widehat{c}_1^* e^{i\theta} + \widehat{c}_2 e^{-2i\theta} + \widehat{c}_2^* e^{2i\theta})$$

$$= \frac{1}{2\pi}(1 + 2(\widehat{a}_1 \cos\theta + \widehat{b}_1 \sin\theta + \widehat{a}_2 \cos 2\theta + \widehat{b}_2 \sin 2\theta)). \tag{3.52}$$

Moreover, the variance-covariance matrix for $\hat{a}_1, \cdots, \hat{b}_2$ reduces to

$$\mathbf{V} = \begin{bmatrix} \frac{1}{2\nu} & 0 & 0 & 0 \\ 0 & \frac{1}{2\nu} & 0 & 0 \\ 0 & 0 & \frac{1}{\nu} & 0 \\ 0 & 0 & 0 & \frac{1}{\nu} \end{bmatrix}. \tag{3.53}$$

The covariance between $\widehat{D}(\theta_1)$ and $\widehat{D}(\theta_2)$ is then to the leading order

$$\mathrm{Cov}(\widehat{D}(\theta_1),\widehat{D}(\theta_2)) = \frac{1}{\pi^2}(\frac{1}{2\nu}\cos(\theta_1-\theta_2)+\frac{1}{\nu}\cos 2(\theta_1-\theta_2)). \tag{3.54}$$

By inserting $\theta_1 = \theta_2$ in the above expression, we obtain

$$\begin{aligned}\mathrm{Var}(\widehat{D}(\theta)) &\approx (\frac{1}{\pi})^2(\frac{1}{2\nu}+\frac{1}{\nu})\\ &= (\frac{1}{2\pi})^2\frac{6}{\nu}\\ &= 3\cdot 2(\mathbb{E}(\widehat{D}(\theta)))^2/\nu. \end{aligned}\tag{3.55}$$

Thus, the sampling variability of the ME-directional estimate for an approximately uniform directional distribution is 3 times the variability of the linear estimates.

It has turned out from computer simulation studies that this result has rather limited validity. For more general distributions an analytical Taylor expansion analysis for the covariance gets very messy. From a series of computer experiments of the variability it was observed that the variability may be substantially larger than for the linear estimates or the ME-estimate for nearly uniform distributions.

3.2 The Wavelet Directional Method

Mark A. Donelan and Harald E. Krogstad

The *Wavelet Directional Method* (WDM) represents an interesting alternative to conventional spectral analysis of directional wave data (Donelan *et al.*, 1996). Wavelet analysis of one-dimensional wave measurements producing time/frequency representations of the signal is well-known, and the WDM extends this to multi-channel data by attaching a wavenumber, and hence a direction, to each wavelet. This is, *de facto*, a time/frequency/wavenumber representation which, by time-averaging, gives frequency/wavenumber distributions,– *wavelet spectra*. Analysis of real data has demonstrated that the wavelet spectra share many of the properties of ordinary spectra, although the exact connection is not always straightforward. The method is computationally simple, and in general simpler than a full frequency/wavenumber spectral analysis of array measurements. At the same time, the enhanced temporal resolution of the wavelet analysis provides a valuable tool for analyzing non-stationary data, and data containing time-localized events. In fact, since the analysis itself is time-localized, the

method may even be applied for data from arrays in slow, irregular motion (see Sec. 4.4), where conventional analysis faces large difficulties.

The wave packet-based stochastic models treated in Chapter 2 form a conceptual basis for the WDM. For the wave packet models, the surface consists of randomly placed wave packets where, in addition, each packet was selected from a distribution of possible shapes. In the present case, the shape is characterized by the frequency and the wavenumber of the packet. The WDM analysis estimates the distribution directly, and the general relation between the distribution and the ordinary spectrum of the surface was given in Eqn. 2.55. Since the present version of the method utilises packets in the form of wave groups, the spectrum will be some kind of convolution between the distribution of shapes and the squared Fourier transform of the envelope of the packet. As the width of packet increases, the spectrum of the surface converges to the shape distribution.

There are still questions related to the use of the WDM, in particular the selection of suitable wavelet frames. The results will to some extent depend on the frame, and in principle one should choose a frame based on physically realistic wave packets. The currently used Morlet wavelet (see below) bears some connection to the Pierson-Neumann packet, but does not satisfy the equations for surface waves.

3.2.1 Algorithm

In principle, the WDM may be applied using any discrete wavelet frame. Donelan *et al.* (1996) use a frame based on the *Morlet wavelet* (Grossmann and Morlet, 1984),

$$m\left(t\right)=\frac{1}{\sigma\sqrt{\pi}}\exp(it-\frac{t^{2}}{2\sigma^{2}}), \tag{3.56}$$

which is recognised as the complex analogue to the Pierson-Neumann wave packet (Sec. 2.4.2) at $\mathbf{x}=0$. The frame consists of the collection $\{w_{ij}\left(t\right)\}$, where

$$w_{ij}\left(t\right)=\omega_{j}^{-1/2}m\left(\omega_{j}\left(t-t_{i}\right)\right),\ j=1,\cdots,N_{\omega},\ i=1,\cdots,N_{t}, \tag{3.57}$$

and the corresponding wavelet transform for a single channel is defined as

$$W_{i,j}=\langle X,w_{ij}\rangle=\int_{t}X\left(t\right)\overline{w_{ij}\left(t\right)}dt, \tag{3.58}$$

which, with a suitable normalisation, gives a time/frequency energy representation $S(t,\omega)$ of the signal in a discrete set of points,

$$S\left(t_i,\omega_j\right)=\left|W_{i,j}\right|^2. \tag{3.59}$$

Due to the shape of Morlet wavelet, a time shift Δt in the signal will show up as a phase shift $\exp\left(i\omega_j\Delta t\right)$ in the wavelet coefficient as long as $\omega_j\Delta t$ is much smaller than σ. In the current implementation of the WDM, the wavelets are assumed to occur in the form of plane waves,

$$w_{ij}\left(t,\mathbf{k}_{ij}\cdot\mathbf{x}\right)=\omega_j^{-1/2}m\left(\mathbf{k}_{ij}\cdot\mathbf{x}-\omega_j\left(t-t_i\right)\right). \tag{3.60}$$

Let $W_{ij}^{\mathbf{x}}$ signify the wavelet coefficient computed from data recorded at the location $\mathbf{x}$. Hence, for an observation at $\mathbf{x}$, and as long as $|\mathbf{k}_{ij}\cdot\mathbf{x}|\ll\sigma$,

$$W_{ij}^{\mathbf{x}}=e^{-i\mathbf{k}_{ij}\cdot\mathbf{x}}W_{ij}^{\mathbf{0}}, \tag{3.61}$$

where $W_{ij}^{\mathbf{0}}$ is the coefficient corresponding to a signal from an origin at the centre of the array. For N different recordings located at $\mathbf{x}_1,\cdots,\mathbf{x}_N$, the phase differences, ψ_{mn}, between any pair of wavelet coefficients, $W_{ij}^{\mathbf{x_m}}$ and $W_{ij}^{\mathbf{x_n}}$, will provide a set of equations for $\mathbf{k}_{ij}$:

$$\psi_{mn}=\mathbf{k}_{ij}\cdot\mathbf{x}_m-\mathbf{k}_{ij}\cdot\mathbf{x}_n=\left(\mathbf{x}_m-\mathbf{x}_n\right)^T\mathbf{k}_{ij},\ m=1,\cdots,n-1,\ n=2,\cdots,N. \tag{3.62}$$

This may be written in the compact form $\mathbf{X}\mathbf{k}_{ij}=\psi$, where $\mathbf{X}$ contains an ordering of $\left(\mathbf{x}_i-\mathbf{x}_j\right)^T$, and ψ a corresponding ordering of ψ_{ij}. The least square (LS) solution for $\mathbf{k}_{ij}$ is

$$\mathbf{k}_{ij}^{(LS)}=\left(\mathbf{X}^T\mathbf{X}\right)^{-1}\left(\mathbf{X}^T\psi\right), \tag{3.63}$$

and a solution exists as long as $\{\mathbf{x}_n\}$ are not co-linear. The accuracy of the solution is expressed in terms of the eigenvalues and eigenvectors of $\mathbf{X}^T\mathbf{X}$. In practice, a simplified solution based on a subset of the possible lags $\mathbf{x}_i-\mathbf{x}_j$ has so far been used to determine $\mathbf{k}_{ij}$.

It is possible to avoid the approximate relation in Eqn. 3.61 by observing that the optimal $\mathbf{k}$ and wavelet amplitude may, alternatively, be defined as the solution of

$$\left(a_{opt},\mathbf{k}_{opt}\right)=\arg\min_{\mathbf{k},a}\sum_{n=1}^{N}\left\|aw_{ij}\left(t,\mathbf{k}\cdot\mathbf{x}_n\right)-X_n\left(t\right)\right\|^{2.}, \tag{3.64}$$

where $\|\|\|$ is the usual Euclidean norm. It may be shown that the optimal value of $\mathbf{k}$ is the value maximising

$$\left| \sum_{n=1}^{N} \langle X_n, w_{ij}\left(t, \mathbf{k} \cdot \mathbf{x}_n\right) \rangle \right|, \tag{3.65}$$

and then the optimal a is the mean of the coefficients from all channels. When Eqn. 3.61 holds, the two solutions coincide.

3.2.2 A Data Analysis Example

The data used here for illustration were obtained from the research tower in Lake Ontario during the Water-Air Vertical Exchange Studies (WAVES) experiment in 1987 – the third and final year of the campaign (Donelan *et al.*, 1999). The tower is fixed to the bottom in 12 m of water at the western end of Lake Ontario. It is exposed to fetches that vary from 1.1 km for westerly winds to 300 km for ENE winds. Wave directional measurements were made with an array of six capacitance wave gauges arranged in a centered pentagon of radius 25 cm.

The first step of the WDM is the calculation of the wavelet transform for the individual wave gauges. As an illustration, Fig. 3.2 shows the time/frequency representation defined in Eqn. 3.59 for an earlier set of data from the same tower (see Donelan *et al.*, 1985). The panels show data from three wave gauges, where the second and third are located 10 m and 21 m, respectively, in the downwind direction from the first. The most energetic waves have a frequency of 0.13 Hz and a wavelength of 72 m. The imprint of the passage of groups from one location to the other is evident and the time lag, though small, may be discerned.

The WDM computes a wavenumber corresponding to each wavelet coefficient using Eqn. 3.63, and histograms of observed wavenumber magnitudes for a case of long fetch (mature) waves is shown in Fig. 3.3.

Each panel of the figure is for a different frequency band. At and near the peak frequency (panel *a*) the observed wavenumbers fall within the expected linear dispersion shell corresponding to the centre (solid) and limits (dashed) of the frequency band. The offset from linear theory is most probably due to a surface current. Figure 3.4 shows the corresponding histograms of wavenumber directions. We note that the waves near the peak have a much narrower spreading than those above the peak.

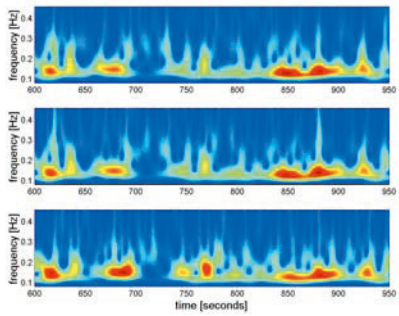

Figure 3.2: Time-frequency plots of the wavelet amplitude from three gauges separated by 10 m and 11 m, respectively, in the downwind direction.

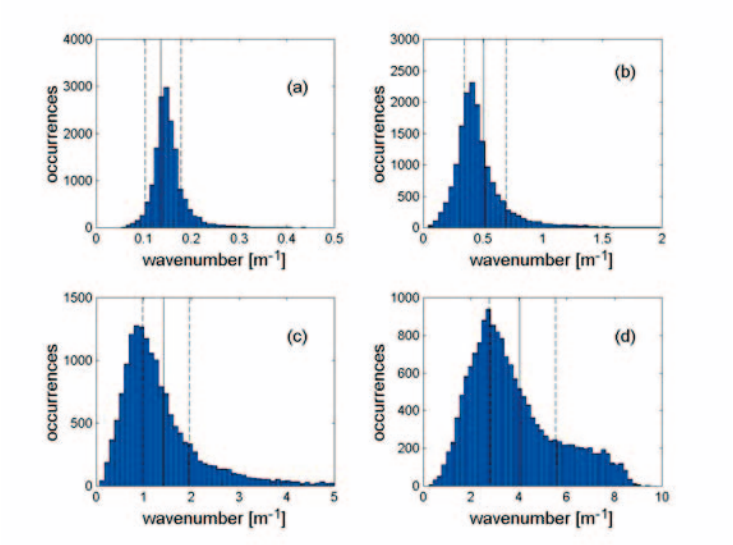

Figure 3.3: Histograms of the observed wavenumbers in particular frequency bands. The solid line is at the location of the wavenumber corresponding to the linear dispersion relation at the centre frequency of the band. The dashed lines are the locations corresponding to the edges of the band. The centre frequencies are 0.177, 0.354, 0.595 and 1.000 Hz. The corresponding wavelengths are, respectively 46.2, 12.5, 4.41 and 1.56 m.

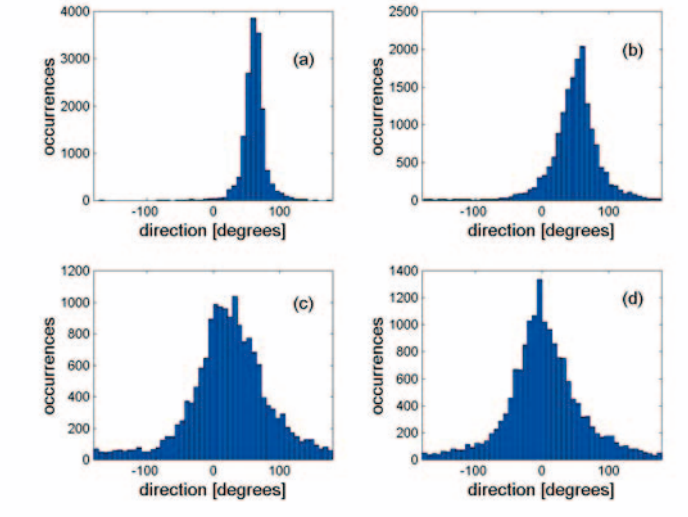

Figure 3.4: Histograms of the observed wavenumber directions in particular frequency bands. The centre frequencies are as in the previous figure.

Each wavenumber magnitude/direction pair is associated with a surface elevation amplitude, and the temporal average of the squared amplitudes, properly scaled, yields an estimate of the 3-D $f/\mathbf{k}$ wavelet spectrum. Estimates of integrated two-dimensional and one-dimensional spectra, analogous to wavenumber or frequency spectra, are formed by additional averaging as in the conventional analysis. The wavelet wavenumber spectrum is shown in Fig. 3.5, and the frequency-direction spectrum in Fig. 3.6.

Figures 3.5 and 3.6 illustrate that the wavelet method shows that the spreading of the spectra away from the peak ($0.136\,\mathrm{m}^{-1}$ and $0.177\,\mathrm{Hz}$) increases, as well as the turning of the waves towards the wind direction for the shorter components and towards the long fetch direction for the longer components (see also Fig. 3.7, and Donelan *et al.*, 1985).

Figure 3.8 shows how the dispersion characteristics of mature wind waves shows up in the frequency/wavenumber spectrum. For these data, the local wind speed was somewhat lower than the phase speed of the longest waves, which approached the tower from the east-north-east, some 60° away from the wind direction. The long waves are thus "overdeveloped" and consequently closely linear. The shorter waves travel slower than the wind and

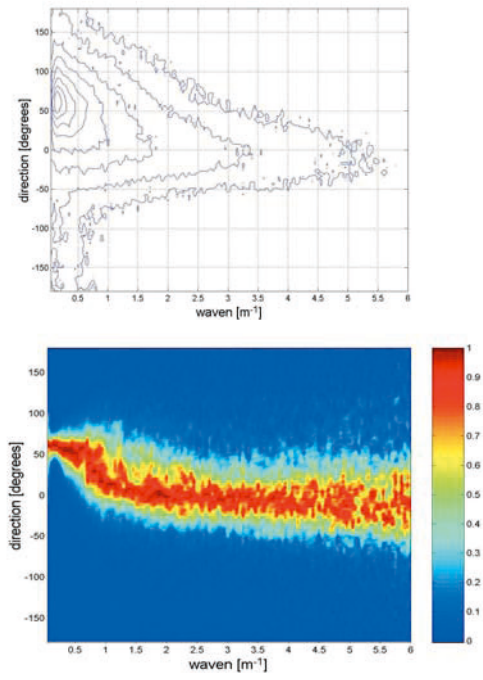

Figure 3.5: *Upper:* The wavenumber wavelet directional spectrum. Logarithmic contour interval, 6dB. *Lower:* The wavenumber spreading function displayed by normalising each wavenumber slice of the directional spectrum by its maximum value.

conform to its direction, but are not strongly forced enough to show much evidence of nonlinearity. The plot is consistent with a nearly linear wave field in which the shorter waves are Doppler shifted by the orbital velocities of the longer waves.

The sampling properties of the WDM estimates are not very well known, and have so far only been investigated empirically. As an illustration, we here show an example for the mean direction using laboratory data in a wind-wave tank. The waves were generated by a constant wind of about 10 m/s at the centre line of the tank – equivalent to 18 m/s at 10 m height. After a stabilisation period of 300 seconds, data were collected for 980 seconds. The basic data set is a time series at 200 Hz from a triplet of *optical wave staffs* arranged in an equilateral triangle of side length 10 mm.

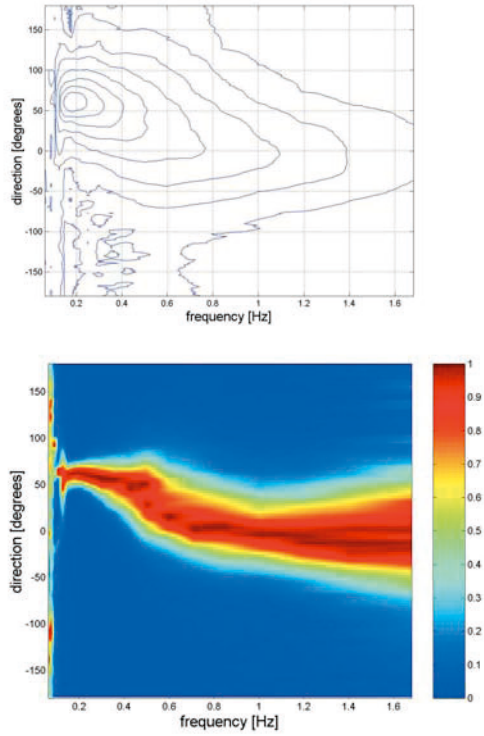

Figure 3.6: *Upper:* The frequency directional spectrum. Logarithmic contour interval, 6dB. *Lower:* The frequency spreading function displayed by normalising each frequency slice of the directional spectrum by its maximum value.

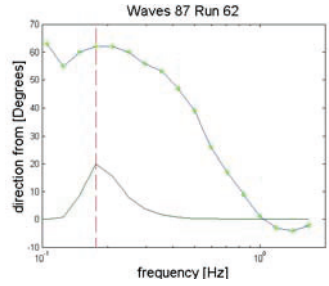

Figure 3.7: The wavelet frequency spectrum (solid line) and the peak direction at each frequency (line with asterisks) showing relaxation from the long fetch direction (east-north-east) to the wind direction (north).

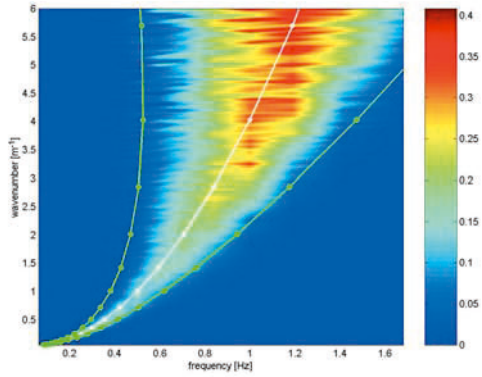

Figure 3.8: Curvature spectrum (k^4 times the wavenumber spectrum) plotted on frequency and wavenumber magnitude. The ridge of the spectrum falls along the linear dispersion curve (white line) and the energy is bounded on both sides by the linear dispersion relation accounting for advection by the standard deviation of the orbital velocities (green lines) i.e. Doppler shifting.

The records were divided into 9 subsets of 109 seconds length, and the mean direction determined at each frequency above the peak in each subset. Figure 3.9 shows the standard deviation of the directional estimates at each frequency versus the number of wave periods observed in the subsets (i.e., record length normalised by the wave period, N). As expected, the variability decreases with increasing normalised record length for the free waves above the peak.

3.2.3 Summary

The methodology of the Wavelet Directional Method (WDM) has been outlined and illustrated by an example from Lake Ontario. The method was developed for an array of wave gauges but may be applied to any of the traditional systems for gathering wave directional information such as pitch-roll-heave buoys and pressure-current meter systems. The ability to derive wavenumber related information directly and to deal with non-steady situations are the principal advantages of the method and makes it well suited to applications in the verification of wave models and calculation of the forces on structures, as well as for detailed analysis of time localised events.

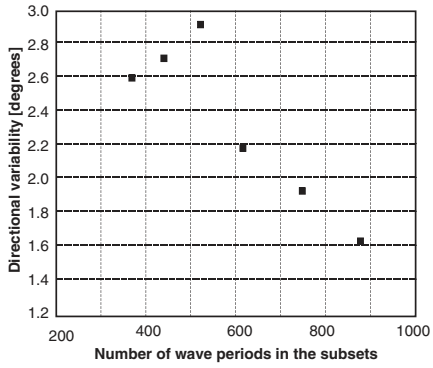

Figure 3.9: The sampling variability of directional estimates of the mean direction in each frequency band versus the number of waves in the subsets.

Acknowledgments

Dr. Bertrand Chapron, IFREMER, provided the Morlet wavelet analysis routines.

3.3 System Calibration and Validation

Harald E. Krogstad

Calibration and validation of wave measurement systems are important tasks for the serious scientist as well as for the professional oceanographic data collector (Tucker, 1993). The price of in-situ wave measurements is considerable, and measurements destroyed by some trivial error are seen all too often. In some cases, *e.g.* when directions of the sensors are mixed up, it may be possible to post-process the data, but in other cases, aliasing and quantization errors, or inadequate data compression routines may have destroyed the data beyond repair. Often quite simple checks are what is needed, and reasonable results should not always be trusted. As an example, the data equations for the first four Fourier coefficients for the popular single point triplet (Eqn. 3.22) will always be meaningful, even if the calibration and hence the results are completely wrong. In many cases, such errors can only be spotted in intercomparison studies with other instruments.

In the present section we shall briefly summarise some of the topics which always need to be considered when collecting the data, and *before* the data are used in an analysis, which typically assume a perfect world. This includes basic sampling considerations, treatment of filters, and data consistency checks.

3.3.1 Aliasing, Leakage and Quantization Errors

All practical signal processing involves *sampling*, and questions about aliasing, spectral leakage and quantization errors must always be sorted out.

Many ocean wave recorders use 1 Hz sampling, which in the open ocean, and with spectra decaying $\sim \omega^{-4.5}$, is quite adequate. However, in more sheltered areas with shorter waves, aliasing will then become a problem. This will turn up as un-physical frequency spectra, and also as a flip of 180° in the wave direction.

Spectral leakage occurs if the recording interval is too short. Usually the recording interval is of the order of 30 minutes and this is quite long compared to the correlation time of the series. Spectral leakage is reduced by a proper tapering of the record, at the expense of some smearing of sharp peaks. Some spectral analysis algorithms are based on averaging spectra from partially overlapping subset of the data series, but as long as there are no particular problems with drift or stationarity, it is usually better to utilise the whole series in one FFT. The resulting periodogram may be used directly for estimating sea state parameters, *e.g.* based on spectral moments.

In general, it has been found that the more complicated directional parameters suffer from larger sampling variability, and hence need somewhat more spectral smoothing than the frequency spectrum.

Quantization errors lead to constant error levels in the spectra, and although easily seen and taken into account in the spectra themselves, they are are less visible in more complicated variables. The effect of quantization errors on directional parameters like the directional spread is discussed in Tucker (1991).

3.3.2 Filters

Measurements are never perfect, but often the distortions may be modelled in terms of filters. As long as the filters are linear, estimated spectra may be

corrected for the filter by applying the inverse of the filter's transfer function. Some of the common situations are discussed below.

We recall that under the assumption of linear wave theory, and also in some more general situations, N ideal wave measurements $\mathbf{Y}(t)$ are connected to the surface elevation by linear, time-invariant filters, $Y_i(t) = \int_{\mathbf{k},\omega} T_i(\mathbf{k},\omega)e^{-i\omega t}dB(\mathbf{k},\omega)$, and the corresponding cross spectrum is $\mathbf{\Sigma}(\omega)d\omega = \int_{\mathbf{k}[\omega,\omega+d\omega]} \mathbf{T}(\mathbf{k},\omega)\mathbf{T}^H(\mathbf{k},\omega))d\chi(\mathbf{k},\omega)$. In practice, observations will always be influenced by additional filters of mechanical or electronic character, *e.g.*

- integration of accelerometers signals to surface elevation
- measuring height by averaging over a finite footprint of the surface
- measuring velocity over a finite volume of water
- applying anti-aliasing filters before sampling
- dynamic response of floating buoys

In general, some of the filters above are non-linear, but for many practical purposes, a linear, time invariant approximation is good enough. Moreover, in most cases, the filters act independently on each channel. In these cases, the filters may be represented by generalised convolutions, and

$$Y_i^{obs} = h_i^{obs} * Y_i = \int_{\mathbf{k},\omega} \hat{h}_i(\mathbf{k},\omega)T_i(\mathbf{k},\omega)e^{-i\omega t}dB(\mathbf{k},\omega). \tag{3.66}$$

The *observed* cross spectrum is therefore,

$$\mathbf{\Sigma}^{obs}(\omega)d\omega = \int_{\mathbf{k}[\omega,\omega+d\omega]} \mathbf{H}(\mathbf{k},\omega)\mathbf{T}(\mathbf{k},\omega)\mathbf{T}^H(\mathbf{k},\omega))\mathbf{H}^H(\mathbf{k},\omega)d\chi(\mathbf{k},\omega). \tag{3.67}$$

A time independent filter, or a directionally independent filter when linear wave theory is valid, will have a transfer function only depending on ω, in which case

$$\begin{aligned} \mathbf{\Sigma}^{obs}(\omega) &= \mathbf{H}(\omega)\mathbf{\Sigma}(\omega)\mathbf{H}^H(\omega), \\ \mathbf{H}(\omega) &= \mathrm{diag}\{\hat{h}_i(\omega)\}. \end{aligned} \tag{3.68}$$

In some cases, it is possible to compute the filters explicitly, or the filters are given by the instrument manufacturer. In other cases, various properties of $\mathbf{\Sigma}$ and $\mathbf{\Sigma}^{obs}$ may be used to deduce properties of $\mathbf{H}$.

An example of a filter having significant amplitude and phase distortion in the frequency range of interest is the Datawell b.v. Hippy 40 A-filter^{TM}, originating from the double integration of the vertical acceleration measurement(Datawell b.v., Hippy 40 documentation, *loc. cit.*),

$$\begin{aligned} A(\omega) &= \frac{1}{\left(1 + i\sqrt{2}\,(\omega_0/\omega) - (\omega_0/\omega)^2\right)(1 + i\omega_1/\omega)}, \\ &\omega_0 = \frac{2\pi}{30.8}\text{Hz},\ \omega_1 = \frac{2\pi}{200}\text{Hz}. \end{aligned} \tag{3.69}$$

Controlled calibration experiments have verified the expression, and the filter is thus easy to account for.

A somewhat different filter stems from the effect of the finite circular footprint of a vertical radar beam, or the finite size of a circular buoy. Then, as a first order approximation,

$$Y^{obs}(t) = \frac{1}{\pi r_0^2}\int_{|\mathbf{x}|\le r_0} \eta(x,t)d\mathbf{x}, \tag{3.70}$$

and the spectral representation leads to the transfer function

$$\begin{aligned} \hat{h}(k) &= \frac{1}{\pi r_0^2}\int_{r\le r_0} e^{i\mathbf{k}\cdot\mathbf{x}}d\mathbf{k} = \frac{1}{\pi r_0^2}\int_{r\le r_0} e^{ikr\cos\theta} r dr d\theta \\ &= \frac{2J_1(kr_0)}{(kr_0)} = 1 - \frac{1}{8}(kr_0)^2 + \frac{1}{192}(kr_0)^4 - ... \end{aligned}$$

The function does not introduce any phase shift, and for linear wave theory and deep water,

$$\hat{h}(\omega) = 2J_1(\omega^2 r_0/g)/(\omega^2 r_0/g) = 1 - \frac{1}{8}\left(\frac{\omega^2 r_0}{g}\right)^2 + ... \tag{3.71}$$

Note that the transfer function is squared in the heave spectrum, and the spectral transfer functions, $\left|\hat{h}(\omega)\right|^2$, for a 2.7 m diameter medium size discus buoy and a 0.9 m diameter spherical buoy are shown in Fig. 3.10. Similar transfer functions may also be derived for more realistic radar footprints and also for volume averaging velocity recorders, *e.g.* for Acoustic Doppler Current Profilers.

3.3.3 Data Consistency Checks

A heave/pitch/roll buoy reacts dynamically to the heave and the slope of the sea surface. The design is a compromise between an ideal sea slope

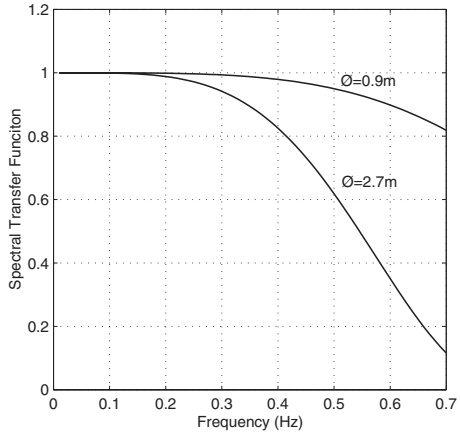

Figure 3.10: Spectral transfer functions for uniformly averaging instruments of two different diameters.

following discus and the requirement for stabilisation. In addition, the effect of the mooring has turned out to be very difficult to assess. Probably the reason why a wildly bouncing buoy is able to measure something meaningful at all, is that the effect of horizontal displacements vanishes to the leading order (see Sec. 3.1.2). The heave eigenfrequency of a circular buoy is approximately

$$\omega_h = \sqrt{\frac{\rho_w \pi (d/2)^2 g}{m + m_a}}, \tag{3.72}$$

where ρ_w is the density of water, d is the buoy's waterline diameter, g is the acceleration of gravity, m is the buoy mass and m_a is the *added mass*, of the order of half the mass for a discus buoy. For most wave buoys, the heave eigenfrequency will be around or above 1 Hz, and thus outside the main frequency range for ocean waves.

The simplest model for the slope excitation is to assume, in accordance with the linear theory for floating oscillating bodies, that the restoring momentum for the buoy comes from a mismatch between the buoy and surface slope. Approximating the slope with the tilt angle, θ, the equation for the buoy motion is

$$\frac{d^2\theta(t)}{dt^2} + 2\lambda\omega_0 \frac{d\theta(t)}{dt} + \omega_0^2 \left(\theta(t) - \theta_s(t)\right) = 0. \tag{3.73}$$

Here the damping ratio, λ, and the eigenfrequency ω_0 are characteristic parameters of the system, and the subscript "s" signifies the surface. In

general, λ and ω_0 will depend on frequency because of frequency dependent added mass. For a circularly symmetric buoy, linear theory further gives that the pitch and roll motions are un-coupled, and the same equations apply to both pitch and roll. We recognise the linear oscillator, which for a regular steady state wave input leads to the transfer function

$$T(\omega) = \frac{1}{1 + 2i\lambda(\omega/\omega_0) - (\omega/\omega_0)^2}. \tag{3.74}$$

The function tends to 1 when $\omega \to 0$, and $T(\omega)$ is purely imaginary at the eigenfrequency. For a circular buoy without large mooring effects, it is reasonable to assume that the transfer functions for the two slopes are equal. However, the transfer functions refer to a *fixed* co-ordinate system and are not in a simple way related to possibly different transfer functions for the sensor output from the pitch and roll sensors, which are fixed to the buoy orientation. Different pitch and roll transfer function could be expected if the buoy is aligned by the mooring in strong currents.

The heave/pitch/roll buoy measures $\eta(\mathbf{x}, t)$, $\frac{\partial \eta}{\partial x}(\mathbf{x}, t)$ and $\frac{\partial \eta}{\partial y}(\mathbf{x}, t)$ at a fixed point $\mathbf{x}$ with the corresponding transfer functions $\mathbf{T}(k, \theta) = [1 \; ik\cos\theta \; ik\sin\theta]'$, irrespective of the validity of Gaussian linear wave theory. Thus, the cross spectrum between heave and one of the slopes should always be purely imaginary, whereas the cross spectrum between the slopes is real. By using Eqns. 3.22 and assuming that the slope transfer functions are equal, we easily see that it is essential to compensate for the modulus of the heave transfer function. The second pair of Fourier coefficients is completely independent of any additional transfer functions, whereas the first pair is dependent only on the phase of the transfer functions. Moreover, the dispersion ratio is dependent on the amplitude of the transfer functions:

$$r^{\text{obs}}(\omega) = \frac{|T_x(\omega)|}{|T_h(\omega)|} r(\omega) \tag{3.75}$$

For other ways of processing the data, similar conclusions do not necessarily hold.

When data are analyzed for phase deviations, one should, because of the sampling variability, average the phase over several spectra after all phases have been changed to be within 0^o to 180^o for σ_{xh} and σ_{yh}, and -90^o to 90^o for σ_{xy}. The averaging could be weighted by the precision of the phase estimate using the fact that the width of the confidence interval for the phase angle is proportional to $\left(|C_{ab}(\omega)|^{-2} - 1\right)^{1/2}$, where $C_{ab}(\omega)$ is the coherence between the records X_a and X_b (Jenkins and Watts, 1968).

Examples of averaged phases for 25 real series from one of the Wavescan buoy configurations is shown in Fig. 3.11. In this case, $f_0 = 0.47\,\mathrm{Hz}$ and $\lambda = 0.10$ provide the best fit to 90°. However, the low value of λ implies a strong attenuation in the resulting slope spectra at around 0.40 –0.45 Hz, and this shows up in the dispersion ratio which is lower than 1 for high frequencies, see Fig. 3.12. The deviation below the spectral peak is probably due to deviations from linear theory. If one accepts the use of the dispersion ratio as an independent constraint, modified and improved transfer functions can easily be derived. Nevertheless, determination of f_0 and λ from the phase test appears to be much more accurate than a direct measurement of the buoy response.

Similar data consistency checks are possible for all single point triplet measurements, although other systems require an assumption about linear wave theory.

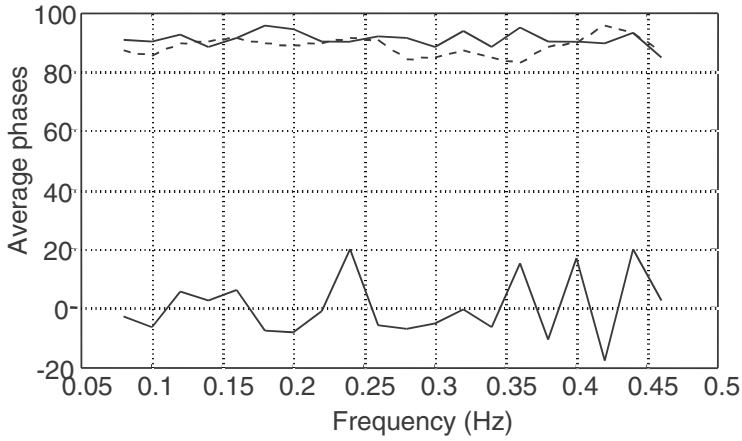

Figure 3.11: Average phase of pitch/heave cross spectrum (solid line), roll/heave cross spectrum (dashed line), and pitch/roll cross spectrum (solid line) after compensation for the slope transfer function (Wavescan buoy).

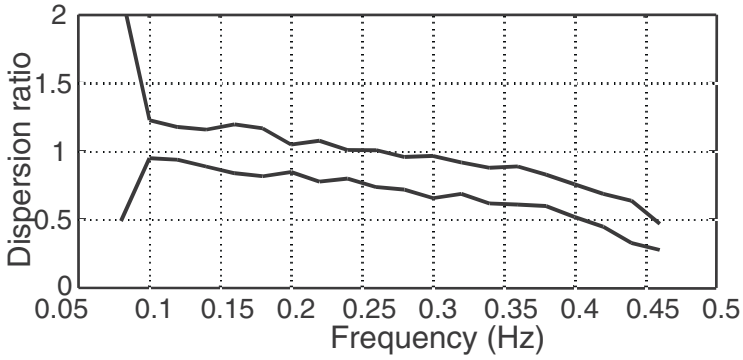

Figure 3.12: Dispersion ratio after compensation of the slope transfer function with the parameters in Fig. 3.11.

Chapter 4

In-situ and Optical Measurement Systems

The present chapter gives a survey of some well-established and some new in-situ measurement systems. The established systems are described only briefly, whereas some of the not-so-common systems are described in more detail.

4.1 Buoys

Harald E. Krogstad

The earliest reference to using a buoy for directional wave measurements appears to be an internal report by N. F. Barber for the Admiralty Research Laboratory in England (Barber, 1946). This paper suggests the basic principle, and the buoy became a reality some fifteen years later as reported by Longuet-Higgins *et al.* (1963). Apart from the *Shipborne Wave Recorder* (Tucker, 1991, pp. 68–73), *in-situ* collection of ocean wave data at sea away from man-made structures has since then been served more or less exclusively by moored buoys. The most successful non-directional wave buoy has been Datawell's *Waverider,* which measures its own vertical acceleration on a gravity stabilised platform. The sensor has subsequently been refined to include tilt in addition to vertical acceleration and is today used in the spherical *Directional Waverider*. Moreover, this sensor, the *Hippy 40*, has been and is still used in many buoys around the world such as the NOAA discus buoys in the US. Although Datawell's sensors have proven to be very robust, the mechanical construction with the accelerometer platform mounted within a floating sphere sometimes leads to problems under transport and handling, and also with extreme temperatures. More compact tilt and ac-

celeration sensors have therefore been developed over the years. *Neptune Science Inc.* has developed robust sensors that may even be used in small expendable wave buoys deployed from aircraft (Earle *et al.,* 1993).

Recently, a number of completely new concepts for tracking the buoy motions have emerged. The idea of utilising the magnetic field vector for azimuth, pitch and roll measurements is reported in Steele and Earle (1991) and Wang *et al.* (1993). The technique compares quite well with the Hippy 40 sensor. The advent of low cost angular rate sensors has made it possible to compute pitch and roll from an arrangement consisting of three orthogonal sensors, and this is developed in a recent paper by Steele *et al.* (1998).

Compact units with no moving parts measuring all six degrees of freedom of the body are now also available. The *Motion Reference Unit* (MRU), manufactured by *Seatex ASA* in Norway, is such a sensor with numerous applications apart from being used in wave buoys. The MRU can be set up to provide time series both for directional measurements in a discus buoy (i.e., heave, pitch and roll), and a spherical buoy (heave and displacement). The sensor has a number of practical advantages including small size, low weight and is not sensitive to rapid rotation under transport or to freezing temperatures (Krogstad and Barstow, 1999a).

4.1.1 The Heave/Pitch/Roll Buoys

The modern heave/pitch/roll buoys are typically medium sized buoys designed for extended unattended operation in the open sea. The optimal shape appears to be a symmetric discus shaped buoy with some stabilisation. The developments in computer technology and solid state memory have made on-board processing and data storage a relatively simple task, and the size of the buoy also makes it a good platform for a variety of met-ocean, chemical and ocean biology observations. On board processing and radio transmission via satellite or link are also common features of modern buoys. What are left as key factors in today's market are therefore robustness, ease of operation, and professional data analysis and calibration software. This section presents some of the more common buoys, but is by no means exhaustive.

The Wavescan (Fig. 4.1) and the NOAA discus buoys (Fig. 4.2) could serve as examples of contemporary heave/pitch/roll buoys. The Wavescan buoy manufactured by Oceanor A/S is the result of development and operation of heave/pitch/roll buoys in Norway for more than 20 years. During this

Figure 4.1: The Wavescan heave/pitch/roll data buoy, Ø2.8 m (*Photograph used by permission*).

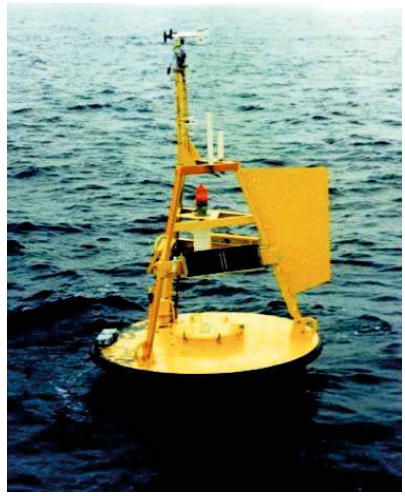

Figure 4.2: The NOAA discus buoy, Ø3.0 m (*Photograph: NOAA/Dept. of Commerce*).

period, the various buoys have been involved in numerous intercomparison experiments leading to significant improvements both in design, operation and data processing. The current model is equipped with an MRU configured for measurements of heave and slope. The MRU is integrated with a 3-axis fluxgate compass for buoy orientation measurements. The diameter of the buoy is 2.8 m and the weight around 920 kg. With a total buoyancy of 3000 kg there is ample room for additional equipment. A single point taut mooring is used for normal conditions and heavily trafficked areas, whilst an s-mooring is used for deep water hostile environments.

As with other state-of-the-art oceanographic instrumentation, raw data as well as on-board processed data may be stored on board or radio-transmitted to shore. The buoy allows in fact two-way communication either via satellite or radio, and the buoy position can also be monitored by means of one-way satellite position tracking.

The variety of buoy instrument and mooring configurations requires a constant need for calibration of the buoy's hydro-mechanical response as discussed in Sec. 3.3.3, and software analyzing Wavescan raw data has been prepared for this purpose.

4.1.2 The Displacement Buoys

The operational principle for Datawell's Directional Waverider (DWR) is based on heave and lateral displacement measurements (Fig. 4.3). Although such buoys by other manufacturers used not to have a very good record, Datawell's DWR has turned out to be quite a success and has been the de facto reference instrument for directional wave measurements during the 1990s. The current Mark II version of the DWR is a spherical buoy with diameter 0.9 m measuring heave and translation by combining the Hippy 40 sensor with a three axis fluxgate compass and two orthogonal horizontal accelerometers. The light weight (~ 250 kg) makes transport and deployment quite easy, and the buoy is routinely used in coastal areas where the size of the mooring is not a concern.

Real time data from the Waverider amount to time series of motion in the vertical, north and west directions as well as directional spectra, optimally coded into a 32 byte satellite transmitted message. The Mark II version appears to have increased the internal sampling frequency from 1.28 to 3.84 Hz, thus covering all waves longer than its physical size.

Another recent spherical buoy on the market with a six degrees of freedom

Figure 4.3: The Datawell Directional Waverider (*Photograph used by permission*).

sensor apparently similar to the MRU is manufactured by *Axys Environmental Systems* in Canada. The buoy is reported to have a sophisticated on-board data analysis module developed in cooperation with the Canadian Hydraulics Centre of the National Research Council of Canada and is fully solar powered, see Fig. 4.4.

A displacement buoy of a fairly complicated shape is Oceanor's Seawatch buoy, Fig. 4.5.The discus-shaped instrument container is surrounded by three vertical 6 meter aluminium legs that are kept together by a top frame,

Figure 4.4: The TRIAXYS directional wave buoy. (*Photograph used by permission*).

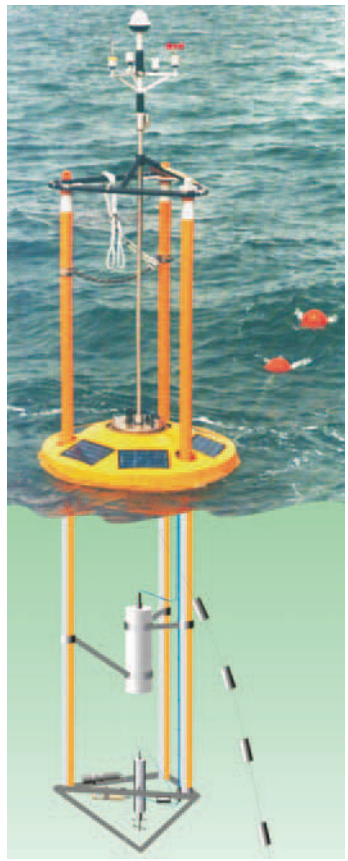

Figure 4.5: The Seawatch buoy (*Illustration used by permission*).

the instrument/processor unit, and the bottom frame. The top frame supports the meteorological sensors and the bottom frame, current meters, temperature and salinity sensors. The first versions of the buoy contained a Datawell Hippy non-directional sensor, but the later versions have directional sensors. Although the design did not seem to favour directional wave measurements, it has been demonstrated in intercomparisons with the DWR (Barstow *et al.*, 1994), that the heave/displacement analysis works surprisingly well also for Seawatch. The present version of the buoy uses the MRU sensor to measure heave and horizontal displacement.

Figure 4.6: The SEATEX ASA's Smart buoy (*Photograph used by permission*).

4.1.3 The GPS buoys

Tracking a buoy's motion by means of the satellite Global Positioning System (GPS) represents in a way the ultimate buoy wave sensor. The buoys will be completely freed from their own sensor and are instead carefully followed by several satellites, which, at least in principle, track all degrees of freedom. GPS consists of 24 satellites orbiting at an altitude of 20,200 km and the radial velocity of the satellite with respect to the receiver is computed from the *ephemerides* (the reference orbit for each satellite) which are transmitted via the satellite message.

The GPS system may be used in a phase tracking mode for determination of position. At the time of writing we are aware of one buoy utilizing the phase tracking principle, reported in Davies *et al.*(1997) and Rossouw *et al.*(2000). However, phase tracking is less robust than Doppler measurements which gives the instantaneous vector velocity of the buoy. The Smart-800 directional wave buoy (Fig. 4.6) manufactured by Seatex ASA relies on Doppler measurements.

In order to obtain more precise Doppler shifts, and, hence, more precise measurements, GPS corrections (obtained either from a local reference station, satellite or by other means) are used in order to remove most of the error sources in the GPS data (Differential GPS mode). The GPS data

are transmitted from the buoy by way of a UHF link (430-450 MHz). The Doppler measurements are, in particular, affected by the rate of change of these errors, the main contribution to which is the Selective Availability (SA), which is the "noise" added by the operators of the GPS system. SA affects the satellite clock frequency and the transmitted navigation message (the ephemerides) leading to degraded satellite coordinates (position and velocity). The SA has recently been turned off.

Normally, the three buoy velocities are sampled at 1 Hz each for 17 min (1024 samples), but improved GPS receivers will allow for higher sampling rates. The logging interval of the time series is flexible. The buoy has a spherically shaped hull, with a diameter of 800 mm, weighs only 80 kg, and contains no moving parts. Also this buoy is a single point triplet device providing the spectrum and the four leading Fourier coefficients of the directional distribution. Since the the wave elevation spectrum has to be obtained by dividing the vertical velocity spectrum by the frequency squared, this has to be carried out with some care in order to avoid a blowup for the very lowest frequencies.

According to information on the Internet, *Makai Ocean Engineering Inc.* in Hawaii is developing a hybrid GPS and 3-axis accelerometer discus buoy which will measure all six degrees of freedom and should therefore be somewhat similar to the Norwegian buoys with the MRU. Three GPS receivers are to be used in an interferometric mode for the buoy's attitude and heading. No further information is however available at the time of writing.

We finally note that the Data Buoy Cooperation Panel of WHO-IOC maintains a web site of oceanographic buoy manufacturers (`http://www.dbcp.noaa.gov/dbcp/`).

4.2 Subsurface Instrumentation

Harald E. Krogstad

Subsurface instruments have a long history for wave measurements. The simplest instruments are high resolution pressure transducers which measure the pressure fluctuations due to the surface waves. The strong signal depth-attenuation with frequency severely limits the high frequency response, and surface elevation profiles, usually obtained by inverse filtering, are typically rather poor unless sophisticated non-linear methods are used. Spatially extended arrays of pressure transducers were the earliest directional instru-

ments, and these are still used for accurate detection of swell directional spectra (Tucker and Hardcastle, 1996). Due to the strong dependence of the transfer function on the wavenumber ($\sim e^{kz}$) the results from subsurface instruments are quite sensitive to the effect of a non-zero mean current.

Extended arrays are directionally sensitive, but for less precision, a compact set-up is more convenient, and over time several systems of so-called *Short Baseline Pressure Arrays* (SBPA) have been used (Howell, 1998). The SBPA dimensions are significantly smaller than the typical wave length, and the *Wave Watch 3D Digital Wave Gage* produced by *Civil Tek Inc.* in the US appears to represent the state of the art of this type of instrument. This is a triangular transducer pressure array with 1.8 m sides. The construction is robust enough to even withstand trawling. As with most contemporary instruments, the gauge has real time analysis capabilities and may store computed parameters for up to 13 months between deployments. The small size of the array enables a simplified directional analysis treating the setup as a single point elevation/slope instrument. We refer to Howell (1998) for further description of the system and the data analysis.

The pressure cell/current meter triplet is another well proven subsurface directional wave sensor. The accuracy is comparable to the SBPA, and numerous systems have been available since the mid-seventies. The depth limitations are similar to the pressure array and in addition current meters are prone to influences from nearby structures, offsets in the mounting and marine growth. The WADIC experiment (Allender *et al.,* 1989) had several pressure/current meters at different depths which made it possible both to investigate the change in the performance with depth and the assumptions about linear wave theory used in the analysis. Some influence from the mounting was however evident in the data (Forristall and Ewans, 1998).

Lee and Wang (1984) have discussed the analysis of bottom pressure data and recommend the use of simultaneous $p - u - v$ (pressure and current) data so that the effect of currents on wavenumber and hence attenuation can be calculated. In very shallow water the effect of non-linearity can also be important. Buchan (1993) also discusses this type of wave-measuring device.

Today, several self-contained units exist where the pressure sensor and the current meters are mounted on a steel rig. Three systems of this type are the *3D-WAVE Acoustic Current Meter* manufactured by *Falmouth Scientific* the *SeaPac 2100 Directional Wave, Tide and Current Gauge* made by *Woods Hole Instrument Systems, Ltd.*, and the *S4 Directional Wave Units* produced

Figure 4.7: The 3D-WAVE Acoustic Current Meter manufactured by Falmouth Scientific (*Photograph used by permission*).

by *Inter Ocean Systems, Inc.* The Falmouth Scientific stand-alone unit is shown in Fig. 4.7.

The InterOcean S4DW directional wave-current meter, see Fig. 4.8, measures high frequency (2 Hz) pressure and simultaneous current vectors. It also has the benefit of providing information on mean water depth and current which permits the accurate calculation of wave-number and wave-current interaction effects. The instrument is mounted on a frame for seabed deployment.

A system consisting of a four beam/one bin acoustic Doppler current meter was tested against a pressure transducer array with excellent agreement by Herbers *et al.* (1991). However, more advanced Acoustic Doppler Current Profilers (ADCPs) have a capability to measure the along-beam current component at a number of locations. Attempts to use horizontally looking ADCPs for wave measurements are reported in for example Pinkel and Smith (1987) and Krogstad *et al.* (1988). A more obvious choice would be to have the ADCP looking upward from the sea bottom, or even from a subsurface moored float below the wave zone. The uppermost measurement locations will then record the wave action, and the data, collected at about 1 Hz data rate, may be analysed as a spatial array. There have been several attempts to use ADCP measurements in this way (Terray *et al.*, 1990; Hashimoto, 1997; and Terray *et al.*, 1997), and the general impression is quite positive. The Maximum Likelihood algorithms and their refinements appear to solve data processing satisfactorily. ADCPs may be placed at larger depths than

Figure 4.8: The InterOcean S4DW directional wave-current meter (*Photograph used by permission*).

instruments measuring at the bottom, and vertical beams may also be used to measure the surface elevation directly (Terray *et al.*, 1997). Since the instrument will at the same time provide the mean current profile over the active water column, the effect of mean currents may be incorporated as described in Sec. 3.1.2.

4.3 Platform-Based Instrumentation

Harald E. Krogstad

A triplet of current meters and pressure cells is sometimes used on platforms as well and has properties similar to the stand alone systems described above. Wave staffs are also still used to some extent although these are being replaced by laser or radar altimeter measurements.

Radar and laser altimeters have been used to track the sea surface elevation from fixed platforms for a long time. The *EMI* laser altimeter is very accurate but the records may be degraded by sea spray and loss of track, resulting in a constant signal for parts of the wave cycle. The pentagon laser array used in WADIC (Allender *et al.,* 1989) worked reasonably well and produced accurate frequency spectra as well as directional spectra using the

Iterative Maximum Likelihood analysis method. The main drawback of this system is the price of the sensors, and we are not aware that cheaper laser based sensors are available.

Whereas the laser has a negligible footprint, the footprint of some of the radar altimeters used from offshore platforms is substantial and therefore severely attenuates the high frequency details of the recordings. The wave profiling differences between radar altimeters and buoys are discussed, *e.g.,* in Prevosto *et al.* (2000). Radar altimeters have been compared to lasers, wavestaffs and buoys in the WACSIS experiment off the Dutch coast (vanUnen *et al.*, 1998).

In the Netherlands, the company *Radac* is currently testing a compact *directional* sensor based on three radar altimeters. The same company is also involved in the development of hybrid sensors where the altimeter is combined with a marine radar.

4.4 The Air-Sea Interaction Spar Buoy, ASIS

Hans C. Graber, Mark A. Donelan and William M. Drennan

The development of the Air-Sea Interaction Spar (ASIS) buoy was driven by the need for measurements of atmospheric, wave and oceanic quantities very close the air-sea interface. Ideally, a suitable platform should be inexpensive and possess a flexible and modular design to accommodate different sensor configurations for high resolution, long term measurements. Several approaches have been tried in the past. These include the use of towers, large spar buoys, and small surface following buoys. Each of these platforms suffers from limitations imposed by the harsh marine environment.

The high stability of towers and large spar buoys (*e.g.* FLIP, Fisher and Spiess, 1963) results in them being limited to measurements well above (or below) the active wave zone. As the wave zone in the ocean is O(10 m) from the mean surface, measurements much closer to the surface are made at considerable risk to the sensors. In addition, the sensitivity of surface measurements (*e.g.* surface elevation) from such platforms will be limited by the high dynamic range required of the sensors.

Surface following buoys are commonly used for wave and near surface meteorological and oceanographic measurements. Buoy networks include those of the US National Data Buoy Center, which operates 3 m diameter and larger discus buoys around the US coasts, and the TAO array of 2.3 m Atlas moor-

ings, operated by the Pacific Marine Environmental Laboratory (US) in the Tropical Pacific. These buoys are attractive in that they offer the possibility of placing sensors close to the surface, typically within 2-5 m. However, their use for high resolution measurements is limited by the disturbance of the buoys themselves to both the wave and wind fields. Also, buoy motions and mooring forces can be large, resulting in considerable contamination of the measurements.

4.4.1 The Instrument Platform

The idea behind the ASIS buoy was to capture the advantages inherent in both the spar and surface following designs. The resonance frequency, ω, of a spar buoy is related to the ratio of the buoy's water-plane area, A, and the sum of its inertial and entrained mass, M: $\omega \propto (A/M)^{1/2}$. In a traditional spar design, a small ω ensures that the buoy is stable to all but the longest waves. For ASIS, the design goal is that the buoy follows the longer waves, and be stable only for shorter waves. ASIS uses a pentagonal cage of small spar columns so as to distribute the buoyancy around the perimeter rather than in a single central column. In addition to providing a righting moment for the buoy, the design serves to protect the sensors. For a given water-plane area, this arrangement results in more wetted area and hence increases ω. The pentagon (0.97 m radius) of spar columns (each 0.22 m in diameter and 3.5 m long) is linked roughly 2 m below the surface to a single 0.3 m diameter column (the 'stem') - see Fig. 4.9. The design resonance period is about 8 sec. In order to minimise the undesirable effects of a resonant spar system, the stem is terminated with a pentagonal drag plate (1 m radius) 7 m below the mean surface level. Further details of the mechanical design of ASIS are provided in Graber *et al.* (2000).

The ASIS buoy is designed as either a moored or free floating platform. In the former configuration, ASIS is connected via a 60 m surface tether to a secondary buoy, which is itself moored - see Fig 4.10. This isolates ASIS from forces on the mooring line. In the latter configuration, ASIS is drogued, with the current shear between the near-surface and drogue depths acting to keep ASIS pointed in a relatively constant direction.

4.4.2 Directional Wave Measurements From ASIS

Directional properties of the surface wave field are derived from measurements from an array of surface elevation sensors. At present these sensors

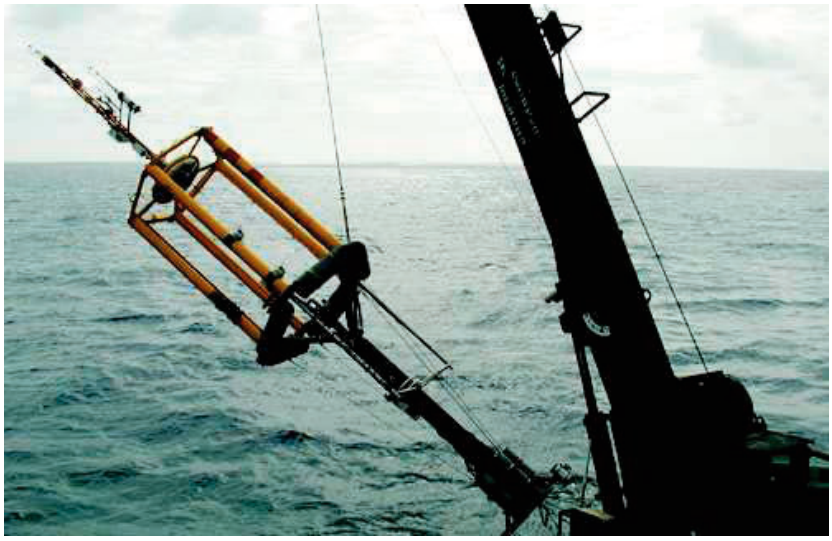

Figure 4.9: ASIS buoy being deployed from the R/V Ron Brown during GASEX, February 2001. For scale, the red and yellow stripes on the uppermost column are 0.30 m high.

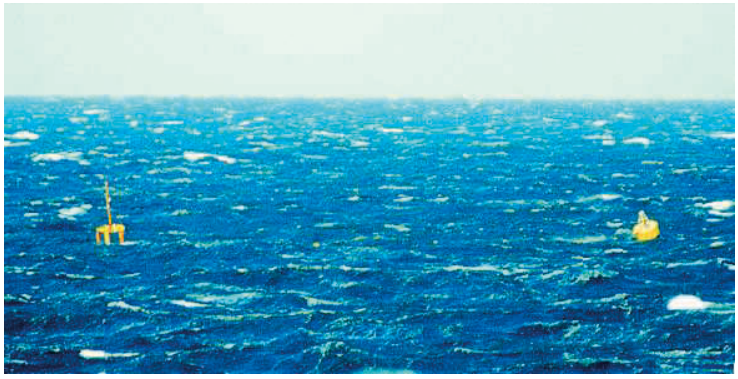

Figure 4.10: ASIS and tether buoys at sea during a Mistral event (FETCH experiment, Hauser *et al.*, 2003). The two buoys are connected by a 60 m floating tether, with the latter buoy moored to the bottom.

are capacitance wave gauges, made from 0.9 mm diameter high carbon steel coated with teflon. The number and spacing of the array elements can be tuned to a particular experimental goal. For most experiments to date, ASIS has been equipped with eight gauges: five positioned in the centres of the open faces of ASIS, forming a pentagon of 0.97 m radius, one at the centre and an additional two forming a right triangle with equal sides of 0.044 m. The six gauges (centre plus outer five) forming a centered pentagon are used to determine the directional distribution of waves of 2 m wavelength and longer; the interior triplet is used for shorter waves.

Many array processing techniques (*e.g.* MLM, WDM) have been developed to obtain directional information from wave gauge data, and a considerable literature has been devoted to intercomparisons of the results from various methods. As this is discussed extensively in Part II of this book, we will not deal with it further here. Instead we discuss the additional signal processing necessary to deal with array data from non-stationary platforms, such as ASIS.

On a moving platform, such as a buoy or ship, individual wave gauges undergo several types of motion: they heave with the platform, and they tilt as the platform itself tilts in the wave field. The response of the platform to the wave field is a function of the platform design, as well as the wave spectrum. Based on transfer functions developed during several field campaigns, ASIS largely follows surface waves with periods greater than 8 seconds, while acting largely as a stationary platform for shorter waves (Graber *et al.* 2000). The exact nature of the transfer function is not important here, because all 6 degrees of motion of the buoy are measured. These measured motion signals are then used to correct the measured surface elevations, converting them to a stationary frame of reference.

ASIS is equipped with a strapped down motion package located in a watertight housing at the foot of the buoy (see Fig. 4.9). The motion package consists of a compass (Precision Navigation TCM-2) and three orthogonally-mounted linear accelerometers (Columbia Research Laboratory SA-307 HPTX), each paired with a solid state angular rate gyro (Systron Donner GC1-00050-100) measuring rotational motion about the accelerometer axis. The accelerometers and rate gyros are mounted in a right-hand coordinate system, with the three components of the acceleration vector $\mathbf{a} = [a_1, a_2, a_3]$ positive towards the bow, the port side and upwards respectively. The measured rotational angles are pitch (θ), roll (ϕ), and yaw (ψ). Because the performance of the rate gyros declines at lower frequencies, low frequency angular motions are determined from the compass (in the case of yaw) or

from the tilt angles derived from the linear accelerometers (in the case of pitch and roll). In all cases the high and low frequency components are combined using a complementary filter with a crossover frequency of 0.04 Hz.

Using the measured buoy motion, the measured surface elevations, z_m, are converted to a stationary reference frame as follows:

$$\eta = z_m \cos\theta\cos\phi + \int\int (\mathbf{a}\cdot[-\sin\theta, \cos\theta\sin\phi, \cos\theta\cos\phi] - g)dtdt$$
$$+ \int [L_2(-\theta_t \sin\psi + \phi_t \cos\theta\cos\psi) - L_1(\theta_t\cos\psi + \phi_t\cos\theta\sin\psi)]dt. \quad (4.1)$$

Here, g represents gravitational acceleration, the subscript t represents time derivative, and the vector (L_1, L_2, L_3) represents the distance from the motion package to the water surface at a given wave gauge. The first two terms in the above equation represent respectively the surface displacement as measured by a wave gauge, corrected for the instantaneous tilt of the platform, and the vertical displacement of the motion sensors. The third term, which on ASIS is much smaller than the first two, accounts for the relative vertical displacement between the motion sensors and the surface due to the relative rotation motion. A derivation of Eqn. 4.1 is given in Anctil *et al.* (1994).

In Fig. 4.11, we plot an example of the surface elevation measured from ASIS. The data, from the 1999 Shoaling Waves experiment (SHOWEX), are representative of mixed sea conditions, with a decaying swell and building wind sea. The significant waveheight is 2.6 m. The actual surface elevation, η, is shown along with the three components from which it is calculated. It is evident that for the longer swell frequencies the dominant component is the buoy displacement itself. At the wind wave frequencies ($f > 0.15$ Hz), on the other hand, the vertical displacement measured with the wave gauges is dominant. This illustrates the ability of ASIS to follow the longer waves, while acting as a stable platform for the shorter ones.

Upon application of Eqn. 4.1, there is a further correction to be made. This arises from fact that while the wave gauges are in a fixed position within the array, the array itself changes its position and orientation within the fluid. On a moored ASIS, the configuration considered here, the principal array motion is a low-amplitude, low-frequency yawing. On a drifting buoy or ship this can also consist of a horizontal displacement through the fluid (*e.g.* Drennan *et al.* 1994). The effect of the yawing motion will be an artificial broadening of the directional width of the spectrum at all frequencies. The

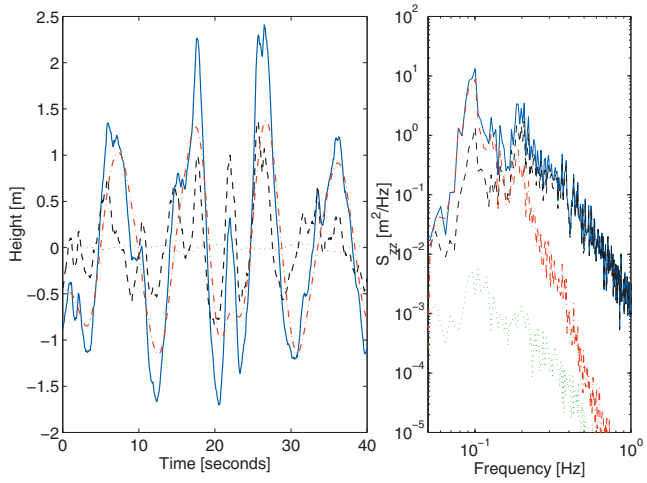

Figure 4.11: Sample time series (left panel) and spectrum (right panel) of surface elevation measured from ASIS on 99.11.03 1106Z, with $H_s = 2.6\,\mathrm{m}$. The four lines show the corrected surface elevation (blue solid) and its three constituent components: buoy heave displacement (red dot-dash), wave gauge signal (black dashed) and vertical displacement due to relative rotational motion (green dots).

degree of broadening is expected to be proportional to the magnitude of the yaw variations. For a typical run in stationary conditions, std(ψ) is of the order of 5°, and the effect on spectral width is small. However, in nonstationary situations, particularly those with turning winds, std(ψ) can be much greater, as ASIS turns to head roughly into the wind. For the purposes of studying the directional wave spectra, cases with std(ψ) $> 15°$ are excluded.

There are several approaches to account for the slow yawing of the array. The surface elevations from the six wave gauges of the centered pentagon define a second order surface. Given time series of yaw deviations from the mean, and of the instantaneous surfaces, time series of surface elevations at fixed positions can be determined. This has been done for several cases, but for typical values of std(ψ), the effects are minimal (i.e. the effects of the yawing on the spectral width are small). An alternative correction can be applied when using wavelet-based array processing techniques. Here directions and spreading are calculated at each time step, instead of as means over a fixed block. For these wavelet methods the instantaneous yaw is used to correct the wave directions at each time.

4.5 Stereo-Photography Techniques

Alain Weill, Christine Guerin, Danièle Hauser and Hélène Dupuis

Small-scale sea surface topography corresponding to horizontal scales ranging from centimeter up to meter scales, is important to document. Indeed waves of these scales are dominant in the process of supporting wind stress, they contribute to the signature in microwave remote sensing and acoustic signals, and to the gas transfer exchange.

Different techniques have been used in the past to analyze the small scale properties of the ocean surface. With classical photography of the surface Cox and Munk (1954a,b) used sun glitter surface information to provide quite fundamental information about the surface. However, after the work of these pioneers, this technique has not been extensively used, probably because it is severely constrained by weather conditions. Digital photography is now an opportunity to collect quantitative sea surface data more easily. Topography of the surface has been retrieved using stereo-photographic data by observing scenes perpendicular to the surface by Shemdin *et al.* (1988), but in their case the observed scales are of limited extent and very close to the observing platform. Airborne stereoscopy has been used by Holthuijsen (1983), but the scales considered are rather large.

Below we shall apply an old technique of stereoscopy (Karara, 1979) for deriving the surface elevation using a system of two commercial digital photographic cameras which can be mounted aboard oceanic vessels or fixed oceanic platforms. The system has been in use on several occasions since 1992. First, from the French oceanographic Vessel Le Suroit, during two experiments in the North Atlantic: SOFIA/ASTEX in 1992 (Dupuis *et al.*, 1993, Weill *et al.*, 1995) and SEMAPHORE in 1993 (Eymard *et al.*, 1996). More recently, it has been used from the French oceanographic vessel Atalante during the FETCH experiment in 1998 in the Mediterranean sea (Hauser *et al.*, 2003), and from the fixed oil platform Casablanca in the Mediterranean sea, during the WISE experiment in 2000 (Camps *et al.*, 2000).

4.5.1 Measurements and Data Processing

Experimental Set-up

Two commercial cameras (CANON POWERSHOT 600) are installed on the top bridge of the oceanographic ships or platform. The cameras have a focal length of 7 mm, and a half field of view of 24.48 degrees in the pointing direction. Typically, the horizontal distance between the cameras is four meters. From ships, the observation is performed in the direction perpendicular to the main axis of the ship. The cameras are installed in such a way that they point towards the surface with a small angle below the horizontal plane. The choice of this angle is a trade-off between the requirement of a good horizontal resolution, and the requirement of minimising the perturbation of the surface by the ship-wake. For the FETCH experiment (on ship) it was 7° below the horizontal plane, whereas for the WISE experiment (platform) it was 15.1°. The height of measurement was 12.5 m during FETCH, and 15.8 m during WISE.

The two camera system is driven by a PC-computer system. Digital photos of 832x624 pixels are recorded on a PC. The time interval between the acquisition of two successive pairs of images, is chosen by the operator. During our first experiments (SOFIA and SEMAPHORE), we chose a one minute interval. In the last experiments, two periods of acquisition were possible: 10 s or 2 min. Because the sea-surface is moving, observation of the same scene from the two cameras requires a good synchronisation between the two cameras. This was achieved with a synchronisation better than 20 ms.

Due to the perspective effect, the horizontal resolution (pixel size) is non constant within the observed area. Typically, it varies from 4 cm to 80 cm from the near-range to the far-range for the conditions of the FETCH experiment.

Principle of Measurement and Processing

We give here an example of the relationship between the coordinates of a point on the surface and the coordinates of the corresponding pixel in the image of each camera, taking into account the fact that the surface is not a plane. A general description of stereo measurement can be found for example in Carbonnel (1989).

Each point P on the surface, referenced by its horizontal (x_p, y_p) and vertical

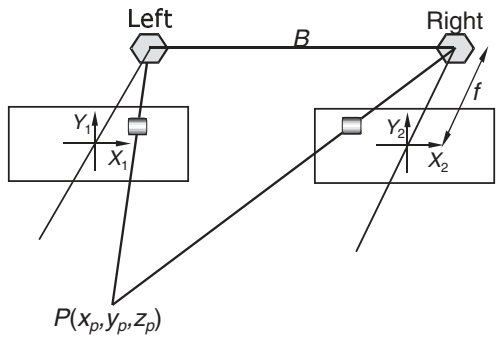

Figure 4.12: Sketch of the geometry of observation in stereo-photography. Here B is the distance between the left and right cameras and f is the focal distance. Each point P of the surface is referenced by its three coordinates (x_p, y_p, z_p). The corresponding pixels in the plane of the left and right images are shown as shaded squares with coordinates (x_1, y_1) and (x_2, y_2) for the left and right camera, respectively.

(z_p) coordinates, is seen by each camera (called 1 and 2). In the frame attached to the images, the coordinates of point P are (x_1, y_1), and (x_2, y_2), for images 1 and 2, respectively, see Fig. 4.12.

The computation of the 3 co-ordinates (x_p, y_p, z_p) of these homologous elements (same elements seen by the two cameras) is easy. The difference $x_1 - x_2$ is the disparity. It is the relative distance between two homologous points in the frame attached with the images, and is reduced to the parallax between the two pictures when there is no relief. From the knowledge of the disparity of the different homologous points one can estimate the 3D topography of the object.

Taking the configuration of two parallel cameras separated by a distance B, one can write:

$$x_p = (B/2)(x_1 + x_2)/(x_1 - x_2), \tag{4.2}$$

$$y_p = By_1/(x_1 - x_2) \tag{4.3}$$

$$z_p = Bf/(x_1 - x_2) \tag{4.4}$$

where f is the focal distance of the cameras.

The common surface observed from the two cameras covers more than 60% of each image, which is considered to be sufficient to perform stereo photography.

The off-line processing includes 5 successive steps: 1) luminosity and contrast adjustment; 2) geometric corrections; 3) homologous point search; 4) three dimensional co-ordinates associated with the sea level; 5) estimate of sea state parameters. Steps 3 to 5 are applied on a sub-part of the image, which excludes the borders (very close to the ship, sky part). Hence, topography and directional wave information is obtained from images of typically 685 x 190 pixels. This corresponds to a size of $40\,\mathrm{m}\times 40\,\mathrm{m}$. We describe hereafter the 5 steps applied on these images.

Luminosity and contrast adjustment. To combine the two images, one needs to have comparable histograms for the two pictures (luminosity and contrast). Since only a subpart of the complete image is useful in the analysis, luminosity and contrast adjustment is applied on a sub-domain of about 300 and 624 pixels for a typical picture of 832 by 624 pixels. The luminosity matrix A_{ij} of this sub-image is averaged along lines and columns to get the mean luminosity, which is subtracted from the raw picture to retrieve comparable histograms between pictures.

Geometric corrections. Due to ship movement, and particularly due to the roll and pitch, the real angle of view is modified by the attitude of the platform. Roll and pitch angles are determined by estimating, for each couple of images, the location and slope of the horizon line. The horizon line is determined from the brightness contrast between the sea and the sky. Then by simple geometric analysis the angles of view $\theta_1$and the tilt angle θ_2 are determined. These angles are used to determine the 3D surface in a reference geometry system.

Homologous point research: The determination of the coordinates x,y,z of a point on the surface requires that the coordinates of homologous points of the surface be found. This means that we must first determine the pairs of homologous points by associating each pixel from the first picture (image 1) to a pixel in the second picture (image 2).

For each pixel in image 1, we determine as a first guess, the position of the corresponding pixel in image 2 by assuming a flat sea and by using the geometric relations associated with the parallax effect for the disparity $x_1 - x_2$ for a flat sea,

$$x_1 - x_2 = \frac{Bf\lambda}{y\cos\theta_1 + h\sin\theta_1}, \tag{4.5}$$

with

$$y = h\left\{\left\{\frac{1}{\tan\theta_1} - \frac{y_1}{\lambda f \sin^2\theta_1\left(1 + \frac{y_1}{\lambda f \tan\theta_1}\right)}\right\}\right\}, \tag{4.6}$$

where h is the altitude of the camera with respect to the mean sea level and λ is the geometric factor relating the real scene and the camera picture and is a constant (specific to the camera).

Then, a window of 64x64 pixels is defined in image 2 (window 2) with x_2, y_2 as origin. Using a window of the same size in image 1 (window 1, with x_1, y_1 as origin), two-dimensional correlation functions between window1 and window2 are calculated. A matrix of 64x64 correlation coefficients is obtained. Correlation is calculated by using Fast Fourier Transforms. The maximum of the correlation coefficients provides the relative shift of window 2 in image 2, with respect to window 1 in image 1, so that the homologous point of (x_1, y_1) is determined in image 2. This procedure is rather time-consuming, so that in fact this process is not done for each pixel of image 1, but a resampling of image 1 is performed. For the results presented hereafter one point out of 10 or 5 is considered in the horizontal or vertical dimension respectively.

Note however, that a good correlation coefficient between points does not ensure that points are homologous. In particular in cases of low topography and homogeneous texture, good correlation values may be obtained for points without any relationship. In order to eliminate those points we choose to add the following criteria:

- the sea does not admit two points with the same coordinates (x,y) but different heights
- the parallax must strictly increase when sweeping the image from the horizon line to the ship.

We therefore eliminate pairs of points, which do not meet these criteria. This is necessary to avoid spurious results. However, this may lead to the result that some points are missing in the topography corresponding to the selected zone of the images.

Three dimensional coordinates associated with the sea level: The co-ordinates (x_1, y_1, x_2, y_2) of homologous points determined on the two photographs in the referential system associated with each picture, provide, in the same reference system, the 3D coordinates $x_p, y_p, z_{p.}$. In order to estimate the topography in an absolute reference system we have to rotate the co-ordinate system from the image-referenced system to the surface-reference system. This is done by taking into account the angle of view θ_1 (corrected from the roll) and the angle of pitch θ_2. In the new system one has

$$\{X\} = \{R\}\{X_p\}, \tag{4.7}$$

where R is the rotation matrix depending on θ_1 and θ_2 angles.

This is done for $\{X_p\}$ provided by one of the images (image 2), but it can be checked that the results are similar if $\{\mathrm{X}_p\}$ from image 1 is used instead.

Estimate of sea state parameters. Once the topography is calculated, the two-dimensional height distribution is computed, and used to calculate the height variance. The directional waveheight spectrum is calculated by using a two-dimensional Fast Fourier Transform (FFT) over the two-dimensional topography re-sampled with 64×64 points. Prior to applying the FFT, we first subtract the mean height which corresponds to the effect of waves larger than the dimension of the observed surface. Results provide complex values, from which the power spectrum is calculated. This spectrum is provided with a 180° ambiguity in direction for 64×64 values with minimum and increment values in wavenumber of approximately 0.157rad/m, for a size of 40 m × 40 m of the processed sub-image.

Illustration of results. Figures 4.13 to 4.16 present a typical product of the method. They correspond to the case of March 24, 16:08 UTC, during the FETCH 98 experiment. Figure 4.13 shows the pair of pictures and Fig. 4.14 shows the corresponding topography. A set of such topographic data is then used to compute statistical or spectral information on the surface. Figure 4.15 shows an example of a mean directional spectrum obtained by combining a set of 14 successive images covering the period 15:58 to 16:30 UTC on March 24. Within the averaging period, only samples including a large number of homologous points have been retained. Figure 4.16(a) shows the corresponding along-wind (solid line) and across-wind (dotted line) energy spectra. The non-directional spectrum (integrated over all directions) is shown in Fig. 4.16b.

Figure 4.16(a) shows that the main energy is concentrated in the along wind direction. The along-wind, across-wind and integrated spectra seem

Figure 4.13: Example of a pair of images (side-looking case) for March 24th, 1998. The width of the surface imaged by the system increases from bottom to top. For the bottom line, located at 20 m from the ship, it is about 20 m. The line located in the middle of the image (intersection between optical axis and surface) is at 100 m from the ship and its width is about 100 m.

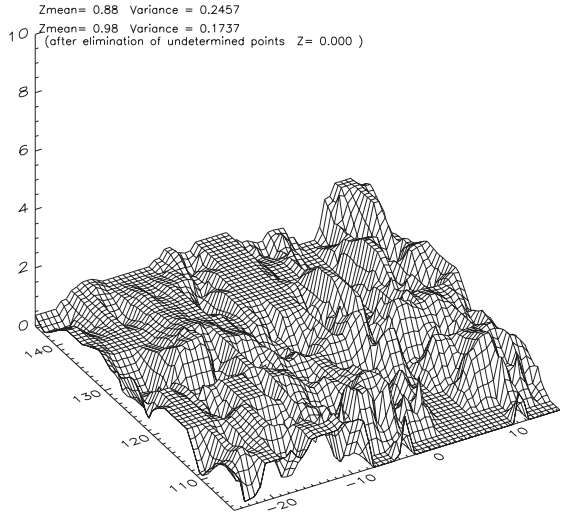

Figure 4.14: Topography of the sea surface corresponding to a sub-part of Fig. 4.13. This sub-part covers 40 m × 40 m and its nearest position from the ship is located at 30 m from the ship.

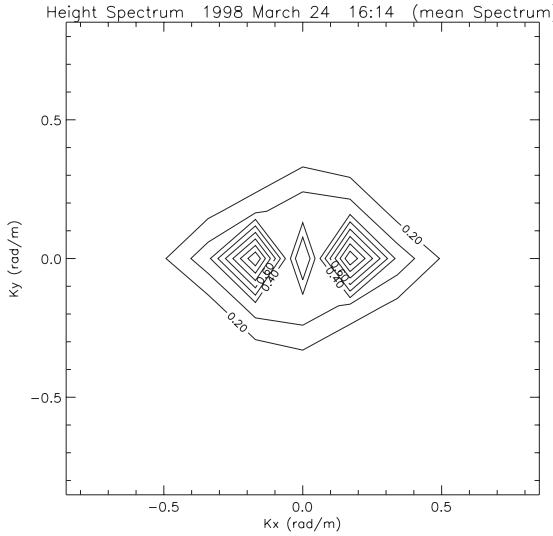

Figure 4.15: Two-dimensional spectrum derived from the topography of Fig. 4.13. The horizontal (vertical) axis corresponds to wavenumbers in the direction parallel (perpendicular) to the ship. Contours represent the energy density normalized by the value at the peak.

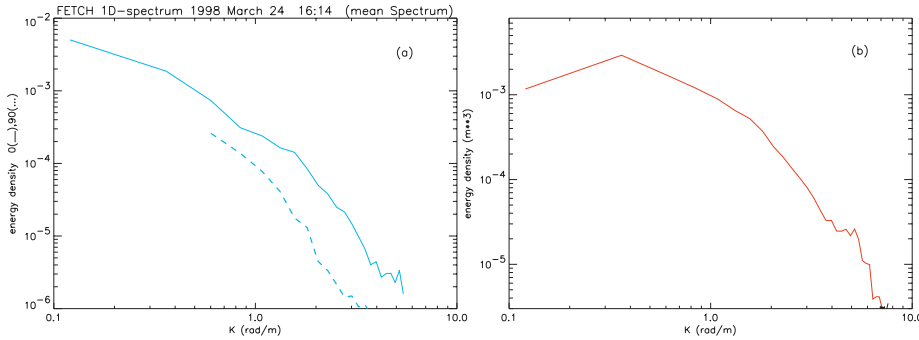

Figure 4.16: (a) Energy density in the along-wind (solid line) and across-wind (dotted line) directions. (b) one-dimensional energy spectrum (integrated over all directions) as a function of wavenumber. Same case as Figs. 4.13 and 4.14.

to indicate two regimes with different wave number dependencies.

It must be noted that a limitation of the method is associated with the undetermined surface elements inside the analysis domain which limits the number of degrees of freedom of spectra and suggests that other analysis techniques than spectral methods should be tested. However, in cases where the surface recovery is better than 90% the method used can be considered to be efficient.

4.5.2 Summary

A numerical stereoscopic method has been developed to derive the sea surface elevation over scales of about 40 m × 40 m. The accuracy on elevation is typically a few centimeters when combining a set of thirty consecutive photographs (one hour of measurements). For this topography, wave statistics and directional spectra can be calculated for wavelengths in the range 40 cm to 40 m. The main difficulty of the method is that the elevation of some points on the surface may be undetermined, due to the problem of finding homologous points in the couple of images. This occurs mainly when the sea surface is flat or close to large breaking events. However, the different criteria used in our processing help to increase the reliability of the method. New CCD systems with a larger number of pixels is certainly a good way to further improve the technique.

The method is unique in that the elevation of the surface is estimated by using spatial observations, as opposed to the methods presented earlier in this chapter. Hence, it avoids the problem of Doppler effects in the measurement of short waves, and provides spectral information directly in terms of wavenumber, which is preferred for comparisons with remote sensing measurements (see the following chapter). An interesting development for the future would be to perform an experiment combining stereo-photo measurements and other techniques such as laser or capacitance wave gauge arrays. This would allow one to further study the relationship between spatial and temporal observations of the statistics and spectral properties of the surface.

Acknowledgments

We acknowledge INSU (CNRS) for helping in the development of this instrument. Special thanks are due to J.P. Vinson, J.Y. Delahaye, F. Baudin for the technical help in the development of this system. Part of the work

has been undertaken, during engineer-school student placements, by F. Renaudon and E. Chaumont with the help of professor J-P. Frangi.

Chapter 5

Radar Wave Measurements

5.1 Overview

Susanne Lehner

Remote sensing techniques allow the measurement of ocean wave fields with both high resolution and large coverage. Ground-based and ship based sensors as well as airborne or space-borne systems provide information on the spatial evolution of ocean wave spectra, currents and near surface windfields.

A classification of remote sensing techniques can be carried out according to the frequency bands used for either active (the sensor transmits and receives signals) or passive (the sensor only receives signals) measurements, see Fig. 5.1.

Although some work has been done on optical measurements of ocean waves (Sec. 4.5), this chapter will concentrate on active radar remote sensing techniques. The main reason for this is the fact that acquisition of active radar data is independent of daylight and cloud conditions. They are therefore believed to be most suited for operational use as well as for many ongoing scientific investigations.

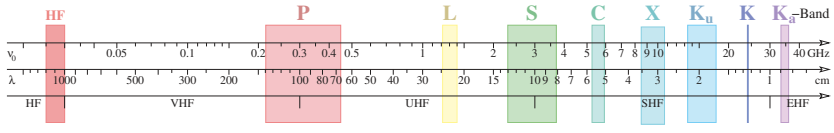

Figure 5.1: Radar frequency bands

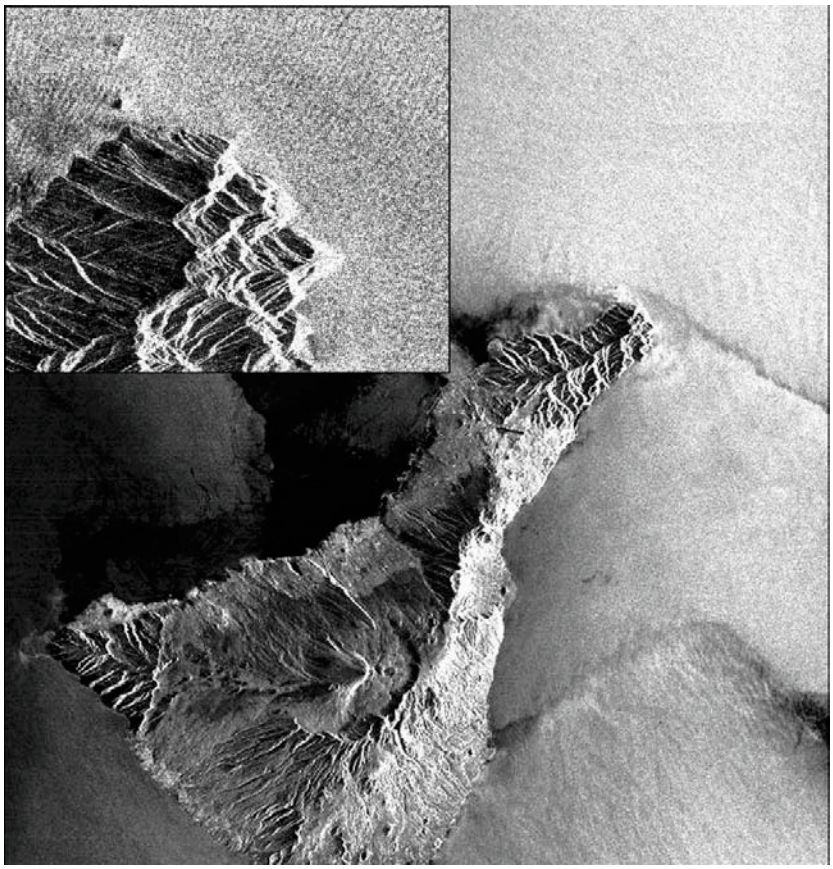

Figure 5.2: $100 \times 100\,\mathrm{km}^2$ ERS-2 SAR image of Teneriffe acquired on October, 13, 1992 at 11:42 UTC.

Table 5.1 gives an overview of various existing radar systems. The table shows a selection of acronyms and the different frequency bands, together with the measuring principles and the platforms that have been used. In addition Fig. 5.30 gives an overview of the satellite missions. An altimeter measures the distance between sensor and sea surface. A real aperture radar (RAR) provides a two dimensional image of the backscatter of the sea surface. While the resolution in range direction is very high (in the order of meters), the resolution in the perpendicular direction is only of the size of the antenna footprint. Therefore, RARs are mainly used on aircraft (e.g. the RESSAC, STORM). A marine radar also provides a two dimensional

Instrument (section)	Acronyms (selection)	Frequency Band	Measuring principle	Platform
Scanning altimeter (5.2)	SRA, SCR	Ka	Topographic map from accurate distance measurements	Aircraft
Marine Radar (5.3)	WAMOS	X	Backscatter modulation at large incidence angles	Ship, coast
Platform Doppler Radar (5.4)	MIROS	C	Backscatter from moderate incidence angles	Ship, platform
HF radars (5.5)	WERA, Pisces, CODAR	HF	Power spectrum of backscattered signal due to moving waves with range and azimuth discrimination	Coast
Non-Doppler Real Aperture Radar (5.6)	RESSAC, STORM, SWIMSAT	C, Ku	Backscatter modulation measured at moderate incidence angles, over 360° in azimuth	Aircraft, satellite (project)
Doppler Real Aperture Radar (5.7)	CORAR	X	Doppler velocity modulation in across-flight direction	Aircraft
Synthetic Aperture Radar (5.8,5.9)	SAR	X,C,L	Travel time (across track) Doppler history (along track)	Aircraft, satellite
Interferometric Synthetic Aperture Radar (5.8,5.9)	INSAR	X,C,L	Two SAR antennas in an along or across track configuration	Aircraft, shuttle, satellite (project)

Table 5.1: Remote sensing instrumentation.

RAR image. As the azimuthal resolution of a RAR would be about 4 km for space borne systems, they are not sufficient to image ocean waves as seen in Fig. 5.2. This problem is overcome by recording the amplitude as well as the phase of the backscattered signal using a synthetic aperture radar (SAR). As the phase contains the information on the Doppler shift due to the relative motion of the radar sensors with respect to the scatterers at the surface, processing of the raw radar data yields a high resolution image both in flight and range direction. As this processing is based on the relative movement of radar to scatterer, individual movements of the scatterers, e.g. due to orbital motions of the sea surface, lead to misplacing and blurring in the image and these have to be corrected for.

The first oceanographic radar satellite SEASAT operated in L-Band in the 30 cm wavelength range. Currently in orbit are C-Band satellites in the 6 cm range, marine radars used on ships or towers operate in X-Band at about 3 cm wavelength, the name HF radar speaks for itself. Satellite missions in the X and L band are in the planning stage.

For flat surfaces the radar beam gets reflected away from the receiving antenna, thus they seem black in the radar image, rough surfaces interact by Bragg scattering with the radar signal at the wavelength of the incoming wave. This the basis for all wind and wave measurements.

There are various measuring techniques based on radar emission. For some of them — spaceborne and airborne radars, and most of the marine radars — the method is based on the analysis of the backscatter intensity of the return radar signal. For the others (HF radar in particular), the method uses both the backscatter intensity and the Doppler spectrum (Doppler effect due to the surface motion of the waves). The mechanism that leads to a scattering of the electromagnetic waves from the surface is dependent on the incidence angle. At small incidence angles with respect to the vertical (less than about 15° to 20°), the main contribution to the backscatter is *specular* or mirror-like reflection, and the roughness scales, which govern the backscattering intensity, cover all scales from about 3 times the electromagnetic wavelength. In this case, the signal reflected from the surface increases when the roughness decreases (for flat surfaces). In contrast, at moderate incidence angles (from about 20° to 70°), the main process is the so-called "Bragg resonant process", which is generated by the waves on the surface which are of the same order of the electromagnetic wavelength. At these incidence angles (typically 20° to 80°) the radar backscatter increases with the surface roughness (i.e energy density of Bragg waves). At larger incidence angles (grazing angles above 70°), other processes affect the radar

backscatter, in particular shadowing effects, although at HF, ground-wave propagation and scattering is also dominated by Bragg resonance at near 90° grazing angles. For radars in the HF range, the backscattered signal provides "direct" information on the wavelengths of interest (because the Bragg wavelength is of the same order). In the other cases, like marine radars, airborne or spaceborne real or synthetic aperture radars to be considered below, the backscatter is related to short wavelengths, but its modulations are related to the wavelengths of interest (several tens of meters). These modulations are then analyzed in terms of properties of long ocean waves (longer than a few tens of meters). For systems that use the Doppler information of the backscattered signal, the principle is to relate the Doppler information to the wave orbital velocity that is in turn related to the wavelength.

Radar images taken at different wavelengths thus show different sea surface features corresponding to the energy at the respective wavelength. Long ocean waves are imaged due to their interaction with the short radar backscattering waves. A review of radar backscattering at the sea surface is given in the book of Geernaert and Plant (Plant, 1990) and by Plant (Plant, 1999).

Remote sensing is successfully used for operational purposes, *e.g.* the monitoring of ocean wave and currents fields around harbors using ground-based sensors or global measurements of wave parameters by using satellite systems. Spaceborne altimeter data are currently used at weather centres for assimilation into ocean wave models to improve wave forecasts. They do not provide, however, any information on the spectral description of the surface (only the significant waveheight and wind speed are provided by space borne altimeters). Significant progress has been achieved in the recent years to develop the analysis of synthetic aperture radar (SAR) data, in order to provide, on an operational basis, spectral information (wavelength and directionality). On a smaller scale, ground-based HF and marine radar data have been assimilated into regional wave models (Wyatt *et al.*, 2003). Synthetic aperture radar measurement system with several antennas provide the possibility of measuring in addition to the backscattered intensity, the digital elevation model and the current field of the sea surface.

Due to their high resolution, two dimensional remotely sensed data are widely used for scientific investigations. Apart from ongoing research to improve forecast models by assimilation of mean wave parameters, SAR images of ocean waves are used to deduce information on extreme waves, wave grouping, directional properties of wave spectra, and wave current interaction.

As an example of SAR imaging of ocean waves, Fig. 5.2 shows a $100 \times 100\,\mathrm{km}^2$ SAR image of Teneriffe acquired by the European remote sensing satellite ERS-1. The blow up in the upper left corner shows ocean wave refraction due to bottom topography. Apart from these local studies spaceborne data are used to analyze ocean wave dynamics on a larger scale, *e.g.* dissipation processes affecting swell propagation.

In the present chapter we give an overview of the basic technical principles of the different sensors as well as the inversion techniques used to derive directional ocean wave spectra. The potential and the limitations of the different sensors is discussed, and current and future developments of the respective systems are summarized, including satellite missions like ENVISAT or SWIMSAT.

Section 5.2 is about an airborne scanning altimeter using the time from transmission to reception of a radar signal reflected from the sea surface as the most straightforward measurement parameter to determine the sea surface elevation.

Then, section 5.3 introduces marine radars, which provide a time series of radar images of the sea surface and thus measurements of three dimensional wavenumber-frequency spectra and currents with a coverage of several kilometers. The Doppler radar described in section 5.4 is another platform-based wave measurement system.

Using two spatially separated antenna stations, the ground based HF-radar (Sec. 5.5) is used to measure two dimensional wave spectra, currents and wind fields on a synoptic scale.

The sections 5.6 and 5.7 deal with different airborne real aperture radars (RAR) with scanning beam antennas providing measurements of two dimensional wave spectra and wind fields.

The last three sections, 5.8 – 5.10, deal with the spaceborne synthetic aperture radar, which measures two dimensional wave spectra and wind fields with very high resolution in both dimensions, but is sensitive to imaging effects due to the motion of the sea surface. This section also gives an introduction to interferometric SAR systems, i.e. systems with several antennas, which provide additional information on currents and orbital velocities.

5.2 Real-Aperture Topography-Measuring Radar

Edward J. Walsh and C. Wayne Wright

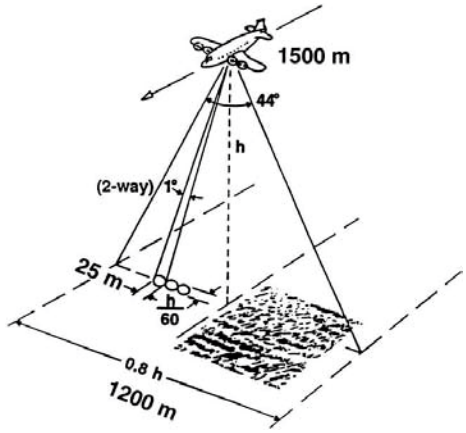

Figure 5.3: Altimeter measurement geometry of the SRA. The specific numbers refer to the Hurricane Bonnie flight on 24 August 1998.

5.2.1 The Scanning Altimeter

The NASA Scanning Radar Altimeter, SRA (Walsh, 1991; Walsh *et al.* 1996), and its predecessor, the Surface Contour Radar (Walsh *et al.* 1985, 1989), were designed primarily to measure the energetic portion of the directional wave spectrum by generating a topographic map of the sea surface. The SRA general measurement geometry is shown in Fig. 5.3; the specific numbers refer to the flight into Hurricane Bonnie aboard a NOAA hurricane research aircraft on 24 August 1998.

The SRA sweeps a radar beam of 1° (two-way) half-power width across the aircraft ground track over a swath equal to 0.8 of the aircraft height, simultaneously measuring the backscattered power at its 36 GHz (8.3 mm) operating frequency and the range to the sea surface at 64 positions. The scan rate was 8 Hz during the Bonnie flight. It is presently set to 10 Hz, but faster scan rates are possible. In real-time, the slant ranges are multiplied by the cosine of the incidence angles (including the effect of aircraft roll attitude) to determine the vertical distances from the aircraft to the sea surface. These distances are subtracted from the aircraft height to produce

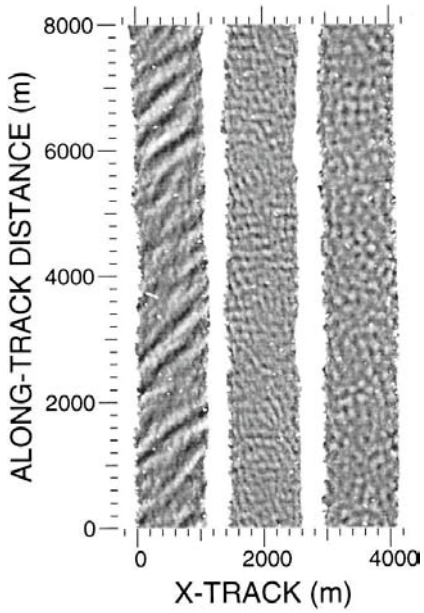

Figure 5.4: Wave topography maps produced by the SRA in different regions of Hurricane Bonnie displayed with the same gray-scale coding (dark troughs and light crests). The isolated white speckles and the white line at 3700 m along-track and 200 m cross-track are data dropouts. The left and middle images involve about 550 cross-track scan lines acquired over 71 s. The right image involves only about 400 scan lines acquired over 51s because the aircraft ground speed was faster.

a sea-surface elevation map, which is displayed on a monitor in the aircraft to enable real-time assessments of data quality and wave properties.

5.2.2 Wave Topography

Figure 5.4 shows three examples of SRA wave topography maps using the same gray-scale coding (dark troughs and light crests). The time sequence of the data progresses up the page for the three 8 km segments, independent of the actual flight-line orientation. At the flight-level of 1.5 km, the SRA swath width was 1.2 km and the images are in proportion. The topography for the left image was obtained while the aircraft was travelling northward about 150 km north of Hurricane Bonnie's eye. The waves were predominantly swell propagating toward 330°, and the periodic oscillation in the height

of the waves associated with the narrow spectral width is apparent in the image. The significant waveheight H_s was about 10 m, and the dominant wavelength was about 300 m.

The NOAA/AOML/Hurricane Research Division surface wind analysis indicated that the wind at this location was directed toward the west at about 40 m/s. A secondary, shorter wavelength system generated by this wind can be seen propagating from right to left across the image, parallel to the wind direction.

The wave topography in the middle image of Fig. 5.4 was obtained while the aircraft was travelling south-eastward about 30 km south and 40 km east of the eye. The significant waveheight H_s was over 6 m, and the wave field was bimodal with approximately the same energy in the two components. The sea surface topography for the image on the right was acquired travelling northward about 120 km east and 90 km south of the eye, where H_s was over 7 m and the wave field was trimodal.

To emphasize that the images of Fig. 5.4 represent wave topography, Fig. 5.5 shows the surface elevation profiles from cross-track positions 30 and 37 (of 64 starting from the left side of the SRA swath) for the interval between 5 and 8 km on the left image in Fig. 5.4. Cross-track position 30 goes through the highest position on the crest of the large wave, 11 m above sea level. It misses the deepest part of the trough, which is lined up directly behind the highest part of the crest in the direction of wave propagation. Cross-track position 37, which is about 100 m to the right of position 30, profiles the deepest part of the trough, which is 8 m below sea level. The crest-to-trough height was 19 m with a 178 m separation, which corresponds to a 356 m wavelength.

5.2.3 Directional Wave Spectra from the SRA

The sea-surface topography measured by the SRA is interpolated to a uniform grid and transformed by a two-dimensional FFT. The artifact spectral lobes are deleted, and the real lobes are Doppler corrected. Wright *et al.* (2001) describe these processes in detail.

Figure 5.6 shows the three wavenumber directional wave spectra generated from the SRA wave topography images of Fig. 5.4. The spectra are in a north, east (k_n, k_e) linear wave number coordinate system with direction being toward that in which the waves are propagating. The thick radial rays indicate the orientations of the boundaries of the half-planes used to

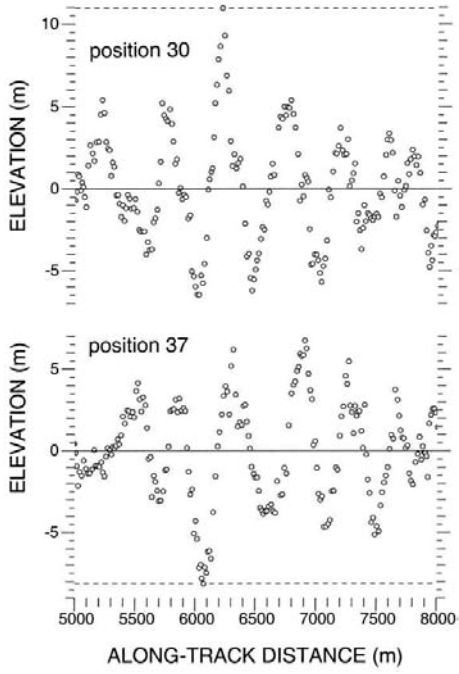

Figure 5.5: Surface elevation profile from cross-track positions 30 and 37 (of 64 starting from the left side of the SRA swath) for the interval between 5 and 8 km on the left image in Fig. 5.4.

eliminate the spectral artifact lobes. To be able to deal with complex situations (such as real spectral lobes in opposite half-planes), there are separate boundaries for wavelengths less than 150 m and greater than 150 m, although in the three spectra shown here, the inner and outer half-planes have the same orientation. All spectral energy is deleted on the artifact side of the boundary, but subsequent Doppler corrections sometimes push the contours past the boundaries.

Two dashed radials are used to partition each spectrum into one to three components. The three pairs of numbers separated by a slash in the header of each spectrum are the waveheight (in meters, equal to four times the square root of the spectral variance within the partition) and the dominant wavelength (in meters, determined from k_n and k_e at the highest spectral value within the partition). The sequence of the three sets of numbers is in clockwise order around the spectrum. When only two wave components

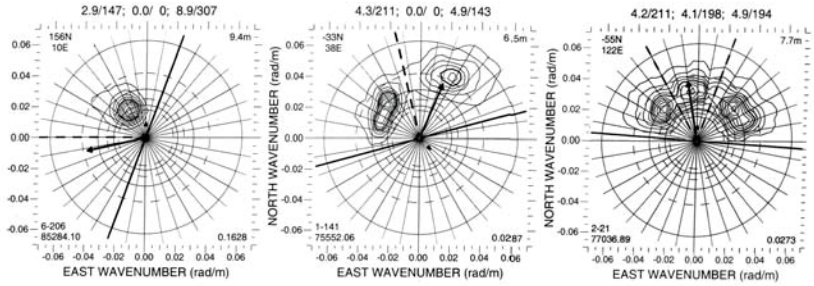

Figure 5.6: SRA directional wave spectra generated from the wave topography shown in Fig. 5.4. Each spectrum contains nine contours, linearly spaced from 10 percent to 90 percent of the peak spectral density of that spectrum, which in $m^4 rad^{-2}$ equals the number in the lower right corner times 81 342. The half-power contour is thicker.

are identified, the two dashed radials are placed coincident between them so the middle elements in the header are zero. When only one component is identified, the two dashed radials are place coincident at one of the half-plane boundaries.

The location north and east of the eye (in kilometers) is indicated in the upper left corner of each spectrum. The total H_s is shown in the upper right corner. In the lower left corner are the flight segment (1 through 10) and spectrum number, separated by a hyphen, and the second of the day (with 86400 s added after midnight).

The outer solid circle on each spectrum indicates a wavelength of 100 m, and the inner circles correspond to wavelengths of 200 m and 300 m. The three dashed circles correspond to wavelengths of 150, 250, and 350 m.

Because the SRA directional wave spectra are represented in terms of ocean wave propagation vectors in wave number space, the wind is referenced to the direction toward which it is blowing rather than the meteorological convention, to make it easier to assess differences in the wind and wave directions on the plots. The arrow superimposed on each spectrum points in the downwind direction given by the NOAA surface wind field. The wind speed values were divided by 1000 before plotting so a speed of 40 m/s corresponds to a length of 0.04rad/m (or approximately the 150 m wavelength circle). The arrow head at a distance 0.01rad/m from the origin always points in the aircraft flight direction.

At 156 km north of the eye (left spectrum of Fig. 5.6), the spectrum was

quite narrow. The header indicates that the swell system in that spectrum has a 8.9 m H_s and 307 m dominant wavelength. The secondary wave system seen propagating toward the west in the left image of Fig. 5.4 is not apparent in the spectrum because its peak energy density was less than 10%. Even though the energy density for the wind-driven sea was below the lowest contour in spectrum, the numbers in the header indicate that the H_s associated with the wind direction was 2.9 m. The wind sea spectrum would have been much broader than the narrow swell spectrum. The wind-driven waveheight was probably higher since the partition boundary was only 12° clockwise of the wind vector, but, for simplicity, the partitioning process was restricted to two radials for boundaries.

The middle spectrum of Fig. 5.6 was approaching the radius of maximum wind and a 143 m wind-driven component is almost at right angles to the 211 m northwest-propagating swell. Fifty-five kilometres south and 122 km east of the eye the wave field was strongly tri-modal (right spectrum of Fig. 5.6), with each of the three components having about 200 m wavelength and over 4 m H_S. The spectral peaks were spread over 100° and the span of the half-power spectral width was about 145°. This would likely be a particularly dangerous location for a boat, since the total H_s was 7.7 m and it was not possible to keep the bow pointed into the approaching waves. An animation of the Hurricane Bonnie wave spectra can be seen at http://lidar.wff.nasa.gov/sra/chs2000.shtml.

5.3 The Marine Radar

J.C. Nieto Borge and Konstanze Reichert

Common marine X-band radars (Table 5.1) may be used as a remote sensing tool to survey ocean wave fields (Atanassov *et al.* 1985; Young 1985). These devices are easily mounted on travelling ships, off-shore platforms, as well as on-shore stations. The present section is based on experience with and developments of the operational marine radar system WaMoS (*WAve MOnitoring System*), see Nieto Borge *et al.*, 1998, Hessner *et al.* 2001.

The measurement of ocean waves with marine radar is due to the interaction of the electromagnetic waves with the sea surface ripples caused by the local wind. This interaction produces a backscatter phenomenon, which is detected by the radar antenna, showing the wave pattern on the radar screen. The pattern is commonly known by sailors as *sea clutter*, and it is

suppressed for navigation purposes, an example of sea clutter image can be seen in Fig. 5.7. Sea clutter is thus the marine radar signal needed to obtain the sea state characterization.

This section deals with the techniques for sea clutter analysis in order to obtain sea state. The method is based on the analysis of the sea clutter's spatial structure and its temporal evolution delivering wave directional spectra, as well as the related sea state parameters, such as significant waveheight, wave period, wave direction, surface current, etc.

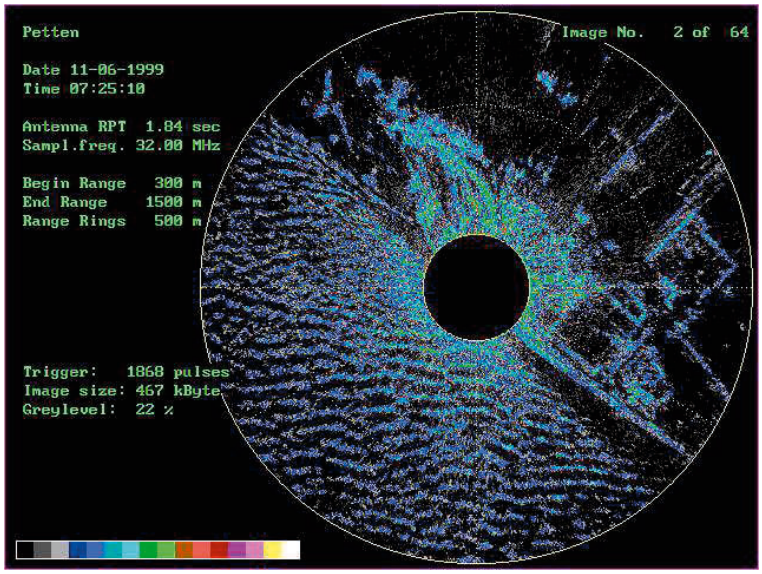

Figure 5.7: Image of a wave field measured by a marine radar. The analog radar video signal was digitally sampled with a *WaMoS II* A/D system. The radar antenna is located in the centre of the image, near to the coast line. The dotted rings give the distance every 500 m, the dotted lines correspond to the angle sectors with a resolution of 30°. In addition, this image shows the wave diffraction phenomena due to variable bathymetry in areas close to the coast line.

The minimum requirements to obtain wave measurements from a marine radar are:

- Antenna rotation speed: 32 *r.p.m.* (or faster).
- Pulse length: 80 ns (or shorter).

- Antenna length: 2.5 m (or longer).
- Azimuthal resolution: 0.8° (or narrower).

In addition, a fast analog/digital converter must be used to sample the analog radar video signal permitting the derivation of the sea state parameters in real time (Dittmer, 1995).

5.3.1 Effects on the Marine Radar Wave Field Images

Marine radar data sets are composed of temporal sequences of consecutive sea clutter images. The sampling interval of this image time series is the antenna rotation period. The spatial resolution of each image is given by the antenna aperture and the pulse length.

Compared to air and space borne remote sensing systems, navigation radar images cover smaller areas but images of the sea surface are obtained at a temporal rate.

Different phenomena appear in the marine radar image, contributing to the final sea clutter shown in the radar screen (see Fig. 5.7):

- *Range dependence*: The radar image intensity decreases when the range increases and this introduces an intensity trend in the measured image if nor compensated for (Croney, 1970).
- *Azimuthal dependence with the wind direction*: It has turned out that the intensity of the image depends on the wind direction. In particular, the return is higher in the directions opposing the wind (Hatten, 1998).
- *Wind speed dependence*: The image intensity increases with wind speed (Hatten, 1998).
- *Azimuthal dependence of the wave propagation direction*: The wave image modulation is stronger along wave propagation direction than perpendicular to it (Reichert, 1994).
- *Tilt modulation*: The tilt modulation is related to the effective slope of the waves. Facets with an orientation close to the antenna direction produce higher backscatter, and therefore the image spectrum for high wavenumbers is enhanced by the tilt modulation (Ziemer and Günther, 1994; Nieto Borge, 1997).

- *Shadowing modulation*: Shadowing occurs when higher waves hide parts of the surface from the radar antenna and is a non-linear phenomenon in the imaging mechanism. This modulation is particularly important in marine radar imaging due to the grazing incidence and the horizontal polarization (Nieto Borge, 1997; Seemann, 1997).

- *Hydrodynamic and orbital modulation*: This is related to the modulation of the short waves (the ripples) when they are riding on the long waves. The modulation causes changes of the backscatter over the long waves, and hence in the visible modulation of the image (Alpers *et al.*, 1981).

5.3.2 Analysis of Marine Radar Data

Inference of the sea state from time series of marine radar images requires inverse modelling methods. However, in addition to obtaining the wave spectrum, the technique also has the additional benefit of providing an estimate of the surface current. As discussed in Chapter 2 for linear wave theory, a steady current $\mathbf{U}$ modifies the dispersion relation as

$$\omega(\mathbf{k}; h, \mathbf{U}) = \sigma(k; h) + \mathbf{k} \cdot \mathbf{U}, \tag{5.1}$$

where $\sigma(k; h)$ is the intrinsic wave frequency. This modification of the dispersion shell shows up in the data and is used to deduce the surface current.

In more detail, the wave spectrum and surface current estimation method consists of the following steps:

1. **Subimage extraction:** Once the sea clutter time series is measured, the next step is to extract an area where the assumptions made above hold. Hence, a subimage time series $\gamma(\mathbf{x}, t)$ is obtained. Figure 5.8 shows an example of marine radar subimage time series.

2. **Fourier decomposition:** The subimage time series of grey levels $\gamma(\mathbf{x}, t)$ is transformed into the spectral domain by using a three dimensional Fourier Transform. Hence, the so-called *image spectrum* $\chi_\gamma(\mathbf{k}, \omega)$ is computed.

   Due to the radar imaging mechanisms, the image spectrum χ_γ contains more information than merely the wave spectrum. There are three main contributions to the image spectrum:

   - Wave spectrum components (Young *et al.*, 1985).

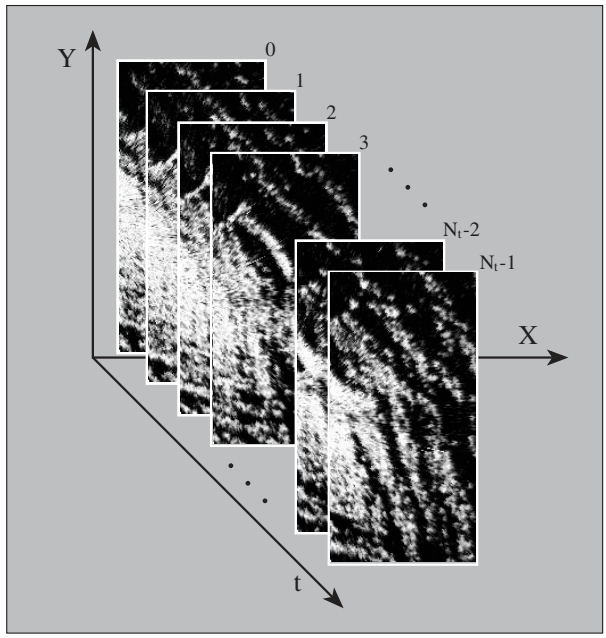

Figure 5.8: Example of a subimage time series measured by a nautical radar. The normal size of each subimage is 1 km ×2 km. For coastal application the subimage size has to be decreased. The data set shown in this figure corresponds to long swell measured in the Bay of Biscay.

- Higher modes of the wave components due to non-linear effects in the radar imaging (Nieto Borge, 1997; Seemann, 1997).
- Background noise due to the local roughness of the sea surface (Seemann, 1997).

In order to extract the wave information it is necessary to separate all the different contributions from the image spectrum $\chi_\gamma(\mathbf{k}, \omega)$. Hence, the inverse modelling technique is applied. The main assumption is to apply the linear theory for ocean waves. Hence, the wave components of the image spectrum is assumed to be located close to the dispersion shell $\omega(\mathbf{k}; h, \mathbf{U})$.

3. **Surface current estimation:** The two components of the surface current $\mathbf{U}$ are computed by minimizing the distance between the position where the spectral energy is located in the image spectrum and its theoretical position given by the dispersion relation (Young *et al.*,

1985). A more recent improvement of this method was carried out taking into account the spectral components of the higher modes of the dispersion relation (Senet *et al.*, 1996).

4. **Filtering the image spectrum:** The wave spectral components are separated from the rest of components by applying the dispersion relation using a bandpass filter (Young *et al.*, 1985). This filter is applied by integrating over all the positive set of frequencies to avoid directional ambiguities. Hence, a two dimensional wave number spectrum $\Psi_\gamma(\mathbf{k})$ is obtained

$$\Psi_\gamma(\mathbf{k}) \;=\; 2 \cdot \int_{\omega>0} \chi_\gamma(\mathbf{k},\omega)\, \delta(\omega - \sigma(k;h) - \mathbf{k}\cdot\mathbf{U})\, d\omega \tag{5.2}$$

where $\delta(\kappa - \kappa_0)$ is the Dirac delta function.

5. **Determination of the directional wave spectrum:** The function $\Psi_\gamma(\mathbf{k})$ is not the directional wave spectrum, because still some additional radar imaging mechanisms exist, which do not vanish due to the bandpass filter given by Eqn. 5.2. These imaging mechanisms are wave field modulations, such as wave tilting, shadowing, etc. The two dimensional wave spectrum $\Psi(\mathbf{k})$ is obtained by applying the inverse of a Modulation Transfer Function $|\mathcal{M}^{-1}|^2(k)$ to the two dimensional spectrum $\Psi_\gamma(\mathbf{k})$ (Ziemer and Rosenthal, 1987).

$$\Psi(\mathbf{k}) \;=\; |\mathcal{M}^{-1}|^2(k) \cdot \Psi_\gamma(\mathbf{k}) \tag{5.3}$$

This function is empirically parameterized as $|\mathcal{M}^{-1}|^2(k) \propto k^\beta$. From comparisons with buoy and marine radar results, as well as Monte Carlo simulations of radar images, the value derived for the exponent is $\beta \approx 1.2$ (Nieto Borge, 1997). Furthermore, the Monte Carlo simulations have shown that, for marine radar (grazing incidence and horizontal polarization), the main modulation mechanism is shadowing (Nieto Borge, 1997; Seemann, 1997).

For practical purposes (i.e. determination of the directional spectra and their related sea state parameters) Eqn. 5.3 provides excellent results, as shown by comparing marine radar results with *in-situ* sensors (Ziemer and Rosenthal, 1993 ; Nieto Borge, 1997 ; Hessner *et al.*, 2001). Nevertheless, as shown in (Nieto Borge, 1997), $|\mathcal{M}^{-1}|^2$ depends on k in a more complicated way and the detailed form is still an open question. In order to obtain more information about the modulation

transfer function $|\mathcal{M}^{-1}|^2$, an exhaustive intercomparison of marine radar data sets with other reliable in-situ measurements is needed. In addition, numerical simulations of wave field surfaces and their related radar images would be valuable.

6. **Computation of other wave spectral representations:** Once the wave number directional spectrum $\Psi(\mathbf{k})$ is obtained, more common wave spectral densities and sea state parameters are derived, such as the *frequency-direction spectrum* $E(\omega, \theta)$, the *one dimensional spectrum* $S(\omega)$, etc. Fig. 5.9 shows an example of directional spectrum $E(\omega, \theta)$ delivered in real time by a marine radar station. The spectrum was estimated following the inverse modelling technique described above. The spectrum obtained corresponds to a bimodal sea state. Marine radars, as well as other measurement methods based on the imaging of the wave field spatial structure, is specially suited to detect such multi-modal sea states (Ziemer, 1991).

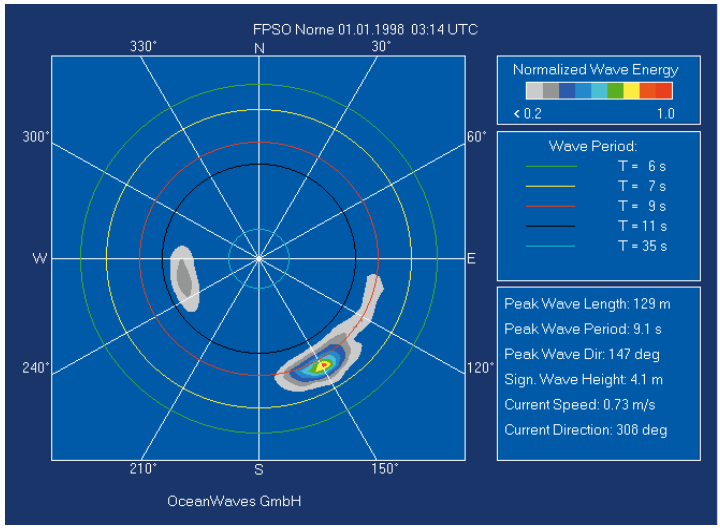

Figure 5.9: Example showing a real time measurement of a frequency-direction spectrum $E(\omega, \theta)$ obtained by the WaMoS system. This spectrum corresponds to a bimodal sea state, which is composed of two independent wave fields propagating with two different wave directions and periods. The measurement was taken in the northern North Sea.

7. **Significant waveheight determination:** The marine radar imaging mechanism depends on how the sea surface backscatters the incident electromagnetic field. That phenomenon is mainly induced by the local wind. Hence, the final grey level pattern of the radar image does not have a direct dependence on the significant waveheight. However, a method to infer waveheights from Synthetic Aperture Radar (SAR) images was developed by Alpers and Hasselmann (1982) and successfully applied (Brüning *et al.*, 1994a; Plant and Zurk, 1997). The basic idea of this method is to relate the measured signal-noise ratio (SNR) with the significant waveheight.

   Due to the existence of the background noise in the image spectrum (Seemann, 1997), marine radars can be calibrated in a similar way to SAR (Nieto Borge, 1997; Nieto Borge *et al.*, 1999). Hence, for a marine radar the significant waveheight is given by

$$H_s = c_0 + c_1\sqrt{SNR} \tag{5.4}$$

   where c_0 and c_1 are calibration constants. Common commercial marine radars are not specifically designed for wave measurements. The antenna gain, as well as the amplifier features are unknown. Hence, the *normalized radar cross section* is not a known parameter. So, the dynamical range of grey level values may change for each marine radar. This fact makes the calibration constants (c_0 and c_1) depend, in principle, on each radar installation.

   The constants c_0 and c_1 are determined after a calibration campaign, correlating significant waveheight estimations from a reference sensor (i.e. buoy, wave laser, etc.) with the root square of SNR derived from the marine radar analysis.

   For marine radars SNR is defined as

$$SNR = \frac{SIG}{BGN} \tag{5.5}$$

   where SIG is the spectral energy of the wave spectrum $\Psi(\mathbf{k})$ and BGN denotes the spectral energy of the background noise. The maximum correlation between H_s inferred by a marine radar and by a reference sensor has been found for the following definitions for SIG and BGN:

$$SIG = \int_{\mathbf{k}} \Psi(\mathbf{k})\, d\mathbf{k} \tag{5.6}$$

$$BGN = \int_{\mathbf{k},\omega} \chi_\gamma(\mathbf{k},\omega)\, d\mathbf{k}\, d\omega - \int_{\mathbf{k}} \Psi_\gamma(\mathbf{k})\, d\mathbf{k} \qquad (5.7)$$

Taking into account the Eqns. 5.6 and 5.7, it is clear that the ratio in 5.5 is always positive. So, the equation 5.4 is well defined from the numerical point of view.

Figure 5.10 illustrates an example of the significant waveheight derived by Eqn. 5.4, and a comparison with a reference *in-situ* sensor.

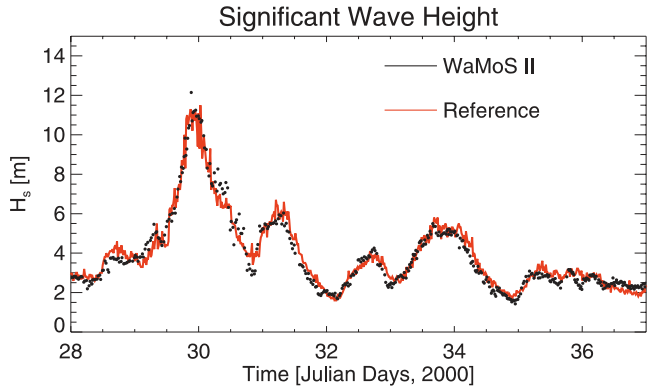

Figure 5.10: Example showing time series of significant waveheight estimated from the marine radar WaMoS (dots) compared to a wave laser in the North Sea (solid line).

5.3.3 Recent Developments

Temporal sequences of sea clutter contain more information than the spectral description of sea states. Some of the recent results are briefly described below:

- **Wind estimation:** Since the sea clutter intensity is highly dependent on the local wind, the local wind may be estimated. Following this idea, a good correlation between the background noise spectral energy BGN and the wind vector has been obtained from measurements on board moving ships (Hatten *et al.*, 1998).

- **Determination of bottom topography:** Analyzing the wave refraction of whole, non-homogeneous sea clutter images, the water

depth for each point has been estimated for coastal areas (Hessner *et al.*, 1999; Bell, 2001).

- **Water depth determination:** in a similar way to the surface current estimation, the water depth h can be obtained. This method assumes homogeneity in the wave field (Outzen, 1998).

- **Wave grouping analysis:** In the frame of the European R&D project *MaxWave*, marine radars are been used to obtain information about wave groupiness, as well as the determination of large individual waves (Hessner *et al.* 2001; Dankert *et al.* 2003).

5.3.4 Concluding Remarks

Common navigation radars are suitable to be used as a remote sensing tool for measuring wave fields. The measurement is possible due to the backscattering of the radar electromagnetic fields by the roughness of the sea surface due to the local wind. Hence, the presence of a minimum amount of wind (about 3 m/s) is necessary to measure wave fields with this sensor.

Marine radars measure all waves with wavelength and period longer than the theoretical Nyquist limits given by the spatial and temporal resolution of the antenna. Thus, for fast rotating antennas (*e.g.* 33.5 r.p.m.), waves with periods longer than 3.6 s can be detected.

Marine radars image local areas of the sea surface in space and time. Once the data sets are collected the image spectrum is computed by using a three dimensional Fourier decomposition. The directional wave spectra, as well as the sea state parameters, are derived from the image spectrum by applying an inverse modelling technique.

New developments on the analysis of wave fields with marine radars have been carried out recently. These methods extend the capabilities of marine radar to provide information other than the wave spectra. From temporal sequences of marine radar images, it is possible to derive parameters such as the wind field over the sea surface, the bottom topography, as well as wave grouping information in space and time.

Figure 5.11: Left: The Doppler wave radar MIROS seen from the front with six horn antennas. The unit is 0.83 m wide and 0.89 m high. Right: The Doppler radar mounted on a platform in the North Sea.

5.4 Platform-Based Doppler Wave Radars

Anne Karin Magnusson and Øistein Grønlie

The MIROS (*Microwave Radar Observing System*) is an example of a platform-based Doppler wave radar manufactured by the Norwegian company MIROS A/S. The system was developed around 1980 to encompass both wave and surface current measurements, and the operational principle is based on the Doppler shift in the backscattered radar signal due to the orbital wave velocity, which in turn is related to the wavelength and wave height by appropriate linear filters (Grønlie, 1995, Tucker, 1991).

A platform based remote sensing system for wave measurements is attractive for the offshore industry first of all because of ease of operation and the reduced maintenance costs. In addition, the high level of activity around platforms often hinders the use of *in situ* instrumentation. Fig. 5.11 shows a front and back view of the radar unit and Fig. 5.12 a sketch of the wave recording and data processing system. It is possible to operate Doppler radars from moving platforms, and a motion compensating system has been developed for the above system. The current motion compensator is utilizing the Seatex' Motion Reference Unit (MRU5), variants of which are also used in wave buoys (Sec. 4.1).

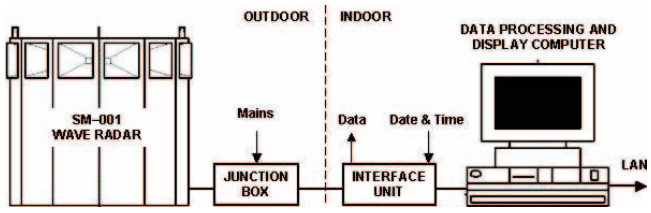

Figure 5.12: Typical data processing and presentation unit for an operational Doppler radar

5.4.1 Measuring Principle

The radar consists of an antenna, a microwave transmitter and receiver, and a signal processor. The directional wave spectra are measured in a pulsed Doppler mode, where linear wave theory is used to transform the deduced velocity spectrum into a wave height directional spectrum.

The MIROS Doppler Radar operates in C-band, that is, the frequency of operation is 5.8 GHz and the corresponding radar wavelength is 5.17 cm. The incidence angle of the radar beam is about 10°, and at such low grazing angles, the dominating scattering mechanism is Bragg scattering from surface ripples with wavelengths close to 2.6 cm. The wind speed at the surface thus has to be sufficient to generate the necessary ripples for the radar to operate.

The sea surface is illuminated with a short pulse, and the received echo is range-gated in order to exclude echoes from the sea surface outside a footprint defined by the pulse-length in range and the antenna beam-width in azimuth. The size of the footprint is of the order of 7.5 m in range and 200 m in azimuth. The footprint is therefore relatively small compared to the wavelength of the gravity waves of interest, but large compared to the scale of the scattering elements. The instantaneous Doppler shift of the echo is proportional to the radial component of the average water particle velocity, averaged over the footprint area.

In order to derive velocity information from the radar echo, the received signal is first frequency-to-voltage converted and low-pass filtered. Velocity "raw" data are collected as 128 s time series sampled at a rate of 2 Hz. During a complete measurement sequence, observations are taken in 6 directions with an angular increment of 30°. This gives a scan over 180° in azimuth, which is sufficient for a complete directional scan, since the radar observes

both approaching and receding waves simultaneously. For each time series, the complex amplitude spectrum is calculated using an FFT-algorithm.

The range of gravity waves to be measured is from about 30 m (limited by the radar range resolution), with no definite upper limit. The directional resolution is approximately equal to the angular width of the footprint (30°), since only the radial components of the orbital velocity of wave components inside the directional sector contribute significantly to the backscatter. However, the angular resolution is a function of wavelength, gradually approaching 90° for the very long swells.

The wave data collected from one fixed radar footprint have an inherent ambiguity of 180 degrees. In order resolve this ambiguity, data are collected *simultaneously* from two closely spaced footprints. The footprint spacing must be less than half the wavelength of the shortest gravity wave of interest. Using the cross power spectrum the ambiguity may be resolved for each frequency component.

The derived velocity spectra are transformed into a directional spectrum using in essence linear wave theory, although the manufacturer retains ownership of the transfer function, which has not been disclosed in full detail.

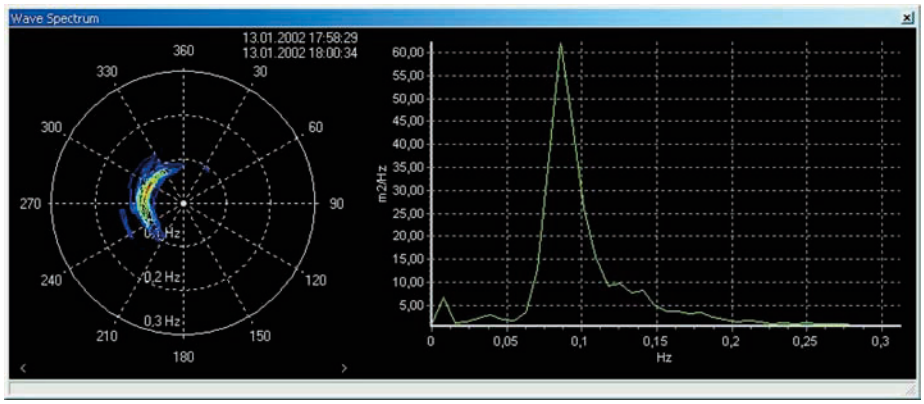

Figure 5.13: Directional wave spectrum as it appears from the MIROS data presentation software. The spectrum was recorded at the Heidrun wave field in the Norwegian Sea with a significant wave height around 6 m.

The final directional wave spectrum is formed by averaging over consecutive scans. The number of scans used for one measurement has varied since 1984, and is currently set so that the directional spectrum is updated every 15 minutes. Frequency resolution is 40 equidistant frequency bands ranging

from 0 to 0.31 Hz. An example of a directional spectrum from MIROS is shown in Fig.5.13.

Validations of the MIROS system have been published in Magnusson (1987a and b), Dobson and Dunlap (1999), and recent intercomparisons between the radar and a directional wave buoy is presented in Part II of this book.

5.5 HF radar systems

Lucy R. Wyatt

Ground wave HF radars are located on the coast providing measurement of radio signals backscattered from locations out to 50 to 300 km from the coast depending on radio frequency. These radars transmit and receive vertically polarized radio signals, either pulsed or frequency-modulated, that can propagate beyond the horizon in ground-wave mode as a result of the conductivity of the sea surface. Figure 5.14 shows the WERA ("Wellen Radar", Gurgel *et al.*, 1999) receive array during an experiment at Gijon on the north coast of Spain.

Groundwave systems have been used routinely for surface current measurement. The potential for wave measurement has been developing over the last ten years. Such measurements require a larger signal-to-nose level than current measurements and hence are available over more restricted ranges.

Figure 5.14: The setup of the HF radar WERA at the Spanish coast

Skywave systems use the ionosphere to observe the sea at over 1000 km from the radar system and are often located inland. Because scatter from the ionosphere introduces additional Doppler shifts to the backscattered

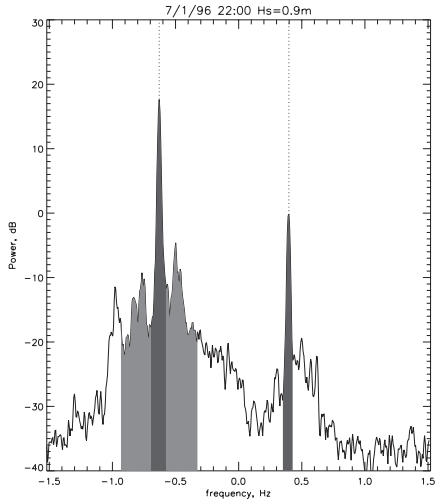

Figure 5.15: Typical low sea-state HF radar Doppler spectrum. Black shaded areas are the first order peaks in this case indicating an offshore wind, dark grey shows the region of the second order continuum used for wave measurement. The spectrum would be shifted to the right of the dotted lines if there were a current towards the radar and vice versa.

signal, operational use has been primarily restricted to surface wind direction measurements and will not be discussed further here (see, *e.g.* Young *et al.* (1997)).

HF radars transmit high frequency (HF 3-30 MHz) radio waves (Table 5.1) which are scattered from ocean waves in all directions with some scattered towards the radar receiver.

The largest contribution to the received signal has been shown (Crombie, 1955, Barrick, 1972) to be due to scatter from ocean waves of half the radio wavelength travelling directly towards or away from the radar (when the transmit and receive sites are co-located) according to whether the wind is blowing in the half plane towards or away from the radar. This produces two peaks in the Doppler power spectrum at a frequency equal to the ocean wave frequency of these Bragg-matched waves. This Doppler frequency is positive if the wave is propagating towards the radar and vice-versa. These peaks can be seen in the Doppler spectrum shown in Fig. 5.15. Their relative height is related to wind direction. If there is a surface current present there is a shift

in peak frequency which is used to measure surface currents (see e.g Paduan and Graber, 1997) and is removed before the data are processed for wave measurements. The rest of the power spectrum consists of a continuum, due to nonlinear wave interactions and scattering processes, and a noise floor. A number of approaches have been developed to provide a theoretical formulation for the power spectrum in terms of the ocean wave spectrum (Barrick and Weber, 1977; Robson, 1984; Walsh and Srivastava, 1987). The perturbation solution developed by Barrick (1971) and Barrick and Weber (1977) is most commonly used and is the basis of all existing HF radar wave measurement.

A number of different radar systems have been used for wave measurement, *e.g.* Pisces (Shearman and Moorhead, 1987, Wyatt, 1990b), OSCR (Wyatt and Ledgard, 1996) and WERA (Gurgel *et al.*, 1999). Pisces operates in the lower half of the HF band (4-18 MHz) and was designed for wave measurement to ranges of 150 km from the coast with a spatial resolution of about 10 km^2. OSCR and WERA both operate at higher HF frequencies (25-30 MHz) and OSCR was designed specifically for surface current monitoring within 40 km of the coast. Both of these have spatial resolution of about 1 km^2. These are all phased array systems. For these the problem of extracting wave measurements is rather easier than is the case for compact antenna systems of the CODAR type (Lipa *et al.*, 1990) where spatial homogeneity in the wave field over a wider area is required.

5.5.1 The Scattering Model

The two peaks in Fig. 5.15 are referred to as first-order peaks because they can be described by the first order solution of a perturbation analysis of the interaction between electromagnetic and hydrodynamic waves. This first order relationship between the power spectrum of the back scattered signal (after radar demodulation) and the ocean directional wavenumber spectrum is described in Barrick (1972), Weber and Barrick (1977), Barrick and Weber (1977). In this discussion the second order parts of the spectrum on either side of the two first order peaks are referred to as sidebands and there are four of these in each spectrum. The sidebands on the zero Doppler side of the first order peaks are referred to as inner sidebands and the others as outer sidebands. Lipa and Barrick (1986) and Holden and Wyatt (1992) present the mathematical formulation for the analysis of second order ocean wave interactions. The last two deal with the solution in the case of finite depth from which the Weber and Barrick work can be derived in the limit

of deep water. The second order electromagnetic analysis is referred to in Lipa and Barrick (1986), Barrick (1971) and is based on the method of Rice (1951).

The resulting equations are presented in Wyatt (2000). A large number of comparisons between the Doppler spectrum obtained by integrating the equation for a given ocean wave spectrum measured using a buoy and the Doppler spectrum measured by the radar at the location of the buoy have been made. In many sea states the agreement between them is good and this has motivated attempts to invert the equation. The equation does not do a good job of describing measured spectra at the peak of storms (Wyatt, 1995a, 1998). The spectrum measured using a radar beam looking into (or away from) the wind direction is significantly enhanced at second order Doppler frequencies over that determined using the equations. Wyatt (1995a) reported that the breakdown of the theory depended on the directional properties of the wave spectrum and these effects are also seen in the OSCR and WERA data. Work (Kingsley *et al.*, 1998) has described the shape of the WERA Doppler spectrum as sea-state increases when looking roughly into the wind and has shown that the slope of the second order spectrum appears to saturate at a significant waveheight of about 4 m. The consequences for the accuracy of wave measurements are described in Wyatt *et al.* (1999) and are discussed further below in Part II, Section 5.2. The main effect is an overestimation of short wave amplitude and, until a new theory emerges, this can probably be dealt with by imposing a waveheight dependent upper limit on the range of ocean wave frequencies for which the inversion is carried out. The alternative is to use a lower radio frequency where saturation will occur at a higher significant waveheight.

5.5.2 The Inversion Problem

The Pisces, WERA and OSCR systems have all been developed as dual-radar systems to avoid problems of direction and amplitude ambiguities that can otherwise arise. Empirical algorithms for extracting significant waveheight and mean period from the Doppler spectrum have been developed (see Wyatt, 2002 for a discussion). These can be used with single-radar systems but the amplitude of the backscattered signal depends not just on significant waveheight but also on the angle between the main wave propagation and the radar look directions. The amplitude is much lower when the radar is looking perpendicular to the main wave propagation direction. It is difficult to develop a robust single-radar significant waveheight estimator

that can deal with this case. A second radar looking at the same area of sea from a different direction can resolve this ambiguity.

The equation used for wave directional spectra measurement is a nonlinear first kind Fredholm equation. Five methods that attempt a solution to this equation have been developed. Three of these remove the non-linearity in the integral equation (i.e. linearise) in order to apply linear integral equation methods: Lipa (1977), Wyatt (1990a), Howell and Walsh (1993). These will be referred to as BL, LW and HW respectively. BL and HW find a solution for the first five Fourier coefficients of the directional distribution whereas LW finds the directional wavenumber spectrum on a wavenumber grid. The fourth method is an optimisation technique developed by Hisaki (1996) to solve the non-linear problem. Recently a Bayesian method has been developed by Hashimoto and Tokuda (1999). The LW method has been extended to tackle the non-linear problem (Wyatt, 2000) but no significant improvements in accuracy were found. The LW method makes use of Doppler spectra measured at the same location from different directions using two radar systems. The HW and Hisaki methods can be used with either a dual or a single radar system but in the latter case provide a reduced range of parameters and the accuracy of these have not been published.

The LW method has been subject to exhaustive testing (Atanga and Wyatt, 1997, Wyatt 1990a, 1991, 1995b, Wyatt and Holden, 1992, 1994, Wyatt and Ledgard 1996, Wyatt *et al.*, 1999, Krogstad *et al.*, 1999b, Wyatt *et al.*, 2003) and, in comparisons with wave buoy data, good accuracy in a range of wave parameters determined from the directional spectrum has been demonstrated.

Linearising methods

Close to the first order Bragg peaks the spectrum is generated by combinations of long waves propagating in all directions, and waves of the same order as the first order Bragg wave and propagating in roughly the same direction. Except in very low sea states these short waves can be assumed to be generated by the local wind and hence modelled with a wind-wave model. This can take the form of a k^{-4} or f^{-5} (or similar) wavenumber or frequency model as is used in the BL, HW inversions or by using a Pierson-Moskowitz spectrum as is used in the LW model when additional information is required to provide the spectral peak. This is obtained using significant waveheight and mean period found directly from the radar spectrum (Wyatt *et al.*, 1985) to determine a wind speed and hence the spectral shape. In

addition a model of the directional distribution is required. In the BL and HW inversions all short waves are assumed to be in the same direction as the first order waves so the directional distribution cancels when the second order is scaled by the first order. The LW inversion extends the range of Doppler frequencies by using a model of the directional distribution around the mean direction to account for the resulting increased range in directions of the short wave components. A method to estimate the parameters of a shortwave directional model has been developed (Wyatt *et al.*, 1997). These two-scale models apply over limited Doppler frequency ranges which reduce as the water depth decreases (Holden and Wyatt, 1992).

LW Linear inversion method

The results presented here and elsewhere in this book use the LW method and hence this is discussed in this section. This method is described in detail in Wyatt (1990, 2000) and Atanga and Wyatt (1997). It is an iterative scheme which solves the direct problem (i.e. integrates the linearised equations for a given wave spectrum) at each iteration and then modifies the wave spectrum at each wavenumber according to the difference between the measured and integrated Doppler spectra at Doppler frequencies influenced by the wavenumber. The modifications at each wavenumber are weighted by the contribution that wavenumber makes relative to all other wavenumbers that contribute at the Doppler frequency. The wavenumbers used in this process are sampled at $\sim 15^\circ$ intervals along the Doppler frequency contours obtained from the delta function constraint in the equation and from the radar signal spectral analysis which sets the discretisation of Doppler frequency. The iterative scheme is initialised with the Pierson-Moskowitz model and directional distribution that was used in the linearisation procedure. The integrations are carried out for each frequency bin within the limited Doppler frequency ranges referred to above and are restricted to the two sidebands surrounding the larger Bragg peak for each of two radar measurements from the same location. Nearest neighbours from the other sideband and radar are identified and used in the adjustment process to ensure that information from more than one sideband and more than one radar are used in the solution for each wavenumber. These nearest neighbours identify the Doppler frequency, wavenumber and propagation direction of the wave closest to the wavenumber vector whose amplitude is being adjusted.

The method produces directional wave spectra on a non-uniform grid of wavenumbers. These are averaged into wavenumber-direction bins, con-

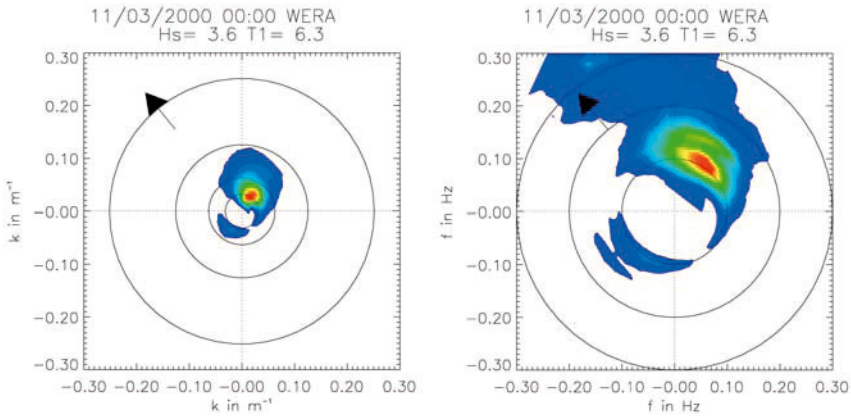

Figure 5.16: Directional spectra measured by the HF radar WERA at the Norwegian coast (Hs in metres and $T1 = Tm01$ in seconds). To the left is shown the wavenumber spectrum with circles shown at wavelengths of 200 m, 100 m, 50 m and 25 m. The directional frequency spectrum is shown to the right. The arrows show radar measured wind direction. The spectral peak is at a wavelength of about 200 m and period of about 9 second propagating towards the north-west. Winds are offshore, generating waves at higher frequencies in the wind direction as can be seen in the frequency spectrum. The colour coding is 20 equally spaced intervals from 0 to the maximum. The windwave peak has an amplitude about 20 percent of the maximum.

verted to directional frequency spectra using the dispersion relationship and then integrated to provide the frequency spectrum and parameters of the directional distribution, *e.g.* mean direction as a function of frequency. Methods to analyse the spectrum directly from the non-uniform grid have been developed (Isaac and Wyatt, 1997) but are not yet capable of handling large quantities of data in an operational way. Current work is directed at developing techniques that should allow solutions on uniform grids and thus simplify the partitioning problem. Fig. 5.16 (left) shows a wavenumber spectrum obtained using WERA at the Norwegian coast. The corresponding directional frequency spectrum is shown in Fig. 5.16 (right). Fig. 5.17 shows WERA measurements of significant waveheight and wind direction across the region of measurement at the same time.

The method has been successfully applied to data collected at a range of radio frequencies (*e.g.* Wyatt and Holden, 1992, Wyatt and Ledgard, 1996, Wyatt *et al.*, 1999). The range of Doppler frequencies used limits the range

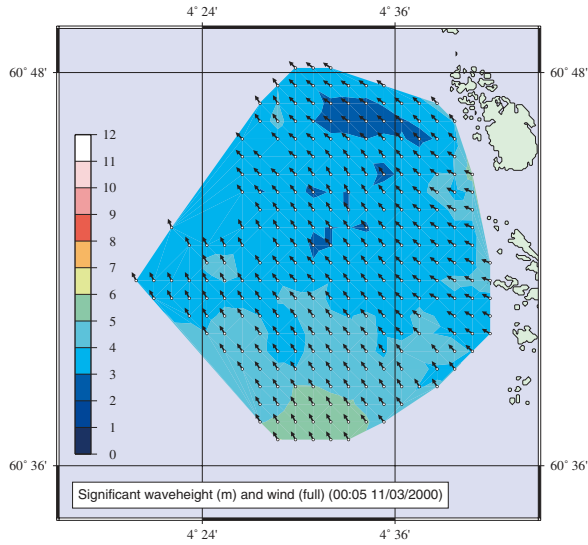

Figure 5.17: Significant waveheight and wind direction over the measurement region at the time of the directional spectra shown in Fig. 5.16.

of ocean wave frequencies for which a solution is found. At 9 MHz the upper limit is about 0.3 Hz and at 27 MHz, about 0.38 Hz.

5.6 Directional Spectra from Real-Aperture Radars

Danièle Hauser and Céline Quentin

The name "real-aperture" radar (RAR) is chosen to distinguish this type of observation from the "synthetic aperture" radar (SAR). In both cases (real-aperture and synthetic-aperture radar), the principle is to use a microwave emission from a radar on a platform (aircraft or satellite) pointing towards the sea surface. The intensity of the electromagnetic signal reflected from the surface (characterised by the backscatter coefficient) is mainly dependent on the small-scale roughness generated by the small wind-waves (a few centimeters). In both cases (RAR and SAR), the principle used to estimate

wave spectra is measurement of the modulations of the backscatter signal intensity associated with the long waves (wavelengths larger than a few tens of meters). Resolution in the radar look direction is typically the same for SAR and RAR (a few meters to a few tens of meters).

Spectral analysis of the modulation of the backscatter coefficient over a certain area yield wave-number spectra of the waves, provided that the transfer function between radar modulation and surface modulation is known. The interest of this approach, usually used from aircraft or satellite, is that it may cover a large spatial area and can be used to document the spatial variation of the spectral characteristics of the waves (energy density as a function of wavelength and direction) along the platform track.

The first difference between the RAR technique and the SAR technique is that the resolution of the radar in the direction perpendicular to the look direction is quite different. In the first case (real-aperture technique), the resolution in the azimuth direction is relatively coarse (at least several hundred of meters). In the second case - synthetic aperture technique with a side-looking beam with respect to the platform track- the signal processing applied to the Doppler information provides a fine resolution in the along-track direction (of the order of 10-20 m). In the case of a real-aperture radar, modulations of the backscatter coefficient are obtained in the direction of look of the radar beam (see Fig. 5.19). A scanning beam antenna is necessary to measure the modulations in each angular direction φ.

The second difference between RAR and SAR is in the transfer function which relates the modulation spectrum to the wave spectrum $\Psi(k, \varphi)$. For RAR the modulation spectrum is linearly related to the slope spectrum of the long-waves when a small incidence angle is chosen (typically less than 20°). For SAR in the same incidence angle conditions, this transfer function is much more complicated and often non-linear. Indeed, for SAR, there is an additional non-linear contribution due to the fact that the analysis technique of synthetic aperture uses the Doppler information to get a high resolution in the azimuth direction. In the case of a moving surface like the ocean, this Doppler shift is not only due to the displacement of the platform, but also to the motion of the scatterers on the surface. This induces Doppler mis-registrations in azimuth (along-track), distortion of the image spectrum and a strong cut-off in the azimuth direction. This effect is proportional to the range-to-velocity ratio of the platform and is maximum for azimuth-travelling waves. For present missions (ERS, Radarsat, ENVISAT) this ratio is high (about 120 s), limiting the information extracted from these SARs in the azimuth direction to long wavelengths (above 150 to 200 m).

This explains why the RAR technique remains an interesting technique. It is an alternative to SAR, for estimating two-dimensional wave spectra from airborne or satellite. An airborne system called RESSAC ("Radar pour l'Etude du Spectre de Surface par Analyse Circulaire") has been developed in France in the 90 s (Hauser et al, 1992a). The system is derived from the one developed by NASA, and called ROWS (Jackson et al, 1985a). The good results obtained from this system in various field campaigns (Hauser et al, 1992a, 1992b, Hauser et al, 1995, Hauser and Caudal, 1996, Eymard et al, 1996, Hauser et al, 2001) as well as those obtained by the NASA group (Jackson et al, 1985a-b, Jackson, 1987, Jackson and Jensen, 1995) incited us to propose a similar system called SWIMSAT (Surface waves Investigation and Monitoring from SATellite) on-board a satellite (Hauser *et al.*, 2001).

In the following, we first present the principle of measurement, the airborne RESSAC system, and illustrate with some results obtained from this system. Chapter 8 in Part II of the present book shows comparisons of the directional information provided by RESSAC and by in situ measurements (a Directional Waverider and an array of capacitance wires).

The development of a coherent RAR (CORAR) developed in the US is described in the following section. In the last section, we also present the project for the satellite-borne system, SWIMSAT, based on the same principle as RESSAC.

5.6.1 The RAR Principle of Measurement

By using a small incidence angle (typically less than 15°), a large footprint (typically of several hundred of meters in both elevation and azimuth direction), and a fine range resolution, it is possible to measure the modulations of the radar cross-section due to the long-waves. These modulations are associated with the local tilt of the surface and the fact that the backscatter coefficient is a function of local incidence angle. Modulations are maximum when the radar beam is aligned with (or opposite to) the direction of propagation of the long waves. It is recognised (Jackson et al, 1985 a,b, Hauser et al, 1992a) that in this configuration (low incidence angle, large footprint with respect to the wavelength of the waves to be measured), the density spectrum of the modulation of the backscattered signal $P_m(k,\varphi)$ is linearly related to the slope spectrum $k^2\Psi\,(k,\varphi)$ of the waves, for wavelengths larger than about 40 m:

$$P_{\,m}(k,\varphi) = \frac{\sqrt{2\pi}}{L_y}\alpha^2 k^2 \Psi(k,\varphi) \tag{5.8}$$

where L_y is the width of the footprint in the azimuth direction, k is the wavenumber of the waves, φ their travelling direction, and α is related to the fall-off of the normalised radar cross-section σ_0 with incidence angle θ,

$$\alpha = \cot(\theta) - \frac{1}{\sigma_0}\frac{\partial \sigma_0}{\partial \theta} \tag{5.9}$$

In α, the derivative of σ_0 is dependent on the small-scale roughness; i.e. wind-conditions. Therefore, it must be estimated for each spectrum. It can be estimated either directly from the radar data (using the measured dependence of σ_0, versus incidence angle, Eqn. 5.9), or indirectly by using an independent measurement of the significant waveheight, H_s, or of wind speed combined with an empirical relation between wind speed and the second term of Eqn. 5.9.

Eqn. 5.8 provides the radial spectrum, $F(k, \varphi)$, in one-look direction. By using a rotating antenna, the complete two-dimensional spectra can be obtained. However, due to the fact that the radar measurement is related to the tilt of the waves which are nearly symmetric with respect to their crest, the directional wave spectra are obtained with an 180° ambiguity in the direction of propagation.

5.6.2 The RESSAC System: Characteristics, Data Processing and Performance

Ressac is a C-Band (5.35 GHz) radar mounted on an airplane with an antenna looking towards the surface with a mean incidence angle of 14° with respect the vertical. It is presently used on board the airplane MERLIN-IV which is operated by the French Meteorological Office (Meteo-France). A large beam antenna is used ($14° \times 3.4°$) which, combined with a high flight-altitude (5800–6000 m), gives a large footprint (about 1500 m × 400 m). The antenna beam of RESSAC scans in azimuth (at a rate of 3 rotations per minute), so that the footprint sweeps the surface in all azimuth directions (0–360°). The signal backscattered from the surface is sampled with a high range (or horizontal) resolution (about 1.5 m in range, i.e. 4 to 12 meters in the horizontal).

The main technical characteristics of RESSAC are summarised in Table 5.2. Figure 5.18 shows the aerial component of the system mounted below the MERLIN-IV fuselage.

Two antennas are used because RESSAC is a radar based on a continuously transmitting wave form (FM/CW or Frequency-Modulated-Continuous Wa-

Figure 5.18: View of the antenna of RESSAC mounted below the fuselage of the MERLIN-IV. The small radome contains the transmitting antenna, The large one the receiving antenna. Both rotate around the vertical axis at a speed of 1 rotation per minute.

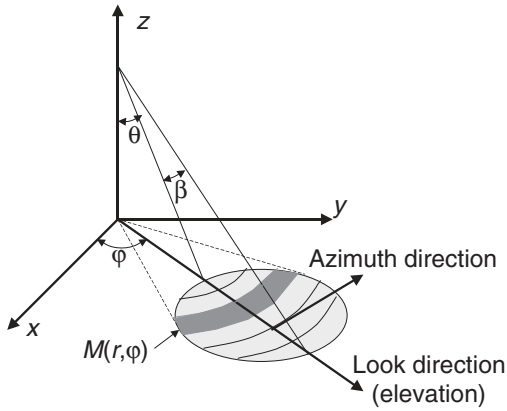

Figure 5.19: Scheme of the RESSAC geometry. The radar is located at an altitude z (usually about 6000 m). It points towards the surface with the mean incidence ($\theta = 14°$). The beam aperture in elevation (β in the figure) is of the order of 14°. The beam can rotate over 360°, thus scanning all the directions φ. The footprint is about 1500 × 400 m. The resolution on the surface ranges from 4 to 13 m from near to far range and is about 6 m at the footprint centre.

ve technology). The small and large radomes contain the transmitting and receiving antenna, respectively. Figure 5.19 illustrates the geometry of the RESSAC observations.

Data processing includes in each look direction (every $1-6\,^{\circ}$, depending on the time-integration choice), geometric corrections to account for the airplane attitude, the Fourier Transform of the auto-correlation function of the relative modulations of σ_0, and corrections to account for noise sources (speckle noise) and the impulse response function. The transfer function is then applied according to Eqn. 5.8. The coefficient α is estimated directly from the radar data (using the measured dependence of σ_0 versus incidence angle, Eqn. 5.8), but has been, on some occasions, post-calibrated using independent measurements of significant waveheight. Finally, an averaging procedure is applied to increase the number of degrees of freedom and decrease the statistical variability. The final product for $F(k,\varphi)$ is usually calculated for 64 wavenumbers covering a range in frequency from 0.05 to 0.25 Hz, in deep water. The energy density is averaged over 15 degrees in the φ direction (24 intervals from 0 to 360° with a 180° ambiguity) and 5 successive scans of the antenna. The time interval of this average (1 min40 s for a 3rpm rate) corresponds to a spatial extension of about 10 km along the airplane-track.

The final product is provided with a resolution in direction of the order of 15°, and a resolution in wavelength depending on the wavelength itself. Typically, it is of the order of 10% of the wavelength for 200 m waves. The statistical variability of the energy density level is defined by the number of degrees of freedom associated with each spectral component. This uncertainty also depends on the wavelength, the footprint, and the number of individual independent samples averaged per azimuth bin (and hence the rotational speed). In the present version of RESSAC, it is estimated to be of the order of $20-25\%$ per 15° azimuth bin in the energy-containing parts of the spectrum, somewhat larger than most *in situ* measurements. For the corresponding non-directional spectra, integrated over all azimuth directions, the number of degrees of freedom reaches $500-600$, depending on the wavenumber and on the situation. This is better than most *in situ* devices. A previous version of RESSAC, used until 1993, had a rotation speed of 1rpm. The number of degrees of freedom was therefore increased by a factor of 3, and the statistical variability of the non-directional energy density was less than 10%. However, the spatial sampling was 3 times less (one average spectrum every 30 km, instead of 10 km, along the flight-track). Hence, there is a trade-off to be chosen between the horizontal sampling for

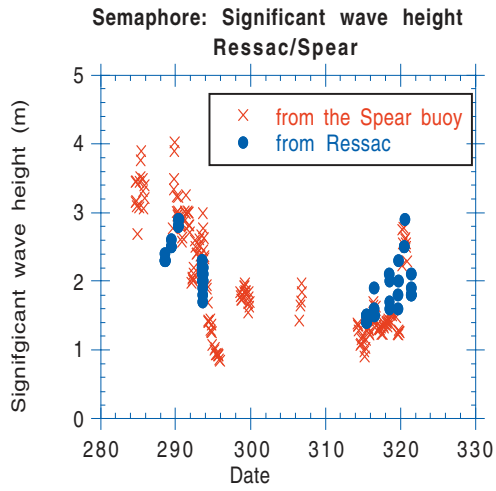

Figure 5.20: Comparison of significant waveheight obtained from RESSAC data and from a waverider (called SPEAR) during the SEMAPHORE experiment.

the two-dimensional spectrum, and the statistical variability in the energy density level.

Due to speckle noise limitations and to the principle of measurement, the present configuration of RESSAC provides reliable estimates of two-dimensional wave spectra for waveheights larger than 1 m and wavelengths larger than about $30 - 40$ m (somewhat dependant on their energy).

Figure 5.20 shows a time-series of significant waveheight obtained from the two-dimensional spectra estimated from the RESSAC observations during the SEMAPHORE campaign (Eymard *et al.*, 1996), and compared to a Waverider measurement.

During this experiment, which took place in the mid-Atlantic (Azores region), swell conditions were mainly encountered. Figure 5.20 shows that the total energy retrieved from the RESSAC data (here without using any calibration procedure of the α parameter) is in good agreement with buoy data.

Figure 5.21 shows frequency spectra obtained in a fetch-limited case in the North Mediterranean Sea during the FETCH campaign (Hauser *et al.*, 2003). This figure illustrates the ability of systems like RESSAC to measure the spatial evolution of wave spectra. In this particular case, the results clearly show the fetch-dependent behavior of the non-directional spectrum,

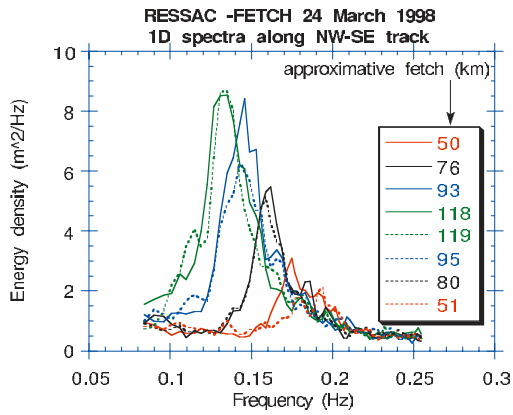

Figure 5.21: Non-dimensional spectra obtained from RESSAC in a fetch-limited case of March 24th 1998 (FETCH experiment). Spectra are plotted at various distances of fetch (see the insert) on the way going forward (solid line) and backward, from the coast to the open sea.

with an increase of the total energy and a decrease of the peak frequency with increasing fetch distance. The overshoot behavior of the wave energy is also clearly visible (more energy around the peak frequency for a given fetch distance than observed at larger fetch distances for the same frequency range). The consistency of the results is confirmed by the agreement of the results obtained along the flight track on the way going offshore (solid lines) and on the way flying back to the shore (dashed lines).

Figure 5.22 shows a comparison of one and two dimensional spectra obtained in a fetch-limited case (20 March 1998 during the FETCH campaign) from RESSAC, and from a wave gauge array installed on the ASIS Spar buoy (Graber *et al.*, 2000). Two-dimensional spectra from this device were calculated using the Maximum Likelihood Method and provided by the University of Miami (W. Drennan). This figure shows that RESSAC is able to detect waves of frequencies up to 0.25 Hz in these conditions. A reasonable agreement is found between RESSAC and the buoy for the one-dimensional spectrum in spite of a slight overestimate of RESSAC energy at low frequency. For the two-dimensional spectra, the main features are also in agreement (peak direction), but the shape of the RESSAC spectrum is narrower and shows more details than the buoy spectrum. A more complete presentation of comparisons between RESSAC and buoy measurements is presented is Chapter 8 of Part II.

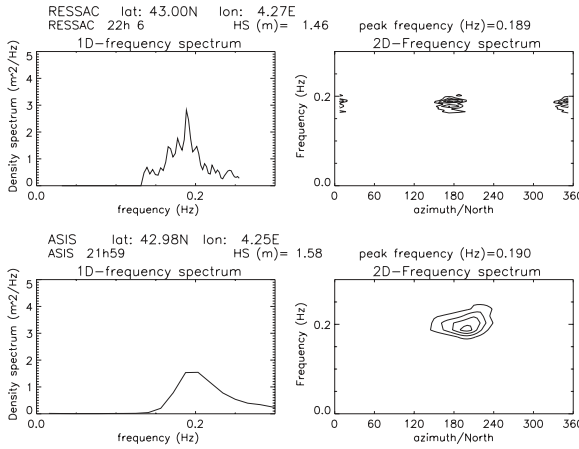

Figure 5.22: Comparison of one-dimensional (left panels) and two-dimensional (right panels) spectra from RESSAC (first line), and buoy data (second line). This case corresponds to the fetch-limited case of March 20th, 1998 of the FETCH experiment.

5.6.3 Real-Aperture Radar on Satellites

The technique used for RESSAC on an aircraft system can be adapted to satellite conditions. The first proposal of this kind was made by Jackson et (1985b), and Jackson (1987). More recently, the SWIMSAT project has been proposed (Hauser *et al.*, 2001), and its development in the context of a satellite mission is under study. With respect to airborne conditions, a satellite project has to take into account additional constraints, related in particular to the size of the antenna and to the signal-to-noise ratio. For SWIMSAT the proposal is to use a Ku-Band radar (13.6 GHz), an incidence angle of 10° and beam-aperture of $2° \times 2°$. With this geometry, assuming an orbit altitude at 500 km, this will give a footprint of about 18 km × 18 km, and a radius of swath of about 88 km. Table 5.2 summarises the main characteristics for the proposed SWIMSAT system, and Fig. 5.23 shows the geometry.

Numerical simulations have been carried out (Hauser *et al.*, 2001) to estimate the performance of such a system. They show that it would be possible to extract spectral information of swell with significant waveheight larger than 1 m, wind waves of a peak wavelength longer than about 70 m, or a combination of both. An additional beam, pointing at nadir (0°) will provide

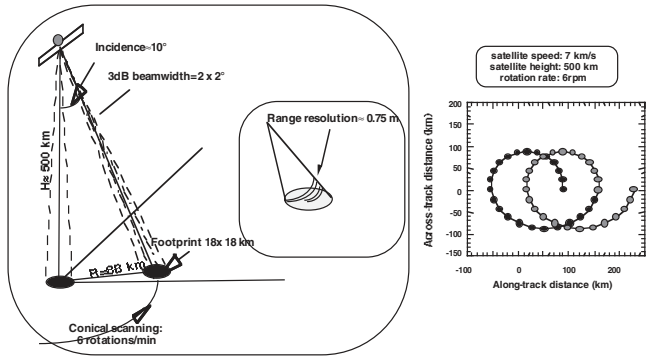

Figure 5.23: Geometry of observation proposed for the SWIMSAT satellite: a dual beam system (0 and 10° from nadir) will be used. The tilt beam will rotate around the vertical axis at a rate of 6 rotations per minute. The corresponding pattern on the surface is shown in the right panel of the figure, for a satellite speed of 7 km/s and a satellite height of 500 km.

significant waveheight and wind-speed as for radar altimeter systems. With the geometry proposed for this system, the two-dimensional spectra of wave energy will be obtained at a scale similar to the grid-sizes scales of wave prediction models running on a global scale (80 to 100 km).

An alternative version of the project is to use a scanning beam antenna which will cover the 0 to 12° incidence range and scan also in azimuth ($0 - 360°$). With such a configuration, it will be possible to improve the spatial resolution of the geophysical products (two-dimensional wave spectra) up to about 50 km × 50 km.

However, to optimise the usefulness of the information provided by SWIMSAT, a method will be developed to take benefit of the radial information acquired for each angular sector (*e.g.* every 15°) at different locations on the surface.

5.6.4 Conclusions

Real aperture radar used on-board airplanes have demonstrated their ability to investigate the spatial variation of waves and of their spectral properties. In particular they can be of great value for regional scale studies in non-homogeneous conditions (near current regions, in coastal zones at regional scale, etc) where *in situ* measurements face limitations.

Instrument	RESSAC	SWIMSAT
Radar frequency	5.35 GHz	13.6 GHz
Polarization	HH	HH
Transmitted wave form	FM/CW, $\Delta f = 168$ MHz, Pulse duration = 7 ms	Chirp, PRF = 4 kHz $\Delta f = 200$ MHz, duration = 7 μs
Peak power	2 Watts	100 Watts
Mean incidence angle	14°	10°
Beam aperture (-3 dB)	14° elev., 3.4° az.	2° elevation, 2° azimuth
Beam rotational speed	3 RPM	6 RPM
Range resolution	1.56 m	0.75 m
Altitude	6 km	500 km
Footprint	1500×400 m	18×18 km
Swath of the beam for a complete beam rotation	Circle, $r = 1.5$ km	Circle, $r = 88$ km

Table 5.2: Main characteristics of RESSAC and SWIMSAT and geometry in standard use

In the context of the development and refinement of remote sensing techniques like altimeter observations (ocean dynamic height, wind and wave measurement) or SAR observations, they are also of great interest because they can help to quantify the influence of wave conditions on the transfer function between radar signal and geophysical parameters (wind estimates from radar altimeters, errors due to the electromagnetic bias for ocean height measurements, and transfer functions between the SAR image spectra and wave spectra). As a matter of fact, recent studies have shown that the long tilting waves (longer than a few meters) may influence these radar signatures, and that the spectral information on waves is important to be known.

The simplicity of the technique used, as well as its advantage with respect to SAR observations (no Doppler analysis, i.e. no artefact due to wave motion in the wave spectra retrieval), make such real-aperture scanning-beam radars good candidates for a space-borne mission. They could efficiently complement SAR systems to estimate the spectral properties of ocean waves at the global scale. Combined with a radar altimeter, they could provide, in addition to significant waveheight and wind speed, the spectral information on waves, which is still lacking for a lot of applications like wave prediction models, offshore installations, ship routing, to mention a few.

5.7 An Airborne Coherent RAR

William J. Plant, William C. Keller and Kenneth Hayes

An X-band, coherent, airborne radar has been developed to measure wind speed and direction simultaneously with directional wave spectra on the ocean. The radar, called CORAR for COherent Real Aperture Radar, measures received power, mean Doppler shifts, and mean Doppler bandwidths from small resolution cells on the ocean surface and converts them into measurements of winds and waves on the ocean. The system operates with two sets of antennas, one rotating and one looking to the side of the airplane. The rotating antennas yield neutral wind vectors at a height of 10 m above the ocean surface using a scatterometer model function to relate measured cross sections to wind speed and direction. The sidelooking antennas produce maps of normalized radar cross section and line-of-sight velocity from which directional ocean wave spectra are obtained.

CORAR was developed to provide simultaneous measurements of winds and waves on the ocean surface. The system operates at moderate incidence angles where backscatter depends strongly on wind speed. It is a coherent system in which surface velocities are used to infer waveheight rather than scattered power levels or the time of flight of a pulse to the surface as is more common (Kenny *et al.*, 1979; Jackson, 1980; Hauser *et al.*, 1992a; Wright *et al.*, 2001). The radar was developed under funding from the U.S. Office of Naval Research (ONR) and has been flown on a DeHavilland Twin Otter airplane during ONR's Shoaling Waves Experiment. CORAR operates in two modes, rotating and fixed, side-looking. In both modes, cross sections, Doppler offsets, and Doppler bandwidths are collected at multiple range bins during data acquisition. In the rotating mode, the stored cross sections are subsequently averaged over small incidence and azimuth angle bins. This produced mean cross sections as a function of azimuth angle from which wind vectors at 10 meters above the ocean surface can be calculated using a scatterometer model function. In the side-looking mode, images of both cross sections and Doppler offsets are produced from which directional wave spectra are obtained. Spectra of the Doppler offset images can be directly converted to waveheight variance directional spectra and their 180° ambiguities can be removed by noting changes in different flight directions. The overall result is that wind vectors and directional ocean wave spectra can be produced simultaneously.

Figure 5.24: CORAR mounted on a Twin Otter aircraft

Principles of Operation

Figure 5.24 shows CORAR installed on the Twin Otter. The white antennas on the side of the airplane are four-foot, slotted waveguide antennas, one operating horizontally polarized and the other vertically polarized. The rotating antennas are mounted inside a radome under the plane. They are two eighteen-inch, slotted waveguide antennas mounted back to back on a stabilized platform. The pulse repetition frequency (PRF) of the radar is 80 kHz but alternate pulses go to the side-looking and rotating antennas so the effective PRF from either antenna is 40 kHz. A switch changes between the H-pol and V-pol antenna of each system after a time interval of about 1/3 second. When collecting data for directional spectral calculations from the fixed antennas, this switching does not occur so that all data are collected

Frequency	9.36 Ghz
Peak Transmitted Power	100 W
Pulse Repetition Frequency per Mode	40 kHz
Vertical Beamwidths	25°
Sidelooking Horizontal Beamwidths	1.8°
Rotating Horizontal Beamwidths	5°
Range Resolution	7.5 m
Nominal Centre Incidence Angle	60°
Rotation Rate	15 rpm
Pulses Averaged	26
Integration Time	256 ms
Time Between Polarization Changes)	370 ms
Samples Transformed	256

Table 5.3: Selected CORAR Specifications

at a single polarization with the side-looking system, usually V-pol.

The system only collects co-polarized data, HH and VV. A pulse width of 50 nsec is obtained by switching; no pulse compression is used in the system. In order to improve signal-to-noise ratio, N pulses are coherently averaged. Therefore, over each 1/3 second interval, the system collects data from each range bin for each mode, rotating and side-looking, at a rate of $40/N$ k Hz, sufficiently fast that Doppler spectra can be calculated for 100 range bins. Signals from the rotating antenna are frequency-shifted so that the spectra remain within the system bandwidth even when a large component of plane velocity exists along the antenna look direction. First and second moments of the Doppler spectra are calculated and stored on hard disk along with the mean received power. A single complete Doppler spectrum from a chosen range bin is also stored for each mode. Each run typically consists of 1000 scans of approximately 1/3 second each. The first 12 scans of each run are used to record a calibration signal and to determine the system noise level. Table 5.3 shows selected specifications of CORAR. Auxiliary information on flight parameters are recorded along with the data. A radar pointing reference system is used to produce records of aircraft pitch, roll, and heading while a differential global positioning system yields ground speed, track, latitude, and longitude.

In subsequent post-flight processing, normalised radar cross sections, σ_o,

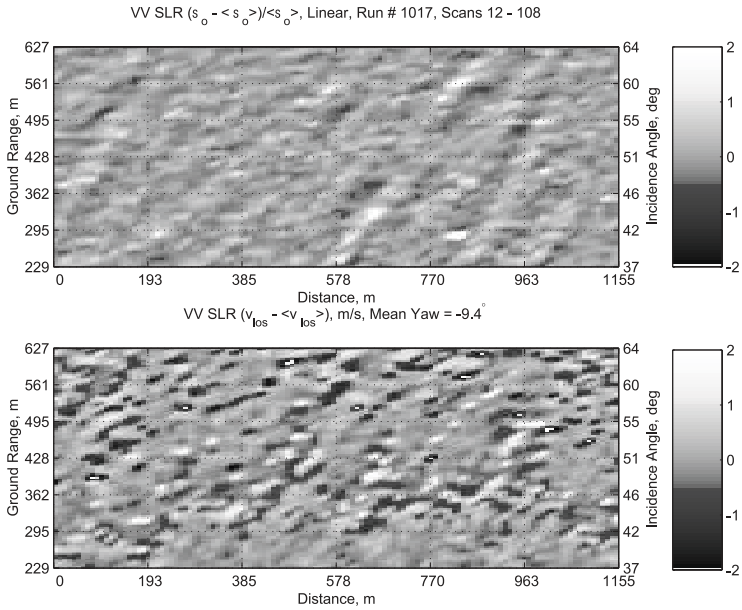

Figure 5.25: Images of normalised modulated radar cross section, σ_0 (upper), and line-of-sight velocity, V_{los} (lower) obtained from CORAR's sidelooking mode.

are obtained for each mode from the difference between the recorded mean received power and noise levels. Line-of-sight velocities are obtained from the stored first moments, f_1, after correction for signal-to-noise ratio (Plant *et al.*, 1998) using the equation

$$V_{los} = \lambda f_1/2, \tag{5.10}$$

where λ is microwave length and f_1 is the first moment of the Doppler spectrum. This moment is corrected for effects of aircraft yaw prior to the velocity calculation. Figure 5.25 shows images of the modulated radar cross section and line-of-sight velocity modulation obtained from the sidelooking mode. After correction for the finite resolution of the range cells and for mapping distortion, the spectrum of the velocity image, $S_v(\mathbf{k})$, may be converted to the wavenumber spectrum as a function of along and cross-track wavenumber, $\Psi(\mathbf{k})$. The relationship, to a very good approximation, is

$$\Psi(k_x, k_y) = S_v(k_x, k_y)/[\omega^2(\cos^2\theta_i + (\frac{k_y}{k_x})^2 \sin^2\theta_i)] \tag{5.11}$$

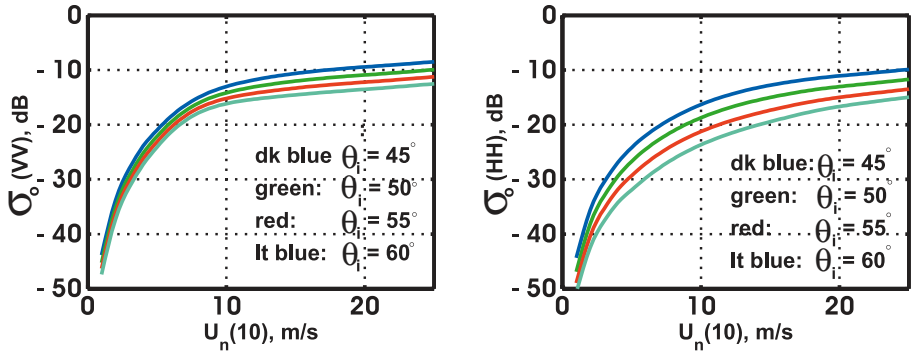

Figure 5.26: The model function developed for use with CORAR to convert normalised radar cross sections in the upwind direction to $U_n(10)$, the neutral stability wind speed at 10 m height.

where ω is wave frequency, and θ_i is the mean incidence angle of the image. For the range of incidence angles covered by CORAR's images, $\theta_i = 47.7°$.

In principal, directional spectra can also be produced from the cross section images and from cross sections and first moments recorded from the rotating mode. The relationship between cross section modulation and waveheight spectra, however, involves the modulation transfer function and has not proven to be accessible to date. Also, waveheight spectra have not yet been produced from first moments for the rotating mode.

Cross sections from the rotating mode averaged over a small range of incidence and azimuth angles yield wind speed and direction via the standard methods of scatterometry, however. The averaged cross sections in the upwind direction are converted to wind speed using the model function shown in Fig. 5.26, which was developed for the system. Unlike model functions used in satellite scatterometry (Schröder *et al.*, 1982), the model function used with CORAR relates wind speed to the normalised radar cross section of the sea only for antenna directions looking into the wind. Since the antenna rotates 360° in four seconds, the aircraft moves only a very short distance during one rotation. Thus measurement of the normalised radar cross section is made in all directions for very nearly the same wind conditions, and the upwind wind direction is determined from the direction of maximum return signal. Wind speed is then determined from the level of the radar cross section in this direction alone.

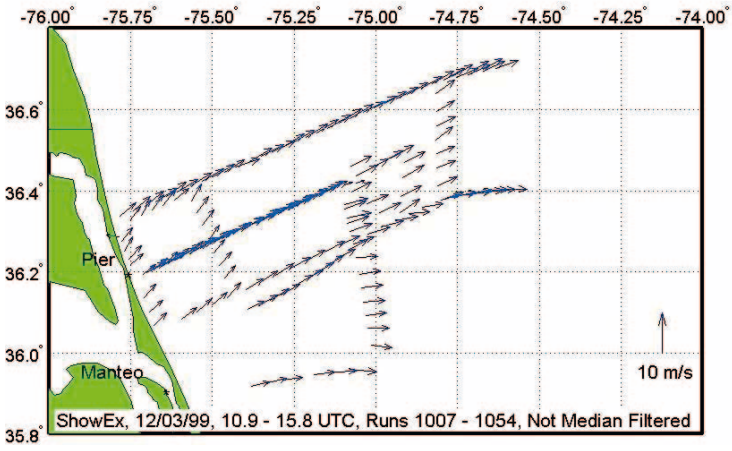

Figure 5.27: Wind vectors measured by CORAR east of Duck, NC on December 3, 1999.

Wind Vectors and Directional Wave Spectra

Wind speed and directions have been measured by CORAR on several days in the late fall of 1999 off the east coast of the United States. Figure 5.27 shows wind vectors measured on December 3, 1999. The offshore winds on this day produced waves propagating in the wind direction. These can be seen in Fig. 5.28, which shows wave spectra observed simultaneously with the wind measurements of Fig. 5.27.

The spectra shown here were collected at latitude 36.3° and longitude −75°. The two left plots in Fig. 5.28 show waveheight variance spectra, the top one as a function of (k_x, k_y) and the bottom one integrated over azimuth angle to produce $\psi(k)$. The plots on the right are similar except that they show wave slope variance spectra. Spectra from images such as those in Fig. 5.25 always yield two-sided wave spectra, one of which is in the incorrect direction. These incorrect peaks have been removed from Fig. 5.28. They were identified by noting that after correction for mapping distortion, they do not always appear to be in the same direction when the plane flies in different directions.

The top plots in Fig. 5.28 are tilted slightly so that north is up. This allows one to identify the wind wave peak as the one in the slope spectrum travelling in the wind direction of Fig. 5.27.

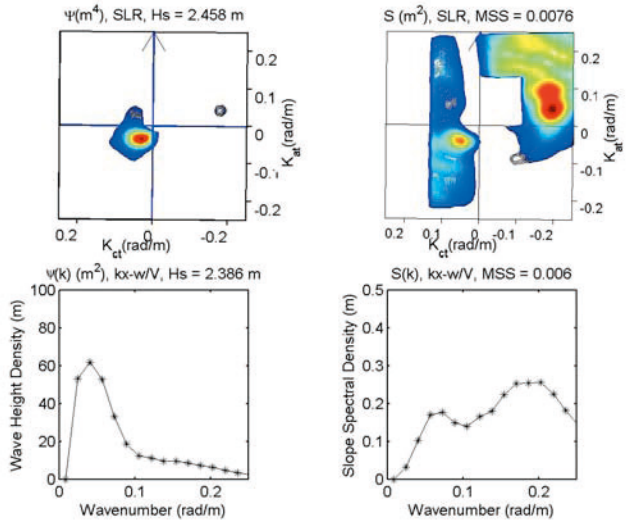

Figure 5.28: Wave spectra measured by CORAR east of Duck, NC on December 3, 1999.

Swell from the northeast is also evident in the spectra; the large height of the swell masks the wind wave spectral peak in the waveheight spectra, although some evidence of it can be seen at high wavenumbers in $\Psi(\mathbf{k})$. One other pronounced peak exists in the slope spectrum in the upper right corner. The origin of this wave train has not yet been identified.

Summary

A coherent, X-band airborne radar capable of making simultaneous measurements of wind vectors and directional wave spectra on the ocean has been constructed and flown. Winds produced by the system are neutral winds at a 10 m height while directional wave spectra are fully calibrated in terms of waveheight or slope. The system obtains wind vectors from the behavior of the normalised radar cross section via scatterometry. To date, it has produced directional wave spectra from the Doppler shifts measured by the side-looking antenna, although three other possible means of deriving directional spectra exist in the recorded data. Development of these other spectral-measurement techniques remains for future work.

5.8 Synthetic Aperture Radar Wave Measurements

Susanne Lehner and Johannes Schulz-Stellenfleth

5.8.1 State of the Art

It has been amply demonstrated that synthetic aperture radar (SAR) images of the sea surface provide directional information on ocean waves (Alpers *et al.*, 1981; Hasselmann *et al.*, 1985c; Hasselmann and Hasselmann, 1991; Krogstad, 1992; Brüning *et al.*, 1994). A closed theory explaining the SAR ocean wave imaging process has been developed and different algorithms for the retrieval of two dimensional wave spectra from SAR data have been proposed by Heimbach *et al.* (1998), Mastenbroek and de Valk (2000) and Krogstad *et al.* (1994). In this chapter the basic SAR ocean wave imaging theory including some recent results on SAR cross spectra is summarised and different retrieval schemes are introduced. Furthermore, first results obtained with a new technique based on interferometric SAR (InSAR) systems are presented (Schulz-Stellenfleth and Lehner, 2001a,b).

Typical spaceborne SAR systems, *e.g.* flown on the ERS-1/2, JERS, RADARSAT and SEASAT satellites or the Space Shuttle operate in C-, L- or X-bands. Microwaves penetrate the atmosphere including clouds nearly unaffected and are therefore especially well suited for continuous monitoring of the oceans and the polar ice caps. Derived geophysical parameters like wind fields, ocean wave spectra, sea ice parameters and ocean surface currents are thus available on a global and continuous basis. SAR image spectra acquired every 200 km along the track by the ERS-SAR are operationally inverted to ocean wave spectra, *e.g.* at the European Centre for Medium-Range Weather Forecast (ECMWF) (Bidlot *et al.*, 2002) and the UK Met office and are used for the validation of the ocean wave models, *e.g.* WAM (WAMDI group, 1988).

Compared to real aperture radar systems, SAR sensors achieve a high resolution in the flight direction (azimuth) of the platform. Typical satellite borne SARs, like the ERS SAR, have resolutions of about 20 m. Airborne systems can provide data with less then 1 m resolution. For processing high resolution images a SAR uses both the amplitude and the phase of the backscattered signals. While the sensor moves along a path it transmits electromagnetic pulses and receives the echoes from each pulse via the same antenna (monostatic configuration). The area illuminated by each pulse is called the antenna footprint and the imaged strip in flight direction the

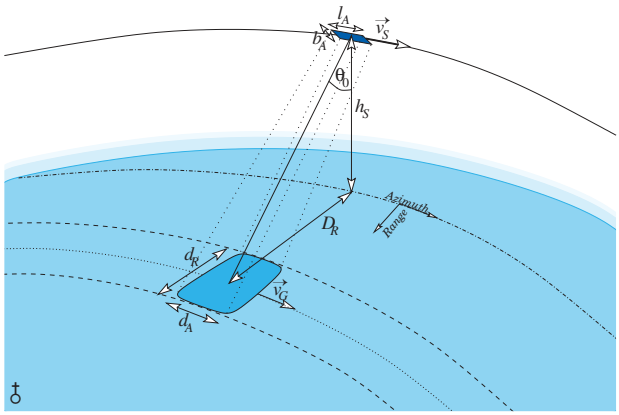

Figure 5.29: Spaceborne SAR imaging geometry

swath. The imaging geometry of spaceborne SAR is illustrated in Fig. 5.29. The main geometrical parameters, incidence angle θ_0, satellite height h_s, the footprint geometry, d_R, d_A and its distance from the sub- satellite track D_R and the satellite parameters satellite speed $\mathbf{v}_s$ and ground speed $\mathbf{v}_g$ is given.

Based on the experience with conventional single antenna SARs interest in multi antenna interferometric SAR systems (InSAR) has been growing in recent years. InSAR measurements are based on the phase difference of the complex signals received by two antennas. If the antennas are separated in the along track direction the interferometric phase contains information on currents and orbital velocities caused by ocean waves. If the baseline of the antennas has an across track component information on sea surface elevation can be extracted.

The section is structured as follows: first an overview of the different SAR missions is given and the available SAR and InSAR data are described. The processing and basic principles of SAR and InSAR data is explained, followed by a short description of SAR ocean wave imaging theory and ocean wave retrieval schemes.

5.8.2 SAR Missions

SAR systems are flown in space as well as on aircrafts. Figure 5.30 shows spaceborne SAR missions carried out since 1978. SEASAT, the first satellite

dedicated to investigate the sea surface using microwaves was launched on June 28 in 1978. It was orbiting around the earth about 14 times a day at a height of 800 km. During its short lifetime of 98 days, it acquired for the first time a whole series of SAR images from space, most of which were still processed optically using conical lenses. These images showed for the first time large spatial coverage of ocean wave fields in near coastal areas.

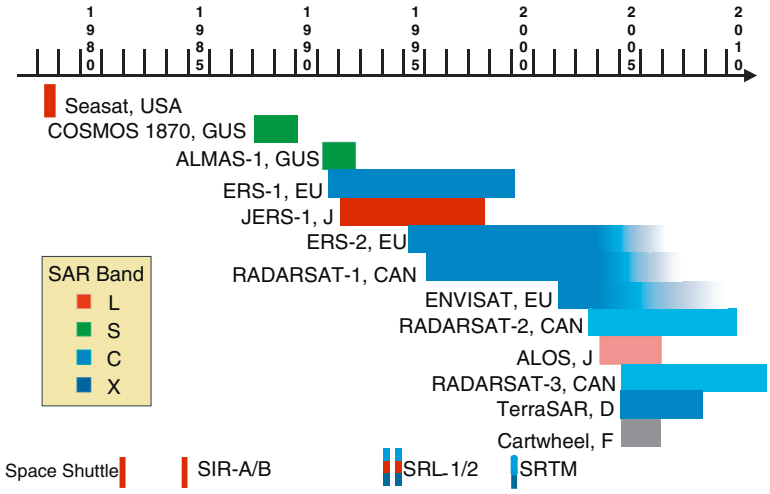

Figure 5.30: Some of the major past and planned spaceborne SAR missions.

Apart from NASA shuttle flights in 1982 and 1984 it took until 1991 until the European Remote Sensing satellite (ERS-1) was launched. Since the start of ERS-1, and its near identical successor ERS-2 launched in 1995, SAR sea surface measurements have been acquired on a global and continuous basis. The ERS satellites thus allowed the operational use of SAR data, *e.g.* at weather centres, for the first time. Most of the data sets investigated in the following were acquired by the ERS satellites or the Canadian RADARSAT-1 launched in 1995. The radar frequency of the ERS SAR is in C-band at 5.3 GHz (Table 5.1) with vertical polarisation in transmit and receive. RADARSAT is operating in C-Band as well, but with horizontal polarisation both for transmission and reception (HH).

During space missions data are acquired on a global basis. Shuttle missions last for about 10 days and are therefore suited for testing new sensors in orbit and for the acquisition of new types of data sets. During the two shuttle missions in April and October 1994 (SIR-C/X-SAR), for the first time SAR data were acquired at different frequencies (L-, C- and X-band). An analysis of the ocean wave data of this mission can be found in Melsheimer *et al.* (1998). During the Shuttle Radar Topography Mission (SRTM) in February 2000 interferometric SAR data were acquired using two antennas in across track geometry. These data are mainly used to derive digital elevation models over land, examples are given in Eineder *et al.*, (2000). Some first results on ocean wave measurements using along track interferometry are given in Bao *et al.* (1999). Satellite missions for interferometric SAR measurements are in the planning stage, *e.g.* Massonnet (2001), Romeiser and Thompson (2000).

5.8.3 Available Types of SAR and InSAR Data

Spaceborne and airborne SAR systems provide SAR data with a large variety of resolutions, coverage and information content. This section gives a brief overview of typical SAR image sizes, coverage and resolutions used for ocean wave measurements in different global or coastal applications.

Conventional SAR Data

ERS SAR data are available at different coverage and resolution. ERS SAR data acquired in image mode have to be down-linked at once as the large amount of raw data cannot be stored on board. For this purpose receiving antenna stations have to be put up in areas of interest. For ERS-1 and 2 the standard image size is 100 km × 100 km at a resolution of 30 m. These images are interesting for studying coastal processes like mesoscale wind fields, and the behavior of two dimensional ocean wave spectra under the influence of bottom refraction and currents. RADARSAT already incorporates the Scan SAR mode covering 500 km × 500 km at a resolution of 100 m, which is not sufficiently high to image ocean waves. This imaging mode is ideally suited for deriving mesoscale wind fields, in particular a synoptic overview of polar lows or hurricanes is possible, which helps to model the ocean wave field in rapidly varying wind field conditions.

The so-called Wave Mode has been acquired on the ERS satellites to ensure global coverage of the oceans. Wave Mode data consist of 5 km × 10 km

SAR raw data taken every two hundred kilometers along the satellite track. This rather small amount of raw data can be stored onboard the satellite, downlinked when in line of sight of receiving stations and processed in real time for fast delivery to the weather centres.

The Advanced SAR (ASAR) on ENVISAT has the capability to acquire global mode data, 100×100 km image mode, and scan SAR data. These data can be stored on board the satellite and are thus available globally.

Interferometric SAR

Interferometric SAR data provide high resolution maps of surface elevation (across track InSAR) or surface motion (along track InSAR) caused either by elevation due to ocean waves (Graber, 1996; Bamler and Hartl, 1998; Bao *et al.*, 1997; Vachon *et al.* 1999; Schulz-Stellenfleth and Lehner, 2001a, 2001b) or surface movement due to currents (Romeiser and Thompson, 2000; Siegmund *et al.* 2003). Spaceborne interferometric measurements over the ocean were, for example, carried out during the SRTM Mission in February 2000. Two airborne experiments with interferometric SAR systems are described in Part II of this book.

5.9 Processing of SAR and InSAR Data

Susanne Lehner and Johannes Schulz-Stellenfleth

A SAR achieves its high azimuthal resolution by recording the Doppler history of the returned signals (Bamler and Schättler, 1993). Consider a single stationary point scatterer located at range R_0. As shown in Fig. 5.31(A), the corresponding SAR raw data are given by a *quadratic chirp* with range dependent frequency modulation rate FM. In fact, FM is related to platform velocity V, range R_0 and radar wavelength λ via

$$FM = -\frac{2\,V^2}{\lambda\,R_0} \tag{5.12}$$

At Doppler centroid time t_c the point scatterer is in the centre of the antenna beam. Doppler zero time t_0 denotes the moment of closest approach (Doppler zero). The width of the chirp envelope (integration time) is in the order of 1 second for typical space-borne sensors.

SAR processing is performed by matched filtering, which corresponds to a multiplication operation in the Fourier domain. Fig. 5.31 (B) shows the

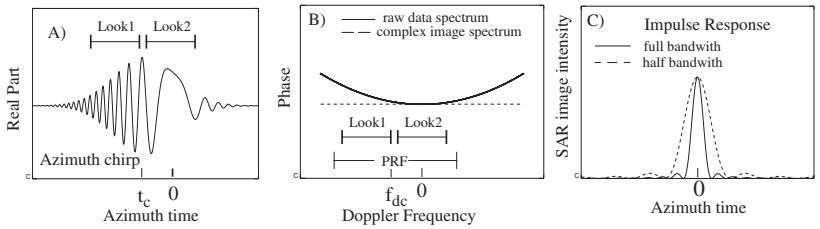

Figure 5.31: (A) Azimuth chirp of single point scatterer in SAR raw data. (B) Phase of raw data azimuth spectrum (solid) and complex image azimuth spectrum (dashed). Frequency bands of looks are indicated. The processed bandwidth is limited by the pulse repetition frequency (PRF) (C) Azimuth impulse response in SAR intensity image using the entire bandwidth (solid) and half bandwidth (dashed)(adapted from Lehner *et al.* (1999)

phase of the raw data spectrum (solid), which is again a quadratic chirp with correspondence between time, t, and frequency, f, given by

$$t = \frac{f}{FM} \tag{5.13}$$

The raw data azimuth spectrum is multiplied with the complex conjugate matched filter spectrum, removing the quadratic phase component. The dashed line in Fig. 5.31 (B) is the phase of the complex image spectrum obtained after this processing step. Fig. 5.31 (C) shows the resulting point scatterer response in the SAR intensity image I using the entire bandwidth (solid) and the half bandwidth (dashed).

Rather than focussing the entire chirp to a single SAR image, subintervals of the integration time are often used to process images (looks) with lower azimuthal resolution. Denoting the complex SAR image by C and the looks by $L_i, i = 1, 2$, these are calculated as

$$L_i = |\mathcal{F}_{az}^{-1}(\mathcal{F}_{az}(F_i\, C))|^2 \quad i = 1, 2, \tag{5.14}$$

where $F_i, i = 1, 2$ are the corresponding bandpass filters and $\mathcal{F}$ denotes Fourier transform. If the corresponding frequency bands are non-overlapping (compare Fig. 5.31 (B)) looks are separated in time according to Eqn. 5.13. The multi-look technique can therefore be used to measure wave motion.

SAR Cross Spectra

Historically, SAR ocean wave measurements were first based on SAR intensity images I and their respective variance spectra P. Although this approach was successfully used to measure ocean wave spectra (Heimbach *et al.*, 1998; Krogstad *et al.*, 1994), it has the disadvantage of ambiguous wave propagation directions. In recent years a new technique was developed, which resolves this ambiguity by making use of the special SAR imaging mechanism (Engen and Johnson, 1995).

The multi-look technique introduced in the previous section allows the measurement of the propagation of the radar cross section patterns associated with ocean waves. For a typical spaceborne SAR the integration time is small compared with the period of waves resolved by the radar. For the ERS SAR the look time separation Δt is in the order of 0.5 s, whereas the shortest waves seen by the radar are about 70 m long, corresponding to about 5 s period.

A standard estimation technique to measure small phase shifts is based on cross spectra. The look cross spectrum $P_{1,2}$ is defined as the Fourier transform of the look cross covariance function ρ_{L_1,L_2}

$$P_{1,2} = \mathcal{F}(\rho_{L_1,L_2}) \tag{5.15}$$

The cross spectrum has symmetric real part and anti-symmetric imaginary part. The propagation direction is indicated by the positive peak of the imaginary part. Fig. 5.32 shows the standard ERS-2 wave mode symmetric spectrum and a cross spectrum computed from the same complex imagette by combining two different looks. A wave system of about 180 m wavelength can be seen propagating to the left. The finer polar grid shown for the cross spectrum will be used for the official ESA ENVISAT cross spectra product.

Compared to conventional SAR image variance spectra, cross spectra have the additional advantage of lower noise levels. This is due to the uncorrelated speckle noise of the two looks (Engen and Johnson, 1995). A more detailed analysis of cross spectrum noise including the issue of cross spectra estimation and sea state dependence can be found in Schulz-Stellenfleth and Lehner (2002).

Basic Principles of InSAR

In imaging radar interferometry complex SAR images of two or more antennas are combined to yield information on sea surface elevation or move-

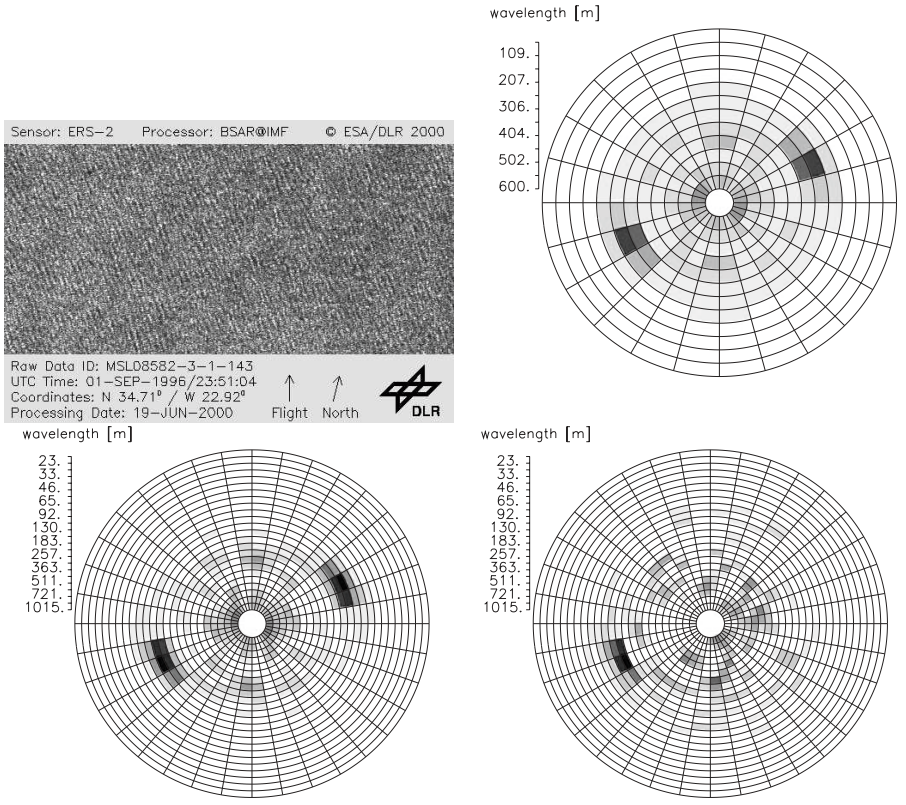

Figure 5.32: Upper left: ERS-2 wave mode imagette (intensity) acquired on Sep 01, 1996 at 34.71 N, 22.92 W showing ocean waves. Upper right: Standard ERS-2 UWA spectrum. Bottom: Real part (left) and imaginary part (right) of a simulated ENVISAT ASAR cross spectrum.

ment. The idea is to use antennas, separated in space, to exploit the phase differences of the received signals. In principle there are two types of interferometry, namely single pass interferometry with all antennas mounted on one platform and multi pass interferometry with one antenna performing sequential acquisitions. Due to the quick decorrelation of the sea surface (within tens of millisecond) only single pass interferometry can be used for ocean applications.

Two complex images c_1, c_2 acquired by two antennas are combined into an interferogram i by taking the expectation value of the complex conjugate

product:

$$i = \langle c_1 \, c_2^* \rangle \tag{5.16}$$

with the asterisk denoting complex conjugation. In general the interferometric phase Φ_i

$$\Phi_i = \arg(i) \tag{5.17}$$

is determined by both the radial velocity u_r (Bao *et al.*, 1999) and the elevation η of the sea surface (Schulz-Stellenfleth and Lehner, 1998). The interferometric phase is then given by a combination of across track and along track components:

$$\Phi_i = m \; k_E \; (\frac{B_x}{V} \; u_r \; + \frac{B_\perp}{R_0 \; \sin\theta} \; \eta_r) \tag{5.18}$$

Here, B_x is the along track component, V is the platform velocity, $B_\perp$ is the baseline component perpendicular to the slant range vector (Bamler and Hartl, 1998) and θ is the incidence angle. The constant m is equal to 2 for monostatic mode and equal to 1 for bistatic mode.

5.9.1 SAR Ocean Wave Imaging Theory

As the backscattering facets on the ocean surface are non-stationary, SAR imaging of the ocean is more complex than standard SAR mapping of solid terrain. Considering again a single backscattering facet on the moving ocean surface. The following effects have to be taken into account:

- A velocity component of the facet in slant range direction leads to a Doppler shift and therefore a shift of the corresponding image point in azimuth ("train off the track effect").
- Similarly, acceleration of the facet in slant range direction causes azimuthal smearing of the SAR image response called acceleration smearing, (Hasselmann and Hasselmann, 1991).
- A lifetime of the facet shorter than the SAR integration time causes degraded azimuthal resolution, called coherence time effect, (Carande, 1994)

A geometrical depiction of the velocity bunching and acceleration smearing effect is given in Fig. 5.33.

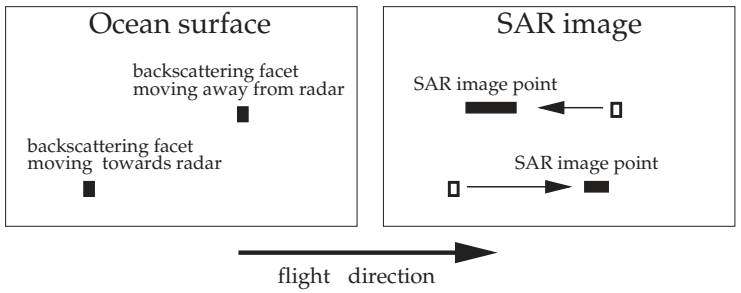

Figure 5.33: Illustration of the velocity bunching and acceleration smearing effect. Two backscattering facets on the ocean surface moving towards the radar and moving away from the radar are shown. The corresponding SAR image points are shifted and smeared in flight direction. The upper facet is assumed to have a smaller velocity and higher acceleration than the lower facet (adapted from Lehner *et al.*,2000).

To relate the relative modulation I_m of a SAR image I

$$I_m = \frac{I - \langle I \rangle}{\langle I \rangle} \tag{5.19}$$

to the sea surface elevation η, a SAR imaging forward model has been developed. The model consists of two parts :

- A real aperture radar (RAR) modulation model, which explains the modulation of the radar cross section by ocean waves.
- A velocity bunching model, which explains the impact of sea surface motion on the SAR image formation process.

The RAR modulation model is based on a two scale model of the ocean surface (Alpers and Rufenach, 1979).

Two Scale Model of the Ocean Surface

According to common theory radar backscatter from the ocean surface for incidence angles between 20° and 60° is dominated by Bragg scattering (Keller and Wright, 1975). Based on this assumption SAR ocean wave imaging can be explained by a two scale model, which divides the sea surface into two spatial scales separated by a wavenumber k_{sep}. The small scale

part with wavelength in the order of the radar wavelength dominates the backscattering process. Longer waves have an indirect impact, modulating the backscatter by tilt, hydrodynamic interaction and orbital velocity bunching.

The separation wavenumber can be chosen either independent of the SAR sensor from pure electrodynamic hydrodynamic considerations (EMH model) or dependent on the SAR resolution (SAR two scale model) (Hasselmann *et al.*, 1985c; Kasilingam and Shemdin, 1990).

As SAR is a coherent imaging system assumptions have to be made about the complex radar reflectivity r of the ocean surface. Independent of the choice of k_{sep} it is widely assumed that the reflectivity r is a spatially white process. The autocorrelation function of r then has the form

$$\langle r(\mathbf{x_1}, t_1)\, r^*(\mathbf{x_2}, t_2)\rangle = \sigma(\mathbf{x_1}, \frac{t_1+t_2}{2})\, \delta(\mathbf{x_1}-\mathbf{x_2})\, \exp\big(-\frac{(t_1-t_2)^2}{\tau_s^2}\big) \quad (5.20)$$

where τ_s is the scene coherence time describing the temporal decorrelation of the sea surface. Scene coherence times have been measured using along track interferometry (Carande, 1994). For C-band τ_s is in the order of 50 ms. Recent theoretical studies have shown a wind dependence in the coherence time (Romeiser and Thompson, 2000).

The RAR Modulation Transfer Function

To first order the modulation of the mean radar cross section $\langle\sigma_0\rangle$ of the sea surface by ocean waves is a linear function of the surface elevation η and can thus be described by a RAR modulation transfer function (RAR MTF) T^{RAR}.

$$I_R := \frac{\sigma_0 - \langle\sigma_0\rangle}{\langle\sigma_0\rangle} = 2\, Re\big[\int \eta_k\, T_k^R\, \exp(i\,\mathbf{k}\cdot\mathbf{x})\, d\mathbf{k}\big] \quad (5.21)$$

Here η_k is the complex Fourier spectrum of η and Re denotes real part. The RAR MTF T^{RAR} is dominated by three independent physical processes:

- *Tilt modulation* : Long ocean waves modulate the local incidence angle and thus the Bragg wavelength (Valenzuela, 1978).
- *Hydrodynamic modulation*: Due to hydrodynamic interactions long waves modulate the energy of short Bragg waves (Alpers *et al.*, 1981).
- *Range bunching*: A pure geometric imaging effect due to the propagation of the ocean waves during the imaging process, causing a modulation of the effective backscattering area by long waves.

Assuming that these three transfer function combine as linear filters, the RAR MTF can thus be written as the sum the corresponding transfer functions:

$$T^R = T^{tilt} + T^{hydr} + T^{rb} \tag{5.22}$$

Analytical expressions for the transfer functions can be found in Brüning *et al.* (1990). It should be noted that there is considerable uncertainty in particular about the phase of the hydrodynamic MTF T^{hydr}. Different attempts to measure T^{hydr} have provided only very coarse estimations (Brüning *et al.* 1994b). Recently a new technique for RAR MTF estimation was proposed based on interferometric SAR measurements (Schulz-Stellenfleth and Lehner 2001a).

Velocity Bunching Model

Based on Eqn. 5.20 it can be shown that SAR imaging of a moving sea surface with normalised radar cross section σ_0 and orbital velocity u_r by a SAR with platform velocity V and slant range R (distance between radar and target) is described by the following expression (Brüning *et al.*, 1990):

$$\begin{aligned} I(\mathbf{x}) \;=\; & \frac{\pi T_0^2 \rho_a}{2} \int \frac{\sigma(\mathbf{x}')}{\hat{\rho_a}(\mathbf{x}')} \exp\Bigg(-\frac{\pi^2}{\hat{\rho}_a^2}\Big(x - x' \\ & -\frac{R}{V} u_r(\mathbf{x}')\Big)^2\Bigg)\, \delta(y' - y)\, dx' dy' \end{aligned} \tag{5.23}$$

Here I is the SAR intensity image, x and y are the azimuth and range coordinates, T_0 is the SAR integration time and $\hat{\rho}_a$ is the degraded azimuthal resolution

$$\hat{\rho}_a = \rho_a \sqrt{1 + \frac{T_0^2}{\tau_s^2}} \tag{5.24}$$

with scene coherence time τ_s. For the ERS SAR the azimuthal resolution ρ_a is about 10 m. There is considerable uncertainty about the (intrinsic) coherence time τ_s, but is estimated to be in the order of about 50 ms for C band (Carande, 1994).

The main mechanism represented by Eqn. 5.23 is the so called velocity bunching effect. According to the "train off the track effect" image points of backscattering facets with range velocity component u_r are shifted by a distance ξ in the azimuth direction.

$$\xi = \frac{R}{V}\, u_r \tag{5.25}$$

In the framework of linear Gaussian wave theory, the slant range velocity u_r can to first order be expressed in terms of the sea surface elevation field η,

$$u_r(\mathbf{x}) = 2\,Re\Big[\int T_k^v\,\eta_k\,\exp(i\,\mathbf{k}\cdot\mathbf{x})\,d\mathbf{k}\Big] \tag{5.26}$$

where T^v is the velocity transfer function, η_k is the complex Fourier spectrum of η and Re denotes real part. Due to the periodicity of u_r, SAR image intensities are stretched and bunched in the azimuth direction. The velocity bunching effect dominates the SAR imaging of ocean waves travelling in the azimuth direction and is in general non linear (Krogstad, 1992).

For the along and across track InSAR, interferogram expressions equivalent to Eqn. 5.23 were derived in Bao *et al.* (1997) and Schulz-Stellenfleth and Lehner (2001b). The two main conclusions of these studies were:

- Like conventional SAR images, interferometric data are affected by the "train off the track effect". However, this mechanism leads to a distortion of the interferogram, which is slightly different to the velocity bunching mechanism (Schulz-Stellenfleth and Lehner, 2002).

- Interferometric data are much less dependent on the RAR modulation mechanism than conventional SAR imagery. As there exist only rough estimates for the RAR MTF, this is a big advantage of InSAR data.

Equation 5.23 provides a mapping relation between one realisation of the ocean surface and the corresponding SAR image (Hasselmann and Hasselmann, 1991) derived an integral transform for the second moments of this process, relating the ocean wave spectrum, F, to the SAR image variance spectrum, P. This expression was later extended to include finite SAR resolution and coherence time (Bao *et al.*, 1993) as well as the SAR cross spectra (Engen and Johnson, 1995). The following integral transform relates F to the SAR cross spectrum, P, of the normalised looks $\hat{I}_i = (I_i - \langle I\rangle)\,\langle I\rangle^{-1}$, $i = 1, 2$ separated by the time Δt.

$$\begin{aligned} P_k(\Delta t) \;=\; & \frac{1}{4\,\pi^2}\exp(-k_x^2(\frac{R}{V})^2\,\rho^{vv}(\mathbf{0}))\;\exp\big(-k_x^2\frac{\hat{\rho}_a^2}{4\pi^2}\big)\int d\mathbf{x}\;\exp(-i\,\mathbf{k}\cdot\mathbf{x}) \\ & \exp(k_x^2(\frac{R}{V})^2\,\rho^{vv}(\mathbf{x}))\cdot(1+\rho^R(x)+i\,k_x\,\frac{R}{V}\,(\rho^{Rv}(\mathbf{x})-\rho^{Rv}(-\mathbf{x})) \\ & +(k_x\,\frac{R}{V})^2(\rho^{Rv}(\mathbf{x})-\rho^{Rv}(\mathbf{0}))(\rho^{Rv}(-\mathbf{x})-\rho^{Rv}(\mathbf{0})) \end{aligned} \tag{5.27}$$

Here ρ^{RR}, ρ^{Rv} and ρ^{vv} are auto and cross correlation functions of the RAR image and the orbital velocity v, respectively.

$$\rho^{RR}(\mathbf{x}) = \langle I_R(\mathbf{0})\, I_R(\mathbf{x})\rangle \tag{5.28}$$

$$\rho^{Rv}(\mathbf{x}) = \langle I_m(\mathbf{0})\, v(\mathbf{x})\rangle \tag{5.29}$$

$$\rho^{vv}(\mathbf{x}) = \langle v(\mathbf{0})\, v(\mathbf{x})\rangle \tag{5.30}$$

For $\Delta t = 0$ and $\hat{\rho}_a = 0$, Eqn. 5.27 simplifies to the well known relation for SAR image power spectra. For the multi look case the integration T_0 in Eqn. 5.24 must be taken as the integration time of each look, *e.g.* $T_0 = 0.4$s for ERS SAR. A simulation based on the integral transform is shown in Fig. 5.34. An ocean wave spectrum with JONSWAP wind sea and a swell system (A) is plotted together with the corresponding real (B) and imaginary part (C) of the cross spectrum.

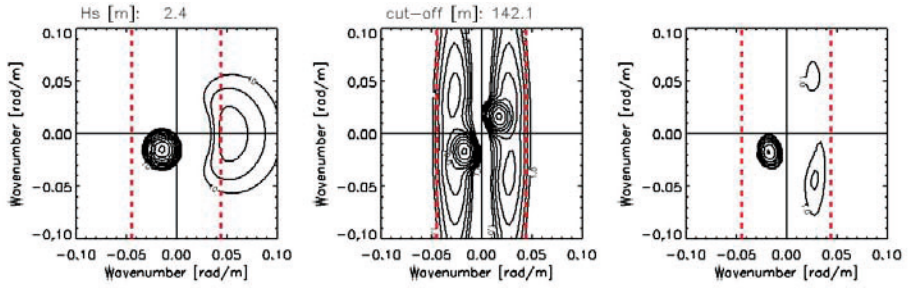

Figure 5.34: (A) Model ocean wave spectrum with JONSWAP wind sea and swell system. (B), (C) Simulated real and imaginary part of the cross spectrum.

Azimuthal Cut Off

The main characteristics of the mapping relation, Eqn. 5.27, is a low pass filtering of the SAR image spectrum in the azimuth direction. A definition of the cut-off wavelength is given by Kerbaol *et al.* (1998) as:

$$\lambda_{cut} = 2\,\pi\,\sqrt{(\frac{R}{V})^2\,\rho^{vv}(\mathbf{0}) + \frac{\hat{\rho}_a^2}{4\,\pi^2}} \tag{5.31}$$

The azimuthal cut-off causes an effective loss of information on ocean waves propagating in the azimuth direction. The shortest wavelength resolved in the range direction is approximately given by twice the range resolution

of the SAR, *e.g.* about 70 m in the case of the ERS-SAR. Depending on the details of the wave spectrum, typical cut-off wavelength for the ERS SAR are between 100 and 300 m. According to Eqn. 5.31 estimated cut-off wavelengths can be used to derive the orbital velocity variance. In Schulz-Stellenfleth and Lehner, (2001a,b) this technique is used to analyze the damping of ocean waves by sea ice in the marginal ice zone (MIZ).

5.9.2 SAR Ocean Wave Retrieval Schemes

Linear Inversion

In principle it is possible to simply neglect the missing information caused by the azimuthal cut-off and to restrict the SAR measurement to the long wave regime. This approach becomes particularly simple using a quasilinear approximation of the forward model (Hasselmann and Hasselmann, 1991). In that case the SAR spectrum is divided by the respective transfer function T^{SAR} yielding an estimate for the two dimensional wave spectrum.

To avoid artifacts caused by noise in spectral regimes where the transfer function is small, parts of the spectrum with significant energy are identified using a spectral partitioning scheme proposed by Gerling (1992). Cross spectra are split into single partitions associated with local maxima. The method is defined by a simple induction rule where each spectral bin is connected to the neighboring bin of highest energy. Only regimes with spectral energy above a certain threshold are considered. Neighboring partitions satisfying criteria like being 'close enough' (Hasselmann *et al.*, 1996) are coalesced. The imaginary part of the cross spectrum is then integrated over each partition to determine the propagation direction of the different subsystems. Finally, the partitions are divided by the transfer function.

As the example in Fig. 5.32 reveals, using only the real part of the cross spectrum cannot resolve the ambiguity. Comparing the result of the partitioning algorithm with the WAM wave spectrum shows that the propagation direction and wave length of the two dominant systems (red and blue) found in the SAR spectrum are in good agreement with the wave model spectrum. An additional system (green) in the centre of the SAR spectrum is due to large-scale noise in the image.

Figure 5.35 shows ocean wave measurements which were carried out using this approach.

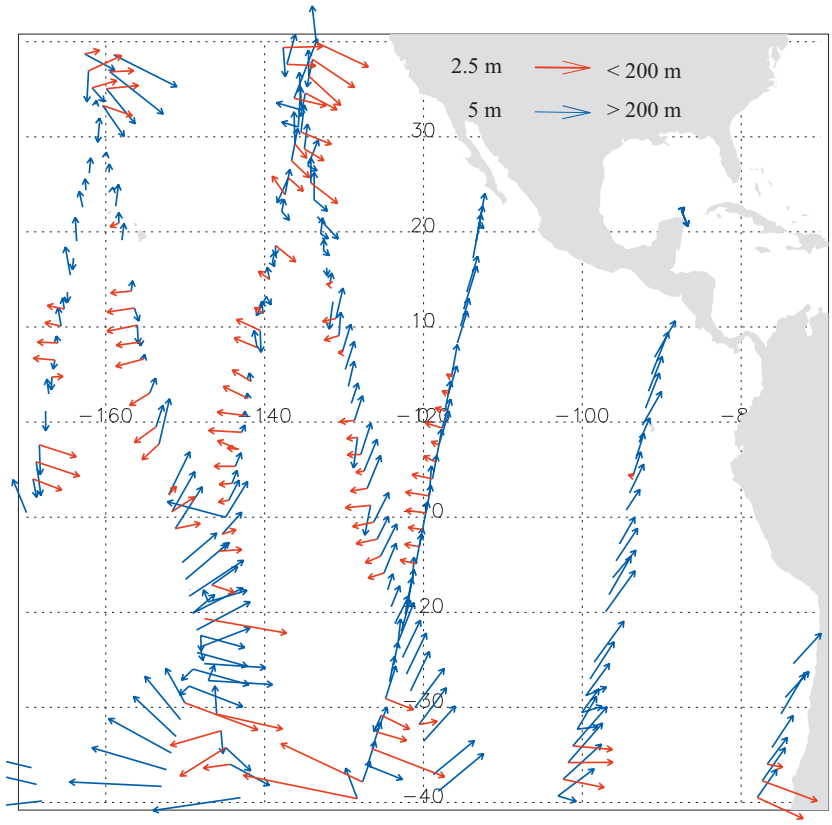

Figure 5.35: Ocean wave propagation direction for June, 1st, 1997 in the south east Pacific. The propagation directions for the two dominant wave systems are shown. Length of the arrows gives the significant waveheight. Scales for the two systems over 200 m (blue) and under 200 m (red) are different.

Non-linear Inversion

Although the above approach is feasible for coarse SAR estimations of longer waves, the method has several drawbacks:

- Due to coupling of different wave components in the SAR imaging process, spectral energy found in the cut-off region can be due to waves which are actually much shorter than the cut-off wavelength. Without using prior knowledge about short waves this SAR spectrum energy is attributed to the wrong ocean wave components in many cases.

- The cut-off wavelength itself is a function of the entire wave spectrum depending on the mean square orbital velocity. Shorter waves have a strong impact due to their higher orbital velocity. Prior information on short waves is therefore necessary to identify the spectral regime where reliable SAR information is available.

- In many cases SAR data contain only parts of the wave systems. In most applications–, *e.g.* wave model assimilation, complete wave systems are needed.

For this reason many SAR ocean wave retrieval schemes make use of some kind of prior information on short ocean waves. The approaches discussed in the literature are:

- Use of wave model spectra as prior information (Hasselmann and Hasselmann, 1991; Krogstad *et al.*, 1994; Engen *et al.*, 1995)

- Use of collocated scatterometer wind measurements to estimate the wind sea part of spectrum (Mastenbroek and de Valk, 2000)

- Use of wind vectors from atmospheric models to estimate the wind sea part of spectrum (official ESA algorithm)

The retrieval of geophysical parameters from airborne or spaceborne sensors using prior information is a standard problem in remote sensing. The main challenge is to combine measurement and prior information in some consistent way. Furthermore it is necessary to use a rigorous theoretical basis for the weighting of the two parts in order allow a clear interpretation of the retrieval results.

A standard retrieval technique used in many different contexts is the maximum a posteriori approach. The method is based on statistical models for both the measurement error and the prior knowledge. The retrieval strategy is to maximise the conditional probability of the wave spectrum F given the measurement P. According to the Bayes formula this probability $P(F|P)$ can be expressed as:

$$P(F|P) = \frac{P(P|F)\,P(F)}{P(P)} \tag{5.32}$$

where $P(P|F)$ describes the measurement error and $P(F)$ represents the prior distribution.

Using Gaussian distributions with diagonal covariance matrix for both the measurement error and the prior distribution, it can be shown that maximising Eqn. 5.32 is equivalent to minimising the following cost function:

$$J(F) = \int \left(\frac{1}{4\ var(P_k)} |P_k(F) - P_k^{obs}|^2 + \frac{1}{4\ var(F_k)} (F_k^{prior} - F_k)^2 \right) d\mathbf{k} \quad (5.33)$$

where F is the retrieved ocean wave spectrum, $P(F)$ the simulated cross spectrum using the forward SAR imaging function in the spectral domain 5.27 and F^{prior} the prior wave spectrum taken e.g. from the WAM model. The integration is over the whole spectrum in $\mathbf{k}$-space.

Although the previous approach was successfully used to estimate two dimensional wave spectra, there are two main points which can be still improved:

- It is not realistic to use a Gaussian model with uncorrelated wave components for the prior wave spectrum. This approach causes distortions of the retrieved wave spectrum, *e.g.* in many cases where the retrieval scheme tries to rotate wave systems of the prior spectrum.

- Due to the unrealistic prior model it is not at all clear how to choose the variance $\mathrm{Var}(F_k)$. The ad hoc weighting functions used in most studies have a strong influence on the retrieved wave spectra. This is a disadvantage in particular for wave model assimilation.

An ad hoc approach to get rid of the distortions caused by the unrealistic prior model was proposed by Hasselmann *et al.*(1996). Although this scheme provides realistic and smooth spectra it has the disadvantage of not being based on a well defined statistical model for the prior spectrum, which consequently leads to problems in the interpretation of the retrieved spectra.

An approach to introduce a more realistic prior model into the maximum a posteriori approach was proposed by Schulz-Stellenfleth and Lehner (2003a). In the PArtition, Rescale and Shift Algorithm (PARSA) probabilities are defined for the wave systems in the prior spectrum to be rotated, shifted in wavenumber or rescaled in energy. The scheme is based on a decomposition of the wave spectrum into different wave systems using the technique proposed by Gerling (1992). Denoting the subsystems with $B^i, i = 1, ..., n_p$ the

prior wave spectrum has a representation:

$$F_k = \sum_{i=1}^{n_p} B_k^i \tag{5.34}$$

For the subsystems stochastic models $\tilde{B}$ are defined as follows:

$$\tilde{B}^i(\Phi, k) = \tilde{X}_{sc}^i \, B^i(\Phi - \tilde{X}_{rot}^i, \tilde{X}_{sh}^i \, k) \quad i = 1, ..., n_p \tag{5.35}$$

Here, $\tilde{X}_{sc}, \tilde{X}_{rot}, \tilde{X}_{sh}^i$ are stochastic variables which are assumed to be independent and Gaussian distributed. The approach has two basic features:

- The shape of the directional distribution is maintained for each subsystem.
- Power laws in k, *e.g.* k^{-4} for wind seas, are maintained for each subsystem.

Using this prior model the following cost function has to be minimised.

$$\begin{aligned} J(X) &= \sum_k H_k \, |P_k(X) - P_k^{obs}|^2 \\ &\quad + \sum_i \left(\frac{(X_{sc}^i - 1)^2}{4(\sigma_{sc}^i)^2} + \frac{(X_{rot}^i)^2}{4(\sigma_{rot}^i)^2} + \frac{(X_{sh}^i - 1)^2}{4(\sigma_{sh}^i)^2} \right) \end{aligned} \tag{5.36}$$

The advantage of the PARSA approach compared to Eqn. 5.33 is the fact that the prior distribution is easier to interpret. If one uses a standard deviation of say 30° for the rotation parameter $\tilde{X}_{rot}$ this means about 95% certainty that the prior wave direction is less than 60° wrong. Basically this kind of confidence measure should be provided with prior wave spectra, *e.g.* provided by a wave model or a buoy.

The direct solution of the minimisation problem stated in Eqn. 5.36 is technically demanding. A feasible numerical scheme which is based on the approximation of the prior distribution Eqn. 5.35 with a multivariate Gaussian distribution can be found in Schulz-Stellenfleth and Lehner (2003b).

Fig. 5.36 shows an inversion performed with the PARSA scheme. The retrieved wave spectrum (A) is shown together with the prior spectrum (B) and the simulated spectra (C), (D) and observed spectrum (E). In all cases the modulus of the cross spectrum is shown.

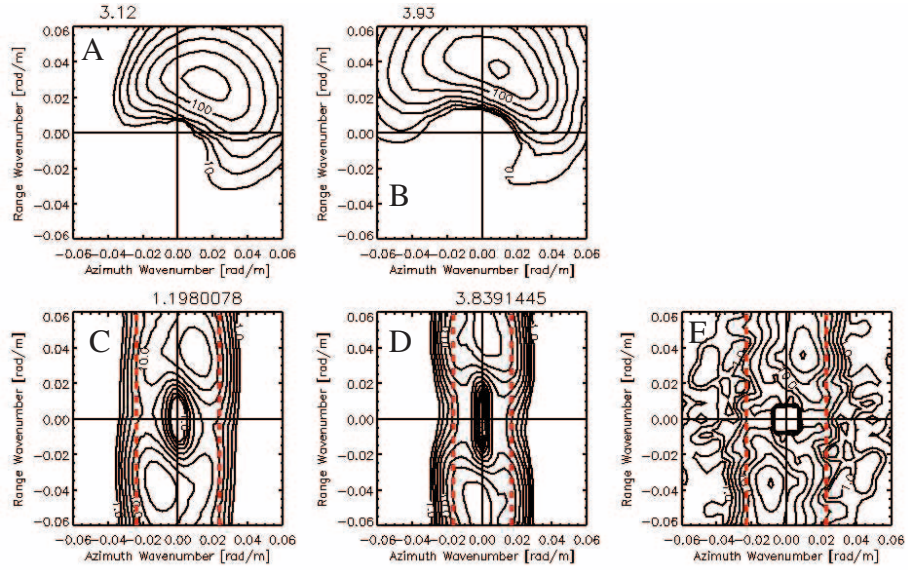

Figure 5.36: (A) Retrieved wave spectrum, (B) Prior wave spectrum, (C) Best simulated SAR spectrum, (D) First simulated SAR spectrum, (E) Observed SAR spectrum (adapted from Schulz-Stellenfleth and Lehner, 2003a).

5.10 Discussion

Susanne Lehner and Johannes Schulz-Stellenfleth

The radar sensors described in this chapter provide reliable new measurement systems for two dimensional wave spectra that will function under extreme weather conditions and will not be as easily destroyed by human impact as in situ devices.

The instruments cover a wide range of resolution and different areas of sea surface are taken into account to derive two dimensional ocean wave spectra and they have, therefore, their own particular applications.

Current spaceborne altimeters give information only on mean parameters such as significant waveheight and are therefore, although important in operational wave modelling applications, not described in this context. The extension to an airborne scanning altimeter yields two dimensional sea surface digital elevation models with all the possibilities to derive information on nonlinear sea surface characteristics. Marine Radars are the only instru-

ments that acquire a series of sea surface images of a size of a few square kilometers, thus in addition to two dimensional wave spectra the propagation of individual waves and wave groups can be measured. Ground based HF radars cover an area of 100 square kilometers or more and can thus be used to monitor the sea state conditions near the coast. Apart from measuring the surface currents, the second order backscattered spectrum yields two dimensional ocean wave spectra. An airborne real aperture radar system was described that has been used mainly for experimental scientific investigations and is now developing as a test system for future spaceborne applications, for example the proposed SWIMSAT mission. This system is independent of sea surface motion imaging artifacts that dominate the synthetic aperture radar images of the SAR.

As the present status of ocean wave modelling is so advanced that measurements of fine details in the directional spectrum are increasingly needed to improve forecast, SAR is of growing interest for operational model assimilation. Currently, space-borne synthetic aperture radar is the only instrument providing directional ocean wave information on a global scale.

An overview was given of the history as well as the present status of ocean wave measurements with synthetic aperture radar. The basic imaging principles were explained and up to date inversion techniques were summarised. SAR cross spectra were shown to resolve the ambiguity of wave propagation direction present in conventional SAR image variance spectra. It was demonstrated that the retrieval of complete two dimensional wave spectra in general requires some prior information on shorter waves propagating in the flight direction. It was emphasised that SAR retrieval schemes should be based on a strict stochastic model which allows a clear distinction between prior information and SAR measurement.

It was shown that first order measurements of long swell are possible using a simple linear or quasilinear inversion technique without any additional prior information. Although the estimated waveheights have a relatively low accuracy, due to uncertainties in the RAR transfer function, this technique is very efficient for monitoring and tracking of wavelengths and directions of swell.

Spaceborne SAR has a history of about ten years of global and continuous measurements, which are of great value for climate change studies. As explained in detail it might be useful to reprocess some of these data to make use of the full SAR information and to make them consistent with data acquired by the coming ENVISAT satellite. A reprocessed test data set of

complex ERS-2 imagettes was presented.

Along and across track interferometric SAR measurements of ocean waves and currents were introduced as an advanced technique providing additional sea state information compared to conventional single antenna SAR systems. InSAR systems simultaneously measure radar cross section, sea surface elevation and orbital velocity. The airborne InSAR systems flown so far are mainly used for scientific studies. However, the technique has reached a status where spaceborne missions for operational use are in the planning stage.

Chapter 6

Spectral Wave Modelling

Jaak Monbaliu and Jean-Michel Lefèvre

Spectral wave models computes the development of the directional spectrum under the action of advection, nonlinear interaction, wind input and spectral dissipation. The present chapter gives a summary of spectral wave modelling as a background for the wave model and data intercomparisons to be found in Part II of this book.

Battjes (1994) considers two families of ocean surface wave models. They are phase resolving (for rapidly varying waves, i.e. waves that have phase-averaged local properties which vary rapidly within distances of the order of one wavelength) and phase averaged models (for slowly varying waves). In most cases the assumption of phase randomness is a good approximation for the description of wind generated waves. It is known that the spectral wave energy distribution contains sufficient information to determine the most important parameters for the description of the wave field. The exact profile of the sea surface is not known in the strict sense but it is in a statistical sense. If at all possible, it is most economical to compute the energy spectrum (a phase-averaged quantity) with a phase averaged model. Phase-resolving models describe the sea-surface as a function of time but are computationally very demanding and should be used only when strictly needed. Only the mathematical description of strong diffraction and possibly of triad interaction requires phase-resolving models like mild-slope equation or Boussinesq models. The discussion here will be limited to phase averaged models, in common use for operational wave forecasting. The emphasis will be on the directional properties of these models.

6.1 The Model Equations

In the general case, incorporating the presence of currents, the equation to be solved is the balance equation for the wave action density (N) as a function of time and space. Wave action density is defined as

$$N(\mathbf{k}, \mathbf{x}, t) = E(\mathbf{k}, \mathbf{x}, t)/\sigma, \tag{6.1}$$

where E is the spectral wave energy density, $\mathbf{x}$ the geographical co-ordinates, t the time, $\mathbf{k} = (k_1, k_2)$ the wavenumber vector, and σ the intrinsic or relative frequency. We recall that the absolute frequency ω is linked to σ by $\omega = \sigma + \mathbf{k} \cdot \mathbf{U}$, where $\mathbf{U}$ is the current vector and $\sigma = \sqrt{gk \tanh(kh)}$. Following Battjes (1994),

$$\frac{\partial N}{\partial t} + \dot{x}_\alpha \frac{\partial N}{\partial x_\alpha} + \dot{k}_\alpha \frac{\partial N}{\partial k_\alpha} = \sum_i S_i, \tag{6.2}$$

where repeated indices means summation, and $\sum_i S_i$ signify the source terms. The characteristic equations for (6.2) are

$$\dot{x}_\alpha = c_{g\alpha} + U_\alpha = \frac{\partial \sigma}{\partial k_\alpha} + U_\alpha, \tag{6.3}$$

$$\dot{k}_\alpha = \frac{\partial k_\alpha}{\partial t} + \dot{x}_\beta \frac{\partial k_\alpha}{\partial x_\beta} = \frac{\partial \sigma}{\partial h}\frac{\partial h}{\partial x_\alpha} - k_\beta \frac{\partial U_\beta}{\partial x_\alpha}, \tag{6.4}$$

$$\dot{\omega} = \frac{\partial \omega}{\partial t} + \dot{x}_\alpha \frac{\partial \omega}{\partial x_\alpha} = \frac{\partial \sigma}{\partial h}\frac{\partial h}{\partial t} + k_\alpha \frac{\partial U_\alpha}{\partial t}. \tag{6.5}$$

The right hand side represents all effects of generation and dissipation of the waves including wind input, S_{in}, white capping dissipation, S_{ds}, non-linear wave-wave interactions, S_{nl}, bottom friction dissipation S_{bf}, and, in very shallow water, depth induced breaking, S_{br}. Non-linear wave-wave interactions may be further split into, S_{nl3}, triad interactions, and S_{nl4}, quadruple interactions. Only the latter are non-zero for deep water.

The computation of the non-linear wave-wave interactions is very time consuming, and in fact so time consuming that the exact calculation of the non-linear transfer is still not possible for operational purposes.

6.2 History

An excellent overview of spectral wave models up to and partially including the development of third generation wave models is given by Khandekar

(1989). The first generation discrete spectral wave models included energy propagation, wind input (Sin) and dissipation (Sds). Sin and Sds were tuned to observed fetch and duration limited characteristics.

The JONSWAP experiment (Hasselmann *et al.*, 1973) clearly illustrated the rapid growth of wave energy on the forward (low frequency) face of the spectrum. This feature together with the observation of the so called 'overshoot' effect could be explained by the non-linear wave-wave interactions. This led to the development of second and third generation spectral wave models.

Second generation models limit the computational effort. In the 'coupled hybrid' models, the wind sea is described by a set of basic sea state parameters (Chapter 2). Swell is propagated independently along rays. In the 'coupled discrete' models both the swell and the wind sea peak are represented at discrete frequencies. The tail beyond the peak is treated parametrically. The non-linear interactions which control strongly the wind sea evolution are parametrised in both type of models. A mechanism is built in to transfer energy between wind sea and swell after every integration time step. These models are still very much in use today, for example U.K. Met Office and Météo-France amongst others, use it as their operational global model.

Third-generation wave models solve the wave transport equation in space and time explicitly without any a priori assumption on the shape of the wave energy spectrum. The break-through was the fact that the non-linear interactions could be calculated explicitly by the approximation of the total integral by a limited number of interaction configurations. Hasselmann *et al.* (1985a, 1985b) found that the exact non-linear transfer could be approximated reasonably well by considering just one mirror-image pair of interaction configurations. Although the calculation of the non-linear transfer was still computationally expensive, it was no longer prohibitive. The method is known as the DIA (Discrete Interaction Approximation) and is still the most widely used method in operational third generation wave models.

The WAM model can be seen as a standard for this type of model (WAMDI, 1988). A detailed description of the WAM-Cycle 4 model can be found in Günther *et al.* (1992) and Komen *et al.* (1994). The WAM-model is a state of the art third generation spectral wave model specifically designed for global and shelf sea applications. It can run in deep or shallow water and includes depth and current refraction (steady depth and current field only). It can be set up for any local or global grid with a prescribed data set, and grids may be nested for fine scale applications. The model is used in many operational centres in the world (*e.g.* at the European Centre for

Medium Range Weather Forecast ECMWF). Other third generation models are, for example, WAVEWATCH (`http://polar.ncep.noaa.gov/waves/`) and the SWAN model developed by T.U.Delft (Booij *et al.*, 1999; Ris*et al.*, 1999; `http://fluidmechanics.tudelft.nl/`).

6.3 Operational Wave Modelling Today

A spectral wave model describes the evolution of the wave energy spectrum. The statistical description assumes stationarity and homogeneity of the wave field at the model mesh size scale. These assumptions break down when the scales of the relevant processes become of the same length and period as the characteristic waves. Global wave models have run with spatial resolutions as large as 3° and time steps of the order of 1 hour (Bidlot and Holt, 1999). Spectral wave models have been run in coastal areas with a spatial resolution of 100 m and have even been used to simulate laboratory experiments where a spatial resolution of 0.5 m was used (Ris, 1997). Note that spectral wave models in coastal areas are very often run in stationary mode, assuming no time variation in the domain considered.

To give a worldwide overview of operational spectral wave modelling is outside the scope of this article. To give some idea however, we refer here to Bidlot and Holt (1999) who recently described the current practice of operational wave forecasting at the European Centre for Medium Range Weather Forecasts (ECMWF) at Reading and at the UK Met Office at Bracknell. Other centres use similar model set-ups, of course adjusted to needs of national interests and specific users. The model of UKMO is a second generation model (as is the model of Météo-France) with 13 frequency components between 0.04 and 0.324 Hz and 16 directional components. Both UKMO, Météo-France and ECMWF run wave models globally and regionally. UKMO runs globally on a regular lat-lon grid with a resolution of 1.25° in longitude and 0.833° in latitude. Regionally it covers the European continental shelf including the Mediterranean and Black Sea at a resolution of 0.4° in latitude and 0.25° in longitude. Météo-France runs a global wave model on a regular lat-lon grid with a resolution of 1° in longitude and 1° in latitude and a regional one covering the European continental shelf and including the Mediterranean and Black Sea at a resolution of 0.25° in latitude and 0.25° in longitude (Guillaume, 1990, Fradon *et al.* 2000). A high resolution model (0.1°) driven by the ALADIN model winds with similar resolution is currently being implemented over a domain covering the

French continental shelf. ECMWF runs the WAM model globally on an irregular lat-lon grid with an effective resolution of 55 km and regionally for the whole North Atlantic, the North Sea, the Baltic Sea and the Mediterranean Black Sea with an effective resolution of 27 km. For the global model they use 25 frequencies between 0.04 and 0.4 Hz and 12 directions. For the regional model the same number of frequencies is used but the number of directions is doubled to 24. On 20th of November 18Z, 2000, at the same as the atmospheric model resolution was upgraded to the spectral resolution T511 (roughly 40 km in grid space), the number of directions in the operational WAM-model at ECMWF increased to 24 as well as the number of frequencies to 30, keeping the same original 25 frequencies and adding 2 low frequency bins and 3 high ones. The horizontal resolution of WAM was kept to 55 km (0.5° at the equator) (Jean Bidlot, *personal communication*).

Bidlot and Holt (1999) indicate that the performance of operational wave models has improved over the last decade. Errors can be attributed to internal wave model errors (incomplete knowledge and/or representation of source terms, inaccurate numerics, ...) and to external errors related to wind field inaccuracies. Especially in forecasting, errors in predicted wind fields soon dominate the other error sources (internal errors).

For a more extended overview and information on practical aspects of operational measurement and analysis, the reader is referred to the "WMO Guide to Wave analysis and forecasting" (WMO, 1998).

6.4 Wave Model Development

Spectral wave modelling is in continuous evolution in terms of physics, numerics and coupling.

Monbaliu *et al.* (2000) described a number of code changes and additions to the original WAM-Cycle 4 code in order to allow the model to run cost-effectively in coastal areas. A depth induced wave breaking dissipation as well as different bottom friction dissipation source term formulations were introduced. The most important change was, however, a relaxation of the condition that the source term integration time step needed to be smaller or equal to the propagation time step.

The development of the SWAN model (Ris, 1997; Booij *et al.*, 1999; Ris *et al.*, 1999) was a result of the need for a spectral wave model for coastal applications. It has an explicit description of all source terms applicable in

such areas, including near-resonant triad interactions. The early versions were to be used in stationary mode only. But recent versions allowed for time evolution. Recently SWAN Cycle-III has been released with, amongst other changes, a higher order propagation scheme and the possibility of using spherical co-ordinates. The SWAN-model, which originally was intended as a near-shore model, can now also be used for large scale applications. The triads are not included in current operational models, but a crude approximation is implemented in the SWAN model.

The use of parallel computers and therefore parallel versions of wave model codes is common. ECMWF, for example, runs parallel since late 1996 (Bidlot *et al.*, 2002). NCEP (National Centers for Environmental Prediction, USA) has replaced their WAM-Cycle4 implementation in early 2000 by the parallel version of the WAVEWATCH-III model (Tolman, 1999).

Developments will continue. It has become clear that the DIA-approach for calculation of resonant four-wave interactions is a relatively poor representation of the theoretical source. More accurate, yet efficient algorithms are being developed (van Vledder *et al.* 2001; van Vledder 2001; van Vledder and Bottema, 2002).

For example, in the "Advanced Wave Prediction Program" of the U.S. Office of Naval Research considerable attention is being paid to the subject of non-linear interactions. Since the non-linear transfer is crucial in the evolution of the wave energy spectrum, a better representation of this process will improve our understanding of the directional features of this evolution. Also other source terms are under discussion and are being investigated. New insights will find their way to operational models. In this respect it is for example interesting to note that WAM and WAVEWATCH employ quite different formulations for the physics of wind input and whitecap dissipation and also use different numerics. In that respect is is also worth mentioning that Schneggenburger *et al.* (2000) use, with apparent success, a non-linear dissipation function to control the evolution of the wave spectrum.

Work has been done to couple wave models with other models. The coupling with current models is getting more and more attention, both in regional and global applications (Ozer *et al.*, 2000; Buckley, 1999). ECMWF runs a coupled wave-atmospheric model since mid 1998 with apparent success (Bidlot *et al.*, 2002). The idea behind the coupling of an atmospheric and a wave model is that waves integrate the effect of wind. Together with the assimilation of altimeter data, it allows for a feedback from the waves to the surface winds. In this respect, assimilation of wave data will become more

and more important in the future. This aspect will be expanded upon in the next section.

6.5 Comparison With Measured Data and Data Assimilation

It is obvious that validation of an operational model needs a systematic comparison with observed data for an extended period of time. For global applications, readily available and reliable wave measurements from buoys are limited. Even fewer buoys provide directional information. Operational centres verify the performance of their operational system against measurements of standard integrated parameters describing the sea-state; see for example Janssen *et al.* (1997). For comparisons with altimeter data, significant waveheight only is used. When buoy data are used in the comparison, the peak or mean period are also compared. Statistics of the results deal with the usual parameters of bias, RMS error and scatter index. Also scatter plots of observed versus modelled data are produced. These comparisons do not say much about how well the full spectrum is reproduced. For a large number of applications a correct match of all frequencies involved in the wave spectrum is essential. For some engineering applications such as dredging operations or surveying, only knowledge of low frequency swell energy is really important. Operational centres acknowledge this and therefore also give the wave parameters in terms of total sea, wind sea and swell. For other applications such as trying to understand the mechanisms of gas transfer across the air-sea interface, probably all frequency components in the spectrum play a role.

Heimbach *et al.* (1998), for example, found that swell energy in the WAM-model set-up that they employed (the operational version of ECMWF since July 1994) was under-predicted by 20-30%, while the wind sea was over-predicted by some 10%, when they compared ERS-1 synthetic aperture radar (SAR) with collocated WAM wave model data for the period between January 1993 and December 1995. Such additional information possibly points at shortcomings such as excessive damping in the WAM model propagation scheme at low frequencies. However, the assimilation of underestimated waveheights from the ERS-1 altimeter in the WAM-model makes such interpretations difficult.

Many operational models include data assimilation of some sort. For example the current practice at ECMWF, UKMO and Météo-France for the

global model includes assimilation of the ERS-2 altimeter waveheight and surface wind speed. At UKMO they use the analysis correction scheme described by Thomas (1988). At ECMWF and Météo-France an optimum interpolation scheme as developed by Lionello *et al.* (1992) is adopted. Although assimilation of waveheight and wind speed have been pointed at as important reasons for improved forecasting skills (see for example Janssen *et al.*, 1997), Voorrips *et al.* (1997) illustrated clearly that assimilating wave information from pitch-and-roll (Wavec) buoys improved the KNMI (Royal Netherlands Meteorological Institute) operational forecast. The impact was greatest (up to 24 hours in the forecast) when swell coming from the Norwegian Sea was detected early enough and assimilated. The assimilation method uses an optimal interpolation technique on wave partitions, i.e. before assimilation, model and buoy data are partitioned into wind-sea and swell components. The methods above however are referred to as single-time level methods, because they adjust the (forecasted) wave field at the time level of assimilation only.

Assimilation techniques should preferably be based on multi-time level methods because they allow for integration of model data and observations in a dynamically consistent framework. Some methods have been proposed in literature, see for example Hersbach (1998) and Voorrips (1998), but are not used operationally, because they are still in development stage or computationally too expensive. One should not forget that data assimilation of wave observations is although common practice now, only developed fairly recently for the practical reason that reliable wave measurements were not available for the largest part of the world. Only about one hundred moored buoys in the world, located in coastal areas, transmit wave data on a regular basis on the Global Transmitting System (GTS). These buoys are almost all located in the Northern Hemisphere. It is only since large amounts of reliable remotely sensed wave information became available (*e.g.* ERS-1 wave data are available since 1991) that research and application interest to assimilate this information has grown considerably. It can therefore be expected that improvements in assimilation techniques for directional wave data will go hand in hand with the availability of a sufficient amount, both in time and in space, of reliable directional wave information. Remote sensing will probably be the only technique capable of providing this information. However, again some restrictions remain. Data from satellites are not available at any time and at any place. Also the information contained in, for example, SAR is limited. Only long wave components are properly resolved. For open ocean applications this is not a restriction, but for applications in

semi-enclosed seas where shorter waves occur most of the time, this kind of information is not effective.

Directional information is important for global wave forecasting/hindcasting. Bauer and Heimbach (1999) demonstrate that the ERS-1 synthetic aperture radar measures waveheights quite well. There seems to be a small but systematic underestimation of the significant waveheight compared to the waveheight as measured by the TOPEX/POSEIDON and ERS-1 altimeters, but it can be attributed to the underestimation of the wind sea part. Swell energy is captured quite accurately. When compared to buoys, the quality of the SAR significant waveheight seems comparable to the ECMWF/WAM model significant waveheight (Voorrips 1998, personal communication). That means that to improve wave analyses and forecasts, additional information from the SAR should be used (period, direction of wave trains, ...). The frequency and directional information present in the SAR signal might therefore make it very suitable for operational wave data assimilation. Note that the operational wave model data assimilation at ECMWF was upgraded on the 15-th of January 2003. It now assimilates in near real time both altimeter (Bidlot, 2001) and SAR data from the ERS-2 satellite (Bidlot, *personal communication*).

Directional information is particularly important in coastal wave studies. The design of harbour protection, the layout of harbour entrance channels, coastal protection measures such as beach-fill or artificial dikes all depend critically on correct directional information. Wave models and/or directional wave measurements, can provide at selected grid points full detail of the wave energy spectrum. Although it is obvious by itself that the representation of a bimodal spectrum by a significant waveheight, a period and a direction cannot describe the full details of the spectrum, the following example of an application at the Belgian coast is given as an illustration. In Fig. 6.1 the measured directional spectrum (Wavec buoy) is shown at Westhinder, a location some 25 km away from the coast (water depth about 30 m).

Also shown (dashed line) is the 'representative' spectrum as it would be constructed if only the significant waveheight, the peak period and the wind direction were given. The measured directional spectrum at Bol van Heist (Wavec buoy), a location some 5 km from the coast with a water depth of about 10 m, is compared to the numerically simulated spectrum. The near shore spectral wave model SWAN-model spectrum (Cycle 2, version 40.01) was implemented for this area and run in stationary mode. If the full directional spectrum is imposed at the sea-ward boundary of the model area (located on a line parallel to the coast and going through the West-

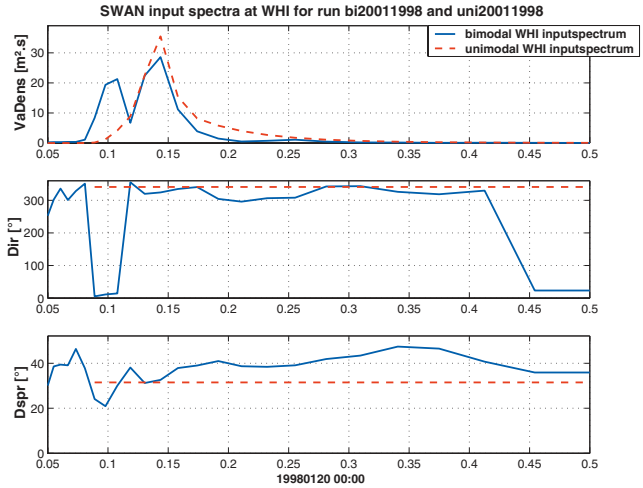

Figure 6.1: Measured bi-modal spectrum at buoy location Westhinder (full line) and representative uni-modal spectrum characterised by the significant waveheight, peak period and wind direction.

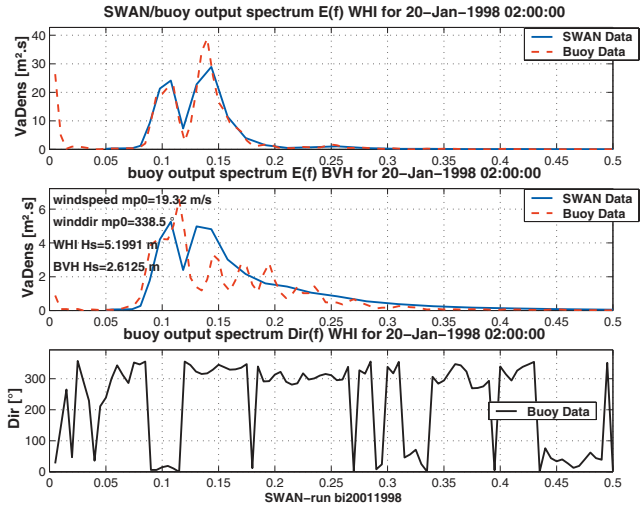

Figure 6.2: SWAN computed (full-line) versus measured spectrum at buoy location Westhinder (off-shore; dashed line upper panel) and measured spectrum at buoy location Bol van Heist (near-shore; dashed line lower panel). Measured spectrum is used as boundary condition for the computations.

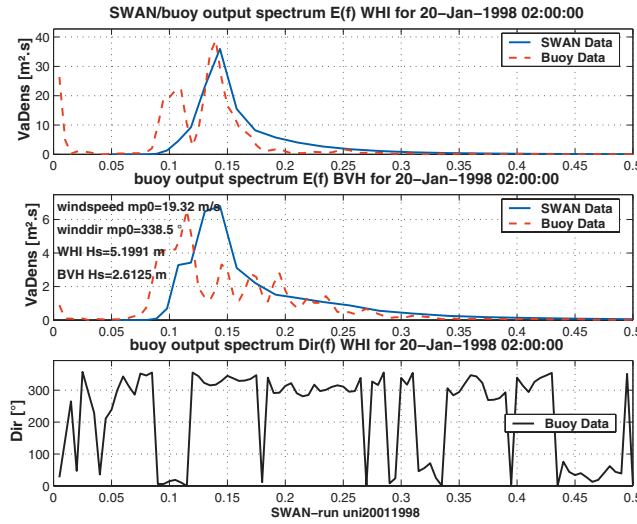

Figure 6.3: SWAN computed (full-line) versus measured spectrum at buoy location Westhinder (off-shore; dashed line upper panel) and measured spectrum at buoy location Bol van Heist (near-shore; dashed line lower panel). Representative spectrum is used as boundary condition for the computations.

hinder location), the agreement between model results and measurement is reasonable, see Fig. 6.2.

However if only integrated parameters are used, the information created at the near-shore location is not reliable (Fig. 6.3). The low frequency peak in the spectrum is completely missed. The availability of directional wave data is therefore crucial for wave climate studies; see for example also the Barstow *et al.*(2000, 2003).

6.6 Conclusions

Although the quality of wave predictions depends in the first place on the quality of the winds, it is clear that the improvement of the performance of operational spectral wave models is, and will be, due to a multitude of interrelated aspects. The improved description of the individual physical processes, improved numerics, coupling of different processes, enhanced resolution both in time and space and assimilation of in situ and remotely sensed data together with ever increasing computational and data processing

power, will all contribute. The enhancement of the resolution in directional space will increase the need to understand and measure the directional characteristics of waves. It can be expected that improvements in assimilation techniques will go hand in hand with the availability of directional data.

Acknowledgement

The support of COST-714 is gratefully acknowledged. The original WAM-Cycle 4 code was obtained from the Max-Planck-Institut für Meteorologie. Buoy data were obtained from the Coastal Service of the Ministry of the Flemish Community.

Chapter 7

Statistical Intercomparisons of Directional Wave Data

Sofia Caires, Lucy R. Wyatt and Harald E. Krogstad

7.1 Introduction

Intercomparison of directional wave data highlights the problems encountered in comparing any data sets. The data are often collected from different kinds of instruments, using different sampling strategies and different analysis procedures. The data may be available in the form of directional spectra, or in the form of parameters derived from the spectra.

Generally speaking, measurements of ocean waves involve estimation of parameters of random models. A central assumption about the random model is that it is stationary or homogeneous, – a property which is never strictly attained in practice. Even if there are optimal space/time windows in which the wave field is stationary and the parameters can be estimated with maximal accuracy, no instrument existing today is close to reaching such accuracy for common sea state parameters.

Consider the intercomparison of two wave instruments independently recording the same sea states. Associated with each measurement there are independent sampling errors, both instruments may have calibration errors depending on the sea state, and there may be temporal and spatial offsets between the recordings. In addition, the underlying sea states vary according to a certain natural variability which is beyond our control. We are thus facing several potential problems which have to be analysed and resolved properly:

- Difference in measurement principles
- Inherent limitations of the measurement principles
- Systematic off-sets due to incomplete calibration
- Inherent and in general different sampling variability
- Incomplete data coverage due to limited variability of the sea states
- Temporal and/or spatial offsets

Different instruments have different applications and, as long as they are known, inherent instrument limitations are not a problem. Whereas buoys are known to be excellent for measuring sea state parameters, their surface profiling capability (for crest height, wave skewness etc.) is less satisfactory. Spatial arrays are in many respects different from point measurements with a sensitivity that may be dependent both on the frequency and direction of the incoming waves.

A proper calibration of the instruments is essential for unbiased measurements, as discussed in Barstow *et al.* (1985). Deriving calibration functions is therefore often the primary objective for intercomparing the measurements. Similar considerations are also relevant when comparing measured data and model results. The sampling variability in real data should not be confused with deficiencies in the model.

In assessing the quality and accuracy of directional wave spectra, we are in principle interested in comparing the full spectra and their variation in wavenumber, $\mathbf{k}$, or frequency and direction, (f, θ). However, detailed quantitative comparisons on a point by point basis of estimated spectra are not feasible or indeed particularly helpful because of the large statistical variability and the fact that most in-situ systems only measure a few integral properties of the spectrum. Directionally integrated parameters like the frequency spectrum, the mean direction and spread as functions of frequency, or frequency integrated parameters like the significant wave height or the so-called main wave direction have less sampling variability than the full spectrum. Although integrated parameters may be sufficient in most situations, they may be inadequate for detailed intercomparisons of complex multi-modal situations. Below we focus on intercomparisons of integrated parameters.

There are various measures for the difference between two data sets, and Willmott *et al.* (1985) discuss measures like the root-mean-square error, the

mean absolute error and index of agreements, and apply the methodology to vector as well as scalar wave data. A set of complementary difference measures is recommended and so is also the 'bootstrap method' for assessing confidence and significance. Zambresky (1989) provides a useful list of standard wave parameters and statistics and Guillaume (1990) recommends some refined wave direction variables and finds the mean relative error to be more useful than the scatter index for comparison of significant wave height. She also uses comparisons of frequency spectra between models and buoy data including confidence limits obtained from the buoy data.

In most intercomparisons of wave measurements, or comparisons of measurements and hindcast results, one measurement is considered to be 'sea truth'. That is, all discrepancies are assumed to be attributable to the other instrument and standard statistical methods and concepts, such as regression analysis, scatter-indices, mean errors, correlation coefficients, *etc.*, are used to study the relationship between the two. Analyses of this type provide useful and easily understood first impressions of accuracy. However, although simple to produce, such presentations alone are, in general, not sufficient to really explain differences between the data sets. As noted above, direct intercomparison of spectra may be the only way to assess differences that show up in integrated parameters such as significant wave height or the overall mean direction.

In reality, all measurements and wave model hindcasts are subject to errors, and possibly bias, and none of them can be considered 'sea truth'. More formally, each of the observations/hindcasts corresponds to the measurement of an *unobserved* or *underlying* quantity, the 'reality' of the measurement and the 'reality' of a model hindcast (equivalently, each of the observations/hindcasts is subject to an unobserved error). In this context, classical linear regression and similar methods are not very appropriate, and more sophisticated tools like *errors-in-variable regression* are needed. When the sampling variability of the wave parameters is known in a statistical sense, weighted *Orthogonal Distance Regression*, ODR, is a reasonable choice (Boggs and Rogers, 1990). The *Pseudo Replication Algorithm* (PRA) (Hussin, 1997) may be used when the sampling variability has to be determined from the data.

There are also alternative approaches like simple non-parametric regression based on ranked observations, principal curve regression (Hastie and Stuetzle, 1989), and non-parametric regression with errors in variables (Fan and Truong, 1993). Applications of these methods to wave data are not known.

For conventional non-directional measurement system like buoys, wave staffs and radar altimeters, the frequency spectrum is obtained by standard time series analyses and the sampling variances in integrated parameters can be estimated using Taylor expansions. This type of analysis was also used to estimate variances of directional parameters from heave/pitch/roll buoys by Long (1980), see Chapter 3. For more complex measurements, *e.g.* HF radar, the sampling variability can only be estimated using simulations (Sova, 1995). Similar techniques have been used by Munthe-Kaas and Krogstad (1985) to confirm the Taylor series approach.

Krogstad *et al.* (1999) review a number of techniques for directional and non-directional wave parameter intercomparisons, and some of these and also more recent work are summarised here.

7.2 Comparison of Scalar Variables

Consider independent scalar measurements X and Y of the wave parameter, μ. Assume that sampling errors are Gaussian such that probability laws of X and Y are

$$\begin{aligned} \mathcal{L}(X) &= N\left(h(\mu), \sigma^2(h(\mu))\right), \\ \mathcal{L}(Y) &= N\left(f(\mu), \tau^2(f(\mu))\right). \end{aligned} \tag{7.1}$$

In general, neither X nor Y are free from systematic errors such that μ may be different from both $f(\mu)$ and $h(\mu)$. It is impossible to determine both $f(\mu)$ and $h(\mu)$, so in the following we assume that $h(\mu) = \mu$ and write x for μ, and y for $f(x)$. We shall furthermore assume that the sampling variability variances $\sigma^2(x)$ and $\tau^2(y)$ are functions of x and y.

For different sea states, x varies according to a certain occurrence density π, which for a long observation interval approaches the long term distribution of x. The observations $(X_i, Y_i)_{i=1}^N$ are thus obtained from a joint density of the form

$$\phi(\xi, \eta) = \int_s g_X(\xi, s, \sigma^2(s)) g_Y(\eta, f(s), \tau^2(f(s)))\pi(s)ds \tag{7.2}$$

where g_X and g_Y are Gaussian densities. The aim is to determine the function $f(x)$ although unbiased estimates of the distribution π may be of independent interest. The above situation suggests an *errors-in-variables*

model,

$$X_i = x_i + \delta_i,$$
$$Y_i = f(x_i) \ + \ \varepsilon_i, \quad i = 1, ..., N.$$

where x_i are unknown and $\mathcal{L}(\delta_i) = N(0, \sigma_i^2)$, $\mathcal{L}(\varepsilon_i) = N(0, \tau_i^2)$. One feature of such models is that they are *symmetric* in the sense that if f is one-to-one, the result of applying the model to some data is independent of which variables are chosen to be X or Y.

An error in variables model in which the underlying variables (x, y) are deterministic is called a *functional relationship model*. If (x, y) are random variables, the model is referred to as a *structural relationship model* (Anderson, 1984).

In our case we will consider the underlying wave parameters to be deterministic variables, and hence use a functional relationship model. Although the wave parameters are random variables, in the sense that they correspond to observations from a hypothetical population of wave scenarios, we are not primarily interested in their statistical behaviour. Instead, we focus on the relationship between the outcomes, that is, between the x and y that happened to occur. Deviations from $y = x$ for simultaneous data indicate lack of a proper calibration or other systematic off-set for one or both of the instruments. In a statistical language, we are interested in studying the relationship between each device or wave model measure (each with its inherent errors) conditionally on a specific 'wave scenario' (the particular occurrence of environmental processes in which measurements took place). A more formal justification can be given on the basis of the conditionality principle (Cox and Hinkley, 1974, p. 38), according to which we should condition on the actual observations ('wave scenario'), and thus regard them as fixed (though unknown), and hence use a functional model. This is the same argument that would lead one to use a regression model if one wanted to predict Y from X even if X is really randomly selected (see for example Cox and Hinkley (1974, Example 2.27, p. 32)).

The *linear* functional relationship, $y = a + bx$, is an important special case. If (X, Y) corresponds to pairs of either different measurements or wave model hindcasts plus their (unobserved) errors, one expects to obtain $y = x$, since both measuring/hindcasting systems aim at the same underlying reality. If this is not the case, this is an indication of a difference between the measurements which may be due to differences in measurement location or time, or it possibly suggests that at least one of the systems needs to be corrected.

Errors-in-variables models have been used in comparisons between HF radar and buoy measurements; see Sova (1995) for a functional relationship model, and Samset *et al.* (1996) for a structural relationship model.

7.2.1 Maximum Likelihood Estimation with Known Error Distributions

Assume that the function f is parametrized in terms of the parameters $\mathbf{p} = \{p_1, \cdots, p_k\}$ such that $y = f(x, \mathbf{p})$. For the linear model $y = a + bx$, $\mathbf{p} = \{a, b\}$. Since the master distribution (Eqn. 7.2) is based on normal densities, a maximum likelihood approach is natural, and the negative logarithm of the likelihood function is

$$\begin{aligned} -\log L(\mathbf{p}, \mathbf{x}|\mathbf{X}, \mathbf{Y}) \quad &\backsim \quad \sum_{i=1}^{N} \Bigg\{ \log \left[\sigma(x_i)^2 \tau(f(x_i, \mathbf{p}))^2\right] \\ &+ \quad \frac{(X_i - x_i)^2}{\sigma(x_i)^2} + \frac{(Y_i - f(x_i, \mathbf{p}))^2}{\tau(f(x_i, \mathbf{p}))^2} \Bigg\} \end{aligned} \tag{7.3}$$

Since $\{x_i\}_{i=1}^N$ are unknown, the model has $N+$ card($\mathbf{p}$) parameters. However, for a given set $\mathbf{p}$, the optimal x_i-s are found by one-dimensional minimizations, which for the simplest cases may be found analytically.

The logarithmic term in Eqn. 7.3 is often slowly varying, and if it discarded, the remaining expression is commonly known as Total Least Square (TLS). Denoting the ratio between the variances, $\gamma(x) = \sigma^2(x) / \tau(f(x, \mathbf{p}))^2$, TLS includes regular Y-on-X regression for $\gamma \to 0$, Orthogonal Distance regression for $\gamma = 1$, and X-on-Y regression for $\gamma \to \infty$. When γ is constant, the linear TLS regression is solvable analytically (Fuller, 1987):

$$\hat{\beta} = \frac{\gamma s_{yy} - s_{xx} + \sqrt{(s_{xx} - \gamma s_{yy})^2 + 4\gamma s_{xy}^2}}{2\gamma s_{xy}}, \tag{7.4}$$

$$\hat{a} = \bar{Y} - \hat{b}\bar{X}, \tag{7.5}$$

$$x_n = \frac{X_n + \beta\gamma(Y_n - \alpha)}{1 + \beta^2\gamma}. \tag{7.6}$$

Here, $\bar{X} = \sum_{n=1}^N W_n X_n / \sum_{n=1}^N W_n$, $\bar{Y} = \sum_{n=1}^N W_n Y_n / \sum_{n=1}^N W_n$,

$$s_{xy} = \sum_{n=1}^{N} W_n \left(X_n - \bar{X}\right)\left(Y_n - \bar{Y}\right), \tag{7.7}$$

and $W_n = \sigma\,(x_n)^{-2}$. For more general functions $y = f(x, \mathbf{p})$, numerical solutions are needed. Highly efficient algorithms for the ODR problem have been developed (Boggs *et al.* 1987) and the Fortran program suite ODRPACK is available from `http://www.netlib.org`.

The above formulation for angular data is slightly different since such data are combined mod(2π). For a valid linear relationship between two angular variables of the form $y = a + bx \mod(2\pi)$, b can only take the values 1, 0 or -1. The natural error distributions for directional data is the *vonMises distribution*, the circular analogue of the normal distribution (Mardia, 1972). It has a probability density function v defined by

$$\begin{aligned} v(x, \mu, \kappa) &= (2\pi I_0(\kappa)^{-1}\, e^{\kappa \cos(x-\mu)}, \\ 0 \le x < 2\pi, &\quad 0 \le \mu < 2\pi, \quad \kappa > 0. \end{aligned} \tag{7.8}$$

where μ is the *mean direction*; κ is the *concentration parameter*; and I_0 is the modified Bessel function of the first kind and of order 0.

With errors distributed according to $\mathcal{L}(\delta_i) = v(\cdot, 0, \kappa), \quad \mathcal{L}(\varepsilon_i) = v(\cdot, 0, \nu)$, the log likelihood for $b = 1$ is

$$\begin{aligned} \log L(a, \mathbf{x}|\mathbf{X}, \mathbf{Y}) \quad &\backsim \quad \sum_{i=1}^{N} \{-\log(I_0(\kappa) I_0(\nu)) + \kappa \cos(X_i - x_i) \\ &+ \quad \nu \cos(Y_i - x_i - a)\}\,. \end{aligned} \tag{7.9}$$

Constant κ and ν should be a realistic assumption for directional data, and with $\gamma = \nu/\kappa$, the problem reduces to

$$\max \left\{ \sum_{i=1}^{N} \{\cos(X_i - x_i) + \gamma \cos(Y_i - x_i - a)\}\,. \right\} \tag{7.10}$$

The optimal x_i for a fixed value of a is easily seen to be

$$x_i = X_i + \arg\left(1 + \gamma e^{i(Y_i - X_i - a)}\right),\ i = 1, \cdots, N, \tag{7.11}$$

which for $\gamma = 1$, simplifies to

$$x_i = \frac{Y_i + X_i - a}{2}. \tag{7.12}$$

The ML estimate for a when $\gamma = 1$ is then

$$\hat{a}_{\gamma=1} = 2 \arg\left(\sum_{i=1}^{N} \exp\left(i \frac{Y_i - X_i}{2} \right) \right). \tag{7.13}$$

For a general γ, a has to be found numerically.

7.2.2 Unknown Error Distributions

If the variances in the linear functional relationship are unknown and cannot be determined using independent methods, they will have to be estimated as a necessary step in the estimation of a and b. However, it turns out that this is impossible without further constraints, such as assuming that $\gamma = \tau^2/\sigma^2$ is known. A method to determine γ is therefore required before maximum likelihood estimates of the unknown parameters, a, b and σ^2, can be obtained. Some complications arise because the maximum likelihood estimate of σ^2 is not consistent and must be corrected 'for degrees of freedom', but what matters is that one can proceed once γ has been given an appropriate fixed value. Hussin (1997) examined problems of this type and proposed a method for estimating γ. In his work he reviews several existing algorithms for estimating the regression coefficients when γ is unknown. He proposes a new algorithm that behaves better than the ones considered and, contrary to them, produces estimates of the ratio of variances γ (and of the variances σ^2 and τ^2 themselves). Extensions of Hussin's PRA method are given in Caires (2000), where further details and algorithms may be found.

The main idea behind PRA is that of creating a *set of pseudo-replicate data*, which allows one to obtain certain estimates of σ^2 and τ^2 by estimating the parameters of the *replicated linear functional relationship model*. This replicated model assumes that, for each i, the underlying variables x_i and y_i, $i = 1, 2, ..., k$, have m_i measurements X_{ij} and Y_{ij}, $j = 1, 2, ..., m_i$, the *replicates*, and that

$$\begin{aligned} X_{ij} &= x_i + \delta_{ij}, \\ Y_{ij} &= a + bx_i + \varepsilon_{ij}, \\ & j = 1, 2, ..., m_i,\ i = 1, 2, ..., k. \end{aligned}$$

The fact that more than one observation is made of the same underlying variable, makes it possible to estimate the parameters by maximum likelihood. Although the created pseudo-replicate data are not truly replicate data, the method consists in estimating the parameters as if they were. Thus, by 'pseudo-replicating' the existing data, one estimates the variances σ^2, τ^2, computes their ratio, and then uses the latter as an estimate (a 'fixed value') of γ to obtain the estimates of the (un-replicated) linear functional relationship model.

The pseudo-replicate data is obtained through a *grouping algorithm*. The algorithm consists in the formation of one family of *pseudo-replicate groups*, a family of subsets or subgroups of the data set $\{X_i, Y_i\}$, $i = 1, 2, ..., N$,

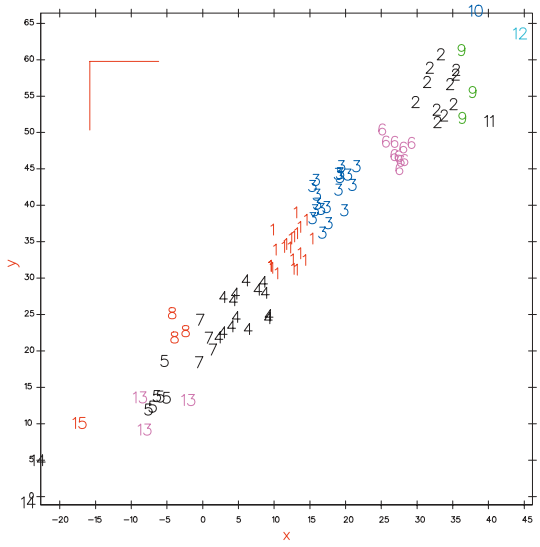

Figure 7.1: Example of pseudo replication of data.

using criteria based on the sample range and sample size. Figure 7.1 shows an example of pseudo replication. In the picture, a set of data $\{X_i, Y_i\}_{i=1}^{N}$, has been divided into groups $\{X_{i,j}, Y_{i,j}\}$, $j = 1, 2, ..., m_i$, $i = 1, 2, \cdots, k$, each data point $(x_{i,j}, y_{i,j})$ being indicated by its group index, i.

Given a family of pseudo-replicate groups obtained by the grouping algorithm, we can use the replicated functional relationship model to estimate the variances σ^2, τ^2, and hence their ratio γ.

Hussins' method consists in using the grouping algorithm to create successive sets of replicate data from which a sequence of γ estimates, γ_p, can be obtained and then to use a line control chart technique to choose the appropriate value for γ. Figure 7.2 shows an example of a line control chart. The full line represents successive values of γ_p and the dashed lines represent the line control limits. Starting from the end of the chart (higher values of p) the last value before the line of the γ_p goes outside the control limits is the chosen value for γ.

When trying to obtain estimates of the *rotation* a and the concentration parameters (κ, ν) between two directional data sets, we were faced with the same problem that occurred in the linear case,– a constraint analogous to that employed in the linear case, *e.g.*, a fixed ratio $\gamma = \nu/\kappa$ is required. Sim-

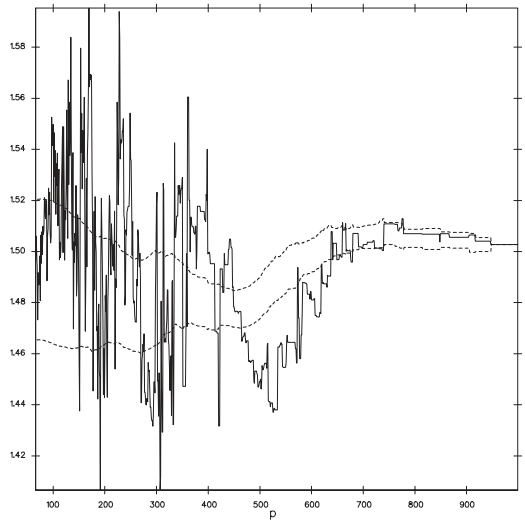

Figure 7.2: Example of a line control chart: λ_p (full line) and line control limits (dashed lines).

ilarly to what happens in the linear case, the estimate of the concentration parameter is inconsistent. Unlike the linear case, this has not been shown theoretically but an analogy with the linear case and the correspondence between variance and concentration parameters has allowed an appropriate correction to be derived. The correction has been confirmed with extensive simulation results (see Caires (2000) for details). The linear PRA method has been extended to allow the determination of the directional parameters.

The models described above deal with observations (X_i, Y_i) affected by errors $(\delta_i, \varepsilon_i)$ whose distributions are assumed normal/von Mises with constant variance/concentration parameter. However, it is likely that errors in measurement or models will depend on the wave conditions. We thus have a problem of *homogeneity,* and need somehow to either homogenize the data or to apply the models above to homogeneous subgroups of the data. In order to homogenize the data, some authors, for instance Samset *et al.* (1996), suggest the use of 'variance stabilizing' transformations, such as a Box-Cox transformation (*e.g.* the logarithm), which is common practice in applied statistics. This is not always an advisable method, because the transformation, which in most cases is non-linear, makes the results difficult to interpret and may change a relationship between variables that was

originally linear into a non-linear one. In our case, this disadvantage seems particularly important. Also, the fact that the variance/concentration parameters of the errors may vary according to wave conditions is itself an important aspect worthy of investigation. A generalised PRA mehods has therefore been developed. The method consists of pooling the data into homogeneous classes (specifically, classes of measurements with approximately the same variance), and then apply the models to each class. This provides estimates of the variances/concentration coefficients of the unobserved errors in each class. Then, a 'global' functional relationship model, in which the variances of the errors are known, can be fitted using the maximum likelihood technique.

7.3 Other Intercomparison Techniques

When different data sets are pooled into a common data base, *e.g.* for climatological analyses, it is important that the data sets are properly calibrated. In particular, the distribution of simultaneous data sets should be the same. This requirement leads to a straightforward method of obtaining a non-parametric regression function $Y = h(X)$ between two arbitrary parameters X and Y. If we for the moment disregard the sampling errors, X and Y will have distribution functions F_X and F_Y, and if the regression function is monotonic,

$$F_X(x) = P(X \leq x) = P(h(X) \leq h(x)) = F_Y(h(x)), \tag{7.14}$$

from which it follows that $y = h(x) = F_Y^{-1}(F_X(x))$. The sampling version, based on an observed data set (X_i, Y_i), $i = 1, .., N$, is the piecewise linear function defined by pairing the ordered observations $X_1^* \leq X_2^* \leq ... \leq X_N^*$ and $Y_1^* \leq Y_2^* \leq ... \leq Y_N^*$. Since sampling errors typically stretch the sampling distributions compared to the exact distributions, this will introduce some bias in the function if the sampling error is large compared to the variations of the variables, or if the sampling errors are highly different for X and Y.

An application to SCAWVEX data in Fig.7.3 shows that the method reveals evidence of a change in the nature of the relationship between HF radar and buoy data in higher sea-states associated with a breakdown in the theory underlying the HF radar data (See also Part II of this book).

A somewhat different approach is the use of *confidence regions* in the scatter diagrams (Allender *et al.*, 1989). The confidence regions are lines which, for

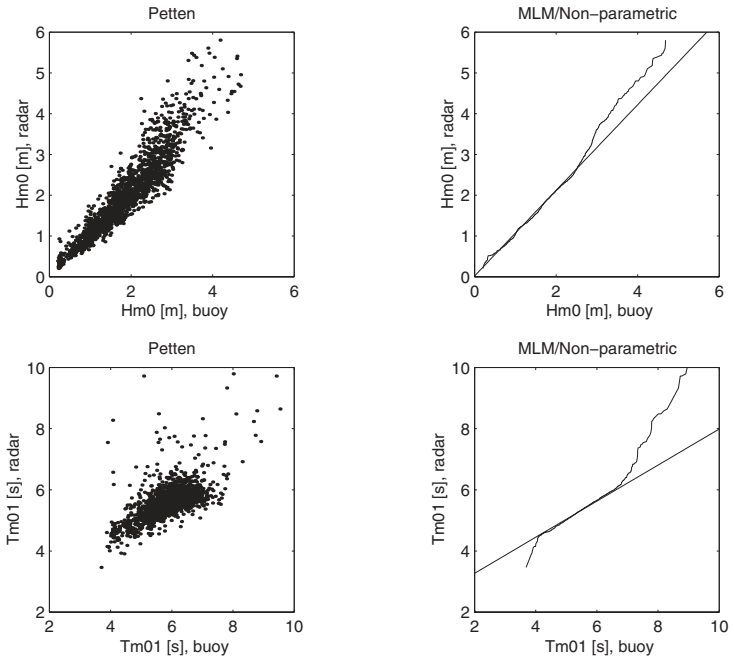

Figure 7.3: ML and nonparametric regression for a data set from the SCAWVEX project. The curves coincide for the bulk of the measurements, but the nonparametric regression indicates some deviation for the extreme measurements.

certain models of the sampling variability, should enclose a given fraction of the data points. As an example, assume that both instruments measure the same apart from the sampling variability, that is, $\mathrm{E}(X) = \mathrm{E}(Y)$ for simultaneous pairs. Assume further that the sampling variabilities are equal but independent with a standard deviation that increases linearly with the expectation,

$$std(X) = std(Y) = c\,\mathrm{E}(X). \tag{7.15}$$

Two lines through the origin which approximately enclose a fraction p of the data points are then given by

$$\begin{aligned} y_{\pm} &= \tan(\pi/4 \pm \delta)x, \\ \sin(\delta) &= c\gamma_p/2^{1/2}, \\ 2\Phi(\gamma_p) - 1 &= p \end{aligned}$$

where Φ is the cumulative standard normal distribution. Using the Hold-

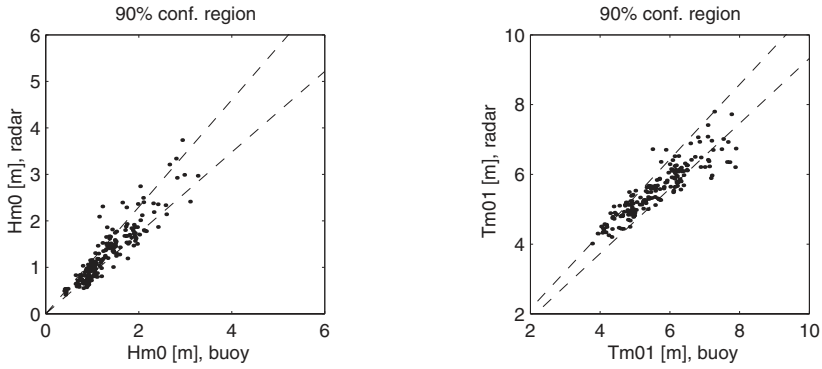

Figure 7.4: Examples of confidence regions for significant wave height and wave period based on the sampling variability of the buoy measurements (Krogstad *et al.* 1999).

erness data from SCAWVEX as an example, the C.O.V. (i.e. standard deviation divided by the expectation) has been found to be 4-6% for the buoy wave height and 3-5% for the radar (Wyatt *et al.*, 1999). For the wave period the C.O.V. was similarly computed to 2-3% for the buoy and 1-2% for the radar. Neglecting the bias for the moment, 90% confidence regions based on a common 6% C.O.V. for the wave height and 3% for the period are shown in Fig.7.4. It turns out that the fraction of the data points inside the 90% limits are merely 57% for wave height and 66% for the wave period. We obtain approximately 90% enclosure by increasing the C.O.V. for wave height to 12% and to 4% for the wave period. We therefore conclude that the sampling variability explains almost all the scatter seen in the wave period (despite an obvious bias seen in the plot), whereas wave height has additional variability not accounted for by the sampling variability.

7.4 Intercomparison of Wave Spectra

One dimensional frequency spectra as well as frequency dependent parameters like the mean direction and the directional spread are conveniently compared using stack-plots with a common frequency scale along the horizontal axis. However, for full two-dimensional spectra, there does not seem to be much possibility apart from contour or color-coded 2D graphs side by side. The large dynamical range of the directional spectrum suggest that

logarithmic contour intervals should applied, but even then rather misleading graphs often appears, in particular when the graphs are auto-scaled. We refer Part II of this monograph for examples of spectral intercomparisons.

Acknowledgements

SC is very grateful to the Portuguese Sub-programa Ciência e Tecnologia do 2^o Quadro Comunitário de Apoio and to the TMR programme of the commission of the European Union for funding her research. SC and LRW are very grateful to Dr. Nick Fieller and Dr. Abdul Hussin for the information provided and useful discussions.Dr. Nick Fieller and Dr. Abdul Hussin for the information provided and useful discussions.

Nomenclature

Symbols

a_n, b_n	Fourier coefficients of the directional distribution $D(\theta)$
$A(\mathbf{k}, \omega)$	Stochastic amplitude for the velocity potential $\Phi(\mathbf{x}, z, t)$
$B(\mathbf{k}, \omega)$	Stochastic amplitude of the surface elevation $\eta(\mathbf{x}, t)$
c_n	Complex Fourier coefficient, $c_n = a_n + ib_n$
c_g	Group velocity, $c_g = \partial\omega/\partial k$
$D(\theta, \omega)$	Directional distribution
$E(\omega, \theta)$	Directional spectrum, $E(\omega, \theta) = S(\omega) D(\theta, \omega)$
$F(\mathbf{k}, \omega)$	Wavenumber-frequency spectrum (also $\Psi(\mathbf{k}, \omega)$ has been used)
f	Frequency, $f = \omega/2\pi$
g	Acceleration of gravity
H_s, $Hm0$	Significant wave height from the spectrum, $H_s = Hm0 = m_0^{1/2}$
$H1/3$	Significant wave height from the time series (not used)
$H(D)$	Entropy functional for the distribution D
h	Water depth
$\mathbf{h}(\theta, \omega)$	Angular part of linear wave theory transfer functions
$J(F)$	SAR inversion functional for the spectrum F
$\mathbf{k}$, k	Wavenumber, modulus of wavenumber
$\mathcal{M}(\mathbf{k})$	Modulation transfer function
m_k	k-th spectral moment, $m_k = \int_0^\infty \omega^k S(\omega)\, d\omega$
$N(\mathbf{k}, \mathbf{x}, t)$	Wave action density
r_n	Modulus of Fourier coefficient, $r_n = \lvert a_n + ib_n \rvert = \lvert c_n \rvert$
R	Radar-surface range
$S(\omega)$	Frequency spectrum
s	Power in the *cos-2s-distribution*
T_p	Spectral peak period
T_z, $Tm02$	Mean wave period from spectrum, $T_z = Tm02 = 2\pi (m_0/m_2)^{1/2}$
T^{RAR}	Real Aperture Radar transfer function
T^{tilt}, T^{hydr}	Tilt and hydrodynamic modulation transfer functions
$T(\mathbf{k}, \omega)$	Linear wave theory transfer function

$\mathbf{U}$	Current velocity
V	Radar platform velocity
$\mathbf{V}$	Variance-covariance matrix for the Fourier coefficients
$\mathbf{W}(n)$	Sampled multivariate wave record, $\mathbf{W}(n)) = \mathbf{Y}(n\Delta t)$
$\mathbf{x}$	Horizontal location
$\mathbf{Y}(t)$	Multivariate record of wave properties
z	Vertical location (positive upwards)

$\eta(\mathbf{x}, t)$	Surface elevation as a function of $\mathbf{x}$ and t
θ	Wave(number) direction
θ_1	Mean wave direction from a_1 and b_1
λ	Wavelength
ν	Degrees of freedom in spectral estimates
ν_i	Intensity of Poisson point process
Ξ	Symbol signifying the dispersion surface
ρ	Water density
$\mathbf{\Sigma}(\omega)$	Cross covariance matrix
σ	Intrinsic frequency (for observations in currents)
σ_0	Radar cross section
σ_1	Directional spread, $\sqrt{2(1-r_1)}$
$\sigma(k, h)$	Dispersion relation, $\sigma(k, h) = \sqrt{gk}\tanh(kh)$
$\Phi(\mathbf{x}, z, t)$	Wave induced velocity potential
$\Psi(\mathbf{k})$	Wavenumber spectrum (Also $F(\mathbf{k})$ is used)
Ψ_γ	Radar image spectrum for the marine radar
$\chi(\mathbf{k}, \omega)$	Wavenumber-frequency spectrum
ω	Angular frequency
ω_s	Sampling frequency

Mathematical notations and functions

$B(x, y)$	Beta function
$\mathrm{Cov}(X, Y)$	Covariance X and Y
$\mathbb{E}()$	Expectation of X
$\mathcal{F}()$	Fourier transform, $\mathcal{F}(f) = \hat{f}$
$g_X(x)$	Gaussian density for X
$H(x)$	Heaviside step function
$I_n(x)$	Modified Bessel function of the first kind and order n
$\Im()$	Imaginary part
$J_n(x)$	Bessel function of order n
$L\left(\Phi, \hat{\Phi}\right)$	Likelihood functional for Φ given an estimate $\hat{\Phi}$
$\mathcal{L}(X)$	Probability law of X
$N\left(\mu, \sigma^2\right)$	Normal distribution with mean μ and st. dev. σ
$P()$	Probability of X
$\Re()$	Real part
$tr(A)$	Trace of the matrix A, $tr(A) = \Sigma_{n=1}^{N} a_{ii}$
$\mathrm{Var}(X)$	Variance of X
$W()$	Winding operation on a function on the real line

Γ	Gamma function
$\delta(\mathbf{k})$	Dirac δ-function
ρ^{XY}	X-Y cross correlation function
Φ^g	Generalized inverse of matrix Φ
$()^H$	Hermitian transposed, $\left(\mathbf{A}^H\right)_{ij} = \overline{a_{ji}}$
$\widehat{()}$	Estimate of a parameter, also used for the Fourier transform
$\dot{}$	Time derivative, $\dot{x} = \partial x / \partial t$
$\#()$	Number of (*cardinality*)

References

Anon., *Ocean Wave Spectra*, Prentice-Hall, Englewood Cliffs, New Jersey, 1963.

Anon., *Ocean wave measurement and analysis*, Proc. of Int. Symp., New Orleans, Louisiana, September 9-11, 1974, ASCE, New York, 1974.

Anon., *Directional Wave Spectra and Applications*, Berkeley, California Publ. by ASCE, New York, 1981.

Akhieser, N. I., and M. Krein, Some questions in the theory of moments, *Transl. of Math. Monographs*, AMS, Providence Rhode Island, 2, 1962.

Allender, J., T. Audunson, S. F. Barstow, S. Bjerken, L. E. Borgman, C. Graham, H. E. Krogstad, P. Steinbakke, and L. Vartdal, The WADIC project; a comprehensive field evaluation of directional wave instrumentation, *Ocean Engng.*, 16, 505–536, 1989.

Alpers, W. R., and C. L. Rufenach, The effect of orbital motions on synthetic aperture radar imagery of ocean waves, *IEEE Trans. Antennas Propag.*, 27, 685–690, 1979.

Alpers, W. R., D. B. Ross, and C. L. Rufenach, On the detectability of ocean surface waves by real and synthetic aperture radar, *J. Geophys. Res.*, 86, 6481–6498, 1981.

Alpers, W. R., and K. Hasselmann, Spectral signal to clutter and thermal noise properties of ocean wave imaging Synthetic Aperture Radars, *Int. J. Remote Sens.*, 3, 423–446, 1982.

Anctil, F., M. A. Donelan, W. M. Drennan and H. C. Graber, Eddy correlation measurements of air-sea fluxes from a Discus buoy, *J. Atmos. Oceanic Technol.*, 11, 1144–1150, 1994.

Anderson, T. W., Estimating linear statistical relationships, *Ann. Stat.*, 12(1), 1–45, 1984.

Atanassov, V., W. Rosenthal, and F. Ziemer, Removal of Ambiguity of Two Dimensional Power Spectra Obtained by Processing Ship Radar Images of Ocean Waves, *J. Geophys. Res.*, 90, 1061–1067, 1985.

Atanga J., and L. R. Wyatt, Comparison of inversion algorithms for HF radar wave measurements, *IEEE J. Oceanic Eng.*, 22, 593–603, 1997.

Bamler, R., and B. Schättler, SAR data acquisition and image formation, in *SAR Geocoding: Data and systems* (Ed.: G. Schreier), Wichman Verlag, Gmbh, Germany, 1993.

Bamler, R., and P. Hartl, Synthetic aperture radar interferometry, *Inverse Problems*, 14, R1–R54, 1998.

Bao, M., C. Brüning, and W. Alpers, A generalized nonlinear ocean wave SAR spectral integral transform and its application to ERS-1 SAR ocean wave imaging, in Proceedings of the Second ERS1 Symp. on Space at the Service of our Environment, Hamburg, ESA SP-361, 1993.

Bao, M., C. Brüning, and W. Alpers, Simulation of ocean waves imaging by an along-track interferometric synthetic aperture radar, *IEEE Trans. Geosci. Remote Sens.*, 35, 618–631, 1997.

Bao, M., W. Alpers, and C. Brüning, A new nonlinear integral transform relating ocean wave spectra to phase image spectra of an along-track interferometric Synthetic Aperture Radar, *IEEE Trans. Geosci. Remote Sens.*, 37, 461–466, 1999.

Barber, N. F., Measurements of the sea conditions by the motion of a floating buoy, *Rep. A.R.L., 103.40, N.2/W*, 1946.

Barber, N. F., and F. Ursell, The generation and propagation of ocean waves and swell, *Philos. Trans. R. Soc. London Ser. A*, 240, 527–560, 1948.

Barrick D. E., Theory of HF and VHF propagation across the rough sea. Part II, *Radio Sci.*, 6, 527–533, 1971.

Barrick D. E., First-order theory and analysis of MF/HF/VHF scatter from the sea, *IEEE Trans. Antennas Prop.*, AP-20, 2–10, 1972.

Barrick D. E., and B. L. Weber, On the nonlinear theory for gravity waves on the ocean's surface. Part II: Interpretation and Applications, *J. Phys. Oceanogr.*, 7, 11–21, 1977.

Barstow, S. F., and H. E. Krogstad: General analysis of directional ocean wave data from heave/pitch/roll buoys, *Mod. Ident. and Control*, 5, 47–70, 1984.

Barstow, S. F., H. E. Krogstad., K. Torsethaugen. and T. Audunson: Procedures and problems associated with the calibration of wave sensors, *Adv. Underw. Techn. and Offs. Eng.*, 4, 55–82, 1985.

Barstow, S.F., M. Athanassoulis, and L. Cavaleri, "EUROWAVES: Integration of data from many sources in a user-friendly software package for calculation of wave statistics in European coastal waters, Proc. *Oceanology International 2000 Conference*, Brighton, UK, March 2000, 269–277, CD-ROM, 2000.

Barstow,S.F., G. Mørk, L. Lønseth, P. Schjølberg, U. Machado, G. Athanas-

soulis, K. Belibassakis, Th. Gerostathis, C. Stefanakos, and G. Spaan, WORLDWAVES, High quality coastal and offshore wave data within minutes for any global site, Proc. *OMAE 2003 conference*, Cancun, Mexico, OMAE2003-37297, June 2003, CD-ROM, 2003.

Battjes J. A., Shallow water wave modelling. Proc. of the *Int. Symp. on 'Waves – Physical and Numerical Modelling'*, Univ. of B. C., Vancouver, I, 1–23, 1994.

Bauer, E. and P. Heimbach, Annual validation of significant wave heights of ERS-1 synthetic aperture radar wave mode spectra using TOPEX/Poseidon and ERS-1 altimeter data, *J. Geophys. Res.*, 104(C6,13), 13345–13357, 1999.

Beal, R. C. (*Ed.*), *Directional ocean wave spectra: measuring, modeling, predicting, and applying*, The Johns Hopkins Studies in Earth and Space Sciences, Johns Hopkins University Press, Baltimore, 1991.

Bell, P.S., Determination of Bathymetry Using Marine Radar Images of Waves, Proc. *ASCE WAVES 2001*, San Francisco, 2001.

Benjamin T. P., and J. E. Feir, The disintegration of wave trains on deep water, *J. Fluid Mech.*, 27, 417–430, 1967.

Bidlot, J.-R., and M. W. Holt, Numerical wave modelling at operational weather centres, *Coastal Eng.*, 37, 409–429, 1999.

Bidlot, J.-R., Assimilation of SAR data into the ECMWF global wave model. Workshop Proceedings, *ECMWF Workshop on Ocean Wave Forecasting*, 2–4 July, 2001, 109–116.

Bidlot, J.-R., J. D. Holmes, P. A. Wittmann, R. Lalbeharry and H. S. Chen, Intercomparison of the performance of operational ocean wave forecasting systems with buoy data, *Weather and Forecasting*, 17, 287–310, 2002.

Boggs, P. T., R. H. Byrd, and R. B. Schnabel, A stable and efficient algorithm for nonlinear orthogonal distance regression, *SIAM Sci. and Stat. Comp.*, 8(6), 1052–1078, 1987.

Boggs P. T., and J. E. Rogers, Orthogonal Distance regression, *Cont. Mathematics*, Vol. 112, *Statistical Analysis of Measurements Error Models and their Applications*, edited by P. J. Brown and W. A. Fuller, 183–194, 1990.

Booij, N., Ris, R. C., and L. H. Holthuijsen, A third-generation wave model for coastal regions. Part 1. Model description and validation, *J. Geophys. Res.*, 104(C4), 7649–7666, 1999.

Borgman, L. E., Maximum-entropy and data-adaptive procedures in the

investigation of ocean waves, Proc. 2nd *Workshop on Maximum Entropy and Bayesian Methods in Applied Statistics*, Laramie, Wyoming 1982.

Brüning, C., W. R. Alpers, and K. Hasselmann, Monte-Carlo simulation studies of the nonlinear imaging of a two dimensional surface wave field by a synthetic aperture radar, *Int. J. Remote Sens.*, 11, 1695–1727, 1990.

Brüning, C., S. Hasselmann, K. Hasselmann, S. Lehner, and T. Gerling, First evaluation of ERS-1 synthetic aperture radar wave mode data, *Global Atmosphere and Ocean Systems*, 2, 61–98, 1994a.

Brüning, C., R. Schmidt, and W. R. Alpers, Estimation of ocean wave-radar modulation transfer function from synthetic aperture radar imagery, *J. Geophys. Res.*, 99, 9803–9815, 1994b.

Brillinger, D. V., *Time Series. Data Analysis and Theory*, Holt, Rinehart and Wilson Inc., New York, 1975.

Buchan, S. J., Wave kinematics, measurement, modelling and application, in *Wave Kinematics and Environmental Forces*, Adv. Underwater Techn., SUT, Kluwer Academic Publishers, 29, 19–33, 1993.

Buckley, A. L., *Wave current interaction for the Met Office Wave Model*, UK Met Office, *internal report*, OA22, 1999.

Burg, J. P. *Maximum Entropy Spectral Analysis*, Ph.D. Thesis, Dept. of Geophysics, Stanford Univ., 1975.

Burg, J. P., D. G. Luenberger, and D. L. Wenger, Estimation of structured covariance matrices, *Proc. IEEE*, 70(9), 963–974, 1982.

Caires, S., *Comparative study of HF radar measurements and wave model hindcast of waves in shallow waters*, PhD Thesis, Univ. of Sheffield, 2000.

Campell, N., The study of discontinuous phenomena, *Proc. Cambr. Phil. Soc.*, 15, 117–136, 1909.

Camps A., I. Corbella, J. Font, A. Julia, J. Etcheto, E. Knapp, WISE experiment, ESA report, *RFQ/3-9650/99/NL/DC*, 38, 2000.

Capon, J., High resolution frequency-wavenumber spectrum analysis, *Proc. IEEE*, 57(8), 1408–1418, 1969.

Capon, J., Maximum-likelihood spectral estimation, in *Nonlinear Methods in Spectral Analysis*, *Topics in Applied Physics*, 34, 155-179, 1979.

Carande, R. E., Estimating ocean coherence time using dual-baseline interferometric synthetic aperture radar, *IEEE Trans. Geosci. Remote Sens.*, 32, 846–854, 1994.

Carbonnel, M., *Photogrammetry applied to surveys of monuments and historical centres*, Rome: ICCROM-165s, ISBN 92-9077-091-X, 1989.

Cox C., and W. Munk, Measurement of the roughness of the sea from photographs of the sun's glitter, *J. Opt. Soc. of America*, 44(11), 838–850, 1954a.

Cox C., and W. Munk, Statistics of sea surface derived from sun glitter, *J. Marine Res.*, 13.2, 198–227, 1954b.

Cox, D. R., and D. V. Hinkley, *Theoretical Statistics*, Chapman and Hall, 1974.

Crombie D. D., Doppler spectrum of sea echo at 13.56 Mc/s, *Nature*, 175, 681–682, 1955.

Croney, J., Civil marine radar, in *Radar Handbook*, Chap. 31, (Ed.: Merril I. Skolnik), 1970.

Dankert, H., J. Horstmann, S. Lehner and W. Rosenthal, Detection of wave groups in SAR images and radar image sequences, *IEEE Trans. Geosci. Remote Sens.*, *in print*, 2003.

Davies, R. E., and L. A. Regier.: Methods for estimating directional wave spectra from multi-element arrays, *J. Marine Res.*, 35, 453–477, 1977.

Davies, J., M, Newling, and A. van Tonder, First results from a revolutionary directional wave buoy making use of differential GPS technology. Proc. IAHR Speciality Seminar S1, Multidirectional waves and their interaction with structures, San Francisco, USA, 1997.

Dittmer, J., Use of marine radars for real time wave field survey and speeding up the transmission/processing, *Proc. WMO/IOC Workshop on Operational Ocean Monitoring using Surface Based Radars*, Geneva, 1995.

Dobson, F. and E. Dunlap, MIROS system evaluation during Storm Wind Study II, *Proc. of CLIMAR 99 WMO Workshop on Advances in Marine Climatology*, Vancouver, 8–15 September 1999, 98–109, 1999.

Donelan, M. A., J. Hamilton, and W. H. Hui, Directional spectra of wind-generated waves. *Philos. Trans. R. Soc. London Ser. A,* 315, 509–562, 1985.

Donelan, M. A., W. M. Drennan, and A. K. Magnusson, Nonstationary analysis of the directional properties of propagating waves, *J. Phys. Oceanogr.*, 26, 1901–1914, 1996.

Donelan, M. A., N. Madsen, K. K. Kahma, I. K. Tsanis, and W. M. Drennan, Apparatus for atmospheric surface layer measurements over waves, *J.*

Atmos. Oceanic Techno., 16(9), 1172–1182,1999.

Drennan, W. M., M. A. Donelan, N. Madsen, K. B. Katsaros, E. A. Terray, and C. N. Flagg, Directional wave spectra from a Swath ship at sea, *J. Atmos. Oceanic Techno.* 11, 1109–1116, 1994.

Dupuis H., J. P. Frangi, A. Weill, Comparison of wave breaking statistics using underwater noise and sea surface photographic analysis during SOFIA/ASTEX experiment under moderate wind speed conditions, *Annales Geophysicae*, 11, 960–969, 1993.

Earle, M. D., R. H. Orton, H. D. Selsor, and K. E. Steele, A sonobuoy sized expendable air-deployable directional wave sensor, *Proc. WAVES'93, ASCE*, 302–315, 1993.

Edge, B., J. M. Hemsley and Y. Goda (*Ed.*), *Ocean wave measurement and analysis*, Proc. 3rd Int. Symp., ASCE, November 3-7, Virginia Beach, Virginia, 1997.

Edge, B., J. M. Hemsley (*Ed.*), *Ocean wave measurement and analysis*, Proc. 4th Int. Symp., ASCE, San Francisco, California, ISBN 0-7844-0604-9, 2001.

Eineder, M., R. Bamler, N. Adam, H. Breit, S. Suchand, and U. Steinbrecher, SRTM/X-SAR interferometric processing – first results, in *Proc. of the EUSAR Conf., Munich*, 2000.

Engen, G., H. Johnson, H. E. Krogstad, and S. F. Barstow, Directional wave spectra by inversion of ERS-1 synthetic aperture radar ocean imagery, *IEEE Trans. Geosci. Remote Sens.*, 32, 340–352, 1994.

Engen, G., and H. Johnsen, SAR ocean wave inversion using image cross spectra, *IEEE Trans. Geosci. Remote Sens.*, 33(4), 1047–1056, 1995.

Engl, H. W., M. Hanke, and A. Neubauer, *Regularization of inverse problems*, in *Mathematics and its applications*, Vol. 375, Kluwer, Dordrecht, 1996.

Eymard L., S. Planton, P. Durand, C. Le Visage, P. Y. Le Traon, L. Prieur, A. Weill, D. Hauser, J. Rolland, J. Pelon, F. Baudin, B. Benech, J. L. Brenguier, G. Caniaux, P. De Mey, E. Dombrowski, A. Druilhet, H. Dupuis, B. Ferret, C. Flamant, F. Hernandez, D. Jourdan, K. Katsaros, D. Lambert, J. Lelievre, P. Le Borgne, A. Marsoin, H. Roquet, J. Tournadre, V. Trouillet, A. Tychensky, B. Zakardjian, Study of the air-sea interactions at the mesoscale: the SEMAPHORE experiment, *Ann. Geophysicae*, 14, 986–1015, 1996.

Fan, J. Q., and Truong Y. K., Nonparametric regression with errors in

variables, *Ann. Stat.*, 21(4), 1900–1925, 1993.

Fisher, F. H., and F. N. Spiess, FLIP Floating Instrument Platform, *J. Acoust. Soc. Amer.*, 35, 1633–1644, 1963.

Forristall, G. Z. and K. C. Ewans, Worldwide measurements of directional wave spreading, *J. Atmos. Oceanic Technol.*, 15, 440–469, 1998.

Fradon, B., D. Hauser and J.-M. Lefevre, Comparison study of a second-generation and of a third-generation wave prediction model in the context of the SEMAPHORE experiment, *J. Atmos. Oceanic Technol.*, 17, 197–214, 2000.

Frasier, S. J., Y. Liu, D. Moller, R. E. McIntosh, and C. Long, Directional ocean wave measurements in a coastal setting using a Focussed Array Imaging Radar, *IEEE Trans. Geosci. Remote Sens.*, 33(2), 428–440, 1995.

Fuller, W. A. *Measurement Error Models*, Wiley, 1987.

Gerling, T. W., Partitioning sequences and arrays of directional ocean wave spectra into component wave systems, *J. Atmos. Oceanic Technol.*, 9, 444–458, 1992.

Goda, Y., Directional wave spectra and its engineering applications, in *Advances in Coastal and Ocean Engineering, Vol. 3*, World Scientific, ISBN 981.02.3016.8, 67–102, 1997;

Goda, Y., A comparative review on the functional forms of directional wave spectrum, *Coastal Engineering Journal*, 41(1), 1–20, 1999.

Goda, Y., *Random Seas and Design of Maritime Structures* (2nd Edition), Advanced Series on Ocean Engineering, World Scientific, ISBN 981-02-3256-X, 2000

Glad, I. K., *Statistiske estimatorer til estimatorer for bølgeretningsestimatorer*. Master thesis (in Norwegian), NTH, April 1990.

Glad, I. K., and H. E. Krogstad: The maximum-likelihood property of estimators of wave parameters from heave, pitch and roll buoys, *J. Atmos. Ocean. Techn.*, 9(2), 169–173, 1992.

Graber H., E. A. Terray, M. Donelan, W. M. Drennan, J. C. Van Leer, D. B. Peters, ASIS – A new air-sea interaction Spar buoy: design and performance at sea, *J. Atmos. Oceanic Technol.h*, 17(5), 708–720, 2000.

Grønlie, Ø., D. C. Brotkorb, B. Natvig, and F. Anderson, MIROS MC - a rig mounted sensor for simultaneous measurement of directional wave spectra, surface current and rig motion, *Proc. OMAE'87*, Houston 1987.

Grønlie, Ø., Microwave Radar Directional Wave Measurements, MIROS Results, *Proc. WMO/IOC workshop on operational ocean monitoring using surface based radars*, Geneva, WHO/TD 694, 73–80, 1995.

Gradshteyn, I. S., and I. M. Ryzhik, *Table of Integrals, Series, and Products*, Academic Press, New York, 1965.

Grossman, A. and J. Morlet, Decomposition of Hardy Functions into Square Integrable Wavelets of Constant Shape. *SIAM J. of Math. Anal.*, 15(4), 723–736, 1984.

Guillaume, A., Statistical tests for the comparison of surface wave spectra with applications to model validations, *J. Atmos. Oceanic Technol.*, 7, 557–567, 1990.

Günther, H., S. Hasselmann, and P. A. E. M. Janssen, The WAM Model Cycle 4 (revised version), Tech. Rept. 4, *Deutsches Klimarechenzentrum*, Hamburg, 91pp., 1992

Gurgel K.-W., G. Antonischki, H-H. Essen and T. Schlick, Wellen Radar (WERA): a new ground-wave HF radar for ocean remote sensing, *Coastal Eng.*, 37, 219–234, 1999.

Hashimoto, N., and K. Konube: Estimation of directional spectra from the Maximum Entropy principle, *Proc. 5th OMAE Symp.*, Tokyo 80–85, 1986.

Hashimoto, N., Analysis of the directional wave spectrum from field data, *Adv. in Coastal and Ocean Eng.*, 3, 103–143, 1997.

Hashimoto, N., and M. Tokuda, A bayesian approach for estimating directional spectra with HF radar, *Coast. Eng. Journal*, 41(2), 137–149, 1999.

Hasselmann, K., T. P. Barnett, E. Bouws, H. Carlson, D. E. Cartwright, K. Enke, J. I. Ewing, H. Gienapp, D. E. Hasselmann, P. Kruseman, A. Meerbrug, P. Müller, D. J. Olbers, K. Richter, W. Sell and H. Walden, Measurements of wind-wave growth and swell decay during the Joint North Sea Wave Project (JONSWAP), *Dtsch. Hydrogr. Z.*, A8(12), 95, 1973.

Hasselmann, S., and K. Hasselmann, Computations and parameterizations of the nonlinear energy transfer in a gravity-wave spectrum. Part. I: A new method for efficient computations of the non-linear energy transfer in a gravity-wave spectrum, *J. Phys. Oceanogr.*, 15, 1369–1377, 1985a.

Hasselmann, S., K. Hasselmann, J. H. Allender, and T. P. Barnett, Computations and parameterizations of the nonlinear energy transfer in a gravity-wave spectrum. Part. II: Parameterizations of the nonlinear energy transfer for application in wave models, *J. Phys. Oceanogr.*, 15, 1378–1391, 1985b.

Hasselmann, K., R. K. Raney, W. J. Plant, W. Alpers, R. A. Shuchman, D. R. Lyzenga, C. L. Rufenach, and M. J. Tucker, Theory of synthetic aperture radar ocean imaging: A MARSEN view, *J. Geophys. Res*, 90, 4659–4686, 1985c.

Hasselmann, K., and S. Hasselmann, On the nonlinear mapping of an ocean wave spectrum into a synthetic aperture radar image spectrum, *J. Geophys. Res.*, 96, 10713–10729, 1991.

Hasselmann, S., C. Brüning, K. Hasselmann, and P. Heimbach, An improved algorithm for the retrieval of ocean wave spectra from synthetic aperture radar image spectra, *J. Geophys. Res.*, 101, 16615–16629, 1996.

Hastie, T. and W. Stuetzle, Principal Curves, *JASA*, 84(406), 502–516, 1989.

Hatten, H., F. Ziemer, J. Seemann, and J. C. Nieto Borge, Correlation Between the Spectral Background Noise of a Nautical Radar and the Wind Vector, *Proc. OMAE 17th Int. Conf. Proc.*, Lisbon, 1998.

Haug, O., and H. E. Krogstad, Estimation of Directional Spectra by ML/ME-Methods, *Proc. WAVES'93*, New Orleans 25–28 July, 1993.

Hauser D., G. Caudal, G.J. Rijckenberg, D. Vidal-Madjar, G. Laurent, P. Lancelin, RESSAC: A new airborne FM/CW radar ocean wave spectrometer, *IEEE Trans. Geosci. Remote Sens.*, 30(5), 981–995, 1992a.

Hauser, D., G. Caudal, and B. Chapron, Observations with the RESSAC airborne radar during Ren 91, Proceedings of the *ERS-1 Geophysical validation workshop*, 47–53, ESA WPP-36 (Penhorst, France, April 1992), 1992b.

Hauser, D., G. Caudal, and L. K. Shay, Behavior of the ocean radar cross-section at low incidence, observed in the vicinity of the Gulf-Stream, *IEEE Trans. Geosci. Remote Sens.*, 33(1), 162–171, 1995.

Hauser D., and G. Caudal, Combined analysis of the radar cross-section modulation due to the long ocean waves around 14 and 34° incidence: implication for the hydrodynamic modulation, *J. Geophys. Res.*, 101(C11,25), 833–25,846, 1996.

Hauser D., E. Soussi, E. Thouvenot, and L. Rey: SWIMSAT: A real-aperture radar to measure directional spectra of ocean waves from space-Main characteristics and performance simulation, *J. Atmos. Oceanic Technol.*, 18(3), 421–437, 2001.

Hauser D., H. Branger, S. Bouffies-Cloché, S. Despiau, W. Drennan, H. Dupuis, P. Durand, X. Durrieu de Madron, C. Estournel, L. Eymard, C. Flamant, H. Graber, C. Gurin, K. Kahma, G. Lachaud, J-M Lefèvre, J.

Pelon, H. Pettersson, B. Piguet, P. Queffeulou, D. Tailliez, J. Tournadre, and A. Weill, The FETCH experiment: an overview, *J. Geophys. Res.*, 108(3), 10.1029/2001JC001202, 2003.

Heimbach, P., S. Hasselmann, and K. Hasselmann, Statistical analysis and intercomparison of WAM model data with global ERS-1 SAR wave mode spectral retrievals over 3 years, *J. Geophys. Res.*, 103(C4), 7931–7977, 1998.

Herbers, T. H. C., R. L. Lowe, and R. T. Guza, Field verification of acoustic Doppler surface gravity wave measurements, *J. Geophys. Res.*, 96(C9), 17, 023–17, 035. 1991.

Hersbach, H., Application of the adjoint of the WAM model to inverse wave modelling, *J. Geophys. Res.*, 103(C5), 10469–10488, 1998.

Hessner, K., K. Reichert, and W.Rosenthal, Mapping of the sea bottom topography in shallow seas by using a nautical radar, *Proc. ITC'99*, Hamburg, 1999.

Hessner, K., K. Reichert, J. Dittmer, J.C. Nieto Borge, and H. Günther, Evaluation of WaMoS II wave data, *Proc. ASCE WAVES* 2001, San Francisco, 2001.

Hisaki Y., Nonlinear inversion of the integral equation to estimate ocean wave spectra from HF radar, *Radio Sci.*, 31, 25–39, 1996.

Holden G. J., and L. R. Wyatt, Extraction of sea state in shallow water using HF radar, *IEE Proceedings–F*, 139, 175–181, 1992.

Holthuijsen L. H., Stereophotography of ocean waves, *Appl. Ocean Res.*, 5(4), 204–209, 1983.

Howell R., and J. Walsh, Measurement of ocean wave spectra using narrow beam HF radar, *IEEE J. Oceanic Eng.*, 18, 296–305, 1993.

Howell, G. L., Shallow water directional wave gages using short baseline pressure arrays, *Coastal Eng.*, 35, 85–102, 1998.

Hussin, A. G., *Pseudo-replication on functional relationships with environmental applications*, Doctoral Diss., Univ. of Sheffield, England, 1997.

Isaac F.E. and L.R. Wyatt, Segmentation of HF radar measured directional wave spectra using the Voronoi Diagram. *Journal of Atmospheric and Oceanic Technology*, 14, 950–959, 1997.

Isobe, M., K. Kondo, and K. Horikawa, Extension of the MLM for estimating directional wave spectra, in Proc. Symp. on *Description and Modelling of Directional Seas*, Paper A6, Lyngby, Denmark 1984.

Jackson, F. C., An analysis of short pulse and dual frequency radar techniques for measuring ocean wave spectra from satellites, *Radio Sci.*, 16(6), 1385–1400, 1980.

Jackson, F. C., W. T. Walton and C. Y. Peng. 1985a. Aircraft and satellite measurement of ocean wave directional spectra using scanning-beam microwave radars. *J. Geophys. Res.*, 90(C1), 987–1004, 1985a.

Jackson, F. C., W. T. Walton and C. Y. Peng. 1985b. A comparison of in situ and airborne radar measurements of ocean wave directionality. *J. Geophys. Res.*, 90(C1), 1005–1018, 1985b.

Jackson F. C., The Radar Ocean-Wave Spectrometer, *Johns Hopkins APL Technical Digest*, 8(1), 116–127, 1987.

Jackson F. C., and E. Jensen, Wave field response to frontal passages during SWADE, *Jour. of Coastal Res*, 11(1), 34–67, 1995.

Janssen, P. A. E. M., B. Hansen, and J. R. Bidlot, Verification of the *ECMWF Wave Forecasting System Against Buoy and Altimeter Data. Weather and Forecasting*, 12, 763–784, 1997.

Jeffreys, E. R., G. T. Wareham, N. A. Ramsden, and M. J. Platts, Measuring directional spectra with the MLM, Proc. *Directional Wave Spectra and Applications*, Berkeley, California Publ. by ASCE, New York, 203–218, 1981.

Jenkins, G. M. and D. G. Watts, *Spectral analysis and its applications*, Holden-Day, San Francisco, 1968.

Kaiser, G., *A Friendly Guide to Wavelets*, Sixth Printing, Birkhauser, Boston, ISBN 0-8176-3711-7, 300pp., 1999.

Karara, H. M. (Ed.), *Handbook of Non-Topographic Photogrammetry*, 2nd ed., American Society of Photogrammetry, Falls Church, VA, 1979.

Kasilingam, D. P., and O. H. Shemdin, Models for synthetic aperture radar imaging of the ocean: A comparison, *J. Geophys. Res.*, 95, 16263–16276, 1990.

Kay, S. M., *Modern spectral estimation: Theory and application*, Prentice Hall, Englewood Cliffs, New Jersey, 1988.

Keller, W. C., and J. Wright, Microwave scattering and the straining of wind generated waves. *Radio Sci.*, 10, 139–147, 1975.

Kenny, J. E., E. A. Uliana, and E. J. Walsh, The surface contour radar, a unique radar remote sensing instrument, *IEEE Trans., Microw. Theory and Tech.*, MTT-27(12), 1080–1092, 1979.

Kerbaol, V., B. Chapron, and P. W. Vachon, Analysis of ERS-1/2 synthetic aperture radar wave mode imagettes, *J. Geophys. Res.*, 103, 7833–7846, 1998.

Khandekar, M. L., *Operational Analysis and Prediction of Ocean Wind Waves*, Springer Verlag, 1989.

Kingsley S. P., A. M. Torregrossa and L. R. Wyatt, Analysis of second order HF radar sea spectra recorded in storm conditions. *Proceedings of Oceans'98, Nice, France, September 1998, publ. by IEEE*, 459–462, 1998.

Kinsman, B., *Wind Waves*, Prentice-Hall Inc., Englewood Cliffs, New Jersey, 1965.

Kitaigorodskii, S. A., V. P. Krasitskii, and M. M. Zaslavskii, On Phillips' theory of equilibrium range in the spectra of wind-generated gravity waves, *J. Phys. Oceanogr.*, 5, 410–420, 1975.

Komen, G. J., L. Cavaleri, M. Donelan, K. Hasselmann, S. Hasselmann and P. A. E. M. Janssen, *Dynamics and Modelling of Ocean Waves*, Cambridge University Press, Cambridge, 1994.

Krogstad, H. E., Maximum likelihood estimation of ocean wave spectra from general arrays of wave gauges, *Mod. Ident. Control*, 9, 81–97, 1988.

Krogstad, H. E., R. L. Gordon and M. C. Miller, High-resolution directional wave spectra from horizontally mounted acoustic Doppler current meters, *J. Atmos. Oceanic Technol.*, 5(4), 340–352, 1988.

Krogstad, H. E., A simple derivation of Hasselmann's nonlinear ocean-synthetic aperture radar transform. *J. Geophys. Res.*, 97, 873–885, 1992.

Krogstad, H. E., O. Samset, and P. W. Vachon, Generalizations of the nonlinear ocean-SAR transformation and a simplified SAR inversion algorithm, *Atmos. Ocean*, 32, 61–82, 1994.

Krogstad, H. E., S. F. Barstow, O. Haug, P.Ø. Markussen, G. Ueland, and I. Rodriguez, Smart-800: A GPS Based Directional Wave Buoy, *Proc. ASCE Waves'97*, Virginia Beach, Virginia, USA, November 1997.

Krogstad, H. E., S. F. Barstow, S. E. Aasen and I. Rodriguez: Some recent developments in wave buoy measurement technology, *Coastal Eng.*, 37, 309–330, 1999a.

Krogstad H. E., J. Wolf, S. P. Thompson and L. R. Wyatt, Methods for the intercomparison of wave measurements, *Coastal Eng.*, 37, 235–258, 1999b.

Krogstad, H. E. and S. F. Barstow, Recent advances in wave measurement technology, *Proc. International Society of Offshore and Polar Engineers*

(ISOPE), Brest, Vol. III, ISBN 1-880653-42-7, 19–25, 1999c.

Kuik, A. J., G. Ph. van Vledder, and L. H. Holthuijsen, A method for the routine analysis of pitch-and-roll buoy wave data, *J. Phys. Oceanogr.*, 18, 1024–1034, 1987.

Laing, A. K., Nonlinear properties of random gravity waves in water of finite depth, *J. Phys. Oceanogr.*, 16, 2013–2030, 1986.

Lee, D. Y., and H. Wang, Measurement of waves from subsurface gage, 271–286 in: Proceedings of the 19th Coastal Engineering Conference, Sept. 3–7, Houston, Texas. Ed. B.L.Edge 1984.

Lehner, S., J. Schulz-Stellenfleth, B. Schättler, H. Breit, and J. Horstmann, Wind and wave measurements using complex ERS-2 SAR wave mode data, *IEEE Trans. Geosci. Remote Sens.*, 38, 2246–2257, 2000.

Lionello, P., H. Günther, and P. A. E. M. Janssen, Assimilation of altimeter data in a global third generation wave model, *J. Geophys. Res.*, C97, 14453–14474, 1992.

Lipa, B. J., and D. E. Barrick, Extraction of sea state from HF radar sea echo: Mathematical theory and modelling, *Radio Sci.*, 21, 81–100, 1986.

Lipa, B. J., Derivation of directional ocean-wave spectra by inversion of second order radar echoes, *Radio Sci.*, 12, 425–434, 1977.

Lipa, B. J., D. E. Barrick, J. Isaacson, and P. M. Lilleboe, CODAR wave measurements from a North Sea semisubmersible, *IEEE J. Oceanic Eng.*, 15, 119–125, 1990.

Long, R. B., and K. Hasselmann, A variational technique for extracting directional spectra from multi-component wave data, *J. Phys. Oceanogr.*, 9, 373–381, 1979.

Long, R. B., The statistical evaluation of directional spectrum estimates derived from pitch/roll buoy data, *J. Phys. Oceanogr.*, 10, 944–952, 1980.

Long, R. B., Inverse modelling in ocean wave studies, in *Wave Dynamics and Radio Probing of the Ocean Surface* (Eds.: O. M. Phillips and K. Hasselmann), Plenum Press, New York and London, 687p., 571–593, 1986.

Longuet-Higgins, M. S. The statistical analysis of a random moving surface, *Phil. Trans. Roy. Soc.*, A 249, 321–387, 1957.

Longuet-Higgins, M. S., D. E. Cartwright, and N. D. Smith: Observations of the directional spectrum of sea waves using the motion of a floating buoy, in *Ocean Wave spectra. Proceedings of a Conference*, Prentice-Hall, 111–136, 1963.

Lukacs, E. *Characteristic functions*, 2nd Ed., Griffin, London, 1970.

Lygre, A. and H. E. Krogstad, Maximum entropy estimation of the directional distribution in ocean wave spectra, *J. Phys. Oceanogr.,* 16, 2052–2060, 1986.

Magnusson, A.K., *MIROS-WAVEC validation study*, Norwegian Meteorological Institute Report, Bergen, Statoil Contract T7183, 1987.

Magnusson, A.K., Wave model results with wind input from a course and a fine-meshed atmospheric model, compared with wave measurements, *Modeling the offshore environment. Proceedings of SUT conference*, London, 1–2 April, 1987, Graham & Trotman Limited, ISBN 0-86010-922-4, 1997.

Magoon, O. T., and J. M. Hemsley (Ed.), *Ocean wave measurement and analysis*, Proc. 2nd Int. Symp., ASCE, New Orleans, Louisiana, July, ISBN 0-87262-922-8, 1993.

Mardia, K. V., *Statistics of Directional Data*, Academic Press, London, 1972.

Massel, S. R., *Ocean surface waves: Their physics and prediction*, Adv. Series on Coast. Eng., 14, World Scintific, 1995.

Massonnet, D., Capabilities and limitations of the interferometric cartwheel, *IEEE Trans. Geosci. Remote Sens.*, 39(3), 506 – 520, 2001.

Mastenbroek, K. and C. F. de Valk, A semi-parametric algorithm to retrieve ocean wave spectra from synthetic aperture radar, *J. Geophys. Res.*, 105, 3497–3516, 2000.

Melsheimer, C., M. Bao, M. and W. Alpers, Imaging of ocean waves on both sides of an atmospheric front by the SIR-C/X-SAR multifrequency synthetic aperture radar, *J. Geophys. Res.*, 103, 8839–18849, 1998.

Mitsuyasu, H., A. Masuda, and Y. Y. Kuo., The dispersion relation of random gravity waves. Part I, *J. Fluid Mech.*, 92, 717–730, 1979a.

Mitsuyasu, H, F. Tasai, T. Suhara, S. Mizuno, M. Ohkusu, T. Honda, and K. Rikiishi, Observation of the power spectrum of ocean waves using a cloverleaf buoy, *J. Phys. Oceanogr.,* 10, 286–296, 1979b.

Mollo-Christensen, E. and A. Ramamonjiarisoa, Modelling the presense of wave groups in a random wave field, *J. Geophys. Res.*, 83, 4117–4122, 1978.

Monbaliu, J., R. Padilla-Hernandez, J. C. Hargreaves, J. C. C. Albiach, W. Luo, M. Sclavo, and H. Günther, The spectral wave model WAM adapted for applications with high spatial resolution, *Coastal Eng.*, 41, 41–62, 2000.

Shearman, E. D. R., and M. D. Moorhead, Pisces: A coastal ground-wave

radar for current, wind and wave mapping to 200 km ranges, *IGARRS'88 proceedings*, 773–776, 1988.

Munthe-Kaas, H., and H. E. Krogstad: Sampling variability of sea state parameters, *ANODA Rep.*, 9, Continental Shelf Institute, Trondheim, January, 1985.

Nieto Borge, J.C., *Análisis de Campos de Oleaje Mediante Radar de Navegación en Banda-X* (in Spanish), Ph.D. thesis Dept. of Physics, University of Alcalá, 1997.

Nieto Borge, J.C., K. Reichert, and J. Dittmer, Use of nautical radar as a wave monitoring instrument, *Coastal Eng.*, 37, 331–342, 1999.

Nieto Borge, J. C., K. Reichert, J. Dittmer, and W. Rosenthal, WaMoS II: A wave and current monitoring system, Proc. of the *COST 714 Conference on Directional Wave Spectra*, Paris, 1998.

Nwogu, A., Maximum entropy estimation of directional wave spectra from an array of wave probes, *Appl. Ocean Res.*, 11,(4), 176–182, 1986.

Ozer, J., R. Padilla-Hernandez, J. Monbaliu, E. Alvarez Fanjul, J. C. Carretero Albiach, P. Osuna, C. S. Yu, and J. Wolf, A coupling module for tides, surges and waves, *Coastal Eng.*, 41, 95–124, 2000.

Outzen, O., *Bestimmung der Wassertiefe und der oberflächennahen Strömung mit einem nautischen Radar* (in German), Diploma Thesis, GKSS 98/E/60. 1998.

Paduan J. D., and H. C. Graber, Introduction to High-Frequency radar: reality and myth, *Oceanography*, 10, 36–39, 1997.

Pawka, S. S., Island shadows in wave directional spectra, *J. Geophys. Res.*, 14, 1800–1810, 1983.

Phillips, O., *The Dynamics of the Upper Ocean*, 2nd Ed., Cambridge University Press, Cambridge, 1977.

Pierson,W. J., G. Neumann, and R.W. James: *Practical methods for observing and Forecasting Ocean Waves by Means of Wave Spectra and Statistics*, U.S. Navy Hydrographic Office Publ. No. 603, 1955.

Pierson, W. J., and G. Neumann, *Principles of physical oceanography*, Imprint Englewood Cliffs, N.J., Prentice-Hall, 1966.

Pierson, W. J., *The Theory and Applications of Ocean Wave Measuring Systems at and Below the Sea Surface, on the Land, from Aircraft and from Spacecraft*, Rep. No. NASA CR-2646, 1976.

Pinkel, R., and J. A. Smith, Open ocean surface wave measurement using Doppler sonar, *J. Geophys. Res.*, 92(C12), 12, 967–12, 973, 1987.

Plant, W. J., Bragg scattering of electromagnetic waves from the air/sea interface, in *Surface Waves and Fluxes*, Vol I+II, Geernaert, G. L. and B. Plant, ed., *Kluwer Academic Publishers*, 1990.

Plant, W.J. and L. M. Zurk, Dominant wave directions and significant wave heights from synthetic aperture radar imagery of the ocean, *J. Geophys. Res.*, 102, 3473–3482, 1997.

Plant, W. J., W. C. Keller, V. Hesany, and K. Hayes, Measurements of the marine boundary layer from an airship, *J. Atmos. Oceanic Technol.*, 15, 1433–1458, 1998.

Plant, W. J., D. E. Weissman, W. C. Keller, V. Hesany, K. Hayes, and K. W. Hoppel, Air/sea momentum transfer and the microwave cross section of the sea, *J. Geophys. Res.*, 104(C5), 11173–11191, 1999.

Prevosto, M., H. E. Krogstad and A. Robin, Probability distributions for maximum wave and crest heights, *Coastal Eng.*, 40, 329–360, 2000.

Reichert, K., *Untersuchung zur azimuthalen Abhängigkeit der Abbildung von Seegang mit dem Achiffsradar* (in German), Diploma Thesis, Univ. of Hamburg, 1994.

Rice, S. O., Reflection of Electromagnetic Waves from Slightly Rough Surfaces, *Comm. Pure Applied Math.*, 4, 351–378, 1951.

Rice, S. O., *Mathematical analysis of random noise*, Bell Syst. Tech. J., 23, 282–332, 1944 and volume 24, 46–156, 1945 [Reprinted in *Selected Papers on Noise and Stochastic Processes*, N. Wax, Ed., New York, Dover, 1954, 133–294].

Ris, R. C., *Spectral modelling of wind waves in coastal areas*, Ph. D. thesis, Delft University of Technology, The Netherlands 1997.

Ris, R. C., L. H. Holthuijsen, and N. Booij, A third-generation wave model for coastal regions. 2. Verification, *J. Geophys. Res.*, 104(C4), 7667–7681, 1999.

Robson R. E., Simplified theory of first- and second-order scattering of HF radio waves from the sea, *Radio Sci.*, 19, 1499–1504, 1984.

Romeiser, R., and D. R. Thompson, Numerical study on the along-track interferometric radar imaging mechanism of oceanic surface currents, *IEEE Trans. Geosci. Remote Sens.*, 38(1), 446–458, 2000.

Rossouw, M., A. vanTonder, U. von St. Ange, L. Coetzee, and J. Davies,

Assessing the quality of directional wave measurement by a differential GPS buoy, *Proc. Int. Conf. Coastal Eng.*, ICCE 2000, Vol. 2, 1240–1253.

Samset, O., H. E. Krogstad, and O. Haug: *Analysis of Holderness data: A comparison between directional waverider and the OSCR HF radar data*, Technical report, SINTEF, 1996.

Schneggenburger, C., H. Günther, and W. Rosenthal, Spectral wave modelling with nonlinear dissipation: validation and applications in a coastal tidal environment, *Coastal Eng.*, 41, 201–235, 2000.

Schröder, L. C., D. H. Boggs, G. Dome, I. M. Halberstam, W. L. Jones, W. J. Pierson, and F.J. Wentz, The relationship between wind vector and normalized radar cross section used to derive SEASAT-A satelline scatterometer winds, *J. Geophys. Res.*, 87(C5), 3318–3336, 1982.

Schulz-Stellenfleth, J., and S. Lehner, Study of SAR ocean wave imaging by using airborne single pass cross track interferometrie: the SINEWAVE experiment, in *Proceedings of the COST 714 conference Paris*, WMO, 1998.

Schulz-Stellenfleth, J., and S. Lehner, Ocean wave imaging using an airborne single pass cross track interferometric SAR, *IEEE Trans. Geosci. Remote Sens.*, 39, 38–44, 2001a.

Schulz-Stellenfleth, J., J. Horstmann, S. Lehner, and W. Rosenthal, Sea surface imaging with an across track interferometric synthetic aperture radar (INSAR) - the SINEWAVE experiment, *IEEE Trans. Geosci. Remote Sens.*, 39, 2017–2028, 2001b.

Schulz-Stellenfleth, J., and S. Lehner, Spaceborne synthetic aperture observations of ocean waves travelling into sea ice, *J. Geophys. Res.*, 107(C8), 10.1029–10.1039, 2002.

Schulz-Stellenfleth, J., and S. Lehner, A parametric scheme for ocean wave retrieval from complex synthetic aperture radar data, submitted to *J. Geophys. Res*, 2003a.

Schulz-Stellenfleth, J., and S. Lehner, A noise model for synthetic aperture radar look cross spectra acquired over the ocean, submitted to *IEEE Trans. Geosci. Remote Sens.*, 2003b.

Seemann, J., F. Ziemer, and C. M. Senet, A Method for Computing Calibrated Ocean Wave Spectra from Measurements with a Nautical X-Band Radar, *Proc. Oceans'97*, 1158–1154, 1997.

Seemann, J., *Interpretation der Struktur des Wellenzahl-Frequenzspektrums von Radar-Bildsequenzen* (in German), Ph. D. thesis, Univ. of Hamburg,

GKSS-Report 97/E/68, 1997.

Senet, C.M., *Untersuchungen zur Bestimmung der oberflächennahen Strömungsgeschwindigkeit mit einem nautischen Radar* (in German), Dipl. Thesis, Univ. of Hamburg, GKSS-Report 97/E/3, 1996.

Sharma, J. N., *Development and Evaluation of a Procedure for Simulating a Random Directional Sea Surface and Associated Wave Forces*, Ph. D. dissertation, Univ. of Delaware, 1979.

Shemdin O. H., H. M. Tran, and S. C. Wu, Directional measurements of short ocean waves with stereophotography, *J. Geophys. Res.*, 93, 13891–13901, 1988.

Siegmund, R., M. Bao, S. Lehner, and R.Mayerle, First demonstration of surface currents imaged by hybrid along and cross track interferometric synthetic aperture radar, *in print*, *IEEE Trans. Geosci. Remote Sens.*, 2003.

Sova, M. S., *The Sampling Variability and the Validation of High Frequency Wave Measurements of the Sea Surface*, Univ. of Sheffield PhD Thesis, 1995.

Steele, K. E., and M. Earle, Directional ocean wave spectra using buoy azimuth, pitch, and roll derived from magnetic field components, *IEEE J. Oceanic Eng.*, 16, 427–433, 1991.

Steele, K. E., D. W. Wang, M. D. Earle, E. D. Michelena, and R. J. Dagnall, Buoy pitch and roll computed using three angular rate sensors, *Coastal Eng.*, 563, 123–139, 1998.

Terray, E. A., H. E. Krogstad, R. Cabrera, R. L. Gordon, and A. Lohrmann, Measuring wave directional using upward looking Doppler sonar, Proc. *IEEE 4th Conf. on Current measurements, IEEE No. 90CH2861*, 252–257, 1990.

Terray, E. A., R. L. Gordon and B. H. Brumley, Measuring wave height and direction using upward-looking ADCPs, Proc. *Oceans97*, IEEE Press, 287–290, 1997.

Thomas, J. P., 1988. Retrieval of energy spectra from measured data for assimilation into a wave model, *Q. J. R. Meteorol. Soc.*, 114, 781–800, 1988.

Tolman, H. L., User manual and system documentation of WAVEWATCH-III version 1. 18, *NOAA / NWS / NCEP /OMB technical note*, 166, 110, 1999.

Tucker, M. J., *Waves in Ocean Engineering; measurement, analysis, interpretation*, Ellis Horwood Series in Marine Science, 1991.

Tucker, M. J., Recommended standard for wave data sampling and near

real-time processing, *Ocean Engineering*, 20, 459–474, 1993.

Tucker, M. J., and P. J. Hardcastle, The Interpretation of Wave Records from Pressure Sensors, *POL Internal Document*, 101(28), 1996.

Vachon, P. W., J. W. M. Campbell, A. L. Gray, and F. W. Dobson, Validation of Along-Track Interferometric SAR Measurements of Ocean Surface Waves, *IEEE Trans. Geosci. Remote Sens.*, 37, 150–162, 1999.

Valenzuela, G. R., Theories for the interaction of electromagnetic and oceanic waves - a rewiev, *Boundary Layer Metereol.*, 13, 61–85, 1978.

van Unen, RF., A. A. van Beuzecom, G. Z. Forristall, J. P. Mathisen, and J. Starke, WACSIS - Wave Crest Sensor Intercomparison Study at the Meetpost Noordwijk Measurement Platform, Proc. *OCEAN'98*, Nice, France, 1998.

van Vledder, G. Ph., T. H. C. Herbers, R. E. Jensen, D. T. Resio and B. Tracy, Improved method for obtaining the integration space for the computation of nonlinear quadruplet wave-wave interactions, Proc. *27th Int. Conf. on Coastal Eng.*, Sidney, Australia, 2000.

van Vledder, G. Ph., Extension of the discrete interaction approximation for computing nonlinear quadruplet wave-wave interactions in operational wave models, Proc. *WAVES 2001*, Sept. 2–6, San Francisco, ASME, 540–549, 2001.

van Vledder, G. Ph. and M. Bottema, Improved modelling of nonlinear four-wave interactions in shallow water, Proc. *28th Int. Conf. on Coastal Eng.*, Cardiff, UK, 459–471, 2002

Voorrips, A. C., V. K. Makin, and S. Hasselmann, 1997. Assimilation of wave spectra from pitch- and roll-buoys in a North Sea wave model, *J. Geophys. Res.*, 102(C3), 5829–5849, 1997.

Voorrips, A. C., *Sequential data assimilation methods for ocean wave models*, Ph. D. thesis T. U. Delft No. 168. 1998.

Walsh, E. J., D. W. Hancock, D. E. Hines, R. N. Swift, and J. F. Scott, Directional wave spectra measured with the surface contour radar, *J. Phys. Oceanogr.*, 15, 566–592, 1985.

Walsh, E. J., D. W. Hancock, D. E. Hines, R. N. Swift, and J. F. Scott, An observation of the directional wave spectrum evolution from shoreline to fully developed, *J. Phys. Oceanogr.*, 19, 670–690, 1989.

Walsh, E. J., Surface contour radar directional wave spectra measurements during LEWEX, in *Directional Ocean Wave Spectra*, ed. R. C. Beal, JHU/

APL, 86–90, 1991.

Walsh, E. J., L. K. Shay, H. C. Graber, A. Guillaume, D. Vandemark, D. E. Hines, R. N. Swift, and J. F. Scott, Observations of surface wave-current interaction during SWADE, *Global Atmos. Ocean Syst.*, 5, 99–124, 1996.

Walsh, J. and S. K. Srivastava, Rough surface propagation and scatter, 1. General formulation and solution for periodic surfaces, *Radio Sci.*, 22, 193–208, 1987.

WAMDI Group, The WAM model–a third generation ocean wave prediction model, *J. Phys. Oceanogr.*, 1775–1810, 1988.

Wang, D. W., C. C. Teng, and R. Ladner, Buoy directional measurements using magnetic field components, *Proc. WAVES'93, ASCE*, 316–329, 1993.

Weber B. L. and D. E. Barrick, On the nonlinear theory for gravity waves on the ocean's surface. Part I: Derivations, *J. Phys. Oceanogr.*, 7, 3–10, 1977.

Weill A., F. Baudin, H. Dupuis, L. Eymard, J. P. Frangi, E. Gerard, P. Durand, B. Benech, J. Dessens, A. Druilhet, A. Rechou, P. Flamant, S. Elouragini, R. Valentin, G. Sèze, J. Pelon, C. Flamnant, J. L. Brenguier, S. planton, R. Rolland, A. Brisson, J. Le Borgne, A. Marsouin, T. Moreau, K. Katsaros, R. Monis, P. Queffelou, J. Tournadre, P. K. Taylor, E. Kent, R. Pascal, P. Schibler, F. Parol, J. Descloitres, J. Y. Ballois, M. André, and M. Charpentier, SOFIA 1992 experiment during ASTEX*, Global Atmos. Ocean Sys.*, 3, 335–395, 1995.

Wiegel, R. L. (*Ed.*), *Proceedings of Conference on Directional Wave Spectra Applications*, ASCE, Berkeley, California, ISBN 0-87262-303-3, 1982.

Willmott C. J., S. G. Ackleson, R. E. Davies, J. J. Feddema, K. M. Klink, D. R. Legates, J. O. Donnell, and C. M. Rowe: Statistics for Evaluation and Comparison of Models, *J. Geophys. Res.*, 90(C5), 8995–9005, 1985.

WMO (World Meteorological Organization), *Guide to wave analysis and forecasting.* MO-No. 702, WMO– Geneva Switzerland, 1998.

Wright, C. W., E. J. Walsh, D. Vandemark, W. B. Krabill, A. Garcia, S. H. Houston, M. D. Powell, P. G. Black, and F. D. Marks, Hurricane directional wave spectrum spatial variation in the open ocean, *J. Phys. Oceanogr.*, 31, 2472–2488, 2001.

Wyatt L. R., G. D. Burrows and M. D. Moorhead, An assessment of a FMICW ground-wave radar system for ocean wave studies, *Int. J. Remote Sens.*, 6, 275–282, 1985.

Wyatt L. R., A relaxation method for integral inversion applied to HF radar measurement of the ocean wave directional spectrum, *Int. J. Remote Sens.*, 11, 1481–1494, 1990a.

Wyatt L. R., Progress in the interpretation of HF sea echo 'clutter': HF radar as a remote sensing tool. *IEE Proceedings–F*, 137, 139–147, 1990b.

Wyatt L. R., HF radar measurements of the ocean wave directional spectrum, *IEEE J. Oceanic Eng.*, 16, 163–169, 1991.

Wyatt L. R., and G. J. Holden, Developments in ocean wave measurement by HF radar, *IEE Proceedings–F*, 139, 170–174, 1992.

Wyatt L. R., and G. J. Holden, Limits in direction and frequency resolution for HF radar ocean wave directional spectra measruement, *The Global Atmosphere and Ocean System*, 2, 265–290, 1994.

Wyatt L. R., High order nonlinearities in HF radar backscatter from the ocean surface, *IEE proceedings–Radar, Sonar and Navigation*, 142, 293–300, 1995.

Wyatt L. R., The effect of fetch on the directional spectrum of Celtic Sea storm waves, *J. Phys. Oceanogr.*, 25, 1550–1559, 1995.

Wyatt L. R., and L. J. Ledgard, OSCR wave measurement – some preliminary results, *IEEE J. Oceanic Eng.*, 21, 64–76, 1996.

Wyatt L. R., L. J. Ledgard and C. W. Anderson, 1997: Maximum likelihood estimation of the directional distribution of 0.53 Hz ocean waves, *J. Atmos. Oceanic Technol.*, 14, 591–603, 1997.

Wyatt L. R., HF radar wave measurements in high sea-states, Proceedings of *Oceans'98,* Nice, France, September 1998, publ. by IEEE, 463–466, 1998.

Wyatt L. R., S. P. Thompson and R. R. Burton, 1999: Evaluation of HF radar wave measurement, *Coastal Eng.*, 37, 259–282, 1999.

Wyatt L. R., Limits to the inversion of HF radar backscatter for ocean wave measurement,. *J. Atmos. Oceanic Technol.*, 17, 1651–1666, 2000.

Wyatt, L. R., An evaluation of wave parameters measured using a single HF radar system, *Can. J. Remote Sens.,* 28, 205–218, 2002.

Wyatt L. R., J. J. Green, K.-W. Gurgel, J. C. Nieto Borge, K. Reichert, K. Hessner, H. Günther, W. Rosenthal, O. Saetra, and M. Reistad, Validation and intercomparisons of wave measurements and models during the EuroROSE experiments, *Coastal Eng.*, 48, 1–28, 2003.

Young, G. S., J. A. Harlan, and T. M. Georges, Application of over-the-

horizon radar observations to synoptic and mesoanalysis over the Atlantic, *Weather and Forecasting*, 12, 44–55, 1997.

Young, I. R., W. Rosenthal, and F. Ziemer, A three dimensional analysis of marine radar images for the determination of ocean waves, *J. Geophys. Res.*, 90, 1049–1059, 1985.

Young, I. R., *Wind generated ocean waves*, Ocean Engineering Series, Elsevier, 1999.

Zambresky, L., *A verification study of the global WAM model, December 1987 – November 1988.* GKSS Forschungszentrum, Geestracht, Techn. Rep. 63, GKSS 89/E/37, 86, 1989.

Ziemer, F. and W. Rosenthal, On the transfer function of a shipborne radar for imaging ocean waves, *Proc. IGARSS'87*, Ann Arbor, Michigan, 1559–1564, 1987.

Ziemer, F., Directional spectra from shipboard navigation radar during LEWEX, in *Directional Ocean Wave Spectra*, (Ed.: Robert C. Beal), The John Hopkins University Press, 1991.

Ziemer, F., and W. Rosenthal, Measurement of two-dimensional wave energy spectra during SAXON-FPN'90, *Proc. Oceans'93*, 2, 326–331, 1993.

Ziemer, F., and H. Günther, A system to monitor ocean wave fields, *Proc. Second Int. Conf. Air-Sea Interaction and Meteorology and Oceanography of the Coastal Zone*, Lisbon, Portugal, 1994.

Part II

MEASURING AND ANALYSING THE DIRECTIONAL SPECTRUM OF OCEAN WAVES

Special Studies

Technical Editor Jaak Monbaliu

Chapter 1

Introduction

Kimmo K. Kahma

Finnish Institute of Marine Research, Helsinki, Finland

1.1 Scope of Part 2

Part 1 of this book presents the theory, analysis techniques and measuring principles of various instruments to measure the directional spectrum. The last chapter of Part 1 discusses the complicated issue of how to compare the instruments and methods involved. Here in Part 2 individual intercomparison studies are presented. Chapters 2, 3 and 4 are devoted to comparisons between in-situ instruments. Chapters from 5 to 9 deal with radar measuring techniques. Chapter 10 compares different partitioning techniques.

Several intercomparisons between various directional wave sensors have been reported before the present study. In an extensive Wave Direction Calibration Project (WADIC) Allender *et al.* (1989) compared seven wave buoys, eight rapid-response vector current meters, pressure transducers and infrared laser altimeters in the North Sea. Beal in Directional Ocean Wave Spectra (1991) reports several comparisons from the LEWEX experiment: Endeco Wavetrack buoy and the Datawell Wavec buoy; Endeco Wavetrack buoy and the Seatex Wavescan; Ship Radar and a Wavescan buoy; Ship Radar and Wavec buoy; SAR with the Wavescan buoy. Recently, Directional Waverider and pitch-and-roll buoys were compared by O'Reilly *et al.* (1996) against a pressure array, and Wyatt *et al.* (1999) compared a Directional Waverider with HF radar.

The comparisons showed that different sensors usually agreed well on one-dimensional spectra and integral parameters related to it, such as significant

wave height H_s and peak wave period T_p. The agreement between directional parameters was less satisfactory. Peak direction and mean direction were usually consistent, but e.g. Foley and Bachan (1991) show a occasional 50° bias in the peak direction between an Endeco Wavetrack buoy and a Datawell Wavec buoy. These differences were attributed to shorter waves that biased the direction of the longer waves in the Wavetrack buoy. Ziemer (1991) similarly shows occasional differences up to 45° between peak directions of a Wavescan buoy and a Ship Radar. The origin of these differences was not obvious.

In these comparisons the directional spreading showed considerable scatter, and between some of the instruments there was very little correlation (Allender *et al.*, 1989). When the full directional spectra were compared, different instruments and analysis methods gave quite different spectra. While the general shape of the spectrum was often similar, there were cases where the one spectrum contained a peak that the other one did not. The conclusion may be drawn that the full directional spectrum with an arbitarily high directional resolution was not available with any of the techniques of that time (Krogstad, 1999).

Part 2 presents several new comparisons, some of which involve new instruments and analysis techniques.

An important aspect to take into account when evaluating the comparisons is that they have not been made in the same year. The instruments are continuously developing and therefore the results reported in different comparisons are not necessarily comparable. Some of the observed shortcomings have been reduced by further instrument development. It should be also taken into account that by the time of this writing several new comparison measurements are being conducted.

The editors did not find it practical to make Part 2 a single coherent presentation of the comparisons. Each contribution is therefore a self-contained article.

1.2 References

Allender, J., T. Audunson, S.F. Barstow, S. Bjerken, H.E. Krogstad, P. Steinbakke, L. Vardel, L.E. Borgman and C.Graham, The WADIC project: a comprehensive field evaluation of directional wave instrumentation, *Ocean Engng.* 16, 505-536, 1989.

Beal, R. C. (Ed.), *Directional ocean wave spectra: measuring, modeling, predicting, and applying*, The Johns Hopkins studies in earth and space sciences, Johns Hopkins University Press, Baltimore, 1991.

Foley, E. W. and R. J. Bachmann, Directional Spectra from the Moored Datawell Wavec Buoy during Lewex, in *Directional Wave Spectra*, Ed. R.C. Beal, Johns Hopkins University Press 1991.

Krogstad, H. E., Reliability and Resolution of Directional Wave Spectra From, Heave, Pitch and Roll Data Buoys, in *Directional Wave Spectra*, Ed. R.C. Beal, Johns Hopkins University Press 1991.

O'Reilly, W. C., T. H. C. Herbers, R. J. Seymour, and R. T. Guza: A comparison of directionalbuoy and fixed platform measurements of Pacific swell, *J. Atmos. Oceanic Technol.*, 13, 231-238, 1996.

Wyatt, L.R., S.P. Thompson and R.R. Burton, Evaluation of HF radar wave measurement. *Coastal Engineering*, 37, 259-282, 1999.

Ziemer, F., Directional spectra from shipboard navigation radar during LEWEX, in *Directional Ocean Wave Spectra*, Ed. R. C. Beal, John Hopkins University Press, 1991.

Chapter 2

Comparisons of Directional Wave Sensors and Buoys

Harald E. Krogstad [a] *and Stephen F. Barstow* [b]

[a] Dept. Mathematical Sciences, NTNU, Trondheim, Norway
[b] Oceanor, Trondheim, Norway

2.1 Introduction

The Norwegian directional wave buoys are briefly described in Part 1. In this section we present some of the calibration and intercomparison studies that have been carried out with the buoys which, until recently, have all been using the Datawell Hippy sensors. However, in 1996, Seatex ASA launched the GPS Smart buoy, and at about the same time, the Motion Reference Unit (MRU). We refer to Krogstad *et al.* (1997, 1999) for more details about the directional wave sensors.

The initial intercomparisons between the Smart and Wavescan buoy were carried out in early spring 1995. Following this test, four different directional buoys, including the Smart-800, were deployed in April 1996. One of the other buoys in this campaign was a Wavescan equipped with both a Datawell heave, pitch, roll sensor (Hippy-120) and an MRU-6 from which synchronous measurements were obtained. This allowed a direct validation of the capabilities of the MRU sensor for measuring directional spectra, as dynamic buoy effects would then be equal for both systems.

During the following winter a more comprehensive test for the Smart buoy to obtain data in higher wave conditions was carried out against a reference Directional Waverider on the exposed coast of mid-Norway. As mentioned

in the general description in Part 1, the Seawatch buoy with its elongated structure was from the outset only equipped with a non-directional Waverider. In 1993, it was decided to test a Directional Waverider in the buoy, and the intercomparisons with a stand alone Directional Waverider turned out better than expected (Barstow *et al.*, 1994). Current Seawatch buoys are equipped with the MRU sensor, and results from a recent intercomparison with a Directional Waverider are reported below.

The MRU and GPS directional wave sensors have no moving parts and both are, therefore, considerably more robust than the conventional accelerometer-based wave sensors. Both sensors have low mass, making for lighter equipment, easier deployment and transportation. In addition, the sensors are not sensitive to extremes of temperature, which is of particular importance to coastal applications and transportation in high latitudes.

2.2 The Smart/Wavescan Intercomparisons

The first open ocean tests of the Smart buoy were carried out in February and March 1995 at the Frøya test site off shore Mid-Norway, where the Smart-800 buoy and a Wavescan heave/pitch/roll buoy, equipped with a Datawell Hippy 120 wave sensor, were moored less than 1 km apart in an area with weak wave gradients and at a depth of approximately 100 m. Seventeen minutes records were obtained every 30 minutes with a sampling frequency of 1 Hz.

An excerpt of a set of time series and the corresponding spectra from the Smart buoy is shown in Fig. 2.1. No extra calibration or filtering have been applied, and we note that a flat spectral level of about $0.01\text{m}^2\text{s}$ is reached below approximately 0.05 Hz. Although this level is most likely a result of second order contributions to the spectrum caused by the buoy's Lagrangian measurement principle, it is at the same time an upper bound for the single measurement noise level, thus limiting the average random error to less than 0.07 m/s.

In Fig. 2.2, scatter plots of the most important sea state parameters from the analysis of about 50 simultaneous records from 23–24 February and 20–21 March are shown (note that the limited resolution for T_p leads to a number of superimposed data points). The weather situation on the 23–24 February was such that a low had developed on the 21^{st} to the south–west of Iceland and moved slowly eastward with strong swell generating westerly winds to the south of the centre. It passed the Faroes on the 22^{nd} and upon reaching

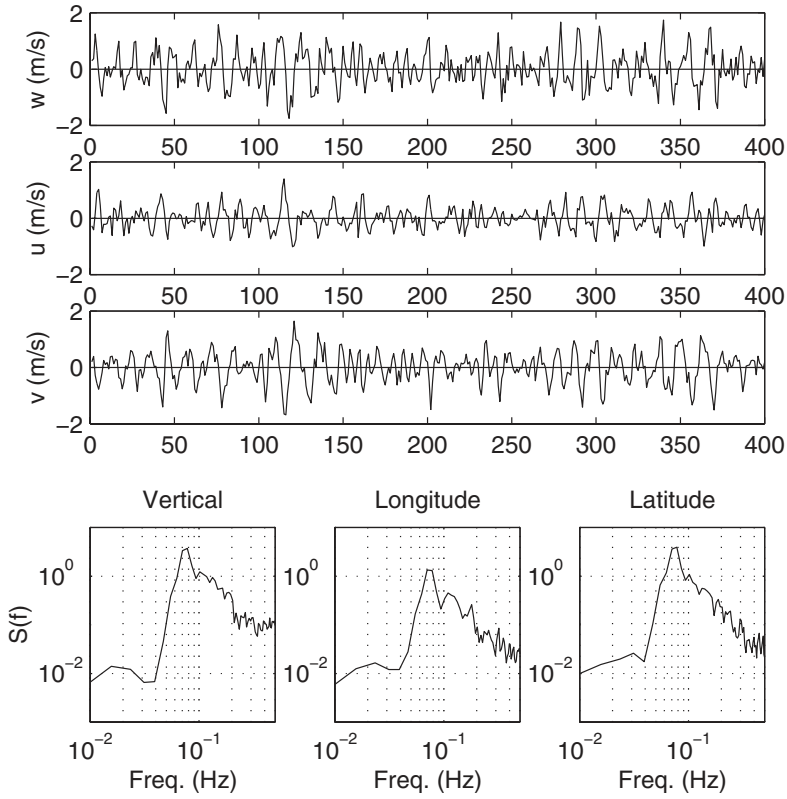

Figure 2.1: Upper: Excerpts of velocity time series obtained from the Smart buoy processing system; Lower: Corresponding spectra from the complete time series.

the Norwegian coast it turned and moved slowly along the coast passing close to the measurement site on the 23^{rd}. Locally at Frøya, winds were not strong and were variable in direction. Swell would therefore have dominated the wave situation over this period. For 20–21 March, a very deep low had moved in from the Atlantic on the 17^{th} and, weakening, moved more or less directly over the measurement site in an easterly direction. As it retreated eastwards, and extensive area of strong northerlies built up in the Norwegian Sea. These northerly wind waves would have dominated the wave spectrum on both these days. Whereas significant waveheight, peak period and the main and mean directions show good agreement, the mean wave period is

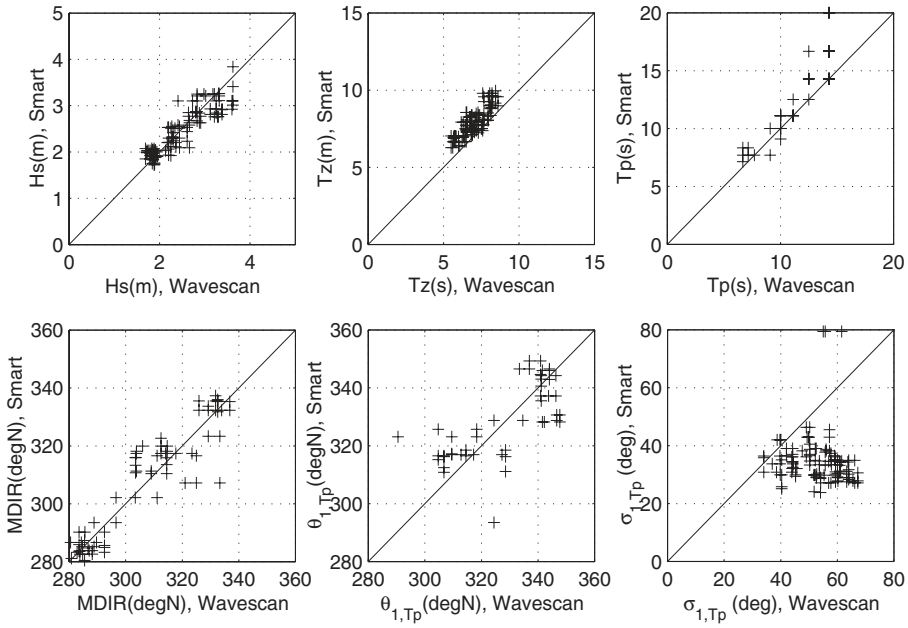

Figure 2.2: Comparison of a selection of wave parameters from the Smart-800/Wavescan sea trials. Note the expanded directional scale for the main and mean directions.

biased compared to the Wavescan and the directional spread around the spectral peak is significantly lower for the Smart buoy (all wave parameters are based on the spectrum and defined in Part 1).

The difference in wave period is explained from an intercomparison of the spectra, where it was found that the spectral ratio $S_{\mathrm{Smart}}(f)/S_{\mathrm{WSC}}(f)$ drops from one around the most energetic parts of the spectra to about 0.5 in the high frequency end at 0.4 Hz.

Examples of simultaneous directional spectra from the two buoys are shown in Figs. 2.3 and 2.4. In these plots, the directional distributions have been computed using the Burg Maximum Entropy estimate (see Part 1). The visual impression of the Smart spectra as significantly more "tight" was evident in all observed cases and is reflected in the strong bias in wave spread between the buoys, see further discussion of Wavescan below.

For a heave-pitch-roll buoy such as Wavescan, we recall the dispersion ratio

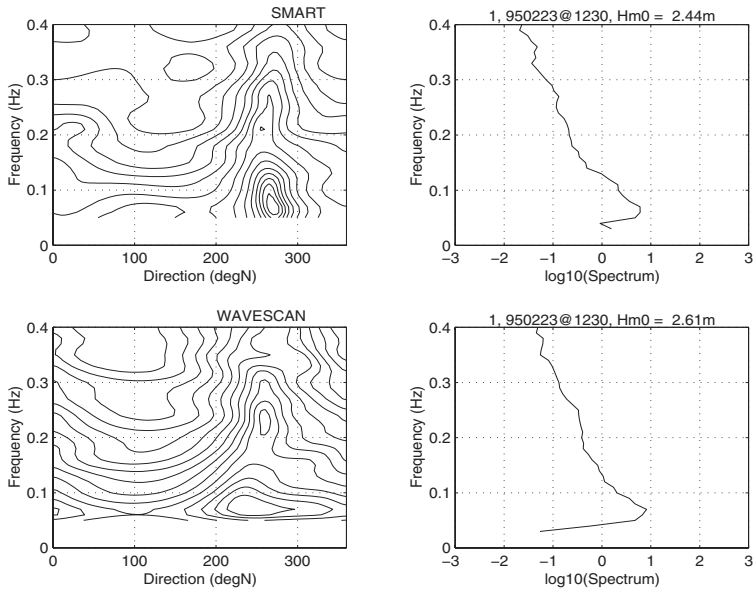

Figure 2.3: Examples of simultaneous directional spectra (left) and frequency spectra (right) from the Smart-800 and Wavescan buoys.

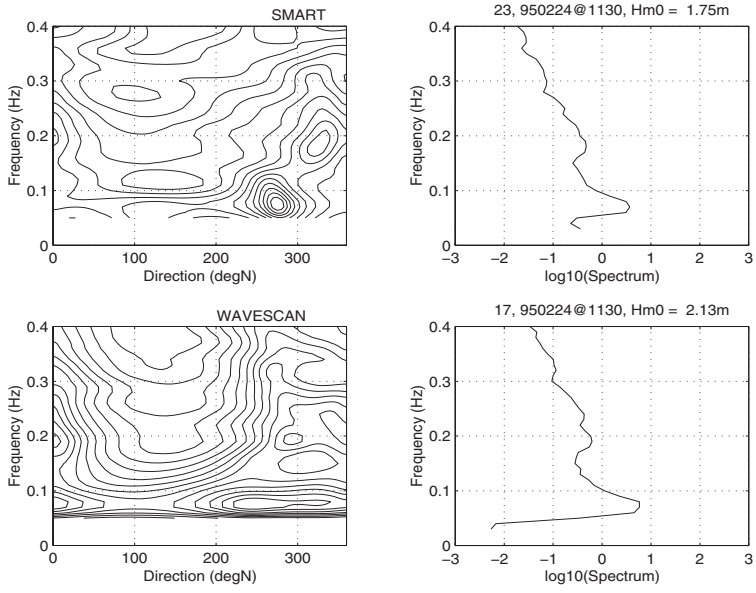

Figure 2.4: See previous figure for legend.

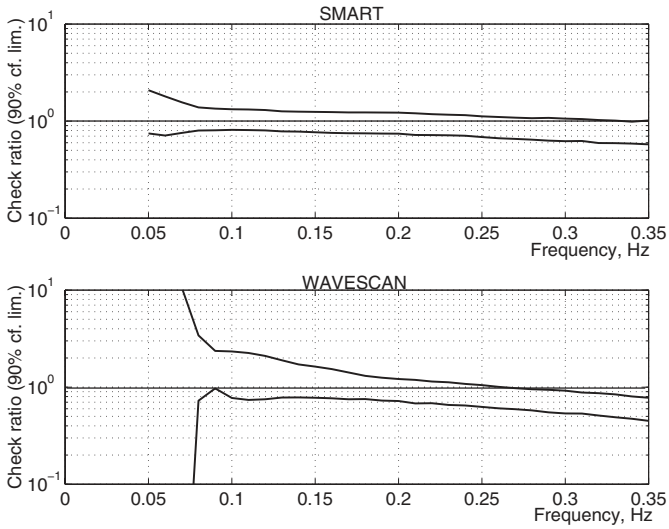

Figure 2.5: Check ratios for the Smart-800 and Wavescan buoys. The graphs signify the 90% variability around the average values. Note that the part of the spectrum below T_p has not been used.

(Part 1, section 3.1 and 3.3.3)

$$r_{\mathrm{WSC}}(f) = \left[\sqrt{\frac{S_{xx}(f) + S_{yy}(f)}{S(f)}}\right] / k(f), \tag{2.1}$$

where S_{xx} and S_{yy} are the slope spectra in the x and y directions, respectively. A similar ratio may also be defined for Smart,

$$r_{\mathrm{Smart}}(f) = \sqrt{\frac{S_{uu}(f) + S_{vv}(f)}{S_{ww}(f)}} \times \tanh^2\left(k(f)h\right) \tag{2.2}$$

In this case S_{uu}, S_{vv} and S_{ww} denote the velocity spectra, and the ratio is 1 for an ideal displacement buoy in a linear wave field. The 90% variability around the average check ratios for both buoys is shown in Fig. 2.5, and it is clear that the ratio for the Smart buoy is somewhat closer to 1 compared to the Wavescan buoy.

2.3 The MRU/Hippy Intercomparison

In April 1996, Seatex deployed a Wavescan buoy for about 5 weeks on the western coast of Norway close to the island Frøya in approximately 100 m depth. The buoy was instrumented with *dual* MRU-6 and Hippy-120 wave sensors which were configured to sample the buoy heave, pitch, roll and heading synchronously at 2 Hz for a 17 minutes interval every 3 hours. The directional data analysis was identical apart from the electronic transfer functions, which were compensated for as specified by the manufacturers. Wavescan's nominal dynamic transfer functions (see Barstow and Krogstad, 1984), which compensate for the buoy's pitch/roll resonance at about 2.4 second, were applied to both sensor spectra.

The initial intercomparison of wave parameters showed quite strange discrepancies, which after some investigation were explained by examining the simultaneous time series.

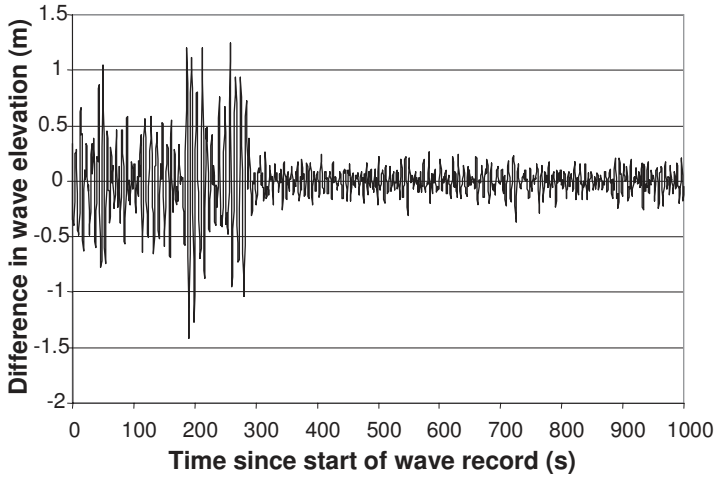

Figure 2.6: Time series (2 Hz) of the difference in wave elevation between the MRU and the Hippy, showing the lack of agreement for approximately the first 5 minutes of the record.

Figure 2.6 shows the difference between elevation recordings. From about five minutes into the series, the difference drops to a very low level. The reason for the discrepancy at the beginning of the file turned out to be due to the operational set up of the MRU sensor. In order to save power, the

MRU sensor is switched on some minutes before measurements commence and what we see is the final initialisation of the system's Kalman filter. The cure for this problem has simply been to increase the "warm-up" time for the sensor.

Following the discovery of the reason for the discrepancy, the intercomparison was repeated based on a directional analysis of the second uncorrupted part of the time series (1024 samples). During the measurement period, a good range of wave conditions were experienced. H_s reached 4 m in two storms, a good mixture of wave directions were measured, and both local wind seas and the occasional long Atlantic swell occurred. Figure 2.7 shows scatter plots of selected wave parameters between the two sensors for the duration of the experiment.

Both H_s and even $H_{\max}$ show close to perfect agreement with less than 1 cm mean difference. The peak wave period (T_p) similarly shows little difference (one large outlier occurs for a strongly bimodal wave spectrum). The maximum spectral density also shows perfect agreement. The main differences are found for the directional parameters. There is some scatter for the wave direction at the spectral peak, $\theta_1(f_p)$, although the overall features are similar and in agreement with the predominant weather conditions. The directional spread at the spectral peak period, $\sigma_1(f_p)$ is, however, systematically higher from the Hippy sensor by as much as 22% on average (See also the Smart/Wavescan intercomparison above). Intercomparisons between the frequency spectra showed almost perfect agreement apart from the very low frequencies where the MRU seems to give slightly higher spectral levels compared to the Hippy.

The reason for the difference in the spread estimates was eventually found by looking at the raw time series of pitch, roll and buoy heading. As was the case for elevation, both sensors give almost identical measurements of pitch and roll. However, it turned out that the buoy heading (compass) series were quite different, as illustrated in Fig. 2.8.

The MRU heading time series (from a 3-axis fluxgate compass) is noticeably smoother than the data from the compass used together with the Hippy sensor, which for the Norwegian buoys was a gimballed 2-axis fluxgate Silva compass. In addition, inspection of several time series shows that spikes are not infrequent on the Silva compass time series. Interestingly enough, by removing the spikes and doing a simple moving average smoothing of the Hippy compass time series, the directional spread drops to the same level as that derived from the MRU sensor.

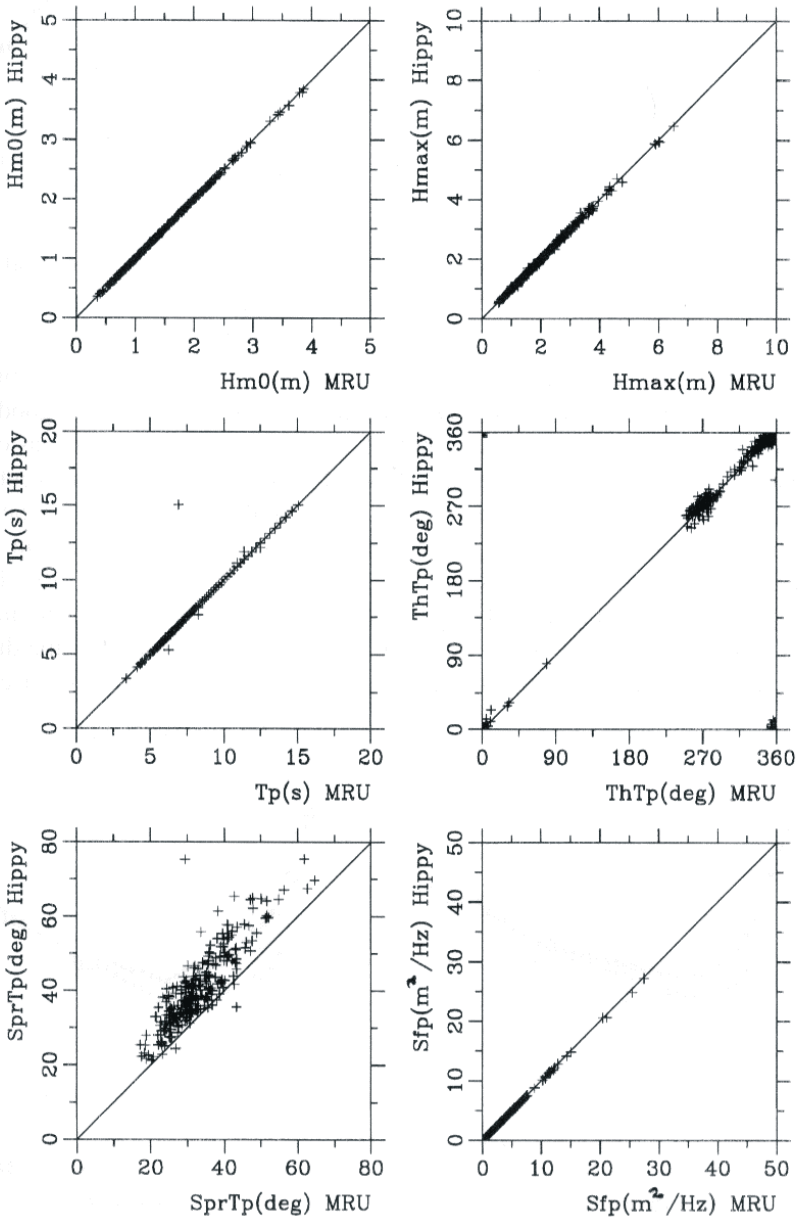

Figure 2.7: Comparison of wave parameters derived from the MRU and the Hippy sensor in the same buoy for the duration of the field trial; a) H_{m0}; b) H_{max}; c) T_p; d) $\theta_1\,(T_p)$; e) $\sigma_1\,(T_p)$, and f) Spectral value at the peak, $S\,(f_p)$.

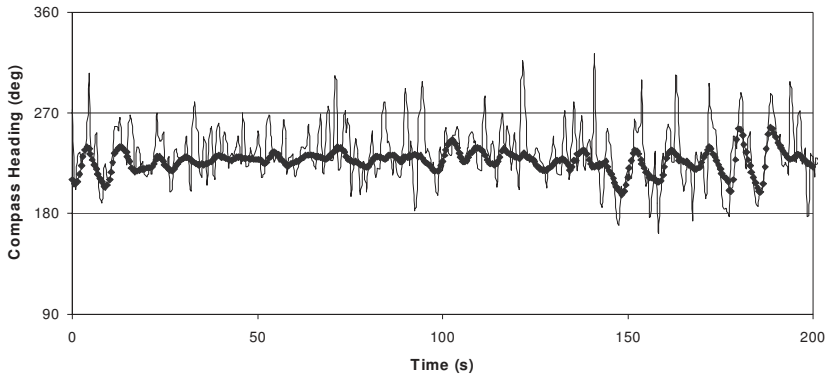

Figure 2.8: Typical time series of buoy heading from the Hippy compass (solid line) and the MRU (diamonds).

2.4 The Smart/Directional Waverider Intercomparison

During the period December 1997 to February 1998, a Smart-800 was moored less than 1km from a Directional Waverider near the Svinøy lighthouse, on the western coast of Norway in a water depth of around 90 m. The DWR data were collected as part of the *FARGIS* project (an operational monitoring system for Norwegian shipping lanes), coordinated by the Norwegian research organisation SINTEF. The Smart-800 receiver station was located at the lighthouse 5 km from the measurement site. The directional wave data from the DWR were based on Datawell's real time analysis carried out and stored on board the buoy. One wave record was available each hour based on a 26 minutes measurement sequence. However, the two system's measurement sequences were not exactly synchronised and short-term fluctuations may add some extra uncertainty. About 400 simultaneous directional spectra were available for the intercomparison.

Simultaneous measurements were matched and scatter plots of various wave parameters are shown in Fig. 2.9.

The Smart-800 significant waveheight shows excellent correlation with the DWR with only 8 cm overall bias and a residual scatter index of 6%, as expected from the sampling variability. A slight tendency for the Smart to overestimate at low sea states is due to a small increase in the spectral ratio

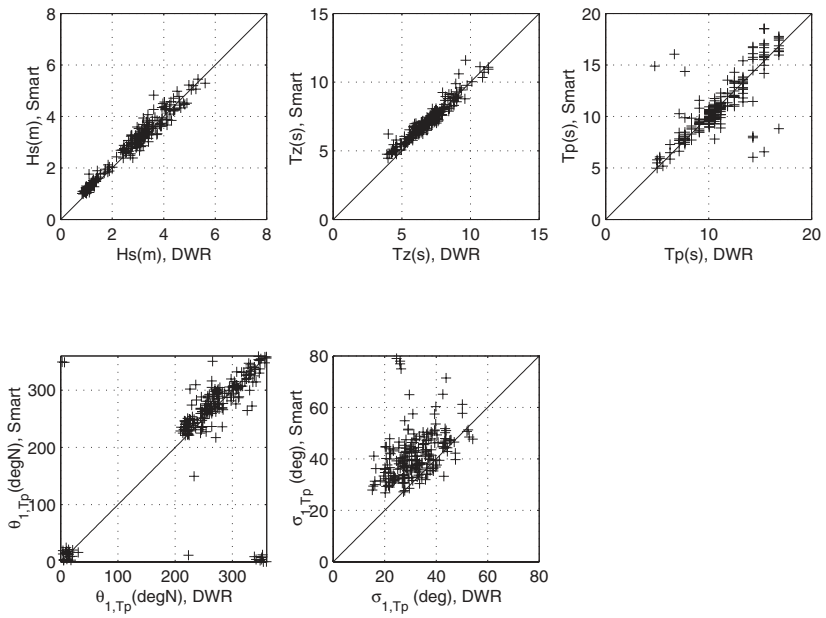

Figure 2.9: Scatter plots of a) H_s; b) T_z; c) T_p; d) $\theta_1\,(T_p)$; e) $\sigma_1\,(T_p)$, and f) $S\,(f_p)$ between the Smart-800 and the Directional Waverider (DWR) during the Svinøy test from December to February 1997-98.

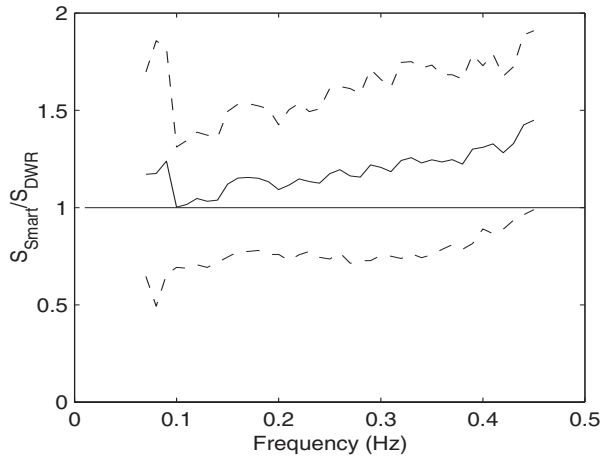

Figure 2.10: Observed mean spectral ratio (solid line) and plus/minus one standard deviation (dashed line) between the Directional Waverider and the Smart buoy (only including data above the spectral peaks).

with frequency (see Fig. 2.10).

Nevertheless, the mean period, T_z, shows excellent agreement. The peak wave period shows normal behaviour, with some outliers occurring in bimodal sea states. The wave direction at the spectral peak $\theta_1(f_p)$ shows overall only a 3 degree bias. Finally, the directional wave spread at the spectral peak ($\sigma_1(f_p)$) is definitely higher from the Smart-800. The largest outliers are for records from the Smart-800 with a peak period at 25 sec. A closer examination of these wave spectra shows that this is due to low frequency noise contaminating the wave spectrum, probably caused by occasional failures to buffer the GPS data at the receiver station. This is a part of the reason for the higher directional spread from the Smart-800, but the overall tendency has not been fully explained.

Figs. 2.11 – 2.13 show direct spectral intercomparisons similar to Figs. 2.3 and 2.4. Taking into account the rather large sampling variability of the maximum entropy directional estimate (Part 1, Section 3.1), a slightly different amount of spectral smoothing, and above all, the highly different operational principles, the agreement is remarkably good. In the first case, the sea state is quite complex. Nevertheless, the various wave fields are found in both spectra. For the higher sea states, the directional characteristics are simpler, and the agreement still good.

2.5 The MRU Sensor in the SEAWATCH Buoy

During a 3 month period in winter 1993 – 94, OCEANOR together with Datawell carried out a direct intercomparison between a stand alone Directional Waverider and a Directional Waverider mounted in a Seawatch buoy. The results, presented at the OCEANS '94 Conference (Barstow *et al.*, 1994), showed, somewhat surprisingly, that the dynamic response of the Seawatch buoy had no negative influence on the quality of directional spectra from the buoy. On the contrary, the data seemed to indicate that the Seawatch system followed the orbital velocities more closely.

In February to March 1999, a validation of the MRU-6 in the Seawatch buoy was carried out at the Frøya test site. This time, the Seawatch buoy was in fact equipped with dual MRU-4 and MRU-6 sensors. This test was designed both to verify the use of the MRU in Seawatch and, in addition, to confirm that the less expensive MRU4 sensor could be used instead of the MRU-6 with no detrimental effect on the directional wave measurements (MRU4 is a scaled down version of MRU-6 requiring about 60% of the power). A

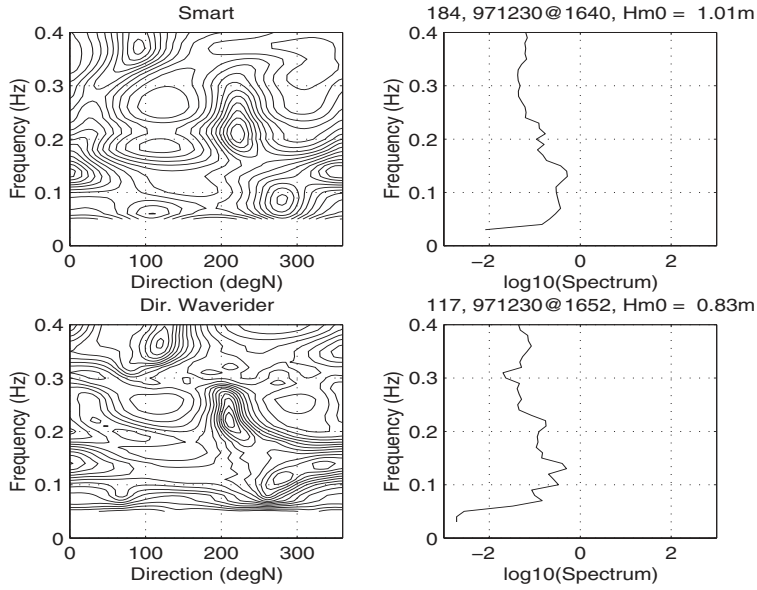

Figure 2.11: Simultaneous directional spectra (left) and frequency spectra (right) from the Smart and Directional Waverider buoys. Low, mixed sea state.

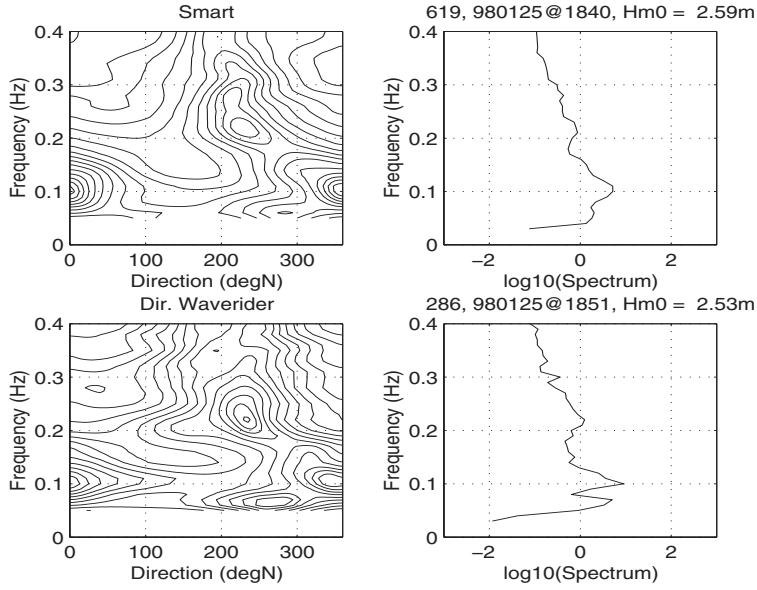

Figure 2.12: See Fig. 2.11. Intermediate sea state.

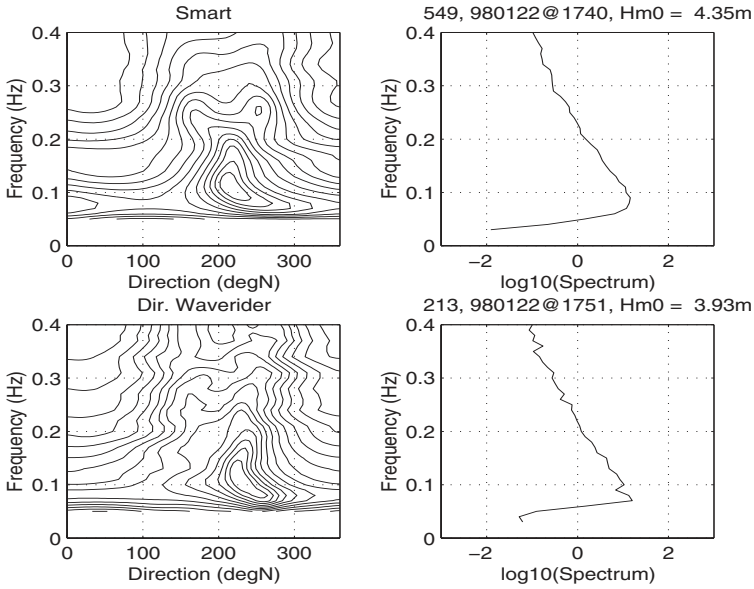

Figure 2.13: See Fig. 2.11. High, unimodal sea state.

comparison of mean frequency spectra over the trial period is shown in Fig. 2.14. The MRU-4 and MRU-6 are very close, whilst the Directional Waverider spectra deviate for the highest frequencies above 0.4 Hz. This is possibly due to differences in the sampling used on the two buoys which is 1 Hz for the Seawatch and 1.28 Hz for the Directional Waverider. In fact, it turned out that all MRU-4 measured wave parameters were practically inseparable from the MRU-6.

An intercomparison of wave parameters between the Seawatch buoy with the MRU-6 sensor and the Directional Waverider is shown in Fig. 2.15. The scatter is similar to the statistical sampling variability, apart from a few outliers for the direction at the spectral peak. The scatter for directional spread is considerable, and one sees a tendency to lower spread from the Seawatch buoy, also observed already in the first field trials (Barstow *et al.*, 1994).

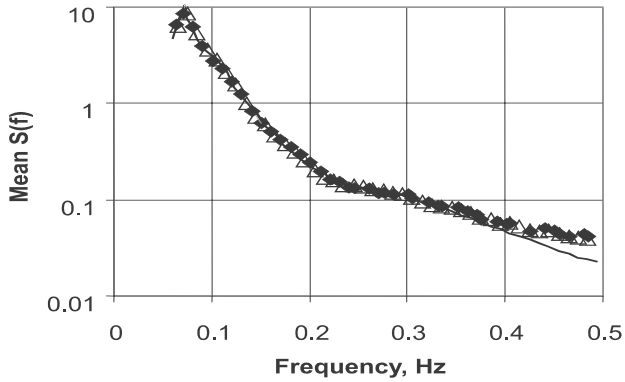

Figure 2.14: Comparison of mean wave spectra for the period 27th February 1999 to March 7th 1999 for which simulataneous wave spectra are available from a) MRU-4 (open triangles), b) MRU-6 (black diamonds) and the Directional Waverider (solid line). Only spectral estimates at and above the spectral peak are included.

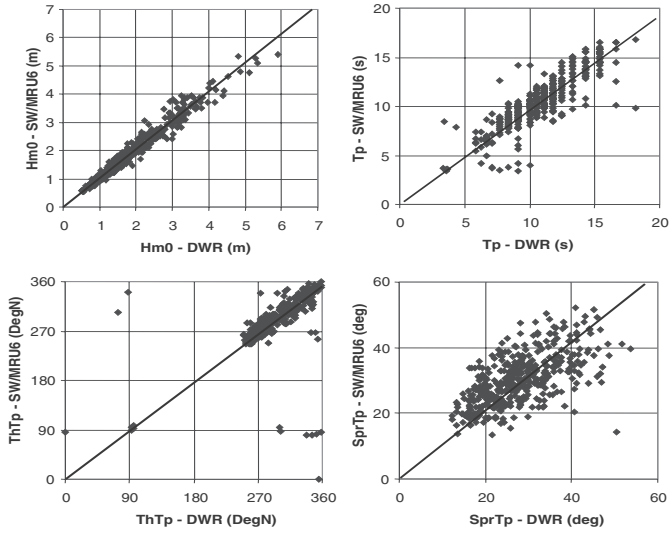

Figure 2.15: Comparison of the significant waveheight ($Hm0 = H_s$), peak wave period (T_p), wave direction at the spectral peak period ($ThTp = \theta\,(T_p)$) and directional spread at the peak period ($SprTp = \sigma_p\,(T_p)$) for the duration of the 1999 intercomparison of the Seawatch equipped with an MRU6 sensor and the Directional Waverider.

2.6 Discussion

This chapter has presented a small selection of intercomparison studies that are always necessary for keeping an up-to-date and trimmed instrument park. The possibilities for unexpected, and in many cases, downright stupid errors in the measurement set-up appear to be never-ending. In the first directional measurements from buoys in Norway, the swell statistics showed a perfect directional shadow caused by the coast,– 90 degrees off, and thus consistent with the square shaped instrument box which could be placed in the buoy in four different ways! The apparent noisy compass series in Wavescan shown above, is an example of a more subtle error. The noise will be mixed up with signal in a complex way by the transformation to a fixed coordinate system and will not be easily visible in the results.

Differences in the non-directional parameters may often be traced back to noise or different dynamic behaviour of the buoys. For example, the high frequency spectra from the Wavescan buoy ($\emptyset$=2.7m) are definitely higher than spectra from the DWR and Smart ($\emptyset$=0.9m). This may be explained by different dynamic behaviour, but the difference between the Smart and the DWR must have other causes, of which mooring effects and operational principles are probable reasons.

For the directional parameters, the present study confirms that the mean direction is a quite stable parameter. The directional spread is on the other hand quite susceptible to noise, and we see that the Wavescan spread is higher than Smart, Smart is higher than DWR, and Seawatch is higher than DWR. The reasons for the discrepancies are most likely the buoy behaviour and mooring effects, both of which are quite hard to assess quantitatively.

The frequency range of the buoys varies. First of all, the sampling frequencies are different, although the parameters considered above are not strongly influenced by the Nyquist frequencies. Also the low frequency response differs. The Smart buoy delivers velocity spectra which blow up in a simple way when converted to displacement. For the Directional Waveriders, the acceleration is twice integrated to displacement internally in the buoy.

The modern wave sensors are, however, promising. Neither the MRU nor the GPS have moving parts and both are, therefore, more robust than the conventional accelerometer based wave sensors.

The MRU wave sensor can be used in both displacement buoys and heave, pitch and roll buoys. The test against the standard Hippy sensor showed that the heave and slope time series are virtually indistinguishable. Being based

on highly different operational principles, this adds significant confidence to both systems.

The sensor in the Smart buoy uses novel differential GPS measurement technology to measure the 3-axis orbital velocities of the buoy, from which directional wave spectra are calculated using analysis routines which are very similar to conventional directional wave buoys. The more obvious principle of tracking the motion itself is possible, but appears to be less stable. However, the GPS technology, where the motion of the buoy is tracked completely independently from any local sensor, represents in a way the ultimate wave sensor on a buoy. Unfortunately, various hardware problems have hampered the further development of the Smart, although the properly working buoy, as reported above, has shown that directional spectra are close in accuracy to buoys with "in-situ" wave sensors. In the future, the GPS-system may well be a part of the instrumentation on any metocean buoy.

2.7 References

Barstow, S.F., and H.E. Krogstad, General analysis of directional ocean wave data from heave/pitch/roll buoys, *Mod. Ident. and Control*, 5, 47–70, 1984.

Barstow, S.F., Haug, O. and T. van der Vlugt, A Field Validation of a Directional Waverider in a Seawatch Buoy. *Proc. OCEANS '94 Conference*, Brest, France, 1994. Vol.2, 32–37.

Krogstad, H.E, S.F. Barstow, O. Haug, P.Ø. Markussen, G. Ueland and I. Rodriguez, Smart-800: A GPS Based Directional Wave Buoy. *Proc. Waves'97 Conference*, Virginia Beach, Virginia, USA, November 1997.

Krogstad, H.E, S.F. Barstow, S.E. Aasen and I. Rodriguez, Some recent development in wave buoy measurement technology, *Coastal Eng.*, 37, 309–329, 1999.

Chapter 3

ASIS-Directional Waverider Comparison

William M. Drennan[a], *Kimmo K. Kahma*[b], *Hans C. Graber*[a], *Heidi Pettersson*[b], *Mark A. Donelan*[a], *Delphine Icard*[a] *and Danièle Hauser*[c]

[a] Rosenstiel School of Marine and Atmospheric Science, University of Miami, Miami (FL), USA
[b] Finnish Institute of Marine Research, Helsinki, Finland
[c] Centre d'étude des Environnements Terrestres et Planétaires (CETP), Vélizy, France

3.1 Introduction

The Air-Sea Interaction Spar buoy (ASIS) is a new multipurpose platform for conducting research at and near the air-sea interface (see Part 1 section 4.4). It has been developed by University of Miami's Rosenstiel School of Marine and Atmospheric Science (RSMAS), and the Woods Hole Oceanographic Institution (Graber *et al.*, 2000). Here we describe a comparison of directional wave measurements from ASIS and a Directional Waverider buoy (DWR), which were made during an experiment in the Mediterranean in 1998. Directional wave measurements on ASIS are made using an array of capacitance wave gauges, each measuring the local surface elevation. See Part 1, section 4.4 for details regarding wave measurements on ASIS. The Directional Waverider is described in section 4.1.2 of Part 1.

In the analysis we apply the guidelines for comparisons given in Part 1. These include the estimation of the sampling variability associated with the data being compared: significant differences between instruments will be indicated by variability greater than the expected sampling variability.

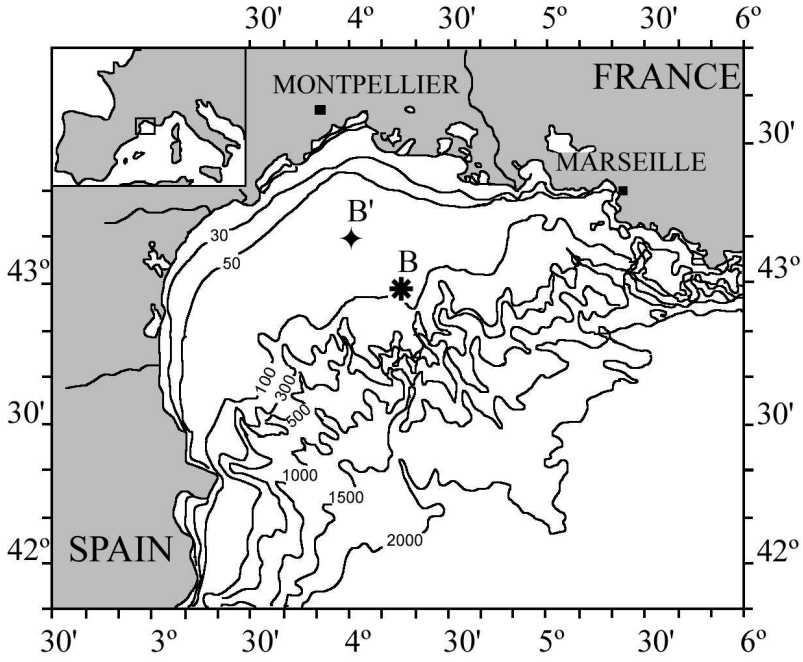

Figure 3.1: Map showing the location of the FETCH experiment. Point B indicates the mooring position of the ASIS buoy. During 16-25 March 1998 the DWR buoy was also at this location. It was then moved to point B'.

3.1.1 The FETCH Experiment

The FETCH (Flux, Etat de la mer et Télédétection en Condition de fetcH variable, or Flux, sea state, and remote sensing in conditions of variable fetch) experiment took place from 12 March to 16 April 1998 in the Gulf of Lion, western Mediterranean Sea (Fig. 3.1). The experiment, part of a MAST-III funded initiative on the Mediterranean basin, included as its goals: i) the study of waves as a function of development (fetch limited), ii) the improvement of wave prediction models, and iii) the measurement and parameterisation of turbulent fluxes at the air-sea interface (Hauser *et al.*, 2003). The experimental strategy was to carry out extensive measurements of waves and fluxes during off-shore high wind events: Mistral winds, blowing south down the Rhone valley, and Tramontane winds, blowing south–eastward, parallel to the Pyrenees. Mistral winds, in particular, are remarkable for their strength and steadiness, with winds of over 20 ms^{-1}

sometimes persisting for days. Hence they represent a relatively rare opportunity to study wave development in steady, high wind conditions.

To achieve these and other goals, the ship *R/V L'Atalante*, two aircraft, and several buoys were instrumented with wave and turbulent flux sensors, and operated in the experimental area; satellite data were also archived. Here we focus our attention on the two moored buoys, the Directional Waverider (DWR) and ASIS. In order to study the fetch dependence of the wave field, the buoys were moored at different fetches, roughly 40 and 60 km from the coast. However, as the principles of measurement of the buoys are quite different, an initial side by side test of the two buoys was carried out. It is the data from this initial period that we discuss here.

During the FETCH intercomparison, the two buoys were moored approximately 2 km apart (to avoid possible entanglement) at 42°58'56"N, 04°15'11" E, along the 100 m isobath. DWR was moored on 1998-03-16 at 12Z. ASIS was deployed two days later, during calm weather, on 1998-03-18 and was operational by 17Z. During FETCH, ASIS was tethered to a secondary buoy using a 60 m surface tether. This mooring configuration is designed to limit the effects of mooring line forces on ASIS. DWR was recovered on 1998-03-25 at 13Z, for redeployment further in-shore. Hence the period of the side-by-side intercomparison between the two buoys was about a week. During this time, the buoys experienced a variety of wind and wave conditions. In Fig. 3.2, the 7 m wind speed and direction (measured by a sonic anemometer on ASIS), along with significant waveheight, H_s, and spectral peak frequency, f_p, from the two buoys, are shown for the period of the intercomparison. Two events of particular interest during the intercomparison period were the Mistrals of 19-21 March and 24 March.

3.2 The Wave Buoys

During the FETCH experiment, the ASIS buoy was equipped with an array of 8 wave capacitance gauges for measuring the directional properties of the wave field. The array consisted of five wires equally spaced around the outer perimeter of the pentagonal cage (radius 0.93 m) and three wires forming a small triangle in the centre. The three wires at the centre are used to measure wave lengths less than 2 metres.

Here we focus on larger scale waves, and use surface elevation data from the 6-element centred pentagon. During the intercomparison period one of the wires at the outer perimeter was broken, hence data from only five of

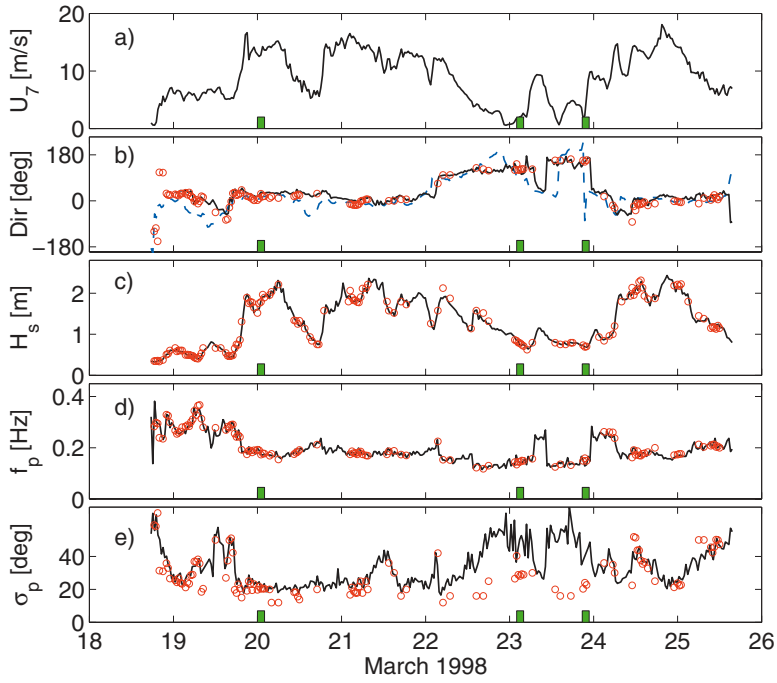

Figure 3.2: Conditions during the FETCH intercomparison period. Unless otherwise indicated, ASIS and DWR data are indicated by solid lines and open circles respectively. The shaded areas indicate specific periods discussed in the text. Panel a) shows the 7-metre wind speed. Panel b) indicates the peak wave directions, along with the ASIS wind direction (dashed). Panel c) shows significant waveheight. Panel d) indicates peak frequency. Panel e) shows the directional spreading at the peak frequency.

the gauges is available. The buoy motion was measured and the waveheight time series corrected as described in Part 1, section 4.4.2. Once the time series are corrected for buoy motion, standard array processing techniques can be applied to extract directional information - see Part 1, chapter 3.

During the comparison measurements the DWR was used in the standard configuration, moored using a double rubber cord mooring line. The spectral density, mean direction, directional spread, skewness and kurtosis in the frequency range $0.025 - 0.58$ Hz were calculated from 1600 second displacement time series on board the buoy, following Longuet-Higgins *et al.* (1963). Each half hour the spectral data and 20 minutes of displacement data (vertical, north and west) were sent to the *R/V L'Atalante* via HF radio. Unfortu-

nately the ship was not in reception range all the time and full spectral data and time series are available only for about half of the intercomparison period. The buoy was also equipped with an ARGOS transmitter, and sent compressed directional spectra (13 frequency bands) via ARGOS satellite. These compressed spectra are available for the whole comparison period.

DWR was calibrated immediately after the experiment by the manufacturer, Datawell b.v.. All calibrated parameters were within the specifications. When calculating one dimensional spectra and significant waveheight, heave was reduced by 0.8%, based on the calibration. The ASIS wave staffs were calibrated at RSMAS prior to deployment in the field. Pre- and post-field calibrations of the ASIS motion sensors were carried out at the National Water Research Institute (NWRI), Burlington, Canada. Previous field deployments (Graber *et al.*, 2000) identified a 10.3° offset in the mean compass direction. The compass directions were corrected for this offset.

3.3 Results

3.3.1 One-dimensional Parameters

In Fig. 3.2c, time series of significant waveheight from the two buoys are plotted for the full intercomparison period. The DWR data set includes data received via ARGOS (appr. 20%). In these data the significant waveheight has been calculated on board the buoy and the the peak frequency is the middle of the frequency band that forms the peak. In Fig. 3.3a, H_s from the two buoys are plotted against each other. As the buoy data are calculated at different times (the DWR data at half hourly intervals, the ASIS data every 28.5 min), the DWR data have been interpolated onto the denser ASIS time base for the comparison. A maximum likelihood regression (assuming equal variability, Orear (1982)) yields H_s-DWR = 1.004 H_s-ASIS + 0.033, which is not significantly different from a 1:1 line. Here the correlation coefficient, γ^2, is 0.993. The dashed lines on the plot represent the 90% confidence limits due to sampling variability (Allender *et al.*, 1989; Krogstad *et al.*, 1999), using a coefficient of variation estimated from the data (COV $\approx$ 0.05). This value is consistent with that reported by Krogstad *et al.* (1999) for a Directional Waverider buoy deployed off Scotland. As 91% of the data fall within the 90% confidence limits, we conclude that the scatter in the comparison is accounted for by sampling variability.

In Fig. 3.2d, time series of peak frequency from the two buoys are plotted.

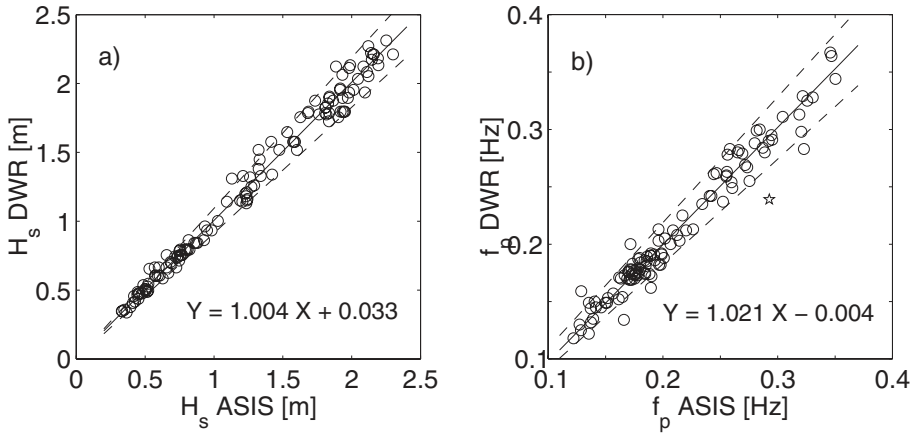

Figure 3.3: Comparisons of significant waveheight (Panel a) and peak frequency (b) as measured by ASIS and DWR buoys. The dashed lines indicate the 90% confidence bands, assuming equal variability for the two sensors. The point denoted by star in (b) represents a bimodal sea, and has been excluded from the regression.

For each buoy, f_p is derived from the frequency spectrum using a parabolic (energy-weighted) fit to the most energetic, and two neighbouring, frequency values. The two f_p's are plotted against each other as a scatter plot in Fig. 3.3b. A maximum likelihood (ML) regression yields f_p-DWR = 1.021 f_p-ASIS - 0.004 (γ^2 = 0.981), which again implies no significant difference between the two estimates, with more than 90% of the points falling within the 90% confidence limits. The point having the largest deviation from the ML regression line is associated with a bimodal sea state, with the two modes containing similar energy and with the two buoys selecting the different modes as 'maximum'. This point is excluded from the regression.

It is evident that the two buoys are in very good agreement in terms of the basic parameters describing the wave field. However, a comparison of the higher order properties, such as the skewness of the waves, indicates significant differences between the two sensors. In Fig. 3.4a we plot the skewness of the surface elevation time series measured by the two buoys versus time. For DWR, only 49 time series that are free of transmission errors are available during the intercomparison period. For equivalence with the DWR sampling, the ASIS data were low pass filtered at 1.3 Hz; for the most part, this made only small, O(1 - 10%), changes to the ASIS skewness. It is evident that both data sets show considerable scatter, and there is no relationship between them. While the ASIS skewness data are correlated

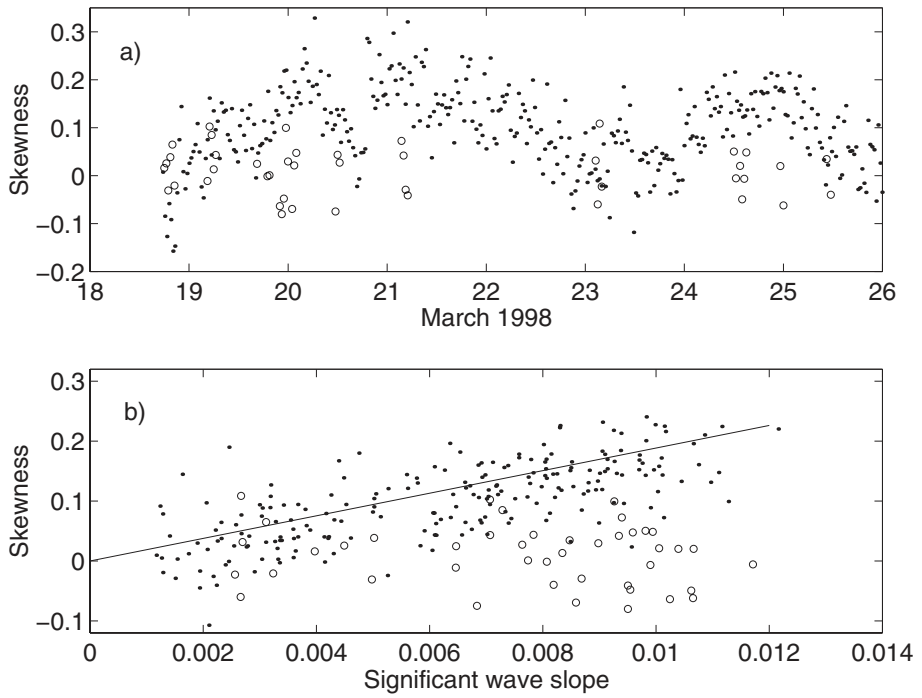

Figure 3.4: Panel a) shows skewness of the surface elevation time series as measured from the two buoys (ASIS •; DWR ○). For the comparison, the ASIS time series were first low passed at the DWR sampling frequency. Panel b) shows the skewness data, averaged over 3 hours, for the entire FETCH campaign plotted against significant slope, $S_s = (\overline{\eta^2})^{1/2}/\lambda_p$. The curve of Srokosz and Longuet-Higgins (1986) is also shown.

with wind, and significant steepness, $S_s = (\overline{\eta^2})^{1/2}/\lambda_p = H_s/(4\lambda_p)$ (Huang and Long, 1980), see Fig. 3.4b, the DWR data are not. In the latter figure, 2 hours of ASIS data have been binned to reduce the variability. Here the skewness, K, of the ASIS surface elevation time series support the general relation with steepness predicted by Srokosz and Longuet-Higgins (1986) for narrow spectra: $K = 6\pi S_s$. Srokosz and Longuet-Higgins (1986) also addressed the question of how a surface follower, such as a DWR, measures the surface elevation skewness. They concluded that to within second order it should be equivalent to wave gauge (Eulerian) measurements. The FETCH data indicate that this is not the case, and support instead the recent conclusions of Magnusson *et al.* (1999).

3.3.2 Directional Parameters

Next we investigate the two-dimensional parameters: spreading angle, σ_1, and mean wave direction, θ_1. For DWR, σ_1 is calculated on board following the method of Longuet-Higgins *et al.* (1963): $\sigma_1 = (2(1 - r_1))^{1/2}$, where $r_1 = \sqrt{a_1^2 + b_1^2}$,

$$a_1 = Q_{12}/\sqrt{(C_{22} + C_{33})C_{11}} \tag{3.1}$$

$$b_1 = Q_{13}/\sqrt{(C_{22} + C_{33})C_{11}} \tag{3.2}$$

where C_{ij} and Q_{ij}, both functions of frequency, are the real and imaginary parts (co- and quad-) of the cross spectrum between sensors i and j. Here, subscripts 1, 2 and 3 refer to displacement in the vertical, north direction and west direction respectively (see also Kuik *et al.*, 1988). For the purposes of comparison, the spreading for the ASIS buoy distribution is calculated in a similar manner. From the wave staff array elevations, the local sea surface slopes (pitch and roll) are calculated. Then, σ_1 is calculated as above where subscripts 1, 2 and 3 in Eqns. (3.1) and (3.2) refer to displacement in the vertical direction, pitch angle and roll angle, respectively (Longuet-Higgins *et al.*, 1963). Although this does not take advantage of the ASIS buoy's higher resolution (and its ability to determine local curvature), it allows for a direct comparison.

As the spreading values at adjacent frequencies varies, the mean spreading at the three frequencies that define the peak frequency is used to get a representative spreading value for the peak of the spectrum. This is also consistent with the ARGOS data: the spreading and mean direction correspond to the mean value of the frequency band that forms the peak of the spectrum.

The time series of the spreading angles at the peak frequency, σ_p, are plotted in Fig. 3.2e. Most of the time the agreement is good, but at some times DWR reports much smaller spreadings (Fig. 3.5a). Most of these cases occurred during the 36 hour period from 22 March (1200) to 23 March (2400). This period is discussed below. If these data, plotted using open circles on Fig. 3.5a, are removed, the DWR and ASIS σ_p agree well, with the DWR σ_p values on average 3° lower than those of ASIS.

When the comparison is extended to all frequencies above the peak, and energy levels above 0.02 E_{max} (Fig. 3.5b), the spreading angles are scattered more evenly. The linear regression (maximum likelihood) in this case, $\sigma_{1,DWR} = 1.2\sigma_{1,ASIS} - 10.6$ is significantly different from 1:1 agreement

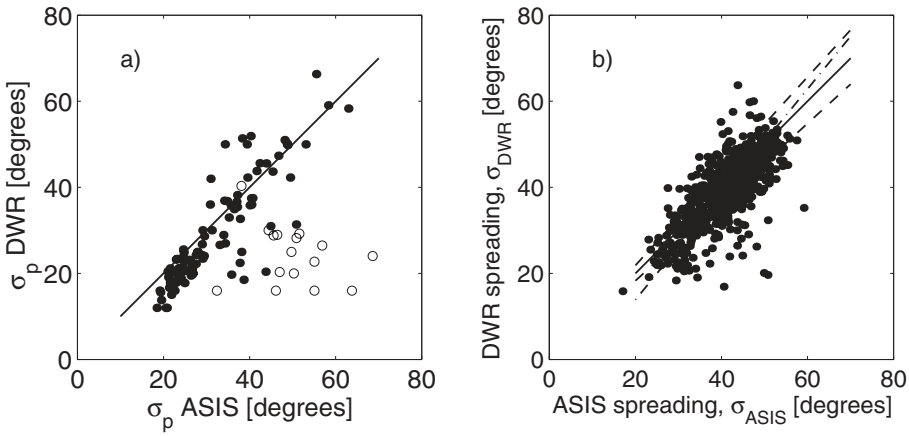

Figure 3.5: Comparison of angular spreading, σ_1, calculated following Longuet-Higgins *et al.* (1963), for ASIS and DWR. Panel a): angular spreading at the peak frequency, where ∘ denotes data collected between 22 March 1200 and 23 March 2400. Panel b): σ_1 at all frequencies above the peak, and with energy $E > 0.02E_{max}$. The dashed lines indicate the 90% confidence bands, assuming equal variability for the two sensors. The dashed-dotted line is a fit to the data and the solid line the 1:1 line. (after Pettersson *et al.*, 2003)

($\gamma^2 = 0.74$). The most systematic differences are associated with the peak of the spectrum, with the largest disagreements again occurring during the swell-dominated, light wind period of 22-23 March (Fig. 3.2). Note that some of the data in panel a) are not included in panel b): only those data where σ_1 is available as a function of frequency are used here.

In order to investigate the performance of the two buoys further, we focus on three events during the intercomparison period. For each event, identified by shading in Fig. 3.2, data from three or four consecutive half hour runs have been averaged together in order to reduce variability. The first event shows a comparison that is typical of most of the data set. The other two events are selected to investigate the disagreement during 23 March. During all three events, meteorological conditions are slightly unstable, with sea-air temperature differences under 1.5°C.

The first event, during the Mistral of 20 March (0000-0200), is marked by strong winds (14 ms^{-1}) and a wind sea with $H_s = 1.9\,\mathrm{m}$. The two buoys show good agreement in both the energy spectra (Fig. 3.6a), and the angular spreading (Fig. 3.6b) at all energetic frequencies. This good agreement is typical of most of the intercomparison period.

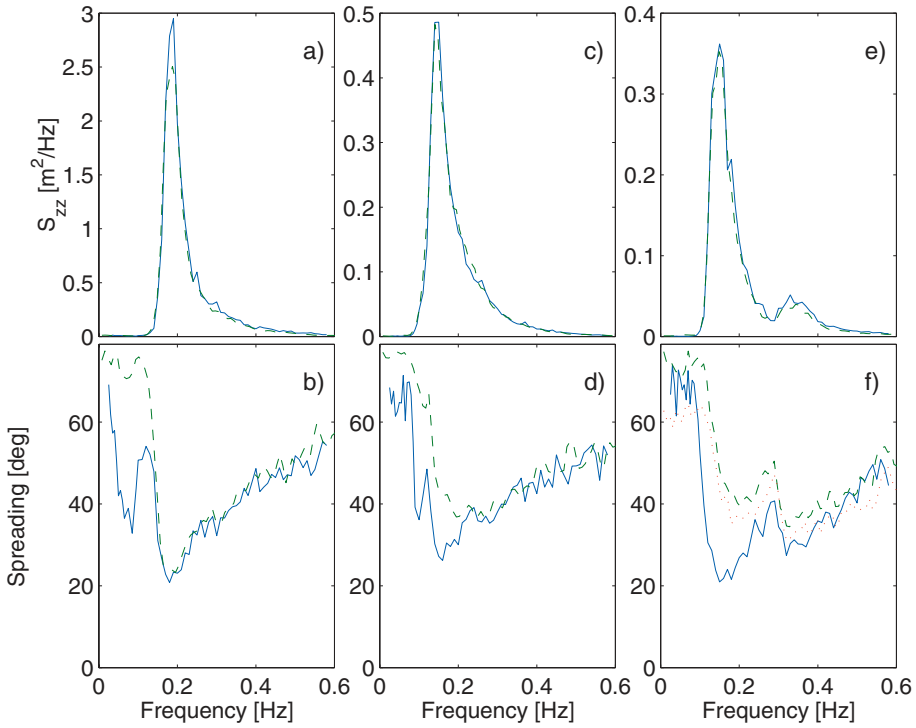

Figure 3.6: Surface elevation spectra (upper plots), and angular spreading (lower plots) for ASIS (dashed line) and DWR (solid line) at selected 2 hour periods starting at 20 March 0000 (a, b), 23 March 0200 (c, d) and 23 March 2100 (e, f). The dotted line in f) shows spreading with the ASIS data analysed in 2-min blocks.

The next two cases are chosen to study the period when the two sensors did not display such agreement. During the interval from 22 March 1200 through 23 March 2400, peak spreading angles from ASIS were considerably larger than those reported by DWR. During these two days, full DWR spectra are only available for two short intervals. These are the two cases discussed below.

On 23 March (0200-0400), the wind speed was low (2 ms^{-1}) and from the east. During the previous 6 hours (Fig. 3.2), the wind was light and variable, shifting from S to E. The wave field was dominated by a swell from the SE, with $H_s \approx 0.8$ m. Energy spectra from the two buoys at this time show excellent agreement at all frequencies (Fig. 3.6c). While the angular spreading of the two buoys compare well at high frequencies (Fig. 3.6d), there are

disagreements around the peak, where ASIS reports higher spreading.

The third event, later on 23 March (2100-2230), occurred during an interval in which the winds turned from S to NE and increased from 2 to 5.5 m/s. The significant waveheight was 0.7 m. The energy spectra (Fig. 3.6e), which in this case are bimodal, compare well. A maximum likelihood method (ML) analysis (Capon, 1969) of the data confirms the presence of a wind sea from the NE, along with a swell from SE. In this case, the comparison of angular spreading (Fig. 3.6f) is poor, with ASIS reporting a much broader distribution at most frequencies. In this case, much of this discrepancy between the platforms can be linked to an assumption made in the ASIS analysis: that of stationarity. During FETCH, ASIS was moored in a tethered configuration, with the buoy heading determined by the wind forcing. When the wind direction changes considerably during the course of a run, ASIS rotates, which results in an apparent broadening of the directional spreading. During this third event, the ASIS heading changed by 80° during a single run. In contrast, for the first and second events the maximum heading changes over 28 min were 3° and 10°, respectively.

In order to quantify this effect, the ASIS data were reprocessed in 2-min blocks, during each of which the mean rotation was small. The results appear as a dotted line in Fig. 3.6f. The agreement between the DWR and reprocessed ASIS spreading angles is now good for the wind sea component of the spectrum, but disagreements remain for the swell component. A comparison of MLM spectra for the original and reprocessed ASIS data also show a significant reduction in spreading (not shown).

During the first event, the DWR spectra show a decrease in spreading at $f \approx 0.08$ Hz (Fig. 3.6b). Such behaviour could be interpreted as an indication of a very low energy swell at this frequency, but we believe that this is not the case. Such low frequency behaviour is not seen in the ASIS data. However, similar narrowing at the same 0.08 Hz frequency has been observed in DWR wave measurements in the Baltic Sea - see, e.g., Fig. 3.7. In this case the wind speed was less than 13 m/s over the whole Baltic Sea during the preceding six days. From the point of view of wind generated waves the Baltic Sea is an inland sea. As the peak frequency of fully developed waves is higher than about 0.1 Hz when the wind speed is below 13 m/s, waves of frequencies around 0.08 Hz could not have been directly generated by such low winds. These facts lead us to suspect that these low frequency narrow spreading angles are spurious and are related to the mooring of DWR. The decrease in spreading at low frequencies occurs where the one dimensional spectrum remains in the background noise level while the spectra of the hor-

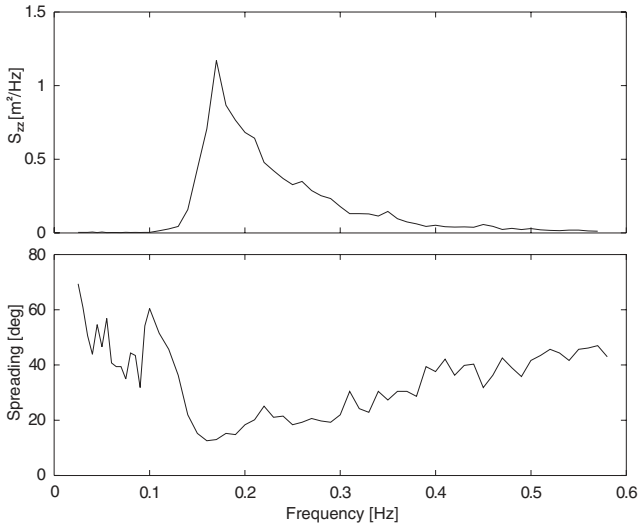

Figure 3.7: Baltic Sea DWR spectrum

izontal displacements (north and west) rise above it. Horizontal movements which are not related to vertical movements are not surface waves.

According to the Datawell manuals, the DWR directional response is sensitive to the asymmetry caused by the mooring forces at and below the natural frequency of the mooring line. For the standard double rubber cord mooring we have used, this frequency is 0.05 Hz. The directional errors caused by the mooring should decrease rapidly towards higher frequencies. For a moored DWR the frequency 0.05 Hz is defined as the lowest limit for directional measurements. Our analysis suggests that an additional requirement for reliable directional measurements with a moored Directional Waverider is that the heave spectrum rises above the noise level at the given frequency.

Finally, we compare the mean wave propagation direction as determined by the buoys. As the DWR calculations are done following Longuet-Higgins *et al.* (1963), we use the same algorithm for the ASIS data. The mean direction, θ_1 is taken to be $\theta_1 = \arctan(Q_{13}/Q_{12})$, where Q_{12} and Q_{13} are defined above. As in the case of the spreading, the mean direction at the peak frequency is defined as the mean of the mean directions at the three frequencies that form the peak of the spectrum. In Fig. 3.2b, the mean direction at the peak frequency, θ_p is plotted for each buoy as a function of time. In general the two are seen to follow each other quite well, with a mean

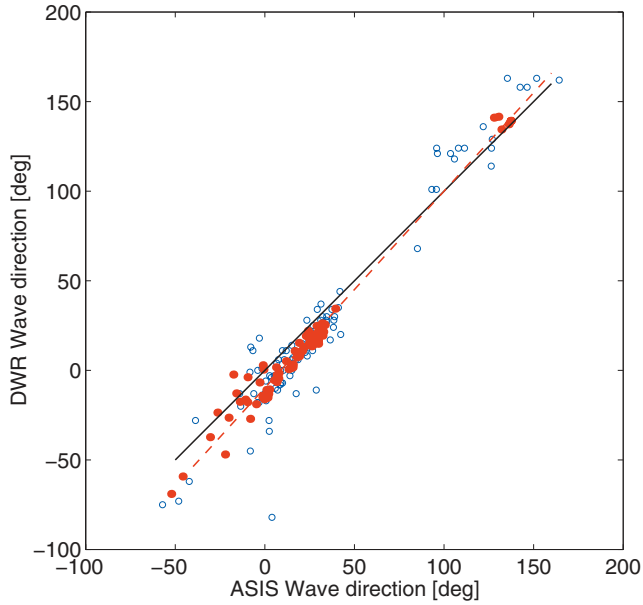

Figure 3.8: Comparison of wave directions for ASIS and DWR. ○ and ● indicate peak and mean (spectrally weighted) directions, respectively. The solid line indicates a 1:1 relationship and the dashed line is a fit to the spectrally weighted data.

difference of 6.7° (Fig. 3.8). As some of the scatter in the figure derives also from differences in f_p, the mean (spectrally-weighted) wave directions, θ_0, are also shown. As DWR spectra are necessary for this calculation, the plot of θ_0 includes only half the data of θ_p. Although the scatter is reduced using θ_0, the conclusions are similar. For the most part the data are well related using $\theta_{0DWR} = 1.1\ \theta_{0ASIS} - 9.8°$.

3.4 Conclusions

In general most wave sensors agree well on the one dimensional spectrum and the basic parameters derived from it, the significant waveheight and the peak period. This was also the case in this study where two wave buoys with different measuring principles were compared. Differences arose when the higher order properties, such as the skewness of the waves, were studied. The wave skewness calculated from the wave array measurements of the Air-Sea Interaction Spar buoy ASIS was correlated with both the wind speed

and the significant slope. The wave skewness measured by the Directional Waverider (DWR), a surface following buoy, showed no correlation with either.

The directional properties of the wave field are more problematic to measure. As the comparisons in this book show, the mean direction and especially the directional spreading from different wave sensors often show considerable scatter and inconsistencies. Also in this study the biggest scatter was with the directional spreading. The mean propagation direction was reported consistently by the two buoys and for the most part, also the spreading values agreed quite well, with DWR yielding slightly lower (3°) spreading angles at the peak. The most pronounced differences were found during the swell-dominated conditions of 22-23 March when ASIS reported higher spreading values around the peak frequency than DWR.

The sensitivity of the spreading parameter to the mooring design manifested itself in certain situations. In the case of DWR, the spurious narrow spreadings at lower frequencies in cases where the one dimensional spectrum was in the background level was suspected to be caused by the mooring line forces. This means that the lowest reliable frequency of directional measurements by a moored DWR is limited to frequencies where there actually are waves. This is obviously no serious limitation, but complicates the use of spreading information. The ASIS buoy was tethered to a secondary buoy to isolate additional downward forces and ASIS did not show the peculiar low frequency behaviour of DWR. However, during turning wind situations, this mooring configuration led to a broadening of the ASIS spectra due to the yawing of ASIS during the course of a run. The disagreement on 22-23 March could be partly explained by the yaw changes, but we are not able to identify the mooring designs or any other characteristics of the instruments (see Part 1) as being clearly associated with the remaining disagreement.

The present study shows the importance of intercomparison measurements when the directional width of the spectrum is studied using different sensors. The performance of the sensors with respect to each other has to be known before comparison of results obtained from different wave sensors can be done reliably.

3.5 References

Allender, J., T. Audunson, S.F. Barstow, S. Bjerken, H.E. Krogstad, P. Steinbakke, L. Vardel, L.E. Borgman and C.Graham, The WADIC project:

a comprehensive field evaluation of directional wave instrumentation, *Ocean Engng.* 16, 505-536, 1989.

Capon, J., High-resolution frequency-wavenumber spectrum analysis, *Proc. IEEE*, 57(8), 1408-1418, 1969.

Graber, H.C., E.A. Terray, M.A. Donelan, W.M. Drennan, J. van Leer and D.B. Peters, ASIS – A new air-sea interaction spar buoy: design and performance at sea, *J. Atmos. Oceanic Tech.*, 17(5), 708-720, 2000.

Hauser D., H. Branger, S. Bouffies-Cloché, S. Despiau, W. Drennan, H. Dupuis, P. Durand, X. Durrieu de Madron, C. Estournel, L. Eymard, C. Flamant, H. Graber, C. Guérin, K. Kahma, G. Lachaud, J.-M. Lefèvre, J. Pelon, H. Pettersson, B. Piguet, P. Queffeulou, D. Tailliez, J. Tournadre, and A. Weill, The FETCH experiment: an overview, *J. Geophys. Res.* 108 (C3), doi:10.1029/2001J001202, 2003.

Huang, N.E. and S.R. Long, An experimental study of the surface elevation probability distribution and statistics of wind-generated waves, *J.Fluid Mech.*, 101, 179-200, 1980.

Krogstad, H.E., J. Wolf, S.P. Thompson, L.R. Wyatt, Methods for intercomparison of wave measurements, *Coastal Eng.*, 37, 235-257, 1999.

Kuik, A.J., G.Ph. van Vledder and L.H. Holthuijsen, A method for the routine analysis of pitch-and-roll buoy wave data, *J. Phys. Oceanogr.*, 18, 1020-1034, 1988.

Longuet-Higgins, M.S., D.E. Cartwright and N.D. Smith, Observations of the directional spectrum of sea waves using the motion of a floating buoy, in *Ocean Wave Spectra*, Nat. Acad. of Science, Prentice-Hall, 111-132, 1963.

Magnusson, A.K., M.A. Donelan and W.M. Drennan, On estimating extremes in an evolving wave field, *Coastal Eng.*, 36, 147-163, 1999.

Orear, J., Least squares when both variables have uncertainties, *Am. J. Phys.*, 50, 912-916, 1982.

Pettersson H., H. C. Graber, D. Hauser, C. Quentin, K. K. Kahma, W. M. Drennan, and M. A. Donelan, Directional wave measurements from three wave sensors during the FETCH experiment, *J. Geophys. Res.*, 108 (C3), 8061, doi:10.1029/2001JC001164, 2003.

Srokosz, M.A., and M.S. Longuet-Higgins, On the skewness of sea surface elevation, *J. Fluid Mech.*, 164, 487-498, 1986.

Chapter 4

Intercomparison of S4DW and DWR

Judith Wolf

Proudman Oceanographic Laboratory, Birkenhead, United Kingdom

4.1 Introduction

Wave data are important in the study of coastal oceanography, being required for studies of coastal erosion, pollutant and sediment transport and surge-tide-wave modelling. The most commonly deployed instrument is probably the surface-following Datawell Waverider buoy. This has mooring limitations in very shallow water and there are several advantages to a bottom-mounted system which is less subject to interference and less exposed to extreme weather. However, due to the attenuation of waves with depth, (the high frequency waves are more severely attenuated than low frequency) the depth in which wave data can be collected by a bottom-mounted system is restricted to less than about 20 m. This makes it complementary to the Waverider in the near-shore zone, since the Waverider cannot be deployed satisfactorily in less than about 10 m depth. More information on subsurface instrumentation can be found in Part 1, section 4.2. Here we discuss the analysis method and results from the bottom deployed InterOcean S4DW (directional wave) instrument which measures the pressure and velocity vector (often called a *p-u-v* instrument).

4.2 The Wave Analysis Method

The linearised wave equations for an individual wave of angular frequency $\sigma = 2\pi f$ where f is the frequency in Hz), wave-number $\mathbf{k}$ and amplitude a, where h is the water depth, are given below.

$$\zeta(\mathbf{x}, z, t) = a\frac{\sinh(k(z+h))}{\sinh(kh)}\sin(\mathbf{k}\cdot\mathbf{x} - \sigma t - \phi) \tag{4.1}$$

where ζ is the vertical displacement of a particle from its rest position at depth z (positive upwards with origin in the undisturbed water surface), $\mathbf{x}$ is the horizontal spatial independent variable and t is time. The expression for the surface displacement is thus:

$$\zeta(\mathbf{x},t) = a\sin(\mathbf{k}\cdot\mathbf{x} - \sigma t - \phi) \tag{4.2}$$

The pressure at depth z is given by

$$p(\mathbf{x}, z, t) = \rho g a\frac{\cosh(k(z+h))}{\cosh(kh)}\sin(\mathbf{k}\cdot\mathbf{x} - \sigma t - \phi) \tag{4.3}$$

where ρ is the water density and g the gravitational acceleration. The pressure attenuation with depth is given by $\cosh(k(z+h)) / \cosh(kh)$.

Horizontal displacement χ is

$$\chi(\mathbf{x}, z, t) = a\frac{\cosh(k(z+h))}{\sinh(kh)}\cos(\mathbf{k}\cdot\mathbf{x} - \sigma t - \phi) \tag{4.4}$$

The wave intrinsic (angular) frequency,σ, is related to the wave number by the dispersion relation:

$$\sigma = \sqrt{gk\tanh(kh)} \tag{4.5}$$

However the observed or apparent frequency, ω, is Doppler-shifted:

$$\omega = \sigma + \mathbf{k}\cdot\mathbf{U} \tag{4.6}$$

where $\mathbf{k}$ is the wave-number vector and $\mathbf{U}$ the current vector, see e.g. Phillips (1977).

The S4DW analysis is based on Trageser and Elwany (1990) except that an additional step of fitting a high-frequency f^{-5} tail above the cut-off

frequency is included and the mean current is also included in the analysis. First the spectra $C_{11}(f)$, $C_{22}(f)$, $C_{33}(f)$ for the pressure and velocity components are computed by fast Fourier transform (FFT). Here subscript 1 denotes vertical displacement of the sea surface or heave, 2 denotes north current, 3 denotes east current, after correction for depth attenuation. The depth attenuation is corrected by applying the inverse relation $\cosh(k(z+h))/\cosh(kh)$, using the correct wavenumber derived from the Doppler-shifted dispersion relation as above. Cross-spectra $C_{12}(f)$ and $C_{13}(f)$ are defined, full definitions of which are given in Wolf (1996), which are used to obtain the angular harmonics, a_n, b_n, of the directional wave spectrum $F(f,\theta)$:

$$\begin{aligned} a_n &= \tfrac{1}{2\pi} \int_0^{2\pi} \cos(n\theta)\, F(f,\theta)\, d\theta \\ b_n &= \tfrac{1}{2\pi} \int_0^{2\pi} \sin(n\theta)\, F(f,\theta)\, d\theta \end{aligned} \tag{4.7}$$

and

$$a_1 = \frac{C_{12}}{\sqrt{C_{11}(C_{22}+C_{33})}},\ b_1 = \frac{C_{13}}{\sqrt{C_{11}(C_{22}+C_{33})}} \tag{4.8}$$

A pitch-roll buoy or *p-u-v* instrument can only resolve the first two angular harmonics of the full directional spectrum. Spectral forms of the standard wave parameters are defined with reference to the spectral moments

$$m_n = \int_0^\infty f^n S(f) df \tag{4.9}$$

Thus the significant waveheight, H_{m0} and wave period, T_{m02}, are:

$$H_{m0} = 4\sqrt{m_0} \quad ,\ T_{m02} = \sqrt{\frac{m_0}{m_2}} \tag{4.10}$$

The high frequency tail improves H_{m0} slightly and produces a dramatic improvement in T_{m02}.

From a_1, b_1 the standard parameters of mean wave direction and spread can be calculated:

$$\begin{aligned} D(f) &= \tan^{-1}(b_1/a_1) \\ s(f) &= \sqrt{(2-2r)}, \text{where } r = \sqrt{a_1^2+b_1^2} \end{aligned} \tag{4.11}$$

More sophisticated models of the wave directional spectra can be fitted e.g. Krogstad et al. (1999), but these are not discussed further here.

4.3 Data Collection

Here we discuss some results from S4DW data collected at Holderness (UK) (Wolf, 1996; 1998) and Petten (Netherlands) (Wolf, 1997) during the EU-SCAWVEX project. Wave data were collected near Holderness on the east coast of the UK for the winters of 1994/95 (Holderness 1) and 1995/96 (Holderness 2) at several stations (see Fig. 4.1). The instruments deployed included a non-directional and 2 directional Waverider buoys, 8 bottom pressure recorders and 2 S4DW (directional wave) current meters, at stations N1 and S1 during Holderness 1 and at N1 and N2 during Holderness 2. Other wave-measuring instruments deployed simultaneously included HF radar, X-band radar, satellite-borne SAR and altimeter and beach-mounted bottom pressure recorders. At Holderness we concentrate on results from station N1. The Petten data are from a location about 10 km off the Dutch coast at station MP_A, location 52°50'40"N 04°33'37"E, in about 20 m of water, at which a PMP (POL Measurement Package) and Directional Waverider (DWR) were deployed. A total of 35 days of good data were collected in November and December 1996 during which significant waveheights in excess of 4.5 m and currents up to 0.7 m/s were recorded. The data displayed some interesting wave-current interaction effects since the waves and currents were often collinear (Wolf and Prandle, 1999).

The S4DW data were analysed with and without a correction for the Doppler shift of apparent (observed) frequency. There is a noticeable tidal modulation of observed wave parameters. This affects both Waverider and bottom pressure recorders but the latter are also affected by an attenuation correction. Inclusion of currents allows more accurate calculation of wave-number and hence attenuation. Clayson and Ewing (1988) discuss the correction of Waveriders for Doppler shift effects including frequency-varying response functions. The correction of the Waverider data is not discussed further, but the shift in frequency from apparent to observed frequency is not very large. The change in attenuation can be more significant. For example, at 0.2 Hz, with a 0.5 m/s current, the error in frequency will be about 12% but the error in attenuation will be about 20%. Surface currents were estimated from the observed near-bed currents by applying a constant factor of 1.4, which was obtained by using Prandle (1982) and was found to give close to

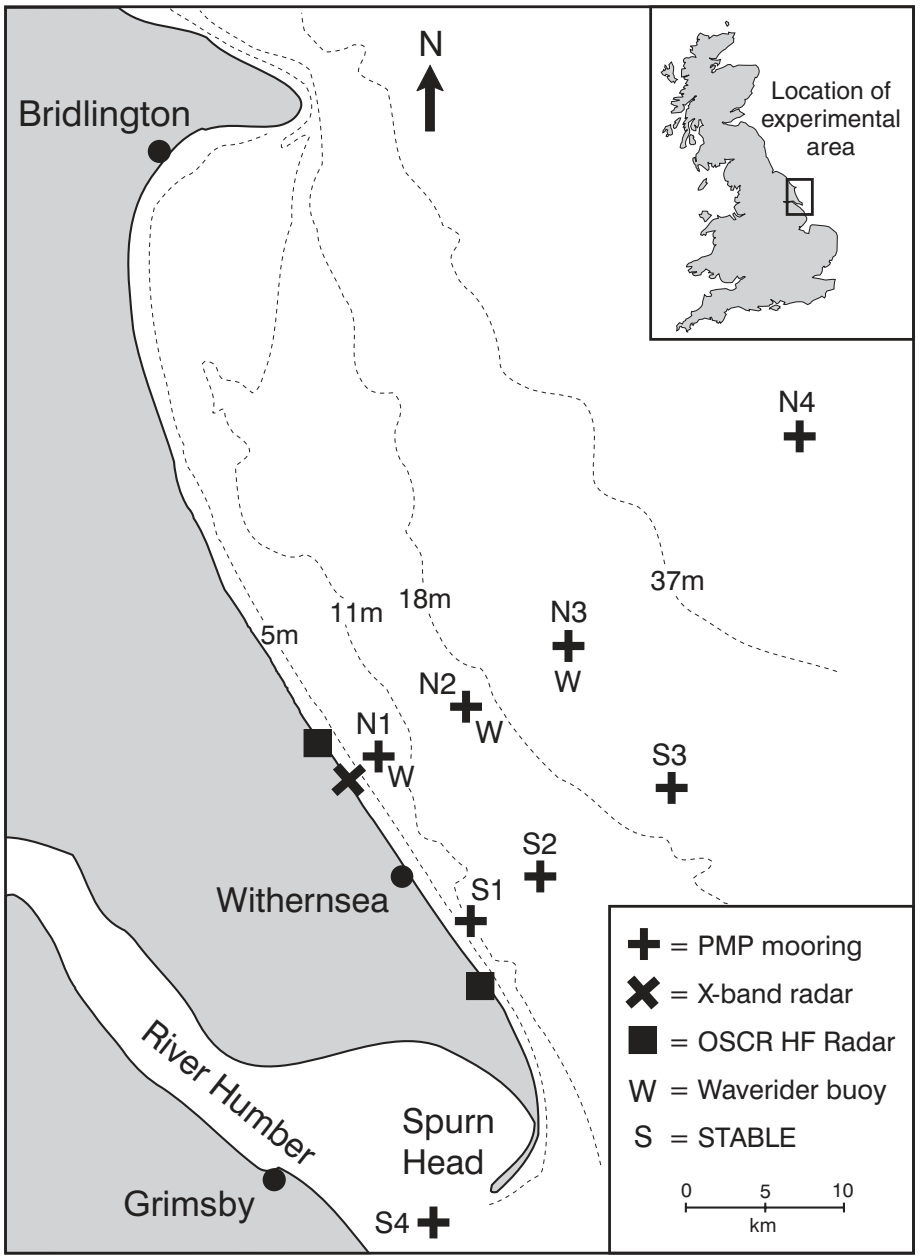

Figure 4.1: Holderness experimental layout.

the optimum correction for Holderness data. After examination of WERA (HF radar) surface currents the following relationship appears a better fit to currents at Petten:

(a) Surface current amplitude is approximately twice the bottom current amplitude

(b) Surface current lags bottom current by about 1 hour

(c) Surface current veers by about 10 degrees.

The inclusion of mean current data in the S4DW analysis was found to improve the Holderness results, which were compared with directional and non-directional Waverider buoy data at stations N1 for Holderness 1 and N1 and N2 for Holderness 2.

One test of the effectiveness of the current correction was the amount of variance at tidal periods which was removed from the T_{m02} time series and also the reduction in the correlation between T_{m02} and the tidal current component in the direction of the high frequency (0.25 Hz) waves. For the 2nd deployment at N1, for example, the correlation reduced from 0.275 to 0.083 after applying the Doppler shift correction. The effect on H_s is quite small, but for T_{m02} the current correction removes about 44% of the variance between 11.9 and 13 hours period (corresponding to the main semi-diurnal tide, centred on 0.08 cycles/hour).

4.4 Intercomparison of S4DW and DWR

The result of the S4DW analysis were compared with directional and non-directional Waverider buoy data at stations N1 for Holderness 1 and N1 and N2 for Holderness 2. The results with and without current correction are referred to as S4DWC and S4DW respectively. Figure 4.2 shows an intercomparison of the S4DWC and DWR data at N1 for Holderness 2, which gives the best results since this is the shallowest station at which directional data can be compared.

Examples of frequency spectra measured at Petten, with and without current correction, are given in Fig. 4.3 for times of maximum current during 12-14 November. During this time the peak wave energy is from the north, thus a north-going (ebb-tide) current is opposing the wave direction. The spectra and H_s are seen to improve for both following and opposing current.

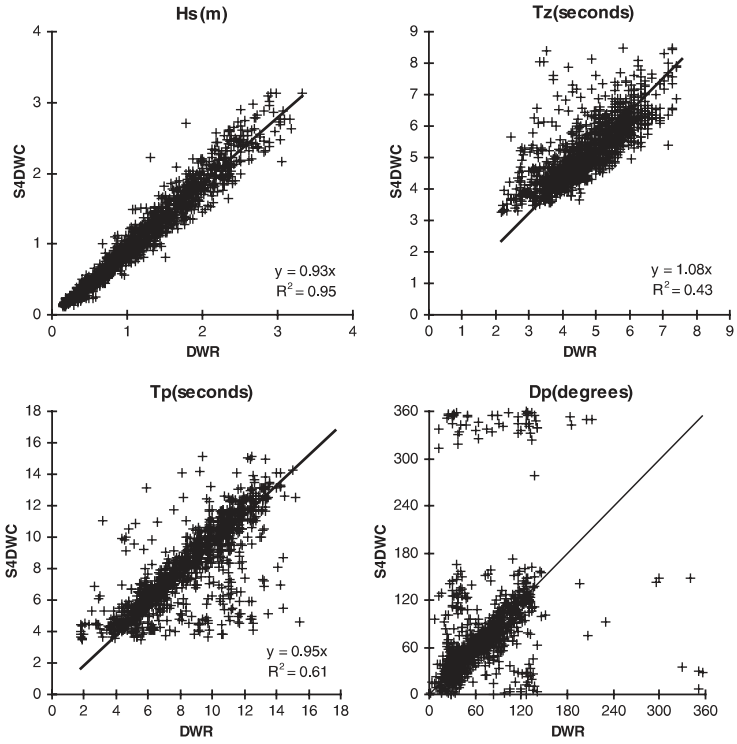

Figure 4.2: Scatter diagrams and correlation coefficients for wave integrated parameters at N1, Holderness 2. $Hs = H_{m0}$ = significant waveheight, $Tz = T_{m02}$ = mean wave period, Tp = peak wave period, Dp = peak wave direction

Although the water depth is rather deep to make bottom-mounted wave measurements the data are in good agreement with the Waverider buoy.

Figure 4.4 shows the spectral ratio for all the Petten spectra, compared with the Waverider. The S4DW spectra often show a low frequency peak coming from the south or south-west, which is sometimes not detected by the DWR. Spread is equivalent for both instruments up to about 0.15 Hz i.e. just above main peak, then the S4DW has much larger spread at higher frequencies.

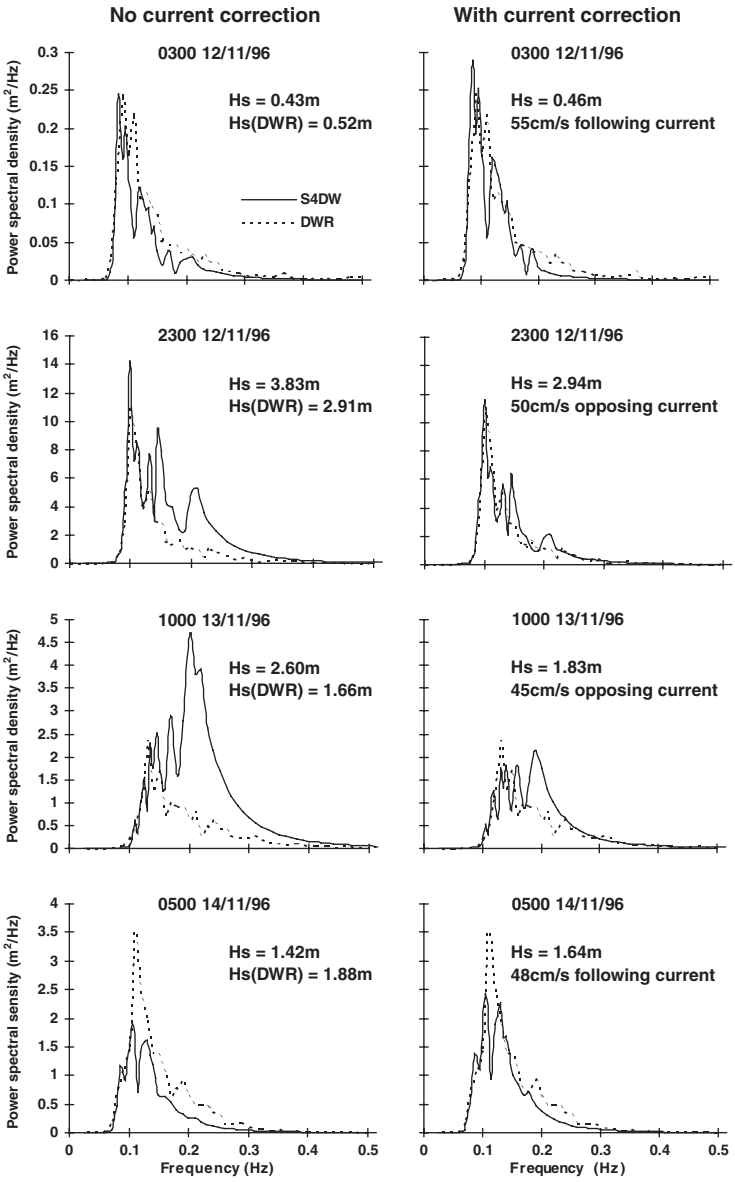

Figure 4.3: Petten spectra. Left-hand column shows spectra with no correction for current, right-hand column includes current correction. Solid line is S4DW, dotted line is DWR. $Hs = H_{m0}$ = significant waveheight.

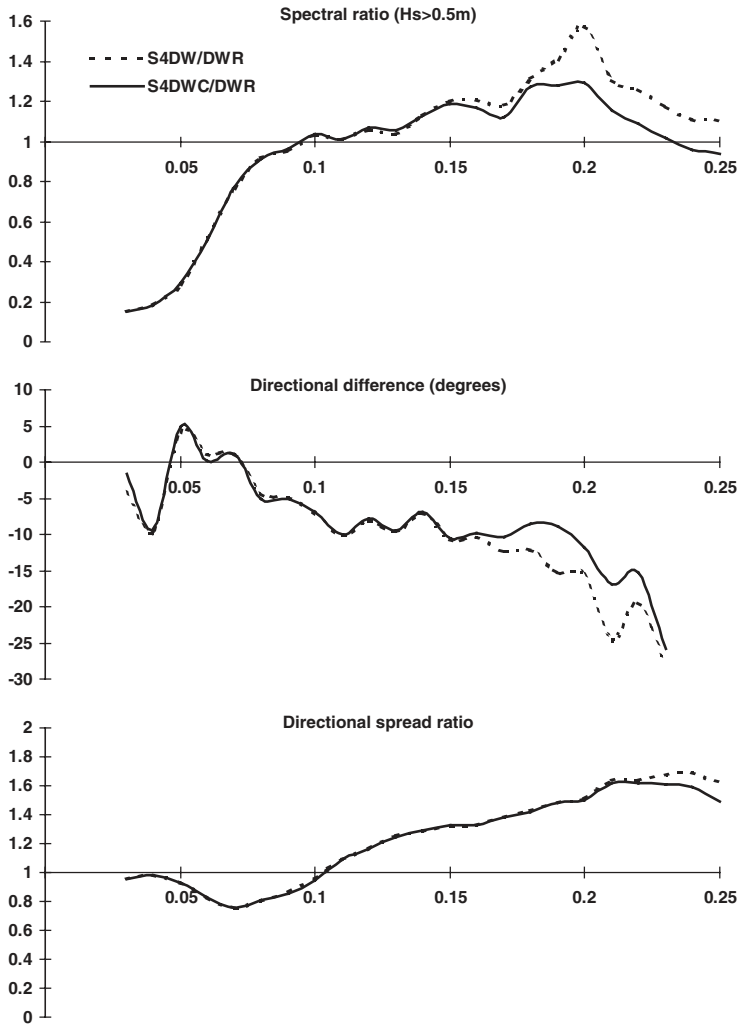

Figure 4.4: Petten spectral ratios. In each case the solid line is for analysis with currents and dotted line is without. $Hs = H_{m0}$ = significant waveheight. Horizontal axis gives frequency in Hz. Vertical axis; top: ratio of energy spectra, middle: directional difference in degrees, bottom: ratio of directional spread.

Acknowledgements

The data were collected for the Ministry of Agriculture, Fisheries and Food under its Flood Protection Commission. Data analysis was carried out under the EU SCAWVEX Project. The following POL staff assisted in various ways: Andy Lane assisted with data analysis, Dave Flatt supplied the S4DW data, Peter Hardcastle supplied the Waverider data and Robert Smith prepared Fig. 4.1.

4.5 References

Clayson, C.H. and Ewing, J.A., Directional wave data recorded in the southern North Sea, Inst. Ocean. Sci., *Deacon Lab. Rep.*, No. 258, 70pp, 1988.

Krogstad, H. E., J. Wolf, S. P. Thompson and L. R. Wyatt, Methods for the Intercomparison of Wave Measurements, *Coastal Engineering, 37*, 3-4, 235-257, 1999.

Phillips, O.M., *The dynamics of the upper ocean*, Cambridge University Press, 336pp., 1977.

Prandle, D., The vertical structure of tidal currents, *Geophysical and Astrophysical Fluid Dynamics, 22*, 29-49, 1982.

Trageser, J.H., and H. Elwany, An integrated solution to directional wave measurements, *IEEE Proceedings*, 154-168, 1990.

Wolf, J., The Holderness Project wave data, *Proudman Oceanographic Laboratory Internal Document no. 89*, 61pp., 1996.

Wolf, J., Waves at Petten, Netherlands, November-December 1996, *Proudman Oceanographic Laboratory Internal Document no. 114*, 1997.

Wolf, J., Waves at Holderness: results from in-situ measurements, pp. 387-398 in *Proceedings of Oceanology'98*, Brighton, UK, March 1998, 1998.

Wolf, J. and D. Prandle, Some observations of wave-current interaction, *Coastal Engineering, 37*, 3-4, 471-485, 1999.

Chapter 5

HF Radar

5.1 Introduction

Lucy R. Wyatt

University of Sheffield, Sheffield, United Kingdom

In this chapter a number of different studies investigating the accuracy of HF radar wave measurement are presented. The first, section 5.2, presents comparisons between HF radar and directional waveriders focussing on two experiments one at Petten in the Netherlands and the other at Fedje in Norway. The first was in the relatively shallow waters of the southern North Sea and the second one the exposed west coast of Norway during a period with a number of storm events. Qualitative and quantitative comparisons are presented. It is still very difficult to make quantitative comparisons of the full directional spectrum and of course directional waveriders do not measure the full spectrum, just a limited number of Fourier coefficients. Section 5.3 provides some qualitative comparisons of individual spectra using the maximum entropy method to provide buoy spectra and thus explores the validity of that method. Some interesting examples of bimodality are presented which raise questions about the maximum entropy method and/or the directional resolution of the radar data. The experiment at Fedje also provided an opportunity for comparisons with the WaMoS X-band radar and the WAM wave model and these are discussed in section 5.4. Finally a detailed comparison between measurements obtained using the OSCR HF radar and the SWAN wave model are presented in section 5.5. This shows that the errors in the HF radar measurements increase away from the centre of the measurement region probably due to antenna sidelobes.

5.2 Comparisons of HF Radar and Directional Waverider

Lucy R. Wyatt

University of Sheffield, Sheffield, United Kingdom

The inversion produces directional wave spectra on a non-uniform grid of wavenumbers (Wyatt, 2000). These are averaged into wavenumber-direction bins, converted to directional frequency spectra using the shallow-water dispersion relationship and then integrated to provide the frequency spectrum, parameters of the directional distribution e.g mean direction as a function of frequency and various frequency integrated parameters such as significant waveheight.

The accuracy and limitations of HF radar wave measurement are discussed here. More details can be found in Wyatt *et al.* (1999). The data were obtained using the WERA radar (Wellen Radar) developed by the University of Hamburg (Gurgel *et al.*, 1999) as part of the SCAWVEX project (Wyatt *et al.*, 1998). Wyatt *et al.* (1999) also discuss results using the OSCR (Ocean Surface Current Radar) developed in the UK. The data that are discussed here were collected during the SCAWVEX experiment at Petten in the Netherlands and during the EuroROSE (Günther *et al.*, 2000) experiment at Fedje on the Norwegian coast. In the latter experiment comparisons have been made with the WaMoS X-band radar and with the WAM wave model. These intercomparisons are discussed in detail in Wyatt *et al.* (2003) and summarised in section 5.4 below.

Figure 5.1 shows time series of wind speeds and directions during both experiments. Wind directions estimated from the radar data (Wyatt *et al.*, 1997) are shown demonstrating good agreement. The wind measurements were made at sites on the coast some 10 km from the radar measurement and therefore some differences could be expected. At the present time there is no acceptable HF radar wind speed algorithm. Petten is on the west coast of the Netherlands and measurements are therefore of southern North Sea waves with fetch limitations in many directions. Fedje is on the west coast of Norway and exposed to Atlantic storms. Similar wind speeds result in very different local wave conditions at these two sites.

Before presenting the detailed intercomparisons it is worth emphasising the ability of HF radar to measure wave variability in time and frequency and

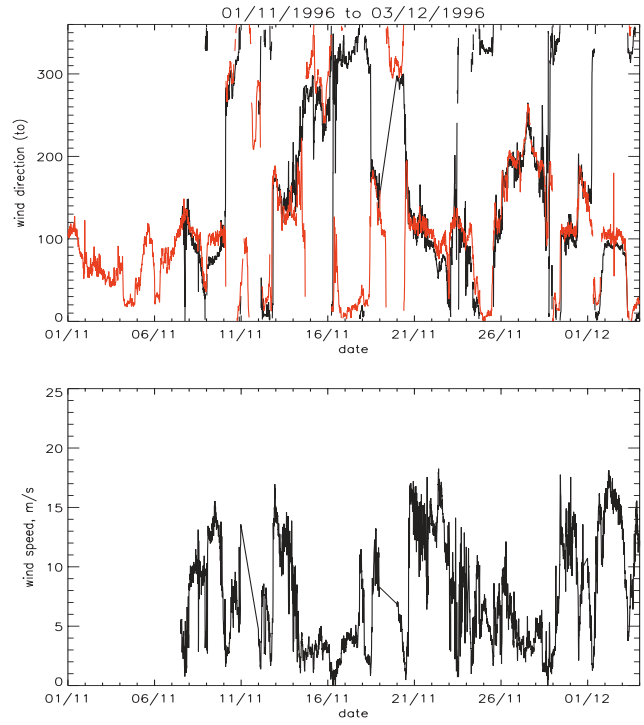

Figure 5.1: Wind direction (above) and speed (below) at Petten (top panel) and Fedje (next page). Red lines are HF radar estimates, black lines are coastal measurements and green lines in the Fedje direction plot are the local wind directions used in the WAM wave model.

in space. Figure 5.2 shows examples from the Fedje experiment with large wind direction (and hence high frequency wave direction) changes during the day of 15/3/2000 although the spectral peak is propagating towards the south–east throughout. These measurements were taken during the decay phase of a storm and waveheights can be seen to decrease from $4-5$ m at 0455GMT through the day.

Wyatt *et al.* (1999) presented comparisons of the radar and wavebuoy data integrated over six fixed frequency bands. In addition, the maximum amplitude value in each individual spectrum was identified and a 10 mHz frequency range either side of this was integrated to provide peak parameters. In this report statistics will be presented for three frequency bands. These are sufficient to highlight the most important features of the comparisons.

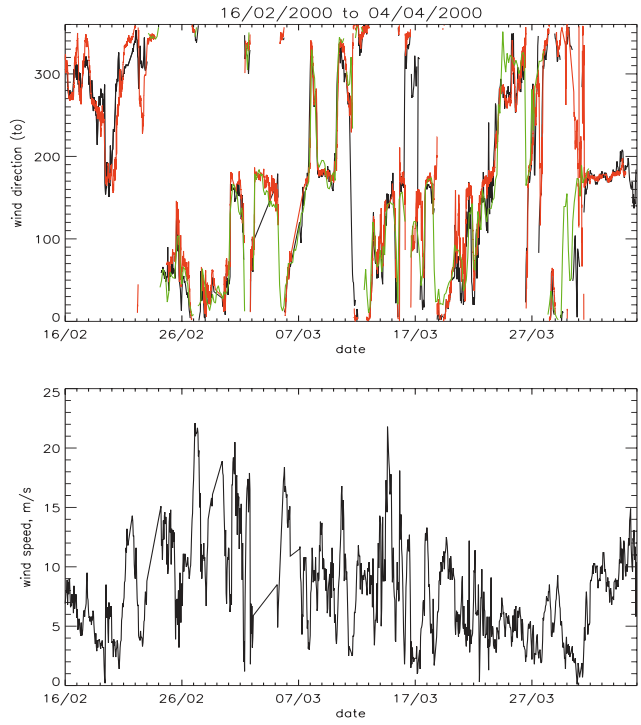

Figure 5.1: Continued.

They are firstly the full frequency range of each intrument/model rather then the fixed range, 0.05 - 0.4 Hz, used in the earlier work. This will therefore be a comparison of reported significant waveheight (for example) for which differences in measured frequency ranges will be one source of differences in parameter estimation. The peak parameters are determined using a frequency range lying between frequencies above and below the peak where the amplitude drops to 80% of peak amplitude. The peak frequency for this definition is at the centroid of this frequency range and is referred to as the 80% centroid below. Finally comparisons in the frequency range 0.2 - 0.3 Hz will demonstrate features of the higher frequency measurements.

The comparisons make use of: some standard statistics; a maximum likelihood analysis using radar variances determined using spectral variance estimates obtained with Monte Carlo simulations (Sova, 1995) and buoy variances obtained using Taylor expansions (see Part 1, Chapter 7); and

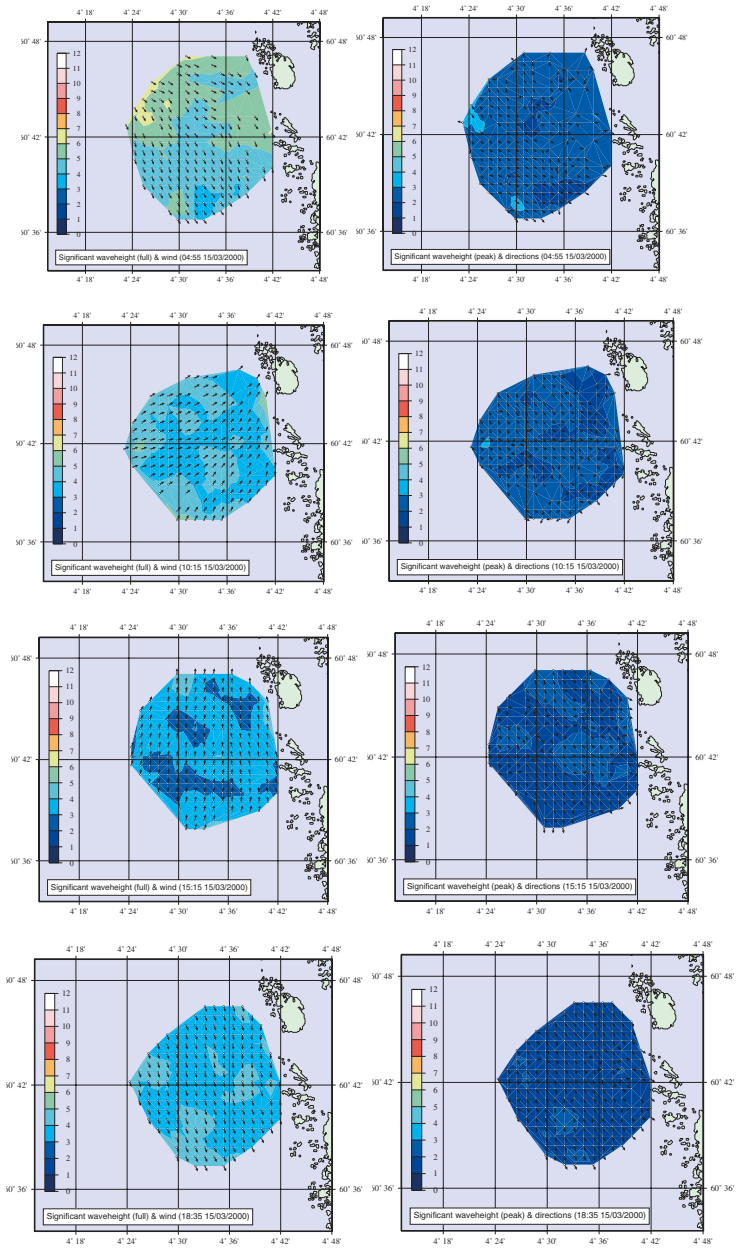

Figure 5.2: Fedje wind direction change on 15/3/2000. Left hand panel shows colour-coded significant waveheight and wind direction towards which the wind is blowing, right hand panel shows contribution to significant waveheight from the spectral peak with direction of propagation of the peak.

a maximum likelihood analysis using radar and buoy variances estimated using the techniques developed by Caires (2000). The analysis is used both to provide information about the accuracy of HF radar measurements and to compare the different methodologies.

5.2.1 The Petten Experiment

The Petten experiment demonstrated that HF radar is capable of measuring wave parameters on a regular basis. WERA backscatter measurements were made every twenty minutes with occasional gaps in wave measurement at particular locations when the quality of the radar measurements was not sufficient. Quality is judged by measuring the signal to noise of key features in the backscatter signal. Often wave measurement is limited by current variability and/or high antenna sidelobe levels both of which distort the first order part of the signal. If the distortion is particularly bad, this is detected by the signal to noise analysis and no inversion is carried out. Figure 5.3 shows time series of radar and wavebuoy significant waveheight for the Petten experiment. Mean direction, period and spread are shown in figures 5.4, 5.5 and 5.6 respectively. The amplitude, direction, period and spread estimates at high frequencies and at the peak of the spectrum are also shown.

While there is qualitative agreement there is an overestimation in significant waveheight when it is high and this is particularly noticeable in the high frequency amplitude contributions. The peak comparison presented here also suggests an overestimation between the radar and wavebuoy compared to an underestimation in the corresponding figure in Wyatt *et al.* (1999). The difference is due to the change in definition of 'peak' here. The comparison now takes in a wider range of frequencies and this obviously masks the underestimation in actual peak amplitude that was reported in Wyatt *et al.* (1999) and is also found at Fedje. The overestimation of high frequency amplitude is directly related to the underestimation in mean period at these times.

Variability in the peak direction could be associated with bimodality in the spectrum with similar amplitude contributions in rather different directions and at different frequencies thus also explaining some of the peak period variability. Some of this bimodality could be artificially introduced through antenna sidelobe contamination of the radar signal. Note also that some of the variability is at times of low amplitude (also contributing to mean period variability).

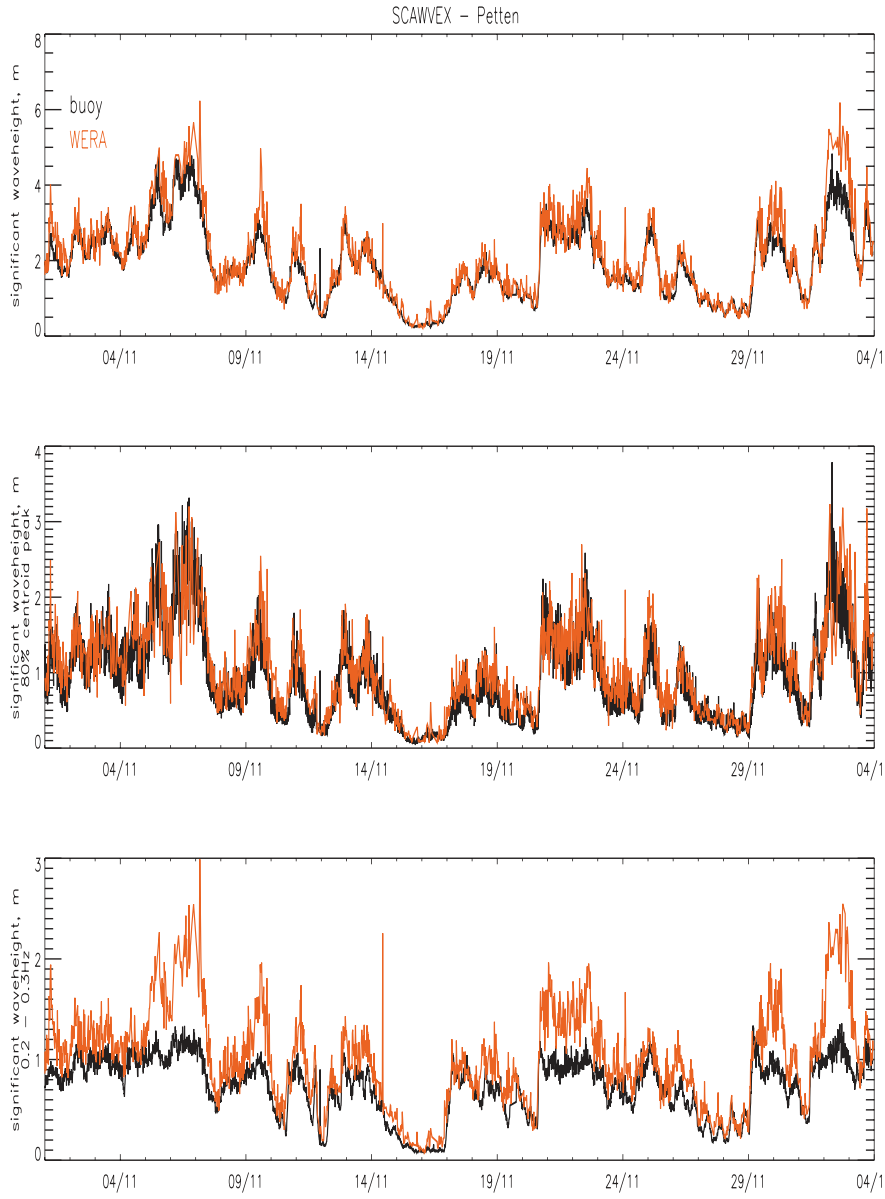

Figure 5.3: Petten significant waveheight (top panel), peak (middle) and high frequency (lower panel) waveheight comparisons between a directional waverider (black) and HF radar (red).

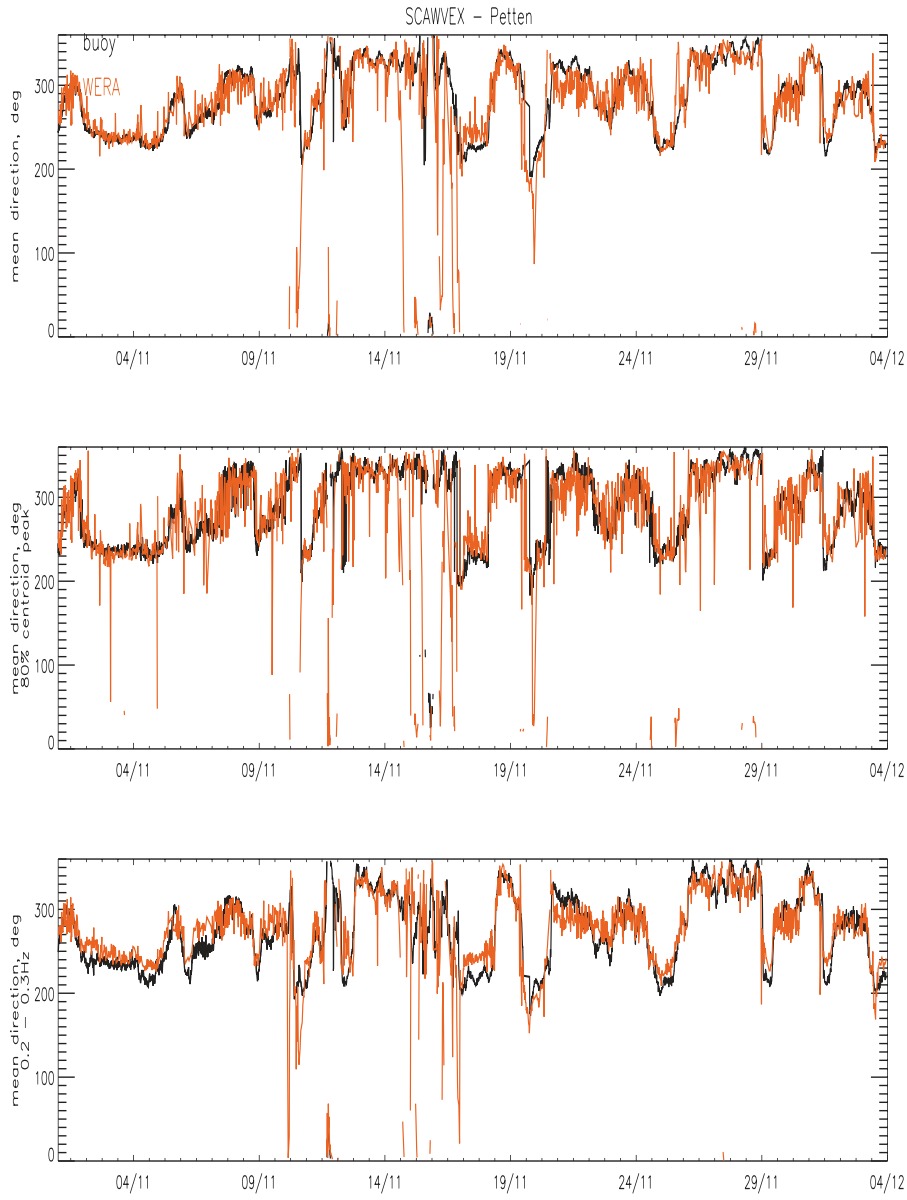

Figure 5.4: Petten mean, peak and high frequency direction comparisons. As Fig. 5.3.

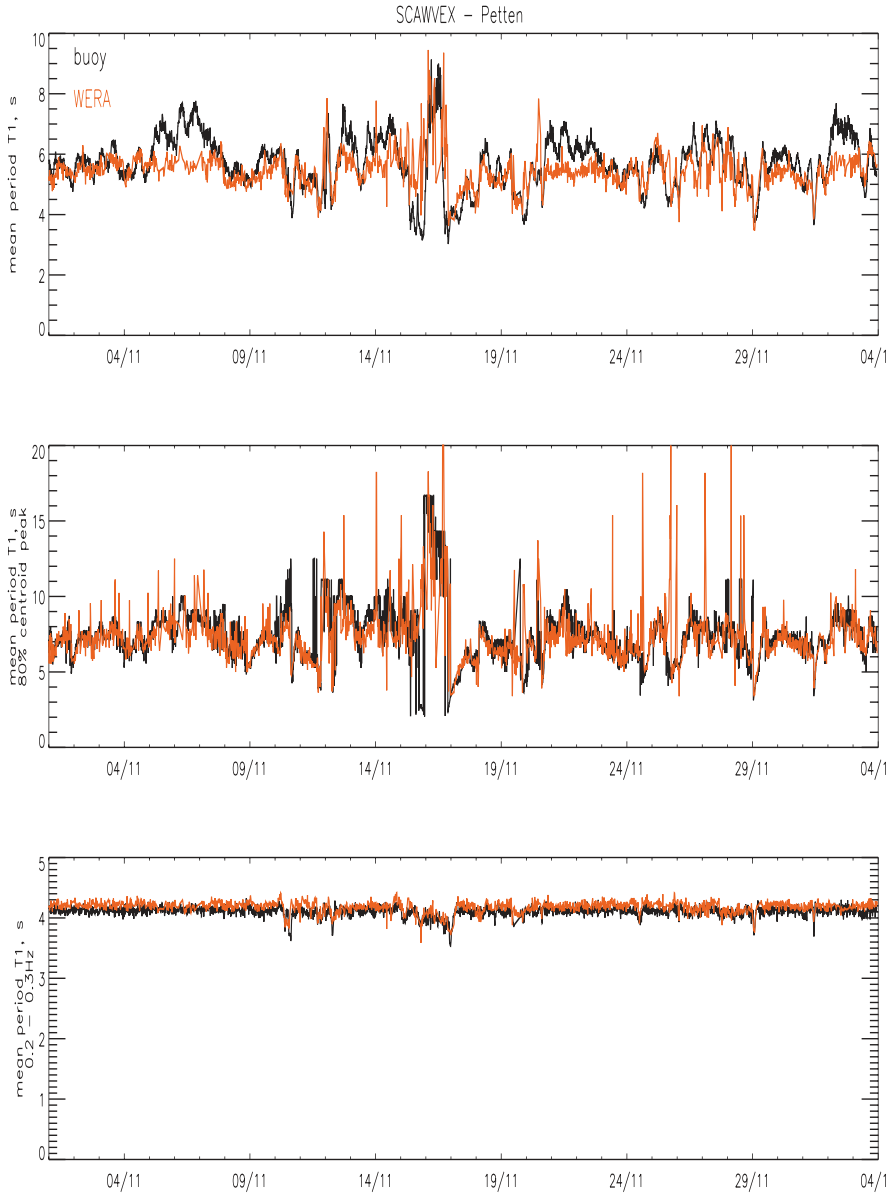

Figure 5.5: Petten mean, peak and high frequency period comparisons. As Fig. 5.3.

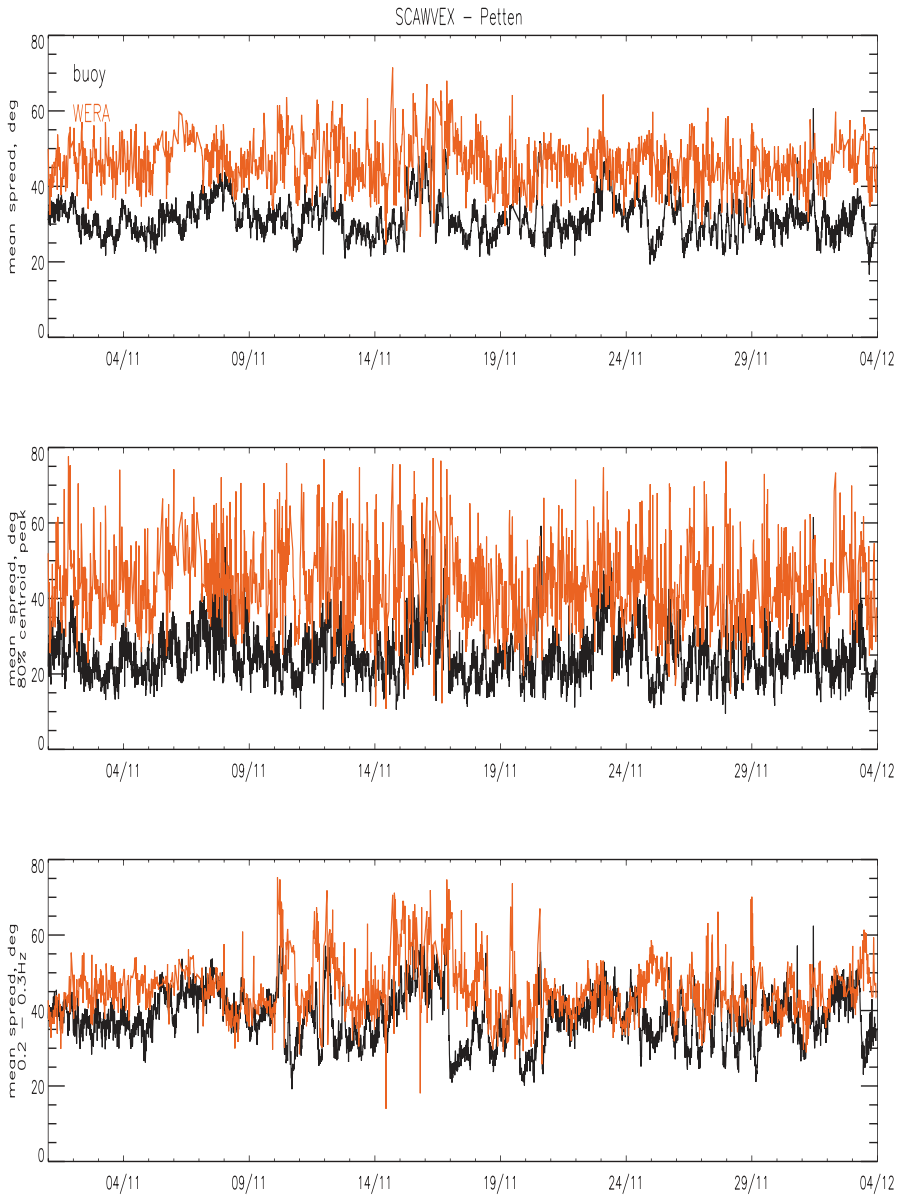

Figure 5.6: Petten mean, peak and high frequency spread comparisons. As Fig. 5.3.

5.2.2 The Fedje Experiment

The Petten experiment demonstrated that HF radar wave measurements become increasingly inaccurate as waveheight increases. This was not an unexpected result. Barrick's formulation for the backscatter spectrum in terms of the ocean wave directional spectrum (part 1, section 5.3) arise from a second order perturbation expansion of the ocean surface. Wyatt (1995) indicated that the theory becomes increasingly inaccurate at waveheights above about 2 m at the operating frequencies used by WERA. During the Fedje experiment a series of storms generating waves of 6 m and over passed through the region. One storm, 6-8 March 2000, generated waveheights of over 8 m for about a day. The HF radar data for this period has been analysed and waveheights of $8-14$ m were measured, but, even though these are of the same order as the buoy measurements, for most of the time the data do not pass all our quality requirements and so these are not included in the analysis below. There does appear to be an upper limit in waveheight for reliable wave measurements of about 7 m at these radio frequencies.

Figures 5.7, 5.8, 5.9 and 5.10 show timeseries of height, direction, period and spread at Fedje. The features of the Petten HF radar comparison are also very clear in this data set. The significant waveheight and 80% peak measurements are qualitatively similar but there is significant overestimation in high frequency amplitude during the storm events. Peak directions are rather noisier in this case, probably because the wave energy is at lower frequencies (see figure 5.8) which are more susceptible to antenna sidelobe and current variability spurii. The mean period comparison is much worse at Fedje and is due to the high frequency of storm events with associated overestimation of the high frequency spectrum. Note that in both cases the high frequency ($0.2-0.3$ Hz) period is more or less constant. This is presumably because the waves in this frequency range were fully-developed most of the time. The directional spreading parameter comparison is not particularly illuminating except at the high frequencies where a correlation can be seen.

Some additional comparisons during this experiment are presented in section 5.4 below.

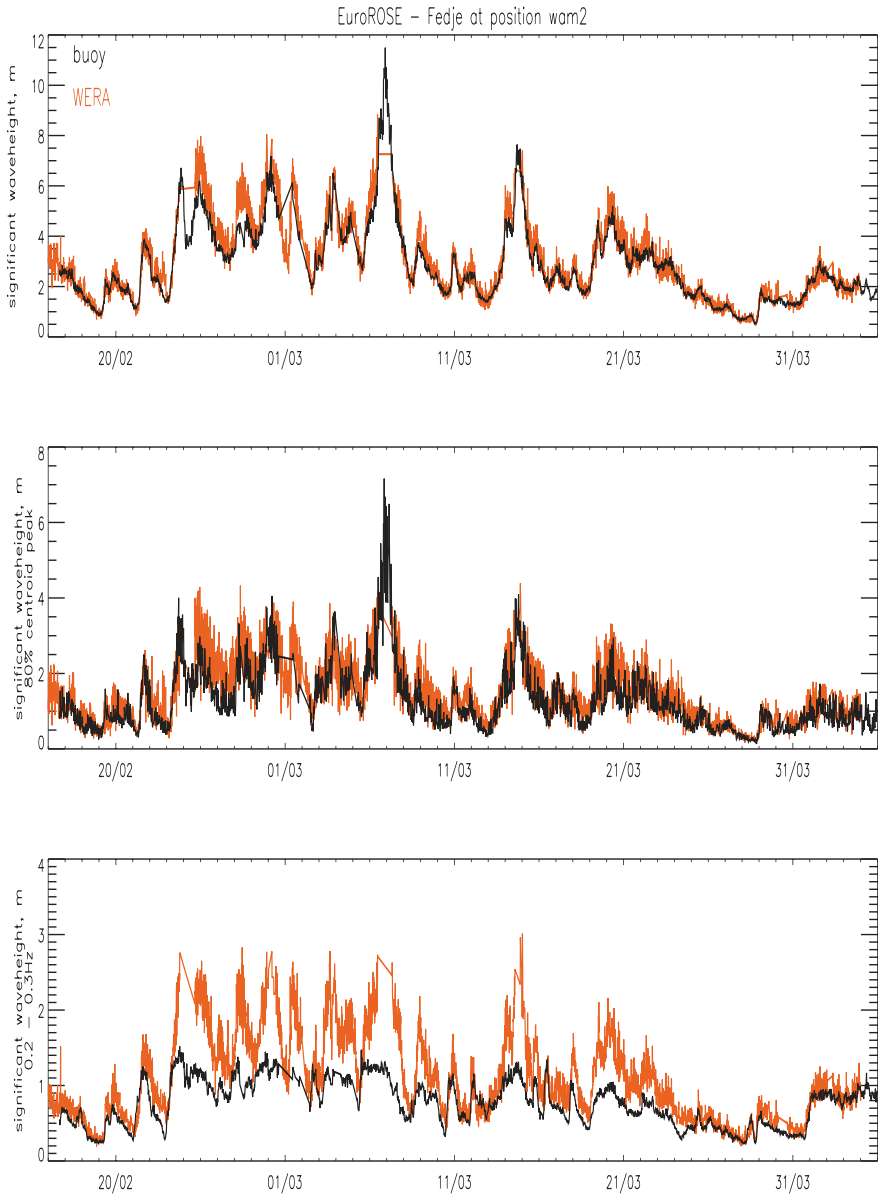

Figure 5.7: Fedje significant waveheight, peak and high frequency waveheight comparisons. As Fig. 5.3.

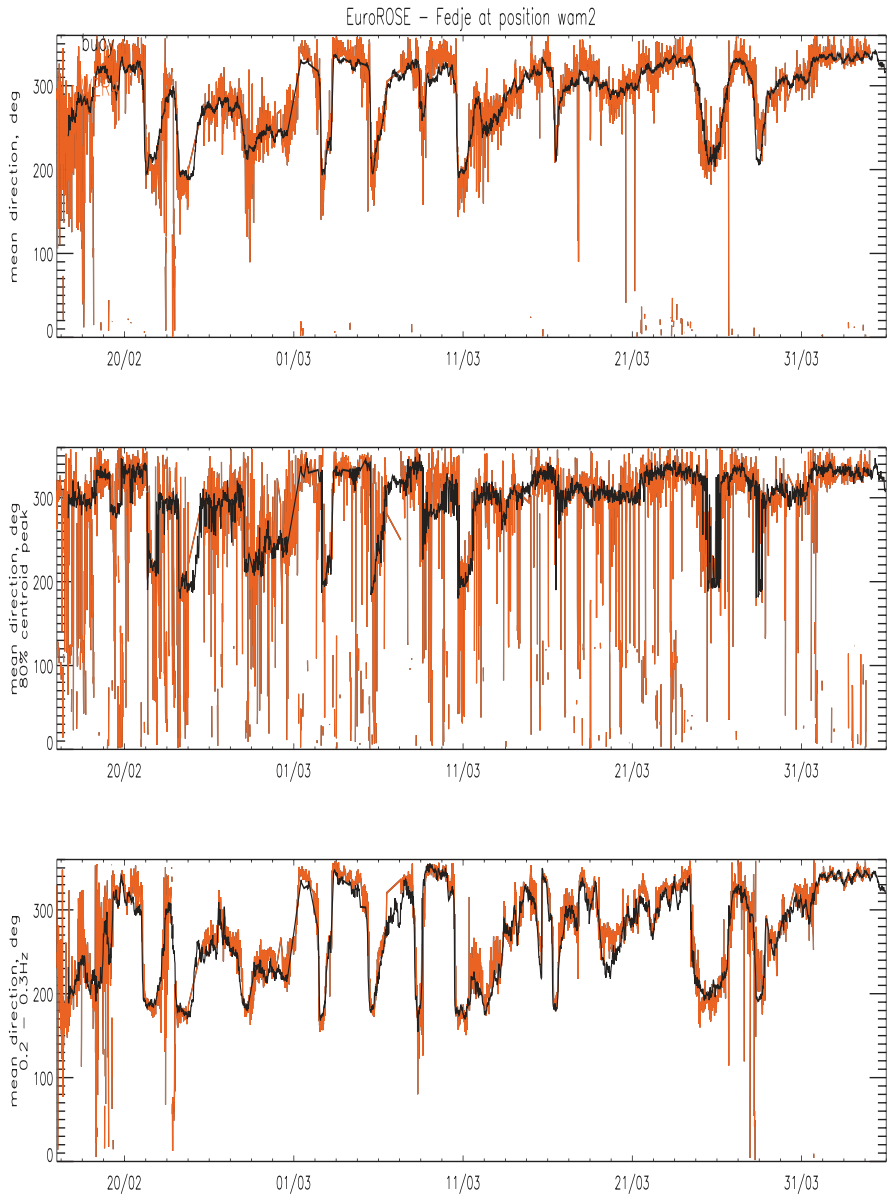

Figure 5.8: Fedje mean, peak and high frequency direction comparisons. As Fig. 5.3.

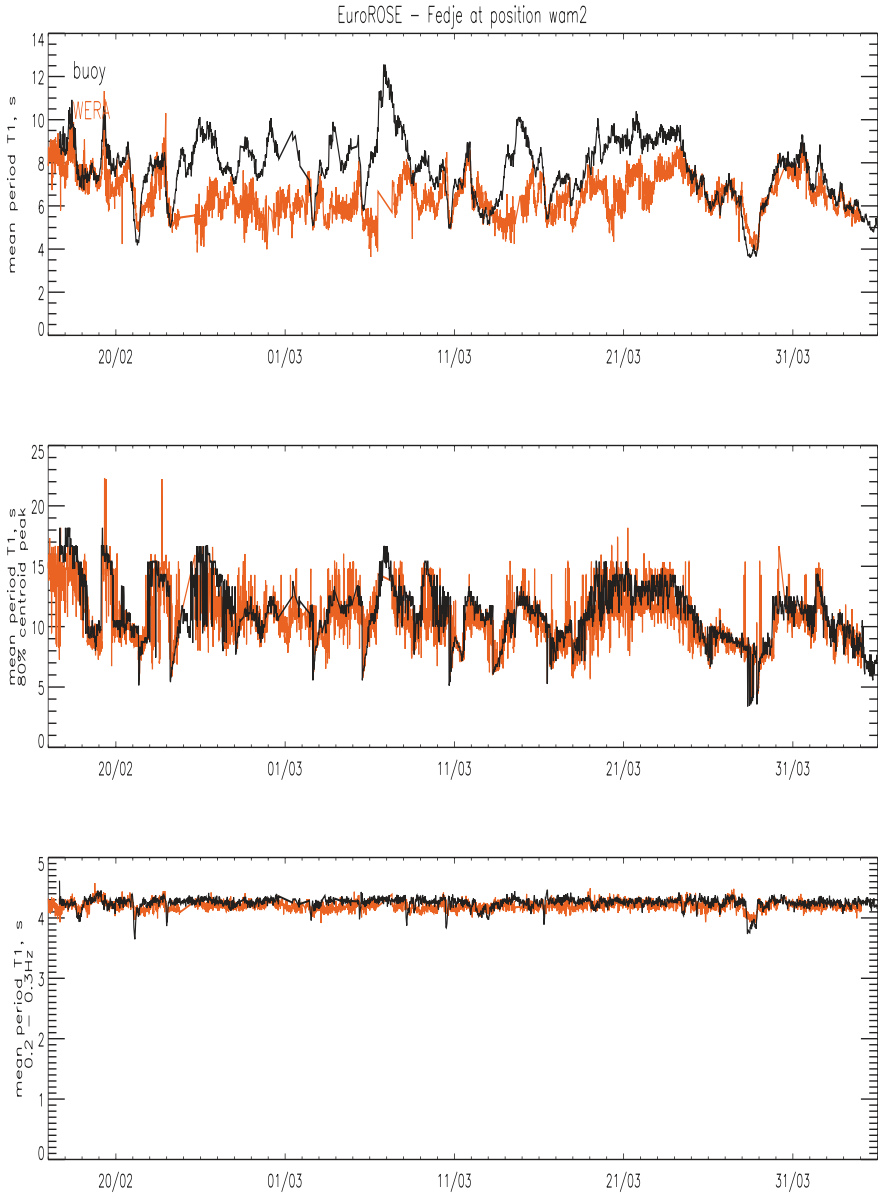

Figure 5.9: Fedje mean, peak and high frequency period comparisons. As Fig. 5.3.

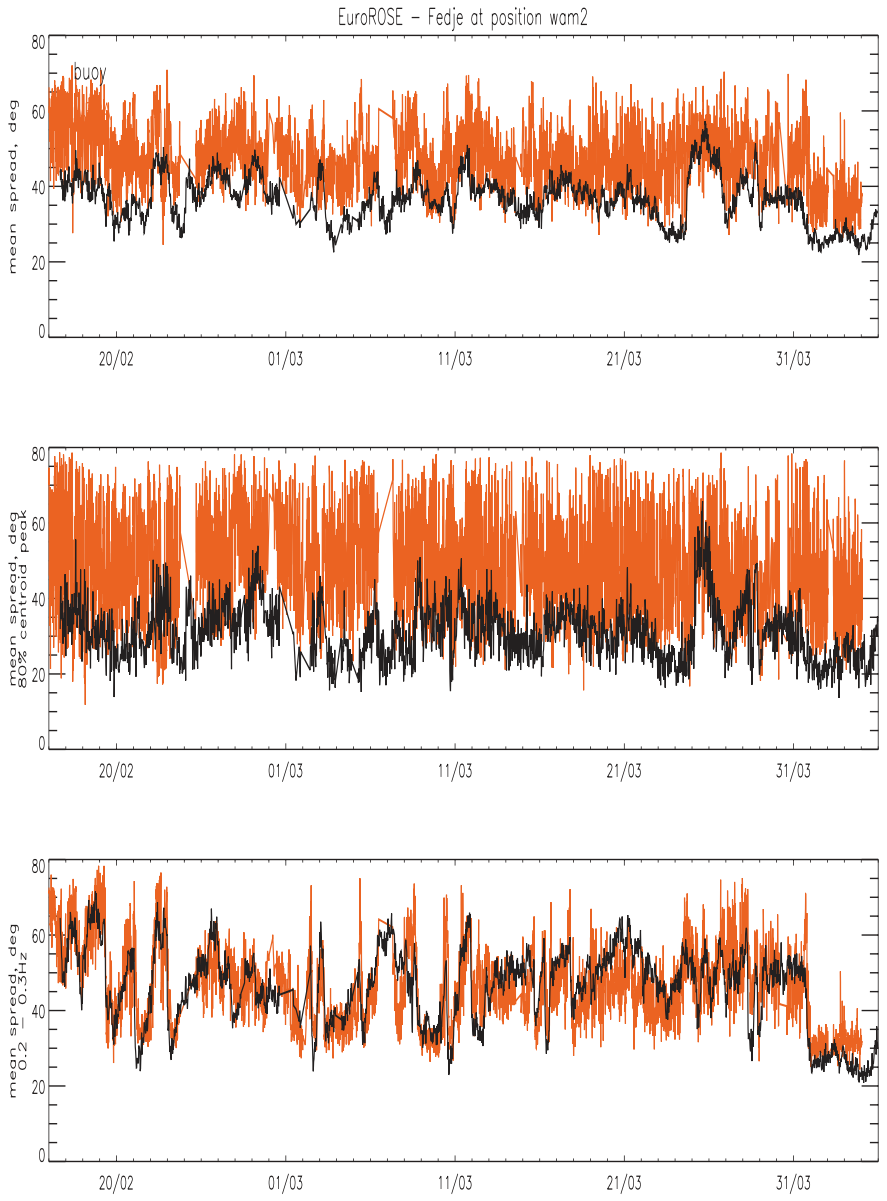

Figure 5.10: Fedje mean, peak and high frequency spread comparisons. As Fig. 5.3.

5.2.3 Statistics of the Comparisons

The above qualitative remarks are confirmed in the statistics presented in Tables 5.1 and 5.2. The work reported in Wyatt *et al.* (1999) showed that although some of the more traditional statistics provide a qualitative picture of the accuracy of the radar measurements, many of them do not help in explaining the origin of the differences. For linear parameters, the relative (rather than mean) error does provide useful information as does the mean directional difference for circular parameters and these are included in the tables. The circular analogue of the correlation coefficient is used for directional data (referred to as circular correlation below) and is the T-linear correlation coefficient defined by Fisher and Lee (1983). Wyatt *et al.* (1999) also demonstrated that it was possible to include the variability associated with both radar and wavebuoy in an analysis of their relative performance as wave measuring systems. This allowed detailed quantitative intercomparisons to be made using a maximum likelihood analysis. The HF radar comparisons show that there are differences in the maximum likelihood relationships found using the two maximum likelihood estimates. The relationships using variances determined from the data seem to be more consistent with the relative error and mean difference estimates. Figure 5.11 shows that the estimated significant waveheight variances both for the radar and the wavebuoy are significantly higher than the sampling variability estimated using the simulation and theoretical approaches referred to earlier. It is not surprising that the HF radar variances estimated using simulations is lower than that estimated from the data. The simulations assume the theory is correct and the measurements have demonstrated that there are substantial differences. In addition, of course, variances estimated from the data will include a contribution from the long wave spurious contributions also not in the simulations. It may be more surprising that the variances estimated for the buoy are similar to those estimated for the radar. The differences correspond to standard deviations in height estimation of $10 - 20$ cm above sampling variability. Buoy variances have also been estimated in the preliminary WAM and WaMoS comparisons and similar values are found there. Difference between sampling and measured variability was also identified in the mean spectral ratio plots presented in Krogstad *et al.* (1999).

Figure 5.12 shows significant waveheight scatter plots for Petten and Fedje HF radar and wavebuoy data. The two maximum likelihood lines are shown on each. In addition a regression line (assuming equal and constant variances for each measurement) through the origin and the non-parametric regression

(Part 1, Chapter 7) are drawn. The non-parametric curve departs from the ML lines earlier in the Petten data set and the two ML lines, which are indistinguishable for the Fedje data, are different at Petten. This could be an indication that the Petten higher waveheight measurements were more contaminated with low frequency sidelobe spurii than similar waveheights at Fedje perhaps because of the different distribution of this energy with frequency in the southern North Sea compared to the exposed Atlantic coast.

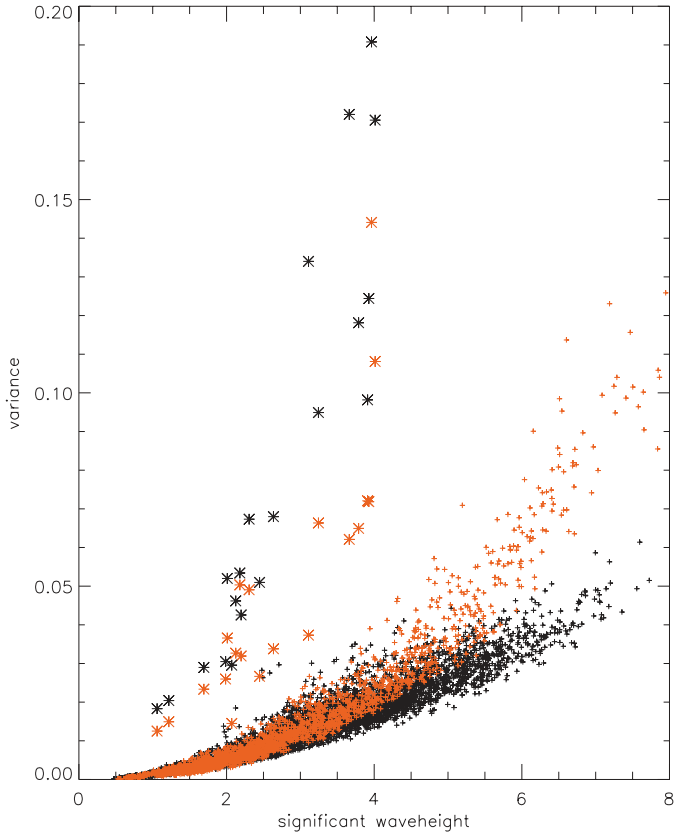

Figure 5.11: Buoy waveheight variance estimated using Taylor series, + in red, HF radar variances estimated using monte carlo simulations, +. Variances estimated from the data *, red for buoy, black for radar.

Table 5.1: Petten HF radar/buoy comparison statistics.

Number of cases 1790	**Full range**	**80% peak**	**0.2-0.3Hz**
Waveheight			
Correlation coefficient	0.93	0.8	0.84
Relative error (standard deviation)	11.2% (21%)	22.6% (41.5%)	38.2% (34.6%)
ML slope/intercept using data estimated variances	1.13/0.0	1.14/0.0	1.38/0.0
ML slope/intercept using theoretical and simulation variances	1.05/0.02	-	1.17/0.001
Period			
Correlation coefficient	0.54	0. 5	0.48
Relative error (standard deviation)	-2.7% (13.8%)	2.7% (35.4%)	1.8% (2.2%)
ML slope/intercept using data estimated variances	0.93/0.0	0.98/0.0	-
ML slope/intercept using theoretical and simulation variances	0.6/2.0	-	0.93/0.28
Direction			
Circular correlation coefficient	0.79	0.64	0.8
Mean difference (standard deviation)	1.6° (27.7°)	3.5° (39.6°)	3.5° (27.5°)
ML difference using data estimated variances	1.7°	2.9°	4.9°
ML difference using theoretical and simulation variances	3.8°	-	4.1°
Spread			
Circular correlation coefficient	0.18	0.14	0.22
Mean difference (standard deviation)	14.5° (7.2°)	17.6° (12.2°)	7.2° (8.9°)
ML difference using data estimated variances	14.4°	17.7°	5.9°

Table 5.2: Fedje HF radar/buoy comparison statistics.

Number of cases 3583	**Full range**	**80% peak**	**0.2-0.3Hz**
Waveheight			
Correlation coefficient	0.96	0.76	0.85
Relative error (standard deviation)	6% (14.7%)	27.8% (43.4%)	37.4% (33.9%)
ML slope/intercept using data estimated variances	1.07/0.0	1.17/0.0	1.33/0.0
ML slope/intercept using theoretical and simulation variances	1.09/-0.08	-	1.6/-0.15
Period			
Correlation coefficient	0.46	0.65	0.33
Relative error (standard deviation)	-13.1% (14.8%)	-3.4% (20%)	-1% (2.3%)
ML slope/intercept using data estimated variances	0.88/0.0	0.94/0.0	-
ML slope/intercept using theoretical and simulation variances	0.6/2.2	-	0.94/0.22
Direction			
Circular correlation coefficient	0.81	0.38	0.85
Mean difference (standard deviation)	1.9° (27.6°)	6.7° (56.6°)	6.9° (25.9°)
ML difference using data estimated variances	2.99°	4.4°	4.1°
ML difference using theoretical and simulation variances	−4.55°	-	−7.95°
Spread			
Circular correlation coefficient	0.38	0.07	0.68
Mean difference (standard deviation)	10.2° (8.1°)	17.0° (14.8°)	0.3° (8.4°)
ML slope/intercept using data estimated variances	10.07°	17.0°	0.48°
ML difference using theoretical and simulation variances	−11.0°	-	0.18°

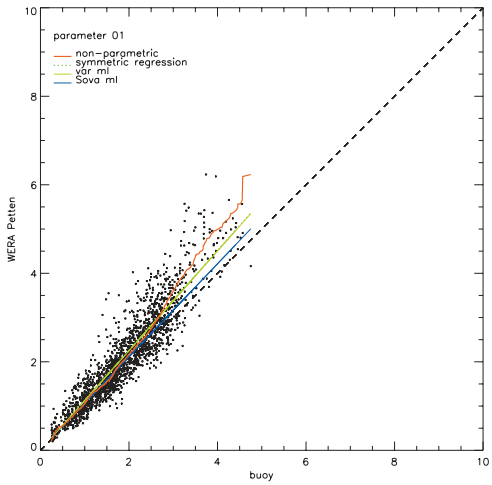

Figure 5.12: a. Scatter plots of significant waveheight at Petten with various relationships as described in the text.

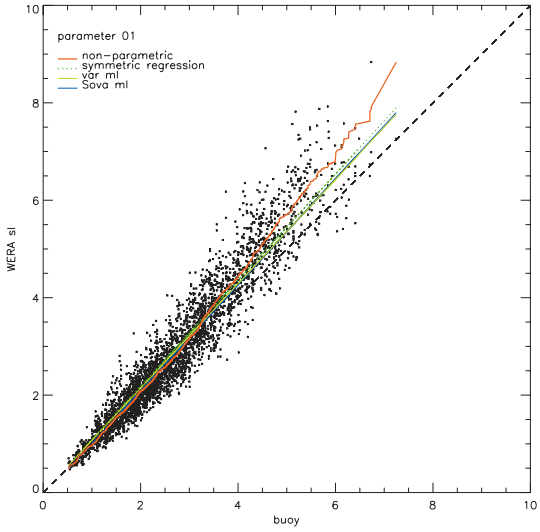

Figure 5.12: b. Scatter plots of significant waveheight at Fedje with various relationships as described in the text.

5.2.4 Concluding Remarks

The Holderness, Petten and Fedje experiments have provided data over a very wide range of conditions and hence provide a very comprehensive data set for assessing the accuracy and limitations of HF radar wave measurement. Two main limitations have been identified by comparisons of particular parameters or of the full directional spectrum. Firstly, short time or space scale current variability and/or antenna sidelobes introduce spurious contributions to the spectrum which are particularly noticeable at low wave frequencies. The other is the problem of applying the inversion based on a theory that is clearly invalid in high sea-states at the operating frequencies of OSCR and WERA. This has been shown to lead to a substantial overestimation in amplitude at high frequencies. One suggestion for dealing with this is to use the maximum likelihood analysis to calibrate the spectrum, an alternative is to limit the frequency range of the inversion and parametrise the amplitude at high frequencies with a f^{-5} (for example) spectral tail. Of course the most satisfactory solution would be to develop a theory that explains the observed backscatter in high seas conditions (Kingsley *et al.*, 1998). This is the subject of investigation at Sheffield. Another alternative is to use a lower radio frequency. The PISCES radar, developed by Neptune Radar Ltd and the University of Birmingham (Shearman and Moorhead,1988), was designed to operate at frequencies from $4 - 18$ MHz in order to provide wave measurements within the contraints of the theory. Measurements at about 7 m with that radar have characteristics in common with measurements at 2 m with WERA (Wyatt, 1995). The PISCES radar is currently in operation on the North Devon coast in England undergoing trials with a view to potential inclusion in a proposed UK wave monitoring network. Comparisons are being made with products from the UK Meteorological Office wave model with the aim of validating the radar measurements and identifying any model problems. At the time of writing waveheights have been limited to less than 4 m. The statistical analysis has two aims. One is to evaluate the HF radar measurements by comparison with the wavebuoy and perhaps to use the maximum likelihood relationships to provide a calibration adjustment. The latter approach depends on consistency of these relationships from experiment to experiment which seemed to be the case in the Wyatt *et al.* (1999) paper for the Holderness and Petten experiments but does not seem to be the case at Fedje. The reason for this seems to be the frequency dependent error sources and their interaction with the details of the energy distribution in the spectrum. The other aim of the analysis is to provide variance estimates for the radar measurements

in order to use them in model assimilation schemes. We have been providing variances based on the simulation work but the more recent work (using the data to estimate variances) is suggesting that those are inadequate for the buoy as well as the radar. This is an area that requires further work.

On the basis of the figures determined here it seems that there is a 5-10% overestimation in significant waveheight mostly attributable to a large overestimation in high frequency amplitude. Standard deviations in Hs estimation are of the same order. On average directions are very good with mean differences of less that 5° across the frequency band and directional spreading at the higher frequencies is also within 5° or so of that measured by the buoy. Over the full frequency range the radar spread measurements are not very useful and are definitely strongly influenced by the error sources. Mean periods are seriously affected by distortions to the high frequency part of the spectrum. This is especially clear in the Fedje data set.

Whilst there remain some problems limiting the accuracy of the HF radar wave measurements this work has shown that the impact of the problems can be clearly identified and it should be possible to factor these into an assimilation scheme in a quantitative way. The limitations also need to be seen against the huge advantage of the spatio-temporal monitoring capabilities of HF radar systems both for operational applications and as sea-truth for satellite missions.

Acknowledgements

This work was partly funded by the EU MAST programme MAS2CT940103 and MAS3CT980168. I am particularly grateful to Klaus Werner Gurgel and his group at the University of Hamburg who collected the WERA data in the SCAWVEX and EuroROSE experiments, Steve Thompson and Jim Green who processed the Petten and Fedje data sets respectively and to all those involved in the provision of in-situ wind and wave data during those experiments.

5.3 Qualitative Directional Spectra Comparisons

Lucy R. Wyatt

University of Sheffield, Sheffield, United Kingdom

The inversion process that generates wave measurements from HF radar Doppler spectra provides the directional wavenumber spectrum on a non-uniform grid. For wavebuoy comparisons, and indeed for all parameter extraction procedures, the data on the non-uniform grid are first averaged into wavenumber (or, using the dispersion relation, frequency-direction bins). A k^{-4} (or f^{-5}) tail is added at those vector wavenumbers not included in the integral inversion.

Wave buoys do not measure the full directional spectrum providing instead a limited number of frequency dependent Fourier coefficients, $[a_i(f), b_i(f)$ i=0,2], of the directional distribution. To construct a directional spectrum from these coefficients the maximum entropy method (Lygre and Krogstad (LK), 1986; see also Part 1, Chapter 3) is used. Expressing the Fourier coefficients in complex form i.e.

$$c_i = a_i + ib_i \tag{5.1}$$

the maximum entropy (ME) estimate of the directional spectrum is given by

$$S(f,\theta) = a_0(f)\left[\frac{1-\phi_1 c_1^* - \phi_2 c_2^*}{\left|1-\phi_1 e^{-i\theta} - \phi_2 e^{-i2\theta}\right|^2}\right] \tag{5.2}$$

where * denotes complex conjugate, and

$$\begin{aligned} \phi_1 &= (c_1 - c_2 c_1^*)\Big/\left(1-|c_1|^2\right) \\ \phi_2 &= (c_2 - c_1\phi_1)\,. \end{aligned} \tag{5.3}$$

The Fourier coefficients are smoothed in frequency before the ME estimate is calculated in order to reduce their variance, e.g.

$$a(f_i) = 0.25 * a(f_{i-1}) + 0.5 * a(f_i) + 0.25 * a(f_{i+1})\,. \tag{5.4}$$

LK note that ME estimates can have a tendency to split peaks but note that in real situations the lack of better measurements of the directional distribution make it difficult to distinguish between real bimodal structure and

artifacts of the estimate. An alternative ME estimate is being investigated (Hashimoto, 1997) which may be more robust with respect to peak splitting. However this method is sometimes numerically unstable when applied to Fourier coefficients, an application directly to the buoy raw data is advised (Hashimoto, private communication). LK compare the ME estimate with a maximum likelihood method (MLM) commonly used in the analysis of data from spatial arrays of wave recorders (e.g. Capon, 1969). They show that the MLM tends to produce broader distributions with poorer directional resolution. A similar comment on the MLM is given in Donelan *et al.* (1996) where it is compared with a wavelet analysis method. The wavelet analysis method gives directional distributions with fairly narrow spreads even at quite high frequencies and wavenumbers.

Fourier coefficients determined from the radar measured spectrum have been used to assess the ME estimates since of course the resulting spectrum can be compared with the original spectrum. The uncertainties raised by LK concerning peak splitting can be addressed in this way.

The spectra are presented using logarithmic contour levels in order to reveal detailed features at high frequencies. They are scaled with respect to the radar maximum in order to provide a clear comparison at high frequencies. Directions are those towards which the waves are propagating.

Figure 5.13 shows examples from Petten, the Netherlands, on 20$^{\text{th}}$ November 1996. The radar measurements are on the upper row, the ME estimates from radar Fourier coefficients on the middle row with the buoy ME estimates below. They are colour-coded with 10 equally spaced logarithmic levels with spacing 1/3 and minimum level (dark blue) –3 to –2.67. Thus three orders of magnitude are represented in order to highlight comparability, or otherwise, at high frequencies. Amplitudes greater than the radar peak are shown in black. The middle row is the radar spectrum estimated from the same number of Fourier coefficients as are used in the buoy estimates on the bottom row. The overall shape of the spectra are in reasonable agreement, the main differences being increased spreading in the radar measurements (both full and ME) and increased peakiness in the buoy estimates. The radar ME estimates are very similar to the full measurements suggesting that this is an appropriate method for reconstructing buoy directional spectra. Note that the Fourier coefficients are only determined for the radar data at frequencies that contribute to the inversion and hence there is a cut off at about 0.37 Hz in these figures.

Ahead of the arrival of a low pressure system (overhead at about 1100GMT)

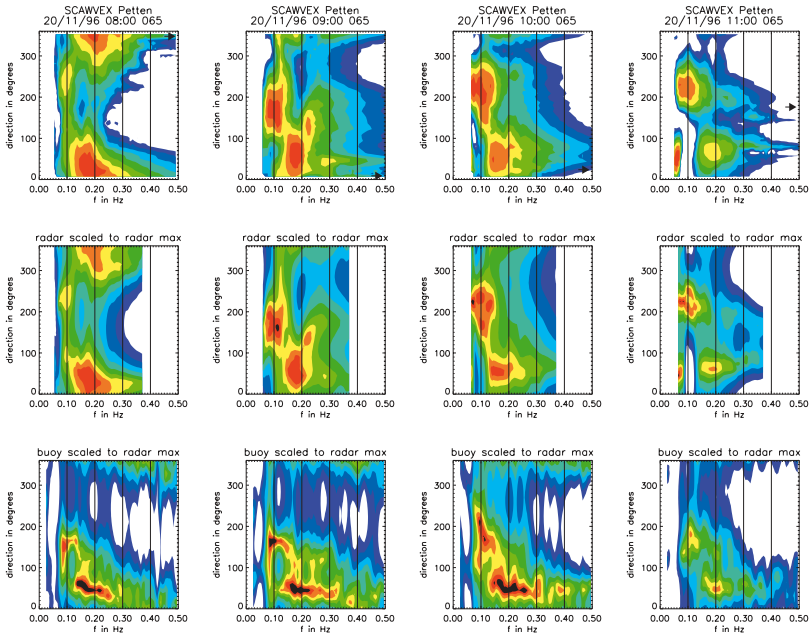

Figure 5.13: Directional spectra measured during the SCAWVEX experiment at Petten, Netherlands in the morning of 20/11/96. Frequency in Hz plotted on horizontal axis and direction towards which the waves are propagating on the vertical axis. The spectra are normalised with respect to the maximum amplitude in the radar measurement (top row) at each time. (For amplitude variation with time see section 5.2.1) Radar estimated wind directions (Wyatt *et al.*, 1997) are shown with arrows on the top row.

the spectrum is dominated by energy propagating from the south in the longer fetch direction (Fig. 5.13). There is also a distinct swell contribution at about 0.1 Hz from the north. The measurement at 1100GMT shows an additional wave component at about 0.07 Hz propagating towards the north–east. This is likely to be either a noise source in the radar data or associated with contamination of the signal by antenna sidelobes. After the low has passed (Fig. 5.14) waves are predominantly to the south–east, i.e. onshore, in the direction of the wind. There are additional peaks in the radar data in Fig. 5.14 which are also attributed to sidelobe problems. More details of this period are presented in Wyatt (1999).

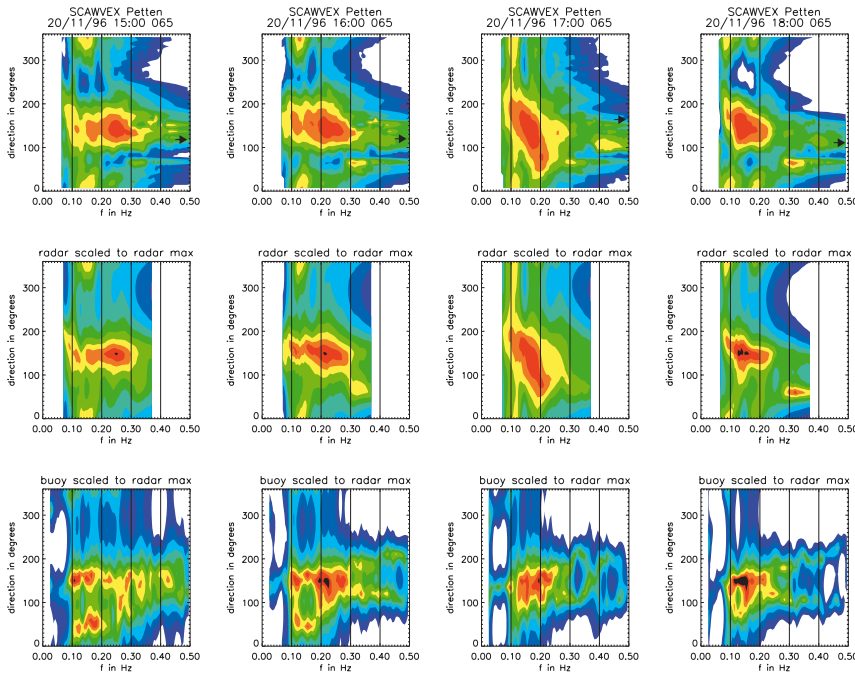

Figure 5.14: As Fig. 5.13 but for later the same day.

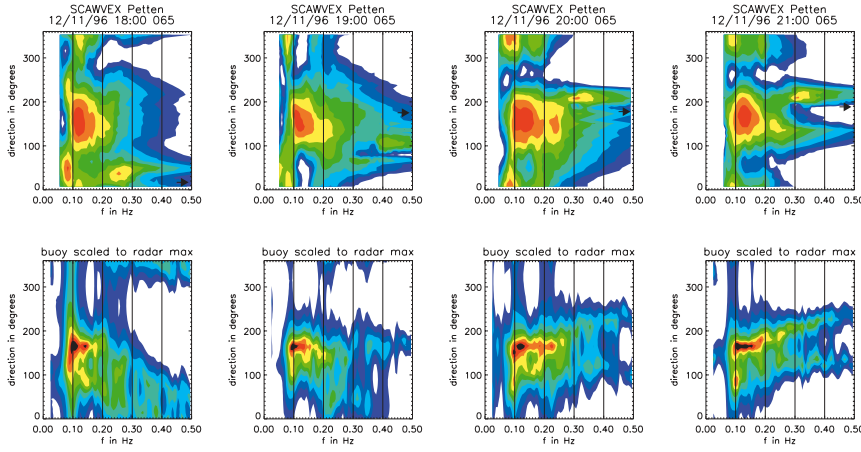

Figure 5.15: As Fig. 5.13 measured on 12/11/96 without the radar ME estimates.

5.3.1 Bimodal Distributions

Of particular interest in a lot of the SCAWVEX data is evidence of bimodality at the higher frequencies both in the radar and wavebuoy measurements. See for example the measurement at 1800GMT in Fig. 5.14. Bimodal spectra have been measured before on a lake (Young *et al.*, 1995) and in the ocean (Ewans, 1998) in fetch-limited conditions. Waves at the Holderness and Petten sites in the North Sea are likely to be fetch-limited in many wind conditions. Examples were also found associated with developing seas. Late on 12/11/96 during the Petten experiment wind direction changed from southerly to northerly and speed increased from 5 to 10-15m/s over a short time and then remained steady for several hours. In Fig. 5.15 there is evidence of bimodality at high frequencies in both the radar and buoy data but it is unclear whether this is associated with the local development of wind waves (and hence consistent with Banner and Young, 1994) or with the combination of newly developing waves with swell and/or a decaying wind wave field. The latter explanation looks more likely when one examines Fig. 5.16 which shows slices through the radar directional spectrum at 2120GMT. At frequencies beyond 0.21 Hz one of the two wave components present seems to be the tail of the main contribution to the spectrum with a peak at 0.13 Hz whereas the second component is developing in the wind direction.

Although the radar examples of bimodality do appear to be consistent with the ME buoy estimates, the amplitudes in the part of the spectrum affected are rather small and it was necessary to be sure that the graphical routines used were not in some way responsible for the apparent appearance of this phenomenon in the radar data. Figure 5.17 shows the radar data (for 1800GMT on 20/11/96) at the output from the inversion procedure i.e. on the non-uniform grid before averaging into frequency (or wavenumber) direction bins, before adding the high frequency tail and before applying the contouring routine. This makes it clear that the radar is not providing measurements over the full range of directions at frequencies beyond about 0.27 Hz. Note that this can also be seen in Fig. 5.16. Higher frequency measurements are concentrated roughly around the radar estimated wind direction. Whilst it is clear that the addition of the high frequency tail and the interpolation used in the contour plotting (as in Fig. 5.14) do accentuate the impression of bimodality, the origins of it can still be seen in the inversion output. (at ~ 0.32 Hz, 70° and ~ 0.4 Hz, 110°). The second question that arises is whether the inversion procedure is really capable of finding

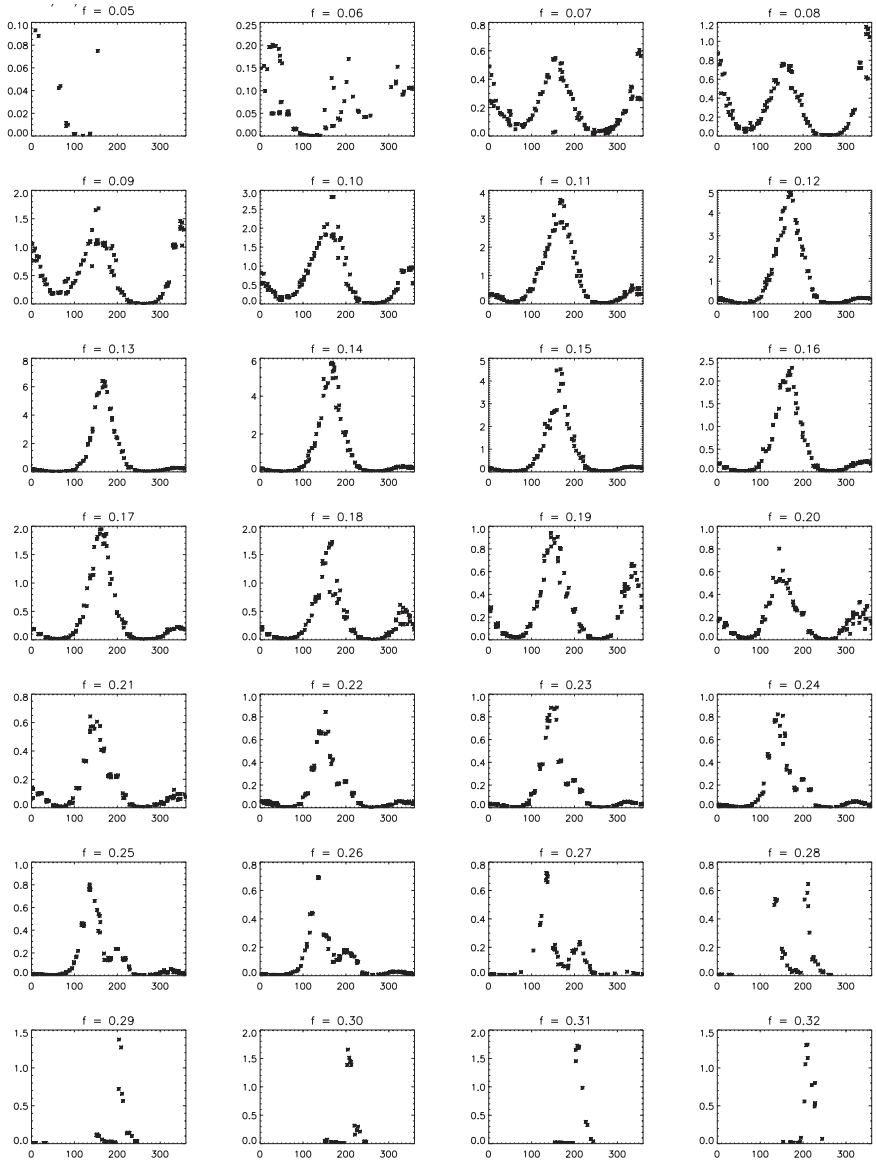

Figure 5.16: Slices through the radar measured directional spectrum in 0.01 Hz wide frequency bins from 0.05 Hz to 0.32 Hz before frequency bin averaging. The vertical scales vary according to the local maximum. Directions are along the horizontal axis.

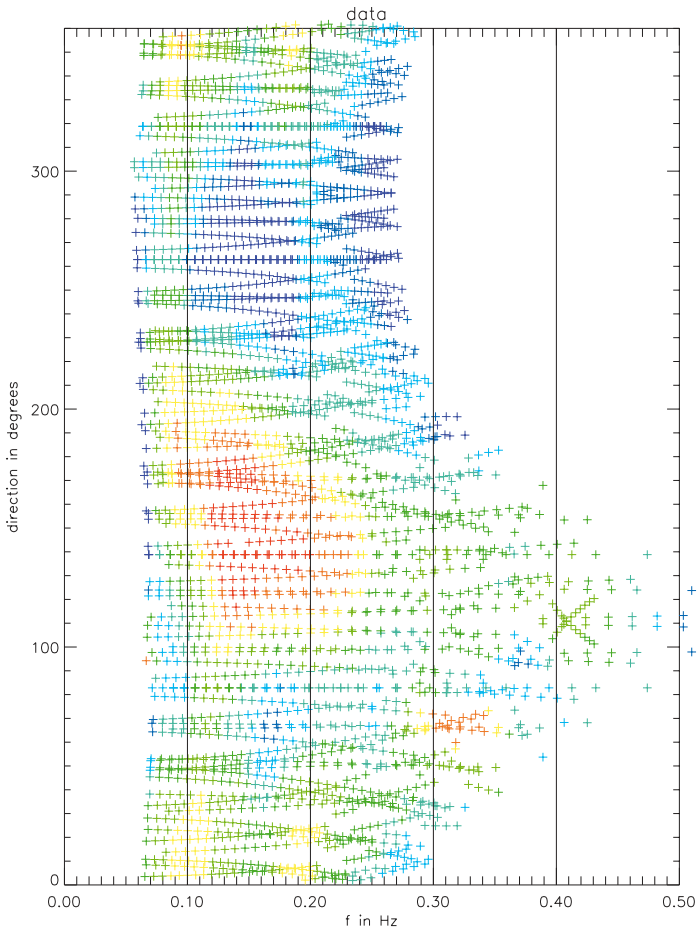

Figure 5.17: The radar measured directional spectrum at the output of the inversion after conversion from wavenumber to frequency displayed and colour coded as in Fig. 5.13. Each + corresponds to a vector wavenumber that was included in the inversion process.

bimodal structure at these higher frequencies. Simulations have been used to show that the inversion process can resolve frequency features of this sort. Figure 5.18 shows an example of this. Note that because of limitations in the simulations it is not possible to model exactly the situation observed on, say, 12/11/96 at 2100GMT. The ability to resolve two (or more) wave con-

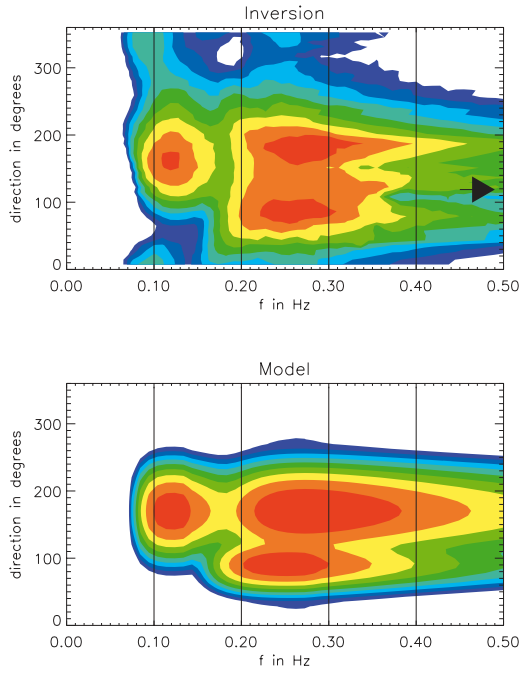

Figure 5.18: The lower figure shows a modelled directional spectrum with three wave components. This is used to simulate radar Doppler spectra which are then inverted to provide the measurement in the upper figure. Displayed and colour coded as in Fig. 5.13.

tributions depends on their relative amplitudes and the wavenumber vector difference between the peaks as was found in an investigation of bimodality at lower frequencies (Wyatt and Holden, 1994).

Kuik *et al.* (1988) proposed a technique to identify multimodal directional distributions using the skewness,γ, and kurtosis,δ, parameters. These are defined in terms of the centred second order Fourier coefficients m_2, n_2(which in turn can be calculated from the regular Fourier coefficients a_2 and b_2) as follows.

$$\gamma = \frac{-n_2}{[(1-m_2)/2]^{3/2}} \tag{5.5}$$

and

$$\delta = \frac{6 - 8r_1 + 2m_2}{\left[2\left(1 - r_1\right)\right]^2} \tag{5.6}$$

where

$$\begin{aligned} r_1 &= \sqrt{a_1^2 + b_1^2} \\ m_2 &= a_2 \cos\left(2\theta_0\right) + b_2 \sin\left(2\theta_0\right) \\ n_2 &= b_2 \cos\left(2\theta_0\right) - a_2 \sin\left(2\theta_0\right) \\ \theta_0 &= \arctan\left(b_1/a_1\right). \end{aligned} \tag{5.7}$$

Based on simulations and measurements they proposed the following relationship between these parameters which would be required for a unimodal symmetric distribution.

$$\delta > 2 + |\gamma| \text{ for } |\gamma| \leq 4 \text{ and } \delta > 6 \text{ for } |\gamma| > 4.$$

Figure 5.19 shows plots of δ versus $|\gamma|$ and of δ as a function of frequency for a case from Fig. 5.13 (0800GMT) and from Fig. 5.15 (2100GMT). The frequencies at which the Kuik *et al.* (1988) criterion suggests bimodality are indicated with symbols on the frequency distribution plot. These plots are consistent with a visual inspection of Figs. 5.13 and 5.15 with Fig. 5.19 implying bimodality at high frequencies in the latter case and at low frequencies in both cases.

The Holderness and Petten observations seemed to support the use of MEM for the analysis of the directional waverider since in nearly all cases when there was bimodality in the wavebuoy data it was also found in the radar data. However recent data obtained off the Norwegian coast at Fedje have provided examples where the buoy data (using MEM and Kuik *et al.*, 1988) shows bimodality whereas the radar does not. One example is shown in Fig. 5.20. The Kuik *et al.* (1988) analysis is shown in Fig. 5.21 and Fig. 5.22 shows slices through the radar measured directional spectrum which shows no evidence of directional bimodality at any frequency whereas Fig. 5.21 suggests bimodality in the buoy data beyond 0.3 Hz. There is therefore still a question mark over the use of ME analysis.

As was the case in the examples shown here, in general it has been found that where bimodality is observed in the radar data, it seems to be associated with cases of new wave development alongside old wave systems rather than the bimodality being associated with the development itself as was suggested by Banner and Young (1994).

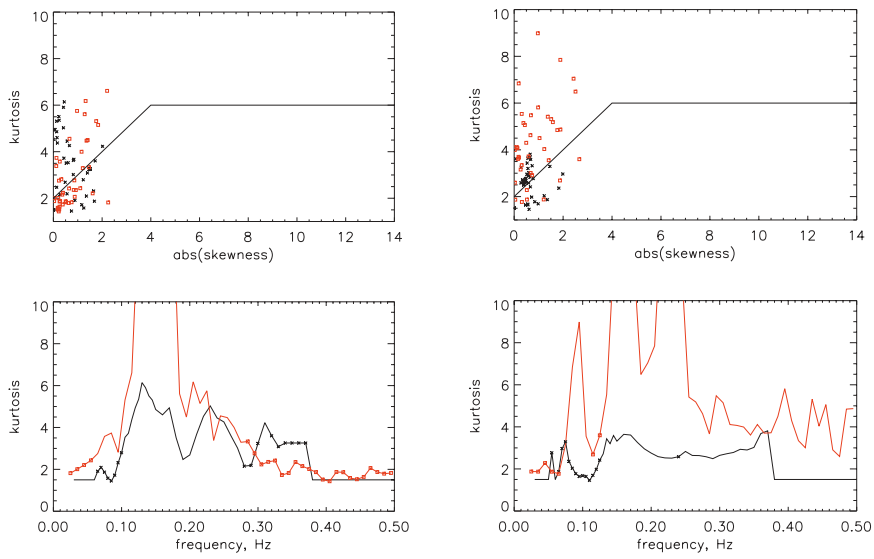

Figure 5.19: Skewness and kurtosis plots as described in the text for (left) 12/11/96 at 2100GMT and (right) 20/11/96 at 0800GMT. The radar measurement is in black and the buoy in red. The cases that fall below the line in the upper diagram are identified with symbols on the lower diagram.

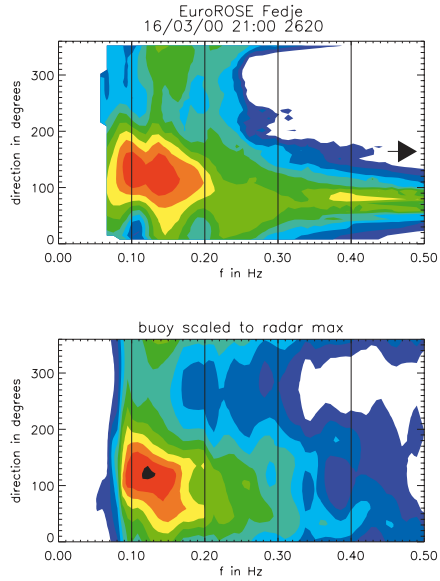

Figure 5.20: Directional spectra measured during the EuroROSE Fedje experiment on 16/3/2000 at 2100GMT displayed and colour coded as in 5.13.

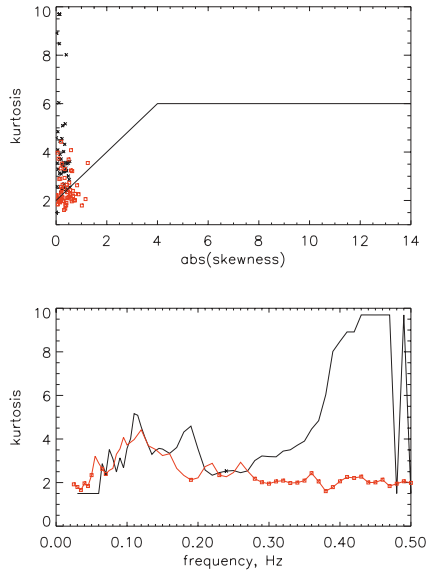

Figure 5.21: As Fig. 5.19 for the data in Fig. 5.20.

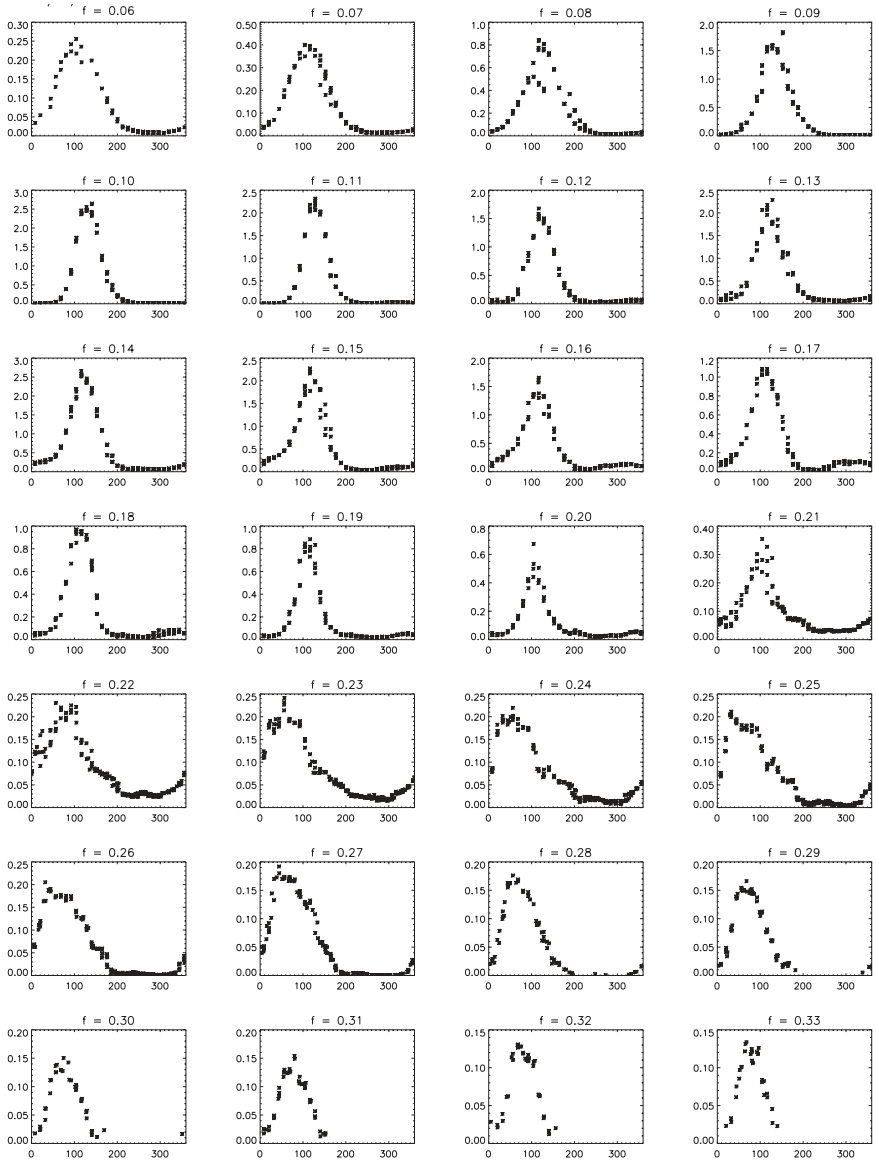

Figure 5.22: As Fig. 5.19 for the data in Fig. 5.20.

5.4 Comparisons with WaMoS X-band and WAM Wave Model

Lucy R. Wyatt [a], *Jim J. Green* [a], *Klaus-Werner Gurgel* [b], *José Carlos Nieto Borge* [c], *Konstanze Reichert* [d], *Katrin Hessner* [d], *Heinz Günther* [e], *Wolfgang Rosenthal* [e], *Øyvind Saetra* [f] *and Magnar Reistad* [g]

[a] University of Sheffield, Sheffield, United Kingdom
[b] University of Hamburg, Hamburg, Germany
[c] German Aerospace Centre (DLR), Oberpfaffenhofen, Germany
[d] Ocean Waves GmbH, Lüneburg, Germany
[e] GKSS, Geesthacht, Germany
[f] ECMWF, Reading, United Kingdom
[g] Norwegian Meteorological Institute, Bergen, Norway

As has already been mentioned, the Fedje experiment provided the opportunity for comparisons between the WERA HF radar wave measurements and those obtained using the WaMoS X-band radar and also with a high resolution implementation of the WAM wave model. These comparisons are described in detail in Wyatt *et al.* (2003) with some additional comparisons in Wyatt *et al.* (2002) and Wyatt and Green (2001). Wyatt *et al.* (2003) also includes a discussion of WERA/WaMoS comparisons in a second EuroROSE experiment at Gijon on the north coast of Spain.

Aspects of the Fedje comparison are summarised here. Some discussion on the WERA/buoy comparisons were already presented in section 5.2 above. Figure 5.23 shows frequency spectra (i.e directional spectra integrated in direction) for WERA, buoy, WaMoS and WAM for the period 23/2/2000 to 12/3/2000 inclusive. Figure 5.24 shows the direction spectra (i.e directional spectra integrated in frequency) for the same period. Directions here are those towards which the waves are propagating. Note that the direction spectra for the buoy are determined from the maximum entropy calculations. Figure 5.25 shows comparisons of significant waveheight, mean period, direction (from which the waves are propagating) and spread. In considering the WaMoS measurements it is necessary to note that these were not made at the buoy location but at a site near the coast much more sheltered from the north and north-west. The sheltering effect leading to refraction of waves towards the coast is seen in Fig. 5.24 and more clearly in the mean direction comparisons in Fig. 5.25 during the period 1-10/3 when the other measure-

ments show waves from just west of north. There is also no doubt some impact on other parameters of the directional spectrum.

The features of the WERA spectra, already described, are clear here in comparison not just to the buoy but also to WAM and WaMoS i.e. overestimation of high frequencies and underestimation of peak frequencies in storm conditions leading to low mean periods, and noisy directional distributions. WAM and WaMoS show generally good agreement with the buoy for the spectral characteristics and hence for the parameters significant waveheight, mean period and direction (when the sheltering effect already referred to is taken into account). Figure 5.23 suggests that WaMoS amplitudes are underestimated at frequencies beyond about 0.2 Hz and this is confirmed in more detailed comparisons presented in Wyatt and Green (2001). However that report also showed that there is still some directional information at the higher frequencies. There are clear differences in directional spreading with the WaMoS measuring much narrower spreads than the others and the WAM spreads being lower than the buoy. Again WERA mean spreads are noisy. Where waveheights are low, < 2 m for this experiment, WaMoS shows noisy mean directions and spreads. The later Gijon experiment showed that there is also a low wind speed limit of about 3m/s on WaMoS performance. As a result of these observations, some additional quality checks are carried out on WaMoS data which would have flagged these noisy events. These are discussed further in Hessner *et al.* (2001) and Wyatt *et al.* (2003). The WAM model in general produces good estimates of the directional spectral parameters over the full frequency range although there is evidence of a slow response to directional change (reported in Wyatt *et al.*, 2002 and 2003) perhaps due to poor temporal resolution in the wind input. In addition comparisons between WAM and WaMoS at the site of the WaMoS measurements suggests that the WAM model is not capturing the impact of sheltering perhaps due to inadequate land boundary resolution. The very high waveheight observed by the buoy on 6/3/2000 is not reflected in either WaMoS or WAM (the WERA measurements were not of sufficient quality at this time). It is also difficult to explain using information from other buoys off the Norwegian coast and taking into account the wind conditions. Note that WaMoS and WAM were measuring similar heights at this time and that these were in turn similar to the other buoys (which were not in the immediate vicinity).

Some comparison have been made between WERA and WaMoS at the Gijon sites where they were more closely co-located. However there were a number of factors (see Wyatt *et al.*, 2003) that limited the amount of data available

for comparison. In addition there was no directional buoy available. In a future experiment it would be useful to co-locate an HF radar, X-band radar and a directional wavebuoy for a more conclusive validation of the two radar systems and indeed of the WAM or other wave model.

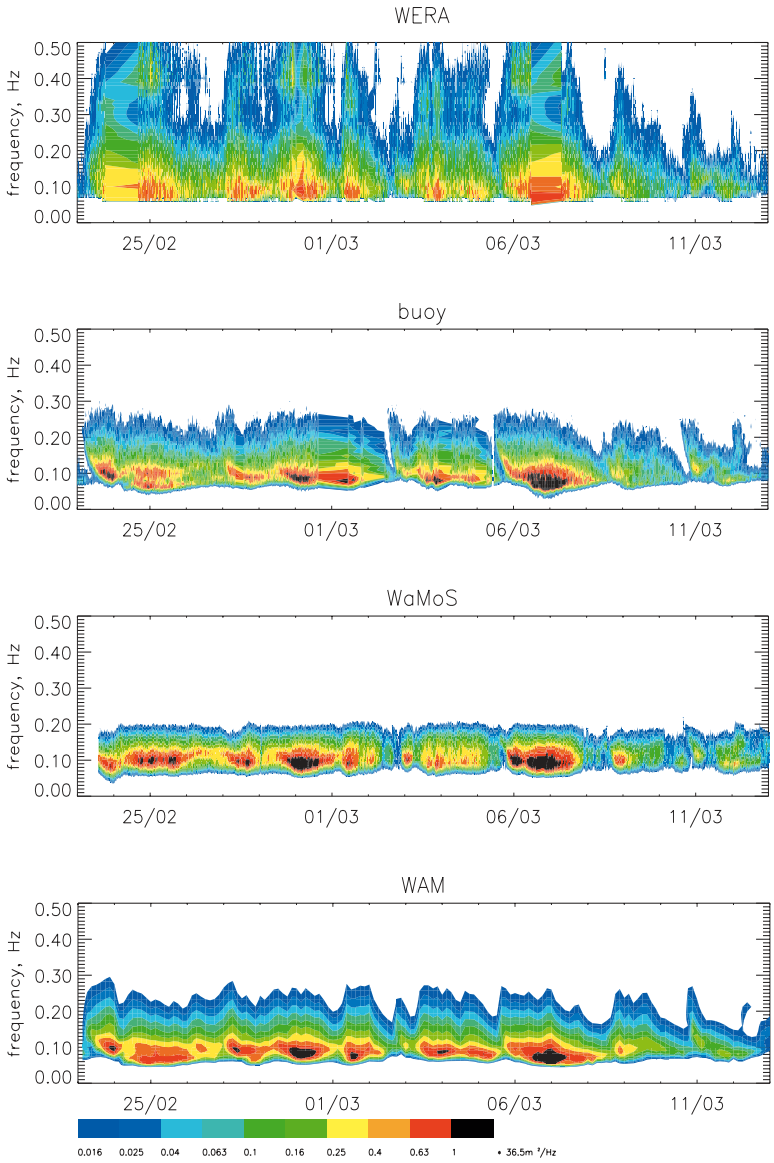

Figure 5.23: Frequency spectra during the Fedje experiment. From top to bottom: WERA, buoy, WaMoS and WAM. The colour scaling is logarithmic as shown and normalised to the maximum value measured by WERA during the whole experiment.

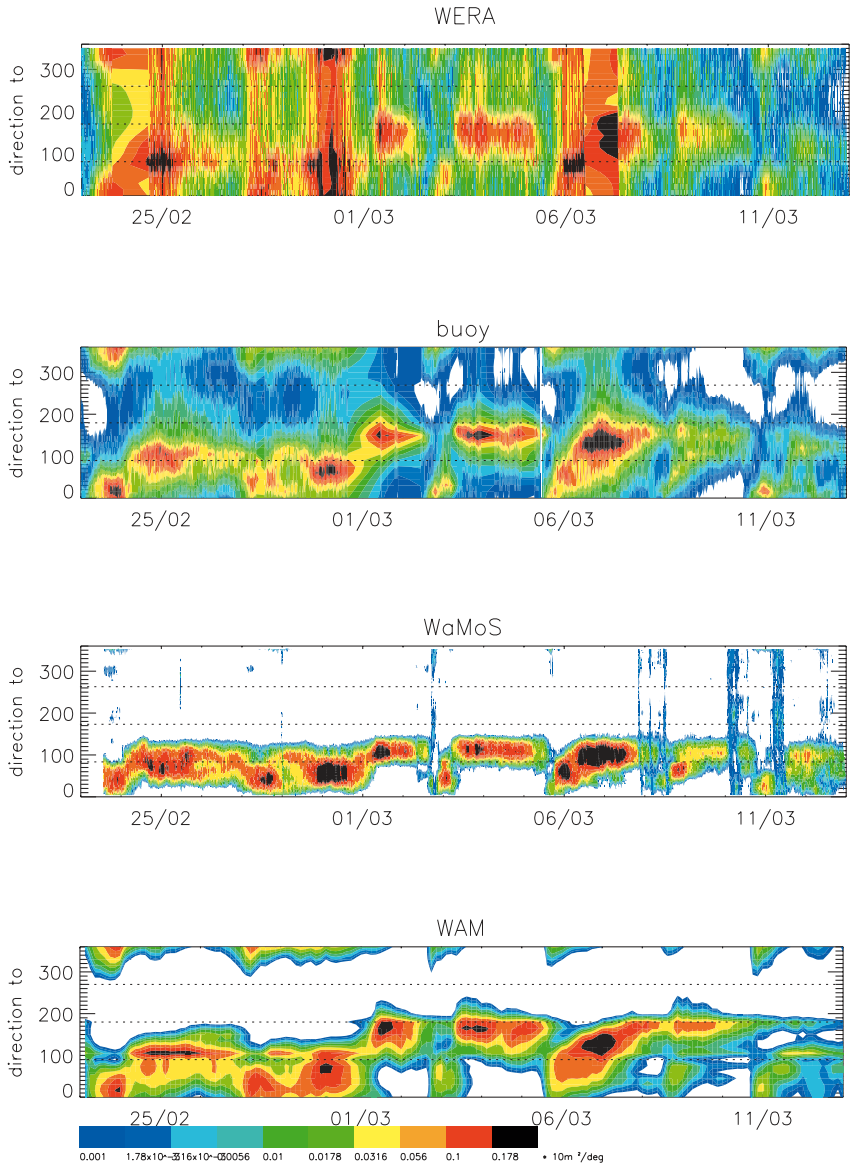

Figure 5.24: Direction spectra during the Fedje experiment. From top to bottom: WERA, buoy, WaMoS and WAM. The colour scaling is logarithmic and is normalised as shown.

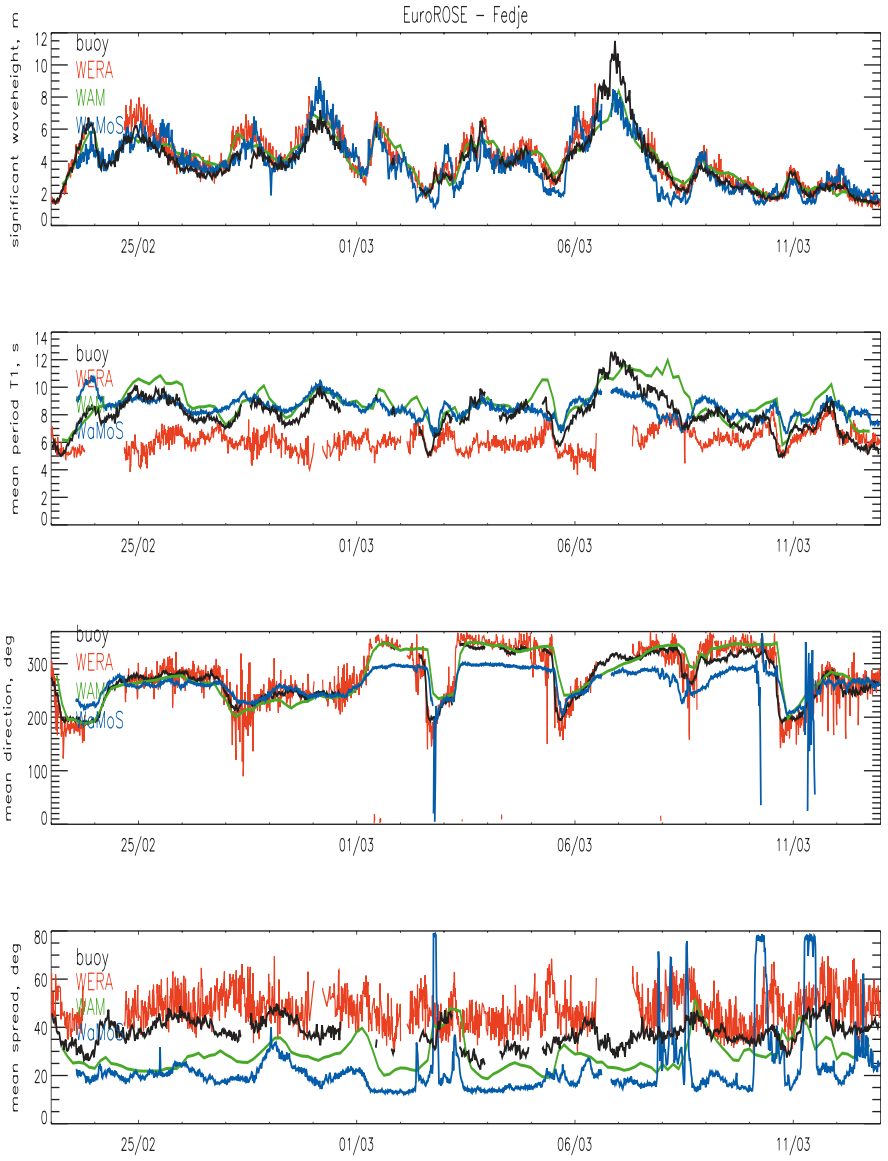

Figure 5.25: Fedje comparisons of significant waveheight, mean period, mean direction and mean spread (from top to bottom). Buoy (black), WERA (red), WAM (green) and WaMoS (blue).

5.5 Comparisons with Wave Model Results

S. Caires [a] *and L.R. Wyatt* [b]

[a] KNMI, de Bilt, the Netherlands
[b] University of Sheffield, Sheffield, United Kingdom

5.5.1 Introduction

The monitoring of coastal wave conditions is of great importance in the modern world. High frequency (HF) radars are well-suited for providing such measurements. Additionally, numerical shallow water wave models can be used to provide predictions.

Both HF radars and wave models, however, still require improvements, and their measurements/predictions need thorough validation assessments. Usually, wave model predictions and radar measurements are assessed by comparison with buoy measurements, but these are restricted to a limited number of locations and therefore do not allow a spatial assessment of the data. Consequently, the assessment of HF radar and wave model data needs to be based not only on comparisons with buoy data but also on comparisons between radar and wave model data.

None of the above types of data can be assumed to correspond to *true* sea state observations; instead, they have to be assumed to be affected by random errors. This characteristic of wave data means that standard statistical methods are not appropriate for a comparative statistical assessment of radar, SWAN and buoy data; the methods presented in Part 1, Chapter 7 are the best suited for this purpose.

In this paper we will present a brief account of an extensive comparative study between HF radar measurements obtained during a 1 month period off the coast of Holderness in the north–east of England and the corresponding wave model results (Caires, 2000). The emphasis is on the accuracy of the whole wave field covered by the radar and SWAN. Previous work has concentrated on local accuracy at the location of, and in comparison with, a buoy. We will only analyse in detail a period of 3 days, and then provide the reader with the main conclusions of the study based on the whole data set. Our exposition is divided into 7 sections. In Section 5.5.2 we describe the hindcasts and measurements. In sections 5.5.3 to 5.5.6 we analyse the data from the 3 day period separately in terms of each of the main wave

parameters: significant waveheight (H_{m0}), mean wave period determined from the first moment of the frequency spectrum (T_{m01}), mean wave direction (MWD) and directional spread ($DSpr$). We finish with the general conclusions of our study in Section 5.5.7.

5.5.2 Description of the Data

The wave model chosen for our study is SWAN (Simulating WAves Nearshore). This is a state-of-the-art, third generation, shallow water wave model developed in Delft University of Technology (Booij *et al.*, 1999 and Ris *et al.*, 1999). The model takes into account wave propagation, refraction, shoaling, wind generation, wave dissipation and quadruplet and triad wave interaction; it calculates the wave spectrum by numerically integrating the action balance wave equation from given wind, bottom and current conditions.

The HF radar measurements available for the study were obtained by an OSCR (Ocean Surface Current Radar) system in two measuring campaigns made off the coast of Holderness, north–east of England, as part of the SCAWVEX (Surface Current and Wave Variability Experiment) project (Wyatt *et al.*, 1998). This experiment was set up partly in response to the growing concern about the amount of coastal erosion on the coast of Holderness. The measurement campaigns, which comprised several wave measuring instruments, took place in the successive winters of 1994-95 and 1995-96. These radar measurements have already been compared with the buoy measurements from this same experiment (Wyatt *et al.*, 1999), and the latter will also be used here as an independent source of information.

Figure 5.26 shows in the top panel the region of the SWAN computational grid with depth contours, the location of the wind grid knots, and the locations where boundary directional wave spectra are taken from WAM model hindcasts. The grid lines coincide with computational grid knots 12 km apart. The bottom panel shows the locations where the HF radar measurements are available and the locations of two buoys that were deployed for the same experiment. Both SWAN and OSCR provide us with directional wave spectra with a resolution of 25 frequencies, equally spaced on a logarithmic scale between 0.03 Hz and 0.5 Hz, and 24 equally spaced directions. The OSCR spectrum results from the processing of data over a 1 hour period, and the SWAN spectrum is computed at the middle of that period. The SWAN hindcasts are computed at each of the OSCR cell locations. The number of locations at which OSCR measurements are available varies from hour to hour, depending on how many Doppler spectra are successfully inverted.

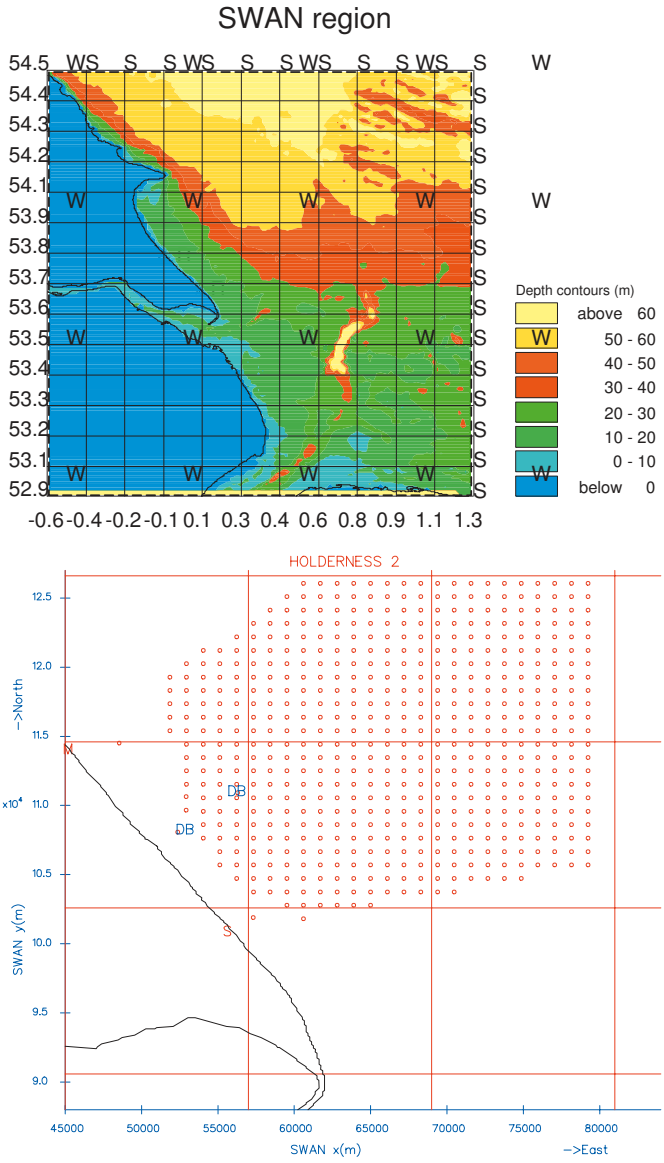

Figure 5.26: Top panel: The region of the SWAN computational grid with depth contours; W - locations of the wind grid knots, S - locations where boundary conditions are given. Bottom Panel: OSCR cells (∘), buoys (DB) locations, master (M) and (S) radar site.

It was not our objective to compare the directional wave spectra point by point, for this would be too time consuming and would not contribute to an understanding of the general character of the data. In order to reduce the data and to make meaningful comparisons between the OSCR and SWAN measurements, we have instead summarised the directional wave spectra in terms of the main wave parameters for different frequency bands.

Additionally, in our extensive comparisons we have classified the data into *wave scenarios*, i.e., data corresponding to sea states whose characteristics are sufficiently important and unique to be worth studying separately. This procedure was essential because the performances of both SWAN and OSCR are expected to depend on the wave scenario, a fact substantiated by our study. In particular, the quality of the SWAN hindcasts is highly dependent on the wave scenario. In the cases studied, the hindcasts are quite good when the wave systems are created within the SWAN computational area, but when the wave scenario is composed by wave systems created outside the computational area, SWAN usually underperforms.

Here we shall be analysing a specific wave scenario, observed during the period from 10 a.m. of the 7th until 7 p.m. of the 10th of January 1996, characterised by fetch limited wave growth, with waves moving mainly towards north–west, parallel to the coast line. The plots in Figure 5.27 compare the histograms of H_{m0}, T_{m01}, MWD and DSpr data from OSCR with the corresponding histograms of data from SWAN for this period. The two top graphs are ordinary frequency histograms; the other two are frequency histograms for circular data, the radius of each of the connected points representing the frequency of observations around its angle/direction. The plots allow a qualitative assessment of the comparisons. Overall, the comparisons seem to be reasonable, apart from a clear 20° offset between the two data sets of mean wave direction.

The following sections assess these data in more detail. The analysis is based on the statistical models presented in Part 1, Chapter 7.

5.5.3 Significant Waveheight

Let us recap the steps necessary to the fitting of the statistical models. Firstly, we classify the data into homogeneous subsets. From the analysis of the radar data a classification on the basis of location was the most appropriate. We then apply the pseudo-replication algorithm, PRA, to each subset, obtaining estimates of the parameters of the local functional relationship

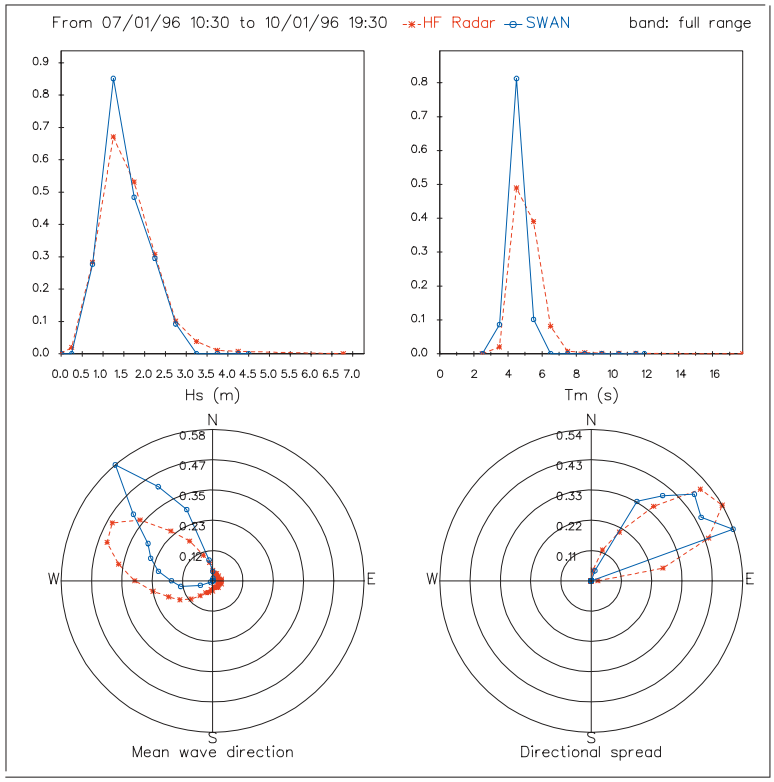

Figure 5.27: Comparison between histograms of the main wave parameters of OSCR and SWAN for the period from 10 a.m. of the 7th until 7 p.m. of the 10th of January 1996.

models. Finally, the data sets are pooled together and used to estimate the global functional relationship model.

Figure 5.28 shows the sample sizes of the local timeseries for the considered period; each sample size appears in the map/SWAN grid as the number at the location of the corresponding timeseries.[1] It is seen that the sample sizes can vary from 60 to 1. We have decided to apply the PRA only to samples with at least 6 observations. For these, we have computed the

[1]We have opted in this and in all other surface plots showing local statistics to print in colour the figures obtained at each location; using this representation instead of just colour contours enables us to assess the space variability of the data without any smoothing.

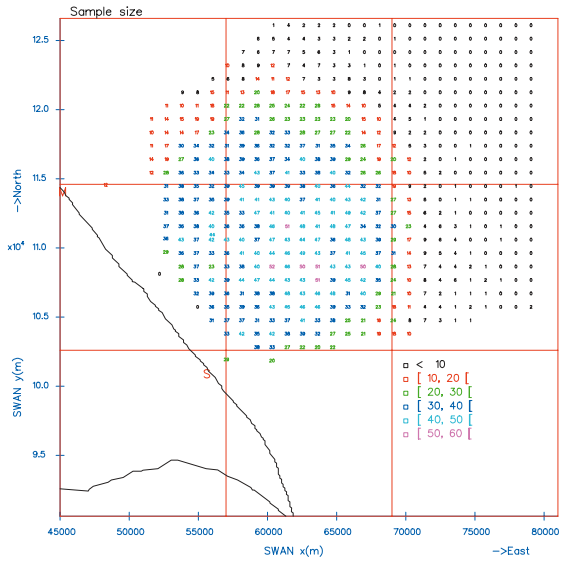

Figure 5.28: Sample sizes of the local timeseries for the period from 10 a.m. of the 7th until 7 p.m. of the 7th of January 1996.

(local) estimates of intercept, α, slope, β, variance of OSCR estimates, σ^2 and ratio of variances, λ, of the local linear functional relationship models.

The analysis of the surface estimates obtained allows the following comments:

- The estimates of α do not vary much spatially. At all cells around the central measuring area the values of $\hat{\alpha}$ vary around 0.2 m; in the north–east region of the measuring area $\hat{\alpha}$ takes negative values.
- The estimates of β to the south of the master radar site are mostly below 1, being very near 1 in an area around the location of the buoys. To the north of the master radar site the values of $\hat{\beta}$ are frequently above 1.
- The standard deviations of the random errors associated with the OSCR measurements range from values as low as 8 cm to values as high as 40 cm. The highest values occur at the cells located further south and east, in the borders of the measuring area. The errors are clearly small around the location of the buoys and a bit further east.

- The values of $\hat{\lambda}$ are mostly below 1, revealing that the errors of the radar are overall slightly larger than SWAN's. Over the region where the errors of the radar have lower standard deviations, the estimates of λ are around 0.8.

Having fitted functional relationship models to the local timeseries, we now have estimates of the local variances of the errors. Using these estimates we may fit a global functional relationship model to the data set obtained by pooling all local timeseries of H_{m0}. This set has a total of $n = 9033$ observations, and the maximum likelihood (ML) estimates of α and β are $\hat{\alpha} = 0.00$ and $\hat{\beta} = 0.97$. The scatter plot of the data with the fitted global functional relationship is presented in Figure 5.29, and suggests a reasonably good agreement between the radar and SWAN for the bulk of the data, whose observed errors are roughly symmetrically distributed.

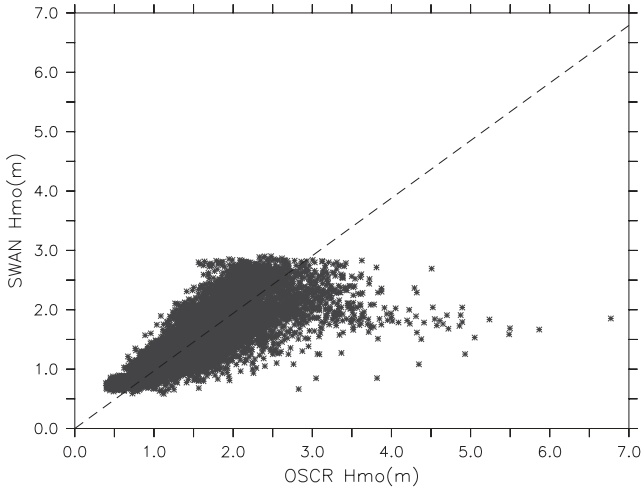

Figure 5.29: Scatter plot of H_{m0} data and fitted global functional relationship model; OSCR: x-variable; SWAN: y-variable.

The megaphone shape produced by the observations shows that the variance of H_{m0} measurements increases roughly linearly with their magnitude. Although the data were not explicitly classified in terms of waveheight, this is a feature associated with the radar measurements since the offshore and outer edge measurements have higher amplitudes and higher variances in general.

There are a number of outlying observations in the OSCR measurements, whose significant waveheights are above 3.5 m, and this is the aspect of the data that the linear model is intrinsically unable to explain. Indeed, the observed errors of the outliers are always positive (corresponding to overestimates of the radar), in clear violation of the assumption of a symmetric distribution for the errors. However these outliers do not affect our estimates (which are nearly the same as those obtained by discarding the outliers), because the global model accounts for the different variances and the outliers correspond to timeseries with large variances (having therefore negligible weight in the estimation process).[2]

In view of these observations, we may conclude that this global model explains the data quite well and provides sensible numerical estimates characterising the relationship between radar measurements and SWAN hindcasts of H_{m0}.

The OSCR measurements in the 0.03 to 0.1 Hz frequency range are often spurious due to sidelobe contamination (see Wyatt *et al.*, 1999 and e.g. section 5.2). Using only the 0.1 to 0.5 Hz range of the spectrum to compute the significant waveheight data (denoted by $H_{mo_{0.1}^{0.5}}$), the agreement is slightly better. For the local estimates we obtain values of $\hat{\alpha}$ even closer to zero, estimates of β considerably closer to 1, and values of $\hat{\sigma}^2$ are slightly smaller than those obtained by considering the full spectral range. This is specially true for those cells located in the south and east boundaries of the measuring area, which shows that bad measurements in these locations occur mainly at low frequencies. The estimates of λ are much closer to 1 than the corresponding estimates obtained with H_{m0} data. Since the estimates of σ^2 (the variance of the errors of the radar) have decreased, this increase in the estimates of λ indicates that there was practically no change in the errors of SWAN. For these data the global estimates of α and β were $\hat{\alpha} = 0.00$ and $\hat{\beta} = 0.98$. Apart from the slightly higher estimate of β and a slightly smaller dispersion around the fitted line, the results are very similar to those obtained with H_{m0} data. Thus, in spite of the systematic improvements observed in the local relationships, the global improvement is not very significant.

[2]Incidentally, if these data had been fitted with a local model (assuming equal variances), then of course the agreement between OSCR and SWAN would be poorer, since the slope of the line would have to decrease for the model to explain the highest observations of the radar. This is clear just from a simple linear regression, which would give us a slope of 0.6.

5.5.4 Mean Wave Period

From the estimates of the local functional relationship models for mean period we can draw the following conclusions. The estimates of β are very low, in most of the cells below 0.3. There are only a few locations, mainly to the north of the master radar site and closer to the shore, with estimates around 0.7. Practically all values of $\hat{\alpha}$ are above 0, and most between 2 and 4 seconds. There is a big scatter in the estimates of σ^2, whose values vary mainly between 0.01 and 0.4. The scatter of the λ estimates is enormous, with values ranging from 0.01 to 100.

A pronounced feature of the OSCR measurements of T_{m01} is that many of them seem to be erroneous or outlying. This is supported by the buoy/OSCR comparisons. Figure 5.30 shows the results of comparing OSCR with the offshore buoy. The left panel of the figure suggests that the correspondence between OSCR and the buoy is quite bad. However, the OSCR observation above 7 seconds seems to be an outlier. A better fit results if this observation is removed from the sample as can be seen the right panel of Figure 5.30. The estimates of $\hat{\alpha} = -0.49$ and $\hat{\beta} = 1.1$ reflect a clear agreement between OSCR and buoy.

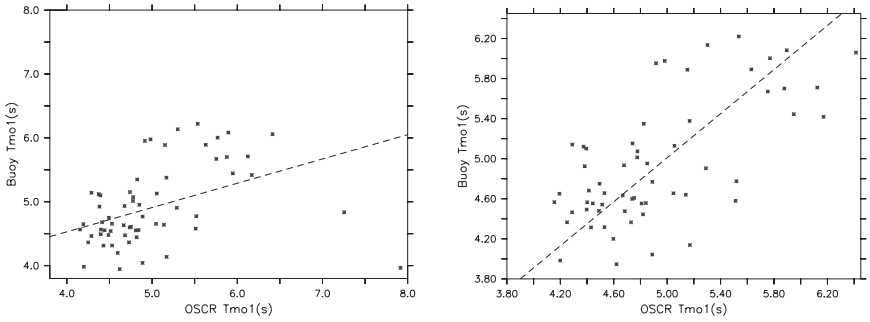

Figure 5.30: Scatter plot of OSCR (x-variable) and offshore buoy (y-variable) T_{m01} data, and fitted functional relationship line. Left panel: Considering all the data. Right panel: Discarding the OSCR observations of T_{m01} above 7 s.

This is an instance of a situation where an observation can be promptly identified as an outlier and its effect on the fitted model assessed on purely empirical grounds. As we have been noting, the poor results of the radar are due to a considerable amount of outlying observations in the data, many

of which are hard to identify.

At the buoy location the agreement between SWAN and the buoy is much worse than that between OSCR and the buoy without the outlying OSCR observation. This indicates that the disagreement between SWAN and OSCR is not solely due to OSCR outlying observations but also to poor SWAN hindcasts.

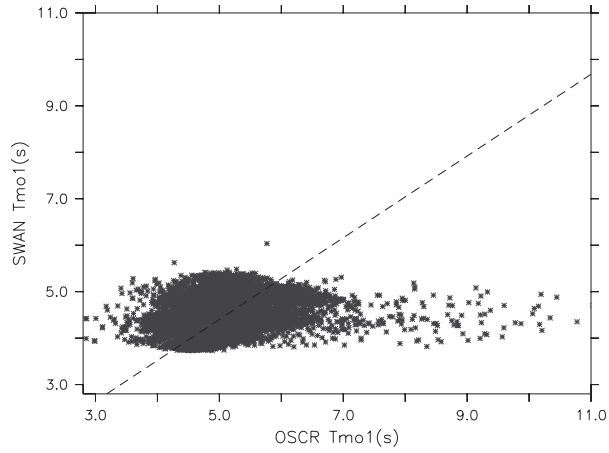

Figure 5.31: Scatter plot of T_{m01} data and the fitted global functional relationship; OSCR (x-variable) and SWAN (y-variable).

Pooling all the local timeseries together and using the estimates of the local variances of the errors, we have fitted a global functional relationship to the T_{m01} data. The scatter plot of the data and the fitted global functional relationship are presented in Figure 5.31. The ML estimates of α and β are $\hat{\alpha} = 0.00$ and $\hat{\beta} = 0.88$ (the sample size being 9033, as in the corresponding analysis of significant waveheight data).

The estimates of α and β are far better than those obtained with any of the local time series. Of course, it is enough to recall the local estimates and to look at Figure 5.31 to see that this does not mean that there is a good correspondence between OSCR and SWAN. What the global results mean, though, is that the radar and the wave model agree on average, but with very large errors. We note again that obtaining a fitted line with slope near 1 with these data is possible because the global model takes into account the different variances of errors; a simple linear regression would give a slope

estimate of about 0.13.

Considering only the 0.1 to 0.5 Hz range, $T_{m01}{}_{0.1}^{0.5}$, the results show that, although there are some improvements in the local comparisons, the estimates of the global model are the same as those obtained with the T_{m01} data, though in this case the data are slightly less scattered and do not contain as many outliers. This shows that the disagreement between SWAN and the radar in terms of the mean wave period is quite large, and that the lack of correspondence is not just restricted to the lower frequencies where the OSCR measurements are often spurious and the SWAN hindcasts may be poor due to inadequate boundary conditions. It is, in fact, a more general problem. Since the mean wave period data are very sensitive to the shape of the frequency spectrum, this indicates that the shape of the frequency spectra of OSCR and SWAN is quite distinct.

5.5.5 Mean Wave Direction

We have obtained estimates of directional difference, $\hat{\alpha}$, OSCR's concentration parameter (the equivalent of the variance for circular variables), $\hat{\kappa}$, and concentration parameter ratio, $\hat{\lambda}$, by fitting circular functional relationship models to the local mean wave direction (MWD) timeseries of OSCR and SWAN from the 3 day period being considered. From the analysis of these estimates, we can conclude the following. The offset between OSCR and SWAN data depends on the location; see Figure 5.32. At the further offshore cells in the middle of the measuring area the estimates of $\hat{\alpha}$ are of about 40°, decreasing to values below 20° in the northern cells and, in the direction of the coast, with values of $\hat{\alpha}$ in some cases below 10° in the cells closer to the shore. The spatial pattern of the α estimates indicates a dependence of the quality of the comparisons on water depth. The worst results are obtained at deep water locations, and the best results at locations with less water depth. This indicates that the wind directions used as input in SWAN are biased, this being particularly clear at the locations where the wave direction is not influenced by water depth. At locations of shallower waters, there is some wave refraction, and therefore a better agreement. — This claim of erroneous winds is also supported by the better agreement between OSCR and buoy measurements ($\hat{\alpha} = 3.5°$, offshore) than that between OSCR and SWAN ($\hat{\alpha} = 11.62°$, offshore).— However, differences are not solely explained by a bias in the wind direction; along with this, there is the fact that the quality of the OSCR measurements is worst in the areas where the correspondence is poorer, as was observed in the H_{m0} and T_{m01}

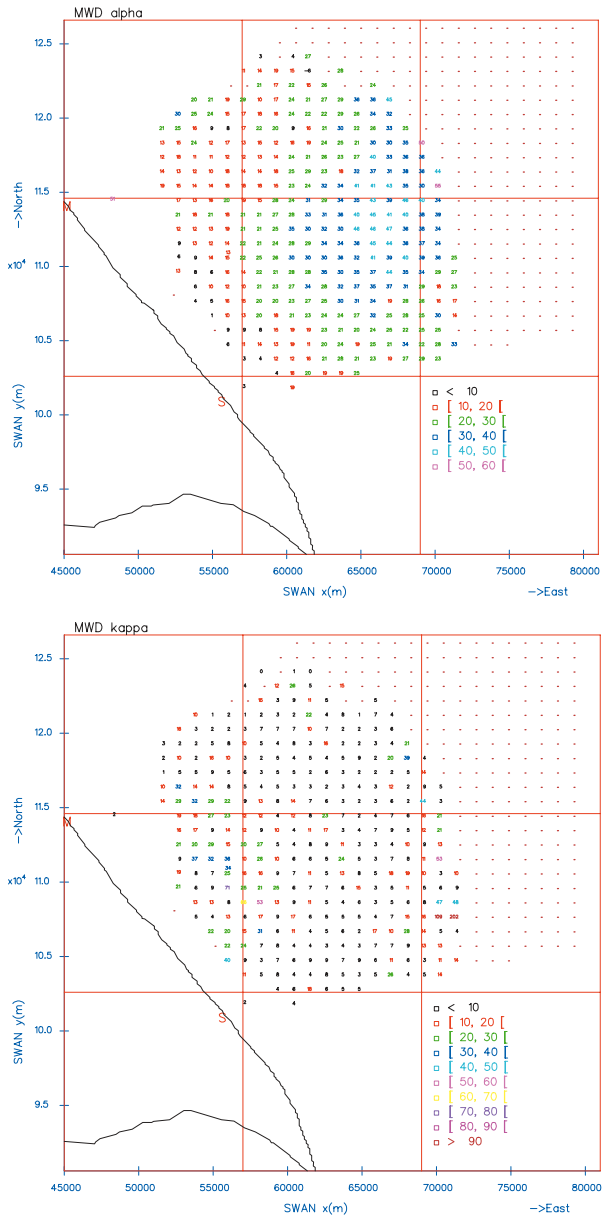

Figure 5.32: Top Panel: α estimates of the local functional relationship models. Bottom panel: κ estimates of the local functional relationship models. MWD of OSCR: x-variable, MWD of SWAN: y-variable.

comparisons. There is also a clear spatial pattern in the κ estimate; see Figure 5.32. If we imagine drawing a circle with centre a bit to the north of the mid point between the two radar sites on the coast and enclosing 6 vertical lines of radar cells in that central region, we see that at the cells enclosed by the circle the estimates of the concentration parameter of the errors associated with OSCR are usually above 20 (standard deviation below 13°), and that as we move away from the circle the values drop below 10. This circle represents roughly the area where more reliable measurements are obtained. The values of $\hat{\lambda}$ are very high. Estimates of λ below 5 are found only in the central measuring area, closer to the shore; elsewhere, most of the estimates are above 5, with higher values in the northern cells. This pattern indicates that the errors associated with SWAN have smaller standard deviations (whose values are usually below 7°) than those of the radar.

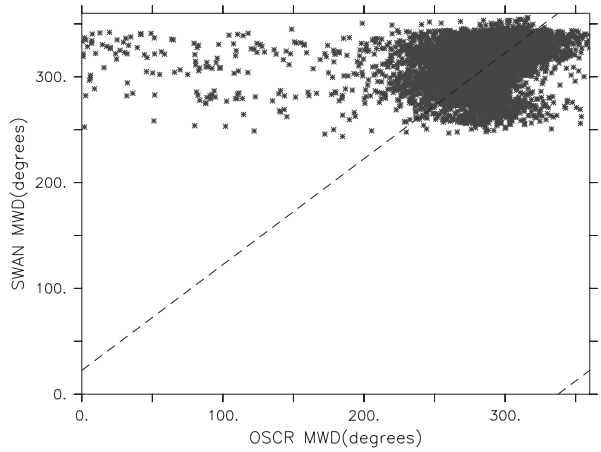

Figure 5.33: Scatter plot of MWD data and fitted global functional relationship model; OSCR: x-variable; SWAN: y-variable.

Figure 5.33 shows the scatter plot of the MWD data of OSCR and SWAN with the fitted global functional relationship model (obtained using the local estimates of the concentration parameter). With these data we get the estimate $\hat{\alpha} = 22.45°$, which gives the overall offset between OSCR and SWAN. Again, care must be taken in interpreting these results: not only is the rotation between radar and wave model data not homogeneous over the whole area, as there is a large quantity of outlying observations, a large

dispersion, and the model does not really fit the data.

For the $MWD_{0.1}^{0.5}$ data the values of $\hat{\alpha}$ are higher than for the MWD data by as much as 10° in some locations, with values ranging from 9° to 50°. The increase in the values of $\hat{\alpha}$ is no indication that the low frequency mean wave direction measurements is good. What is happening here is that there is a clockwise angular difference between the OSCR measurements and the SWAN hindcasts for frequencies above 0.1 Hz, and an anticlockwise angular difference between the OSCR measurements and the SWAN hindcasts in the low frequency part of the spectrum. The offset in the low frequencies is a lot higher than over the rest of the spectrum, and the net effect in MWD is to falsely show an agreement between the two data sets.

5.5.6 Directional Spread

In the analysis of directional spread data (see Figure 5.34) we find that, although there is some spatial dependence in the estimated rotation parameter, the concentration parameters of the errors show no clear dependence on the location. We have also investigated whether there was a dependence of the errors on other factors, but no evidence of such dependence was found. Thus, contrary to what was found about the other parameters, the random errors associated with the directional spread data seem to be quite homogeneous.

The maps in Figure 5.34 show α and κ estimates of the local circular functional relationship models fitted to OSCR and SWAN data of directional spreading ($DSpr$). Looking at Figure 5.34, we can see that the values of $\hat{\alpha}$ vary between -10 and 10°, with the negative values occurring mainly at the offshore boundary of the measuring area and at the cells to the north of the master radar site. The estimates of κ are high, usually above 30, and in some locations exceeding 200. The lower values occur at the further offshore locations to the north of the master radar site. The corresponding values of $\hat{\lambda}$ (not shown here), have no well defined spatial pattern, being mostly greater than 1, indicating lower standard deviations of the errors of SWAN hindcasts than the standard deviations of the errors of OSCR.

Pooling all $DSpr$ data of OSCR and SWAN and fitting a global circular functional relationship to it, we obtain an estimate of $\hat{\alpha} = 2.64°$. The scatter plot of these data is shown in Figure 5.35 with the fitted line. As can be seen from the picture, there is a big scatter in the observations, and the low value of $\hat{\alpha}$ only indicates an average agreement.

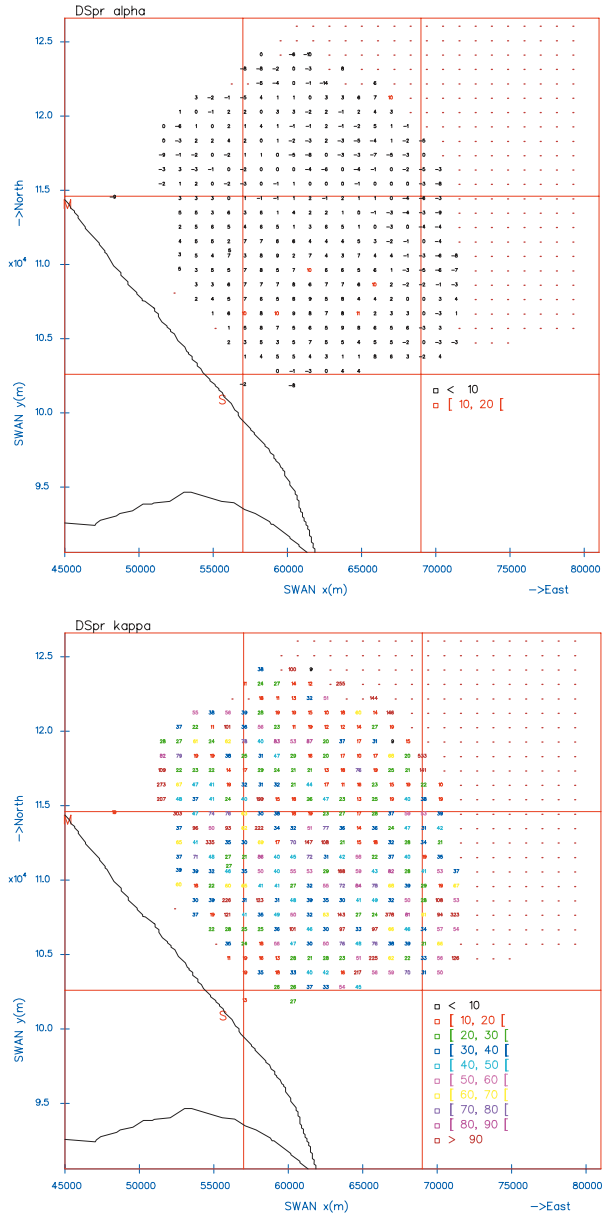

Figure 5.34: Top panel: α estimates of the local functional relationship models. Bottom panel: κ estimates of the local functional relationship models. *DSpr* of OSCR: x-variable, *DSpr* of SWAN: y-variable.

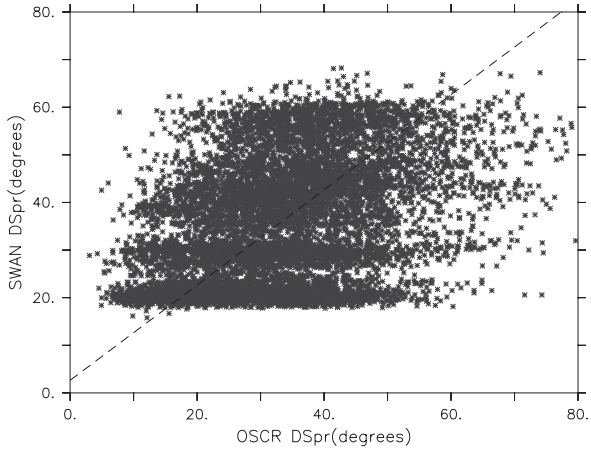

Figure 5.35: Scatter plot of *DSpr* data and fitted global functional relationship model; OSCR: x-variable; SWAN: y-variable.

Discarding the low frequency observations we would obtain a rotation of $\hat{\alpha} = -0.02^\circ$ degrees, and still a big scatter in the observations, specially in the OSCR measurements, although less than that observed in the comparisons accounting for the whole frequency range.

5.5.7 Conclusions

The main conclusion of our extensive study—of which we have only analysed a small period here—were that on average OSCR is able to measure the sea state but with a very large variation and many outliers. The best performance is achieved in the 0.1–0.5 frequency range and the wave parameter that is better measured is the significant waveheight. The quality of the measurements depends on the spatial location at which they are made, and the more reliable measurements are obtained at the radar cells within shorter range from the two radar sites and at the centre of the measuring area. We note that it is in this region where all previous quantitative assessments of HF radar data quality have been made. The radar performance is worse in terms of the mean wave period. This parameter is very sensitive to the actual shape of the frequency spectrum, and a good match will always be hard to find. However, the radar seems to behave quite well when the

outliers are successfully identified. The radar measurements of mean wave direction are good in most of the cases, but the occurrence of bad measurements seems to be quite random and difficult to identify. There is a big question mark on the accuracy of the directional spread measurements. Although on average the measurements are in fact quite good, the scatter of the data is so large that this might even be regarded as purely coincidental.

Regarding the quality of the radar measurements in terms of spectral frequency (not presented here), the best radar measurements correspond to the central area of the spectrum in the 0.1–0.3 frequency range. The low frequency measurements are often spurious due to sidelobe contamination (see Wyatt *et al.*, 1999 and e.g. section 5.2). This is a clear handicap of these radar systems, since the waves at these frequencies are the most important in terms of structural design of offshore and coastal structures and clearly a solution for this problem must be sought.

In terms of the random errors associated with each of the main wave parameters of OSCR, the main result of our research is that the contribution of the spatial location over which the measurement is made bears much more importance than the sampling variability associated with each measurement.

The above are conclusions on the performance of the radar. We shall now state the conclusions about the performance of SWAN.

The quality of the SWAN hindcasts is highly dependent on the wave scenario. In the cases studied, the hindcasts are quite good when the wave systems are created within the SWAN computational area. When the wave scenario is composed by wave systems created outside the computational area, SWAN usually underperforms.

In terms of the mean wave period, SWAN's performance is quite poor. As said, this parameter is very sensitive to the shape of the wave frequency spectrum. SWAN's underestimation of the swell energy, due to the poor quality of the boundary waves, along with the errors in the current velocity field, affecting the shape of the high frequency spectrum, and the possible errors in the driving wind fields velocities, contribute to an overall bad performance of SWAN in terms of the mean wave period in the whole frequency range.

The quality of SWAN's mean wave direction hindcasts is highly dependent on the quality of the driving winds, specially in the deeper water locations. At these locations, quite large offsets between SWAN and the measuring instruments were found. In shallower waters the discrepancies are not so large, indicating a proper modelling of wave refraction by SWAN.

SWAN's directional spread hindcasts seem to be reasonable in terms of what is currently known about this parameter. Although there are some discrepancies between SWAN's hindcasts and the corresponding radar and buoy measurements of the directional spread, specially in the low frequency part of the spectrum. Because the quality of the measurements seems to be dubious we do not have enough information to further comment on this.

The estimated variances/concentration parameters associated with SWAN's hindcasts of the main wave parameters are consistently lower than those associated with the radar. Contrary to the radar, the SWAN errors are highly dependent on the wave scenario and do not change much spatially. This is expected since the SWAN predictions result from the numerical integration of several quantities and consequently are expected to have considerably less variability.

5.6 References

Banner, M.L. and I.R. Young, Modeling spectral dissipation in the evolution of wind waves. Part 1: Assessment of existing model performance. *Journal of Physical Oceanography*, 24, 1550-1571, 1994.

Booij, N., R.C. Ris, and L.H. Holthuijsen, A third-generation wave model for coastal regions. 1. Model description and validation. *J. of Geophys. Res.*, 104 (C4), 7649-7666, 1999.

Caires, S., Comparative study of HF radar measurements and wave model hindcasts of waves in shallow waters. PhD thesis (unpublished), University of Sheffield, 2000.

Capon, J., High resolution frequency wavenumber spectrum analysis. *Proceedings of the IEEE*, 57, 1408-1418, 1969.

Donelan, M.A., W.M. Drennan, and A.K. Magnussen, Nonstationary analysis of the directional properties of propagating waves. *Journal of Physical Oceanography*, 26, 1901-1914, 1996.

Ewans, K.C., Observations of the directional spectrum of fetch-limited wave. *Journal of Physical Oceanography*, 28, 495-512, 1998.

Fisher, N.I. and A. J. Lee, A correlation coefficient for circular data. *Biometrika*, 70, 327-332, 1983.

Günther H., K.-W. Gurgel, G. Evensen, J. Guddal, J.-C. Nieto Borge, and L. R. Wyatt, European radar ocean sensing. *Proceedings of EurOCEAN*

2000, Hamburg, 2000, 443-448, 2000.

Gurgel K.-W., G. Antonischki, H-H. Essen and T. Schlick, Wellen Radar (WERA): a new ground-wave HF radar for ocean remote sensing. *Coastal Engineering*, 37, 219-234, 1999.

Hashimoto, N., Analysis of the directional wave spectrum from wave data. *Advances in Ocean and Coastal Engineering*, 3, 103-143, 1997.

Hessner K., K. Reichert and J. Dittmer, *EuroROSE Experiment 2 – October/November 2000, Cabo Peñas – Cabo de Torres*, May 2001, OceanWaveS GmbH, internal report, 2001.

Kingsley S.P., A.M. Torregrossa and L.R. Wyatt, Analysis of second order HF radar sea spectra recorded in storm conditions. *Proceedings of Oceans'98, Nice, France, September 1998, pub IEEE*, 459-462, 1998.

Krogstad H.E., J. Wolf, S.P. Thompson and L.R. Wyatt, Methods for intercomparison of wave measurements. *Coastal Engineering*, 37, 235-258, 1999.

Kuik, A. J., G. Ph. van Vledder, and L. H. Holthuijsen, A method for the routine analysis of pitch-and-roll buoy wave data. *Journal of Physical Oceanography*, 18, 1020-1034, 1988.

Lygre, A. and H.E. Krogstad, Maximum entropy estimation of the directional distribution in ocean wave spectra. *Journal of Physical Oceanography*, 16, 2052-2060, 1986.

Ris, R.C., L.H. Holthuijsen, and N. Booij, A third-generation wave model for coastal regions. 2. Verification. *Journal of Geophysical Research*, 104 (C4): 7667-7681, 1999.

Shearman, E.D.R. and M.D. Moorhead, PISCES: A coastal ground-wave radar for current, wind and wave mapping to 200km ranges. *IGARSS'88 proceedings*, 773-776, 1988.

Sova, M.G., The sampling variability and the validation of high frequency wave measurements of the sea surface. PhD thesis, University of Sheffield, 1995.

Wyatt, L.R. and G.J. Holden, Limits in direction and frequency resolution for HF radar ocean wave directional spectra measurement. *The Global Atmosphere and Ocean System*, 2, 265-290, 1994.

Wyatt, L.R., High order nonlinearities in HF radar backscatter from the ocean surface. *IEE proceedings–Radar, Sonar and Navigation*, 142, 293-300, 1995.

Wyatt, L.R., L.J. Ledgard, and C.W. Anderson, Maximum likelihood esti-

mation of the directional distribution of 0.53 Hz ocean waves. *Journal of Atmospheric and Oceanic Technology*, 14, 591-603, 1997.

Wyatt, L.R., K.-W. Gurgel, H.C. Peters, D. Prandle, H.E. Krogstad, O. Haug, H. Gerritsen, G.J. Wensink, The SCAWVEX Project. *Ocean wave measurement and analysis, Proceedings of WAVES 97*, Eds. B.L.Edge and J.M.Hemsley, vol 2, 1457-1467, 1998.

Wyatt, L.R., HF radar measurements of the development of the directional wave spectrum. *The Wind-Driven Air-Sea Interface. Electromagnetic and acoustic sensing, wave dynamics and turbulent fluxes*, ed M.L. Banner, School of Mathematics, UNSW, Sydney, Australia, 433-440, 1999.

Wyatt, L.R., S.P. Thompson and R.R. Burton, Evaluation of HF radar wave measurement. *Coastal Engineering*, 37, 259-282, 1999.

Wyatt, L. R., Limits to the inversion of HF radar backscatter for ocean wave measurement. *Journal of Atmospheric and Oceanic Technology*, 17, pp. 1651-1666, 2000.

Wyatt, L. R. and J. J. Green, The EuroROSE Project–Validation and Intercomparison of wave measurements and models at Fedje. *SCEOS report*, University of Sheffield, 2001.

Wyatt, L. R., J. J. Green, K.-W. Gurgel, J.-C. Nieto Borge, K. Reichert, K. Hessner, H. Günther, W. Rosenthal, O. Saetra and M. Reistad, Comparisons of wave measurements during the EuroROSE Fedje experiment. *Ocean wave measurement and analysis, Proceedings of WAVES 2001*, Eds. B.L. Edge and J.M. Hemsley, vol 1, 201-210, 2002.

Wyatt, L. R., J. J. Green, K.-W. Gurgel, J.-C. Nieto Borge, K. Reichert, K. Hessner, H. Günther, W. Rosenthal, O. Saetra and M. Reistad, Validation and intercomparisons of wave measurements and models during the EuroROSE experiments. *Coastal Engineering*, 48, 1-28, 2003.

Young, I.R., L.A. Verhagen and M.L. Banner, A note on the bimodal directional spreading of fetch-limited waves. *Journal of Geophysical Research-C*, 100, 773-778, 1995.

Chapter 6

Marine Radar

6.1 Comparison of WaMoS II with In-situ Measurements

Katrin Hessner[a]*, José Carlos Nieto Borge*[b]

[a] OceanWaveS GmbH, Lüneburg, Germany
[b] German Aerospace Centre (DLR), Oberpfaffenhofen, Germany

6.1.1 Introduction

In the last 30 years routine sea state measurements were carried out mainly using moored wave buoys. As these devices are easily subject to damage and loss, considerable interest has been shown lately in the use of remote sensing techniques. One method to remotely measure the sea state is based on the analysis of radar backscatter signals from the sea surface, received in the near range of a nautical X-Band radar. Such a system was developed at the German research centre GKSS and is now commercially available from OceanWaveS GmbH. This system has been designed for the automatic wave monitoring from coastal sites, off-shore platforms and from board all types of ocean going vessels. For more detailed information about the measurement technique see section 6.1.2 in this Part 2 and section 5.3 of Part 1. In contrast to in-situ wave sensors like e.g. buoys, which are based on the temporal analysis of the buoy motion using accelerometer and tilt sensors, radar measurements of the sea state are based on the analysis of the temporal and spatial evolution of the radar backscatter information. Hence the resulting wave information from WaMoS II measurements include also

spatial information of the sea state. This allows the direct determination of directional properties of the sea state with high accuracy. In order to obtain statistically representative wave measurements, in-situ sensors like buoys or lasers sample typically the sea surface elevation for about 20-30 minutes. From these time series the wave energy spectrum and hence the sea state parameters like significant waveheight, peak wave period, peak wave direction, etc. are determined. For a single standard wave measurement, WaMoS II analyses a time series of radar images taken within one minute covering an area of about 2 km × 1 km. In order to cover a similar temporal time domain with WaMoS II measurements as with in-situ measurements, the resulting WaMoS II wave spectra are averaged over the same time interval. This allows all directional information to be retained. From the mean wave number spectrum the frequency direction spectrum, the energy spectrum and hence all standard wave parameter are determined. These parameters represent spatial means over an area of 2 km × 1 km and temporal means over the chosen time interval (20-30 minutes). In contrast to that, the in-situ sensors like buoys or down looking lasers are temporal means of point measurements.

In this chapter operationally collected WaMoS II wave data are compared to in-situ measured wave data. For the main sea state parameters, such as significant waveheight, peak wave period and peak wave direction, error statistics are applied. The measurements are from a safety and rescue vessel (*Golfo de Vizcaya*, Spain), from deep water off-shore oil platforms (*Ekofisk*, Norway; *FPSO Norne*, Norway; *FPSO Terra Nova*, Canada), from an oil shuttle (*Navion Oceania*, Norway), and from a shallow water coastal station (Heligoland, Germany).

6.1.2 Description of WaMoS II System

WaMoS II (Wave Monitoring System) is an operational wave monitor consisting of a high speed video digitising and storage device, a marine radar, and a standard PC for wave analysis, data storage, and/or communication (see Fig. 6.1). The analog radar video signal is read out and transferred to the PC where analysis software carries out the computation of sea state parameters in real time. Data can be accessed either directly, via removable media or on-line via modem, local area network, Internet, etc. (Hessner *et al.*, 1999).

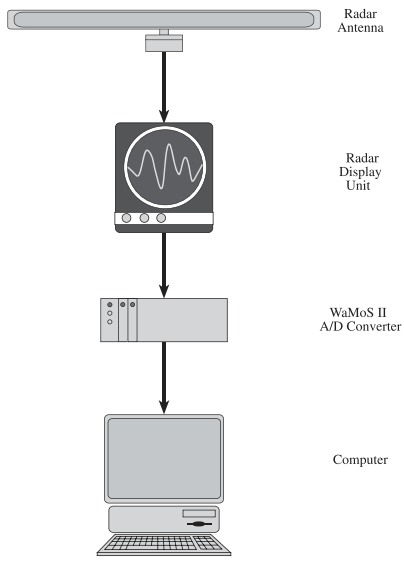

Figure 6.1: Scheme showing a WaMoS II installation. The data are digitised by the WaMoS II A/D converter and transferred to a PC, where the data analysis, storage and remote communications are carried out.

Description of WaMoS II Data Sets

The WaMoS II wave analysis raw data sets are composed of time series of consecutive images of the sea surface. For standard wave analysis, a common WaMoS II time series has 32 sea surface images, each one formed of 128 times 256 pixels. For common X-band nautical radars and a WaMoS II sampling frequency of 20 MHz (pulse length 50 ns) those data sets have a spatial resolution of 7.5 m and a coverage of about 1 km in range times 2 km in azimuth. With an antenna repetition rate of about 2 s, time series duration is about 1 minute. Thus the total WaMoS II measurement time, that includes data acquisition plus wave analysis, is about one minute.

To compare WaMoS II results with time domain in-situ sensors, such as buoys, lasers, etc., it is necessary to set up the WaMoS II software control parameters to cover a similar temporal coverage to the in-situ sensor, typically between 20 and 30 minutes (Reichert *et al.*, 1998; Reichert *et al.*, 1999). Therefore the single wave spectra are averaged over the same period. Hence assuming a single WaMoS II wave measurement every 2 minutes, the

20 minute means consist of 10 single measurements. Therefore the wave spectral estimates are smoothed with 20 degrees of freedom (d.o.f).

WaMoS II Wave Data Processing

The result of the WaMoS II analysis is the wave number spectrum $\Psi(\boldsymbol{k})$ from which other spectral density functions of the wave field can be derived. The frequency-direction spectrum $E(\omega, \theta)$ is computed taking into account the dispersion relation $\omega(\boldsymbol{k}; h, \boldsymbol{U})$ and the appropriate Jacobian function to convert from $\boldsymbol{k}$-space to (ω, θ)-space (Nieto Borge *et al.*, 2000):

$$E(\omega, \theta) \;=\; \Psi(\boldsymbol{k}(\omega; h, \boldsymbol{U}))\, k\, \frac{dk}{d\omega} \tag{6.1}$$

where $\boldsymbol{k}(\omega; h, \boldsymbol{U})$ is the inverse function of the dispersion relation and $dk/d\omega$ is the inverse value of the wave group velocity. The one dimensional frequency spectrum $S(\omega)$ is computed by integrating $E(\omega, \theta)$ over all the possible wave directions:

$$S(\omega) \;=\; \int_0^{2\pi} E(\omega, \theta)\, d\theta \tag{6.2}$$

Knowing $E(\omega, \theta)$ and $S(\omega)$, the directional spreading function is computed by:

$$D(\omega, \theta) \;=\; \frac{E(\omega, \theta)}{S(\omega)} \tag{6.3}$$

The function $D(\omega, \theta)$ provides the full description about the directional motions of the wave field. The standard directional parameters, such as mean wave direction, peak direction, angular spreading, etc. are derived directly from $D(\omega, \theta)$. For example, the mean wave direction $\bar{\theta}(\omega)$:

$$\bar{\theta}(\omega) \;=\; \tan^{-1}\left[\frac{b_1(\omega)}{a_1(\omega)}\right] \tag{6.4}$$

and the directional spread (see Part 1 in this book):

$$\sigma_1(\omega) \;=\; \sqrt{2\left[1 - \sqrt{a_1^2(\omega) + b_1^2(\omega)}\right]} \tag{6.5}$$

where $a_1(\omega)$ and $b_1(\omega)$ are the first coefficients of the Fourier expansion for $D(\omega, \theta)$

$$a_1(\omega) = \int_0^{2\pi} D(\omega,\theta)\,\cos\theta\,d\theta \quad ; \qquad b_1(\omega) = \int_0^{2\pi} D(\omega,\theta)\,\sin\theta\,d\theta \tag{6.6}$$

From the $S(\omega)$ the standard wave parameter peak wave period T_p and peak wave direction θ_p are inferred:

$$T_p = \frac{2\pi}{\omega_p} \tag{6.7}$$

$$\theta_p = \bar{\theta}(\omega_p) \tag{6.8}$$

where ω_p is the location of the energy maximum in $S(\omega)$

$$S(\omega_p) = \max[S(\omega)] \tag{6.9}$$

The WaMoS II estimator of T_p uses the centroid formula (PIANC-IAHR, 1986):

$$T_p \approx 2\pi \frac{\int_{\omega_1}^{\omega_2} \hat{S}(\omega)d\omega}{\int_{\omega_1}^{\omega_2} \omega\,\hat{S}(\omega)d\omega} \qquad ; \text{where } \hat{S}(\omega_1) = \hat{S}(\omega_2) = 0.8 \cdot \max[\hat{S}] \tag{6.10}$$

and $\hat{S}$ is the smoothed periodogram (the discrete Fourier transform estimation of $S(f)$). The expression 6.10 is the recommended T_p estimator by the International Navigation Association (PIANC-AIPCN) and the International Association for Hydraulic Research (IAHR-AIRH).

In contrast to wave parameters like e.g. T_p and θ_p which can be determined directly from the radar images, the significant waveheight H_s cannot be determined directly. The reason for this is the non-linearity of the imaging mechanism of ocean waves in radar images. Alpers and Hasselmann (1982) developed a method to derive the significant waveheight (H_s) from synthetic aperture radar (SAR) imagery obtained by ERS-1 over the ocean. The basic idea of this method is that H_s is assumed to be linearly correlated with the square root of the signal-to-noise ratio (SNR) of the radar image, where

the signal is the relative wave energy in the image spectrum, and the noise energy is due to the speckle spectral components closely connected with the wind speed responsible of the local roughness on the sea surface.

$$H_s = c_0 + c_1\sqrt{SNR} \tag{6.11}$$

where c_0 and c_1 are calibation constants dependant on the radar installation. The calibration is needed because the radar intensity images are measured with a relative grey level scale and there is not a direct information about the radar cross section (see section 6.1.2 in the Part 1 of this book).

The successful use of this method also for the determination of the significant waveheight from nautical radar images has been shown for various installations (Ziemer and Günther, 1994; Nieto Borge, 1998; Nieto Borge *et al.*, 1999).

6.1.3 Comparisons

For the comparisons WaMoS II measurements at various types of applications were used:

- Rescue and safety vessel: *Golfo de Vizcaya*, Oil vessel: *Navion Oceania*.
- Coastal site: Island of Heligoland.
- Off-shore platform: *Ekofisk*, *Norne* and *Terra Nova*.

The comparisons were carried out with different in-situ sensors

- Pitch and roll buoy.
- Shallow water buoy, directional.
- Laser.

and for different sea state properties, such as spectral wave information $S(\omega)$, $\bar{\theta}(\omega)$, $\sigma(\omega)$ and main wave parameters significant waveheight H_s, peak wave period T_p and peak wave direction θ_p.

For the comparison one needs to know that in-situ sensors like buoys determine the significant waveheight H_s directly from the spectrum, or from the

statistical analysis of the wave elevation time series, while WaMoS II uses the signal to noise ratio relation (Eqn. 6.11).

The buoy peak period used here have been estimated by locating the frequency of the maximum energy in the periodogram. This estimator presents a high variability and depends on the frequency resolution and each specific realisation of the wave elevation stochastic process. The WaMoS II uses the centroid method (Eqn. 6.10) for the determination of T_p.

Installation on Moving Ships

In this section two data sets are presented. The first one was obtained in February 1995 in the Bay of Biscay. For this data set a comparison of spectral directional wave properties obtained by WaMoS II onboard *Golfo de Vizcaya* and a pitch-roll buoy is shown. The second data set was obtained in the northern North Sea. For this data set, a comparison of H_s, T_p and θ_p is presented.

Bay of Biscay A Seatex WaveScan buoy (Hippy-120) was used as in-situ sensor. The buoy was deployed in deep water (600 m mooring depth) in the Bay of Biscay, close to the northern coast of Spain. It measured time series of heave, pitch and roll motions, and compass with a duration of 24 minutes and a sampling rate of 1 s. Pitch-roll buoys measure three geometrical properties of the wave field at a fixed point of the ocean. Those are heave $\eta(t)$, west–east wave slope $\eta_x(t)$ and south–north wave slope $\eta_y(t)$. It is well known that, with these three wave properties, only the first four Fourier coefficients (a_1, a_2, b_1 and b_2) of the directional spreading function $D(f,\theta)$ can be estimated by:

$$\begin{aligned} D(\omega,\theta) &= \frac{1}{\pi}\left\{\frac{1}{2} + a_1(\omega)\cos\theta + b_1(\omega)\sin\theta \right. \\ &\quad \left. + a_2(\omega)\cos 2\theta + b_2(\omega)\sin 2\theta\right\} + \Delta(\omega,\theta) \end{aligned} \tag{6.12}$$

where $\Delta(\omega,\theta)$ is the unknown part of $D(\omega,\theta)$. Therefore only estimations of $a_1(\omega)$, $a_2(\omega)$, $b_2(\omega)$ and $b_2(\omega)$, as well as parameters derived from them, are used for comparison.

The WaMoS II data were obtained on board the safety and rescue vessel *Golfo de Vizcaya* which was passing the buoy anchoring position, at a speed

of 4 knots. The WaMoS II was connected to a radar with the following characteristics: antenna rotation period of 2.5 s, pulse length of 80 ns (range resolution of 12 m), azimuthal resolution of 0.8° and a nominal emission power of 10 W. For this installation the WaMoS II measurements represent spatial means over 1536 m × 3072 m (4.7 km^2) and temporal means over 80 s. While the ship was passing the buoy, the sea state was a long swell case coming from north-west. For the comparison 6 independent WaMoS II measurements taken in the direct vicinity of the buoy are used. Figure 6.2 shows the 4 directional Fourier coefficients (a_1, a_2, b_1, b_2) as obtained by WaMoS II (solid line) and the WaveScan buoy (dotted line)

It can be seen that there is generally good agreement between the buoy and the WaMoS II measurements. The main differences are located in the region of high frequencies, where the effect of a Doppler shift due to a relative motion between the radar and the wave field is largest. In the standard WaMoS II analysis the effect of the motion can be corrected by taking into account the Doppler part of the dispersion relation. This is possible because WaMoS II can determine the necessary current information from the spatial and temporal evolution of the wave field. Buoys measure only the temporal surface elevation, hence additional current information would be needed in order to compensate the effect of the current. Figure 6.3 shows the estimated frequency spectra $S(\omega)$ (top right) the mean direction $\bar{\theta}(\omega)$ (bottom left) and the angular spreading $\sigma(\omega)$ (bottom right) measured on February 14, 1995 at 11:00GMT. The solid line represents the WaMoS II data, the dotted line the Wavescan buoy data. Note, the WaMoS II spectral estimates are smoothed with 12 degrees of freedom (d.o.f.). The buoy results were smoothed with 16 d.o.f.

Only the common frequency domain has been plotted. This WaMoS II measurement has a lower Nyquist limit than the buoy, because of the difference in the sampling time of the sensors: 2.5 s for the radar and 1 s for the buoy.

There is a good agreement between both results. Both sensors have an energy peak at about 0.7 Hz. The corresponding wave direction is about 315°, which represents a swell system with about 13 seconds peak period coming from north–west. The wave spreading for both sensors is about 30°-40° also lowest at the peak.

Northern North Sea The time series of WaMoS II wave parameters was obtained onboard the oil shuttle *Navion Oceania* (Statoil, Norway) from February 10 - 22, 2000. During this time the *Navion Oceania* stayed in the

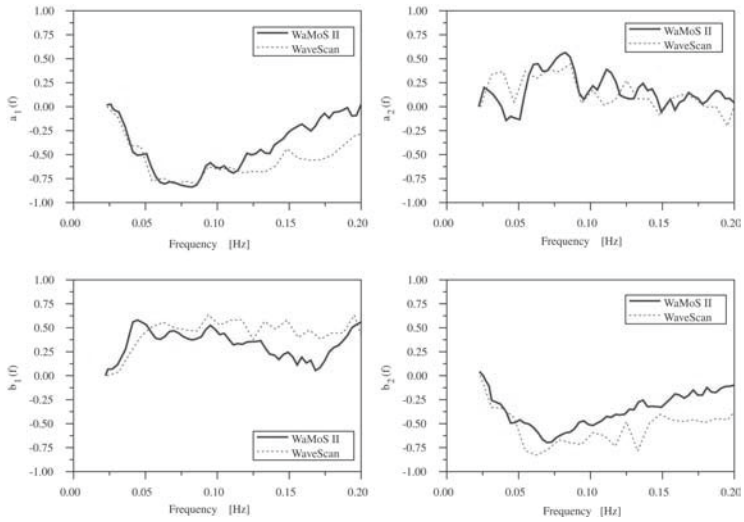

Figure 6.2: Comparison of the first four Fourier coefficient of the directional spreading function for a swell case measured in the Bay of Biscay in 1995. Solid lines indicate WaMoS II, dotted lines the WaveScan pitch-roll buoy results.

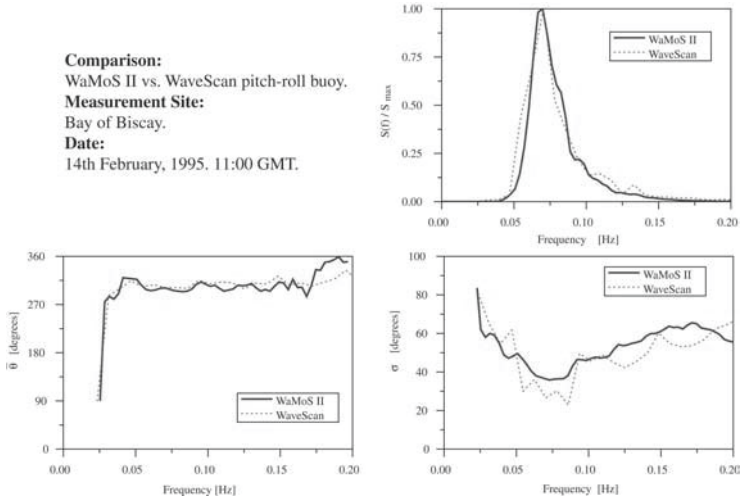

Figure 6.3: The frequency spectrum $S(\omega)$ (top right), the mean direction $\bar{\theta}(\omega)$ (bottom left) and the angular spreading $\sigma(\omega)$ (bottom right) were measured on February 14, 1995 at 11:00GMT. The solid line represents the WaMoS II data, the dotted line the WaveScan buoy data.

vicinity of the FPSO *Norne* (66°1.23'N, 8°6.4'E), where reference data from a buoy deployed nearby was available. The buoy data are 20 minute mean values. In Fig. 6.4 the main sea state parameters, significant waveheight H_s, peak wave period T_p, and peak wave direction θ_p are shown. The WaMoS II measurements are 30 minutes mean values and cover an area of about 1.8 km^2.

The time series of all three wave parameters show good agreement between the two measurements. Again small deviations due to natural variations of the significant waveheight are visible. Further it has to be taken into account that the two sensors do not exactly cover the same areas and local variations of the sea are possible. Two sensors of the same kind deployed, for example, about 200 m apart, deliver deviation of about 10%.

The statistical analysis of the data delivered the following relative error for H_s, T_p, and θ_p given in Table 6.1. Note that these errors include also the error of the buoy measurements.

Wave Parameter	Symbol	Relative error
Significant waveheight	H_s	11%
Peak wave period	T_p	3%
Peak wave direction	θ_p	10°

Table 6.1: WaMoS II error statistics, *Navion Oceania* at Norne February 1999.

Off Shore Sites

In this section two data sets are presented. The first one was obtained at Ekofisk located in the central North Sea. The second one was obtained at Terra Nova, Grand Banks, Canada. For both data sets a comparison of H_s, T_p and θ_p is presented.

Central North Sea, Ekofisk The radar data presented in this section were obtained at a WaMoS II site located in the Ekofisk oil field in the central North Sea, operated by Phillips Petrol. The standard sea state parameters are transferred in real time to the Norwegian Met Office (DNMI). Since 1992 these data have entered DNMI's Extreme Wave Warning program. The wave data presented were obtained from January 28 - February 6, 2000. In this

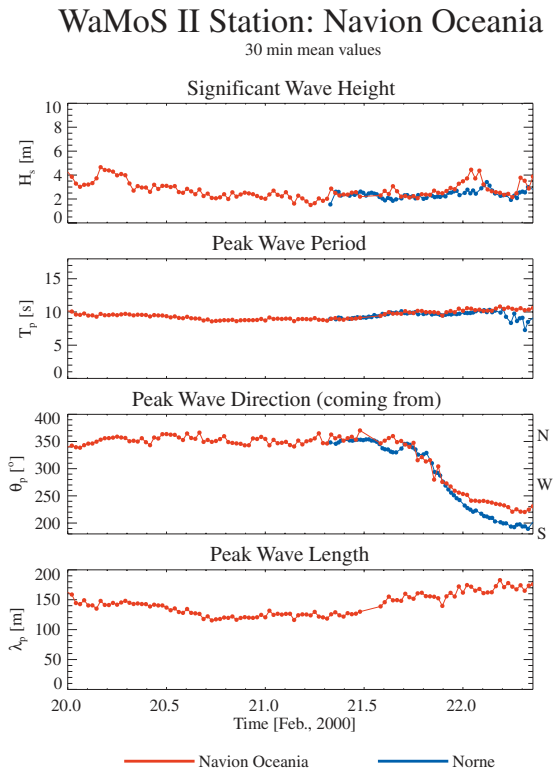

Figure 6.4: Timeseries of the the significant waveheight (H_s), peak wave period (T_p) and peak wave direction (θ_p) as obtained by WaMoS II onboard Navion Oceania (red) and by the Norne (blue) buoy for the period of February 2000.

area the mean water depth is about 70 m. The radar was in operation with a rotation period of about 1.55 s, a pulse length of 50 ns (range resolution of 7.5 m), azimuthal resolution of 0.27° and a nominal emission power of 15 W. For this installation the WaMoS II measurements represent spatial means over 960 m × 1920 m (1.8 km^2) and temporal means over 20 minutes.

Two down looking lasers, deployed on gas platform about 2 nm (3.5 km) south of the WaMoS II location and about 1 nm from each other, are used as reference sensors. The wave lasers measure the sea surface elevation at 20 m over the mean sea level with a sampling time of 0.5 s. The laser data were collected and processed by DNMI, Norway.

Figure 6.5 shows the time series of the significant waveheight H_s as obtained by WaMoS II and two wave lasers.

In the time series the natural spatial and temporal variability is visible. Also the two lasers do not provide exactly the same results. The best agreement is found in high sea states with regression coefficients of 0.93 and 0.92 for the two lasers (see Table 6.2 for relative errors of H_s as a function of waveheight).

Grand Banks, Terra Nova The radar data presented in this section were obtained at a WaMoS II site onboard the Petro-Canada FPSO Terra Nova at the Grand Banks, Canada. The X-band radar onboard Terra Nova operates with a repetition rate (antenna revolution time) of about 1.8 s. The WaMoS II radar sampling rate of 32 MHz provides radar information with a spatial resolution of 4.7 m. The wave analysis is carried out in a range between 500 m and 1200 m from the radar antenna and for 3 different directions (0°, 55°, and 305° relative to the ship heading). WaMoS II on board Terra Nova measures continuously every 5 minutes. The data output is a smooth average over 30 minutes (over about 6 single measurements). Hence each WaMoS II measurement represents a spectral mean value of the area of about 600 m × 1200 m and 30 minutes.

Wave Parameter	Range	Relative error
Significant waveheight	$H_s < 5$m	9%
Significant waveheight	5m $< H_s <$ 10m	8%
Significant waveheight	10m $< H_s$	7%

Table 6.2: WaMoS II error statistics for H_s, *Ekofisk*, North Sea, Jan/Feb, 2000.

A DataWell WaveRider Buoy, located at the platform Henry Goodrich, was used as in-situ reference sensor. The buoy was located about 1 nm south of the WaMoS II at a water depth of 96 m. It runs with a sampling frequency of 2.56 Hz and a sampling period of 20 minutes. The buoy data were collected and processed by OCEANS Ltd., St. John's.

Figure 6.6 shows the time series of the significant waveheight H_s as obtained by WaMoS II and the buoy. Error statistics for H_s are given in Table 6.3. Again both sensors show good agreement.

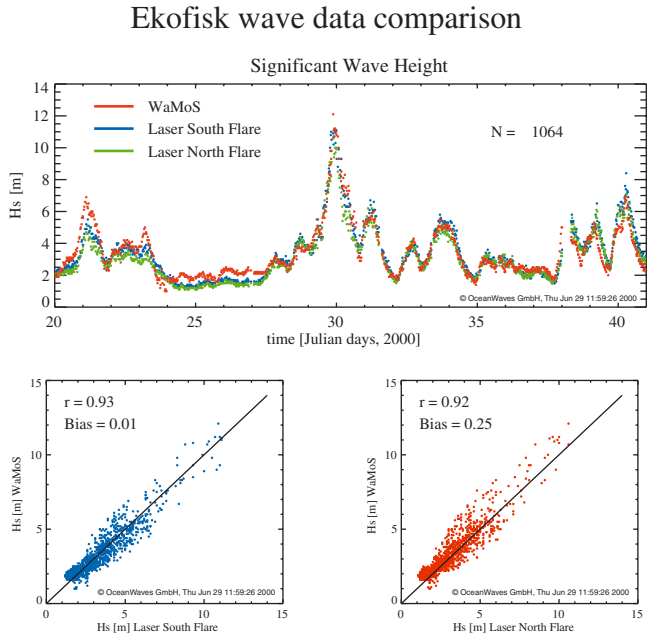

Figure 6.5: Time series of H_s as obtained by WaMoS II and the two wave laser located in the Ekofisk oil field, central North Sea (top), and linear regressions between each laser and the WaMoS II result (below).

Parameter	Symbol	Value
Correlation coefficient	R	0.91
Relative error	Rel	0.10

Table 6.3: H_s error statistics FPSO *Terra Nova*, Canada, August-September 2001.

Coastal Sites

The wave data presented in this section were obtained at the coastal station Heligoland from October 10 - November 29. 1999. The radar antenna of the WaMoS II was deployed on the island, Heligoland, about 70 m above mean sea level. The observing area was about 500 m off the coast at a water depth between $7 - 10$ m (depending on the tide). The radar was operating with a rotation period of about 2 s, a pulse length of 31.25 ns (range resolution

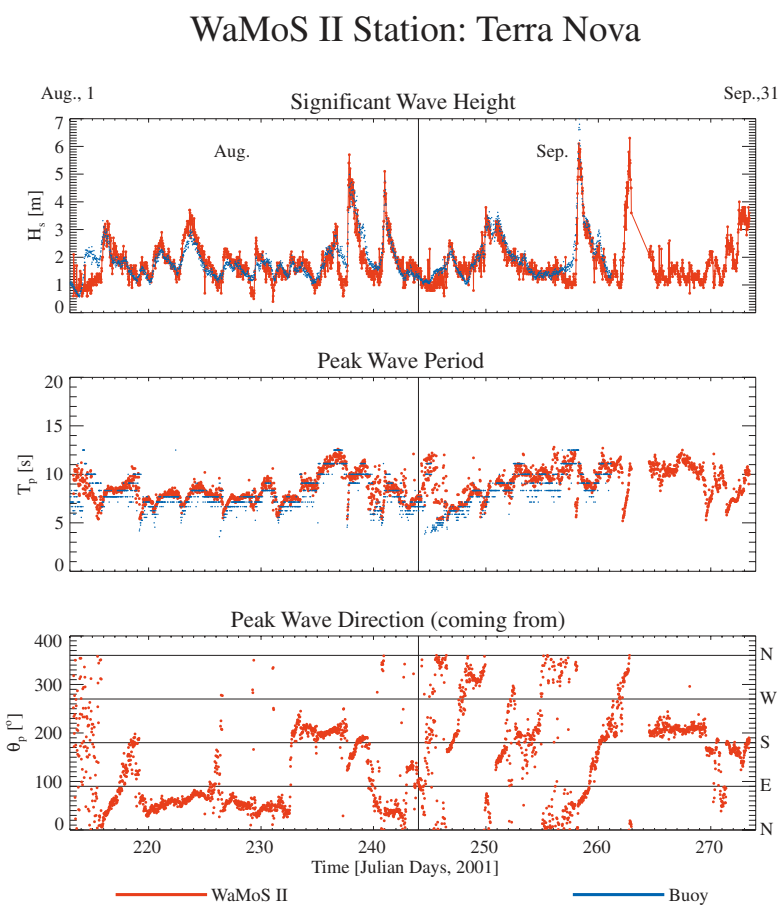

Figure 6.6: Time series of H_s as obtained by WaMoS II and a buoy located at Terra Nova, Grand Banks, Canada.

4.7 m) azimuthal resolution of 0.8° and a nominal emission power of 10 W. For this installation the WaMoS II measurements represent spatial means over 600 m × 1200 m (0.8 km^2) and temporal means over 64 s.

A directional DataWell WaveRider buoy (Hippy-40) was used as in-situ sensor. The buoy was deployed in the centre of the WaMoS II observing area, south–west of the radar antenna. It measured time series of heave, horizontal displacements in west–east and south–north directions with a duration of 20 minutes and a sampling rate of 0.5 s. The buoy data were collected

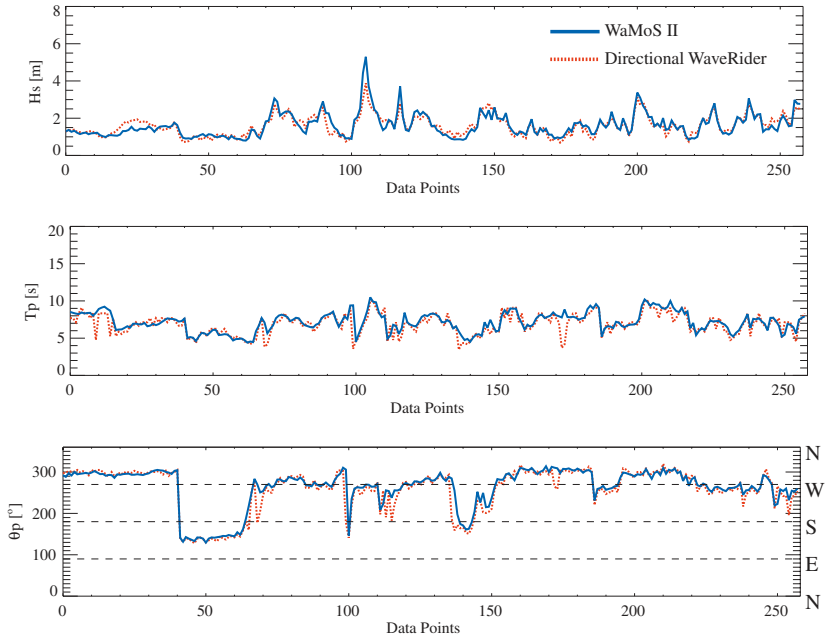

Figure 6.7: Time series of sea state parameters measured in shallow waters in Heligoland, Germany: Significant waveheight H_s (upper plot), peak period T_p (central plot) and peak wave direction θ_p (lower plot). The WaMoS II data are noted with the solid line and the Directional WaveRider buoy data with the dotted one.

and processed by BSH, Germany.

In a similar way to pitch-roll buoys, the Directional WaveRider measures three different wave properties. Hence only the first four directional Fourier coefficients and their related directional parameters can be estimated.

In Fig. 6.7 time series of the main sea state parameters H_s, T_p, and θ_p as obtained by WaMoS II (solid line) and the buoy (dotted line) at Heligoland are presented.

The time series of all three wave parameter show good agreement between the two sensors. Again small deviations due to natural variations of the significant waveheight are visible.

The linear regressions between the WaMoS II and the buoy measurements for the wave parameters can be seen in Fig. 6.8. Relative errors for the wave parameters are given in Table 6.4.

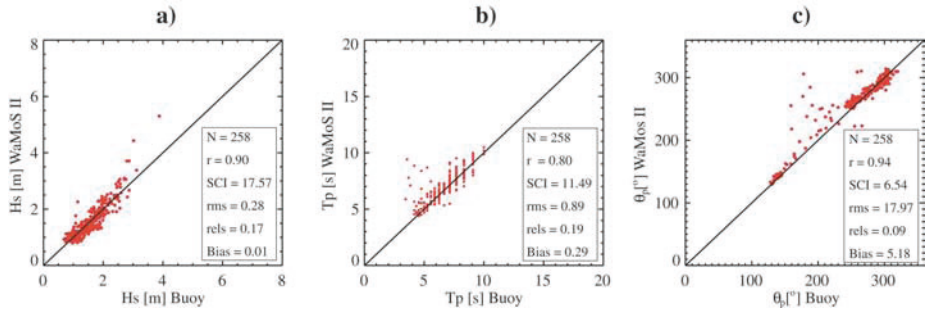

Figure 6.8: Linear regressions of the sea state parameters showed in Fig. 6.7: significant waveheight (a), peak period (b) and peak wave direction (c).

Wave Parameter	Symbol	Relative error
Significant waveheight	H_s	11%
Peak wave period	T_p	5%
Peak wave direction	θ_p	8°

Table 6.4: WaMoS II error statistics, Heligoland, North Sea,October/November 1999

6.1.4 Summary and Conclusions

In this section an inter comparison of wave measurements carried out by the remote sensing system WaMoS II and in-situ sensors is presented. The main difference between the two kinds of measuring techniques is that WaMoS II analyses sequences of radar backscatter images, while in-situ sensors analyse the temporal evolution of the sea surface. Hence WaMoS II measurements represent temporal and spatial means while in-situ data are temporal means of point measurements. For the comparison it has further to be noted, that the WaMoS II and in-situ measurements may not have been carried out at the exact same location, hence local effects can lead to deviations. The presented comparisons were carried out for different types of WaMoS II sites: moving ships, off shore platforms and for a coastal station. For ship measurements carried out in the Bay of Biscay a comparison of the first four Fourier coefficients and spectral wave information was presented. It was shown that both sensors observe the same sea state directional properties.

Small deviations can be explained by the difference in the analysis method, especially with respect to the effect of a current and by the different location of the measurements. For the other stations the derived main sea state parameters, significant waveheight H_s, peak wave period T_p, and peak wave direction θ_p are compared.

The H_s measurements presented here ranged up to 12 m. The statistical comparison with reference sensors yield a relative error for WaMoS II measurements of less than 10%. A separate error analysis for different classes of waveheights (< 5 m, 5-10 m, > 10 m) yields the same order for the relative error. This result indicates that WaMoS II measures with the same accuracy over the full range of waveheights and has no upper limitation. Depending on the radar installation geometry the lower limitation of WaMoS II measurements is about 0.5 m. The presented T_p ranged from 7 - 15 seconds with a relative error of 5%. The frequency resolution and range of WaMoS II measurements are related to radar constants with the limits given by the sampling rate, antenna length, and radar antenna repetition time. The relative error is independent of the occurring wave periods. The θ_p presented here ranged over all directions with an error of about 10°. The directional resolution of WaMoS II is only limited by the navigational radar itself. The angular resolution of a standard X-band radar is about 0.5° varying slightly with the antenna length. Therefore the expected theoretical accuracy of directional properties is less than 1°. The difference between the theoretical estimation and the relative error of the previously discussed data sets is related to the measuring principals. In contrast to spatial measuring devices (WaMoS II) point measurements (buoys or lasers) have a strong limitation in the directional resolution, hence the point measurements are expected to have a higher error.

Acknowledgements

The authors would like to thank Statoil, Norway; Phillips Petrol, Norway, and Norwegian Met Office (DNMI), Norway for providing the WaMoS II and buoy, laser data for the Ekofisk and Norne sites. We want to thank Petro-Canada and OCEANS Ltd., St. John's, Canada for the data obtained at Terra Nova, Grand Banks. For the data obtained at Heligoland we want to thank the *Bundesamt für Seeschifffahrt und Hydrography* (BSH). For the data obtained in Spain we want to thank the Spanish Port and Harbor Administration, *Puertos del Estado* and the Spanish Safety and Rescue Society (SASEMAR).

6.2 X-band Radar at Holderness

Judith Wolf

Proudman Oceanographic Laboratory, Birkenhead, United Kingdom

6.2.1 Introduction

Here we discuss the results of an X-band radar deployment to measure directional wave spectra at Holderness. As described in Chapter 4, wave data were collected near Holderness on the east coast of the UK for the winters of 1994/95 (Holderness 1) and 1995/96 (Holderness 2) at several stations (see Fig. 4.1).

The instruments deployed included a non-directional and 2 directional Waverider buoys, 8 bottom pressure recorders and 2 S4DW (directional wave) current meters, at stations N1 and S1 during Holderness 1 and at N1 and N2 during Holderness 2 (Wolf, 1996). Other wave-measuring instruments deployed simultaneously included HF radar, X-band radar, satellite-borne SAR and altimeter and beach-mounted bottom pressure recorders. The X-band radar results and the intercomparison with the measurements from other sensors are discussed here. Waves were measured by an X-band radar deployed on the cliff-top at Tunstall (53° 45.83' N, 00° 00.83' W), being the shoreward end of line N1-N3, at a height of approximately 10 m above sea level (see Fig. 4.1). The analysis methodology follows that developed by GKSS (Young *et al.*, 1985; Ziemer and Rosenthal, 1987), with some refinements. Details are given in Wolf and Bell (2001). The novel aspects lie in the method of calibration of the radar spectra, derivation of the empirical transfer function, determination of water depth and the comparison of the radar wave data with a new data set from conventional wave measuring devices. The radar spectra have been compared with non-directional spectra obtained by bottom-pressure recorder and Waverider at a nearby station N1 and directional spectra measured by a bottom-mounted InterOcean S4DW at the same location. An estimate of the empirical transfer function has been derived, allowing estimates of the wave spectra to be computed from the image spectra. Various integrated parameters are then derived from these spectra and compared with the conventional observations, finally producing an optimised calibration procedure.

6.2.2 Data Analysis

Within a rather limited frequency range (the upper limit is at about 0.17 Hz) the X-band radar gives the full wave-number frequency spectrum of the radar image of the waves. Beyond the high frequency limit a tail-fitting procedure improves the agreement with conventional in-situ wave measurement devices. It is necessary to apply a transfer function to relate the image spectrum to the actual wave spectrum. An empirical transfer function has been derived which relates the wave spectrum to the square of the image spectrum multiplied by frequency to the fifth power, using the Waverider and S4DW wave spectra at N1. The X-band radar can give useful estimates of the directional wave spectra in a coastal application and is also being developed to obtain nearshore bathymetry (Bell, 1999).

It is essential to the analysis to provide an estimate of water depth. An approximate estimate of depth can be made, without external information, by examination of the main spectral peak, for images with sufficient contrast (which is also related to a minimum waveheight). The error in the radar-estimated depths is about ±2m due to the rather coarse wavenumber and frequency resolution. The near-range and far-range parts of the image can be analysed separately and give results consistent with expected values. Alternatively the depth observed locally e.g. by the S4DW can be used to improve the analysis.

A depth survey at the site showed evidence of an offshore bar within a few hundred metres of shore with height $2-3$ m. This would be likely to broaden the spectra by spreading the energy over a wider wavenumber (and hence frequency) range. The depth at N1 was used in the analysis, which does have quite a significant effect on the energy spectrum, although less effect on direction and spread. The main effect of an error in the depth is a shift in the frequency of the longest waves, especially important near the spectral peak. Shallower depths would lead to a shift of energy towards the lower-frequency end of the spectrum. An independent estimate of the water depth in the radar footprint is desirable. The tidal variation in water depth in such shallow coastal regions has a significant effect.

Only the Holderness 1 results have been processed although the quality of data from Holderness 2 is probably better. For Holderness 1 a non-directional Waverider and S4DW at N1 were used for calibration and comparison. Scatter plots of the main wave parameters are given in Fig. 6.9. Note that H_s here is calculated from the spectrum, i.e. H_{m0} in Eqn. 4.10.

Figure 6.10 shows the radar spectra compared with Waverider and S4DW

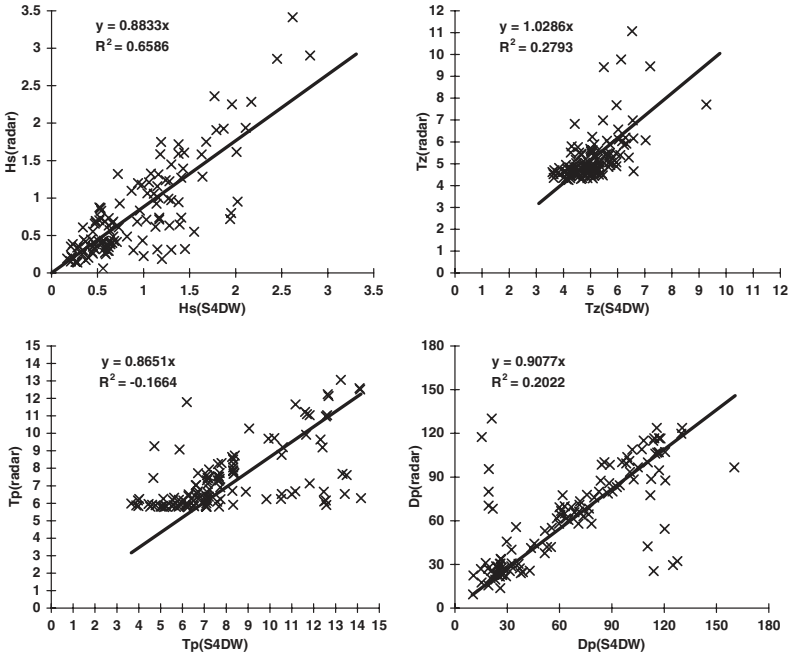

Figure 6.9: Intercomparison of an X-band radar vs. the directional Waverider at Holderness.

spectra at 09:00 on 26 January 1995, the time of maximum waveheight during the period for which simultaneous data were collected by all 3 instruments.

The two different radar analyses, labelled NR=0 and NR=1, refer to use of the 'noise-reduction' option. For NR=1, only energy in the spectrum close to the linear dispersion shell is included in the analysis. The peak wave direction is well observed by the radar. Figure 6.11 shows the spectral ratio and mean spectra for the radar compared to the Waverider and S4DW, after application of the empirical transfer function.

6.2.3 Discussion

The radar gives much more backscattered energy at low frequencies (below the spectral peak) than at high frequencies, where a rather sharp cutoff is observed. The full mechanism of microwave radar backscatter at low (grazing)

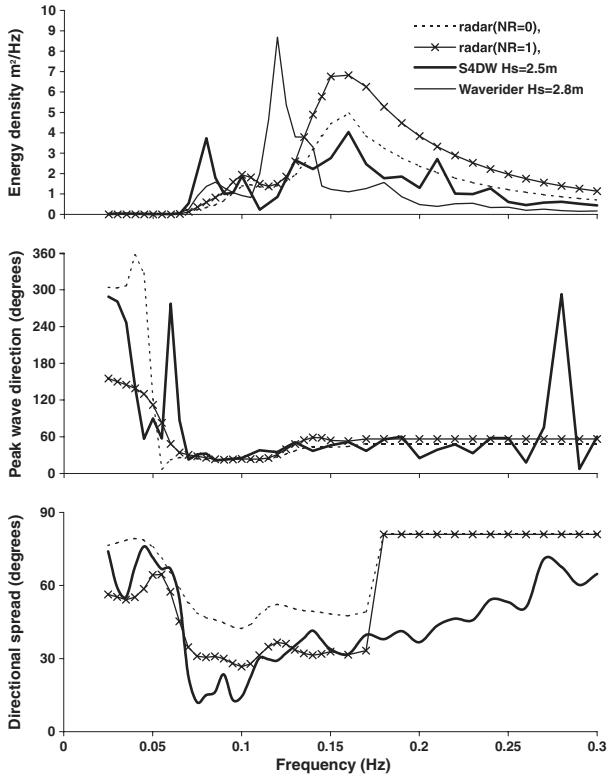

Figure 6.10: Frequency spectra from the X-band radar vs. S4DW and directional Waverider at the station N1 at Holderness.

incidence is not known. An empirical transfer function between the image spectra and wave spectra has been derived for the simultaneous Waverider, S4DW and radar spectra. The transfer function is best fitted as a power of the frequency. This does not agree with theory for the Bragg scattering model, which depends on the modulation of the Bragg-resonant waves by the longer waves imaged by the radar. If the hypothesised hydrodynamic and tilt modulation mechanisms are important, then the controlling parameters would be expected to be wave slope and orbital velocity. Both these mechanisms would amplify the backscatter at higher frequencies - here the lower frequencies are amplified. From the images, the forward face of the longer waves appears more reflective to radar energy than shorter waves. Other mechanisms that could be implicated in the backscatter are bubbles

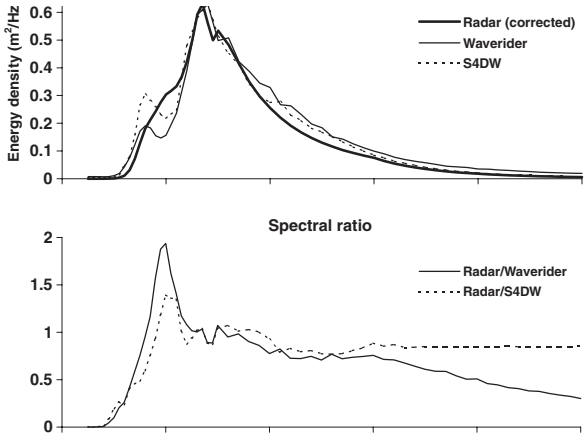

Figure 6.11: Spectra and spectral ratio between the X-band radar and the directional Waverider and S4DW.

and local wave breaking. The local wave steepness may be more significant than the spectral wave steepness. The shadowing effect at grazing incidence would be wave-height related so that larger waves, i.e. near the peak of the spectrum, would be enhanced relative to smaller waves.

Frequency is less well resolved than wavenumber in this particular radar configuration. This could be improved by using a longer recording interval. Also averaging several data samples would reduce the confidence limits on the spectral estimates.

Acknowledgements

The data were collected for the Ministry of Agriculture, Fisheries and Food under its Flood Protection Commission. Paul Bell collected the X-band radar data. Data analysis was carried out under the EU SCAWVEX Project. Andy Lane assisted with data analysis, Dave Flatt supplied the S4DW data. Peter Hardcastle supplied the Waverider data. Thanks to Robert Smith for Fig. 4.1.

6.3 References

Alpers, W., and K. Hasselmann, Spectral signal to clutter and thermal noise properties of ocean wave imaging synthetic aperture radars, *Int. J. Rem. Sens.*, 3, 423-446, 1982.

Bell, P.S., Shallow water bathymetry derived from an analysis of X-band marine radar images of waves. *Coastal Engineering*, 37, 3-4, 513-527, 1999.

Hessner, K., K. Reichert, and J. Dittmer, Coastal application of a wave monitoring system based on nautical radar, *IGARSS'99 Proc.*, Hamburg, 1999.

Nieto Borge, J.C., Significant wave height estimation from nautical radar data sets, *GKSS 98/E/28*, GKSS Research Center Geesthacht, Geesthacht, 1998.

Nieto Borge, J.C., K. Reichert, J. Dittmer, W. Rosenthal, WaMoS II: A wave and current monitoring system, *COST 714 conference Proc.*, Paris, 1998.

Nieto Borge, J.C., K. Hessner, and K. Reichert, Estimation of the significant wave height with X-band nautical radars,*OMAE'99 Proc.*, St. John's, 1999.

Nieto Borge, J.C., R. Sanz González, K. Hessner, K. Reichert, and C. Guedes Soares, Estimation of sea state directional spectra by using marine radar imaging of sea surface, *OMAE'00 Proc.*, New Orleans, 2000.

PIANC–IAHR, List of sea state parameters, *PIANC Bulletin*, 52, 1986.

Reichert, K., J.C. Nieto Borge, and J. Dittmer, WaMoS II: An operational Wave Monitoring System, *Oceanology International Proc.*, Brighton, 1998.

Reichert, K., K. Hessner, J.C. Nieto Borge, J. Dittmer, WaMoS II: A a radar based wave and current monitoring system, *ISOPE'99 Proc.*, Brest, 1999.

Wolf, J, The Holderness Project wave data, *Proudman Oceanographic Laboratory Internal Document no. 89*, 61pp, 1996.

Wolf, J. and Bell, P.S., Waves at Holderness from X-band radar, *Coastal Engineering*, 43 (3-4), 247-263, 2001.

Young, I.R., Rosenthal, W. and Ziemer, F., A Three-Dimensional Analysis of Marine Radar Images for the Determination of Ocean Wave Directionality and Surface Currents. *Journal of Geophysical Research*, 90(C1), 1049-1059, 1985.

Ziemer, F. and Rosenthal, W., On the Transfer Function of a Shipborne Radar for Imaging Ocean Waves. *Proc. IGARSS '87 Symp.*, Ann Arbor,

Michigan, pp. 1599-1564, 1987.

Ziemer, F., and H. Günther, A system to monitor ocean wave fields, *Int. Conf. on Air-Sea Interaction and Methology and Oceanography of the Coastal Zone*, Lisbon, 1994.

Chapter 7

MIROS Doppler Wave Radar

A.K. Magnusson

Norwegian Meteorological Institute (DNMI), Bergen, Norway

7.1 Introduction

Wave observations gathered with the MIROS Doppler wave radar have been compared to observations given by other conventional wave measuring instruments in several studies. Many of these studies are unfortunately performed under contract and are not available. One study was performed at DNMI (the Norwegian Meteorological Institute) under contract with Statoil (contract no. T7183, 1987). Five months of measurements (November 1986 – March 1987) were analysed. With the permission of Statoil, some of the results are shown in this chapter.

The MIROS analysing software and hardware has changed slightly since the 80's. The studies performed in the 1980's showed among other things that the averaging period had to be shortened to give measurements comparable to those obtained from other in-situ instruments like buoys.

7.2 Comparison with a Wavec Directional Buoy

7.2.1 Introduction

In a study supported by Statoil, MIROS measurements from the platform Gullfaks A (61.2°N, 2.2°E) operated by Statoil were compared to Wavec

measurements at North Cormorant (61.2°N, 1.2°E), an oil field exploited by Shell. Wavec data were kindly provided by Shell for this study. Results were discussed in a DNMI report (Magnusson, 1987).

The report has two main sections. One is dealing with integral parameters like significant waveheight (H_{m0}), wave peak periods (T_p) and peak wave direction, the other is dealing with directional spread. A short review of the first section is given hereunder, followed a more detailed review of the part dealing with directional parameters.

7.2.2 Integral Wave Parameters

Wave conditions during the 5 months were quite rough. Data retrieval was poor in the first one and a half months. Most of the simultaneous records (602 in total) analysed are from the last 3 months. Statistics of the significant waveheight is given in Table 7.1.

Sensor	Mean value $< H_{m0} >$	Standard deviation	Regression line between the 2 datasets	Correlation	RMSE
Wavec	3.41	2.18	Y = 0.93 X + 0.46	0.934	0.586
MIROS	3.17	2.20	Y = 0.94 X – 0.030		

Table 7.1: Comparison between MIROS and Wavec significant waveheight

On average, MIROS gives lower significant waveheight. The same trend is seen in the results for the peak wave period ($< T_{pWavec} > = 10.12$ sec, $< T_{pMIROS} > = 9.88$ sec).

The differences could be caused by several conditions:

- The two sites in question (Gullfaks A and North Cormorant) are about 50 km apart. This was found to influence some of the cases with high discrepancy (especially peak wave period in swell conditions).
- The sampling period for one record was at that time 72 minutes for the MIROS and 30 minutes for the Wavec. This was also found to explain some of the discrepancies in the storm maxima of significant waveheight.

A more important finding in the study is that the discrepancy was larger for wave conditions where the MIROS would see the back face of the waves

(receding waves). The average significant waveheight given by the MIROS in these conditions (waves coming from sector 270°-30°) was 12% lower than the value given by the Wavec. In the southerly conditions the measurements were more in agreement. The discrepancy in the receding conditions was independent of waveheight and wave period. It was therefore concluded that interference of waves with the platform constructions is not a major cause for the discrepancy. Non-linearity in the waves, giving different Doppler effects on the forward and backward faces was assumed to be a more probable cause. To reduce the discrepancy, the down looking angle of the MIROS radar was thereafter reduced. The choice of angle is a balance between having the least shadowing effect in the waves and the least disturbance in the waves due to interference with the constructions. Personnel from the MIROS-company indicated also thereafter that they would look more closely at the transfer function between the Doppler signal and the wave spectrum (private communication with Øystein Grønlie).

Measurements of peak wave direction were found to be in quite good agreement. This was seen in the time series from both instruments. Also, in 430 of the 602 simultaneous cases, the difference in peak wave direction was less than 30° (disregarding the 180° ambiguity).

7.2.3 Directional Spread

The directional wave spectrum is assumed to be given as a product of the frequency spectrum and a frequency dependent directional distribution function $D(f, \theta)$:

$$E(\theta, f) = D(f, \theta) \cdot E(f) \tag{7.1}$$

where $D(f, \theta)$ has the characteristics of a probability function, and can therefore be characterised by parameters such as mean direction, directional spread, skewness and kurtosis.

Directional spread is calculated in quite different ways for the buoy and the MIROS radar. The MIROS gives a frequency spectrum in 6 different directions, allowing for a simple calculation of directional spread: it is calculated as the square root of the circular variance around the mean direction at the peak or around the total mean direction, according to the following formulae (Grønlie, 1986):

$$\sigma_o = \sqrt{2 \cdot \sum_j [1 - \cos(\theta_j - \overline{\theta})] \cdot \frac{E(\theta_j)}{\sum_j E(\theta_j)}} \tag{7.2}$$

where $\overline{\theta}$ is either the mean direction at the peak frequency or for the total spectrum, and $E(\theta_j)$ is either the directional spectrum at the peak or integrated over frequencies.

Calculations of directional spread from the measurements given by the Hippy sensor in the Wavec buoy are more elaborate. The analysing method relies on the method of Longuet-Higgins *et al.* (1963) for heave-pitch-and-roll sensors. A complete description of the development of the expressions can be found in Kuik *et al.* (1988). The parameters are described using mainly the first 4 Fourier coefficients of the directional distribution resulting from the standard cross-spectral analysis of the signals.

In Magnusson (1987) the spreading values given by the 2 instruments (spread at the peak, given in degrees) were compared to a $\cos^{2s}$ type of directional distribution function expressed as a function of frequency f and propagation direction θ (Mitsuyasu *et al.*, 1975):

$$D(f, \theta) = \alpha(f) \cdot \cos^{2s(f)} \left(\frac{(\theta(f) - \overline{\theta}(f)}{2} \right) \tag{7.3}$$

where $\alpha(f) = 2^{2s(f)} \cdot \frac{\Gamma^2(s+1)}{2\Gamma(2s+1)}$ is a normalising constant ensuring $\int D(f, \theta) \cdot d\theta = 1$.

An empirical relation for $s(f)$ was first proposed by Mitsuyasu *et al.* (1975):

$$\frac{s}{s_p} = \left(\frac{f}{f_p} \right)^{\mu} \tag{7.4}$$

where s_p is the spreading exponent at the peak of the spectrum ($f = f_p$), and

$$\begin{aligned} \mu &= -2.5 \text{ for } f \geq f_p \\ &= 5 \quad\quad \text{for } f < f_p \end{aligned}$$

They introduced a U_{10}/c_p dependence of s_p (U_{10}: wind speed at 10 m above m.s.l.; c_p: phase velocity at peak frequency), suggesting:

$$s_p = 11.5(U_{10}/c_p)^{-2.5}, \text{for } 0.7 \leq U_{10}/c_p \leq 1.2 \tag{7.5}$$

Hasselmann *et al.* (1980) adopted the same parameterisation for the JONSWAP data, but finally proposed new expressions suggesting that the maximum spread was constant (value depending on f being smaller or larger than f_p) after finding no significant dependence on U_{10}/c_p.

Haver (1986) proposed, after a synthesis of the two results of Hasselmann *et al.* (1980) and Mitsuyasu *et al.* (1975), together with measurements in the North Sea, an expression for $s(f)$ depending on $T_p/\sqrt{H_{m0}}$, where T_p is the peak period and H_{m0} is the significant waveheight. But, due to uncertainty in measurements, Haver (1986) sets upper and lower limits for s_p:

- lower limit: $s_p = 6.5$ for all $T_p/\sqrt{H_{m0}}$
- upper limit:

$$\begin{array}{ll} s_p = 13.0 & \text{for } T_p/\sqrt{H_{m0}} \leq 5 \\ s_p = 0.132 \cdot 10^{-5}(T_p/\sqrt{H_{m0}})^{10} & \text{for } T_p/\sqrt{H_{m0}} > 5 \end{array}$$

With these parametrisations in mind, the values of directional spread at the peak given by the Wavec and MIROS systems were compared.

The relation between directional spreading (σ_1) and the factor s in the $\cos^{2s}$distribution model is easily found

$$\sigma_1 = \{2/(s+1)\}^{1/2} \tag{7.6}$$

and

$$s = (2/\sigma_1^2) - 1 \tag{7.7}$$

Note that σ_o is in radians and s is dimensionless.

In the MIROS-Wavec comparison, a first check of the data was done to ensure that the respective values of directional spread referred to the same sea, since the distribution model is only appropriate to uni-model seas. The difference in peak direction was constrained to 30° (430 simultaneous records). A second constraint was that the absolute relative error in peak wave period ($|(T_{pWavec} - T_{pMIROS})/T_{pWavec}|$ should be less than 0.2 seconds. This reduced the number of simultaneous cases satisfying both conditions from 602 to 397.

The MIROS spreading is mostly between 20° and 50°, while Wavec values are more spread: at the minimum 13° and in many cases up towards 60°. Spreading values below 20° are rare. The relatively small span of the values of directional spread given from the MIROS are probably due to the coarse directional resolution of the directional spectrum (30°). The same results are seen when putting further constraints on the cases (using wind direction and mean and peak period). A comparison of the directional spread from the two sensors is shown in Fig. 7.1 in the resulting 109 cases. Comparison of the directional spreading factor s_p is shown in Fig. 7.2. We see a tendency for a relation between the two datasets (increasing MIROS value is simultaneous with increased Wavec value), but the span of values is the same.

In Kuik *et al.* (1988), the value of σ_1 is said to be strongly influenced by noise in the measurements. An example is given where, for a true value of $\sigma_1 = 10°$, with a noise of 5% in the three basic heave and slope signals, the directional spread will be given a value of 20°. The uncertainty is said to decrease as σ_1 increases. There are only a few values below 20° in the data set considered.

The relation of the s-factor to $T_p/\sqrt{H_{m0}}$ was also examined in the report (Magnusson, 1987). Figure 7.3 shows a comparison of $T_p/\sqrt{H_{m0}}$ values from the two sensors in the 109 cases, and Fig. 7.4 shows the directional spreading factor s_p as function of $T_p/\sqrt{H_{m0}}$ for each sensor (Wavec: left panel, MIROS: right panel). In Fig. 7.3 we see that not all the cases are identically observed. Nonetheless, the results given in Fig. 7.4 do not indicate relations such as those mentioned above.

The results demonstrate:

- Values of s_p given by the Wavec are mostly between 2 and 15. This span is independent of $T_p/\sqrt{H_{m0}}$, a factor that expresses the 'wave age'.
- The span of s_p is smaller when measured with the MIROS. This is most probably due to the coarse directional resolution of the system. No dependence on wave age (or $T_p/\sqrt{H_{m0}}$) can be noticed.

7.3 Concluding Remarks

In 2001 five platforms in the Norwegian sector report meteorological observations to the GTS system of WMO (World Meteorological Organisation),

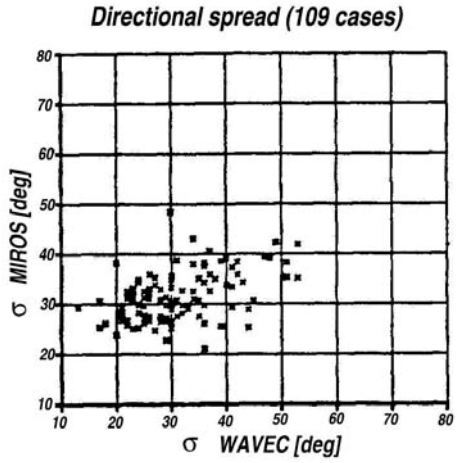

Figure 7.1: Comparison of directional spreading (degrees) from the MIROS and the Wavec. Constraints are set on the data so that the comparison is made in cases with uni-modal seas.

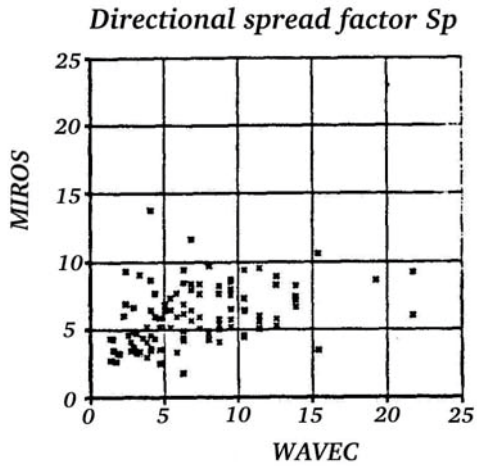

Figure 7.2: Comparison of directional spreading (power s_p) from the MIROS and the Wavec.

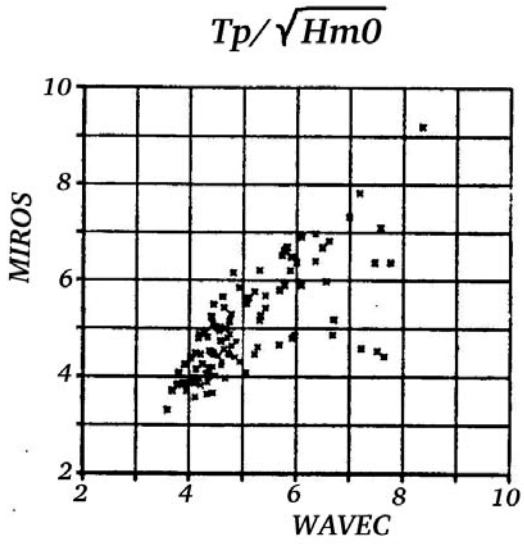

Figure 7.3: Comparison of $T_p/\sqrt{H_{m0}}$ calculated with values from the MIROS and the Wavec.

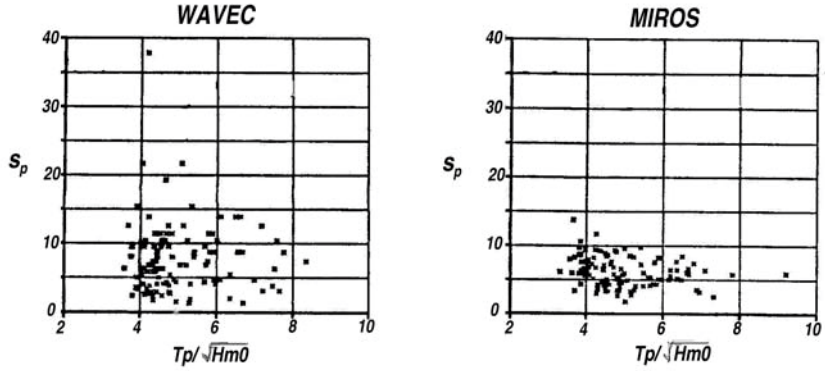

Figure 7.4: Directional spreading factor s_p as function of $T_p/\sqrt{H_{m0}}$ for the Wavec (left) and the MIROS (right).

including wave observations given by a MIROS. Several other platforms also use wave information for operational purposes from this sensor. From the 15 years this instrument has been operating, the experience at the marine forecasting centre in Bergen (Norwegian Meterorological Institute) is that the standard wave parameters that are reported are of good value. Directional information is seldom used. Directional spreading is not used operationally for forecasting, but it is in use for calculations of fatigue on constructions.

Results presented here do not give high confidence to measurements of directional spread. The unidirectional conditions are not always fulfilled for the cos^{2s} model to be adequate. When there is unimodality, the spreading value is dependent on the sensor. The MIROS Doppler wave radar has a coarse directional resolution, and the spreading values are therefore constricted to a smaller range than the spreading values given by the Wavec directional buoy. In the range where MIROS resolution is adequate (20-50 degrees), the comparison shows there is some correlation between the two systems, but there is still a large uncertainty in the spread.

7.4 References

Grønlie, Ø., Estimation of wave direction and directional spread, *Internal MIROS report*, Doc. no. TN/046/86/ØG/6105/D, 1986.

Haver, S., On the modeling of short-crested sea for structural response calculations, *Statoil report*, 1986.

Hasselmann, D.E., M. Dunckel, and J.A. Ewing, Directional wave spectra observed during JONSWAP 1973, *J. Phys. Oceanogr.*, Vol.10, 1264-1281, 1980.

Kuik, A. J., G. Ph. van Vledder, and L. H. Holthuijsen, A method for the routine analysis of pitch-and-roll buoy wave data. *Journal of Physical Oceanography*, 18, 1020-1034, 1988.

Longuet-Higgins, M.S., D.E. Cartwright, and N.D. Smith, Observations of the directional spectrum of waves using the motion of a floating buoy, in *Ocean Wave Spectra*, 111-136, Prentice-Hall, 1963.

Magnusson, A.K, MIROS-Wavec validation study. Comparison of the measurements of sea state parameters, *DNMI report under contract no T7183 with STATOIL*, 1987.

Mitsuyasu, H., F. Tasai, T. Suhara, S. Mizuno, M. Ohkusu, T. Honda, and

K. Rikiishi, Observations of the directional spectrum of ocean waves using a cloverleaf buoy, *J. Phys. Oceanogr.*, Vol 5, 750-760, 1975.

Chapter 8

Comparison of Airborne Radar and Buoy Data

Danièle Hauser [a], *Céline Quentin* [a], *Kimmo K. Kahma* [b], *Heidi Pettersson* [b], *William M. Drennan* [c], *Hans C. Graber* [c]

[a] Centre d'étude des Environnements Terrestres et Planétaires (CETP), Vélizy, France
[b] Finnish Institute of Marine Research (FIMR), Helsinki, Finland
[c] Rosenstiel School of Marine and Atmospheric Science (RSMAS), University of Miami, Miami (FL), USA

8.1 Introduction

Although the behaviour in frequency and energy of wave spectra has been extensively studied in the past (in particular from the JONSWAP experiment, Hasselmann *et al.* (1973)), there is still a need to better document the angular distribution of the surface waves. The questions are in particular: what is the shape of the distribution? How does the spread vary with parameters such as fetch (or wave age) and wind speed? What is the effect of swell on the angular distribution of wind-sea? Answers to these questions are quite important to better understand the physics of the waves (non-linear interactions, wave growth and dissipation, ..), to improve parameterisations in wave-prediction models (and the wave forecast), to estimate the effect of long waves on remotely-sensed parameters. A good estimate of the directional spread is also necessary for many applications (e.g., ship design, offshore industry).

Here we present spectral data obtained from the real-aperture airborne radar RESSAC and a comparison with buoy observations.

The principle of measurement of RESSAC (see section 5.6 in Part 1 for more details) is based on the measurement of modulations of the radar backscatter coefficient due to the slopes of long waves. A spectral analysis is applied to these modulations, providing modulation spectra, which are linearly related to wave slope spectra. So, as opposed to the case of most of the in situ measurement techniques, the estimate of the directional spectrum is rather direct, provided that the transfer function between radar modulation spectra and wave spectra is known. Indeed this approach provides radial cuts of the 2D spectra $F(k, \phi)$ for each look direction ϕ. With a scanning beam antenna, the complete spectra over 360° is obtained, with however a 180° ambiguity in the propagation direction. Another interest of this airborne system is its ability to provide 2D spectral information at a regional scale with a rather good sampling (every 10 km along the flight-track).

In contrast, waverider or pitch-roll buoys provide observations at a single location. The wave measurements are based on the recording of three independent wave signals (e.g. heave, pitch, roll) at the same location, from which auto- and cross-correlation spectra are calculated (Barstow *et al.*, 1991). The same principle of analysis can also be applied to other types of measurements such as those obtained from arrays of sensors (laser array, network of capacitance wires, etc). The most basic parameters relative to the angular distribution are derived from these observations using a combination of "integral" parameters. They are usually estimated by assuming that the directional distribution can be expanded as a truncated Fourier series (see Longuet-Higgins *et al.*, 1963). In each frequency band the first order parameters of the angular distribution (mean direction, angular spread) are calculated from the co- and quad spectra, and eventually higher order parameters (skewness, kurtosis). More sophisticated approaches are used to derive a 2D directional spectrum. The Maximum Likelihood Method or the Maximum Entropy Method or Variational Inverse Techniques are usually applied to estimate such a "synthetic" 2D spectrum (see Benoit and Goasguen, 1999 for a review). From these 2D spectra, moments of the angular distribution (mean direction, angular spread,..) can be calculated a posteriori. But, they may provide results different from what would be estimated directly from co and quad spectra of couples of measurements (Benoit and Goasguen, 1999).

So, because the methods of measurement and analysis are completely different between in situ and radar observations, there is a need to better know

how they compare. This is the goal of this chapter, where we present results on the properties of the angular distribution deduced from the airborne real-aperture radar RESSAC and from wave gauge measurements (directional waverider DWR and spatial array of capacitance wave gauges). The Longuet-Higgins approach was used to obtain the mean direction and angular spread from the DWR and wave gauge array. For the radar data, the 2D wave spectra estimated from the radar observations were used to calculate a posteriori the same parameters (mean direction and spread or exponent s of a $\cos^{2s}$ angular distribution), which can be directly compared to buoy data.

The data were collected during the FETCH experiment (Hauser *et al.*, 2003), which took place in March-April 1998 in the north Mediterranean Sea (Gulf of Lions, France). This experiment was devoted to the study of air/sea interactions using in situ measurements (ship, buoys) and remote sensing observations (airborne radar and lidar, data from the ERS-2 and TOPEX-POSEIDON satellites). One of the objectives was to study the behaviour of surface waves in fetch-limited and high wind conditions.

8.2 The Data Set

The experimental area of the FETCH experiment is shown in Fig. 3.1.

In situ wave measurements during FETCH were performed using:

- an array of wave gauges (5 or 6 capacitance wires) installed on the SPAR buoy "ASIS" of the University of Miami (Graber *et al.*, 2000, and section 4.4 of Part 1, this book). This buoy was anchored at the approximate location 42°59.06N, 04°14.71N at a 90 m water depth (point B in Fig. 3.1)

- a directional waverider (DWR) of the "Datawell" company, deployed by the Finnish Institute of Marine Research (FIMR), see chapter 3, Part 2 of this book

- a non-directional drifting waverider (SPEAR buoy deployed by Météo-France).

During the first half of the experiment (from 18 to 25 March) the DWR and ASIS buoy were moored close to each other (distance of 2 km between

them). After March 25th, the DWR buoy was moved and moored at location 43°09.56N, 04°06.25E at a water depth of about 80 m.

The airborne radar RESSAC (Hauser *et al.*, 1992, and section 5.6 in Part 1 of this book) was used from the MERLIN-IV airplane of Météo-France to measure the directional spectra of the waves along the track of the airplane. It was also used in a second mode of operation to estimate the wind vector at different positions along the track (this latter data set will not be discussed here). During each flight, tracks of the airplane passed over one of the wave buoys, so that a set of co-located measurements of waves from buoys and airborne radar has been collected. Some of the RESSAC tracks were also co-located and simultaneous with the TOPEX/POSEIDON passes, providing a further documentation of spatial variations of the significant waveheight and wind speed in this area.

Standard meteorological measurements (and in particular wind measurements) were performed on the instrumented " ASIS " buoy (point B in Fig. 3.1) and on the research vessel "L'ATALANTE" which cruised within the area marked by a heavy-line rectangle in Fig. 3.1. L'ATALANTE generally cruised into the wind along legs passing nearby the ASIS buoy. These two platforms were also equipped to measure the turbulent fluxes (of heat and momentum on L'ATALANTE and of momentum on the ASIS buoy).

The data sets presented here correspond to three different cases of observations (24 March, 3 April, and 7 April 1998). The first case corresponds to an off-shore wind situation (Mistral event with wind blowing from north). April 3rd corresponds to a general surface flow from the south–west preceding the arrival of an atmospheric surface front. April 7th corresponds to a mixed sea case a few hours after the passage of an atmospheric front, with wind-sea from west superposed with swell from the south. The main characteristics of each situation are presented in Section 8.6.

8.3 RESSAC Data

The principle of measurement and main steps of the processing are explained in section 5.6, Part 1 of this book. We just recall here that the final product obtained with RESSAC is a 2D spectrum in the form of $F(k, \theta)$ where k is the wavenumber and θ the angle of propagation with respect to the north (with an ambiguity of 180°). The present data sets have been obtained for 64 wave number bins up to 0.2617 cpm, which corresponds (for the deep-water

gravity wave dispersion relation) to the frequency range [0.05,0.25] Hz. The energy density was averaged over 15° in the θ direction (24 intervals from 0 to 360° with 180° ambiguity) and 5 successive scans of the antenna. The time interval of this average (1min40s) corresponds to a spatial extension of about 10 km along the airplane-track. Note that for the FETCH experiment we had some problems to estimate the α coefficient of the transfer function Eqn. 5.8 given in section 5.6, Part 1 of this book. So we used external data (significant waveheights from TOPEX-POSEIDON) to normalise the total energy of the waves and from that, $F(k, \theta)$ was normalised. Since in the present study we focus on the angular distribution, the absolute normalisation of the wave spectra is anyhow not important.

Figs. 8.1a-c present the flight track during the RESSAC measurements. The numbers indicated along the tracks refer to the location of the directional spectra discussed in the following. In each of the studied cases, there are co-located data between RESSAC and at least one of the directional buoys (DWR or ASIS). In section 8.7, we present not only comparisons between RESSAC and these buoys, but also an analysis of the spatial variation of the directional properties of waves obtained from RESSAC along each track.

8.4 Buoy Data

The directional waverider of FIMR is presented in Chapter 3, Part 2. During FETCH, the buoy was moored by the standard mooring-line, which includes two 15 m rubber cords. The spectra were calculated on board the buoy from displacement time series of 1600 seconds, following Longuet-Higgins *et al.* (1963). Every half an hour, a spectrum, -energy, mean direction, directional spreading and second order Longuet-Higgings coefficients- in the frequency range 0.025 to 0.58 Hz, were sent via HF radio to the receiver on R/V L'ATALANTE, together with the 20-minutes of displacement data (vertical, north and west). The datalogger was not used in this experiment and during the periods when the ship was beyond the reception range data were lost. The buoy also sent spectra (13 spectral bands) via Argos to cover these periods.

The ASIS buoy is presented in section 4.4 of Part 1. For this comparison, we use data collected from an array of 6 capacitance wave gauges mounted in a centred pentagon of 0.93 m radius, with one gauge on each of the five faces of the buoy, and a sixth in the centre. Note that only five gauges were functional during the March period of FETCH; all six were operational

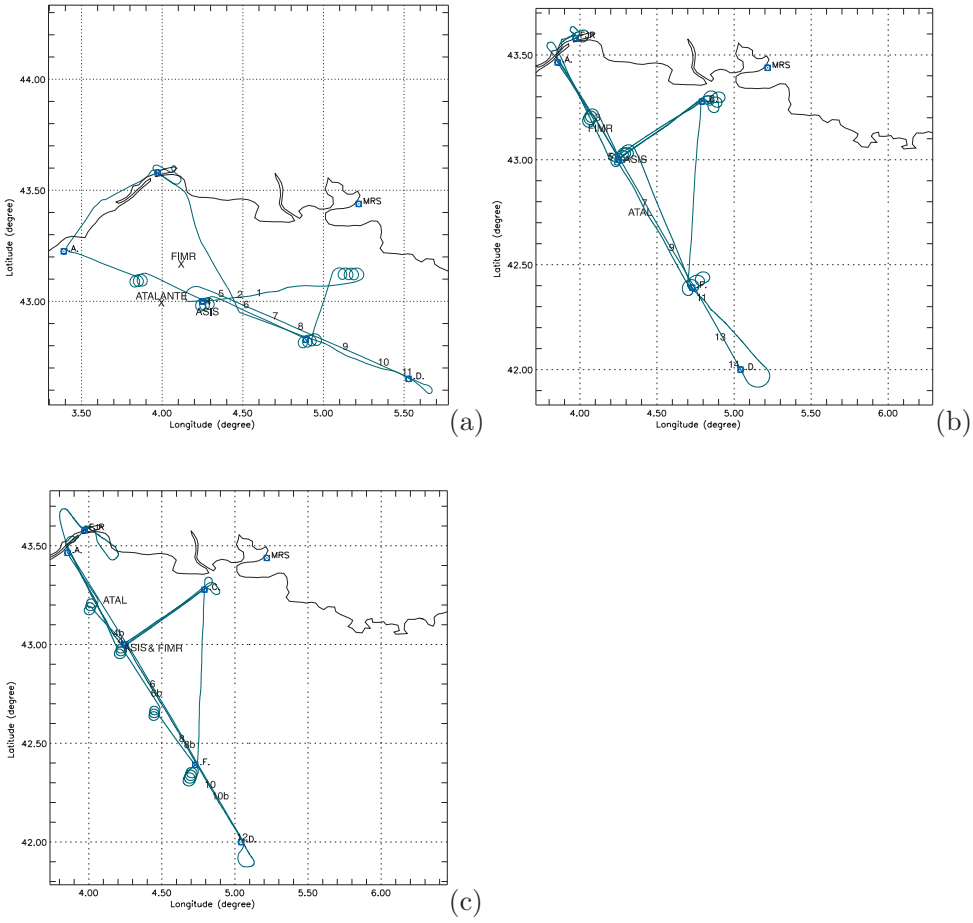

Figure 8.1: Flight tracks of the MERLIN-IV airplane, which carried the RESSAC radar. The numbers along the track refer to the positions of the 2D spectra discussed in the paper. The position of ASIS, DWR (labeled as FIMR) and ATALANTE are indicated. (a): 24 March; (b): 3 April; (c): 7 April.

during April. The wave gauge data were combined with the measured buoy motion data to obtain the true surface elevation (see section 4.4, Part 1 of this book). During FETCH, ASIS data were analysed in blocks of 28.5 min. For the purposes of comparison with other sensors, the spreading parameters for ASIS are calculated in a similar fashion to those of the waverider buoy. That is, the local surface slopes are calculated (by differencing appropriate combinations of surface elevation data from the array), and the slopes along with the vertical surface displacement were used in a classical Longuet-Higgins *et al.* (1963) analysis.

8.5 Method of Comparison Between RESSAC and Buoy Data

In order to complement the qualitative comparison of 2D spectra obtained from RESSAC and buoys, we have developed a quantitative comparison of the directional properties. The approach was to calculate, from the 2D spectra of RESSAC, the same parameter as provided by the buoys (mean direction and spread). RESSAC spectra have been converted into frequency spectra $F(f,\theta)$ using the dispersion relationship for deep-water gravity waves. From these frequency spectra, the co-and quad spectra have been calculated according to their definitions:

$$\begin{aligned}
&C_{11}(f) = \int_0^{2\pi} F(f,\theta)d\theta,\ C_{22}(f) = \int_0^{2\pi} k^2 F(f,\theta)\cos^2\theta d\theta,\\
&C_{33}(f) = \int_0^{2\pi} k^2 F(f,\theta)\sin^2\theta d\theta,\ Q_{12}(f) = \int_0^{2\pi} kF(f,\theta)\cos\theta d\theta,\\
&Q_{13}(f) = \int_0^{2\pi} kF(f,\theta)\sin\theta d\theta,\ C_{23}(f) = \int_0^{2\pi} k^2 F(f,\theta)\sin\theta\cos\theta d\theta
\end{aligned} \tag{8.1}$$

As is done in the standard processing for waveriders, we have assumed that the directional distribution $D(f,\theta)$ can be expanded as a Fourier series truncated at the second order:

$$D(f,\theta) = \frac{1}{2\pi}\left[1 + 2\sum_{n=1}^{2} r_n(f)\cos\left(n(\theta-\theta_1)\right)\right] \tag{8.2}$$

where D(f,θ) = F(f,θ) /S(f), S(f) is the 1D spectrum, θ_1 is the mean direction, and r_1, r_2 are the first and second order parameters related to the

directional spread. These quantities are related to the co- and quad-spectra through:

$$\theta_1 = \arctan(Q_{13}/Q_{12}) \tag{8.3}$$

$$r_1 = \sqrt{\frac{(Q_{12})^2 + (Q_{13})^2}{C_{11}\,(C_{22} + C_{33})}} \tag{8.4}$$

$$r_2 = \sqrt{\frac{(C_{22} - C_{33})^2 + (2C_{23})^2}{C_{11}\,(C_{22} + C_{33})}} \tag{8.5}$$

From r_1, the first-order angular spread is defined by $\sigma_1(f) = [2(1-r_1(f)]^{1/2}$. For DWR and ASIS, parameters θ_1 and $\sigma_1(f)$ were those provided by the processing of the co-and quad spectra of the time series. In addition, 2D spectra were also calculated from the buoy data using the MLM (Capon, 1969, Isobe *et al.*, 1984). The plots of the directional spectra for ASIS and DWR which appear here in the text correspond to the spectra calculated with this MLM.

For RESSAC, parameters θ_1, r_1 (or σ_1), r_2, have been estimated from Eqns. 8.1 to 8.5, with co- and quad- spectra calculated from the 2D spectrum $F(f, \theta)$. For this calculation, the integral functions of Eqn. 8.1 are in fact calculated by summing over an angular interval of 180°. This means that we have removed the 180° ambiguity in the RESSAC data. This has been done by choosing a direction of propagation from external information. Note that for this comparison with the buoy data, we have chosen to reduce the information from the 2D spectra of RESSAC to the above-mentioned parameters.

As discussed by Krogstad and Barstow (1999, and chapter 2.5 in Part 1 of this book), the relationship between r_1 and r_2 is an indicator of the shape of the distribution $D(f, \theta)$, assuming that this distribution is symmetric. Our RESSAC data have been used to analyse this $r_1 - r_2$ relationship.

For a $\cos^{2s}$ angular distribution, parameter r_1 is related to the exponent s by:

$$s(f) = \frac{r_1\,(f)}{1 - r_1\,(f)}. \tag{8.6}$$

Note that for all the results of RESSAC, we have limited the analysis of the angular spread σ_1(f) and associated parameters r_1, r_2, s, to the most

energetic part of the spectrum, i.e. for frequencies where the energy density is above 0.1 times the maximum value of the non-directional spectrum S(f). This was done to avoid uncertainty due to the smaller accuracy in the energy density at low energy.

8.6 Environmental Conditions for the Selected Data Set

Environmental conditions are known from the meteorological parameters measured on the ASIS buoy and on the R/V "L'ATALANTE". Atmospheric models are also used to place these local measurements in their larger scale environment. In particular, we use here the wind fields provided by the atmospheric circulation model "ALADIN" from Météo-France. This model is a regional adaptation of the global atmospheric model of Météo-France. It is run twice a day (0 and 12 UTC), and provides atmospheric variables every 3 hours with a resolution of about 10 km over our region of interest.

Figs. 8.2 to 8.4 illustrate, for each situation (March 24$^{\text{th}}$, April 3$^{\text{rd}}$, April 7$^{\text{th}}$), the time series of wind speed and wind direction measured on the ASIS buoy and on L'ATALANTE. These two platforms were not always close together, which explains most of the differences in Figs. 8.2 – 8.4 between the data of these two platforms. The significant waveheight from ASIS and DWR buoys is also plotted. ASIS and DWR were close together on March 24$^{\text{th}}$ but not during the two other situations.

The case of March 24$^{\text{th}}$ corresponds to a "Mistral" event. Mistral is a regional wind often occurring during high-pressure situations over France, when there is a well-established northerly flow over France associated with a low-pressure system over the Gulf of Ligure (6-10°E, 43-44°N). Northerly winds blowing over the south–east part of France are accelerated in the Rhone valley, due to orographic effects and to the pressure field at low levels. In such situations, high winds generally last for several days. On March 24$^{\text{th}}$, north–northeasterly winds are observed for the whole day at the ASIS buoy and ATALANTE locations (see Fig. 8.2). Wind speed is relatively variable but increases during the day, with values from 6 to 14 m/s in the morning and from 12 to 18 m/s in the afternoon. The ALADIN wind field indicates that close to the time of the RESSAC measurements (17:20 to 19 UTC), the RESSAC track is entirely within the region of northerly winds, but very high winds from the north–east exist in the region located north–east of

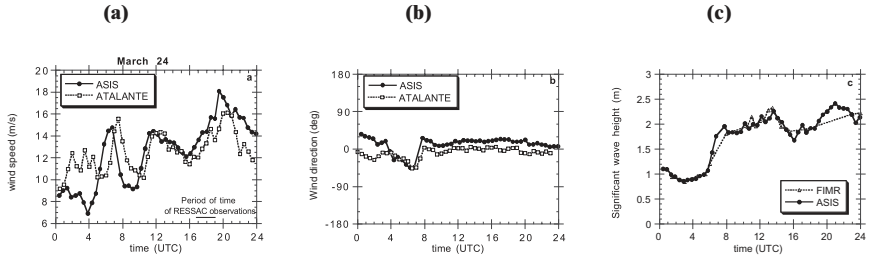

Figure 8.2: Wind and wave conditions on March 24^{th} from ASIS (heavy line), L'ATALANTE (light line) and DWR (light line, labeled as FIMR in the enclosed box). Left panel: wind speed. Middle panel: wind direction. Right panel: significant waveheight. The position of L'ATALANTE is close to the one of ASIS from 12 to 15 UTC. RESSAC data were obtained between 17:20 and 19:00 UTC.

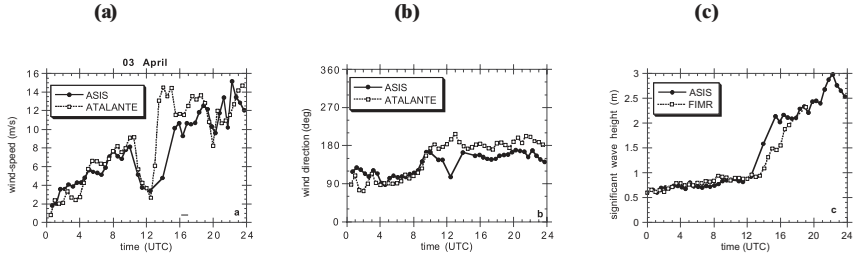

Figure 8.3: Same as Fig. 8.2, but for April 3rd. The position of L'ATALANTE is close to the one of ASIS from 12 to 18 UTC. Note that DWR is located about 25 km north–west of ASIS at this date. RESSAC data were obtained between 16:20 and 17:00 UTC.

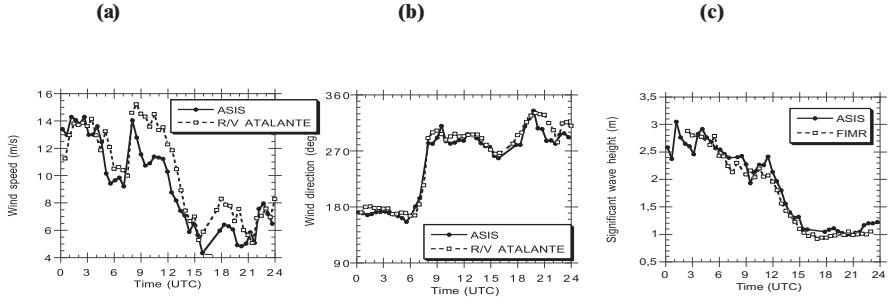

Figure 8.4: Same as Fig. 8.3, but for April 7th. The position of L'ATALANTE is close to the one of ASIS from 13 to 14 UTC and at 21 UTC. RESSAC data were obtained from 16:15 to 16:50 UTC.

our experimental area. These high north-easterly winds started during the night before our measurements and are due to the low-pressure trough over the Gulf of Ligure. We'll see, in the discussion of the results that this has some influence on the wave field measured along the RESSAC track. The significant waveheight measured at the ASIS and DWR locations gradually increases after the first wind increase in the morning and reaches about 2 m at the time of the RESSAC observations.

On April 3rd, the general meteorological situation corresponds, to a dominant surface wind from the south–west over the western Mediterranean sea for the whole day. This circulation is associated with the warm air preceding a frontal atmospheric discontinuity which moved eastward from the Atlantic to Spain and France. We could conclude from the ALADIN model (not shown here), that the easterly winds measured at the buoy and ship locations until 12 UTC (see Fig. 8.3) are, in fact, associated with a cyclonic circulation of relatively small scale (about 100 km in diameter) embedded in the general soutwesterly flow. This cyclonic circulation is very likely related to the orographic effect of the Pyrénées mountains located around 42.0-42.5°N at the French-Spanish border. In the morning, the centre of this cyclonic structure is located a few tens of kilometers south–west of the ASIS buoy. This induces light winds from the east at the ASIS position. But in the afternoon (after 15 UTC), this structure has moved to the north–west with respect to its previous position, so that at the ASIS position, wind is much higher (10-14 m/s) and from the south–southeast. Because L'ATALANTE is located further south–east (see Fig. 8.3) in the afternoon, winds from this ship are more oriented from the south. The ALADIN model shows that high winds from the south–west blow along the Spanish coast, south–west of our experimental area. Significant waveheights measured by ASIS and DWR show a rapid increase after the wind increase (after 12 UTC) with values of 1.7 to 2 m observed during the RESSAC measurements (16:20 to 17 UTC).

On April 7th, an atmospheric frontal discontinuity passed over the experimental area in the morning. In front of this discontinuity, (before 8 UTC at the ASIS location) wind was blowing from the south with wind speed above 10 m/s (see Fig. 8.4). After this front passage, wind blew from west–northwest. At the ASIS location, it started to decrease more or less regularly from above 14 m/s (at 8 UTC) to about $4-7$ m/s at 15 UTC. After 15UTC, wind speed remained between 4 and 8 m/s, depending on the location (ATALANTE or ASIS) and on the exact time. During the RESSAC observations (16:15 to 16:50 UTC), wind at the ASIS location was light (about 4 m/s).

Due to the southerly flow existing during the previous hours, a swell system with waveheight up to 3 m was present in the morning before the frontal passage. Significant waveheight measured at the two buoy locations are very similar and decrease from about 3 m in the morning to about 1 m in the afternoon.

8.7 Results

8.7.1 March 24th

Figure 8.5 presents a selection of 1D and 2D spectra derived from RESSAC on March 24th. These spectra correspond to locations 4, 6, 8, 10 in Fig. 8.1a. The corresponding fetch distance, is 50, 76, 93, and 118 km, respectively. This distance was calculated as the distance between the measurement point and the coast assuming a wind direction from north (0°). Note that in the RESSAC spectra the more or less constant level of energy at low frequency (smaller than the peak) is spurious (due to imperfect corrections in the radar data processing). It should not be considered in the interpretation. In particular, for RESSAC spectra 4 and 6, the analysis should be restricted to wave frequencies above 0.15 Hz.

Non-directional spectra on March 24th (left plots in Fig. 8.5) exhibit features in agreement with what is expected for fetch-limited situations, with an increase of the energy and decrease of the peak frequency f_p for increasing fetch distances. Note that there is a very good correspondence between the 2D spectra obtained from RESSAC on the way going offshore and on the way coming back, separated by about 1 hour (not shown). Compared to the JONSWAP relationship (Hasselmann *et al.*, 1973), we found good agreement for the variation of f_p with fetch, if a wind speed of the order of 15 m/s is assumed. For the energy (both from RESSAC and from the TOPEX-POSEIDON data), the increase for this wind speed is slightly more rapid than the JONSWAP relationship.

RESSAC 2D spectra (right part of Fig. 8.5) also show a significant evolution with distance along the flight-track. At the most northern part (spectra 1 to 6), the 2D energy density is spread around the north-south direction (180–210° ±180°). The relatively broad distribution (with a visible double-peaked structure) in spectra 4 to 6 may be due to the fetch effect associated with the shape of the coast. Further along the track (spectra 7–13), two wave-trains are observed, one in the north–south direction, and another one

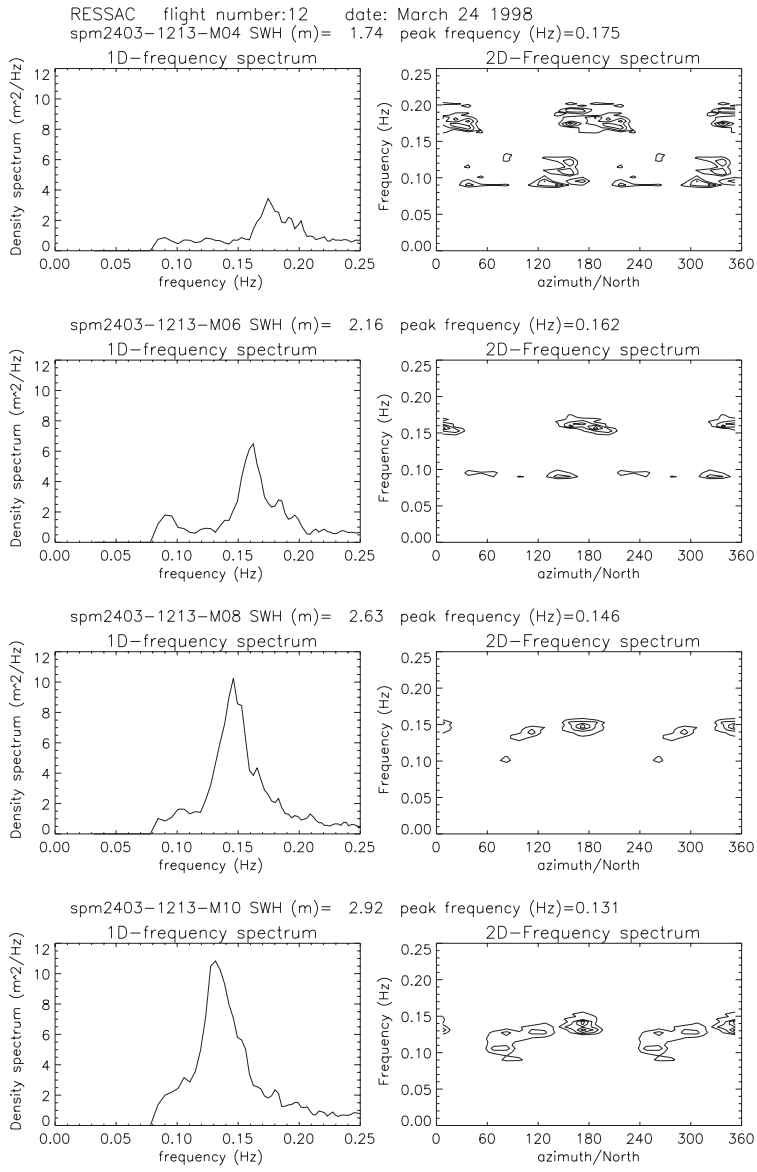

Figure 8.5: 1D (left) and 2D (right) spectra along the RESSAC flight track on March 24$^{\text{th}}$. For the 2D spectra, the energy density is normalised to its maximum value and is plotted versus direction (horizontal axis) and wave frequency (vertical axis). Contours levels are each 0.2 from 0.3 to 0.9. From top to bottom, the spectra correspond to positions 4, 6, 8, 10 in Fig. 8.1a

spread in the northeast-east direction. The first one probably corresponds to wind-waves generated in the measurement area, whereas the latter one is likely to be associated with the waves generated in the Gulf of Ligure (6-10°E, 43-44°N) by the high north-easterly winds blowing there (see section 8.6).

The comparison of RESSAC spectra with ASIS data is shown in Fig. 8.6. There is a good agreement between the non-directional spectra (Fig. 8.6, left panels) with similar peak frequency and energy density. The directional distributions are also in good agreement between RESSAC and ASIS (Fig. 8.6, right panels), although it is evident that the RESSAC spectrum shows more detail than the ASIS spectrum derived with the MLM. Although the peak direction is around 180° for both ASIS and RESSAC, the RESSAC spectrum shows two wave modes near the peak frequency, while the ASIS energy density is more spread in direction and centred around a single peak. The continuous presence of the bimodal sea along the RESSAC flight track indicates that this is a real feature, probably linked to the geometry of the coast line and to the presence of winds from north–west close to the coast as indicated by the atmospheric model ALADIN.

Figure 8.7 shows the spread angle versus the normalised frequency f/f_p for RESSAC and for the wave buoys (DWR and ASIS). Note that the data from DWR were recorded about 2.5 hours earlier than those of ASIS or RESSAC, but we have verified that the conditions correspond to fetch limited stationary conditions. The directional spread obtained from RESSAC is in very good agreement with the ones estimated from ASIS and from the DWR in the energy containing part of the spectrum ($0.8 < f/f_p < 1.5$). Note that in spite of the broader 2D spectrum observed by ASIS, there is a good consistency of the angular spread values. These latter are calculated from the co- and quad spectra for the buoy data but from the 2D spectra for RESSAC. Hence, the broader spectra for ASIS seem to be explained by the MLM which is known to have tendency to provide such broad distributions.

Figure 8.8 shows the spread angle plotted for the subset of RESSAC spectra (4-6-8-10) obtained along the track of RESSAC. The spread angle plotted versus frequency f (not shown) or plotted versus the normalised frequency f/f_p (Fig. 8.8) look similar: they do not show any clear fetch dependence. This is in contradiction with results from Mitsuyasu *et al.* (1975) and Hasselmann *et al.* (1980) who find a dependence of the parameter s (of a $\cos^{2s}$ distribution) with wave age.

To analyse further the spread parameters of RESSAC, the complete set of

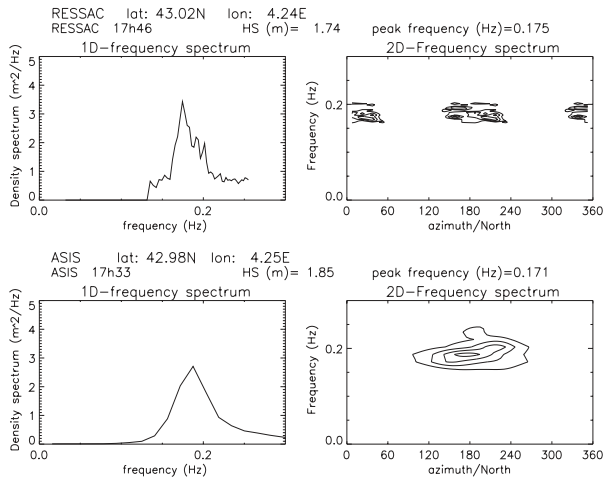

Figure 8.6: 1D (left panels) and 2D (right panels) spectra obtained from RESSAC (top panels) and from ASIS (bottom panels) on March 24, 1998. For the 2D spectra, the energy density is normalised to its maximum and is plotted versus direction (horizontal axis). Contour levels are each 0.2 from 0.3 to 0.9. Time and location, as well as significant waveheight and peak frequency are also indicated on top of the panels.

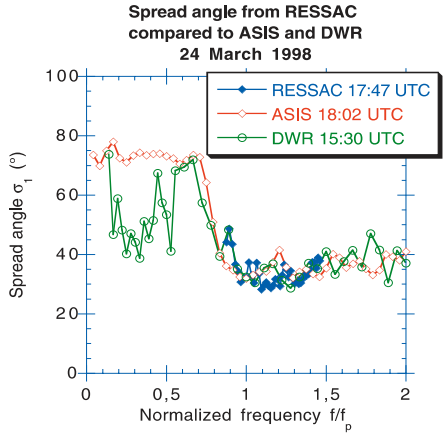

Figure 8.7: Comparison of the spread angle E(f) between RESSAC data and buoy data on March 24$^{\text{th}}$. Data from RESSAC at 17:47 UTC are plotted with the corresponding available data closest in time: DWR at 15:30 UTC, and ASIS at 18:01 UTC.

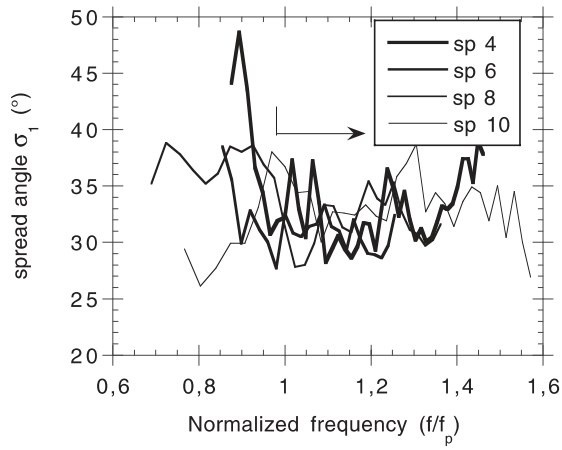

Figure 8.8: Spread angle calculated from the 2D spectra of RESSAC on March 24$^{\text{th}}$ for 4 spectra located at different fetch distances from 50 to 118 km (spectra labeled 4, 6, 8, 10 in Fig. 8.1a).

spread angles and exponent s are plotted in Fig. 8.9.

Overall, we find a minimum value of the spread near the peak frequency. However the scatter is rather large, and in the range of f/f_p which can be analysed from RESSAC, there is not a large variation of the spread. Spread values at the peak are of $32 \pm 4°$ whereas the mean value over all frequencies analysed with RESSAC, is $34 \pm 4°$. The equivalent s exponent shows maximum values at the peak frequency with a mean value of 5.5 $\pm$1.6. In Fig. 8.9b, we also compare these results with the empirical relationships given by Mitsuyasu *et al.* (1975) and Hasselmann *et al.* (1980) for the dependence of coefficients with f/f_p and with wave age. Inverse wave age, defined as the ratio of wind speed U to phase speed C_p at the peak frequency was estimated to range from 1.2 to 1.7 (assuming a constant wind speed of 15 m/s). Figure 8.9b shows that our data span approximately the range of values given by the relations of Mitsuyasu *et al.* (1975) and Hasselmann *et al.* (1980), but the scatter is much larger than predicted by these fetch-dependent relations. In addition our data do not follow the relations proposed by Mitsuyasu *et al.* (1975) and Hasselmann *et al.* (1980). It must be noted however that there is not yet a consensus on the dependence of the angular spread on fetch or wave age. Indeed, Donelan *et al.* (1985) show that the dependence of the angular spread with wave age disappears when the angular spread

is evaluated by using the half-height width of the angular distribution instead of the σ_1 parameter, indicating a probable spurious effect of noise in the estimation of σ_1. Ewans (1998), who presented an analysis of pitch-roll buoy near the coasts of New-Zealand concluded that the dependence of the s parameter on wave age was either very weak or non existent.

The relationship between the r_1 and r_2 spread parameters is shown in Fig. 8.10 ($\sqrt{r_2}$ is plotted versus r_1).

In this figure are also plotted the theoretical curves as given by Krogstad *et al.* (1999) and also shown in section 2.5.3 - Fig. 2.5 in Part 1. Different shapes of the theoretical distributions are plotted (Poisson, sech^2 distribution from Donelan *et al.* (1985), wrapped normal, $\cos^{2s}$ distributions). We find that at large values of r_1 (r_1 >0.8, i.e angular spread less than about 35°), our data are consistent with both the Donelan *et al.* (1985) sech^2 distribution and the $\cos^{2s}$distribution. It is not possible to determine which one of these two relations is in best agreement with the observations, because the theoretical curves are very close together (see also section 2.5.3 in Part 1). In particular, near the peak frequency where the spectra are narrower, it appears that our data are consistent with both the Donelan *et al.* and the $\cos^{2s}$ distribution, but it seems that the Poisson distribution can be excluded. When smaller r_1 values are considered (larger spreads), our data seem to be significantly closer to the $\cos^{2s}$ distribution than to the Donelan *et al.* distribution. When including these smaller r_1 values, the $r_1 - r_2$ relation is even to the right of the $\cos^{2s}$curve, which seems compatible with the bimodal distribution of Ewans (1998) mentioned by Krogstad and Barstow (1999). Compared to the results obtained by Krogstad and Barstow (1999) from in situ data, it appears that the global scatter in the $r_1 - r_2$ relations of RESSAC is much less. Jackson *et al.* (1985) also concluded from the same kind of analysis applied on comparable radar observations, that his $r_1 - r_2$ relations were much less scattered than the corresponding relations from buoy observations. The same conclusion was obtained by Walsh *et al.* (1985) who used an airborne scanning altimeter. This seems to show that radar data contain more information on the directional distribution than in situ devices like wave riders or wave gauge arrays. Another reason may be, as mentioned by Jackson *et al.* (1985), that the quantities used to calculate r_1 and r_2 from radar data are derived from the same measurement, whereas for buoys, they are derived from different sensor outputs.

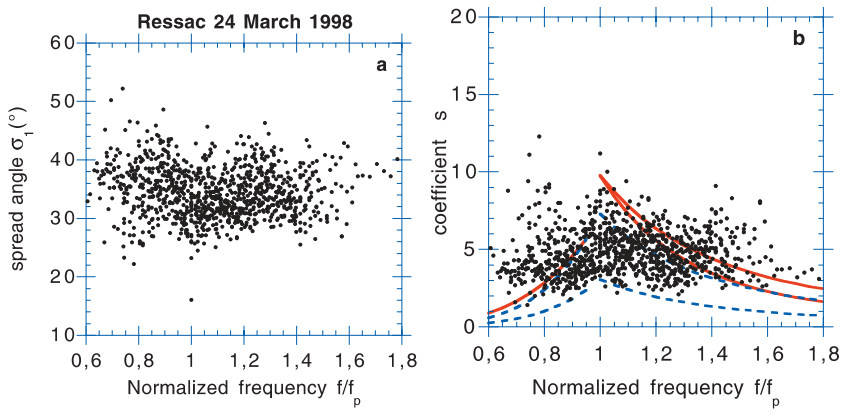

Figure 8.9: Spread angle (a) and coefficient s of a $\cos^{2s}$ angular distribution (b) for the RESSAC data of March 24$^{\text{th}}$. In panel b relationships from the literature also plotted for two values of U/C_p: U/C_p=1.2 and 1.7, for upper and lower lines of the same type, respectively, solid lines for Hasselmann *et al.* (1980) dashed lines, for Mitsuyasu *et al.* (1975).

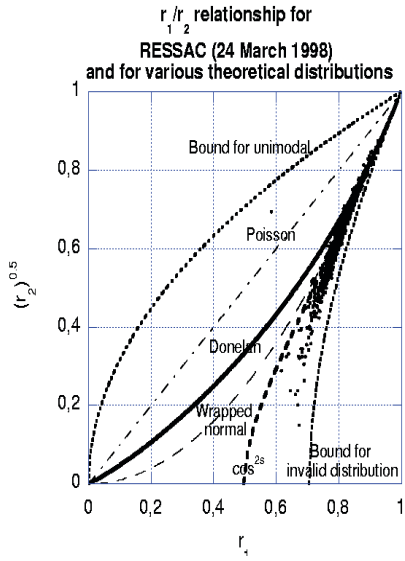

Figure 8.10: Scatter plot of $\sqrt{r_2}$versus r_1 for the RESSAC data on March 24$^{\text{th}}$. The relationship for various angular distribution are also indicated: Poisson distribution, Donelan *et al.* (1985) sech^2 distribution, wrapped normal, and $\cos^2$s distribution.

8.7.2 April 3rd

Figure 8.11 shows a selection of 1D and 2D spectra derived from RESSAC on April 3rd. These spectra, correspond to locations 3, 5, 7, 9 in Fig. 8.1b. Along the track of RESSAC shown in Fig. 8.1b (from positions 3 to 14), significant waveheight ranges from about 1.0 to 2.1 m with maximum values (larger than 1.8 m) observed from positions 4 to 7. The difference in the significant waveheight of RESSAC between locations 3 and 5 is in agreement with the difference observed between DWR and ASIS: 1.9 m measured by DWR near position 3, and 2.1 m by ASIS near position 5. These data indicate that the wave field is not very homogeneous. In the northern part of the track (positions 1 to 7), this is due to the small-scale cyclonic circulation embedded in the general southwesterly flow, as explained in Section 8.6. Evolution between the northern part (positions 1 to 7) and southern part (7 to 14) is probably due to a sheltering effect associated with the Spanish coast. As a matter of fact, we observe a progressive shift of the peak direction (coming from) from 180° to about 230° when going from positions 3 to 14. In addition, a broader distribution is observed on the RESSAC data at positions 7 to 11. It seems that two maxima can be distinguished, corresponding to a north–south (180° ±180°) and northeast–southwest (230° ±180°) direction. This is consistent with a wind-wave component from the south generated locally (winds are from the south at the ATALANTE position), mixed with a swell component from the south–west (230°). As shown by the ALADIN atmospheric model, this swell is probably generated by the high south–westerly winds which have been blowing for several hours south–west of our experimental zone. Both components have a similar peak frequency, so that it is difficult to separate them by looking at the 1D spectra. In direction, the energy is spread over angles 180-230°, so that the result is a broadening of the directional distribution.

Figure 8.12 shows a comparison of the 1D and 2D spectra of RESSAC with the corresponding spectra of DWR (at position 3) and of ASIS (at position 5). At both locations, RESSAC is in good agreement with the buoy data: same shape of the 1D spectrum, same peak frequency and good agreement in the shape of the angular distribution. The difference of about 10 cm in the significant waveheight between RESSAC and ASIS has probably to be attributed however to the non-homogeneous and non stationary situation (see section 8.6). Here again, as for the case of March 24th, the 2D spectrum obtained from ASIS is broader than the corresponding one of RESSAC.

Figure 8.13 shows the spread parameter $\sigma_1(f)$, obtained from RESSAC com-

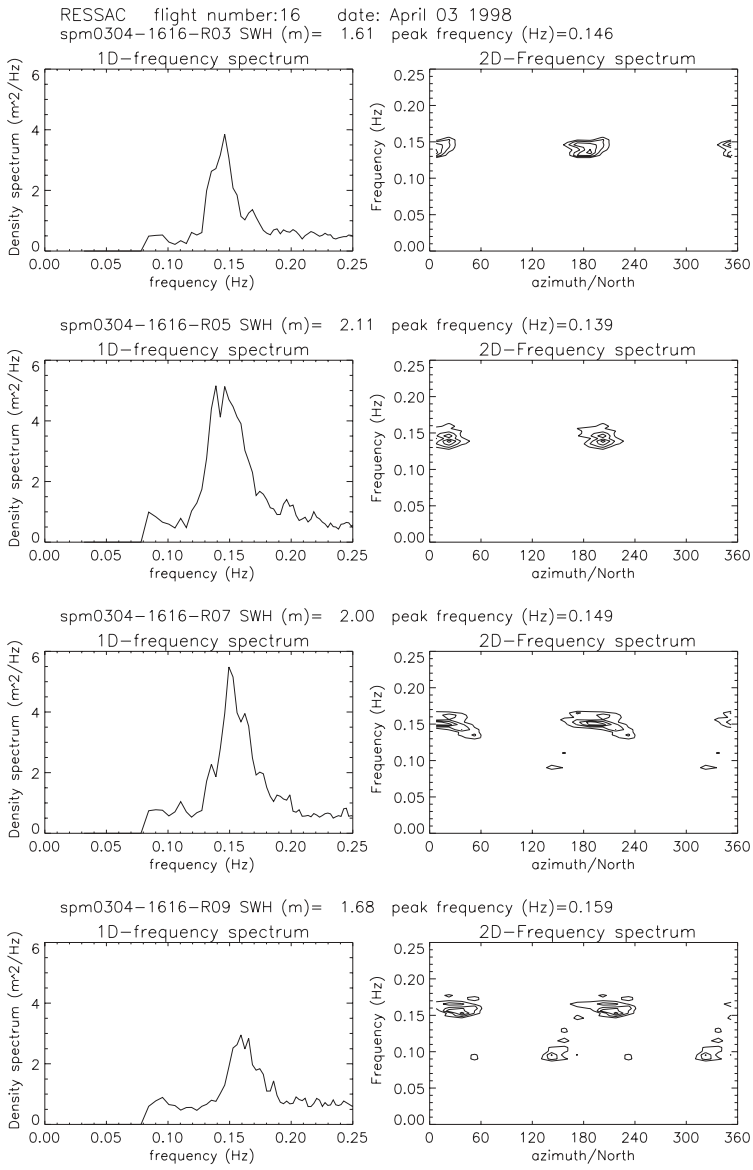

Figure 8.11: 1D (left) and 2D (right) spectra along the RESSAC flight track on April 3^{rd}. For the 2D spectra, the energy density is normalised to its maximum value and is plotted versus direction (horizontal axis) and wave frequency (vertical axis). Contours levels are each 0.2 from 0.3 to 0.9. From top to bottom, the four spectra correspond to positions 3,5,7,9 in Fig. 8.1b.

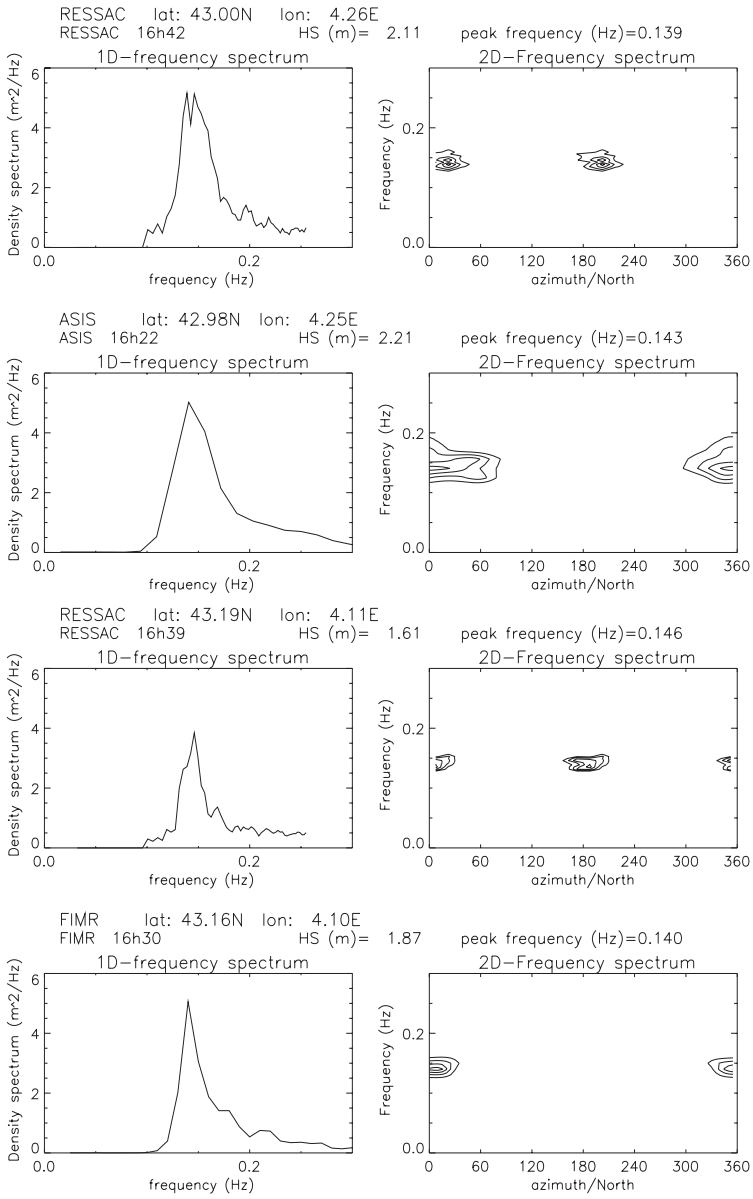

Figure 8.12: Comparison of the 1D (left panels) and 2D (right panels) spectra of RESSAC (first and third lines) with the corresponding spectra of ASIS (second line) and DWR (fourth line) on April 3, 1998.

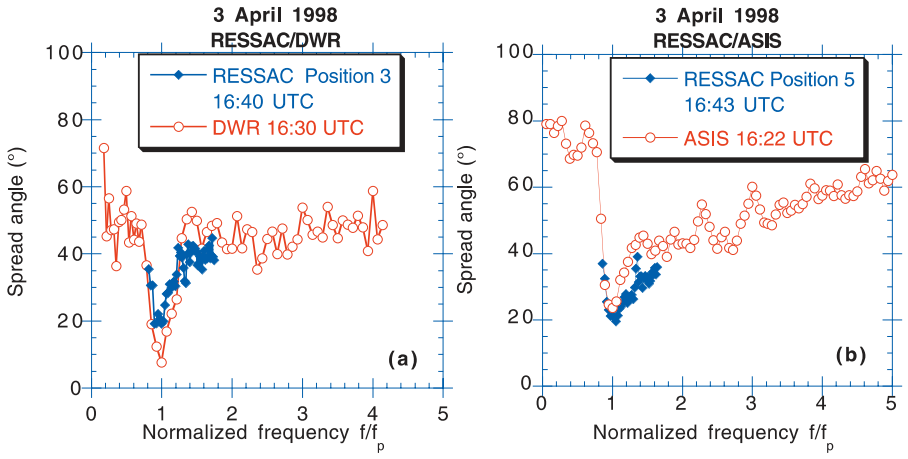

Figure 8.13: Comparison of the spread angle $\sigma_1(f)$ between RESSAC data (solid diamonds) and buoy data (open symbols) on April 3rd.. (a) spectrum at location 3 of RESSAC compared to DWR. (b) spectrum at location 5 of RESSAC compared to ASIS.

pared with that deduced from DWR (Fig. 8.13a) and ASIS (Fig. 8.13b). In each case, minimum of spread is found near the peak frequency, with increasing spreading at lower and higher frequencies. The order of magnitude of the spread is similar for RESSAC and DWR, although the minimum at the peak frequency is about 10° smaller for DWR. RESSAC and ASIS report also consistent angular spread although RESSAC shows a slightly narrower distribution above the peak.

In this case, and in spite of the non-homogeneous and non stationary feature of the situation, there is also a good agreement between the directional properties observed by RESSAC and by the buoys ASIS and DWR.

The non-homogenous situation is further illustrated by the analysis of the spread parameter for a set of RESSAC observations along the track (Fig. 8.14).

The different curves are relative to the locations 3, 5, 7, 9, and 13 indicated in Fig. 8.1b. At all locations, the spread is minimum near the peak of the spectrum. Larger values of spread at the peak of the spectrum are obtained for positions 7 to 13, compared to positions 1 to 6. This is consistent with the double wave system observed on the 2D spectrum south of location 7, with very close peak frequencies, but different directions.

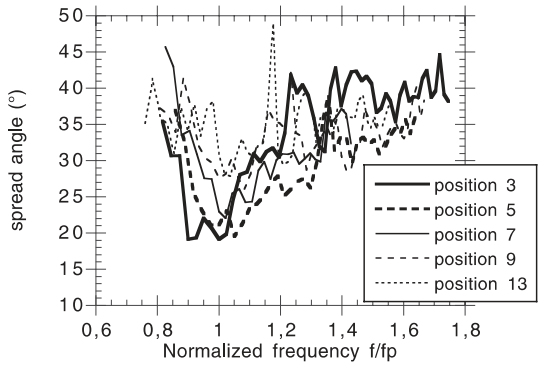

Figure 8.14: Spread angle versus normalised frequency on April 3rd, for 5 spectra of RESSAC located at different distances along the track (positions 3, 5, 7, 9 and 13 in Fig. 2.b).

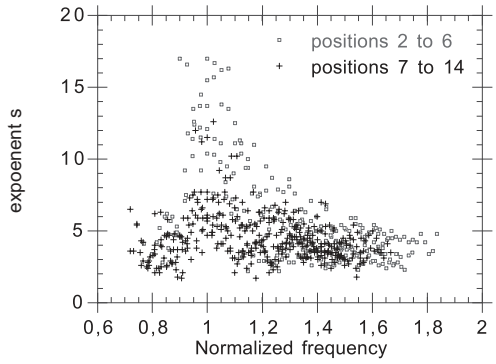

Figure 8.15: Exponent s of a $\cos^{2s}$ angular distribution for all the 2D spectra measured by RESSAC on April 3rd. The two symbols (crosses and dots) discriminate between results for the first half (closest to the shore) and second half of the track (off-shore).

Figure 8.15 shows the coefficient s of the $\cos^{2s}$ angular distribution calculated for the RESSAC positions 2 to 14 as a function of the normalised frequency f/f_p.

The s values range from about 2 to 18, with maximum values (narrower distribution) near $f = f_p$. The result also show that most of the data points with $s \geq 8$ (narrow distributions) are associated with positions 2 to 6 where only one wave system was visible on the RESSAC data. So it turns out that the energy near the peak is more widely spread in direction when the second south–west system is present. Because the two wave systems have very close peak frequencies, but slightly different peak directions, the spread parameter calculated from the 2D spectra increases. Compared to the spread parameter of March 24$^{\text{th}}$, the angular spread is similar, except in positions where only one wave train is observed (positions 2 to 6), which shows a narrower distribution.

The relation between parameters r_1 and r_2, was also analysed for this case. We obtain the same kind of results (not shown), with distributions which are close to a Donelan *et al.* (1985) shape or a $\cos^{2s}$ shape at small spreads, but are closer to a $\cos^{2s}$ shape at larger spreads. As for March 24$^{\text{th}}$, the $r_1 - r_2$ relation at large spread is also consistent with a bimodal distribution.

8.7.3 April 7$^{\text{th}}$

Figure 8.16 shows a selection of 1D and 2D spectra obtained from RESSAC along its track. They correspond to positions 6, 8, 10 in Fig. 8.1.c. For the whole set of data, the significant waveheight from RESSAC ranges between 1 and 1.7 m, with increasing values between positions 6 and 11. Positions 1 to 5 are characterised by a small waveheight (of the order or less than 1 m). Because of this low energy it is difficult to analyse the RESSAC data from this region in detail. As seen in Fig. 8.17 (top left panel), the 1D spectrum from RESSAC near ASIS is noisy, and the peak energy is not very large with respect to the background noise level. In addition, ASIS shows that a significant part of the energy is located at high frequencies (> 0.20 Hz) where the sensitivity of RESSAC is less. ASIS shows two wave components (Fig. 8.17, bottom panels), propagating towards east and north, respectively. On the RESSAC spectra, some energy in these two directions is also observed although the shape of the buoy spectrum is not retrieved by RESSAC, because of the limitations just mentioned. So, only a very rough agreement is found between RESSAC and ASIS, because of the low wave energy. For this reason also, we do not present any comparison between

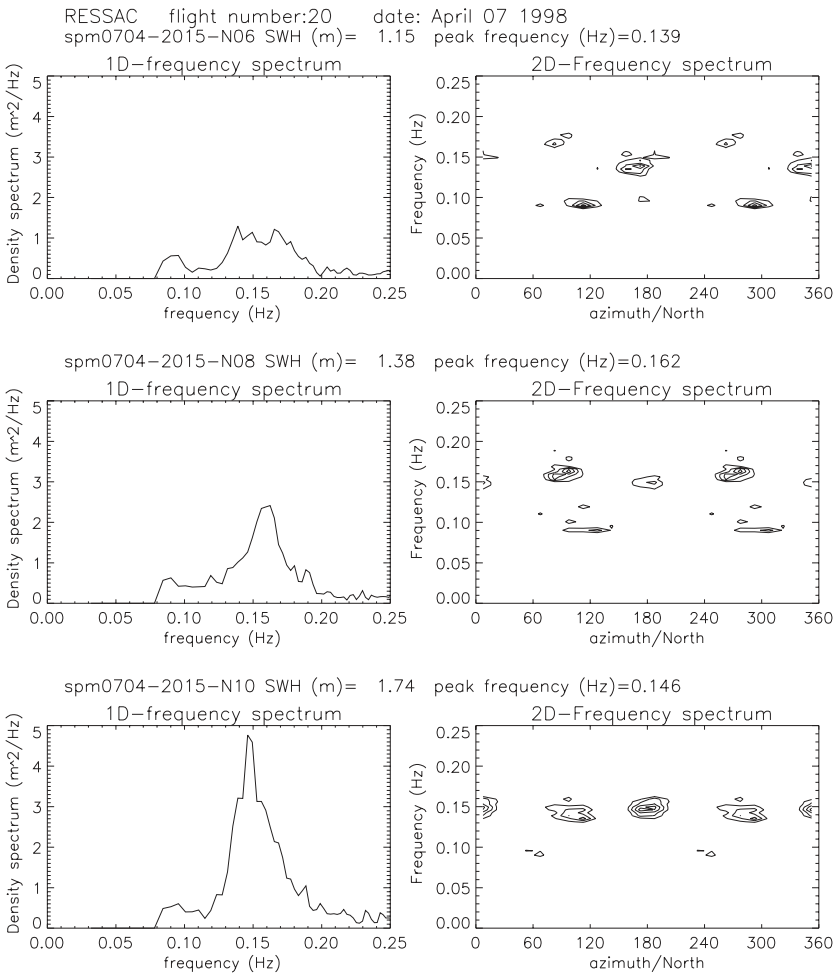

Figure 8.16: 1D (left) and 2D (right) spectra along the RESSAC flight track on April 7$^{\text{th}}$. For the 2D spectra, the energy density is normalised to its maximum value and is plotted versus direction (horizontal axis) and wave frequency (vertical axis). Contours levels are each 0.2 from 0.3 to 0.9. From top to bottom, the spectra correspond to positions 6, 8, 10in Fig. 8.1c.

RESSAC and buoy directional spread for this case.

However, it is possible to discuss the variations of the directional properties seen by RESSAC along its track from 4 to 11, where wave energy is larger. Close to the ASIS buoy (spectra 4-6), the 2D spectra are all characterised by a low energy system aligned in the east–west direction (see Fig. 8.16 top panels). From positions 6 to 10, two wave components are visible, one in the north–south direction, the other one in the east–west direction (middle and bottom panels in Fig. 8.16). The first one corresponds to the swell system propagating towards the north, and generated from the southerly winds of the previous hours and previous day. The second system is probably wind-sea generated by the westerly winds occurring after the frontal passage. The peak frequency of the swell system remains constant (0.15 Hz) over the region sampled by RESSAC, whereas the peak frequency of the wind-sea system decreases from positions 6 to 10 from 0.17 to 0.15 Hz. This is consistent with an increase of fetch between these positions. Hence, between position 6 and 10, we observe a superposition of a fetch-limited wind sea and a cross swell.

The spread parameter σ_1 for the spectra 6, 7, 8, and 10 is shown in Fig. 8.18a as a function of frequency f. The corresponding 1D spectra are also plotted in Fig. 8.18b.

Because there is a double peak in frequency in some of the 1D spectra, we have plotted the data versus f and not f_p. The spread parameter shows a behaviour different from the other studied cases. Indeed, at positions 8 and 10, there is no marked minimum of the spread angle near the peak frequency. The same result is obtained at all positions between 8 and 11 (not shown). In contrast, for spectra 6 and 7, a minimum exists near one of the peak frequencies. It is likely that the absence of a minimum for spectra 8 to 11 is due to the double-peaked system with wave trains very well separated in direction but very close in frequency. When these two wave trains are more separated in frequency (spectra 6 and 7), the spread angles shows this minimum, near the peak frequency of the swell system.

The $r_1 - r_2$ relationship for this case was also analysed. Results are similar to the case of March 24$^{\text{th}}$, showing shapes of distribution compatible with either Donelan *et al.* (1985) or $\cos^{2s}$ distributions when the data set is limited to spread values less than about 35° ($r_1 > 0.8$) or to bimodal distributions when all $r_1 - r_2$ values are considered.

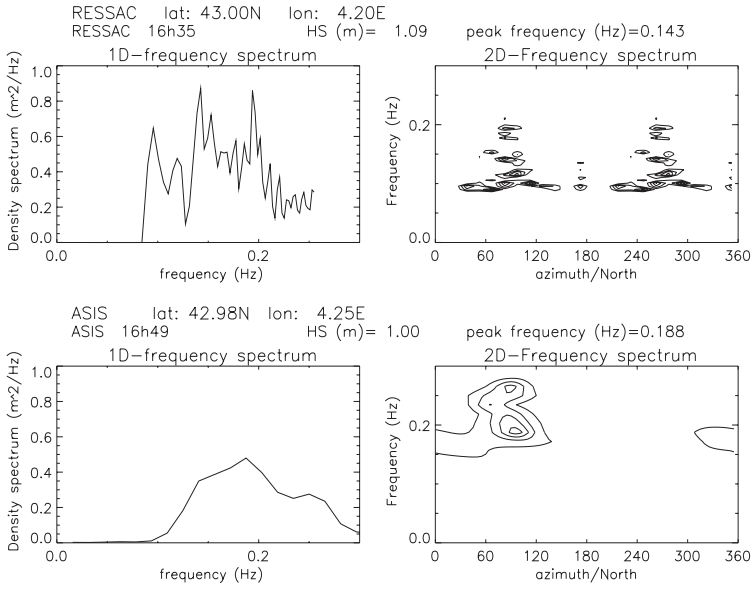

Figure 8.17: Comparison of the 1D (left panels) and 2D (right panels) spectra of RESSAC (first line) with the corresponding ASIS data (second line) on April 7, 1998.

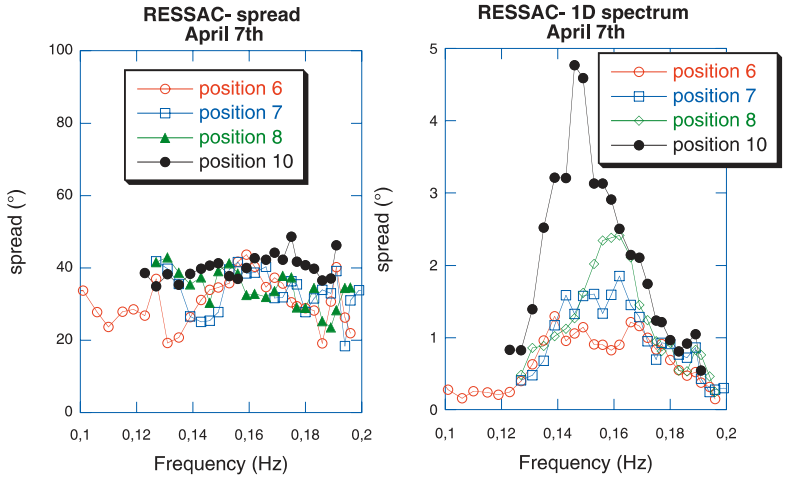

Figure 8.18: Spread (left panel) and 1D spectrum (right panel) from RESSAC on April 7$^{\text{th}}$ at positions 6, 7, 8, 10 indicated in Fig. 8.1c.

8.8 Conclusions

We have presented results on directional spectra of waves deduced from the RESSAC airborne radar observations during the FETCH campaign. In order to compare with buoy observations and to study the spatial variation of the angular distribution of these 2D spectra, we have calculated a spread angle and exponent s of a $\cos^{2s}$ distribution, based on the quantities usually estimated from buoy data analysis (coefficients of a Fourier series related to co-and quad spectra). During the fetch-limited case of March 24$^{\text{th}}$, the agreement for the spread angle between RESSAC and both the DWR waverider and the ASIS wave array is good. The same order of magnitude is found for the spread and the same trend with frequency is observed (minimum values at the peak frequency with increasing values for lower and higher frequencies). At the ASIS location, it seems that a non-homogeneous and/or non-stationary wave-field can be invoked to explain the difference between RESSAC and ASIS.

The comparison between RESSAC and the data from the ASIS and DWR buoys for the case of April 3$^{\text{rd}}$ also shows good general agreement for the directional spread in spite of the non-homogeneous and/or non-stationary character of the situation. In this case, as in the case of March 24^{th}, the 2D spectra provided by ASIS are however significantly broader than the corresponding spectra of RESSAC. The use of the MLM to estimate the 2D spectra from ASIS is probably one of the causes.

In the fetch-limited case (March 24$^{\text{th}}$) no clear variation with wave age or fetch was found for the spread of the angular distribution, as opposed to what was expected from results from Mitsuyasu (1975) and Hasselmann (1980), but in agreement with the analysis of Donelan *et al.* (1985) or Ewans (1998).

In the on-shore wind case (April 3$^{\text{rd}}$), spatial variations of the spread at the peak frequency were identified. They seem to be related to the change from a wind-sea system in the north to a mixed sea situation in the south of the RESSAC track. The mixed sea part shows larger spread of the distribution.

In the third case (April 7$^{\text{th}}$), a combination of fetch-limited wind sea and swell with very distinct directions was present. In that case, the combination of two orthogonal systems with energy well separated, leads to a relatively high spread ($>30°$) all over the energy containing part of the spectrum. The minimum of spread near the peak frequency was only present when the two systems have different peak frequencies.

Results obtained from these three different situations show that our mea-

surement and the proposed approach is able to show variations in the angular distribution when these are present. However some care must be taken before drawing conclusions about the variations of this directional spread, in the presence of bimodal wave systems of the same frequency with well-separated wave trains in direction. This was the case on April 7^{th}. In this case, the spread parameter is probably not representative of any of the two systems, and it would be better to analyse the spread parameter on each of the wave trains after applying a wave-separation algorithm.

Relations between the first order r_1 and the second order r_2 parameter was investigated from the radar data, and compared to theoretical relations for different shapes of the angular distribution. The scatter in the r_1-r_2 relations of RESSAC is much less than that discussed by Krogstad and Barstow (1999) for in situ data. Jackson *et al.* (1985) and Walsh *et al.* (1985) also concluded that $r_1 - r_2$ relations obtained from radar observations were much less scattered than the corresponding relations from buoy observations. This seems to show that due to the direct estimate of the 2D spectrum from a unique device, and to the good resolution in angle, radar data contain more information on the directional distribution than in situ devices like wave riders or wave gauge arrays. From our three data sets, we find that the r_1-r_2 relationship is consistent with a $\cos^{2s}$ distribution or sech^2 distribution, and there is some evidence of a bimodal distribution.

This study has shown that airborne radar is a useful tool to study the 2D distribution of the wave energy. The angular distribution was discussed qualitatively with the 2D spectra, and a quantitative study was performed by estimating the angular spread of the waves. We have shown that a lot of information is provided by the directional analysis and that 1D spectra give only limited information when complex sea-states exist, e.g. in coastal regions.

8.9 References

Barstow S.F., G. Ueland, H.E. Krogstad, and B.A. Fossum, The wavescan second generation directional buoy, *IEEE J. on Oceanic Technology*, vol.16 No 3, 254-266, 1991.

Benoit, M., and G. Goasguen, Comparative evaluation of directional wave analysis techniques applied to field measurements, *Proc. of the 9^{th} International Offshore and Polar Engineering Conference*, Brest(France), 31 May-4

June 1999, Paper No99-MP-04, 1999.

Capon, J., High-resolution frequency-wavenumber spectrum analysis. *Proc. IEEE*, 57(8), 1408-1418, 1969.

Donelan, M., A.J. Hamilton, and W.H. Hui, Directional spectra of wind-generated waves, *Philos. Trans. Roy. Soc. London*, Se. A, 315, 509-562, 1985.

Ewans, L.C., Observations of the directional spectrum of fetch-limited waves, *J. Phys. Oceanogr.*, 28, 495-512, 1998.

Graber, H., E.A. Terray, M. Donelan, W. M. Drennan, J.C. Van Leer, and D.B. Peters, ASIS- A new air-sea interaction Spar buoy: design and performance at sea, *J. Atmos. Oceanic Technol.*, 17, 708-720, 2000.

Hasselmann, K., T.P. Barnett, E. Bouws, H. Carlson, D.E. Cartwright, K. Enke, J.I. Ewing, H. Gienapp, D.E. Hasselmann, P. Kruseman, A. Meerbrug, P. Müller, D.J. Olbers, K. Richter, W. Sell, and H. Walden, 1973. Measurements of wind-wave growth and swell decay during the Joint North Sea Wave Project (JONSWAP). *Dtsch. Hydrogr. Z.*, A8(12), 95 p., 1973.

Hasselmann, D.E., M. Dunckel, and J.A. Ewing, Directional wave spectra observed during JONSWAP 1973, *J. Phys. Oceanogr.*, Vol.10, 1264-1281, 1980.

Hauser, D., G. Caudal, G.J. Rijckenberg, D. Vidal-Madjar, G. Laurent, and P. Lancelin, RESSAC: A new airborne FM/CW radar ocean wave spectrometer, *IEEE Trans. Geosci. Remote Sensing*, 30, 981-995, 1992.

Hauser D., H. Branger, S. Bouffies-Cloché, S. Despiau, W. Drennan, H. Dupuis, P. Durand, X. Durrieu de Madron, C. Estournel, L. Eymard, C. Flamant, H. Graber, C. Guérin, K. Kahma, G. Lachaud, J.-M. Lefèvre, J. Pelon, H. Pettersson, B. Piguet, P. Queffeulou, D. Tailliez, J. Tournadre, and A. Weill, The FETCH experiment: an overview, *J. Geophys. Res.* (C3), doi:10.1029/2001J001202, 2003.

Isobe, M., K. Kondo, and K. Horikawa, Extension of MLM for estimating directional wave spectrum. *In: Proc. Symp. on description and modelling of directional seas*, paper A-6, Lyngby, Denmark, 1984.

Jackson F.C., T.W. Walton, and P.L. Baker, Aircraft and satellite measurement of ocean wave directional spectra using scanning-beam microwave radars, *J. Geophys. Res.*, Vol. 90, No. C1, 987-1004, 1985

Krogstad H.E., and S. Barstow, Directional distributions in ocean wave spectra, *Proc. of the 9th International Offshore and Polar Engineering Confer-*

ence, Brest, May 30- Jun 4, 79-86, 1999.

Longuet-Higgins M.S., D.E. Cartwright, and N.D. Smith, Observations of the directional spectrum of sea waves using the motions of a floating buoy, *Ocean Wave Spectra*, Prentice Hall, 111-136, 1963.

Mitsuyasu H., F. Tasai, T. Suhara, S. Mizuno, M. Ohkusu, T. Honda, and K. Rikiishi, Observations of the directional spectrum of ocean waves using a cloverleaf buoy, *J. Phys. Oceanogr.*, Vol 5, 750-760, 1975.

Walsh E., D. Hancock, and D. Hines, Directional wave spectra measured with the surface contour radar, *J. Phys. Oceanogr.*, 15, 566-592, 1985.

Chapter 9

SAR Data Analysis

Susanne Lehner, Danielle Hoja, Johannes Schulz-Stellenfleth

German Aerospace Centre (DLR), Oberpfaffenhofen, Germany

9.1 Introduction

In this chapter ocean wave measurements obtained with spaceborne SAR and airborne interferometric SAR systems are compared to in situ data, ground based sensors and numerical wave models.

The objective is to illustrate both the potential as well as the limitations of SAR wave measurements and to give some idea about the expected accuracy.

Extensive statistical analysis on a global and annual scale comparing ERS-2 SAR wave measurements to the numerical model WAM can be found in Heimbach *et al.* (1998) and elsewhere. Similar comparisons with in situ buoy data were presented in Mastenbroek and de Valk (2000). These studies were based on SAR image spectra (UWA), which are coarsely gridded, symmetric image spectra available as an ERS-2 standard product every 200 km along the track.

The first global statistical comparisons of ERS-2 wave mode SAR images with models results and collocated scatterometer measurements were presented in Kerbaol *et al.* (1998) and Lehner *et al.* (2000). In this chapter some recent results are presented, using a reprocessed data set of ERS-2 complex imagettes, which are similar to the data currently becoming available from the ENVISAT satellite as a standard product.

9.2 Complex ERS-2 SAR Data Analysis

In this section different studies based on spaceborne and airborne synthetic aperture radar data which have recently become available are presented. The analysed data sets have several new features compared to, for example, the standard ERS-2 UWA wave mode product, which make them particularly interesting for the measurement of two dimensional ocean wave fields. The data were obtained by either new SAR systems in dedicated experiments, e.g. by multi-antenna interferometric sensors, or by the reprocessing of existing SAR raw data.

9.2.1 Reprocessed Complex ERS-2 Wave Mode Data

Operating in wave mode the European Remote sensing satellites ERS-1 and ERS-2 acquire SAR images of 10 by 5 km size (imagettes) every 200 km along the track. With an orbit inclination of 98° the ERS satellites allow SAR data sampling on a nearly global scale covering latitudes up to 81.5 ° N/S. The advanced SAR (ASAR) flown on the satellite ENVISAT launched on March 1, 2002 has a similar operating mode but with acquisitions every 100 km.

For ENVISAT the European Space Agency (ESA) provides the full SAR information contained in complex images, while only coarsely gridded SAR image variance spectra are available from the ERS wave mode. The new complex data have the following advantages with respect to ocean wave measurements:

- the ambiguity of wave propagation direction present in conventional SAR image variance spectra can be resolved;
- SAR look cross spectra have lower noise levels than power spectra;
- the availability of the full image information allows additional analysis of the ocean wave field (not only second statistical moments) like e.g. homogeneity, extreme individual waves or atmospheric disturbance.

To take advantage of the full high resolution image information, ERS-2 wave mode raw data were processed to single look complex SAR imagettes using the BSAR processor developed at the German Space Centre (DLR). In total 34 310 SAR imagettes were processed representing 27 days of data between August 21, 1996 and June 2, 1997. Studies on the use of ERS wave mode

data for wind and wave measurements were published in Kerbaol *et al.* (1998), Lehner *et al.* (2000), Horstmann and Lehner (2001), Heimbach *et al.* (1998), Hasselmann *et al.* (1996) and Schulz-Stellenfleth *et al.*(2001b).

Apart from ocean wave measurements, calibrated imagettes can be used for wind speed estimation. Wind direction can be retrieved from wind induced streaks and wind speed from the mean normalised radar cross section of the SAR imagette using the C-band model CMOD4 originally developed for the ERS scatterometer (SCAT), Horstmann *et al.* (2003). Furthermore, imagettes can be used for sea ice observations providing information on small scale structures like ice floe size.

As an example, Fig. 9.1 shows two ERS-2 imagettes from the reprocessed data set with ocean wave patterns. Details about the processing and a first comparison with ocean wave model data provided by the European Centre for Medium-Range Weather Forecasts (ECMWF) can be found in Lehner *et al.* (2000).

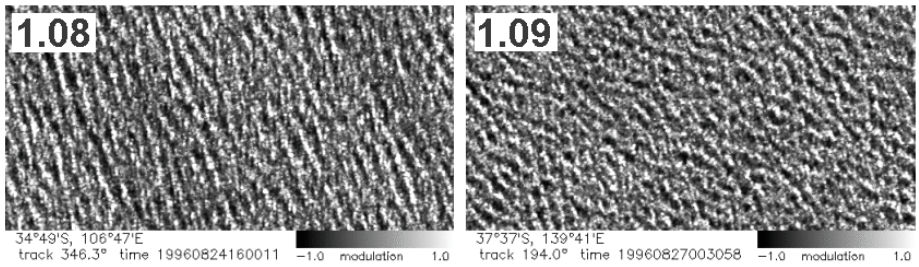

Figure 9.1: Two ERS-2 imagettes reprocessed from wave mode raw data using the DLR BSAR processor.

9.2.2 Comparison of ERS-2 Cross Spectra with WAM Model Data

The reprocessed ERS-2 imagette data set allowed the cross spectra technique described in Engen and Johnson (1995) to be applied on a global scale for the first time. In this section a couple of consistency checks are presented to test the reliability of the new phase information contained in the cross spectra.

Comparison of First and Second Moments

Figure 9.2 (A) shows the imaginary part of the azimuth look cross-spectrum derived from an ERS-2 imagette acquired on June 1, 1997, 06:27 UTC indicating a wave system of about 200 m length propagating to the right. In Fig. 9.2 (B) the collocated ECMWF wave spectrum with 2.6 m significant waveheight is plotted. It can be seen that wave propagation direction and peak wavelength are in good agreement in this case.

The imagette cross spectra were analysed on a statistical basis using all imagettes with collocated ECMWF ocean wave spectra (n=1089). The time gap between SAR observations and model spectra is less than 3 hours and the spatial distance is less than 100 km. Figure 9.3 (A) shows a contour plot of the cross correlation between the range cross spectrum imaginary part (> 0) and the corresponding range wave spectrum. It can be seen that the highest correlations are found along the diagonal plotted in dashed, while negative correlations are found in the upper left and bottom right quarter. Although the absolute correlation values are relatively small, showing a maximum of about 0.6, this pattern indicates a reasonable propagation direction ambiguity resolution for waves travelling in range direction. For the azimuth case Fig. 9.3 (B) shows a similar behaviour, although the correlation pattern is more stretched in the azimuth direction of the ECMWF wave spectrum. This is due to the velocity bunching mechanism, which causes short wave systems travelling in the azimuth direction to be shifted towards lower azimuth wave numbers in the SAR spectrum.

Partitioning of Spectra

Individual wave systems are analysed by a so-called partitioning algorithm of Gerling (1992), see Chapter 10 in Part 2. The method can be applied to cross spectra as well as to ocean wave spectra. Partitioning of WAM ocean wave spectra was done by Hasselmann *et al.* (1996) as part of an algorithm for SAR image spectra inversion. For the partitioning of cross spectra the respective modulus is taken (Fig. 9.4 (A)) and the directional ambiguity of the wave propagation direction is resolved using the imaginary part (Fig. 9.4 (B)). Figure 9.5 shows the partitioning sequence for the cross spectrum shown in Fig. 9.4. The partitioning scheme divides the given spectrum into regions that can be associated with different wave systems (Fig. 9.5 (A)).

The number of partitions found in the first place is in general unrealistically

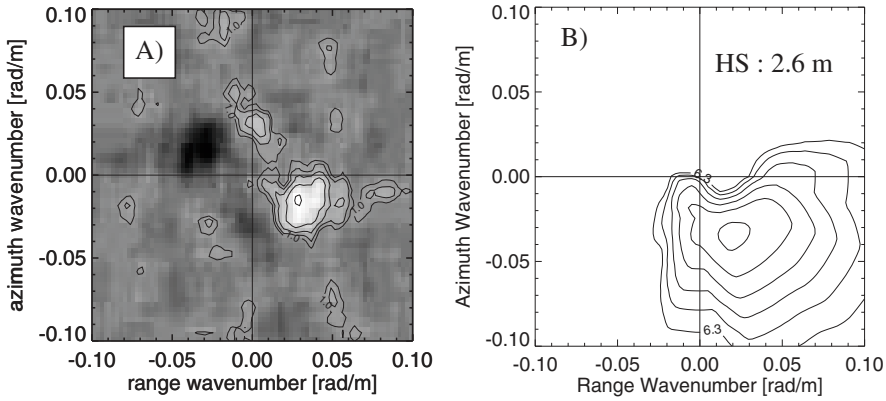

Figure 9.2: A) Imaginary part of cross-spectrum computed from complex ERS-2 imagette acquired on June 1, 1997 06:27 UTC at lat -8.8 lon 56.51 (B) ECMWF ocean wave spectrum with 2.6 m significant waveheight computed for June 1, 1997 06:00 UTC, 9°S 56.63°E

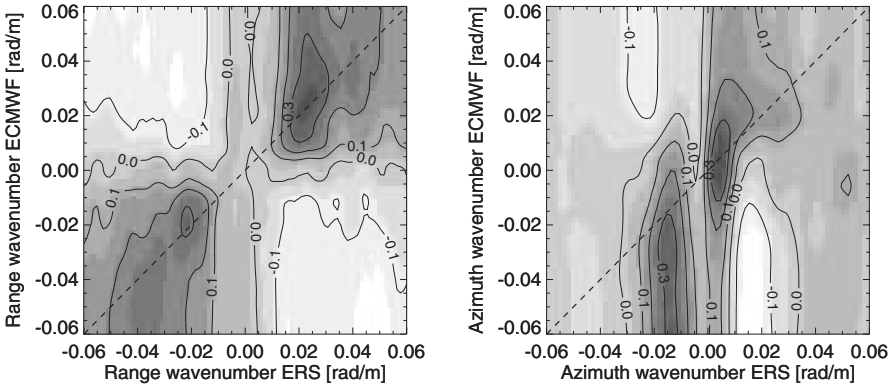

Figure 9.3: (A) Cross-correlation in range direction between cross-spectrum imaginary part (> 0) and collocated ECMWF ocean wave spectrum estimated from 30000 collocations. (B) Cross-correlation in azimuth direction between cross-spectrum imaginary part (> 0) and collocated ECMWF ocean wave spectrum.

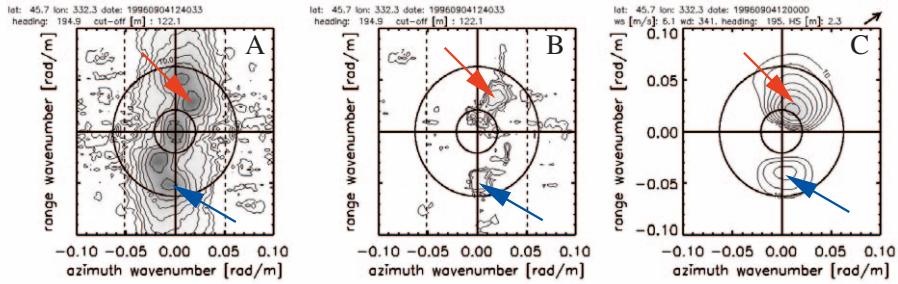

Figure 9.4: (A) ERS-2 cross spectrum modulus showing two different wave systems. (B) Imaginary part (> 0) of cross spectrum. (C) Collocated ECMWF spectrum.

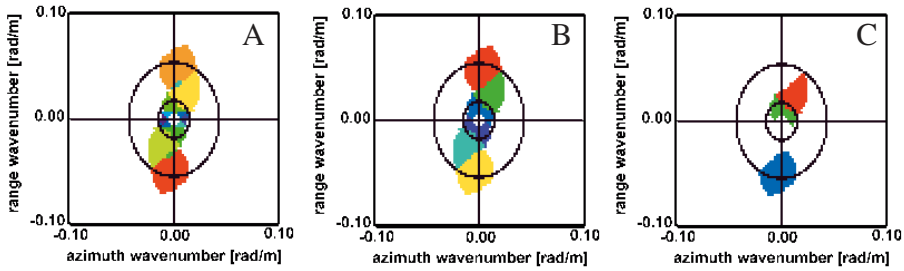

Figure 9.5: (A) Partitioned cross spectrum (modulus) (compare Fig. 9.4). (B) Partitioned cross spectrum with coalesced partitions. (C) Final partitions selected according to the cross spectrum imaginary part.

high due to small scale variations, sampling variability, and directional ambiguities. To remove these artefacts neigbouring partitions meeting additional criteria (Hasselmann *et al.*, 1996) are merged together. Furthermore, only partitions with positive values in the imaginary part of the cross spectrum are taken into account (Fig. 9.5 (C)) resolving the directional ambiguity.

Integral parameters such as mean wave direction, mean wave length, and waveheight are calculated for each spectral partition of the wave spectrum. To obtain first order estimates for these parameters, SAR cross spectra are inverted into ocean wave spectra using a simple quasi-linear inversion method. The dominating wave system in Fig. 9.5 (C) for the example shown in Fig. 9.4 has the following parameters: wave length 266 m, significant

waveheight 2.9 m (after linear inversion), and wave direction 155° (clockwise from north).

Model Comparison

Retrieval of ocean wave information from SAR cross spectra requires a model for the SAR imaging process. Basically there are two ways of comparing model wave spectra with cross spectra observations taking into account the full nonlinear imaging mechanism:

- compare cross spectra simulated from model wave spectra with observed cross spectra (Hoja *et al.*, 2002);
- use nonlinear inversion methods to estimate wave spectra and compare these to model output (Hasselmann *et al.*, 1996; Krogstad *et al.*, 1994; Engen and Johnson, 1995; Mastenbroek and de Valk, 2000).

A description of the different SAR inversion methods is given in Part 1, Section 5.6. The partitioning algorithm is applied to all spectral data sets (imagette cross spectra and quasi-linear inverted ocean wave spectra, wave model ocean wave spectra and forward simulated cross spectra).

Using the comparison of imagette cross spectra with wave model forward simulated cross spectra, cases of significant inconsistencies between SAR measurements and model data in wave length, wave direction and waveheight (only relative) can be detected. This shows the areas of the ocean in which model improvement by assimilation of SAR data can be achieved.

Figure 9.6 shows such a map on August 21, 1996. The arrow length indicates the contribution to the SAR image variance of the different wave systems.

Figure 9.7 shows a map with significant waveheights computed with the PARSA inversion scheme (Schulz-Stellenfleth and Lehner, 2003), described in Part 1, Chapter 5. The scheme takes into account the nonlinear effects in the SAR imaging process and blends SAR information and prior information from the model to estimate a complete two dimensional wave spectrum.

Figure 9.8 shows a scatter plot of SAR inverted versus WAM model significant waveheight H_s. The superscript 12 indicates that only energy with periods greater than 12 seconds were considered in the computation of H_s.

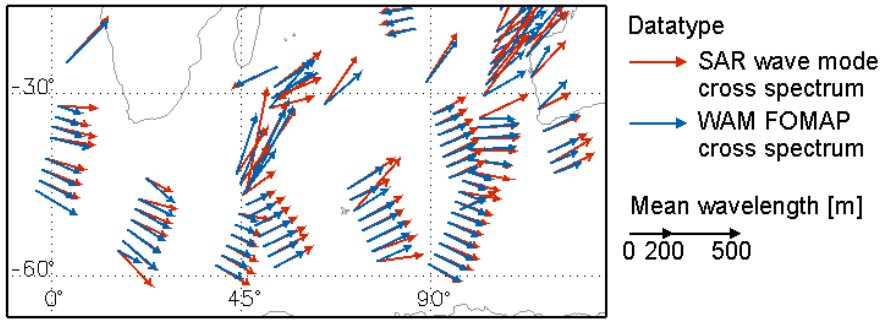

Figure 9.6: Comparison of simulated and observed wave systems found in ERS-2 cross spectra acquired over the South Atlantic and South Indian Ocean on August 21, 1996. The simulations are based on collocated ECMWF ocean wave model data.

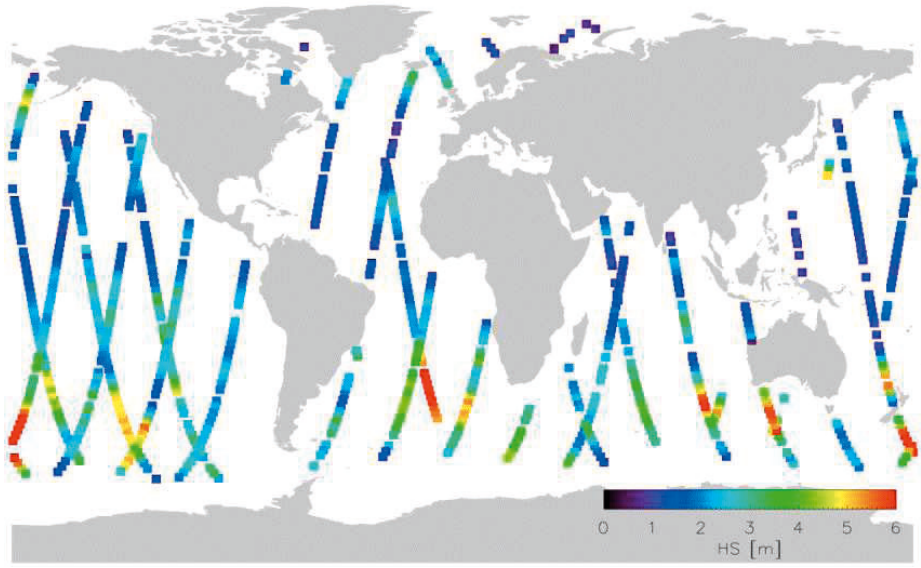

Figure 9.7: Global map of significant waveheight derived from reprocessed ERS-2 wave mode data acquired on September 1, 1996 using the PARSA inversion scheme.

9.3 Interferometric SAR Data Analysis

In this section two experiments carried out with an airborne interferometric SAR system are presented. The first experiment (SINEWAVE) was based

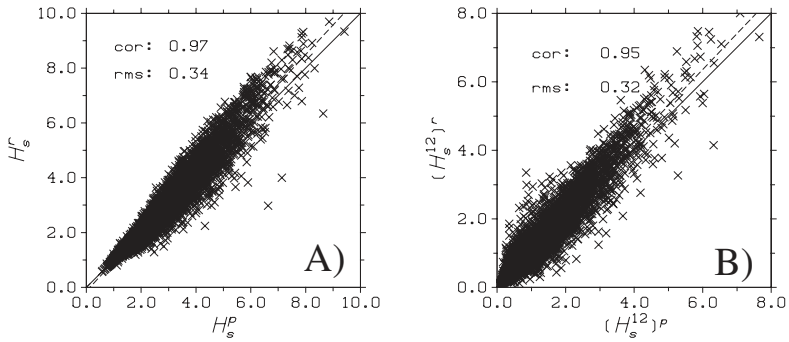

Figure 9.8: A) Scatterplot showing ECMWF waveheights H_s^p versus PARSA derived waveheights H_s^r. B) The same as A) for H_{12}, which is the waveheight of waves with periods greater than 12 s.

on a two antenna sensor with an across track configuration, yielding information about the sea surface elevation field. In the second experiment (TAIWAN) three antennas were used yielding additional information on the orbital velocity and current field. The experiments had the objective to answer the following questions:

- is an across track InSAR system, originally designed to measure elevation models of stationary terrain, capable to provide information on a moving sea surface elevation field?
- what is the impact of wave motion on the InSAR data formation process ?
- what is the impact of inevitable along track components of the baseline on the interferogram?
- does a three antenna interferometric SAR system allow to decouple along and across track components of the baseline yielding independent information on orbital velocity and sea surface elevation?
- do interferometric data contain information on the real aperture radar (RAR) modulation mechanism, which is a key factor in conventional SAR ocean wave measurements?

9.3.1 SINEWAVE Experiment

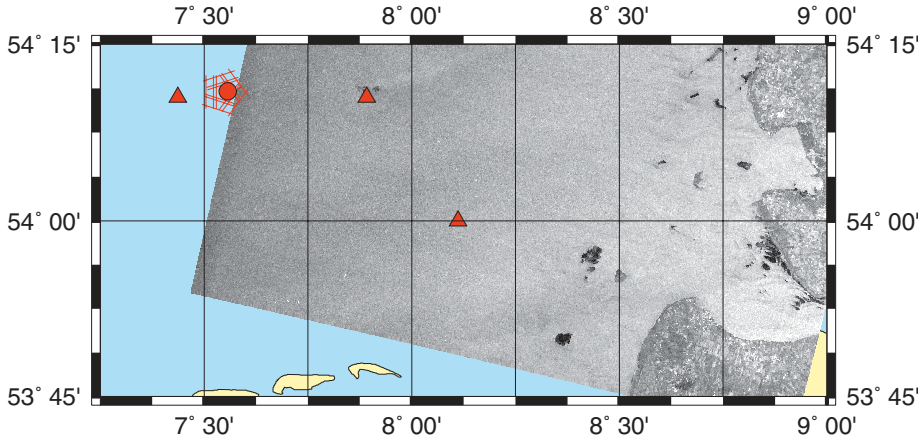

Figure 9.9: Map showing the German Bight with the location of the SINEWAVE experiment 11 nm west of the island Heligoland. An ERS-2 SAR image acquired during the experiment on February 12, 1998 at 12:16 UTC (orbit 14720, frame 2511) is partly superimposed. The red circle indicates the position of a directional wave rider buoy used for in situ ocean wave measurements. The positions of two buoys and a tower on Heligoland used for wind measurements are given by triangles.

The **S**AR **I**nterferometry **E**xperiment for validation of Ocean **Wave** Imaging Models (SINEWAVE) experiment Schulz-Stellenfleth *et al.* (2001a) was carried out in the North Sea 11 nm west of the island Heligoland on Feb 12, 1998. In the experiment the ocean surface was imaged by the AeS-1 across track InSAR system with simultaneous measurements of two dimensional ocean wave spectra by a directional wave rider buoy. The parameters of the AeS–1 system are given in Table 9.1. A map of the experiment location is shown in Fig. 9.9. The size of the map is 120 km x 55 km with the river Elbe estuary on the lower right and the island of Heligoland on the upper inside left. The ERS-2 SAR image superimposed on Fig. 9.9 was acquired at 12:16 UTC (orbit 14720, frame 2511). There is open sea in the dominant wind direction (west) resulting in a long fetch and well developed wave systems. The area has a low variation of bottom topography with an average water depth of about 37 m.

Several ground truth measurements were acquired in the area around Heligoland. The circle in Fig. 9.9 indicates the position of a directional wave

Operating frequency	9.6 GHz
System bandwidth	200 MHz
Polarisation	HH
look direction	right
Incidence angle	20°- 50°
Flight velocity	70 m s^{-1} - 100 m s^{-1}
Azimuth resolution	10 m
Range resolution	10 m
Height resolution	0.26 m-0.50 m
Swath width	1500 m - 2500 m

Table 9.1: Radar parameters of the AeS-1 system developed and operated by AeroSensing GmbH

rider buoy, which provided measurements of 2D wave spectra every 30 minutes. A wind sea system of about 80 m wavelength was measured propagating in an easterly direction. The peak ocean wave frequency is about 0.13 Hz. The significant waveheight H_s decreased slightly from 2.4 Hz to 2.3 Hz.

The red triangles in Fig. 9.9 indicate locations of in situ wind measurements by two buoys *Elbe 1* and *Deutsche Bucht* and from a tower at Heligoland. The wind was blowing from the west with wind speeds of about 13 m/s.

Across track InSAR data were taken at a pentagon flight pattern over the buoy as indicated by lines in Fig. 9.9 (upper left) at flight levels of 500 m, 1200 m, and 30700 m. The size of the tracks is about 3 km in azimuth and about 2 km in ground range. In Fig. 9.10 geocoded intensity images acquired by the master antenna at 1200 m can be seen for all five tracks together with the corresponding bunched digital elevation models (DEMs) and coherence images. Each subimage represents an area of 512 m × 512 m and is oriented north upwards. The solid and dashed arrows represent the aircraft heading.

Comparison with Buoy Data

Fig. 9.11 shows a comparison of two dimensional (2D) spectra calculated from across track InSAR data with collocated buoy measurements. The

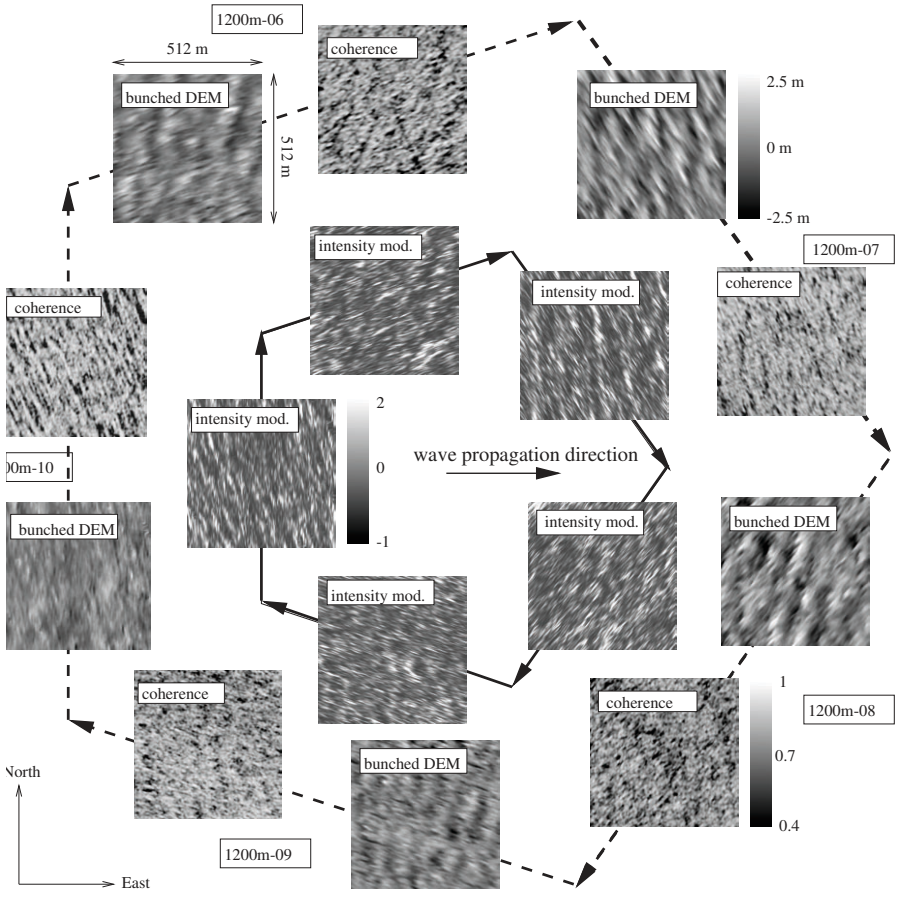

Figure 9.10: Intensity image modulation m (solid line) and bunched DEMs (dashed line) acquired on five tracks in 1200 m height during the SINEWAVE experiment. In addition the respective coherence γ is given (dashed line). All images are of 512×512 m^2 size and are oriented north upwards. The arrow in the centre indicates the peak ocean wave direction. The arrows at the two pentagons indicate flight directions.

2D buoy spectrum (A) is shown together with the bunched DEM spectra acquired at tracks 1200m-07 (B) and 3000m-07 (C). All three spectra are given in the range azimuth reference system of the InSAR. To make the isolines and grey values of the buoy spectrum and the symmetric bunched

DEM spectra comparable, the left plot (A) shows the ocean wave spectrum divided by two. One can see that for the 1200 m case, (B), the wave system visible in the bunched DEM spectrum is slightly rotated anti-clockwise. The energy levels and the shape of the wave system is in good agreement with the buoy spectrum. For the 3000 m flight level the impact of the bunching mechanism is stronger. The wave system visible in the bunched DEM is exactly in the range direction, which is about 30° anti-clockwise with respect to the buoy spectrum. This observation can be explained by a higher slant range to platform velocity ratio of about 40 seconds at 3000 m height compared to about 15 seconds at 1200 m height. Note, that peak rotations of more than 30° (depending on the local wind field) were also detected in spectra of X-band SAR intensity images acquired during the SIR-C/X-SAR mission (Melsheimer *et al.*, 1998).

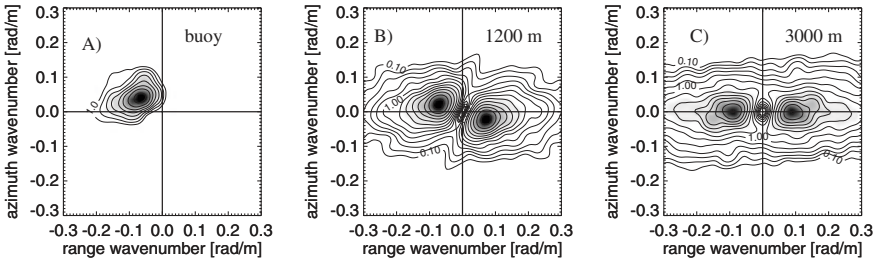

Figure 9.11: (A) Buoy spectrum (divided by two) in the range-azimuth reference system of track 1200m-07. (B) Bunched DEM spectrum of track 1200m-07. (C) Bunched DEM spectrum of track 3000m-07.

For a closer comparison of buoy spectra and bunched DEM spectra with respect to spectral energy and dominant wavelength and direction, Fig. 9.12 shows the respective angular distribution and wavenumber distribution of spectral energies for track 1200m-06 and 1200m-07. Angle is given clockwise from north. To allow comparison with bunched DEM spectra, the spectral energies of the buoy spectrum were divided by two in the angular distribution. At track 1200m-06, the ocean wave is near azimuth travelling, whereas it is propagating in the near range direction at track 1200m-07. One can see that the angular distribution of the bunched DEM acquired at track 1200m-07 (A) is shifted by about 20° towards the range axis (65°) with respect to the buoy spectrum, whereas the respective wavenumber spectra are in very good agreement (B). The bunched DEM spectrum acquired at track 1200m-06 shows smaller spectral energy levels than the buoy. The angular

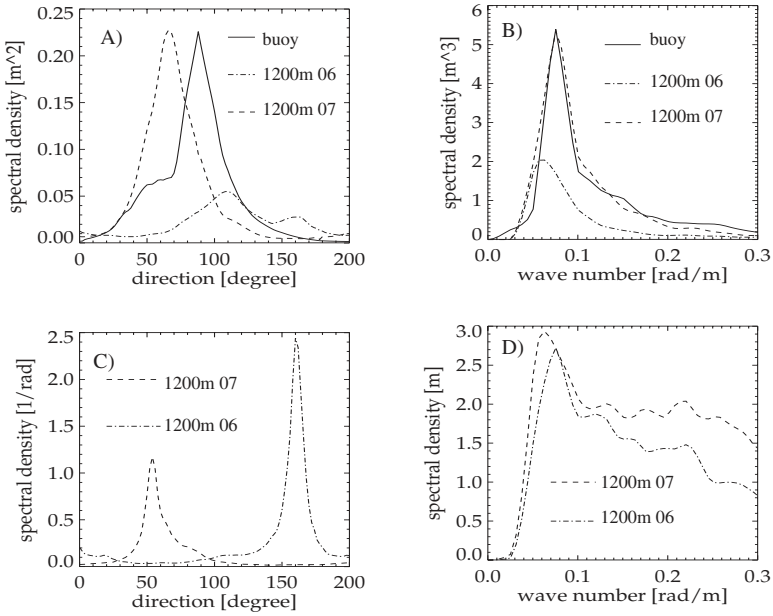

Figure 9.12: (A): Angular distribution of spectral energy of buoy spectrum (solid line) and bunched DEM spectra (dashed–dotted line) derived from tracks 1200m-06 and 1200m-07 (dashed line). Angles are clockwise from north. Spectral density of the buoy is divided by two to account for symmetry of bunched DEM spectra. (B) Corresponding 1D wave number spectra. (C) Angular distribution of spectral energy of SAR intensity images derived from tracks 1200m-06 and 1200m-07. (D) Corresponding 1D wave number spectra of SAR intensity images.

distribution shows a local maximum at 110°, which is 20° clockwise with respect to the maximum of the buoy spectrum. Another local maximum can be found in the exact range direction (162°). The wavenumber spectrum (B) shows a peak wavelength of about 100 m, which is about 20 m longer than the peak wavelength measured by the buoy.

Figure 9.12 (C) and (D) show the same as Fig. 9.12 (A) and (B) for the respective SAR intensity image spectra. As one can see for both tracks the angular distributions are dominated by the high spectral energies, which are found in the range direction. The wavenumber distributions show peak wavelength of 90 m for track 1200m-06 and 80 m for track 1200m-07.

9.3.2 TAIWAN Experiment

In the framework of the EUROROSE project, sponsored by the European Union, sea surface parameters were derived at the north coast of Spain in November 2000 by simultaneous satellite, airborne, and in situ radar measurements (Günther *et al.*, 2000). The objective of the project was to provide a guidance system for ships entering the harbor of Gijon, by monitoring and forecasting wind, ocean wave, and current fields. Making use of the unique coverage with ground based sensors and in situ measurements, the area was used as a test site for a new three antenna InSAR system, which provides simultaneous information on sea surface elevation and orbital velocity (Lehner *et al.*, 2003).

In the **T**hree **a**ntenna **i**nterferometric **wa**ve measureme**n**t (TAIWAN) experiment the airborne three antenna InSAR system AeS-1 developed by Aero-Sensing Radarsysteme GmbH was used. Two antennas are placed along the aeroplane flight direction and one antenna is placed across the flight direction (see Fig. 9.14). The system is thus a combination of along-track and across-track InSAR used for oceanic applications for the first time.

The radar was operated in the following modes simultaneously:

(1) one antenna in the along-track direction transmitted radar pulses and three antennas received the signals;

(2) two antennas in the along-track direction transmitted radar pulses and three antennas received the signals.

Experimental Setup

The TAIWAN experiment took place in the Golf of Biscay on November 11, 2000 as part of the EUROROSE project. Ocean wave and current measurements were carried out by different sensors near the coast between the harbor of Gijon and Cabo de Peñas. Gijon has one of the main harbors at the northern coast of Spain. The city shore and its harbor are affected by the typical sea states and metereological conditions, which are present in the Bay of Biscay, e.g. with long swell coming from the north–west due to storms in the North Atlantic and local wind sea storms coming from north to east.

A map with the experiment location is shown in Fig. 9.13. Two WaMoS stations and HF radar arrays (see Chapter 5 in Part 1 for details on the

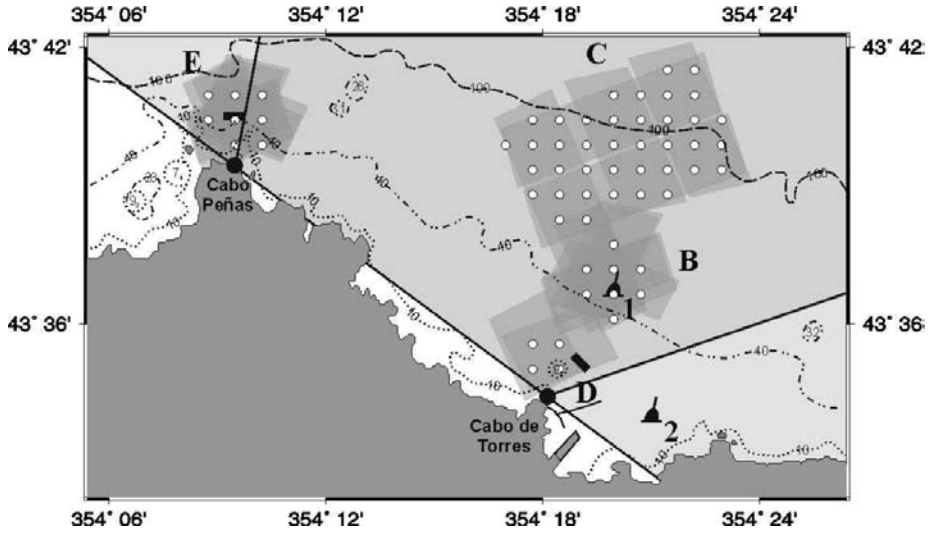

Figure 9.13: Map of the experiment area at the coast of Gijon with tracks acquired by the InSAR system and collocated HF radar measurements indicated by dots. The city of Gijon is located just south-east of Cabo de Torres.

instruments) were located at Cabo de Peñas 43°34.35'N 5°42.05'W and Cabo de Torres 43°39.5' 5°52.2'W about 15 km apart. The water depths in the area increases gradually moving away from the coast with 10 m depth about 1 km from the coast to 50 m about 5 km offshore.

The HF radar covers the area between the two stations with a range of about 20 km. The WaMoS radars used in the Gijon experiment had a range of about 1.5 km. The InSAR acquisition were carried out within the area covered by the HF radar with maximum distance to the coast of about 15 km. The location of the InSAR tracks and the collocated HF radar measurements (indicated by dots) are shown in Fig. 9.13.

The flight pattern of the InSAR has tracks in four equally spaced directions. The orientation of the the pattern was fixed one hour before take off based on wave measurements taken by the WaMoS system located at Cabo de Penas. The orientation was chosen such that the flight pattern contains tracks with the dominant wave system propagating in the approximate across flight direction (range) and along track direction (azimuth) respectively. The WaMoS spectrum taken at Cabo de Penas showed a dominant swell system of about 160 m wavelength with significant waveheight of about 2.5 m coming from the north–east.

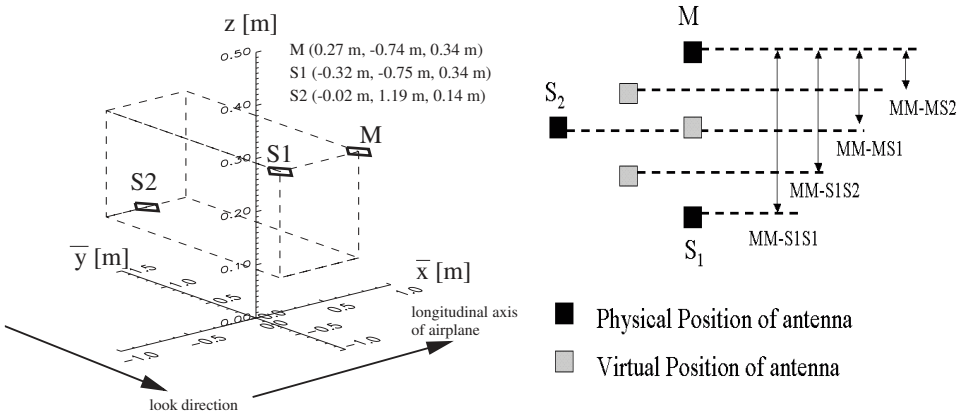

Figure 9.14: Imaging geometry of the three antenna InSAR system used in the TAIWAN experiment (left figure). Top view of the three InSAR antennas with added virtual antennas (grey) representing the different monostatic and bistatic modes of the system (right figure).

InSAR acquisitions took place between 8:30 and 14:00 UTC starting at 3000 m flight level. Due to strong gustiness, data takes had to be interrupted after descending to 1500 m flight level at 11:50. Acquisition was continued at the lower flight level at 14:47 UTC.

Wind measurements were taken near Cabo de Torres. Wind speed was varying between 5 and 10 m/s coming from the south–west at that location. Peak periods and significant waveheights as measured by the two buoys are shown in Fig. 9.15.

First Results of the TAIWAN Experiment

The raw data acquired by the three antenna system were processed to 5 interferograms corresponding to different antenna combinations and bistatic and monostatic modes respectively. Figure 9.16 (E) shows e.g. a 500 m $\times$ 500 m subimage of the interferogram phase measured by the antenna combination master-slave 2 in bistatic mode. The corresponding amplitude image is given in Fig. 9.16 (B). As can be seen in Fig. 9.14 the respective baseline has both along and across track components. The InSAR phase therefore

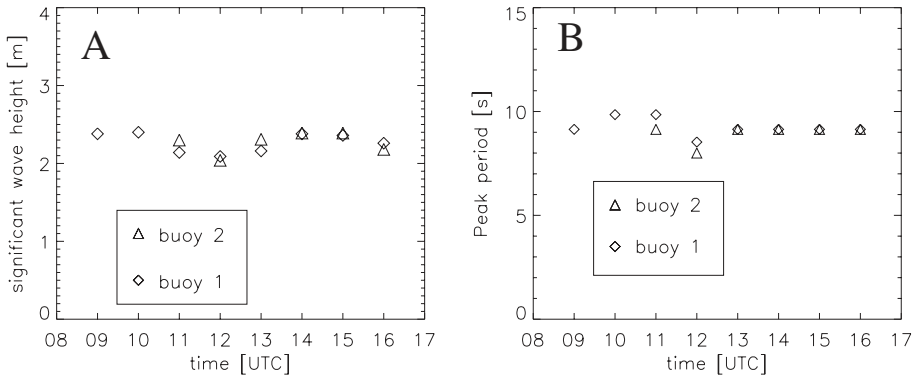

Figure 9.15: Time series of significant waveheight (A) and peak period (B) measured by buoy 1 and buoy 2 deployed at 43°34'N, 5°39'W and 43°36.7'N, 5°40'W respectively on November 9, 2000. The respective water depth are 23 m for buoy 1 and 43 m for buoy 2.

contains information on orbital velocity as well as sea surface elevation. A cut through the InSAR phase in wave propagation direction is shown in Fig. 9.16 (A) (dashed dotted line). A wave system of about 200 m wavelength can be clearly seen.

In order to separate along and across track contributions to the InSAR phase, different interferograms were used in combination. Figs. 9.16 (C) (D) show the resulting elevation and orbital velocity fields. The respective cuts are plotted in Fig. 9.16 (A). The significant waveheight of 2.3 m derived from the measured elevation field is in good agreement with the corresponding WaMoS and buoy measurements of around 2.5 m. The measured orbital velocities of $\pm$ 0.5 m/s are consistent with the velocities expected in the framework of linear wave theory.

Figure 9.17 shows a more detailed comparison of the two dimensional wave spectrum measured by the WaMoS system and the collocated spectrum derived solely from the along track interferogram acquired by the master and the first slave antenna (compare Fig. 9.14). Again it can be seen that wave propagation direction, wavelength and waveheight are in good agreement. The InSAR spectrum seems to be slightly bunched in the platform flight direction compared to the WaMoS spectrum, due to Doppler shifts of the returned radar signal caused by wave motion (velocity bunching). At least to some extent these distortions could be corrected using inversion methods.

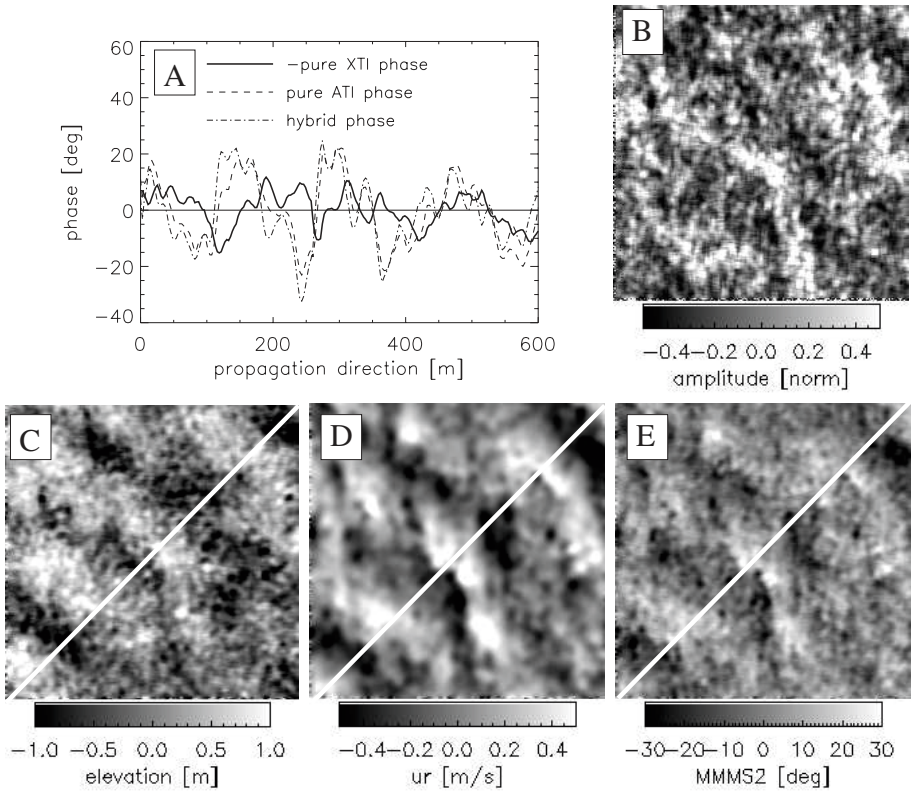

Figure 9.16: Interferometric data acquired by the AeS-1 system during the Gijon experiment at track bb02-05.

9.3.3 SRTM Measurements of Ocean Waves

The capability of spaceborne InSAR systems to image ocean waves has been demonstrated using data acquired during the SRTM (Shuttle radar topography mission) in February 2000. During the SRTM mission, which took place between February 11 and February 22, 2000, interferometric data were acquired on a global scale using the first spaceborne single-pass SAR interferometer. The SRTM system flown on the space shuttle had a bistatic InSAR system with the receiving antenna mounted on a 70 m long mast and the transmitting antenna installed in the cargo bay. The system acquired data in both X and C band, however only C-band data were available for our study. The imaging attitude of the system in space is shown in Fig. 9.18 (B). The main goal of the mission was the derivation of a global digital

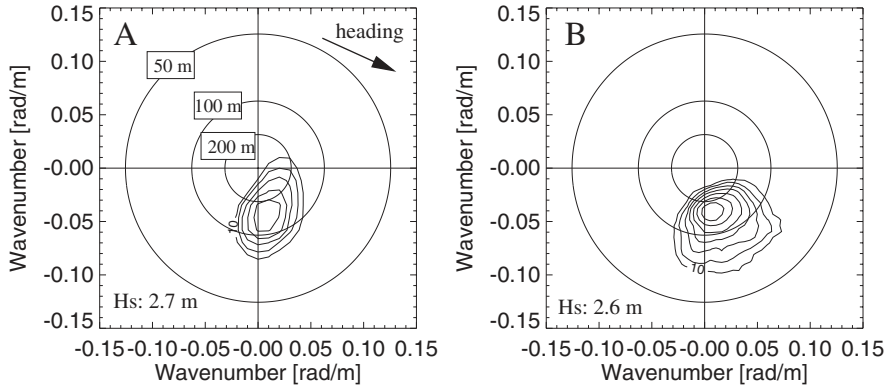

Figure 9.17: Comparison of two dimensional spectra derived from InSAR along track data (left) and WaMoS system (right).

elevation model (DEM) of high precision (about 5 m relative accuracy) over land.

Although the mission was originally devoted to pure land application the system had an additional along track baseline component of about 7 m due to technical reasons. As it turned out this along track baseline allows estimation of orbital velocities associated with ocean surface gravity waves and currents. Figure 9.18 (A) shows the expected interferometric SRTM phase (C-band) as a function of orbital velocity in slant range u_r and sea surface elevation η. It can be observed that a typical orbital velocity of about 1 m/s corresponds to a phase shift caused by an elevation of about 1 m for this InSAR configuration.

Figure 9.19 (A) shows a phase image of 3 by 3 km size which was acquired near the Californian coast (120°W31°N) on Feb 17 at 17:55 UTC. The image is orientated with flight direction (35.6°) upwards. A swell system of about 300 m wavelength can be seen propagating in the range direction. A more detailed analysis presented in Bao *et al.* (2001) showed that the wave patterns are in fact associated with a swell wave. It turned out that interferometric phase is dominated by the along track component of the baseline, see Fig. 9.18, which means that the phase modulations are mainly due to variations in the orbital velocity associated with the swell system.

The SRTM data represent the first demonstration of the ocean wave imaging capability of spaceborne InSAR systems. Taking into account that the

system was by no means optimised for this kind of application, the results obtained are very promising in particular for spaceborne along track interferometry.

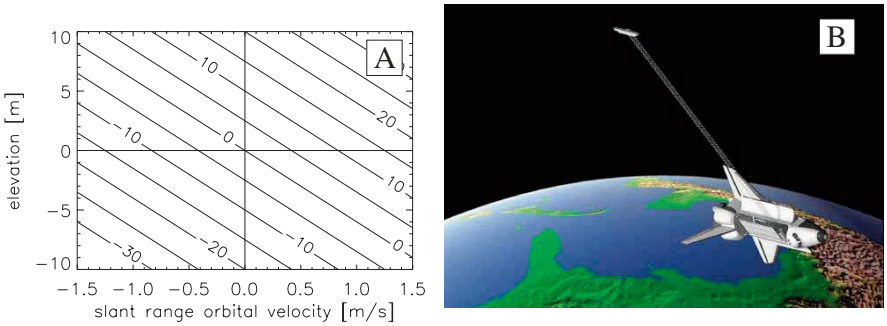

Figure 9.18: (A) SRTM interferometric phase in degrees as a function of sea surface elevation η and orbital velocity in slant range u_r. (B) Artist's view of the Space shuttle with mounted interferometric system during the SRTM mission.

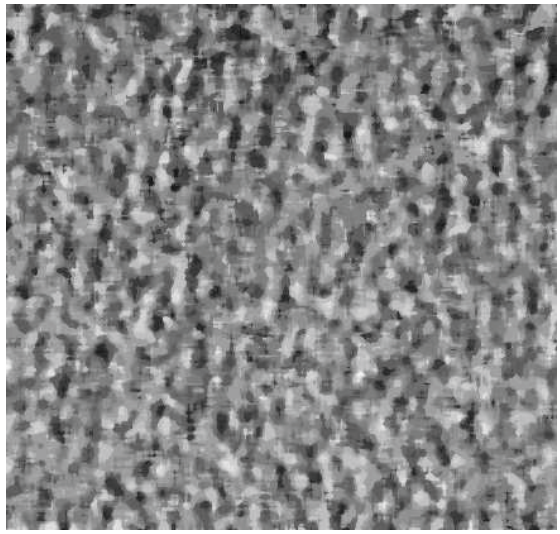

Figure 9.19: (A) SRTM phase image of 3 by 3 km size acquired near the California Coast (120°W31°N) on Feb 17 at 17:55 UTC.

9.3.4 Conclusion

In conclusion one can say that across track InSAR data provide additional information compared to conventional SAR data. In particular the wave measurements are less sensitive with respect to the real aperture radar modulation mechanism (RAR), which contains uncertain components like the hydrodynamic modulation mechanism.

An interesting feature of the system is also its capability to provide simultaneous information on radar cross section and sea surface elevation. This information can, for example, be used to analyse the phase shift between the cross section modulation pattern and the corresponding surface wave. Knowledge about this relationship is also of general importance for SAR wave measurements from spaceborne systems like ENVISAT.

9.4 References

Bao, M., S. Lehner, J. Schulz-Stellenfleth, and M. Eineder, First results on ocean wave imaging from the Shuttle Radar Topography Mission (SRTM), *Proceedings of the IGARSS2001 Conference*, Sydney, 2001.

Engen, G., and H. Johnson, SAR-ocean wave inversion using image cross spectra, *IEEE Trans. Geosci. Rem. Sens.*, 33, 1047–1056, 1995.

Gerling, T. W., Partitioning sequences and arrays of directional ocean wave spectra into component wave systems, *J. Atmos. and Oceanic Technology*, 9, 444–458, 1992.

Günther H., K.-W. Gurgel, G. Evensen, J. Guddal, J.-C. Nieto Borge, and L. R. Wyatt, European radar ocean sensing. *Proceedings of EurOCEAN 2000, Hamburg, 2000*, 443–448, 2000.

Hasselmann, S., C. Brüning, K. Hasselmann and P. Heimbach, An improved algorithm for the retrieval of ocean wave spectra from synthetic aperture radar image spectra, *J. Geophys. Res.*, 101, 16615–16629, 1996.

Heimbach, P., S. Hasselmann, and K. Hasselmann, Statistical analysis and intercomparison with WAM model data of three years of global $ERS-1SAR$ wave mode spectral retrievals, *J. Geophys. Res.*, 103, 7931–7977, 1998.

Hoja, D., J. Schulz-Stellenfleth, S. Lehner, and T. Koenig, Global Analysis of Ocean Wave Systems from SAR Wave Mode Data, *Proc. Int. Geosci. Remote Sens. Symp.*, Toronto, Canada, 2002.

Horstmann, J., and S. Lehner, Wind Retrieval using spaceborne synthetic aperture radar, *Proceedings of the 4th Berlin Workshop on Ocean Remote Sensing*, 2001.

Horstmann, J., H. Schilles, J. Schulz-Stellenfleth, S. Lehner, Global wind speed retrieval from SAR wave mode data, *IEEE, TGARS*, in print, 2003.

Kerbaol, V., B. Chapron, and P. W. Vachon, Analysis of ERS-1/2 synthetic aperture radar wave mode imagettes, *J. Geophys. Res.*, 103, 7833–7846, 1998.

Krogstad, H., O. Samset, and P. W. Vachon, Generalizations of the nonlinear ocean-SAR transformation and a simplified SAR inversion algorithm, *Atmos. Ocean*, 32, 61-82, 1994.

Lehner, S., J. Schulz-Stellenfleth, B. Schättler, H. Breit and J. Horstmann, Wind and wave measurements using complex ERS-2 SAR wave mode data, *IEEE, TGARS*, 38, 2246–2257, 2000.

Lehner, S., *et al.*, Ocean wave and current measurements with a three antenna interferometric synthetic aperture radar, the Gijon experiment, submitted to *IEEE, TGARS*, 2003.

Mastenbroek, C., and C. F. de Valk, A semi-parametric algorithm to retrieve ocean wave spectra from synthetic aperture radar, *J. Geophys. Res.*, 105, 3497–3516, 2000.

Melsheimer, C., W. Alpers, and M. Gade, Investigation of multifrequency/ multipolarization radar signatures of rain cells over the ocean using $SIR-C/X-SAR$ data, *J. Geophys. Res.*, 103, 18,851–18,866, 1998.

Schulz-Stellenfleth, J. and J. Horstmann, S. Lehner, and W. Rosenthal, Sea surface imaging with an across track interferometric synthetic aperture radar ($InSAR$) - The SINEWAVE experiment, *IEEE Transactions on Geoscience and Remote Sensing*, 9, 39, 2017–2028, 2001a.

Schulz-Stellenfleth, J., S. Lehner, and D. Hoja, Retrieval of ocean wave spectra from complex synthetic aperture radar data, *Proceedings of the 4th Berlin Workshop on Ocean Remote Sensing*, 2001b.

Schulz-Stellenfleth, J. and S. Lehner, A parametric scheme for ocean wave retrieval from complex synthetic aperture radar data, submitted to *J. Geophys. Res.*, 2003.

Chapter 10

Partitioning of Wave Spectra

Jean-Michel Lefèvre[a], *Céline Quentin*[b], *Danièle Hauser*[b] *and Jean-Raymond Bidlot*[c]

[a] Météo-France, Toulouse, France
[b] Centre d'Etude des Environnements Terrestres et Planétaires (CETP), Vélizy, France
[c] European Centre for Medium Range Weather Forecast (ECMWF), Reading, UK

10.1 Introduction

The two-dimensional wave energy spectrum is commonly used to describe how the mean sea surface elevation variance due to wind waves is distributed as a function of frequency and propagation direction. The number of frequencies times the number of directions used to describe a wave spectrum is typically more than a few hundred, therefore the common practice when comparing sea states is to reduce the spectral information to a few parameters obtained by integration over the spectrum. The most widely used parameters are the significant waveheight and the mean wave period. However, in order to analyse in more details the spectral properties of the waves, Gerling (1992) introduced the concept of spectral partitioning. The method allows for the computation of the significant waveheight, the mean period and the mean direction of a small number of distinct segments of the two-directional wave spectrum. Since then, several changes have been proposed and several methods are now available. The main differences between them arise from the extraction of the wind sea system. It depends whether the

wind vector is known beforehand or not. We describe here the main methods and illustrate the interest of wave partitioning by presenting comparisons between prediction model results and in situ observations obtained during the FETCH experiment (Hauser *et al.*, 2003).

10.2 Schemes

10.2.1 Gerling (1992)

The scheme proposed by Gerling (from here on referred to as G92) is based only on the geometrical properties of the spectrum. The algorithm for the partitioning of the wave spectrum among the various wave trains can be summarised as follows. It first investigates whether the support of the spectrum which is defined as the domain in the frequency and direction space where there is some energy, is connected. If so, then a certain level is searched such that the support of the spectrum crossing this level is not connected. If such a level does not exist the spectrum has only one mode. Otherwise, if such a level exists, the lowest value is investigated and two wave trains are defined. Then, the procedure just described is iterated for each of them.

Because only the geometrical properties of the spectrum are taken into account, the number of wave trains may depend strongly on the measurement sampling variability or on the numerical schemes for wave model data. The geophysical properties of the sea state are not taken into account, as for example by building a new wind sea associated with a wind rotation. In such a case, G92 may define a single wave train with large angular width.

To overcome these difficulties, Guillaume (1994) and then Hasselmann *et al.* (1996) add constraints on the geophysical properties of the sea-state to the schemes based on geometrical properties. These schemes are respectively referred to as G94 and H96.

10.2.2 Guillaume (1994)

In Guillaume (1994, from here on referred to as G94), the extraction of individual wave trains starts from the peak of the 2D-spectrum. The surrounding bins underneath that peak are investigated in order to select a region for the first wave train. A maximum angular width of investigation from the selected peak is introduced in order to allow for the definition of

a secondary wave train due, for example to the building of a new wind sea. This procedure is then iterated.

For each wave train, the energy, the mean period and the mean direction are computed. The wave trains are ordered according to their mean period, from the lowest values to the highest value. Then, trains are merged together into larger partitions if they are too close to each other. Finally, wave trains are ordered according to their energy from the highest value to the lowest value and partitions with a total energy below a certain value are removed. The threshold parameters are rather arbitrary.

In the final stage of the scheme, the wind sea is chosen amongst the wave trains as the one whose peak frequency f_p fulfils the condition:

$$f_p > f_{PM} \tag{10.1}$$

where f_{PM} is the peak frequency of the Pierson-Moskowitz (PM, 1964) fully-developed wind sea which is function of the wind speed U at a height of 10 m:

$$f_{PM} = 1.3/U \tag{10.2}$$

Amongst these wave trains, the nearest to the wind direction within an imposed limit is chosen. The other wave trains are named swell.

10.2.3 Hasselmann (1996)

Hasselmann *et al.* (1996, referred to as H96) proposed a more efficient method for the partitioning of the wave spectrum, also based on its geometry. A partition is defined as a region where all points, following the path of steepest ascent in the energy density starting from any of these points, lead to the same local maximum of the energy spectrum.

As in G94, partitions are merged together into larger partitions if they satisfy the following conditions that are slightly different from G94. If they are too close to each other, or if the contrast between two peaks is too low, or if the total energy of a partition is below a chosen threshold value, the partitions are merged. Here again, the thresholds are rather arbitrary and Voorrips *et al.* (1997) have chosen slightly different ones from H96.

The wind sea is then chosen as the wave train amongst the remaining wave trains which fulfills:

$$1.3U/C_p cos(\theta - \varphi) > 1 \tag{10.3}$$

where C_p is the phase speed at the peak frequency as derived from the linear theory of waves, U is the wind speed, φ is the wind direction, and θ the wave propagation direction.

The extraction of individual wave trains starts from the peak of the 2D-spectrum.

More recently, other approaches have been chosen in order to extract the wind sea from the spectrum. The first one referred to as G94_2G is an adaptation of G94 for the wave prediction model VAG, which is a second-generation model developed and operated by Météo-France (Fradon *et al.* 2000). The second one is implemented in the WAM model (which is a third-generation model) operated at ECMWF, and is referred to as B01_3G (Bidlot, 2001).

10.2.4 Guillaume Modified

In a second generation wave model, the wind sea part of the spectrum is built following an iterative procedure after wind input and dissipation. The idea is to select spectral components which are of direction less than 90 degrees either side of the local wind direction, and of frequency higher than a minimum frequency f_{min} dependant on the projection of the wind speed in the wave propagation direction:

$$f_{min} = 0.8 * 1.3/(U cos(\theta - \varphi)) \tag{10.4}$$

This relation is based on the limit in peak frequency for a fully-developed wind sea, as given by Pierson-Moskowitz (Eqn. 10.2).

The $cos(\theta - \varphi)$ factor takes into account the projection of the wind in the direction of each wave. The 0.8 coefficient is there to include the forward face of the spectrum.

Then the total wind sea energy (E_{WST}) corresponding to the frequencies larger than f_{min} is computed to determine a new minimum frequency using a relation between the total energy of a PM spectrum and its peak value :

$$f_p = 0.032(E_{WST})^{-1/4} g^{1/2} \tag{10.5}$$

This leads to a second approximation of the total wind sea energy (E_{PMT}) by integration of the spectrum over the selected frequency bins. Then, using an equation derived from the JONSWAP experiment (Guillaume, 1990), the final value of the minimum frequency is inferred:

$$f_{min} = F_{PM}(E_{WST}/E_{PMT})^{-3/10} \tag{10.6}$$

Finally, the wind sea part of the spectrum is reshaped following a JONSWAP spectrum and a $\cos^n$ type angular distribution. This method, modified from Guillaume (1994) by Lefèvre, and referred to as G94_2G, is used to produce wave train parameters operationally from the VAG model at Météo-France.

10.2.5 Bidlot (2001)

In a third generation wave model, there is no need to reshape the wind sea part of the spectrum and the wind sea region can be defined as the segment where the wind input source term is positive. The components of the wind sea are those which are still under the influence of the local wind forcing.

In the WAM model operated at ECMWF, spectral components are considered to be subject to forcing by the wind when :

$$1.2(U/c)cos(\theta - \varphi) > 1 \tag{10.7}$$

where $c = c(f)$ is the phase speed and φ is the wind direction. The rest of the spectral components are referred to as swell.

Note that Eqn. 10.7 is equivalent to:

$$f > 1.3/(Ucos(\theta - \varphi)) \tag{10.8}$$

The difference with Eqn. 10.4 comes from the factor 0.8 which has been introduced by Guillaume to include the forward face of the spectrum.

The advantage of this method, further referred to as B01_3G, lies in its very low computer time cost, in comparison with the others. However, the partitioning is limited to two wave trains, the wind sea and the swell. The swell is a combination of all individual swell trains.

10.2.6 Quentin (2002)

In order to compare spectra from different models or measurements, a common partition scheme has to be chosen. Since the wind speed is not always available with wave measurements, the method should not use the wind speed information in the partitioning procedure.

In the framework of the FETCH experiment (Hauser *et al.*, 2003), the partitioning method used (referred as to Q02) to compare spectra from WAM, VAG, remote sensing observations and buoy data is based on a method very close to G94. The determination of the wind sea train is based on a criteria proposed by Donelan *et al.* (1985). A wave train is identified as wind sea if it satisfies the following criterion:

$$1.2(U/C_p)cos(\theta_m - \varphi) > 1 \tag{10.9}$$

C_p is calculated with the mean period instead of with the peak frequency, in order to smooth the effect of the discretisation. θ_m is the mean direction of the wave train. The other wave trains are classified as swell.

Note that Eqn. 10.9 is equivalent to:

$$f_p > 1.3/(Ucos(\theta_m - \varphi)) \tag{10.10}$$

In summary, partitioning methods can be classified into two main categories. In the first category, the separation between wind sea and swell is done in a first step. Then, the partitioning is applied to the swell spectra. B01_3G, G94_2G belong to this category. That means that the wind vector is needed when doing the partitioning. In the second category, the partitioning procedure is applied to the whole spectrum and then, the wind sea may be chosen amongst the wave trains. Q02, G94 and H96 belong to this second category. The wind vector is not required for the partitioning, so methods of the second category are very useful when no wind measurements are available. However, for these schemes a main drawback happens when the wind is slightly decreasing but with the same direction after having generated an almost fully developed wind sea. Since the peak (or mean) frequency of the main wave train does not change much, it does not satisfy the condition given by Eqn. 10.7 anymore. The old wind sea wave train is therefore considered as swell and the new wind sea is set to zero since its energy is merged in the main wave train.

However, all methods should give similar results in most of the cases and in particular when the wind sea is not fully developed.

10.3 Some Results Using the Wave Train Partitioning

10.3.1 Wave Train Decomposition of One Example Spectrum

As an example we present here results of the wave train decomposition for a spectrum obtained from a directional wave rider (Datawell) operated during the FETCH experiment by the Finnish Institute of Marine Research and for a spectrum provided by the VAG model at the same location and time during the FETCH experiment. These spectra are shown in Fig. 10.1 and the result of the decomposition is presented in Table 10.1. The directional spectrum for the directional waverider (DWR) was estimated by using the Maximum Likelihood Method (MLM) introduced in the context of ocean wave spectra by Davies and Regier (1977). For the spectrum from the wave model, two methods were applied (G94_2G and Q02), while only Q02 was applied for the wave rider data. As discussed above, there are some minor differences between Q02 and G94_2G for the same spectrum. Two wave trains are identified by Q02 (wind sea and swell), whereas a third wave train with very low energy and a very high frequency (0.26 Hz) is given by G94_2G. The comparison with the decomposition from the waverider spectrum indicates that the wind sea from west/south–west is slightly underestimated by the wave model, in agreement with the mean periods and the small differences observed (0.19 Hz for FIMR and 0.22 Hz for VAG/ALADIN). The swell from south/south–west is slightly overestimated by the wave model and the mean frequency of the dominant swell provided by the model (0.15 Hz) is in relatively good agreement with that of the buoy one (0.13 Hz).

10.3.2 Wave Train Evolution

One of the applications of the decomposition method is to follow with time or with distance the evolution of wave trains, and to compare this evolution between different sources of data. Figure 10.2 presents wave trains obtained in a case of fetch-limited off-shore wind during the FETCH experiment (March 24^{th} 1998). Results obtained from the VAG model and from the ASIS buoy

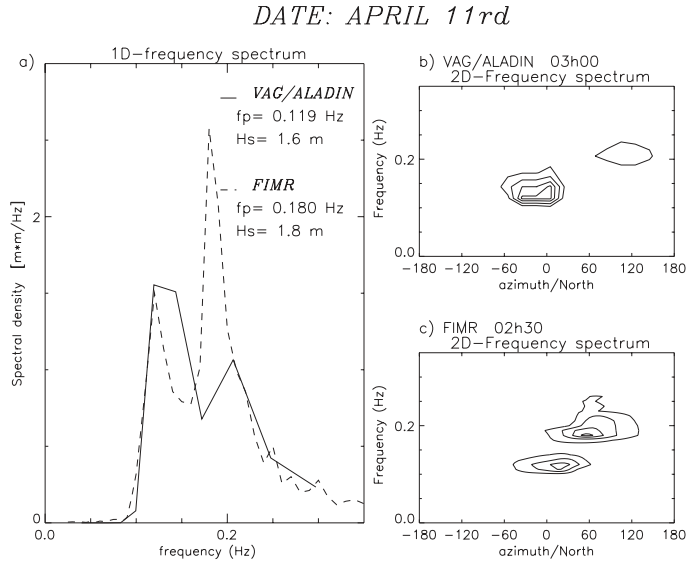

Figure 10.1: 1-D wave spectra at the location of the ASIS buoy on April 11 1998 at 02H30 GMT, as deduced from the ASIS buoy (FIMR) and from the VAG/ALADIN model (left panel), the corresponding 2-D: spectra are represented on right panel.

	Mean Frequency (Hz)	H_{m0} (m)	Wave train direction ($^\circ$/north)	Total H_{m0}	Wind speed (m/s)	Wind direction ($^\circ$/North)
FIMR	0.19	1.18	64.	1.8		
Q02	0.13	0.93	28.			
	0.20	0.47	127.			
VAG/ALADIN	0.22	0.90	107.	1.6	7.75	114.
Q02	0.15	1.26	-11.			
VAG/ALADIN	0.23	0.92	115.	1.6	7.75	114.
G94_2G	0.15	1.26	-3.			
	0.26	0.27	57.			

Table 10.1: Results of the wave train decomposition for the spectra obtained from the FIMR buoy and the VAG model, on April 11 1998 at respectively 02h30 and 03h00 GMT. The first wave train corresponds to the wind sea.

(see Chapter 3 of Part 2) are plotted in Fig. 10.2 (upper panel), together with the wind vector from the numerical weather prediction (NWP) model ALADIN (ALADIN International Team, 1997) and from the in situ measurements of the ASIS buoy (bottom panel). There is a good agreement between the wind direction and wind speed measured by the buoy and predicted by the ALADIN model. The decomposition shows that wavelength and energy of the wind sea predicted by VAG/ALADIN are comparable to the corresponding parameters identified from the in situ observations. Note that there is a non zero angle between the wave model wind sea direction and the atmospheric model wind direction because of the partitioning method used (Q02). This angle is zero when G94_2G is used. The decomposition also shows that a coherent secondary wave train (with waves coming from north–east and wavelength of the order of that of the wind-sea) is identified from the in situ data but not reproduced by the model. This secondary wave train is confirmed by airborne radar observations (see Chapter 8 in Part 2) and is due to the generation of waves farther to the north–east of the domain in a cyclonic non-stationary system.

10.3.3 Model Performance for Wind-Sea and Swell

Another application of the partitioning method is to analyse model behaviour separately for wind sea and swell. In the study presented below, the performance of two wave prediction models forced by wind fields from 3 different atmospheric models is analysed. This study was carried out in the context of the FETCH experiment.

The wave models are i) VAG, which is a second-generation model (Fradon *et al.* 2000) developed at the beginning of the 80's and implemented for operational use at Météo-France in the end of the 80's, ii) WAM, which is a third-generation model developed in the end of the 80's by an international group of modellers (WAMDI Group, 1988) and is operational at the European Centre for Medium-range Weather Forecast since June 1992. The WAM model used for the hindcasts has been modified according to Hersbach and Janssen (1999) in order to improve the performances of the wave model in short fetch situations.

The atmospheric models are the ECMWF/IFS model (Simmons *et al.*, 1989), the ARPEGE/IFS model (Courtier *et al.*, 1991), and the ALADIN model (ALADIN international team 1997). The first two models have a spectral horizontal grid, and the latter has a real grid. The spectral truncation for the ECMWF model is T213, with a Gaussian distribution with latitude, cor-

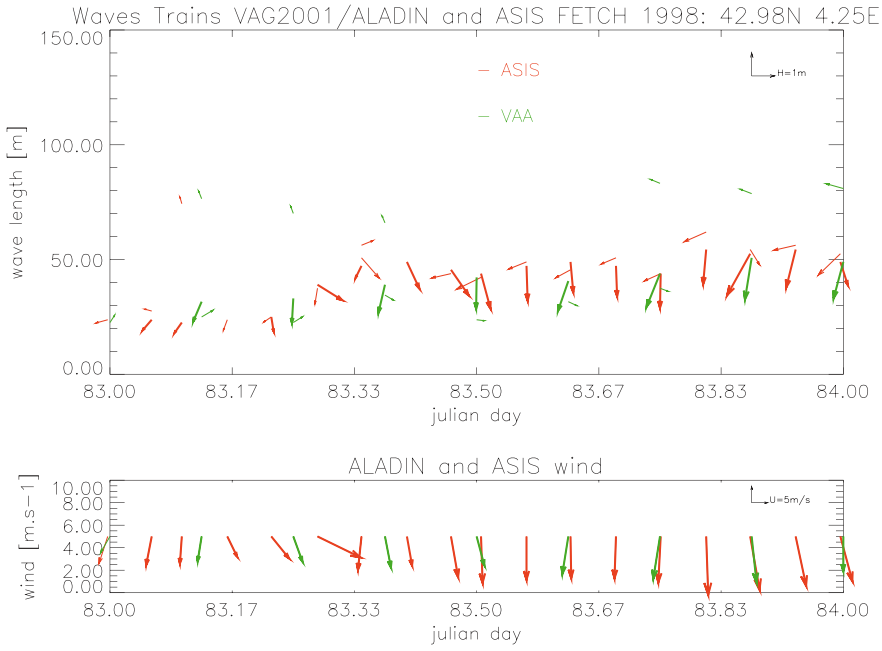

Figure 10.2: Mean direction (arrows direction), wavelength corresponding to the mean period (y axis) and height (proportional to the length of the arrows) of the wind sea and the total swell on March 24^{th} 1998 as a function of time (horizontal axis). Green vectors are for the model. Red vectors are for the ASIS buoy data.

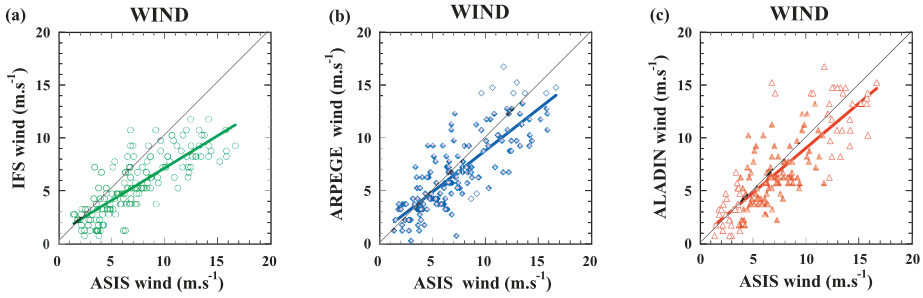

Figure 10.3: Statistical comparison of wind measured on ASIS and predicted by IFS (a), ARPEGE (b), ALADIN (c).

responding to an approximate grid spacing of about 50 km in the FETCH area. ARPEGE is the short-range oriented version of the jointly developed IFS/ARPEGE NWP software package (Courtier *et al.*, 1991). The horizontal resolution is varying with location and is about 20 km in the FETCH area. ALADIN is the extension of the IFS/ARPEGE software to a Limited Area Geometry. The operational ALADIN-France version has a mesh size of 9.5 km.

Before analysing the wave model results, it is necessary to discuss the quality of the forcing winds. Figure 10.3 presents a comparison of the wind speed from the 3 models (U10) with the in situ wind measurements on the ASIS buoy. It is clear that due to the relatively low resolution of IFS, high winds are underestimated by the model. The underestimation is less with ARPEGE, and even less with ALADIN. However, the scatter is similar for the 3 models. The orographic effects are very important in the experiment area and the model resolution is crucial for the quality of the winds.

For the FETCH hindcasts, the model resolution of VAG and WAM is 0.25 ° x 0.25 ° when they are forced by IFS and ARPEGE winds and is 0.1 ° x 0.1 ° when they are driven by ALADIN winds. When analysing the different runs (Fig. 10.4) one observes that in spite of the better accuracy of ALADIN winds (due to the finer resolution), there is not a large difference between the different wave model runs in terms of total significant waveheight.

However, the separation of the energy spectra into windsea and swell provides more details about the performance of these different runs. The significant waveheight H_{m0} from the windsea and from the swell are plotted respectively in Fig. 10.5 and 10.6. For the windsea, there is an improvement for both VAG and WAM (Fig. 10.5) when using the atmospheric model with a higher resolution. The fact that there is hardly any improvement for the swell (Fig. 10.6) when using the ALADIN winds instead of ARPEGE winds, shows that the improvement in the wind speed is probably limited to a relatively small area surrounding the buoy location (i.e. near-shore).

10.4 Conclusions and Perspectives

The partitioning concept is now widely used by many national meteorological services to reduce the complex information delivered by operational numerical wave models. It is also very useful to analyse wave model behaviour and to compare spectra from different sources. Its use should be

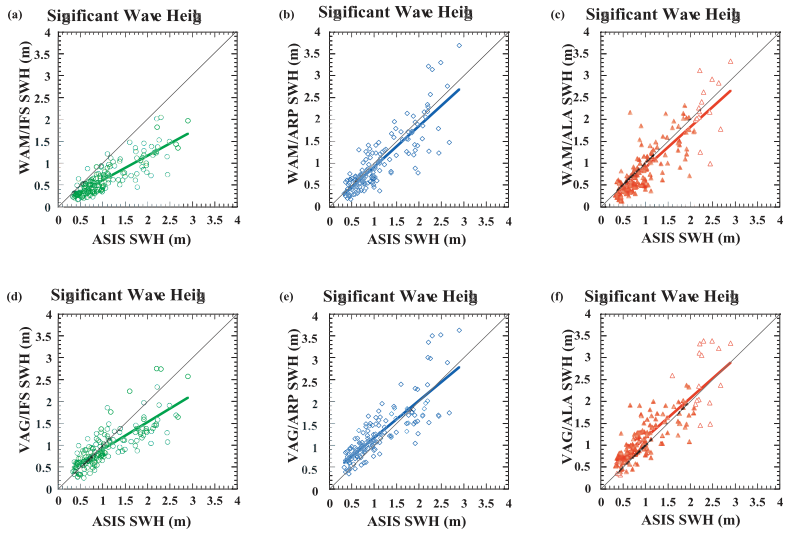

Figure 10.4: Scatter plot of collocated total significant waveheight data from the ASIS buoy and from two Numerical Sea State Prediction models driven by three different NWP's. (a) WAM/IFS model, (b) WAM/ARPEGE model, (c) WAM/ALADIN model (d) VAG/IFS model, (e) VAG/ARPEGE model, (f) VAG/ALADIN model.

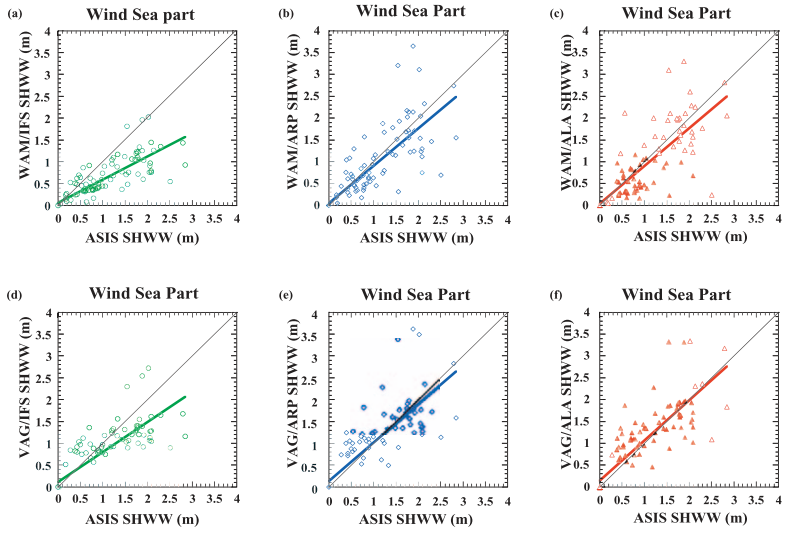

Figure 10.5: Same as Fig. 10.4 but for the Wind sea component only.

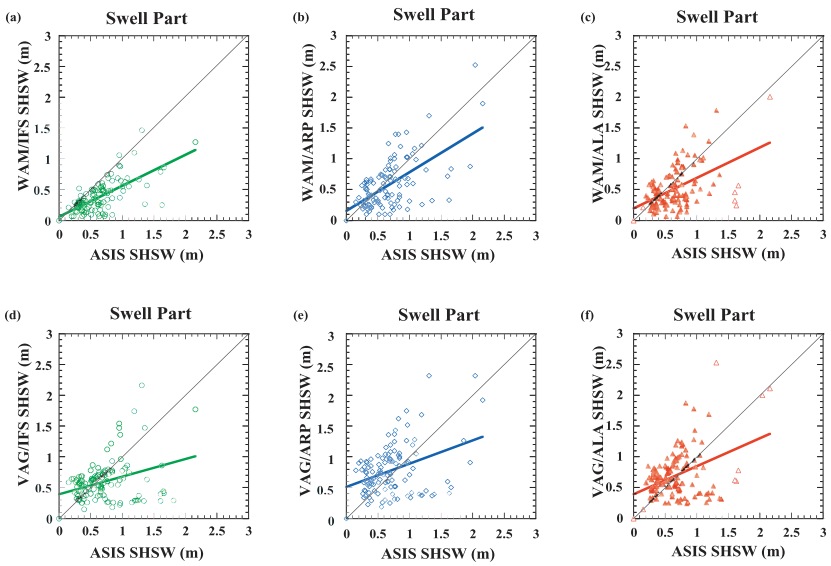

Figure 10.6: Same as Fig. 10.4 but for the Total Swell component only.

also extended to wave spectra observations for operational purposes since SAR observations should be more widely used in the future, as input to assimilation schemes for wave prediction models or for the improvement of the models themselves, in particular in the swell domain of the wave spectra.

10.5 References

ALADIN International Team, The ALADIN project: Mesoscale modelling seen as a basic tool for weather forecasting and atmospheric research, *WMO Bulletin*, 46/4, 317-324, 1997.

Bidlot, J., 2001: ECMWF wave model products, *ECMWF Newsletter*, N0. 91, 2001.

Courtier, P., C. Freydier, J.-F. Geleyn, F. Rabier, and M. Rochas, The ARPEGE project at Météo-France, In ECMWF 1991 *Seminar Proceedings: Numerical methods in atmospheric models*, ECMWF, 9 – 13 September 1991, Vol. II, 193-231, 1991.

Davies, R.E, and L.A. Regier, Methods for estimating directional wave spectra from multi-element arrays, *J. Mar. Res.*, 35, 453-477, 1977.

Donelan, M. A., J. Hamilton, and W. H. Hui, Directional spectra of wind generated waves, *Philos. Trans. R. Soc. London, Ser. A*, 315, 509-562, 1985.

Fradon, B., D. Hauser D., and J.-M. Lefèvre, Comparison study of a second-generation and of a third-generation wave prediction model in the context of the SEMAPHORE experiment, *J. Atmos. Oceanic Technol.*, Vol 17, 2, 197-214, 2000.

Gerling, T.W., Partitioning Sequences and Arrays of Directional Ocean Wave Spectra into Component Wave Systems, *J. Atmos. Oceanic Technol.*, vol. 9, 444-458, 1992.

Guillaume, A., 1990. Statistical tests for the computation of surface gravity wave spectra with application to model validation, *J. Atmos. Ocean. Techn.*, vol. 7, 552-567, 1990.

Guillaume, A., Analyzing directional evolution ocean waves for operational research applications, *International conference on sea-air interaction and on meteorology and oceanography of the coastal zone*, AMS, 1994.

Hasselmann, S., C. Brüning, K. Hasselmann, and P. Heimbach, An improved algorithm for retrieval of ocean wave spectra from synthetic aperture radar image spectra, *J. Geophys. Res.*, 101, 16615-16629, 1996.

Hauser D., H. Branger, S. Bouffies-Cloché, S. Despiau, W. Drennan, H. Dupuis, P. Durand, X. Durrieu de Madron, C. Estournel, L. Eymard, C. Flamant, H. Graber, C. Guérin, K. Kahma, G. Lachaud, J.-M. Lefèvre, J. Pelon, H. Pettersson, B. Piguet, P. Queffeulou, D. Tailliez, J. Tournadre, and A. Weill, The FETCH experiment: an overview, *J. Geophys. Res.* (C3), doi:10.1029/2001J001202, 2003.

Hersbach, H., and P.A.E.M. Janssen, P., Improvements of the short fetch behaviour in the Wave Ocean Model (WAM), *J. Atmos. Oceanic Technol.*, 16, 884-892, 1999.

Pierson, W.J., and L. Moskowitz, A proposed spectral form for fully developped wind sea based on the similarity theory of S.A. Kitaigorodskii, *J. Geophys. Res.*, 69, 5181-5190, 1964.

Quentin, C., *Etude de la surface océanique, de sa signature radar et de ses interactions avec le flux turbulent de quantité de mouvement dans le cadre de l' expérience FETCH*, Thèse de l'Université Paris 6, April 2002. (in french)

Simmons, A. J., D. M. Burridge, M. Jarraud, C. Girard and W. Wergen, The ECMWF medium-range prediction models development of the numerical formulations and the impact of increased resolution, *Meteorol. Atmos.*

Phys., 40, 28-60, 1989.

Voorrips, A.C., V.K. Makin, and S. Hasselmann, Assimilation of wave spectra from pitch- and roll-buoys in a North Sea wave model, *J. of Geophys. Res.*, 102, C3, 5829-5849, 1997.

WAMDI Group, The WAM Model - A third generation ocean wave prediction model, *J. Phys. Oceanogr.*, 18, 1775-1810, 1988.

Affiliations and Addresses of Contributors:

Stephen F. Barstow
Fugro Oceanor, Pir-Senteret, N-7462 Trondheim, Norway.
www.oceanor.com

Jean-Raymond Bidlot
European Centre for Medium Range Weather Forecasts (ECMWF), Shinfield Park, Reading RG2 9AX, United Kingdom.
www.ecmwf.int

Sofia Caires
Sheffield Centre for Earth Observation Science, Department of Applied Mathematics, University of Sheffield, Sheffield S3 7RH, United Kingdom.
www.shef.ac.uk/~sceos/
At present: Meteorological Service of Canada (MSC) and Koninklijk Nederlands Meteorologisch Instituut (KNMI), P.O.Box 201, NL-3730 AE De Bilt, The Netherlands.
www.knmi.nl

Mark A. Donelan
Rosenstiel School of Marine and Atmospheric Science (RSMAS), University of Miami, 4600 Rickenbacker Causeway, Miami, FL 33149-1098, USA.
wwww.rsmas.miami.edu

William M. Drennan
Rosenstiel School of Marine and Atmospheric Science (RSMAS), University of Miami, 4600 Rickenbacker Causeway, Miami, FL 33149-1098, USA.
wwww.rsmas.miami.edu

Hélène Dupuis
Département de Géologie et d'Océanographie, Centre National de la Recherche Scientifique (CNRS), Université Bordeaux 1, Avenue de Facultés, F-33405 Talence Cedex, France.
www.epoc.u-bordeaux1.fr

Hans C. Graber
Rosenstiel School of Marine and Atmospheric Science (RSMAS), University of Miami, 4600 Rickenbacker Causeway, Miami, FL 33149-1098, USA.
wwww.rsmas.miami.edu

J. Jim Green
Sheffield Centre for Earth Observation Science, Department of Applied Mathematics, University of Sheffield, Sheffield S3 7RH, United Kingdom.
www.shef.ac.uk/˜sceos/

Øistein Grønlie
MIROS A/S, P.O.Box 364, N-1372 Asker, Norway.
www.miros.no

Christine Guérin
Centre d'Etude des Environnements Terrestres et Planétaires (CETP), 10-12 Avenue de l'Europe, F-78140 Vélizy, France.
www.cetp.ipsl.fr

Klaus-Werner Gurgel
Institute of Oceanography, University of Hamburg, Bundesstrasse 53, D-20146 Hamburg, Germany.
www.ifm.uni-hamburg.de

Heinz Günther
Institute for Coastal Research, GKSS Research Center, Max Planck Str. 1, D-21502 Geesthacht, Germany.
www.gkss.de

Danièle Hauser
Centre d'Etude des Environnements Terrestres et Planétaires (CETP), 10-12 Avenue de l'Europe, F-78140 Vélizy, France.
www.cetp.ipsl.fr

Kenneth Hayes
Applied Physics Laboratory, University of Washington, 1013 NE 40th St., Seattle WA 98105-6698, USA.
www.apl.washington.edu

Katrin Hessner
OceanWaveS GmbH, Munstermannskamp 1, D-21335 Lüneburg, Germany.
www.oceanwaves.de

Danielle Hoja
German Aerospace Center (DLR), Institute of Remote Sensing Technology, Oberpfaffenhofen, Postfach 1116, D-82234 Weßling, Germany.
www.dlr.de

Delphine Icard
Rosenstiel School of Marine and Atmospheric Science (RSMAS), University of Miami, 4600 Rickenbacker Causeway, Miami, FL 33149-1098, USA (in 2002).
wwww.rsmas.miami.edu

Kimmo K. Kahma
Finnish Institute of Marine Research (FIMR), P.O.Box 33, FIN-00931 Helsinki, Finland.
www.fimr.fi

William C. Keller
Applied Physics Laboratory, University of Washington, 1013 NE 40th St., Seattle WA 98105-6698, USA.
www.apl.washington.edu

Harald E. Krogstad
Department of Mathematical Sciences, Norwegian University of Science and Technology (NTNU), N-7491 Trondheim, Norway.
www.math.ntnu.no

Jean-Michel Lefèvre
Météo-France, Direction de la Prévision, Division Marine et Océanographie, 42 Avenue G. Coriolis, F-31057 Toulouse Cedex 1, France.
www.meteo.fr

Susanne Lehner
German Aerospace Center (DLR), Institute of Remote Sensing Technology, Oberpfaffenhofen, Postfach 1116, D-82234 Weßling, Germany.
www.dlr.de
At present: Rosenstiel School of Marine and Atmospheric Science (RSMAS), University of Miami, 4600 Rickenbacker Causeway, Miami, FL 33149-1098, USA.
wwww.rsmas.miami.edu

Anne Karin Magnusson
Norwegian Meteorological Institute (DNMI), Division Western Norway, Allégaten 70, N-5007 Bergen, Norway.
www.met.no

Jaak Monbaliu
Katholieke Universiteit Leuven, Hydraulics Laboratory, Kasteelpark Arenberg 40, B-3001, Heverlee, Belgium.
www.kuleuven.ac.be

José Carlos Nieto Borge
German Aerospace Center (DLR), Institute of Remote Sensing Technology, Oberpfaffenhofen, Postfach 1116, D-82234 Weßling, Germany.
www.dlr.de

Heidi Pettersson
Finnish Institute of Marine Research (FIMR), P.O.Box 33, FIN-00931 Helsinki, Finland.
www.fimr.fi

William J. Plant
Applied Physics Laboratory, University of Washington, 1013 NE 40th St, Seattle WA 98105-6698, USA.
www.apl.washington.edu

Céline Quentin
Centre d'Etude des Environnements Terrestres et Planétaires (CETP), 10-12 Avenue de l'Europe, F-78140 Vélizy, France (until 2002).
www.cetp.ipsl.fr

Konstanze Reichert
OceanWaveS GmbH, Munstermannskamp 1, D-21335 Lüneburg, Germany.
www.oceanwaves.de

Magnar Reistad
Norwegian Meteorological Institute (DNMI), Division Western Norway, Allégaten 70, N-5007 Bergen, Norway.
www.met.no

Wolfgang Rosenthal
Institute for Coastal Research, GKSS Research Center, Max Planck Str. 1, D-21502 Geesthacht, Germany.
www.gkss.de

Øyvind Saetra
European Centre for Medium Range Weather Forecasts (ECMWF), Shinfield Park, Reading RG2 9AX, United Kingdom.
www.ecmwf.int
At present: Norwegian Meteorological Institute (DMNI), P.O. Box 43 Blindern, N-0313 Oslo, Norway.
www.met.no

Johannes Schulz-Stellenfleth
German Aerospace Center (DLR), Institute of Remote Sensing Technology, Oberpfaffenhofen, Postfach 1116, D-82234 Weßling, Germany.
www.dlr.de

Edward J. Walsh
NASA Goddard Space Flight Center, USA, on assigment at NOAA Environmental Technology Laboratory, 325 Broadway, Boulder, CO 80303-3328, USA.
www.noaa.gov

Alain Weill
Centre d'Etude des Environnements Terrestres et Planétaires (CETP), 10-12 Avenue de l'Europe, F-78140 Vélizy, France.
www.cetp.ipsl.fr

Judith Wolf
Proudman Oceanographic Laboratory (POL), Bidston Observatory, Bidston Hill, Prenton CH43 7RA, United Kingdom.
From Dec. 2004: Proudman Oceanographic Laboratory, Joseph Proudman building, 6 Brownlow Street, Liverpool L3 5DA, United Kingdom.
www.pol.ac.uk

C. Wayne Wright
NASA Goddard Space Flight Center, Wallops Flight Facility, Wallops Island, VA 23337, USA.
osb.wff.nasa.gov

Lucy R. Wyatt
Sheffield Centre for Earth Observation Science, Department of Applied Mathematics, University of Sheffield, Sheffield S3 7RH, United Kingdom.
www.shef.ac.uk/~sceos/

List of Acronyms

ADCP	Acoustic Doppler Current Profiler
ALADIN	Name of the limited-area atmospheric circulation model of Meteo-France
ARGOS	Name of the Global Data Telemetry and Geo-positioning Services
ARPEGE	Name of the global circulation atmospheric model of Meteo-France
ASAR	Advanced Synthetic Aperture Radar
ASIS	Air-Sea Interaction Spar buoy
ASTEX	Atlantic Stratocumulus Transition EXperiment
ATALANTE	Name of a French research vessel
BSAR	Name of the SAR processing algorithm at DLR
BSH	Bundesambt für Seeshiffart und Hydrography
CETP	Centre d'étude des Environments Terrestes et Planétaires
CMOD4	Name of the empirical algorithm used to estimate wind speed from radar cross-sections estimated with C-Band radars
CODAR	COastal raDAR (also product name of *CODAR Ocean Sensors*, Los Altos, California, US)
CORAR	COherent Real Aperture Radar
COV	Coefficient of Variation
CW	Continuous Wave
DEM	Digital Elevation Model
DLR	Deutschen Zentrum für Luft- und Raumfahrt (German Space Centre)
DMNI	Norwegian Meteorological Institute
DOF	Degrees Of Freedom, also written d.o.f. (used here for the amount of averaging in the spectral analysis)
Dsp	Directional Spread
DWR	Directional WaveRider (*Waverider* and *Directional*

	Waverider are product names of *Datawell bv*, Haarlem, The Netherlands)
EC	European Community
ECMWF	European Centre for Medium-Range Weather Forecasts
EMH	ElectroMagnetic/Hydrodynamic (model)
ENVISAT	ENVIronment SATellite (Satellite operated by ESA)
ERS	European Remote sensing Satellite (The satellites ERS-1 and ERS-2 are operated by ESA)
ESA	European Space Agency
EU	European Union
EuroROSE	European Radar Ocean SEnsing
FARGIS	FAiRway Geografical Informations System
FETCH	Flux, Etat de la mer et Télédétection en Conditions de fetcH variable
FFT	Fast Fourier Transform
FIMR	Finnish Institute of Marine Research
FLIP	FLoating Instrument Platform
FM	Frequency Modulation
FMI	Finnish Meteorological Institute
FPSO	Floating Production, Storage and Offloading
GASEX	GAS EXperiment
GKSS	Research Centre from the Hermann von Helmholtz Society of German Research
GMT	Greenwich Meridian Time
GPS	Global Positioning System
HF	High Frequency
IAHR-AIRH	International Association for Hydraulic Research
IFS	Integrated Forecast System at ECMWF
IMLM	Iterative Maximum Likelihood Method
INSAR	INterferometric Synthetic Aperture Radar
JONSWAP	JOint North Sea WAve Project
KNMI	Koninklijk Nederlands Meteorologisch Instituut (Royal Netherlands Meteorological Institute)
MAST	Marine Science and Technology Program of the European Community

ME/MEM	Maximum Entropy/Maximum Entropy Method
MERLIN-IV	Name of a research aircraft (from Fairchild) of Meteo-France
MIROS	Microwave Radar Observing System (also the company name of *MIROS AS*, Norway)
ML/MLM	Maximum Likelihood/Maximum Likelihood Method
MRU	Motion Reference Unit (product name of *Kongsberg Seatex*, Norway)
MSL	(or m.s.l.) Mean sea level
MTF	Modulation Transfer Function
MUSIC	MUltiple SIgnal Classification
MWD	Mean Wave Direction
NOAA	National Oceanographic and Atmospheric Administration
NWP	Numerical Weather Prediction
NWRI	National Water Research Institute
OCEANOR	Norwegian environmental monitoring company
ODR	Orthogonal Distance Regression
OSCR	Ocean Surface Current Radar
PARSA	Partition-based inversion algorithm for ocean spectra from SAR
PIANC-AIPCN	International Navigation Association
PISCES	HF wave radar developed by Neptune Radar Ltd., UK
PM	Pierson-Moskowitz spectrum
PMP	POL Measurement Package
POL	Proudman Oceanographic Laboratory
PRA	Pseudo Replication Algorithm
PRF	Pulse Repetition Frequency
RADARSAT	RADAR SATellite (Canadian remote sensing satellite)
RAR	Real Aperture Radar
RESSAC	Radar pour l'étude du Spectre des Surfaces par Analyse Circulaire
RSMAS	Rosenstiel School of Marine and Atmospheric Sciences, University of Miami

SA	Selective Availability
SAR	Synthetic Aperture Radar
SASEMAR	Spanish Safety and Rescue Society
SBPA	Short Baseline Pressure Arrays
SCAT	Scatterometer Instrument
SCAWVEX	Surface Current And Wave Variability EXperiment
SCR	Surface Contour Radar
SEATEX	International marine electronics manufacturer (Now *Kongsberg Seatex*)
SEMAPHORE	Structure des Echanges Mer-Atmosphère, Propriétés des Hétérogénéités Océaniques: Recherche Expérimentale
SHOWEX	SHOaling Waves EXperiment
SINEWAVE	SAR Interferometry Experiment
SINTEF	The Foundation for Scientific and Industrial Research at the Norwegian University of Science and Technology
SNR	Signal-to-Noise Ratio
SOFIA	Surface of the Ocean, Fluxes and Interaction with the Atmosphere
SRA	Scanning Radar Altimeter
SRTM	Shuttle Radar Topography Mission
STORM	Système de Télédétection pour l'Observation par Radar de la Mer
SWAN	Simulating WAves Nearshore (shallow water wave model)
SWIMSAT	Surface Waves Investigation and Monitoring from SATellite
S4DW	Interocean directional wave measurement device
TAIWAN	Three Antenna Interferometric Wave measurement
TOPEX/POSEIDON	Name of the American/French altimeter satellite mission
UK	United Kingdom
UKMO	United Kingdom Meteorological Office
UTC	Universal Time, also known as Greenwich Mean Time
UWA	User Wave Annotated product

VAG	Name of the 2nd generation wave prediction model of Meteo-France
WACSIS	WAve Crest Sensor Intercomparison Study
WADIC	WAve DIrection Calibration project
WAM	WAve Model (spectral wave model used by ECMWF)
WAMOS	WAve MOnitoring System
WAVES	Water-Air Vertical Exchange Studies
WDM	Wavelet Directional Method
WERA	WEllen RAdar
WISE	WInd and Salinity Experiment (also *Waves in Shallow Environments*, a scientific workgroup on shallow water waves)
WMO	World Meteorological Organization

COST Office

COST domain: Meteorology

EUR 21367 — COST Action 714 — Measuring and analysing the directional spectra of ocean waves

Editors: Danièle Hauser, Kimmo Kahma, Harald E. Krogstad, Susanne Lehner, Jaak A. J. Monbaliu, Lucy R. Wyatt

Luxembourg: Office for Official Publications of the European Communities

2005 — XV, 465 pp. — 21 x 29.7 cm

ISBN 92-898-0003-8